Jordan Journal of Mechanical and Industrial Engineering (JJMIE)

JJMIE is a high-quality scientific journal devoted to fields of Mechanical and Industrial Engineering. It is published by The Jordanian Ministry of Higher Education and Scientific Research in corporation with the Hashemite University.

SUBMISSION ADDRESS:

Prof. **Mousa S. Mohsen**, Editor-in-Chief
Jordan Journal of Mechanical & Industrial Engineering,
Hashemite University, PO Box 330127, Zarqa, 13133 , Jordan
E-mail: jjmie@hu.edu.jo

Hashemite Kingdom of Jordan

Hashemite University

Jordan Journal of Mechanical and Industrial Engineering

JJMIE

An International Peer-Reviewed Scientific Journal

Special issue devoted for selected papers presented at the International Conference and Exhibition on Green Energy and Sustainability for Arid Region and Mediterranean Countries; ICEGES , November 10-12, 2009, Amman, Jordan.

http://jjmie.hu.edu.jo/

ISSN 1995-6665

Jordan Journal of Mechanical and Industrial Engineering (JJMIE)

JJMIE is a high-quality scientific journal devoted to fields of Mechanical and Industrial Engineering. It is published by The Jordanian Ministry of Higher Education and Scientific Research in corporation with the Hashemite University.

Introduction: The Editorial Board is very committed to build the Journal as one of the leading international journals in mechanical and industrial engineering sciences in the next few years. With the support of the Ministry of Higher Education and Scientific Research and Jordanian Universities, it is expected that a heavy resource to be channeled into the Journal to establish its international reputation. The Journal's reputation will be enhanced from arrangements with several organizers of international conferences in publishing selected best papers of the conference proceedings.

Aims and Scope: Jordan Journal of Mechanical and Industrial Engineering (JJMIE) is a refereed international journal to be of interest and use to all those concerned with research in various fields of, or closely related to, mechanical and industrial engineering disciplines. Jordan Journal of Mechanical and Industrial Engineering aims to provide a highly readable and valuable addition to the literature which will serve as an indispensable reference tool for years to come. The coverage of the journal includes all new theoretical and experimental findings in the fields of mechanical and industrial engineering or any closely related fields. The journal also encourages the submission of critical review articles covering advances in recent research of such fields as well as technical notes.

Guide for Authors

Manuscript Submission

High-quality submissions to this new journal are welcome now and manuscripts may be either submitted online or mail.

Online: For online submission upload one copy of the full paper including graphics and all figures at the online submission site, accessed via E-mail: jjmie@hu.edu.jo. The manuscript must be written in MS Word Format. All correspondence, including notification of the Editor's decision and requests for revision, takes place by e-mail and via the Author's homepage, removing the need for a hard-copy paper trail.

By Mail: Manuscripts (1 original and 3 copies) accompanied by a covering letter may be sent to the Editor-in-Chief. However, a copy of the original manuscript, including original figures, and the electronic files should be sent to the Editor-in-Chief. Authors should also submit electronic files on disk (one disk for text material and a separate disk for graphics), retaining a backup copy for reference and safety.

Note that contributions may be either submitted online or sent by mail. Please do NOT submit via both routes. This will cause confusion and may lead to delay in article publication. Online submission is preferred.

Submission address and contact:

Prof. **Mousa S. Mohsen**, Editor-in-Chief
Jordan Journal of Mechanical & Industrial Engineering,
Hashemite University,
PO Box 330127, Zarqa, 13133 , Jordan
E-mail: jjmie@hu.edu.jo

Types of contributions: Original research papers

Corresponding author: Clearly indicate who is responsible for correspondence at all stages of refereeing and publication, including post-publication. Ensure that telephone and fax numbers (with country and area code) are provided in addition to the e-mail address and the complete postal address. Full postal addresses must be given for all co-authors.

Original material: Submission of an article implies that the work described has not been published previously (except in the form of an abstract or as part of a published lecture or academic thesis), that it is not under consideration for publication elsewhere, that its publication is approved by all authors and that, if accepted, it will not be published elsewhere in the same form, in English or in any other language, without the written consent of the Publisher. Authors found to be deliberately contravening the submission guidelines on originality and exclusivity shall not be considered for future publication in this journal.

Supplying Final Accepted Text on Disk: If online submission is not possible: Once the paper has been accepted by the editor, an electronic version of the text should be submitted together with the final hardcopy of the manuscript. The electronic version must match the hardcopy exactly. We accept MS Word format only. Always keep a backup copy of the electronic file for reference and safety. Label the disk with your name. Electronic files can be stored on CD.

Notification: Authors will be notified of the acceptance of their paper by the editor. The Publisher will also send a notification of receipt of the paper in production.

Copyright: All authors must sign the Transfer of Copyright agreement before the article can be published. This transfer agreement enables Jordan Journal of Mechanical and Industrial Engineering to protect the copyrighted material for the authors, but does not relinquish the authors' proprietary rights. The copyright transfer covers the exclusive rights to reproduce and distribute the article, including reprints, photographic reproductions, microfilm or any other reproductions of similar nature and translations.

PDF Proofs: One set of page proofs in PDF format will be sent by e-mail to the corresponding author, to be checked for typesetting/editing. The corrections should be returned within 48 hours. No changes in, or additions to, the accepted (and subsequently edited) manuscript will be allowed at this stage. Proofreading is solely the author's responsibility. Any queries should be answered in full. Please correct factual errors only, or errors introduced by typesetting. Please note that once your paper has been proofed we publish the identical paper online as in print.

Author Benefits

Page charge: Publication in this journal is free of charge.

Free off-prints: Three journal issues of which the article appears in along with twenty-five off-prints will be supplied free of charge to the corresponding author. Corresponding authors will be given the choice to buy extra off-prints before printing of the article.

Manuscript Preparation:

General: Editors reserve the right to adjust style to certain standards of uniformity. Original manuscripts are discarded after publication unless the Publisher is asked to return original material after use. If online submission is not possible, an electronic copy of the manuscript on disk should accompany the final accepted hardcopy version. Please use MS Word for the text of your manuscript.

Structure: Follow this order when typing manuscripts: Title, Authors, Affiliations, Abstract, Keywords, Introduction, Main text, Conclusions, Acknowledgements, Appendix, References, Figure Captions, Figures and then Tables. For submission in hardcopy, do not import figures into the text - see Illustrations. For online submission, please supply figures imported into the text AND also separately as original graphics files. Collate acknowledgements in a separate section at the end of the article and do not include them on the title page, as a footnote to the title or otherwise.

Text Layout: Use double spacing and wide (3 cm) margins. Ensure that each new paragraph is clearly indicated. Present tables and figure legends on separate pages at the end of the manuscript. If possible, consult a recent issue of the journal to become familiar with layout and conventions. All footnotes (except for table and corresponding author footnotes) should be identified with superscript Arabic numbers. To conserve space, authors are requested to mark the less important parts of the paper (such as records of experimental results) for printing in smaller type. For long papers (more that 4000 words) sections which could be deleted without destroying either the sense or the continuity of the paper should be indicated as a guide for the editor. Nomenclature should conform to that most frequently used in the scientific field concerned. Number all pages consecutively; use 12 or 10 pt font size and standard fonts. If submitting in hardcopy, print the entire manuscript on one side of the paper only.

Corresponding author: Clearly indicate who is responsible for correspondence at all stages of refereeing and publication, including post-publication. The corresponding author should be identified with an asterisk and footnote. Ensure that telephone and fax numbers (with country and area code) are provided in addition to the e-mail address and the complete postal address. Full postal addresses must be given for all co-authors. Please consult a recent journal paper for style if possible.

Abstract: A self-contained abstract outlining in a single paragraph the aims, scope and conclusions of the paper must be supplied.

Keywords: Immediately after the abstract, provide a maximum of six keywords (avoid, for example, 'and', 'of'). Be sparing with abbreviations: only abbreviations firmly established in the field may be eligible.

Symbols: All Greek letters and unusual symbols should be identified by name in the margin, the first time they are used.

Units: Follow internationally accepted rules and conventions: use the international system of units (SI). If other quantities are mentioned, give their equivalent in SI.

Maths: Number consecutively any equations that have to be displayed separately from the text (if referred to explicitly in the text).

References: All publications cited in the text should be presented in a list of references following the text of the manuscript.

Text: Indicate references by number(s) in square brackets in line with the text. The actual authors can be referred to, but the reference number(s) must always be given.

List: Number the references (numbers in square brackets) in the list in the order in which they appear in the text.

Examples:

Reference to a journal publication:

[1] M.S. Mohsen, B.A. Akash, “Evaluation of domestic solar water heating system in Jordan using analytic hierarchy process”. Energy Conversion & Management, Vol. 38, No. 9, 1997, 1815-1822.

Reference to a book:

[2] Strunk Jr W, White EB. The elements of style. 3rd ed. New York: Macmillan; 1979.

Reference to a conference proceeding:

[3] B. Akash, S. Odeh, S. Nijmeh, “Modeling of solar-assisted double-tube evaporator heat pump system under local climate conditions”. 5th Jordanian International Mechanical Engineering Conference, Amman, Jordan, 2004.

Reference to a chapter in an edited book:

[4] Mettam GR, Adams LB. How to prepare an electronic version of your article. In: Jones BS, Smith RZ, editors. Introduction to the electronic age, New York: E-Publishing Inc; 1999, p. 281-304

Free Online Color: If, together with your accepted article, you submit usable color and black/white figures then the journal will ensure that these figures will appear in color on the journal website electronic version.

Tables: Tables should be numbered consecutively and given suitable captions and each table should begin on a new page. No vertical rules should be used. Tables should not unnecessarily duplicate results presented elsewhere in the manuscript (for example, in graphs). Footnotes to tables should be typed below the table and should be referred to by superscript lowercase letters.

JJMIE
Volume 4, Number 1, January 2009
ISSN 1995-6665
Jordan Journal of Mechanical and Industrial Engineering

Preface

This special issue of Jordan Journal of Mechanical and Industrial Engineering contains papers contributed to the International Conference and Exhibition on Green Energy & Sustainability for Arid Region & Mediterranean Countries (ICEGES 2009) held on November 10–12th, 2009 in Amman (Jordan); the Conference was organized by the Hashemite University. This conference was an attempt to answer a fundamental question: how to handle the problem of facing growing prospects of climate problems that are blamed on current fossil fuel energy consumption because of massive CO_2 release into the atmosphere and associated global pollution, so our civilization will survive in the future without experiencing lack of energy. If the use of fossil fuels continues, our civilization will face environmental catastrophe in the near future. In a future energy scenario, our civilization may use nuclear energy, non-nuclear renewable energy, fossil energy with CO_2 sequestration, more efficient energy technologies, energy saving, etc. To design the scenario for the use of renewable energy, the Conference discussed the following themes: wind energy systems, environmental and sustainable development, solar thermal energy systems, reduction of CO_2 emissions, photovoltaic and thermoelectric energy, and green energy technologies.

Energy is one of the most essential human needs. Energy in different forms has enabled the accomplishments of human civilization, and created human good living. Its use has been affordable, efficient and extensive. However, like other human activities, energy consumption created (global and local) pollution. Through the release of CO_2 into the atmosphere, consumption (through combustion) of fossil fuels developed the most dangerous form of pollution – global pollution.

Prior to this special issue, a book of Proceedings with a total of eighty eight contributions had been published at the date of the conference. The growing interest in this conference is clearly seen by the large number of authors from all over the world. The presentations are meanwhile coming from more than twenty countries all over the world, mainly from Europe, Japan, Middle East, Far East and the United States. This selection of papers of the conference contains a total of thirty papers that were peer-reviewed by at least two expert referees and were accepted on the basis of their scientific or technical merit and significance to the field. The activities of the conference included twelve keynote lectures carried out by distinguished scientists from the international scientific community in the field of energy and renewable energy; their lectures covered the main themes of the Conference.

Following the objective of the conference as a forum for scientists, researchers, and engineers in the field of energy and renewable energy, it contains both scientific and technical, application-oriented papers. The unique combination of papers on the latest results from the science and technology of green energies with application- and production-related aspects and market analyses is to be regarded as one of the strengths of this conference for the energy community.

We would like to thank the members of the International Scientific Advisory Committee, authors, as well as the reviewers, for their advice which have certainly helped to improve the quality, accuracy and relevance of this conference program and publications. We would also thank the Hashemite University; the main sponsor of ICEGES 2009, and all organizations for supporting the conference, as well as the organizing committee.

Prof. Mousa S. Mohsen
Editor-in-Chief
Hashemite University
Zarqa, January 2010

JJMIE

Volume 4, Number 1, Jan.2010
ISSN 1995-6665

Jordan Journal of Mechanical and Industrial Engineering

PAGES	PAPERS
1 – 8	Integrated Energy and Water Planning on an Arid Island, Case of S. Vicente, Cape Verde *Raquel Segurado, Luís Alves, Neven Duić, Goran Krajačić*
9 – 14	Smart Grid Applications in the US: Technical Potential and Regulatory Barriers *Homayoon "Amir" Abtahi*
15 – 20	Development of Multistage Converter for Outdoor Thermal Electric Cooling (TEC) Applications *Wael Salah , Soib Taib , Anwar Al-Mofleh*
21 – 28	Effect of Pressure and Inlet Velocity on the Adiabatic Flame Temperature of a Methane-Air Flame *Rana Haj Khalil , Ahmad Sakhrieh, Mohammad Hamdan , Jamil Asfar*
29 - 34	Incentives for Technology Development and Project Based Mechanisms: Case of Renewable Energy Project *H. Imai, J. Akita, H. Niizawa*
35 – 44	Laboratory and Field Scale Bioremediation of Tetrachloroethene (PCE) Contaminated Groundwater *J. Ibbini, S. Santharam, L. C. Davis, L. E. Erickson*
45 – 48	Renewable Energy Potential and Characteristics in Jordan *M. Al zou'bi*
49 - 54	Study and Control of a Power Electronic Cascade using Photovoltaic Cell-Multilevel Inverter *Dalila Beriber, Abdelaziz Talha, Farid Bouchafaa, Mohamed Seghir Boucherit*
55 - 60	The Measurement of Overall Elastic Stiffness and Bulk Modulus in Solar Photovoltaic Devices *Imad Alhayek, Mohamed S. Gaith*
61 - 68	Thermodynamic Simulation Modelling of Low-Temperature Geothermal Source Located in Arid-Zone Area North Africa *S. Masheiti, B. Agnew*
69 - 74	Solid Waste Landfills as a Source of Green Energy: Case Study of Al Akeeder Landfill *H. Abu Qdais, F. Abdulla and L. Qrenawi*
75 - 78	A Novel Dual Effect Soot Filtering System *Saud Aldajah, Yousef Haik and Emad Elnajjar*
79 - 90	Characterization of Horizontally Grown Silicon Nanowires in Aluminum Thin Films *Khaleel N. Abushgair, Husam H. Abu-Safe, Hameed A. Naseem, Mahmoud A. EL-Sabagh, Brian L. Rowoen, Avnish K. Srivastava, Samir M. El-Ghazaly*

JJMIE

Volume 4, Number 1, Jan.2010
ISSN 1995-6665

Jordan Journal of Mechanical and Industrial Engineering

91 - 110 Comparison of Biogas Supply Chains Using the Example of the Conditions of a Municipality
B. Noche, A. Al Mansi, G. De La Torre

111-116 A Comparison between the Electrical and Optical Properties of CdS: In Thin Films for Two Doping Ratios
Shadia J. Ikhmayiesa, Riyad N Ahmad-Bitar

117 - 120 Energy Management for Stand Alone PV System
Achour Mahrane, Madjid Chikh, Ahmed Chikouche

121 - 128 Evaluation of Solar Electric Power Technologies in Jordan
Omar Badran, Emad Abdulhadi, Rustum Mamlook

129-134 Interference Pigment Coated Solar Cellsfor Use in High Radiant Flux Environments
Faiz Rahman, Kamran Abid , Christoph Schmidt, Gerhard Pfaff , Friedrich Koenig

135-142 Development Chances of Distributed Energy Production on Small Scale
S. Alsaqoor, M. AlAjlouni, K. AlQdah, H. Kruczek, E. Pelińska-Olko

143 - 150 Modelling and Optimisation of Wind Energy Systems
A. Benatiallah, L.Kadi, B. Dakyo

151 - 154 New Method for Quality Evaluation of Mc-Si Wafers Implied in the Fabrication of Photovoltaic Cells
Mohamed FATHI, Ahmed CHIKOUCHE

155 - 162 Numerical Modeling of Coal Tire-Shred Co-Gasification
Ilham Talab, Zaki Al-Nahari, Rana Qudaih, Isam Janajreh

163 - 168 Performances of Photovoltaic Generator Multi-Level Cascade
Abdelaziz Talha , Dalila Beriber, Mohamed Seghir Boucherit

169 - 176 Power Quality and Stability Improvement in Wind Park System Using STATCOM
V.Suresh Kumar, Ahmed F.Zobaa, R.Dinesh Kannan, K.Kalaiselvi

177 - 192 Solar Net Collective Flux and Conversion Efficiency of the Nickel-Pigmented Aluminium Oxide Selective Absorber Prepared by Alternate and Reverse Periodic Technique in Different Prototype Volumes
A. Wazwaz, J. Salmi, R. Bes

193 - 204 Transient Analysis and Output Characteristics of DC Motors Fed by Photovoltaic Systems
Mohammad S. Widyan, Anas I. Al Tarabsheh, Issa Y. Etier, Rolf E. Hanitsch

JJMIE

Volume 4, Number 1, Jan.2010
ISSN 1995-6665

Jordan Journal of Mechanical and Industrial Engineering

205-210 Wind-Solar Hybrid Electrical Power Generation in Jordan
Ghassan Halasa

211 - 216 Rapidly Shrinking Dead Sea Urgently Needs Infusion of 0.9 km3/a from Planned Red-Sea Channel: Implication for Renewable Energy and Sustainable Development
Shahrazad Abu Ghazleh, Stephan Kempe, Jens Hartmann, Nils Jansen

217 - 224 Seawater Desalination System Integrated to Single Effect and Double Effect Absorption Heat Transformers
Rabah GOMRI

225 - 230 A Study of Fuel Cell Hybrid Auto Rickshaws Using Realistic Urban Drive Cycles
Mohammed Abu Mallouh, Bradley Denman, Brian Surgenor, Brant Peppley

JJMIE

Volume 4, Number 1, Jan. 2010
ISSN 1995-6665
Pages 1 - 8

Jordan Journal of Mechanical and Industrial Engineering

Integrated Energy and Water Planning on an Arid Island, Case of S. Vicente, Cape Verde

Raquel Segurado [a,*], Luís Alves [a], Neven Duić [b], Goran Krajačić [b]

[a] *Department of Mechanical Engineering, Instituto Superior Técnico, Lisbon, Portugal*

[b] *Power Engineering Department, Faculty of Mechanical Engineering and Naval Architecture, University of Zagreb, Zagreb, Croatia*

Abstract

In general, most islands depend for energy supply mainly on the imports of fossil fuels. Arid islands also depend on water desalination, again often depending on fossil fuel imports. On the other hand, most of the islands present a considerable potential in renewable energies. Several initiatives have been carried out in some islands, mostly in Europe, for the use of this potential in the production of electricity and fresh water. Due to high energy costs, the islands present an excellent experimentation platform for the introduction of new energy technologies. Some islands are trying to become renewable islands, to satisfy their energy and water demand mainly or entirely from indigenous and renewable sources, thus increasing the security of supply and employment opportunities, without necessarily increasing the costs. Islands that have renewable energy sources, such as hydro or geothermal energy, can easily integrate them into the power system, but those with mainly intermittent renewable energy sources (wind, solar) have to tackle the need of energy storage. Here, advanced energy planning must be used to combine different intermittent and regular sources in order to match electricity demand and assure security of supply. The main objective of this paper is to analyse different scenarios for increasing the penetration of renewable energies in the energy system of S. Vicente Island in Cape Verde, using the H2RES model, a tool designed to simulate the integration of renewable sources in the energy systems of island or other isolated locations. This island is extremely dry, and fresh water is provided to the population by sea water desalination, a very high energy intensive process. The electricity supply system is based on diesel and wind (still low penetration). S. Vicente has significant wind resources that are not fully used because of its intermittent nature. In this paper, an integrated approach is used to analyse the electricity and water supply systems in order to increase their efficiency. In the centre of the island there is a 774 meters high mountain. The present study incorporates the possibility of using reversible hydro as a storage technique to increase the penetration of renewable energy sources, using desalinated sea water.

Keywords: Renewable Energy, Islands, H2RES Model, Reversible Hydro, Desalination..

1. Energy Planning in Islands

With respect to energy production, most islands depend mainly on the importation of fossil fuels, with all the economical problems that causes mainly due to the high costs of transporting the fuels. In most cases there is no way to connect the islands to the energy production network, making it difficult to implement solutions that reduce the environmental costs, such as atmospheric pollution and greenhouse gas emissions.

Generally, tourism is one of the most important economic activities in islands, being the energy and water consumption in this sector very high, mainly in high seasons, when the cooling and water needs are very high. Usually in these locations, the energy production systems and the air conditioned systems present a very low efficiency, while the availability and storage of fresh water is deficient. Tourism is equally an activity that produces a great amount of waste, which is a big problem for a closed ecosystem that is an island. [1]

Integrate renewable energy sources in energy systems of small islands presents several advantages, because their high technological cost is compensated by the high cost of the conventional sources of energy due to the small dimension of the energy systems and because of a very expensive security of supply. In order to achieve sustainable development it is very important the integration of renewable energy sources for the production of electricity, together with suitable policies and regulations regarding rational use of energy. The electricity production technologies are rarely adapted to

* Corresponding author, email: raquelsegurado@ist.utl.pt.

the conditions of isolated areas and can seriously damage the vulnerable ecosystems and natural habitats. It is important to develop energy supply infrastructure taking into consideration the seasonal variations caused by the tourist activity, without destroying the local environmental or produce too many emissions.

Other environmental local problems related with fossil fuels are the pollution and contamination of the water and the land by the oil products and residues due to their leak during transport, handling and storage.

Many of these islands present numerous sources of renewable energy that could represent a large fraction of the total energy distribution. However, the intermittent nature of most of these sources (wind and solar) as well as the small energy systems of islands introduce barriers to their penetration, like the struggle to match the demand with the supply and the problems related with the integration in the network.

Renewable energy resources can be separated into two categories in terms of availability: the ones that are constant and continuous, that have an intrinsic storage capacity, such as biofuels, hydro, geothermal; and the ones that are variable and intermittent, that do not own this capacity. This category is subdivided in resources that vary periodically and cyclically, such as solar and tidal energy, and resources that vary randomly, such as wind and wave energy.

The integration of intermittent renewable energy sources in energy systems requires the development of energy storage technologies, energy management technologies and a bigger sophistication of these systems.

2. H2RES Model

The H2RES model (Figure 1) simulates the integration of renewable sources and hydrogen in the energy systems of islands or other isolated locations. It is based on hourly time series analysis of demand (water, electricity, hydrogen, heat), storage (reversible hydro, batteries, hydrogen, heat) and resources (wind speed, solar radiation, precipitation). The main purpose of this model is energy planning of islands and isolated regions which operate as stand-alone systems, but it can also serve as a planning tool for single wind, hydro or solar power producer connected to a central power system. Throughout time, the model is evolving and several new modules have been developed such as wave, biomass, solar heat and desalination.

Several papers describe H_2RES model with details of its operation [1], [2], [3], [4]. The version that has been used for calculating Portugal case study has been updated with a wave module.

The main characteristic of H_2RES model is that it uses technical data of equipment, hourly meteorological data for intermittent sources and according to description in [3] energy balancing is regulated by equations.

Wind velocity, solar radiation and precipitation data obtained from the nearest meteorological station are used in the H_2RES model. The wind module uses the wind velocity data at 10 metres height, adjusts them to the wind turbines hub level and, for a given choice of wind turbines, converts the velocities into the output.

The load module, based on a given criteria for the maximum acceptable renewable electricity in the power system, puts a part or all of wind and solar output into the system and discards the rest of the renewable output. The hourly load of the power system is obtained from the local utility.

The excess renewable electricity is then stored either as hydrogen, pumped water or electricity in batteries. The energy that is stored can be retrieved later, and supplied to the system as electricity. The rest is covered from diesel blocks.

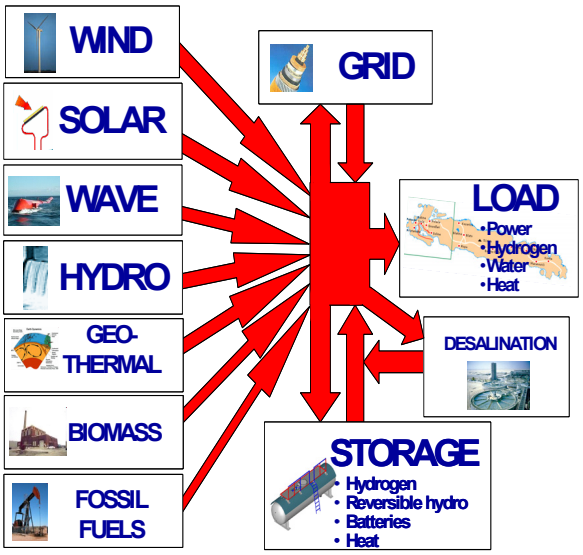

Figure 1. H_2RES computer model v2.8.

The desalination module uses the electricity produced from excess wind to supply the desalination units, that produce drinkable water and put it on the lower reservoir, this reservoir is then used to supply the population. This module takes into account the total capacity of these units (m^3 of water produced per hour) and their electricity consumption per unit of water produced. At each hour, the desalination module verifies if the lower reservoir has at least one day of water demand, if it does not, and if the user allows this option, the desalination units are supplied with electricity from the fossil fuel blocks.

Figure 2. S. Vicente Island [16]

3. The Island of S. Vicente

S. Vicente is the second most crowed island, with about 74,031 inhabitants in 2005 [15], in the Archipelago of Cape Verde, which is composed of ten islands and is situated at about 450 kilometres of the West African coast, in the Atlantic Ocean.

This island has about 228 square kilometres of area and is semi-plane, having just one high point – Mont Verde – located at 774 meters of altitude.

The island is extremely dry, the fresh water is provided to the population by sea water desalination. There are five desalination units in the island, three use reverse osmosis, each one with a capacity of 1,000 m^3 per day, one uses mechanical vapour compression, with a capacity of 1,200 m^3 per day, and the other uses multiple effect distillation, with a 2,400 m^3 per day capacity. A sixth unit was installed in 2007, with a capacity of 1,200 m^3 per day, this unit also uses reverse osmosis.

Regarding electricity production, there are three types of technologies installed in the island: diesel production, wind production and thermal (cogeneration) production. However, this last one is in a deactivation process.

In the following table the electrical power installed in São Vicente by the end of 2005, is stated.

Table 1. Installed capacity in São Vicente by the end of 2005 [17]

Plant	Thermal plant powered by fossil fuel (kW)	Wind (kW)	Cogeneration (kW)
Matiota	11,680	-	780
Lazareto	7,440	-	-
Selada Flamengo	-	1,050	-
Total	19,120	1,050	780

The hourly electricity load of the island in 2005 is depicted in the graphic of the next figure.

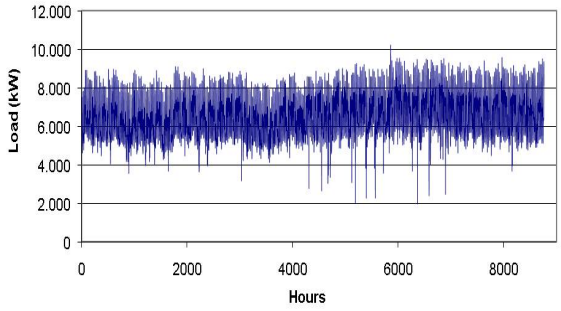

Figure 3. Hourly electricity load of São Vicente in 2005.

In 2005, the electricity production in São Vicente was about 57.173.807 kWh, and the peak power was 10.200 kW.

The electricity demand is relatively stable throughout the year, as there are not large climate variations.

The island has important wind resources. The hourly wind speed of 2005 was collected from the local meteorological station. In this year, the average wind speed was about 7.9 meters per second.

4. Scenarios

In order to apply the H_2RES model to the Island of São Vicente, five scenarios were elaborated, having all as base the year of 2005.

The first scenario is the Business As Usual (BAU), as it only considers the projects that are already foreseen for the island. Regarding the evolution of the demand, a study made by the Research Group on Energy and Sustainable Development was considered. This study, elaborated in the scope of the National Energy Plan for Cape Verde [18], considered the forecast of the evolution of the Gross Domestic Product and of the resident population in order to forecast the growth in the consumption of electricity in the different islands of Cape Verde (Table 2).

Table 2. Forecast of the annual demand growth of electricity in the island of S. Vicente [18]

Period	Annual growth
2006 – 2009	7.92%
2010 – 2014	6.40%
2015 – 2019	4.20%
2020 – 2024	3.36%
2025 – 2030	3.08%

Nowadays, wind energy can be considered economic viable in islands, as long as it does not surpasses a certain limit of penetration. The base scenario is then defined delimiting 30% of the hourly renewable energy penetration, which means that only 30% of the load of one hour can be covered by electricity generated from wind.

According to ELECTRA, the local utility, it is foreseen the installation of more 6,800 kW of wind turbines in the island, and most probably they will be eight turbines of 850 kW each.

The second scenario considers the supply of electricity produced from wind to the desalination plants already installed on the island. This scenario considers the construction of a 30,000 m^3 reservoir, at low altitude, where the water that comes out of the desalination plant will be stored before being supplied to the population. It is believed that S. Vicente has several reservoirs of smaller dimension spread through the island. When the excess electricity from wind is not enough to desalinate all the water needed, the diesel blocks are used to supply the remaining required electricity.

The succeeding scenario maximizes the desalination from wind electricity. Scenario four considers the storage of the excess wind production through pumping of the desalinated water. This scenario contemplates the construction of a dam or water reservoir with about 50,000 m^3 at 500 meters of altitude. Thus, the wind park would supply electricity to a desalination plant and to a pumping

station that puts desalinated water in the upper reservoir. When it is necessary to supply water and electricity to the population, the water is turbinated from the upper to the lower reservoir (Figure 4).

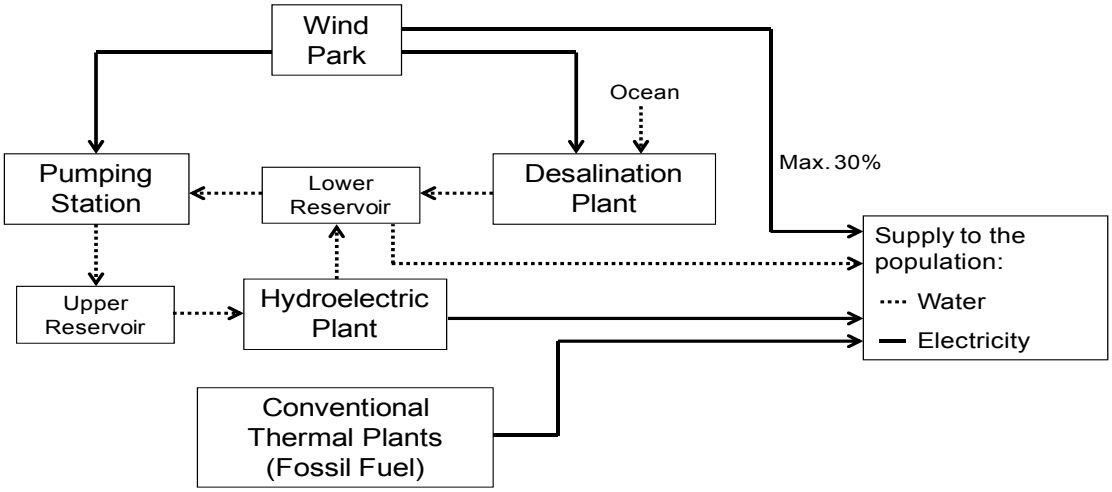

Figure 4. Scheme of scenario 4.

5. Results

Scenario 1 – BAU

Regarding the first scenario, the electricity production in São Vicente from 2005 to 2030 is stated in the following figure. It was considered the above mentioned installation of 6,800 kW of wind energy by 2010 and the addition of diesel blocks to satisfy the growth of the demand.

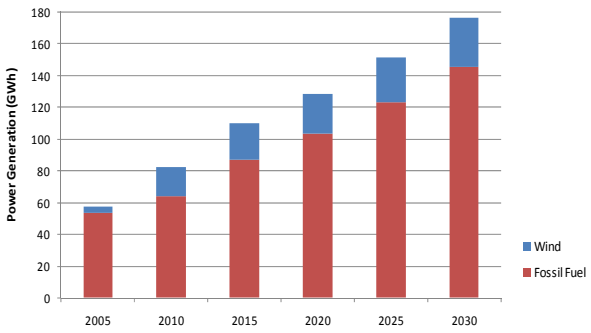

Figure 5. Power production in S. Vicente from 2005 to 2030, for the BAU scenario

It is clear that the penetration of the wind electricity production increases from 2005 to 2010, due to the installation of the new wind turbines, it increases from 6 to 22%. However, from then on, it decreases, as no more wind turbines are added to satisfy the demand growth, only diesel blocks.

In this scenario, the electricity produced from wind has a large amount that is rejected, especially in 2010, with 45% of wind electricity rejected. As the years go by, this rejection decreases due to the growth of demand and the non installation of more wind turbines, in 2030 it reaches about 9%.

Scenario 2 – Desalination from wind

An excellent way to decrease the wind electricity rejected is to supply the desalination plant with this excess electricity. However, when modelling this scenario, the first conclusion reached was that the wind produced was not enough to desalinate all the water needed. Hence, it was considered the supply of electricity from the diesel blocks, when the electricity from wind was not enough.

The evolution of the water demand was considered to be the same as the electricity demand. These calculations considered desalination units already installed in the island, and the addition of desalination units to satisfy the growth of the demand over the years.

The load considered in the first scenario included the electricity needed to desalinate water and to supply the population, thus, in this scenario, there was the need to subtract the electricity used for desalination. According to [17], 14% of the electricity produced in S. Vicente in 2005 was to supply the desalination units. Hence, and because hourly consumption of water does not vary very much, as there are not large water storages, this percentage was deducted from the hourly load.

Regarding the supply of electricity from wind, although there is a 30% limit for the supply of the population, there is no limit for the supply to the desalination units. A reservoir of 30,000 m^3 was considered, in order to have water storage with a capacity of about five days of the demand of 2010.

In this scenario, the penetration of wind electricity reaches higher levels than in the previous one. The proportion of wind electricity rejected in this scenario is much lower, reaching its higher value, about 23%, in 2010.

Scenario 3 – Maximize the desalination from wind

In order to maximize the desalination from wind, the influence of the wind turbines installed, of the capacity of the desalination units and of the capacity of the lower reservoir was studied. Although the most important factor was the power of the wind turbines installed, the increase of this value leads to an increase of the wind electricity rejected. To avoid this, the capacity of the desalination units needs also to increase. Hence, the number of wind

turbines and desalination units was optimised so that yearly wind desalination was maximised while keeping the rejected wind electricity close to 10% [5].

With the installation of wind turbines throughout the year, it is possible to increase the penetration of wind electricity and keep it more or less constant along the years. The production of desalinated water, by electricity from wind and from the fossil fuel blocks is stated in the next figure.

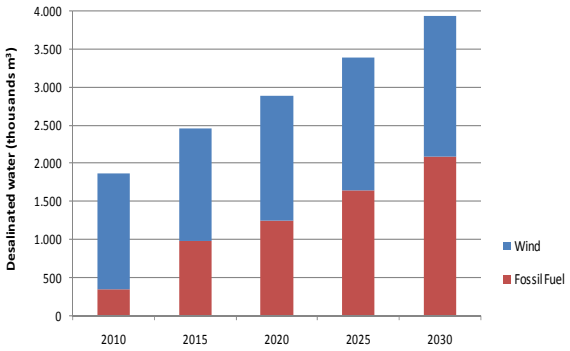

Figure 6. Production of desalinated water in S. Vicente from 2005 to 2030, for scenario 3.

The fraction of desalinated water produced from wind reaches 82% in 2010, and although it decreases slightly in the following years, it never goes below 47%.

Scenario 4 – Reversible hydro and desalination

This scenario considers the pumping of desalinated water to the upper reservoir, and its later supply to the population producing also electricity from de hydroelectric plant. It was considered that the hydroelectric plant is used for peak shaving, about 80% of the weekly peak. The capacity load factor of the hydro turbines was kept above 20%.

Scenario 5 – Maximize RES penetration

In order to maximize the RES penetration in the energy supply system of the island of S. Vicente, the installation of more wind turbines is crucial. However, when modelling this scenario, there was the need to, when testing all the possibilities; verify if none of the reservoirs overflowed. This is a very important issue, especially in an island as dry as S. Vicente. Thus, the two restrictive factors in maximizing RES penetration were the prevention of overflow of the reservoirs and the control of the intermittent rejected. The electricity production along the years for this scenario is indicated in figure 7.

In 2010, the hydroelectric plant produces about 3% of the total electricity produced in the island, 35% is produced from wind, totalizing 38% of RES electricity.

100% hourly intermittent energy penetration scenarios

These scenarios allow the hourly intermittent energy penetration rate to reach 100%. The number of wind turbines was optimised so that yearly wind penetration was maximised while keeping the rejected wind electricity close to 30%. [5]

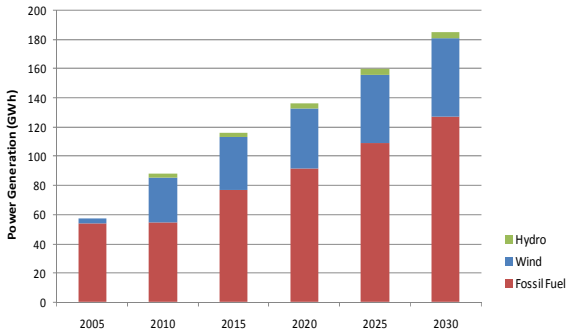

Figure 7. Power production in S. Vicente from 2005 to 2030, for scenario 5.

Unsurprisingly, in these scenarios the penetration of wind electricity is much higher. In scenario 7, where the desalination from wind is maximized, this value reaches 88% in 2010 and around 70% in the following years. The electricity produced from wind is about 70%.

In scenario 9, where the RES penetration is maximized, the hydroelectric plant produces about 7% of the total electricity produced in the island in 2010, 69% is produced from wind, totalizing 76% of RES electricity.

Comparison between scenarios

In the following figure the power generated to supply the island of S. Vicente in the year 2020 in stated for four different scenarios.

It is clear that in scenario 9 the renewable energy sources have a higher fraction. In this scenario, the avoided electricity production from fossil fuel reaches 62.2 GWh. Using an overall electricity emission factor of diesel generators of 0.75 $kgCO_2$ per converted kWh [10], the avoided greenhouse gas emissions are 46,671 $tonCO_2$.

Considering the 30% of hourly penetration limit (scenario 5), the avoided electricity production from fossil fuel reaches 11.8 GWh which corresponds to 8,860 $tonCO_2$ of avoided greenhouse gas emissions.

The next figure illustrates the amount of desalinated water produced from wind and from fossil fuel in the different scenarios

In scenarios 3 and 4, the desalination from wind is always balanced with the desalination from fossil fuel. In 2020, these scenarios present a fraction of desalinated water produced from wind of 53% and 56% respectively. Scenarios 7 and 9 have a higher fraction of desalinated water produced from wind, 75% and 59% respectively.

6. Conclusions and Future Developments

This paper analyses the way to increase the penetration of renewable energy sources in the island of S. Vicente, in Cape Verde. Based on existing load data and meteorological data, several scenarios were built and modelled using the H_2RES model. The scenarios considered wind, reversible hydro and desalination technologies.

The maximization of desalination from wind resulted in fractions of desalinated water produced from wind of about 80% in 2010 for most of the scenarios, but from the following years, this value decreased to around 50%.

The maximization of renewable energy sources in this supply system resulted in a penetration of about 38% of these technologies, with a major fraction from wind and a much lower contribution from hydroelectricity.

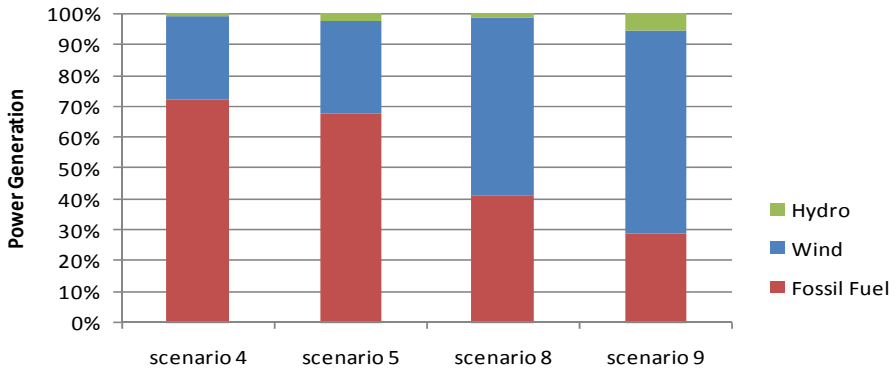

Figure 8. Power production in S. Vicente in 2020, for four scenarios

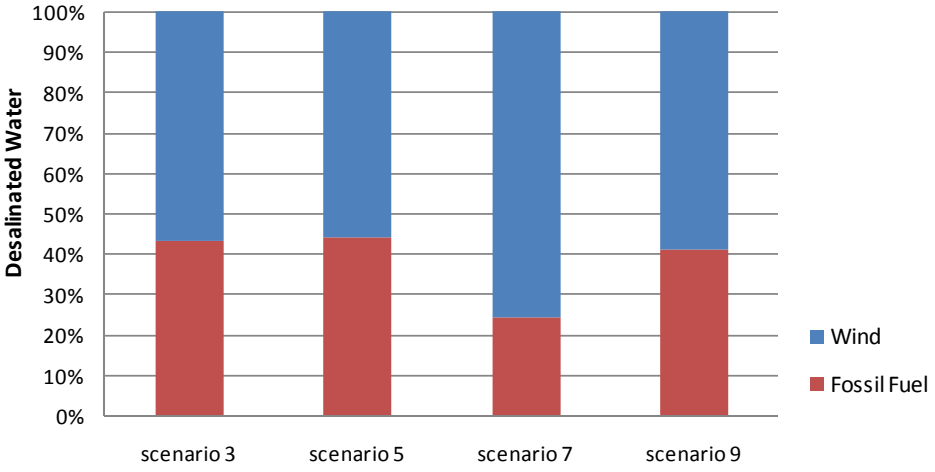

Figure 9. Desalinated water produced in S. Vicente in 2020, for four different scenarios

If an hourly intermittent energy penetration rate of 100% is allowed, the percentage of desalinated water produced from wind can reach 81-88% in 2010 for the scenarios 9 and 6, but for the following years, this value reduced to 60-68%. Regarding the maximization of renewable energy sources, the penetration of these technologies in this supply system reached 76%, with 69% of wind and 7% of hydroelectricity.

These scenarios need to be analysed in environmental and financial terms. There is also the need to examine the sites were the reservoirs can be built and the wind turbines installed, for instance to determine if it is possible to install reservoirs with this dimension, and what is the effect of the local environment.

In order to improve the input data of the first scenario and the baseline year, an update of the forecast of the demand growth will be carried out, together with an assessment of the demand in water and energy of the tourist projects foreseen for the island.

Later work will be done on modelling the fog occurrence in Mont Verde, and consider its collection to the upper reservoir.

Acknowledgments

The authors acknowledge the contribution of the Portuguese National Foundation of Science and Technology of the Ministry for Science and Technology by supporting Raquel Segurado with a Ph.D. grant (SFRH/BD/31663/2006). The authors would also like to thank the company ELECTRA S.A., namely Eng. Rui Paisana for its availability in supplying the necessary data for this study.

References

[1] N. Duić, G. Krajačić, M.G. Carvalho, "RenewIslands methodology for sustainable energy and resource planning for islands". Renewable and Sustainable Energy Reviews, Vol. 12, 2008, 1032–1062.

[2] N. Duić,M.G. Carvalho, "Increasing renewable energy sources in island energy supply: case study Porto Santo". Renewable and Sustainable Energy Reviews, Vol. 8, 2004, 383–399.

[3] N.Duić, M. Lerer, M.G. Carvalho, "Increasing the supply of renewable energy sources in island energy systems". International Journal of Sustainable Energy, Vol. 23, No. 4, 2003, 177-186.

[4] F. Chen,N. Duić, L.M Alves, M.G. Carvalho, "Renewislands - Renewable energy solutions for islands". Renewable and Sustainable Energy Reviews, Vol. 11, No. 8, 2007, 1888-1902.

[5] M. Lerer, N. Duić, L.M. Alves, M.G. Carvalho, "H2RES, Energy planning tool for increasing the penetration of renewable energy sources in island energy supply". International Conference on New and Renewable Energy Technologies for Sustainable Development, Évora, Portugal, 2004.

[6] E.A.F.A. Fadigas, J.R. Dias, "Desalination of water by reverse osmosis using gravitational potential energy and wind energy". Desalination, Vol. 237, 2009, 140-146.

[7] C.R. Henderson, J.F. Manwell, J.G. McGowan, "A wind/diesel hybrid system with desalination for Star Island, NH: feasibility study results". Desalination, Vol. 237, 2009, 318-329.

[8] A.A. Setiawan, Y. Zhao, C.V. Nayar, "Design, economic analysis and environmental considerations of mini-grid hybrid power system with reverse osmosis desalination plant for remote areas". Renewable Energy, Vol. 34, No. 2, 2009, 374-383.

[9] M. Folley, T. Whittaker, "The cost of water from an autonomous wave-powered desalination plant". Renewable Energy, Vol. 34, No. 1, 2009, 75-81.

[10] A. Corsini, F. Rispoli,M. Gamberale, E. Tortora, "Assessment of H_2- and H_2O-based renewable energy-buffering systems in minor islands". Renewable Energy, Vol. 34, No. 1, 2009, 279-288.

[11] K. Udono, R. Sitte, "Modeling seawater desalination powered by waste incineration using a dynamic systems approach". Desalination, Vol. 229, 2008, 302-317.

[12] D. Ipsakis, S. Voutetakis, P. Seferlis, F. Stergiopoulos, C. Elmasides, "Power management strategies for a stand-alone power system using renewable energy sources and hydrogen storage". International Journal of Hydrogen Energy, Vol. 34, 2009, 7081-7095.

[13] J. Koschikowski, B. Heijman, "Renewable energy drives desalination processes in remote or arid regions". Membrane Technology, Vol. 8, 2008, 8-9.

[14] A. Bermudez-Contreras, M. Thomson, D.G. Infield, "Renewable energy powered desalination in Baja California Sur, Mexico". Desalination, Vol. 220, 2008, 431-440.

[15] National Statistics Institute of Cape Verde, "Demographical Predictions by Geographical Code and Year", 2005 (in Portuguese). www.ine.cv

[16] biztravels.net

[17] Electricity and Water Company (ELECTRA – Empresa de Electricidade e Água S.A.R.L.), "Annual Report 2005", 2006 (in Portuguese). www.electra.cv

[18] Ministry of Economy, Growth and Competitivity of Cape Verde, "National Energy Plan – Energy Policy Plan for Cape Verde", 2003 (in Portuguese).

JJMIE

Volume 4, Number 1, Jan.2010
ISSN 1995-6665
Pages 9 - 14

Jordan Journal of Mechanical and Industrial Engineering

Smart Grid Applications in the US: Technical Potential and Regulatory Barriers

Homayoon "Amir" Abtahi

Florida Atlantic Universit,y, Boca Raton, Florida, USA

Abstract

Smart Grid refers to the design and implementation of a modern electrical power transmission and distribution system that incorporates intelligent controls. The sophistication of the control strategy and the controllers is a subject for debate and discussion. In this paper, a general review of the many interpretations of Smart Grid is presented, and available and proposed Smart Grid technologies are discussed. Various systems are described, and a matrix of potential benefits or risks is analyzed. The hierarchy of the more prevalent Smart Grid protocols are assessed and weighted against the risks for the overall safety of the grid and the benefits for the users. Finally, some case studies of utility experiences with pilot projects are reviewed and discussed.

Keywords: Smart Grid; Grid Connected Storage; Photovoltaic Generation; Renewable Energy Systems; Micro-Grid; Smart Appliance; Automated Meter Reading; Real-Time Pricing.

Nomenclature

AMI : Advanced Metering Infrastructure.
AMR : Automated Meter Reading.
CML : Customer Minutes Lost.
CPP : Critical Peak Pricing.
DG :Distributed Generation.
DNP3 :Distributed Network Protocol
HAN :Home Area Network
MDM :Meter data management
NERC :North American Electric Reliability Corporation
NSTB :National SCADA Test Bed
PHEV :Plug-in Hybrid Electric Vehicle
PV :Photovoltaic
SAIDI :System Average Interruption Duration Index
SCADA : Supervisory Control and Data Acquisition
TCP :Transmission Control Protocol
TOU :Time of Use

1. Introduction

Utilities all across the United States are implementing "Smart Grid" (SG) networks in small, medium and even large metropolitan markets. The networks are cooperative efforts between a local utility and private sector power distribution and software suppliers. City of Miami plans to develop a Smart Grid in cooperation with Florida Power & Light (FPL), General Electric and Cisco. The $200 million project has been called a "Blueprint for the Future of Power" by Time Magazine. FPL has made commitments to replicate the program for all of its 4.5 million customers. University of South Florida and Progress Energy have teamed up to design and implement a Smart Grid application that includes solar power generation and bio-diesel cogeneration In Tampa, Florida. PECO, a utility that operates in Pennsylvania, is investing $600 million to convert its power distribution system into a Smart Grid. Drexel University and the University of Pennsylvania are partners in that effort.

On the national level, in April 2009 Vice President Joe Biden unveiled a plan to develop a nationwide Smart Grid with a $3.3 billion investment. One of the many proposed long term plans is to develop local Smart Grid hubs that eventually link up with regional and then a national Smart Grid network. Most of these efforts are funded with Federal Stimulus funds, but a review of the various initiatives indicates that not all the participants have the same understanding of a Smart Grid, nor is there a consensus on the level to which a utility can micro manage its customers' loads. There is a great potential to make the power generation and distribution system more efficient, and safer when dealing with traditional electrical distribution problems. However, there are also risks involved in developing a network that can as a whole - or in its parts - be subject to software errors, cyber-attacks, and network issues that are usually associated with the internet. In addition, there are legal and regulatory barriers that may impede or even disallow some of the proposed Smart Grid (SG) technologies.

One can argue that the earliest application of Smart Grids were the rudimentary controllers that allowed phase and

* Corresponding author. amir.abtahi@gmail.com

voltage quality conditioning in the early days of grid development in the 1950's. The great Blackout of 1965 may have been the earliest warning sign that a more advanced monitoring and control strategy was required for the interconnected grid. A more recent grid failure that affected 50 million people in August 2003 was shorter but alerted the utilities that minor transmission failures could have disastrous consequences, and the vulnerability of the grid to physical or cyber-attacks was also exposed. The need for a resilient, reliable, self-healing power delivery system has become even more evident with the introduction of the first generation two-way communication between the suppliers and the consumers. The basic communication protocols for these systems parallels the infrastructure and the software that supports the internet and is therefore vulnerable to the same risks and failures.

Aside from system reliability and security, automated meter-reading (AMR), and transmission/distribution monitoring and control, the new Smart Grid needs to enable the needs of numerous stakeholders. The utilities are interested in more aggressive load shedding tools, such as smart appliances, Plug-in Hybrid Electric Vehicle (PHEV) storage, and consumption management. They are also looking at the Smart Grid for timely and efficient management of large-scale wind and solar assets that is coming online at accelerated rates. Consumers are hoping that SGs will help curtail ever increasing utility costs with time of use (TOU) electric rates, and net-metering options that allow two-way power transmission and accounting. The Federal and State governments want to assure a secure system that can handle any conceivable threat, whether natural, man-made, accidental or intentional. The matrix of interactions and interests between all the members, and the distinct elements that will eventually become a Smart Grid is complex and will require extensive analysis and discussion. Numerous studies are under way by Federal agencies such as the Department of Energy (DOE) and National Laboratories such as the Idaho National Laboratory (INL) and the Pacific Northwest National Laboratory (PNL), utilities and the Electrical Power Research Institute (EPRI). Numerous university research programs and consultants are also working to understand, set basic rules, and establish overall design criteria for SG. This paper deals with reviewing some of the more prominent configurations, and offering an analysis of the proposed architectures.

2. Elements of the Smart Grid

The predominant SG architecture is based on the current infrastructure of utility implemented control systems that monitor and manage generation and distribution of power. The current "semi-smart" system is in fact smarter and better equipped that even the grid of 2003, when the Ohio initiated blackout event occurred. It has gone through numerous iterations to deal with natural disasters by implementing self-healing features that re-route power, and sensors that can detect the location of a fault with increasing accuracy. Sub-station controllers incorporate two-way communication, and advanced cyber-security and protection elements. The "Smart Grid System Report" by US DOE [1], reviews and summarizes the requirements and a general definition for the Smart Grid. The SG, according to this report, shall be built upon the existing infrastructure, be capable of handling distributed generation, and provide reliable, secure and efficient delivery of power. Since the Smart Grid of the future has new stakeholders, new technologies and features need to be implemented. Among these:

Utility Interests that include:

- Incorporation of solar photovoltaic, solar thermal and wind resources owned or controlled by the utility into the supply stream.
- Load shedding, real-time and time of use (TOU) pricing, and peak shifting with storage such as PHEV
- Integration of consumer-owned and non-utility distributed generation at utilities' discretion
- System integrity and noise reduction due to potentially non-conforming sources
- Cyber-Security and asset protection

Consumer Interests that include:

- Cost savings from peak load reduction
- Export of solar or wind generated power at consumers' discretion to maximize financial benefits
- Less reliance on utilities if so desired
- Asset protection, including PHEV battery life
- Environmental Factors and consumer preferences

Governmental and Regulatory Interests

- National and Local security
- Environmental treaties and agreements
- Consumer Protection
- Utility and National Asset Protection

Figure 1 shows a typical Smart Grid configuration. The various interpretations of a smart grid do not always include every element shown in this schematic. The current configuration of the grid for most of the utilities in the United States, is a straight line from the grid through the local utility's control center, terminating at customer's meters. The INL Report [2] has compiled 74 initiatives in the US that include some elements of the new SG. As of the end of March 2009, there are 28 utility-initiated AMI projects, 18 AMI trial/pilot initiatives, 20 AMR projects, and 8 SG projects and pilots in the installation phase. The utilities with some SG initiative will grow exponentially in the next 3 to 5 years, especially with more than $3.6 Billion in stimulus funding that was awarded in October 2009.

On the supply side, as the utilities discover the benefits of distributed generation, and the return on investment picture for wind and solar improves, the wind/solar component will be a more frequent addition to the SG configuration. The intermittent nature of wind generation in continental US, and the cyclical nature of solar energy requires the addition of large scale storage or interaction with residential/commercial generators.

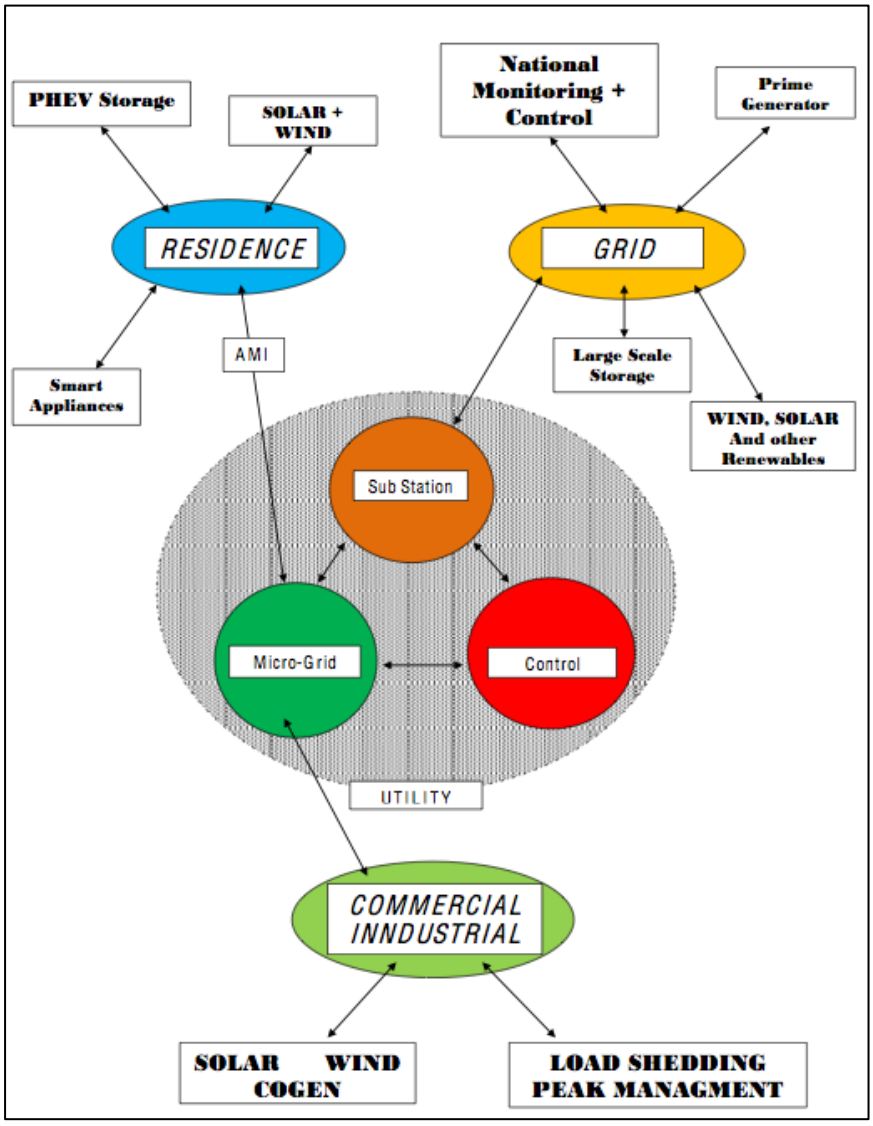

Figure1. a typical Smart Grid configuration.

Energy storage technologies will be critical for the successful implementation of a SG that rely on renewable energy sources. The technology for large scale energy storage is still in its early developmental stages.

Battery performance and cost are barriers to large scale energy storage. New battery technologies and ultra-capacitor development may change the storage options in the coming decade, but at this point in time, utilities will need to rely on residential storage systems. While this may be a short term solution, it is not clear that homeowners will jeopardize the integrity of the PHEV batteries to participate in a national storage landscape, not until battery cycling is decoupled from battery life.

The other major difference between the configuration shown above, and the more widely publicized schematics, such as the block diagram developed at INL [2], is the prominence of the Micro-Grid (MG) block. The MG is usually a passive pass-through part of the network, where local monitoring, fault-detection, and self-healing features are implemented. There are a number of operational and regulatory protocols that constrain the Micro-Grid as an integral part of the grid, with no capability for autonomous operation unless the entire grid is operational. One example is that even though a commercial solar/cogeneration component within the MG is generating power, the utility command and control (UCC) will not allow the flow of electricity from this generating source to let's say a residential customer within the MG. With the current grid and even some of the anticipated SG designs, there are no contingencies for this to occur. However, disabling local distribution in case of a large scale power outage, steals away some of the more valuable qualities of distributed generation: security, redundancy, and active grid re-formation after a massive fault. Wilson Clark, one of the earliest advocates of distributed power generation in the context of a modern grid, attributed distributed power generation in Japan [3] to the difficulty encountered by the allies in its defeat.

Another important feature of the SG advocated by utilities is the Smart Appliance component. A recent study co-sponsored by Portland General Electric, a local utility with PNL and Whirlpool Corporation [4], tested the application

of smart appliances for SG responses. The actual effect of this technology needs further evaluation. The experience with many of the appliance control programs around the US has had a limited success rate. The incentives offered by utilities, such as FPL in Florida are not enough to encourage the consumers to transfer the control of major appliances such as air conditioning equipment to the utility. Programs that offer real-time pricing may do better, but the interactive systems need to be user-friendly and result in real and tangible benefits and savings. There is a general distrust of intrusive technologies, and while the concept of being green and energy efficient does have some traction, when it is in conflict with personal choices or habits, especially inside one's home, may lose its momentum. There is a risk that too much control could backfire, especially if the smart appliance is vulnerable to a smarter virus that may penetrate the controller through the two-way communication path with SG. One wholesale failure of a smart appliance group would seriously affect the entire program.

3. Benefits and Risks

There is no doubt that the grids in the US and around the world need to be re-configured to adapt to new generation and distribution realities. Some countries such as Germany and China have already started this process. The case for the US is more challenging. With numerous private utilities, local cooperatives, and regional entities such as the Tennessee Valley Authority, the design and operation of a central UCC is a formidable task. There are operational challenges for improving service while implementing rigorous interoperability standards between the SG components. Ipakchi [5] reports that US System Average Interruption Duration Index (SAIDI) or Customer Minutes Lost (CML) is 120-160 minutes, while Western Europe with a higher degree of automation maintains 60-80 minutes, and some utilities in Asia have a CML target of 5 minutes, with "substantial monitoring and control, high reliance on automation and extensive self-healing grid design." The ultimate goal of an advanced SG is to achieve these higher goals for service quality, operate two-way communication with the end-user, integrate the grid with large scale renewable generation, and accommodate distributed generation of the end-user. There are certainly risks. Bi-directional communication is vulnerable. There can be natural disasters, man-made accidents, and intentional attempts at harming the system infrastructure, or the communication links. Loss of data between UCC and a group of smart appliances may develop into a major disaster. Minor software glitches in monitoring or control of even the lowest controller in the SG hierarchy could lead to bi-directional damage harming both the supplier and the consumer.

It is conceivable that the need to integrate solar, wind and other renewable has the greatest single impact on the design of the new SG. Peak shaving, remote appliance control, and TOU electric rates were introduced and implemented almost 40 years ago. Even the thermal solar systems that were introduced in the 1970's were initially received as potential peak shavers, but because their utilization cannot be controlled, they were eventually lost to low cost gas and TOU electric rates in the US. What distinguishes Concentrating Solar Thermal Power (CSTP) and solar photovoltaics (PV), is that they are ideal as peak generators. Solar irradiance does for many utilities coincide with peak demand. Wind, through less predictable than solar energy on a daily basis, has a better long-term predictability functions and has become more competitive and a favorite of utilities as a reliable component in their supply chain. With political, regulatory and environmental pressures on utilities to generate cleaner energy that reduces emissions and imports, renewable energy has finally been embraced by mainstream electric producers. No one however predicted the public's desire to generate their own rooftop electricity. Even as recently as 1990's, the promulgation of rooftop solar installations could not have been predicted. European utilities paved the way by introducing Feed-in-Tariff (FIT) and showing that utilities could benefit from rooftop solar.

The integration of centralized and distributed renewable energy, and awareness of energy efficiency were once considered as visionary and futuristic. Utilities now consider these as integral to their overall generation and power delivery strategies. Smart Grid can benefit the utilities, power generators, and the consumers. There are certainly risks involved. Some of the threats can be predicted, and many are yet to be discovered. The hesitation of some utilities to move slowly in adopting SG is understandable. The benefits for utilities may at some point conflict with the benefits to consumers. Regulatory guidelines and standards are still being developed, and not all the stakeholders are at the design table.

4. Conclusions

A standard definition or description of the Smart Grid is still in the development stage. While there is a general understanding of what an SG implies, a standard has not yet been developed, and no metrics have been developed to classify Smart Grids. There will certainly be a great deal of input from utilities both public and private, academicians, consumers, and technology representatives on how best to design and implement an SG. There will probably be variations, exemptions, and numerous addenda. What is clear is that a sustainable SG should be built on an equitable distribution of potential benefits, minimize the risks, and provide reliable and secure power. It should also provide opportunities for those consumers who want to contribute, encourage distributed power generation, and their preferences with regards to emissions and global warming issues, and their choice of energy sources.

For the Smart Grid to be successful, it is essential that it demonstrates to the consumers that it can lead to energy saving and user friendly interaction, resolve potential issues, and be self-learning and continuously improve itself. While no element or protocol in the SG configuration should in anyway jeopardize the security or the reliability of the system, the needs and interests of end-users shall not be compromised, and the concept of a localized micro-grid that can operate autonomously in case of grid-wise failure shall be evaluated and considered.

References

[1] US-DOE, "Smart Grid System Report", Report to Congress by Energy Secretary as per Section 1302 of Title XIII of Energy Independence and Security Act of 2007, July 2009.

[2] Boyer, W.F., and Scott A. McBride, "Study of Security Attribute of Smart Grid Systems-Current Cyber Security Issues", Idaho National Laboratory, USDOE, Under Contract DE-AC07-05ID14517, April 2009

[3] Clark, Wilson, Energy for Survival, The Alternative to Extinction, Garden City, Anchor Books, 1974

[4] Conrad, E., Horst, G., Hammerstrom, D., " Appliance Interface for Grid Responses", Paper C-12, pp. 103-106, Grid-Interop Forum, Albuquerque, New Mexico, Nov. 7-9, 2007

[5] Ipakchi, A, "Implementing the Smart Grid: Enterprise Information Integration", Paper C-79, pp.121-122, Grid-Interop Forum, Albuquerque, New Mexico, Nov. 7-9, 2007

JJMIE

Jordan Journal of Mechanical and Industrial Engineering

Volume 4, Number 1, Jan. 2010
ISSN 1995-6665
Pages 15 - 20

Development of Multistage Converter for Outdoor Thermal Electric Cooling (TEC) Applications

Wael Salah* , Soib Taib , Anwar Al-Mofleh

School of Electrical and Electronic Engineering, Engineering Campus, Universiti Sains Malaysia,

14300 Nibong Tebal, Seberang Perai Selatan, Pulau Pinang, Malaysia

Abstract

The design of Transformer-less DC-DC converter for low voltage and high current thermoelectric cooling (TEC) applications is presented in this paper. The design of the converter was based on the combination of buck and boost converters topology. The prototype of the converter had been constructed and tested. The simulation results and measured data of the power circuit are analyzed and discussed. The maximum efficiency of the converter was about 80%, and it found to be suitable to be connected to the TEC load powered from solar panel power source.

Keywords: SMPS, Transformerless Converter, DC Converter, MOSFETs, Cuk converter, Voltage Divider, TEC.

1. Introduction

The switching power supplies are based on the regulating elements, the switching power supplies consist of transistors that rapidly opened and closed the power switches. The resultant train of pulses is coupled to the output network which provides a smoothing of the DC output. [1]. The unregulated power supplies consist of a rectifier and filter which is not capable of providing a ripple free DC output voltage whose value remains reasonably constant.

The power conversion in consumer electronics devices uses characteristically high-efficiency switched mode power supplies (SMPS). Yet, reflecting the trend toward energy conservation there are increasing demands for power supplies with higher efficiency, lower loss and reduced stand-by waiting power [2][5]. Power processing has always been an essential feature of most electrical equipment. The differences in voltage and current requirements for different applications have led to the design of dedicated power converters to meet their specific requirements [1]. The most significant differences between the linear and the switch mode regulators involve their efficiency, size, weight, thermal requirements, response time, and noise characteristics.

A switching power supply could be used for powering the thermoelectric cooling module (TEC) prototype load. The thermoelectric modules (TEC) are solid-state heat pumps that operate on the Peltier effect. A thermoelectric module consists of an array of “p” and “n” type semiconductor elements heavily doped with electrical carriers. The array of elements is soldered so that it is electrically connected in series and thermally connected in parallel. This array is then affixed to two ceramic substrates, one on each side of the elements [7].

The TEC found in many applications, also TEC cooling modules are potential candidates for use in the thermal management of high temperature electronics applications for their widely commercially availability. The TEC modules have a maximum rated operating temperature of 200"C makes thermoelectric cooling an interesting option in the thermal management of high temperature electronic packaging [8,9].

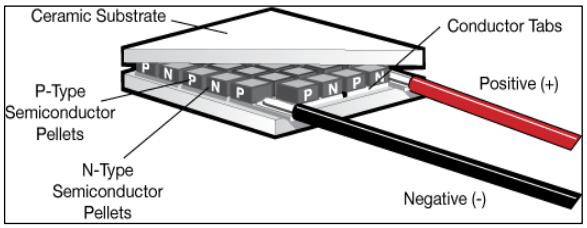

Figure1. Typical TEC Module.

2. Methodology

In switching supplies, the regulating elements consist of series connected transistors that act as rapidly opened and closed switches. The input AC is first converted to unregulated DC which will be chopped by the switching element operating at a rapid rate using high frequency

Corresponding Author. wael_sal@eng.usm.my

PWM signal. The resultant pulse train is transformer-coupled to an output network which provides final rectification and smoothing of the dc output. Regulation is accomplished by control circuits that vary the on-off periods (duty cycle) of the switching elements if the output voltage attempts to chance.

Switching converters occupies between two type of converters which are the line regulated and the quiestiant resonant converters, the main problem of line regulator relates to the high power losses that is dissipated as a heat and also low overall efficient which is around 40%. On the other hand this type of regulators are cheep and simple compared to questiant resonant which are complex and costly but provide high efficient [5].

The elimination of magnetic elements and the use of switches and capacitors as a based design elements for the design of DC-DC converters, then light weight converter can be realized [2]. The idea of switch-capacitor (SC) is to charge capacitors is series, this will provide division of voltage and so wide range of step down achieved, then the charged capacitors have to be discharged in parallel in order to supply the stored energy to the load [4].

The Cuk converter basically derived from connecting a boost converter followed by a buck stage as shown in Figure 2. A practical realization of a Cuk converter could be as follows, the output polarity is inversed relative to input side [3].

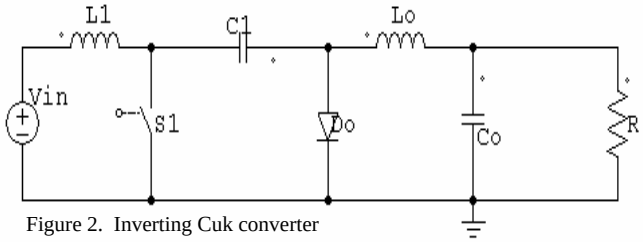

Figure 2. Inverting Cuk converter

The Cuk topology is an inverting topology in which the output polarity opposes the input one, for the purpose of obtaining same polarity referring to the input, a diode and a switch has to be added to a non-inverting Cuk converter. As shown in Figure3 the addition of D1 and S2 enable the transfer of energy stored in C1 with the same polarity from input relative to the output side. And then by combining the common element a single stage non-inverting Cuk stage is constructed [1].

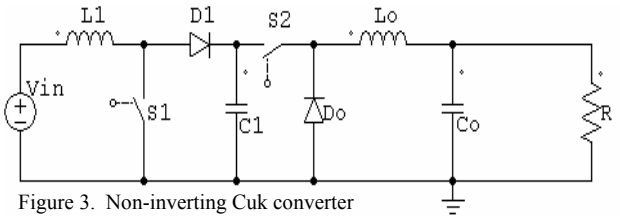

Figure 3. Non-inverting Cuk converter

By considering the topology of the non-inverting Cuk converter, then the new topology can be basically principled on dividing input voltage to charge series connected capacitor during switch on-time and the discharge the capacitor during switches off-time as shown in Figure4.

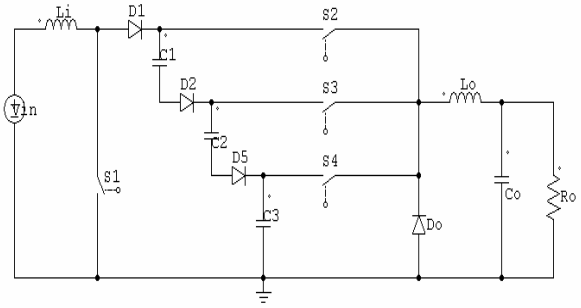

Fig 4. The 3-Stage non-inverting Cuk converter

The DC step down conversion associated with the use of transformer will lead to small value range of duty ration this will make it hard to switch ON and OFF the static switches. So the use of the proposed topology then large step-down voltage can be achieved without very small duty ratio and without usage of transformer. Therefore the losses related to usage of transformer can be eliminated [2,5].

The other advantage of this topology is that the energy transfer from input to the output is through the capacitors. These capacitors are charged on series during Off-time of the power switches and discharged on parallel during On-time of switches [6].

The use of high-voltage, fast switching power transistors, fast recovery diodes, and new filter capacitors with lower series resistance and inductance, could makes the switching supplies in a position of great concern in the power supply industry.

The heat pumping capacity of a TEC module is proportional to the current and is dependent on the element geometry, number of couples, and material properties [9,10]. By the use of thermoelectric modules it could effectively enhancing the thermal performance of air-cooled heat sinks [11].

The micro TEC (Thermo-Electric Cooler) can be used for hot spot cooling system of electric device in which it combined with heat sink. With the use of micro TEC lower maximum temperature at the hot spot can be obtained [12]. The performance of the TEC could be affected by the design of the cooling prototypes, it was found out that TEC combined with spreading devices could significantly extend air cooling performance [13]. The TECs with high cooling power capacities are nominal, a significant thermal enhancements could be achievable when currents and cooling configurations are optimized [14].

With the successful implementation of the multistage converter this cooling arrangement can be easily supplied from a PV panel with a DC-DC converter. The input power to the DC converter will be supplied from an input solar panel, the use of PV as a source of power for the converter, in which it could be a reliable solution for outdoor cooling applications where it is hard to find a source for powering the cooling components for the system.

3. Analysis

The non-inverting capacitance voltage divider current stress on static switches is quit reliable, whereas during the On-state of switch the boost originally switch handle the

input current, and the other switches the current passes through S2,S3 and S4 is Io/3 per switching leg, which leads to reduction of the dissipated power.

With a similar way of analysis of single stage converter, the input/output voltage relation can be derived as given by:

$$V_o = \frac{DV_i}{3(1-D)} - \frac{D^2 V_{RS}}{3(1-D)} - DV_{RD} - DV_{RS} \quad (1)$$

By neglecting the voltage drop (V_{RS}, V_{RD}) then the output voltage is given by

$$V_o = \frac{DV_i}{3(1-D)} \quad (2)$$

And

$$D = \frac{3V_o}{V_i + 3V_o} \quad (3)$$

where D is the duty cycle.

4. Applications

Plate 1 shows a developed prototype for TEC cooling. This prototype uses 4 TECs of 15x15x3 mm size attached to the four sides. This prototype is tested using the converter and draw a current of 2 to 5 amps.

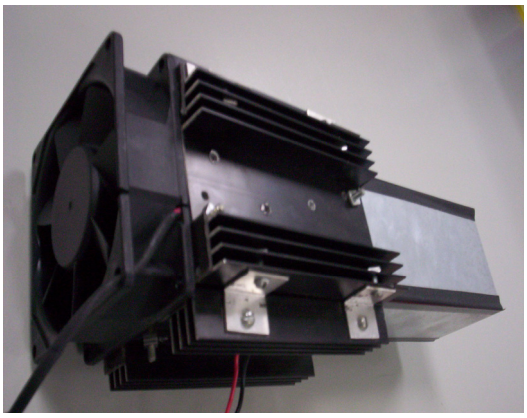

Plate 1: A pre-developed TEC cooling prototypes.

The Plate 2 shows the TEC modules attached to heat sink (30x17x4 cm), then the spaces have to be filled by polytetrafluoroethylene (PTFE) thin sheets, the cold side of TEC modules then being covered by an aluminum sheet as shown in Plate 2.

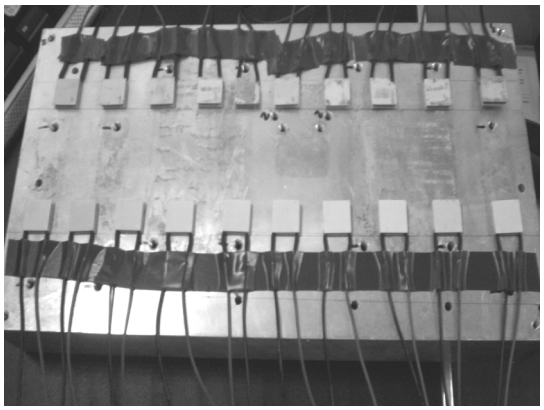

Plate 2: TEC modules attached to heat sink

The testing carton box been coated with a polytetrafluoroethylene (PTFE) sheets is used as a cabinet enclosure for testing the TEC functionality. The TEC was connected as a parallel of two series connected TEC's, these TEC's require a current of about 12A, which is provided by the converter.

5. Results

A. Simulation Software

The SIMCAD program is used for the evaluation of the proposed circuit. The PWM control driving signal for power MOSFETs can be generated by PWM IC control model using current or voltage mode voltage regulation. The useful of power measurement integrated feature allows easier observation for system dynamic performance. The power switched considered to be ideal thought out circuit simulation, so it will be operated as a traditional switch in ON and OFF states.

B. Measured and Simulated Results

Figure 5 shows the simulation of input and output current waveforms, the upper is the converter output current and the lower is the input current.

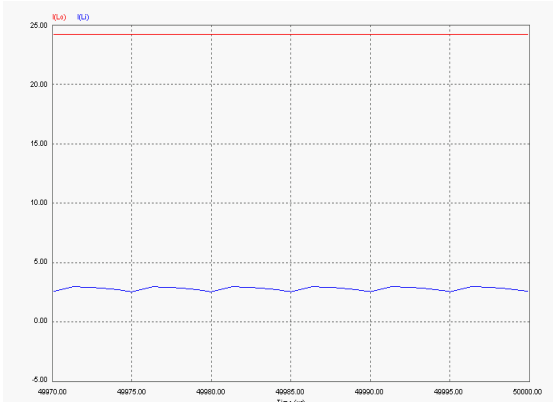

Figure 5. The input and output current waveforms

Figure 6 show the measured waveform of the voltage across the power switch S1 was matched with the waveform obtained from simulation that is illustrated in Figure 7. Also Figure 7 shows the simulated current

through the switch S1, the maximum current being about 3.5A

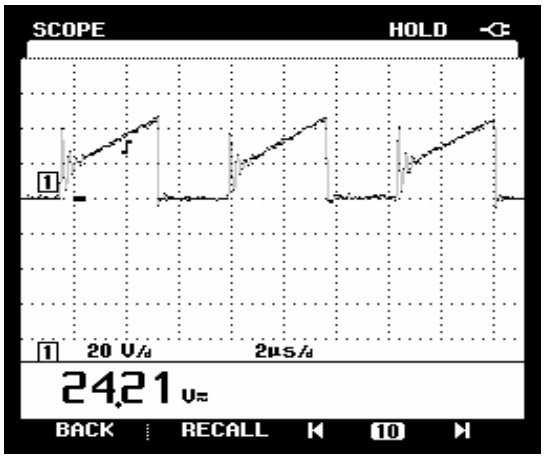

Figure 6 Measured voltage across MOSFET S1

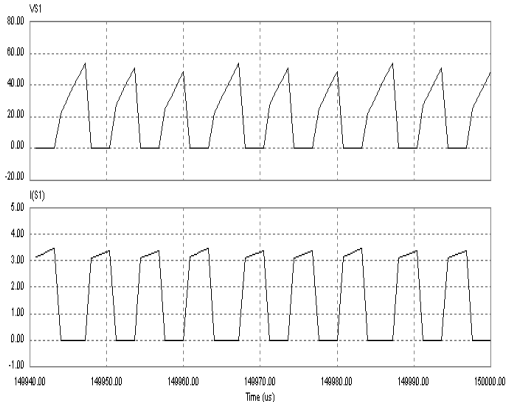

Figure 7 Simulation waveforms of MOSFET switch S1

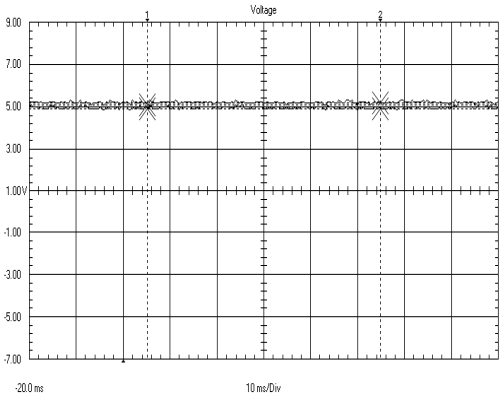

Figure 8. Measured output voltage V_o with Fluke power quality analyzer

Figure 8 shows the measured output voltage analyzed buy Fluke power quality analyzer software. The simulation results of output current and voltage are shown in Figure 9, the upper waveform shows the output current, and the lower one shows the output voltage.

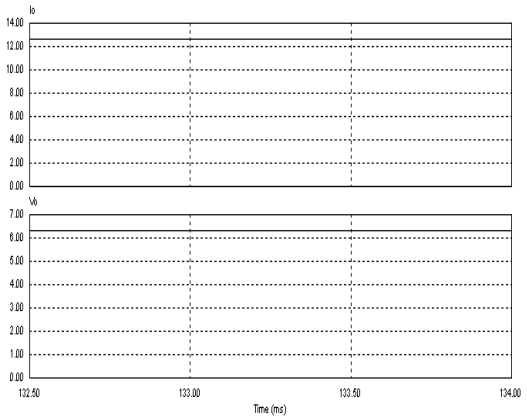

Figure 9. Simulated output voltage and current

Figure 10 shows the converter efficiency versus output power. The figure shows the efficiency at power ranges up to 70W. The figure also shows the converter ability to supply the rated load with efficiency up to 80%. As illustrated in the figure the converter efficiency varies with load change from 35% up to 80% at full load.

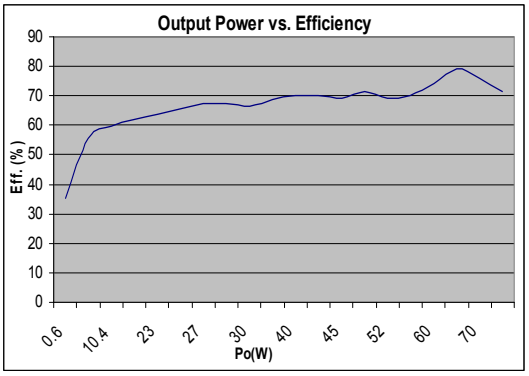

Figure 10 Output power versus efficiency

Plate 3 shows the practical implementation of the power circuit PCB board of the converter, and Plate 4.4 shows the power circuit PCB board.

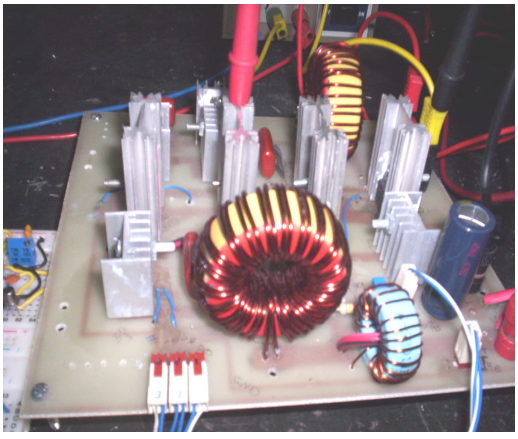

Plate 3. Power circuit PCB board

6. Conclusion

The design of transformer-less converter for low voltage and high current is presented in this paper. The topology was used for device cooling system. For application up to 70 W the topology had show a maximum efficiency of 80%. The implemented converter found to be suitable to supply TEC load connected to PV power source for outdoor application.

References

[1] W. Huang, K. Yen, G. Roig, and E. Lee, "Voltage divided noninverting Cuk converter with large conversion ratios", in IEEE Proc. 1991, II-1005-II-1007.

[2] R. D. Middlebrook, "Transformerless DC-to-DC Converters with Large conversion Ratios", in IEEE Transaction on Power Electronics Vol. 3, NO.4, 484-488, October 1988.

[3] B. Bryant, M.K. Kazimierczuk, "Derivation of the Cuk PWM DC-DC converter circuit topology" in Proc. 2003 International Symposium Circuits and Systems, III-292-III-295.

[4] K. Kumabara and E. Miyachika, "Switched-Capacitor DC-DC Converter", Telecommunications Energy Conference, 1988. INTELEC '88., 10th International, 213 – 218 ,1988, Japan.

[5] J. Liu, Z. Chen, Z. Du, Switched capacitor DC-DC converters enable electronic products to become more compact, in Proc. 1996 IEEE Semiconductor Electronics, Conf., 234–237.

[6] S.V. Cheong, S.H.Chung, and A. Ioinovici, Development of power electronics converters based on switched-capacitor circuits, in Proc. 1992. IEEE Circuits and Systems, 1907-1910.

[7] Optimizing TEC Drive Current Application Note. Available at: www.ilxlightwave.com, 2008.

[8] Thermoelectric Handbook, Available at: www.melcor.com, 2008.

[9] Jin, W., Z. Ke, and J. Friend. Minimum power loss control thermoelectric technology in power electronics cooling. Proc of IEEE Energy Conversion Congress and Exposition (ECCE). 2009.

[10] K.A. Moores, Y.K. Joshi, G. Miller. Performance assessment of thermoelectric coolers for use in high temperature electronics applications. Eighteenth International Conference on Thermoelectrics, 1999, 31 – 34.

[11] Bierschenk, J. and M. Gilley. Assessment of TEC thermal and reliability requirements for thermoelectrically enhanced heat sinks for CPU cooling applications. in International Conference on Thermoelectrics, ICT, Proceedings. 2006.

[12] Kim, O.J. and K.H. Lee. A study on the application of micro TEC for hot spot cooling. in International Conference on Thermoelectrics, ICT, Proceedings. 2007.

[13] Ikeda, M., et al. Thermal performance of thermoelectric cooler (tec) integrated heat sink and optimizing structure for low acoustic noise / power consumption. in Semiconductor Thermal Measurement and Management Symposium, 2006 IEEE Twenty-Second Annual IEEE. 2006.

[14] Zhang, H.Y., Y.C. Mui, and M. Tarin, Analysis of thermoelectric cooler performance for high power electronic packages. Applied Thermal Engineering. Vol. 30, No. 6-7, 2009, 561-568.

JJMIE

Volume 4, Number 1, Jan. 2010
ISSN 1995-6665
Pages 21 - 28

Jordan Journal of Mechanical and Industrial Engineering

Effect of Pressure and Inlet Velocity on the Adiabatic Flame Temperature of a Methane-Air Flame

Rana Haj Khalil [a,*] Ahmad Sakhrieh [b], Mohammad Hamdan [c,*] and Jamil Asfar [b]

[a] *Department of Mechanical Engineering, Philadelphia University Jerash, Jordan*

[b] *Department of Mechaanical Engineering, University of Jordan, Amman, Jordan*

[c] *Al-Zaytoonah Private University of Jordan, Amman, Jordan*

Abstract

The present study focuses on the effect of pressure and high inlet velocity of turbulent premixed flames on the adiabatic flame temperature of a methane-Air Flame. Turbulent premixed flames are widely spread in technical applications and are used especially in stationary gas turbines for a high-efficient and low emission energy conversion of gaseous fuels. The simulation process was performed using Fluent software. The pressure was varied between 2 atmosphere and 10 atmosphere, while the inlet velocity varies between 5 and 10 m/s. it was found that and in general the temperature increase with pressure

Keywords: High pressure combustion, Methane fuel; High Veleocity; Gaseous Combustion.

1. Introduction

Although combustion has been used by mankind for already more than one million year, it is still the most important technology providing the energy supply for our modern day civilizations. Utilization of combustion leads to the release of unwanted pollutants such as carbon monoxide, unburned hydrocarbons and nitric oxides which affect our environment.

Environmental awareness and the need for better and more efficient power generation systems have fueled development of gas turbines for the past two decades. The improvement efforts were focused on reducing NO_X, CO and other pollutant levels in the exhaust, improving efficiency and increasing the reliability of equipments.

Flame temperature is one of the most important properties in combustion, since it has a controlling effect on the rate of chemical reaction. The flame temperature is determined by the energy balance between the reactants and the products at equilibrium. If the reaction zone is spatially very thin in comparison to the rest of the domain of interest, then it is a common practice to denote the maximum temperature in the reaction zone to be the flame temperature. If the combustion process takes place adiabatically, with no work, or changes in the kinetic or potential energy, then the flame temperature is referred to as the adiabatic flame temperature. This is the maximum temperature that can be achieved for the given reactants because any heat transfer from the reaction zone and any incomplete combustion would tend to lower the temperature of the products.

One of the most important parameter in any combustion system is its adiabatic flame temperature, which is the temperature under the condition of no heat loss takes place from the combustion system. This importance arise from the fact that it plays an important role in the pollutants emitted from the system such as carbon oxides and nitrogen oxides, in addition the temperature also affect drastically the thermal stresses set up in the combustion system, such stress may lead to the deterioration of the chamber if not well controlled. Consequently, it is essential and before the construction of the combustion chamber, a simulation process for the temperature distribution within the combustion system must be carefully carried to avoid local thermal stresses and to minimize both nitrogen and carbon dioxides. The concentration of oxides of nitrogen (NO_X) and carbon monoxide (CO), pollutants of great concern, are very much dependent on the flame temperature. [1-4].

2. Theoretical Background

The effect of both pressure and inlet velocity on the adiabatic flame temperature was simulated using a computational fluid dynamics (CFD) software package to simulate fluid flow problems. It uses the finite-volume method to solve the governing equations for a fluid. It provides the capability to use different physical models such as incompressible or compressible, inviscid or viscous, laminar or turbulent, etc. Geometry and grid generation is done using GAMBIT which is the preprocessor bundled with FLUENT.

Corresponding Author. mashamdan@yahoo.com

The model takes into account the following main equations:

Conservation of mass

-The rate of change of mass within any open system is the net flux of mass across the system boundaries

$$\frac{dm}{dt} = \sum_j \dot{m}_j$$

Conservation of species

– Equations tracking the evolution of species within the combustion chamber will be developed on a mass basis .

$$\dot{Y}_i = \sum_j \left(\frac{\dot{m}_j}{m} \right) \left(Y_i^j - Y_i^{cyl} \right) + \frac{\Omega_i W_{mw}}{\rho}$$

where 'm' denotes the total mass within the control cylinder. The species equations are deduced from their multi-dimensional counterparts by neglecting species diffusion terms, consistent with the zero-dimensional assumption.

Conservation of energy.

–The generalized energy equation for an open thermodynamic system may be written as

$$\underbrace{\frac{d(mu)}{dt}}_{\text{Internal Energy}} = \underbrace{-p\frac{dV}{dt}}_{\text{Displacement Work}} + \underbrace{\frac{dQ_{ht}}{dt}}_{\text{Heat Transfer}} + \underbrace{\sum_j \dot{m}_j h_j}_{\text{Enthalpy Flux}}$$

3. Discussion of Results

The general trend of the obtained data is a rapid increase in the temperature within the reaction zone, where the temperature reaches a peak value; this is due to the heat generated as a result of burning of the combustible mixture. Moving away from the reaction zone the temperature either remains almost constant (with a slight drop) or it decreases, this depends on both the pressure within the chamber and on the inlet velocity of combustible mixture.

As indicated in figures 2 though 6, temperature value depends on the pressure, and at any location within the combustion chamber, the temperature increase with pressure, this is due to the fact that the combustion products at this high temperature behaves as an ideal fluid The temperature increases with pressure which is a general behavior of the ideal gas law this is an agreement with Sakhrieh [5]. He studied the effect of pressure on the adiabatic flame temperature at stocichiometric conditions and ambient initial air temperature which is given by the following equation:

Figures 7 through 11 show the variation of adiabatic flame temperature along the combustion chamber as a function of both the pressure and inlet flow velocity. It may be noticed that at any location and for low pressure values (2 to 6 bar), the temperature increases with the inlet velocity of the combustible mixture. This is caused by the increase in the amount of the combustible mixture entering the combustion chamber as a result of the increase in the velocity. Consequently, more heat is generated and hence the temperature increases. However, at high pressure (8 and 10 bar), the adiabatic flame temperature is dominated by the pressure and it decreases with pressure in spite of increasing the inlet velocity, this is might be due to the fact that the high pressure inside the combustion chamber creates a back pressure that apposes the flow of the entering mixture into the chamber and hence a drop in the heat generation and hence lower temperature.

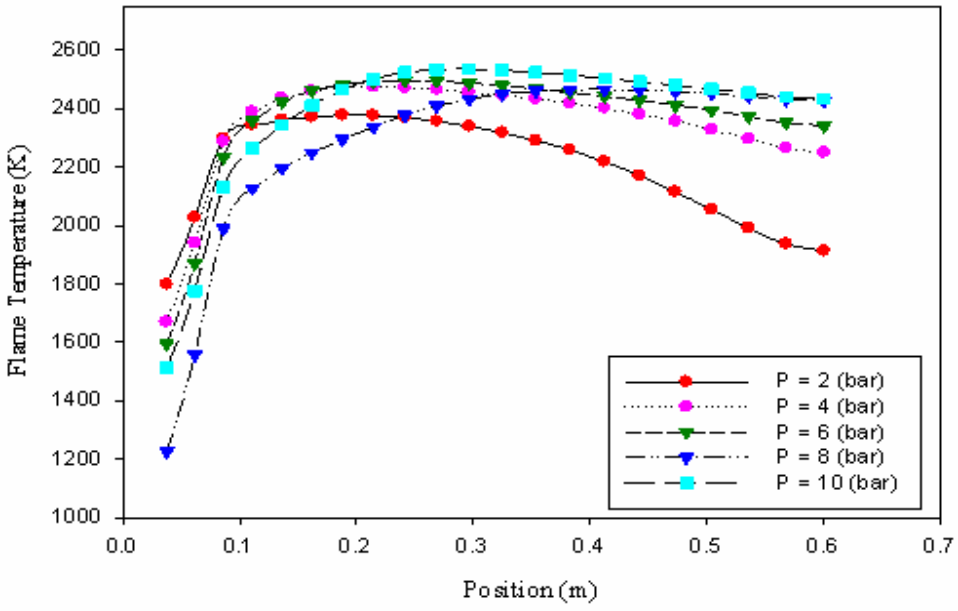

Figure 1. Flame Temperature Distribution, (Velocity = 5 (m/s), at Different Pressures).

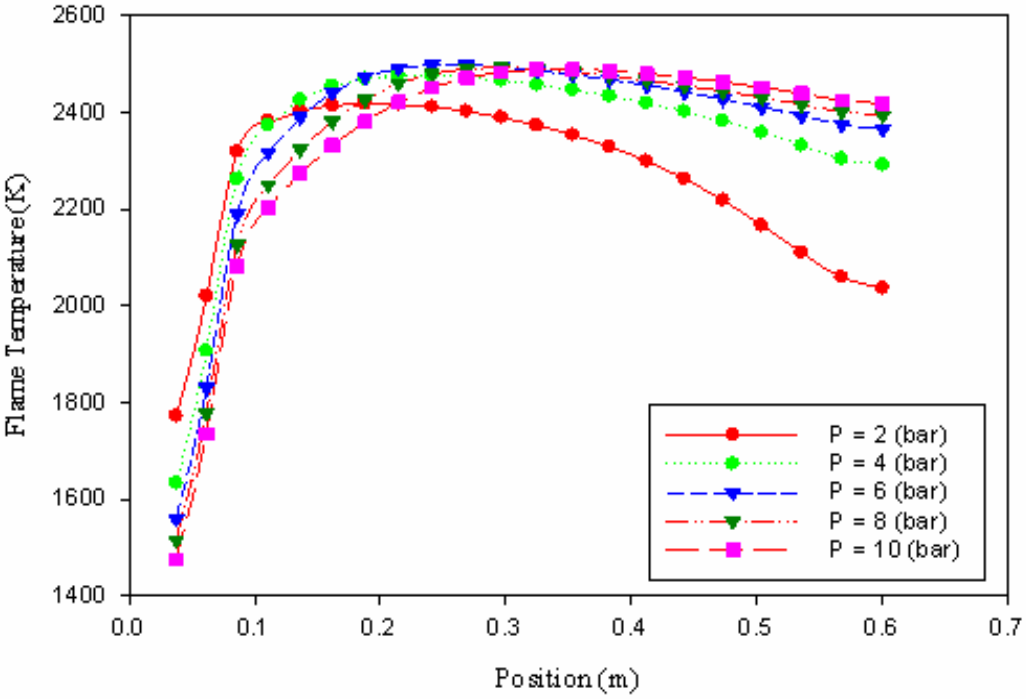

Figure 2. Flame Temperature Distribution, (Velocity = 6 (m/s), at Different Pressures).

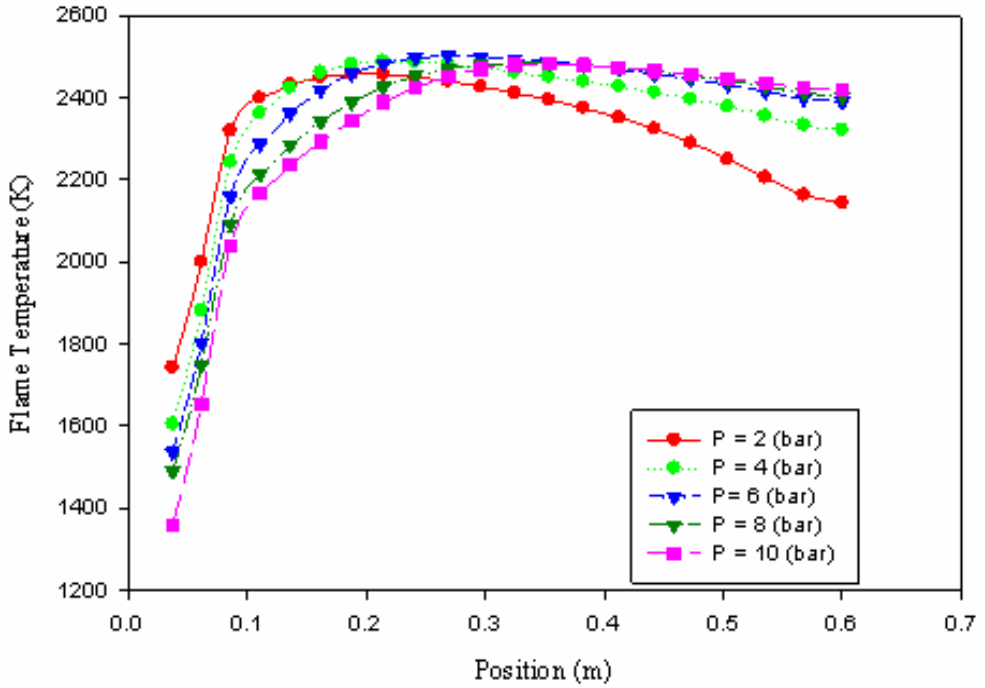

Figure 3. Flame Temperature Distribution, (Velocity = 7 (m/s), at Different Pressures).

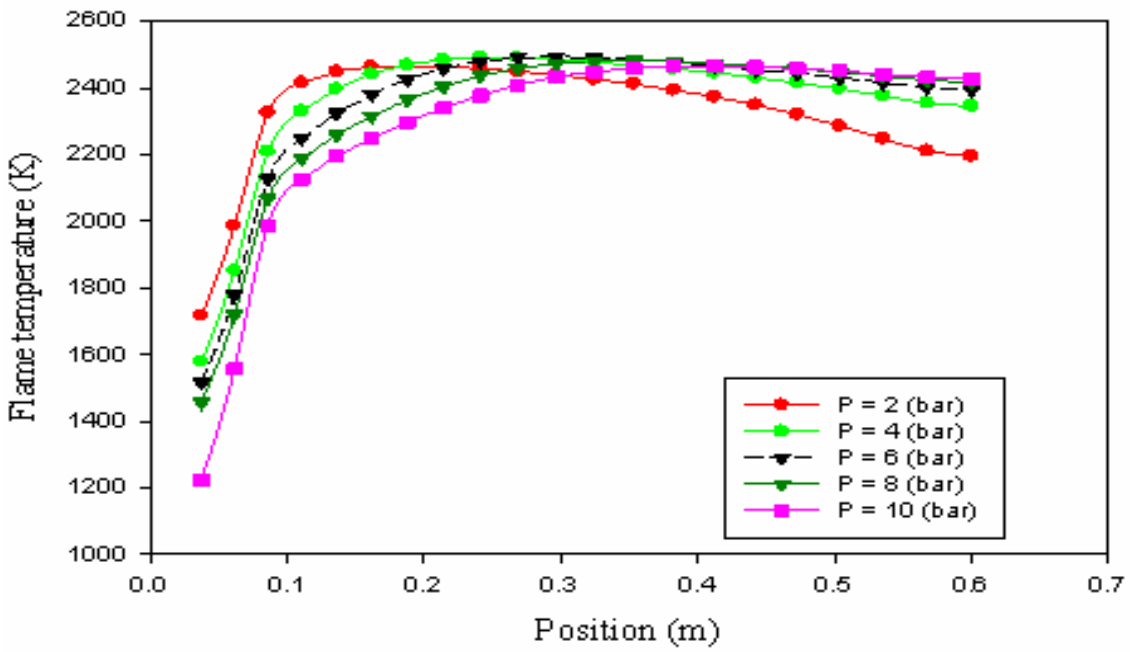

Figure 4. Flame Temperature Distribution, (Velocity = 8 (m/s), at Different Pressures).

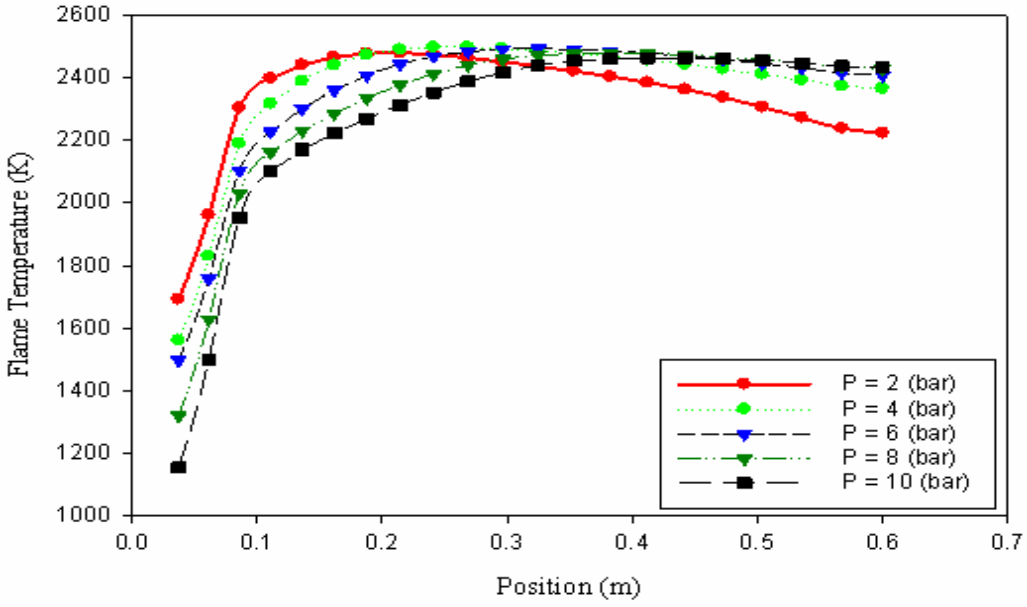

Figure 5. Flame Temperature Distribution, (Velocity = 9 (m/s), at Different Pressures).

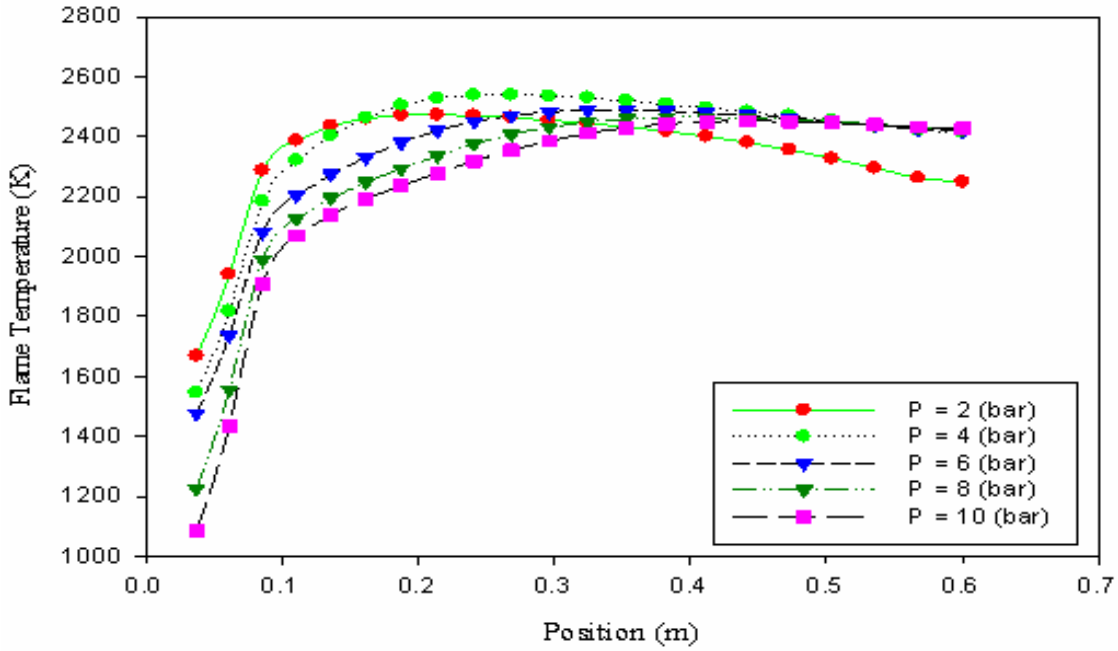

Figure 6. Flame Temperature Distribution, (Velocity = 10 (m/s), at Different Pressures).

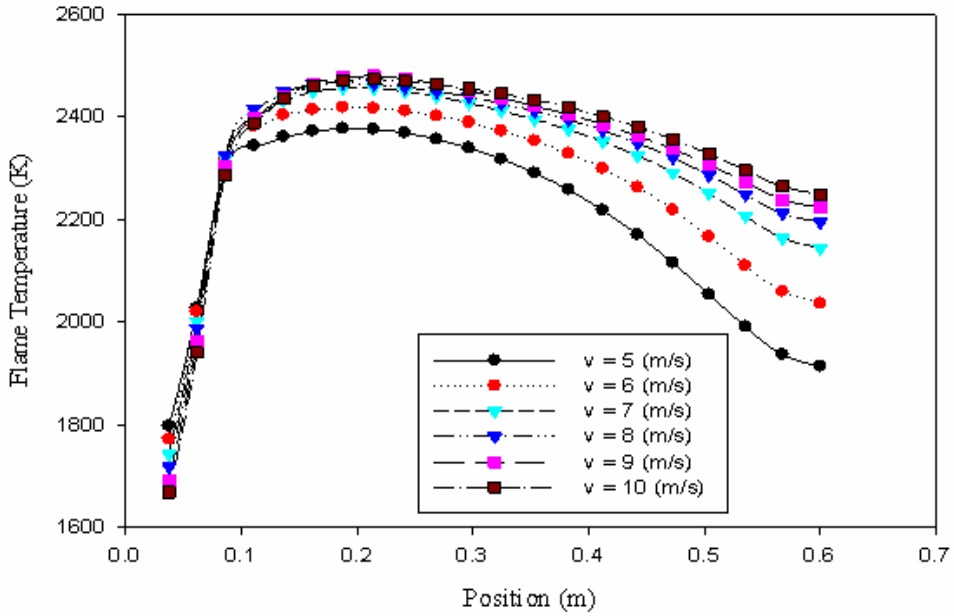

Figure 7. Flame Temperature Distribution, (P = 2 (bar) at Different Velocities).

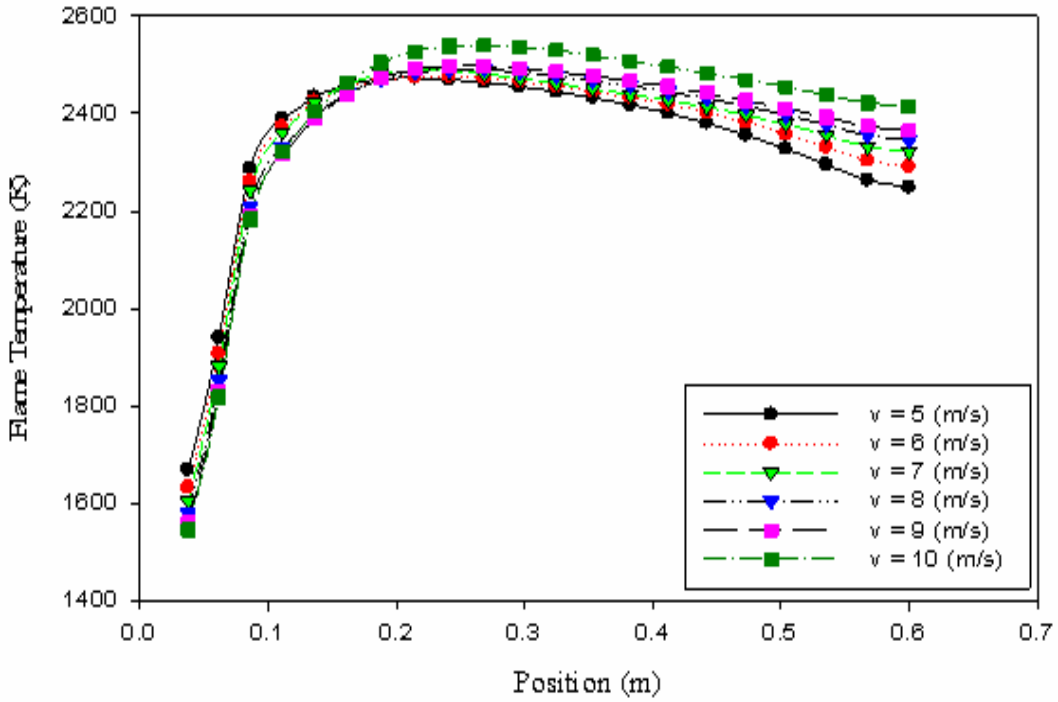

Figure 8. Flame Temperature Distribution, (P = 4 (bar) at Different Velocities).

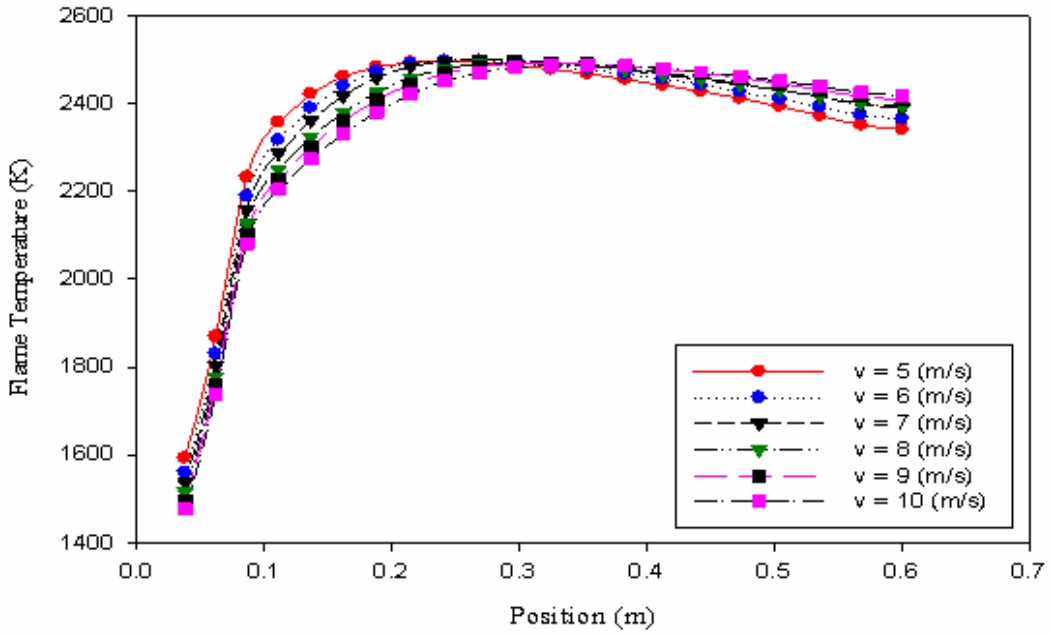

Figure 9. Flame Temperature Distribution, (P = 6 (bar) at Different Velocities).

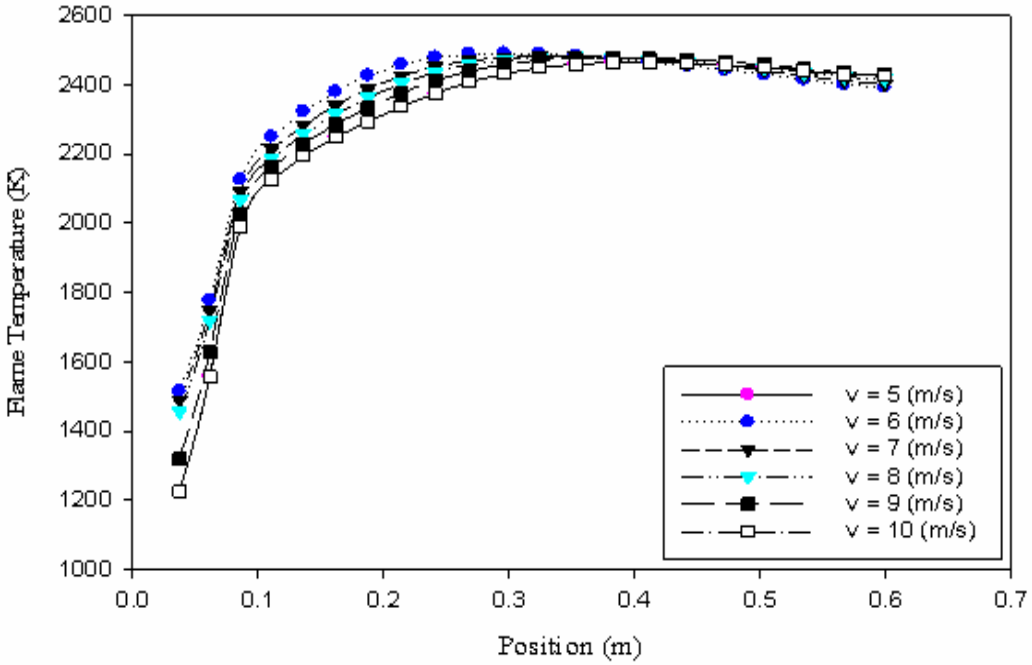

Figure 10. Flame Temperature Distribution, (P = 8 (bar) at Different Velocities).

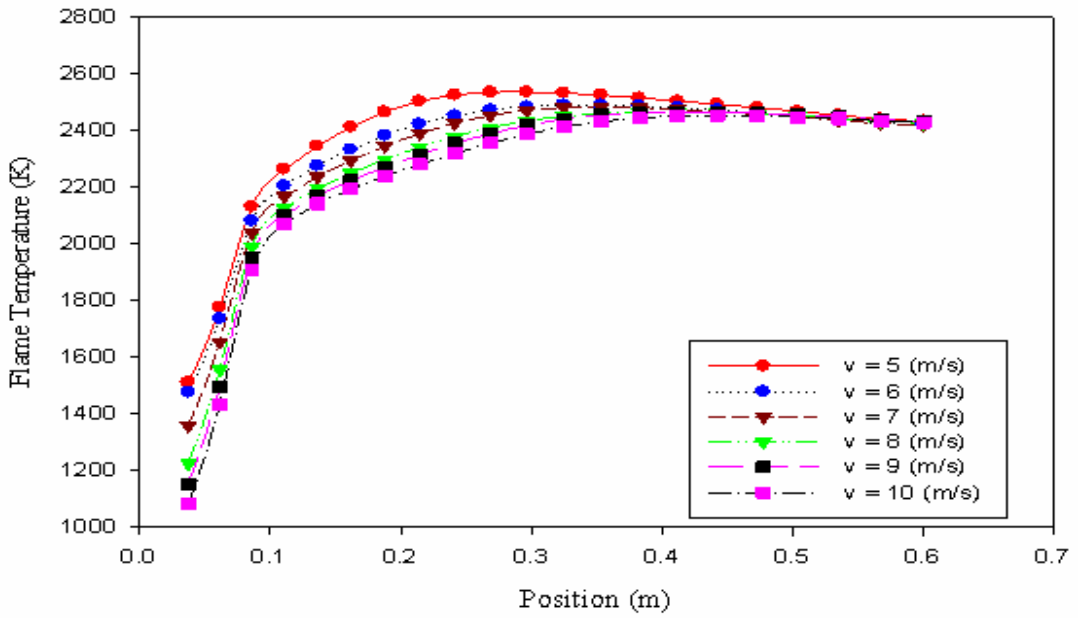

Figure 11. Flame Temperature Distribution, (P = 10 (bar) at Different Velocities).

4. Conclusions

It may be concluded from this work that the Fluent software was successfully used to simulate the variation of adiabatic flame temperature of Methane/air flame turbulent premixed flame. A further will be followed to completely simulate such flame.

References

[1] K.K. Kuo, Principles of combustion, 1st ed. John Wiley & Sons, 1986.

[2] J.F. Griffiths and J.A. Barnard, Flame and combustion, 3rd ed. Blackie Academic & Professional, an imprint of Chapman & Hall, 1995.

[3] I. Glassman, Combustion, 2nd ed. Academic Press, Inc., Florida, 1987.

[4] F.A. Williams, Combustion theory, 2nd ed. Addison-Wesley Publishing Company, California, 1985.

[5] A. Sakhrieh. Reduction of pollutant emissions from high pressure flames using an electric field. Phd thesis. Der Technischen Fakultät der Universität Erlangen-Nürnberg. 2006

JJMIE

Volume 4, Number 1, Jan. 2010
ISSN 1995-6665
Pages 29 - 34

Jordan Journal of Mechanical and Industrial Engineering

Incentives for Technology Development and Project Based Mechanisms: Case of Renewable Energy Project

H. Imai [a,*], J. Akita [b] and H. Niizawa [c]

[a] Kyoto Institute of Economic Research,Kyoto University, Kyoto, Japan

[b] Department of Economics, Tohoku University, Sendai, Japan

[c] School of Economics, University of Hyogo, Kobe Japan

Abstract

Currently, project based mechanisms under Kyoto protocol are prospering while its critical appraisal and examination of alternative options are undergone in the negotiation for post Kyoto schemes. Here, we investigate the mechanism from the viewpoint of new technological development, which is much awaited as the ultimate resolution for the climate change problem. We first lay out a theoretical model based upon economic theory and hint at possible problems. Then taking up the case of renewable energy projects, we illustrate the presence of the possibly negative effect, and compare this mechanism with other policy options raised in the course of negotiation, utilizing theoretical model based on game theory and theory of industrial organization.

Keywords: Clean Development Mechanism (CDM), Renewable Energy Projects, Technology Development, Entry Barrier.

1. Introduction

Project based mechanisms (CDM (Clean Development Mechanism) and JI (Joint Implementation)) are schemes introduced in Kyoto protocol (1997) as the first attempt to introduce a baseline-credit scheme for emission reduction project in developing country (and hence without an assigned limit) as well as in some developed countries (mostly former socialist counties) so that one could utilize those credits into the amount of emission reduction toward the fulfillment of assignment of Green House Gas (GHG) emissions on the part of developed countries (more exactly, signatory of Kyoto protocol called Annex I (or B) countries). These schemes are more complicated than a mere subsidy scheme for emission reduction, and contains immense conceptual difficulty, which made some people dubious of the functioning of this mechanism (see Bohm and Carlen (2002) for example).

Actually, after years of trial and errors, number of registered projects surpassed 1000 (as of 2008) and now, inclusive of proposed projects (i.e. those in pipeline), expected credits may reach 1.2 billion tones, (as of 2008) which may be sufficient to fill the gap between demand and supply in the upcoming emission trade scheme under Kyoto protocol (2008-2012) according to some speculation. (For a general overview of the current state of CDM, see Capoor and Ambrosi (2008) , Lecocq and Ambrosi (2007) for instance.) Many developing countries were rather skeptical of the mechanism when it was proposed, but now they seem to find more interests in this mechanism and the category of eligible projects as CDM projects tend to be expanded (to include programmable CDM and further policy CDM or sector CDM is proposed). By contrast, some parties start criticizing complicated procedure of CDM as a burden, and propose to replace the mechanism by simpler schemes. In short, even though CDM seems to have launched successfully, but there remains a room for farther controversy. JI is similar but since its formal start line is later (i.e. from 2001 for CDM while 2008 for JI), here we shall mostly deal with CDM, and so below CDM is used synonymously with a project based mechanism.

One issue we have raised concerning CDM earlier is the baseline methodologies (Imai and Akita (2003)). Then we analyze the same issue for a private firm operating in an imperfectly competitive industry (Imai, Akita, and Niizawa (2008)). In this paper, we again consider a private firm in an imperfectly competitive industry, but now our focus is on the incentive to undertake CDM projects for firms whose decisions are related through market demands, and its effect on technology development. Many researchers agree that the technological breakthrough is the key to any successful scheme to cope with climate change problem, and the desire for technology transfer is one driving force for project based mechanisms (Youngman et al (2007), and de Coninck et. al. (2007) estimate the extent to which CDM contributes to

* Corresponding author. imai@kier.kyoto-u.ac.jp.

technology transfer). Hagem (2009) deals with this problem based on the same imperfect competition model of Cournot competition. There, the focus is on whether investment is undertaken or not and a comparison is made between CDM and cap-and-trade scheme. Here, our interests are focused on an incentive for technological development from a dynamic viewpoint if an early adoption of a CDM project by some firm affects the incentives of other firms to do so with a possibly improved technology (in terms of emission reduction), and if so, positively or negatively. Earlier, we have investigated a related question if an adoption of a CDM project by one firm could induce other firms to follow the suit (in Imai, Akita, and Niizawa (2007) to find that the possibility is relatively slim). Therefore under the most modes of oligopolistic competition, such effect is negative, and hence incentive for technological development also tends to be hampered, which is what we show below.

2. MODEL

2.1 Setup

Our base model considers the incentive consequences of the CDM in an industry where multiple firms potentially compete. Especially we are interested in the effect of the so-called rate-based (Fischer (2005)), or relative (Laurikka (2002)) (or ex post (Imai and Akita (2003)) baseline upon the firms' decisions and ultimately its impact upon emission saving R&D. (As a matter of fact, this coupled with a cap is the most commonly used baseline setting methods, when applicable.)

We start out with a simplistic setup where there is an incumbent monopolist in the industry, and has a chance to engage in a CDM project. After this period, a potential entrant comes up with a new invention which would lower emission further, and faces a decision whether to engage in a new CDM project based on this invention.

(We could consider a similar problem where two firms face similar decision using the same technology under the same time structure. This gives a certain advantage over the incumbent monopolist under some occasions, which parallels the preemption by an earlier investment opportunity, illustrating some advantage incumbent firms may have, as pointed out in the industrial organization literature. Here, implicitly assuming that different technology is monopolized by each firm. Obviously there are various patterns of the ownership of inventions, and what we assume here is one specific case, with some other arrangement discussed in a separate section below.)

In evaluating the effects of CDM project on the production technology, several factors appear as candidates to be affected other than emission levels and investment costs, i.e. fixed and variable costs of production in general. Here to simplify the analysis, we assume that production is carried out through a technology involving no fixed costs and constant unit costs, which are not affected by the projects. Also we assume that emission level is given by a constant emission factor representing emission level per output. Specifically, we assume that by the incumbent monopolist's project, emission factor is lowered from e(0) to e(1) (<e(0)), while the potential entrant's project brings it down to $0 < e(2) < e(1)$. Investment costs for each project is $I > 0$, and $J > 0$ (with implicit assumption that $J > I$).

The most important supposition we have is the way baseline is set under CDM project. When it is appropriate to consider that without CDM credits, nobody adopts the emission reducing projects, then the use of e(0) as the baseline setting emission factor would be approved by the CDM Executive Board. In fact this is along the spirit of the Marrakech Accord and many registered projects employ this type of baseline setting methodology where the emission level from the project can be safely regarded as emission factor times the scale of operation. Thus, for the incumbent monopolist, if the project is admitted, its credit revenue would be (e(0)-e(1))rq, where q is the output level of the monopoly firm and r is the price of emission right determined by the emission trading market. (Throughout, we assume that the project is small so that the emission price is not affected by the project.)

What would be an appropriate baseline setting would be a more arguable issue for the potential entrant. If the incumbent monopolist did not adopt the project, then e(0) may be safely assumed to be the baseline. What if the monopolist adopted the project? We view that e(1) would become the baseline, as when the entrant's project is introduced, prevailing technology is that of the monopolist and hence e(1) gives the natural standard for that period. This creates a twist in the incentives as the monopolist can affect the marginal revenue (or negative costs) of the entrant by adopting the CDM project. An alternative may be to set baseline at e(0), but unless the entrant had some record of operation with the old technology, we believe it is some what not in line with the possible baseline setting methods listed in Marrakech Accord.

The sequence of decisions is very simple. First, the incumbent monopolist decides whether to adopt the CDM project or not in the period 1. Observing the consequence of the period 1, in period 2, the potential entrant decides whether to enter with its CDM project or not. We analyze the subgame-perfect equilibrium outcome of this game.

2.2 Equilibrium Conditions

First, it would help state the gist of the analysis in terms of abstract framework. Let us $\Pi(c,c')$ stand for profits of a firm (net of CDM investment costs) with the own parameter c while the opponent's parameter c'. Writing by $\Pi(c)$, we indicate that profit when the firm is the monopolist. (Like earlier studies, here we utilize the assumption that the firm maximizes the total profits without specifying the sharing scheme among project participants, meaning investors and hosts. This can be justified by assuming that parties are risk neutral or more conveniently the project is a unilateral CDM project, although which makes the assumption that the technology utilized is a new innovation in doubt.)

Relevant comparisons are the cases where c's stand for constant marginal costs inclusive of CDM (marginal) revenue. That is, c_0 stands for the marginal costs when the incumbent monopoly firm without CDM, c_1 for the monopoly firm with a CDM project, and c_2 for the entrant firm entered with a new CDM project when the incumbent monopolist firm has adopted the CDM project, while c_3 for the entrant firm entered with a new CDM project when the incumbent monopolist firm has not

adopted the CDM project. (we assume that $c_0 > c_1 > c_3$ and $c_2 > c_3$) Thus, $\Pi(c_3, c_0)$ stands for profits of the entrant firm (at period 2) when the monopoly firm did not adopt the CDM project in period 1, and $\Pi(c_0, c_3)$ represents that of the monopoly firm. With a discount factor $\delta > 0$, the total profits of the monopoly firm in this case is given by $\Pi(c_0) + \delta\Pi(c_0, c_2)$. Similarly, $\Pi(c_2, c_1)$ and $\Pi(c_1, c_2)$ represent profits of the entrant firm and the incumbent monopoly firm in period 2 when the incumbent firm engaged in the CDM project, and its total profits are given by $\Pi(c_1) + \delta\Pi(c_1, c_2)$. Finally, if the entrant stayed out, then depending on whether the monopolist employed the CDM project or not, its gross profits are given by $\Pi(c_1) + \delta\Pi(c_1)$ or by $\Pi(c_0) + \delta\Pi(c_0)$. Note that in some occasion, some firm may be forced to exit (or entry is de facto deterred), because of the equilibrium output level becomes 0, but we keep notation for duopoly in the notation we employ here. (As a matter of facts, we shall not focus upon such cases below.)

Now, the equilibria can be classified in terms of these notations:

Case 0: $\Pi(c_3, c_0)$ <J: even without CDM, entry is not worthwhile, and this case is subdivided into two sub-cases—

Case00: $\Pi(c_0) + \delta\Pi(c_0) \geq \Pi(c_1) + \delta\Pi(c_1) - I$: The incumbent firm does not employ the CDM project.

Case01: $\Pi(c_0) + \delta\Pi(c_0) < \Pi(c_1) + \delta\Pi(c_1) - I$: The incumbent firm chooses to adopt the CDM project;

Case 1: $\Pi(c_2, c_1) - J < 0 \leq \Pi(c_3, c_0) - J$: without CDM, the entrant enters;

Case10:

$\Pi(c_0) + \delta\Pi(c_0, c_3) \geq \Pi(c_1) + \delta\Pi(c_1) - I$:the monopolist prefers entry without the own CDM than blocking the potential entry;

Case11:

$\Pi(c_0) + \delta\Pi(c_0, c_3) < \Pi(c_1) + \delta\Pi(c_1) - I$:the monopolist chooses the CDM project for the sake of entry prevention;

Case 2: $0 \leq \Pi(c_2, c_1) - J \leq \Pi(c_3, c_0) - J$: the entry occurs whatever the monopolist chooses;

Case20:

$\Pi(c_0) + \delta\Pi(c_0, c_3) \geq \Pi(c_1) + \delta\Pi(c_1, c_2) - I$: the monopolist still does not wish to engage in the CDM project;

Case21:

$\Pi(c_0) + \delta\Pi(c_0, c_3) < \Pi(c_1) + \delta\Pi(c_1, c_2) - I$: the monopolist adopt the CDM project.

3. Renewable Energy Project

Now, we apply the above model to a renewable energy project. One of the characteristics of energy industry is that there is a tendency for it to be regulated. Regulation often implies that price is not a choice variable for the firm in consideration. Further, the characteristic of some power plants is that it is only economical to operate at its maximal capacity level, so that at least at the plant level, supply of output is more or less fixed.

As for the case of renewable energy supply, there are several instances. In some countries, distribution of power is monopolized, while the market for power generation is competitive, with power distribution company is obligated to purchase supply of renewable energy within certain limit. We shall model this situation below as a simpler case, with another simplifying assumption that the price the entrant receives is the same as the consumer price.

Suppose there is a single firm granted the position of monopolistic distribution firm, which is also a monopolist in power generation at its inception. Potential entrant is a power generation firm with renewable energy. Market demand is fixed at Q, and when the entrant enter, its size of supply is also fixed at q < Q. Price is fixed by the regulator, which we normalize at 1 and all the relevant marginal costs are assumed to be below 1.

Now, the profits for the firms are

$$\Pi(c_0) = (1-c)Q$$

$$\Pi(c_1) = (1-c+r)Q$$

$$\Pi(c_0, c_3) = (1-c)(Q-q)$$

$$\Pi(c_1, c_2) = (1-c+r)(Q-q)$$

$$\Pi(c_2, c_1) = (1-c'+r')q$$

$$\Pi(c_3, c_0) = (1-c'+r+r')q$$

The most interesting case is Case 11, where monopolist adopts CDM project just for the purpose of blocking the entry, and entrant's attempt to enter is deterred. The conditions for this case were:

CDM project itself was not attractive for the monopolist

$$\delta\Pi(c_0) > \delta\Pi(c_1) - I$$

but it is attractive to deter entry

$$\delta\Pi(c_0, c_3) < \delta\Pi(c_1) - I$$

And for the entrant, entry with CDM is attractive if the monopolist has not adopted its CDM project yet,

$$\Pi(c_3, c_0) > J$$

But if the monopolist has adopted its CDM project, entry is not attractive

$$\Pi(c_2, c_1) < J$$

Combining these conditions, we have

$$\delta(rQ + (1-c)q) > I > \delta rQ$$

$$(1-c'+r+r')q > J > (1-c'+r')q$$

This yields simple inequalities for this case to take place.

As we assumed that Q > q, one may question that relationship between I and J may depend upon the size of the operation too, and hence one may alter the setup so that the investment costs are IQ or Jq to eliminate the effect of the size. This yields a slight modification to the above formula

$$\delta(r + (1-c)q/Q) > I > \delta r$$

$$(1-c'+r+r') > J > (1-c'+r')$$

One notable difference would be the role of relative size of encroachment enters into the formula, with an obvious interpretation.

One interesting sub-case worthy of further investigation would be the case where the incumbent monopolist itself adopts a renewable energy project as CDM. In this case, we had better assume J < I, because otherwise, there would be no point for the entrant to enter. Along with the analysis carried out as above, entrant would enter even though there

is no CDM benefits, because its output is purchased by the monopolist as a requirement, whereas monopolist adopts renewable energy already. Thus to consider the potential problems which might occur under this circumstance, one must rethink the supposition that the monopolist's CDM project covers all of its production capacities, or the presumption that the monopolist must purchase all the supplies, which lies outside of the scope of this exercise.

4. Ownership Structure

One important exercise is an examination of the effect of ownership of invention. Suppose the outside R&D firm has the invention corresponding to the technology which we assumed that the potential entrant owns. Then we ask if this R&D firm would sell this technology to the monopolist or to the potential entrant. In other words, which firm would pay higher price for this invention?

To this end, we retain our assumption that the monopolist with own CDM project must apply for the new CDM project (rather than applying for a deviation from the ongoing project) and in that event, baseline is given by the own CDM project. As to the timing of purchase, we assume that the monopolist firm first decides whether to go for its own CDM or not and then together with the potential entrant, it bids for the invention. To examine this situation, there are several alternatives which would affect conclusions. In particular, the way price of invention is set and the possible commitment by parties for the future actions would affect the result significantly. Here, mostly for the purpose of illustrating the similarity of the situation with the case we have already looked at, we employ the assumptions that the R&D laboratory has the power to set the price and that commitment by contract is not possible. Also we omit the first period payoffs, to yield an extensive game.

First, the R&D firm decides whether it invests J to generate this invention or not. Then the monopolist decides whether to its own CDM project (at the cost I) or not. In case where the monopolist has not adopted its own CDM, if the potential entrant obtained the technology, then monopolist's payoff is $\Pi(c_0, c_3)$ while that of the entrant is $\Pi(c_3, c_0) - B$ where B is the price of invention paid. If the monopolist obtained the invention, then its payoff would be $\Pi(c_3) - B$ (assuming that B is all what is necessary to carry out the investment) while entrant's payoff is 0. Thus the maximal amount the monopolist would pay for the invention is $\Pi(c_3) - \Pi(c_0, c_3)$, while that of the entrant is $\Pi(c_3, c_0)$. Therefore, if

$$\Pi(c_3) - \Pi(c_0, c_3) > \Pi(c_3, c_0)$$

then the monopolist obtains the technology and adopts CDM project with this new technology with $B = \Pi(c_3) - \Pi(c_0, c_3) > 0$, while if the opposite inequality holds, then the entrant enters with $B = \Pi(c_3, c_0)$ provided that B covers all the investment costs. (We may add the option for the R&D company not to sell the technology if the price turns out to be negative, but here, non-negativity of the price is assured.)

Next, suppose that the monopolist has adopted CDM project with its own technology. Then the maximal amount the entrant pays for the invention would be $\Pi(c_2, c_1) - B$, with the payoff for the monopolist being $\Pi(c_1, c_2)$. When the monopolist obtains the invention, its payoff would be $\max\{\Pi(c_2), \Pi(c_1)\} - B$, as it can choose to shelve the invention, while entrant's payoff is 0. Thus the price would be $\Pi(c_2, c_1)$ if

$$\Pi(c_2, c_1) > \max\{\Pi(c_2), \Pi(c_1)\} - \Pi(c_1, c_2)$$

And the entrant obtains the technology while when the reverse inequality holds, the monopolist obtains the invention and either applies for the new CDM or shelves the patent. (We assume that the monopolist does not choose to use the technology but not apply for the new CDM, in which case according to the methodology of the old CDM its deviation is too much and so credits would not be awarded. Still there would be a possibility that such technology may bring benefits to the firm by itself, if the new marginal cost other than marginal credit revenue is substantially lowered by the invention.)

The solution of the game we use is again the subgame perfect equilibrium (which is given by a procedure called backward induction, part of which we have already described). In fact the optimal solution is easily understood once one realizes that in the event that the monopolist has not adopted its own CDM project, then irrespective of the identity of the firm which obtained the technology, the monopolist's payoff is given by $\Pi(c_0, c_3)$ whereas in the event that the monopolist firm adopted its own CDM project, then its payoff would be $\Pi(c_1, c_2)$. This yields exactly the same result as we had before which is due to the assumption that the R&D firm has the right to set the price.

Another possibility would be the case where the potential entrant possessing the new technology may sell (or the monopolist can buy out) the technology. This essentially is tantamount to the case of merger and so by this the problem of mal-alignment in incentives would be eliminated.

5. Sectoral Credits and Other Policy Measures

One proposal as a replacement of CDM is sectoral credit system. Under this scheme, the government of a developing country delineates a certain sector with a target emission level, and any reduction in emission achieved relative to this target level is awarded as credits, which are supposed to be traded in the emission trading markets. No penalty is imposed even if emission turned out to be above the target level (called the "no lose" feature. Other than that the system works more like ex ante baseline, the difference is more on the type of actors, i.e. in CDM, private entities are the main actors, while under this system, government is the primary actor. Of course, in order to provide incentives for the sector to cut down emission beyond the target level, the government could employ several measures, like a domestic cap-and-trade system or other reward system where the government provides reward in proportion to the emission reduction, for instance, but it is up to each government. Note that some

reduction by one firm may be cancelled out by the extra emission by another firm and so there may be no smooth connection of the domestic market with the international emission trading market.

Since one cannot pin down a particular policy measure the government would employ domestically, direct comparison is not that easy. One possibility is that the government can internalize all the difficulties raised above by ideally rewarding the new and improved technology, so that within the confine of market-based incentive, sectoral credit system works better. However, as is the case with the grand-fathering according to the past performance in the allocation of quota, there could be a beneficial treatment biased toward existing firms which may hamper the development incentives of potential entrants in the case of domestic market. In fact, in the case discussed above, if the monopolist is allocated the amount the same as the emission level in the previous period, while the new entrant has no allocated amount (but with renewable energy, no emission results), the incentive for the entrant to enter with better technology is worse. Some strange effect is that now the monopolist may welcome new entrant because by the amount of demands it loses, extra emission right could be sold, (if it can be sold to entities in the other sector). Let us formulate this problem.

Despite of the caveat above, suppose that the emission price is the same as the world market price. The monopolist's profit would be

$$\Pi(c_0) = (1-c)Q$$

$$\Pi(c_1) = (1-c+r)Q$$

$$\Pi(c_0, c_3) = (1-c)(Q-q) + \pi q$$

$$\Pi(c_1, c_2) = (1-c+r)(Q-q) + \pi q$$

$$\Pi(c_2, c_1) = (1-c')q$$

$$\Pi(c_3, c_0) = (1-c')q$$

Now, in this setup, one easily sees that there is no entry deterrence, as the profits for the entrant remains the same regardless of monopolist's adoption of the emission reduction technology on its own. At the same time, there is no extra incentive for the entrant to introduce better technology. By contrast, the monopolist wishes the entrant to enter, as its own emission is reduced by the amount the entrant steals from the monopolist. The decision to adopt its own emission reduction technology is now made purely by its own profit criterion. This is a quite extreme story. However, it seems that the defect of cap-and-trade system in this regard deserves further attention.

For developing countries joining the CAP-and-trade system either sector-wise or nationally is another alternative. This shares the same properties as above without the possible gap between domestic and international emission credits. R&D incentive of this scheme with patent system in comparison with public reward scheme is a well known topic in the theory of R&D economics.

Yet another policy option is the GIS (Green Investment Scheme) where world organization or developed nation provides money in an upfront manner, with a promise of developing nation engaging in an emission reduction project. This scheme overcomes the difficulty of transaction costs associated with baseline-credit scheme, while the well known problems are the ability to evaluate the appropriate amount to be given for the project before actual project is carried out and the lack of incentives to monitor after the fact as to whether the execution of the announced project is exactly carried out or not. Although immune from the problems raised in this paper, the extent to which this scheme contributes to the incentive to develop technology depends upon the way the reward is given, detail of which is not that clear at this moment.

6. Further Extensions

Numerous extensions are possible and desirable. Among those, we pick up three such possibilities.

First, one of the fundamental nature in the environmental problem is the presence of uncertainty associated with it, and so incorporating uncertainty into our model would be of primary importance. In the current context, one uncertainty may be that of emission price. This issue is related to the problem that if in developing countries, entrepreneurs are more risk averse, which is in part disproved by the prevalence of unilateral CDM, while some claims that the fact that not many ambitious projects are undertakes in CDM may substantiate the above claim to some extent.

Another natural extension would be considering multiple firms. For instance, one can think of the case with multiple incumbent firms. Here, as is well known (and as we show in Imai, Akita, and Niizawa (2008)), the impact of a single firm's entry becomes alleviated, and thus the incentive to preempt again is mitigated. One could similarly extend toward multiple entry firms, and a sequence of entrants in the multi-periods setting.

Finally, and related to the above issues are the dynamic nature of the issues. Especially, development of one technology affects the future incentive for further development. There are several simple dynamic models in the industrial organization literature, and examination of this problem along with those models would be fruitful.

All these are the agenda for future research.

Acknowledgments

The authors acknowledge the financial aid by Japanese Ministry of Education, Culture, Sports, Science and Technology (MEXT), Grant-in-Aid for Scientific Research (B) 18310031.

References

[1] Bohm, P., and Carlen, B., A Cost-effective Approach to Attracting Low-income Countries to International Emissions Trading: Theory and Experiments, *Environmental and Resource Economics*,Vol. 23, 2002, 187-211.

[2] Capoor, K. and Ambrosi, P. .State and trends of the carbon market 2008., The World Bank and International Emissions Trading Association, 2008.

[3] De Coninck, H., Haake, F., and van der Linden, N. Technology transfer in the Clean Development Mechanism. *Climate Policy*, Vol. 7, 2007, 444-56.

[4] Fischer, C..Project based mechanisms for emission reductions: balancing trade-offs with baselines. *Energy Policy*, Vol.33, 1807-1823.

[5] Hagem, C. , The clean development mechanism versus international permit trading: the effect on technological change. *Resource and Energy Economics*, Vol. 31, 2009, 1–12.

[6] Imai, H. and Akita, J. On the incentive consequences of alternative CDM baseline schemes., in T.Sawa (ed.) *International Frameworks and Technological Strategies to Prevent Climate Change*, Tokyo: Springer Verlag, 2003, 110-126..

[7] Imai, H., Akita, J. and Niizawa, H. *CDM domino*, in L. Petrosjan and N. Zenkevich eds., *Contributions to Game Theory and Management*, Graduate School of Management, St. Petersburg State University, 2007, 177-188.

[8] Imai, H., Akita, J. and Niizawa, H. Effects of alternative CDM baseline schemes under imperfectly competitive market structure., A.Dinar, J.Albiac and J.S.Soriano (eds.) *Game Theory and Policy Making in Natural Resources and the Environment*, Routledge, 2008, 307-333.

[9] Laurikka, H..Absolute or relative baselines for JI/CDM projects in the energy sector?., *Climate Policy*, Vol. 2, 2002, 19-33.

[10] Lecocq, F. and Ambrosi, P.The clean development mechanism; history, status, and prospects., *Review of Environmental Economics and Policy*,Vol. 1, 2007, 134-151.

[11] Youngman, R., Schmidt, J., Lee, J. and de Coninck, H. , Evaluating technology transfer in the Clean Development Mechanism and Joint Implementation. *Climate Policy* Vol. 7, 2007, 488-99

JJMIE

Volume 4, Number 1, Jan. 2010
ISSN 1995-6665
Pages 35 - 44

Jordan Journal of Mechanical and Industrial Engineering

Laboratory and Field Scale Bioremediation of Tetrachloroethene (PCE) Contaminated Groundwater

J. Ibbini [a,*], S. Santharam [b], L. C. Davis [c] and L. E. Erickson [d]

[a] *Hashemite University Zarqa, Jordan,* [b]*Engineering associate in the Municipal Programs Section, Bureau of Water, at Kansas Department of Health and Environment, Topeka, U.S.A*

[c] *Department of Biochemistry, Kansas State University, Manhattan, KS, U.S.A,* [d]*Department of Chemical Engineering, Kansas, U.S.A*

Abstract

Bioremediation studies were conducted at a tetrachloroethene contaminated site located in Manhattan Kansas. A former dry cleaning facility was in operation for 30 years. Shallow and deep aquifers down gradient from contaminated site were found to be contaminated with PCE and it's degradation products all above their Maximum Contamination Limits (MCL's). PCE concentration in groundwater at the pilot study area was about 15 mg/L (ppm) in the deep zone and 1 mg/L in the shallow zone. Lab scale microcosms were prepared with different nutrients like soy oil methyl esters (SOME), yeast extract (YE), glucose, lactate, methanol and cheese whey for biostimulation experiments, and commercially available KB-1 bacterial culture was used to bioaugment PCE degradation. Biostimulation of the natural ground water and soil microflora did not completely degrade PCE as cis-DCE (c-DCE) accumulated in the sample. Bioaugmented microcosms containing YE and SOME created reducing conditions for KB-1 culture, resulting in ~ 90% dechlorination of PCE. Cheese whey microcosms with concentrations of (0.01% to 0.025%) reduced PCE, while 0.05% cheese whey and higher inhibited the KB-1 culture. This inhibition was due to a drop of pH that inhibited the bacterial culture activity. At pilot study area, tracer studies were conducted to monitor the direction and velocity of groundwater before during and after remediation experiments. Several nutrient feeding events took place during biostimulation and bioaugmentation. Results indicate that complete degradation of PCE occurred when KB-1 culture containing *Dehalococcoides* bacteria was introduced under anaerobic conditions. The total chlorinated ethenes (CEs) decreased by about 80% in the pilot study area due to bioremediation. Biodegradation of CEs continued for a long term (several months) after the addition of nutrients.

Keywords: Bioremediation; Chlorinated ethenes; PCE; Dehalococcoides.

1. Introduction

Tetrachloroethene, also known as Perchloroetheylene (PCE) is a common groundwater and soil contaminant. It's widespread application mainly at degreasing and dry cleaning sites has lead to its accumulation in natural systems (SCRD, 2007). Chlorinated solvents are considered the second most abundant contaminants after petroleum hydrocarbons (Sutfin, 1996). Acute (short term) exposure to PCE through inhalation may include irritation to upper respiratory tract and eyes, kidney dysfunction, dizziness, headache, sleepiness, and unconsciousness. While Chronic (long term) inhalation of tetrachloroethene have neurological effects, including sensory symptoms such as headaches, impairments in cognitive and motor neurobehavioral functioning and color vision decrements (U.S. EPA, 1994).

A number of abiotic processes may degrade chlorinated ethenes under both aerobic and anaerobic conditions. Abiotic pathways include hydrolysis, elimination, dehydrohalogenation and hydrolysis. Many abiotic transformations of chlorinated ethenes occur at rates that are too slow to have significance in contaminant removal (AFCEE, 2004). Bioremediation, both natural and enhanced, has proven to be a powerful approach for remediating chlorinated solvents, including PCE (Cupples et al. 2004; Lee et al. 1997; Maymo-Gatell et al. 1997). Under anaerobic conditions PCE is sequentially reduced to less-chlorinated and or non-chlorinated ethenes were chlorine atom is replaced by hydrogen in a process called reductive dechlorination that is also referred to as halorespiration (Bradley and Chapelle, 1999) (Figure 1). PCE, which contains four chlorine atoms, is sequentially degraded to TCE to DCE to VC and then to ethene. The process depends on environmental factors that include the presence of strongly anaerobic conditions, availability of fermentable substrates, generation of molecular hydrogen (H2) and the presence and viability of the appropriate microbial population to facilitate the reaction (Major et al., 2002). So far Dehalococcoides bacteria can degrade PCE to the final end products and they depend on hydrogen as the electron donor. The role of other anaerobic bacteria in

Corresponding author, jhibbini@hu.edu.jo

the culture comes in providing the Dehalococcoides with the necessary hydrogen by fermenting utilizable substrates such as lactate, molasses, hydrogen releasing compound (HRC), emulsified vegetable oil, chitin, etc. (Newell et al. 2000). In this work, a biostimulation/bioaugmentation studies were carried out in lab scale microcosms and field pilot scale designed for a PCE contaminated site in Manhattan, KS (Figure 2). Biostimulation and bioaugmentation were used to enhance the rate and extent of biodegradation.

2. Materials and Methods

Ground water sampling

Ground water samples were collected from monitoring wells using a three stage pump. Three water samples were collected from each monitoring well with 5 ft (1.5 m) spacing between them, across the lower portion of the screened zone. Shallow wells were sampled at 18 (5.5 m), 23 (7 m) and 28 (8.5 m) ft below ground surface (bgs), while water from the deep wells was collected at 42 ft (13 m), 47 ft (14.3 m) and 52 ft (16 m) bgs. This sampling allowed detection of a concentration gradient in the monitoring wells and /or it could be considered as triplicate sampling from the same well. Order of sampling was always from the top to the bottom of the well. Samples were collected in 16.5 mL glass vials, filled to the top, and then immediately capped with mininert caps. Vials were then transported to the lab, and 1 mg/L resazurin added as a redox indicator. A 5 mL sample was taken out of the vial with a syringe leaving 5 mL of headspace. While liquid removed, the cap was loosened to allow air replacement. Vials were manually shaken and let stand at least an hour before head space analysis. The water removed was preserved in glass vials, closed with screw caps and stored in a cold room (4ºC) for ion analyses the same day.

3. Microcosms Preparations

Reagents and Supply

Chemicals used in this research included, D-Glucose (Fisher Scientific, Fair Lawn, NJ), Yeast Extract (Sigma-Aldrich, Inc. St. Louis, MO), Soy Oil Methyl Ester (AG Environmental Products, L.L.C.), Methanol (Certified A.C.S. Fisher scientific Co. Fair lawn NJ), Lactic acid (Sigma-Aldrich, Inc. St. Louis, MO), Cheese Whey (AlmaCreamery, KS), Resazurin (Baltimore Biological Laboratory Inc. Baltimore, MD). Chlorinated ethenes were obtained from: PCE (Certified A.C.S., Fisher Scientific Co. Fairlawn NJ), TCE (Aldrich Chemical Co. Inc., Milwaukee WI), cis-1,2-DCE (Chem. Service. West Chester PA. Purity 99.4%), VC (Chem. Service. West Chester PA), methane (Matheson Gas Products, A division of Will Ross Inc., E. Rutherford, NJ). The microbial culture KB-1, which was used in microcosm experiments was kindly provided by SiREM laboratories in Ontario, Canada. A 20 L batch of of KB-1 was purchased from SiREM for the pilot study (Figure 2.3). Hamilton gas tight syringes (Hamilton Company, Reno, Nevada) were used to inject gas phase samples into the gas chromatograph with 26 gauge needles, (SUPELCO, Bellefonte, PA). The clear glass 16.5 mL vials fitted with mininert Teflon caps were obtained from SUPELCO (Bellefonte, PA).

4. Water Microcosms

Water microcosms were prepared from different monitoring wells, at different times, to study the appropriate combinations of nutrients for biostimulation and bioaugmentation studies. Water was collected from wells into 1 L glass bottles, filled to the top, immediately capped, and brought to the lab. Microcosms were prepared by adding treatment nutrients to 16.5 mL glass vials, and then transferring water collected from the site so that final volume was 11 mL. Resazurin was added (1 mg/L) as a redox indicator. Vials were flushed with either argon or nitrogen to maintain anaerobic head space and sealed with mininert Teflon caps. Then 0.5 mL of PCE saturated gas was introduced to the treatment vials for water collected from monitoring wells other than MW-5 (which already contained high PCE). The vials were shaken and allowed to equilibrate for a few hours to overnight before analysis. Vials were maintained under ambient conditions for the duration of the experiment. Headspace analysis was done with a gas chromatograph. The KB-1 bacterial consortium from SiREM was used for bioaugmentation. The culture is sensitive to oxygen, so microcosms were first stimulated with nutrients before adding 10 µL of KB-1, usually after 2-3 days, when resazurin was reduced from blue to colorless. Redox potential at the colorless stage of resazurin is -100 mV or lower, which is optimum for KB-1 microorganisms.

5. Cheese Whey Microcosms

Several microcosm experiments were prepared using liquid cheese whey. Cheese whey contains 5% lactose and therefore different concentrations were used in microcosms ranging from 0.01 to 0.5 percent of lactose content. Whey was used as sole nutrient and carbon source, or amended with soy oil methyl esters. One set used cheese whey that was filtered through 0.22 µm filter (CAMEO 25 NS Nylon filter) to eliminate microbial competition with KB-1. Microcosms with and without KB-1 were compared. Water from monitoring wells 5D, 8D and 9D was used for different sets of vials and the same method was used, as described above in water microcosms section. All microcosms were prepared in 16.5 mL clear glass vials, topped with mininert caps. Total volume of liquid phase was 12 mL. Resazurin (1 mg/L) was added as a redox indicator, and vials were flushed with nitrogen gas (30 s) after preparation and sealed immediately.

6. Pilot Study

Bioremediation Implementation

Nutrient injection

Table 1 lists the amount of each supplement and the tracer added to the nutrient solution during the injection on August 18, 2005. Glucose (40 g) and yeast extract (10 g)

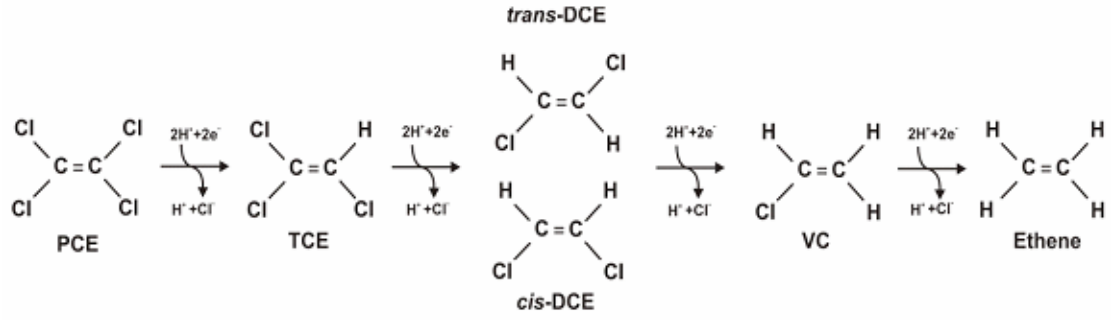

Figure 1. Sequential reduction of PCE to ethene by anaerobic reductive dechlorination adapted from (AFCEE, 2004).

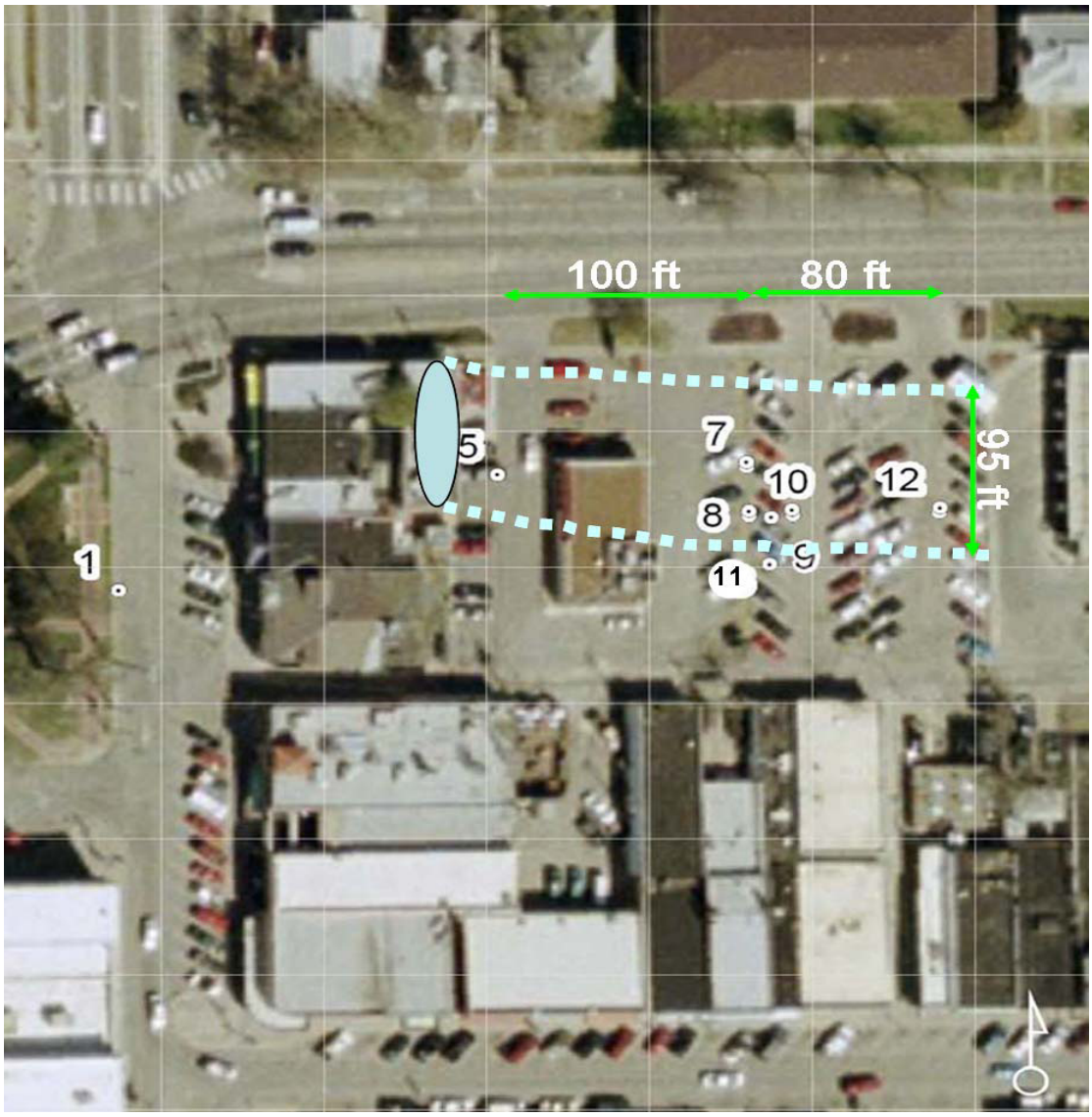

Figure 2. GIS aerial map showing location of PCE source (Oval shape), direction and width of contaminating plume (Dashed lines) in the pilot study area.

Table 1. Amount of SOME, lactate, yeast extract and KBr added in the nutrient solution for injection on August 18, 2005.

	Deep Zone		Shallow Zone	
Water (L)	188		197	
Nutrient/Tracer	**Mass (kg)**	**Concentration (%)**	**Mass (kg)**	**Concentration (%)**
SOME	8	4	2	1
Lactate	0.8	0.4	0.8	0.4
YE	2	1	0.2	0.1
KBr	0.2	0.1	0.2	0.1

were added to approximately 200 L of groundwater on August 15, 2005 and incubated to obtain the anaerobic chase water. Soy oil methyl ester (SOME) acts as a slow electron donor while lactate and glucose (in chase water) act as fast electron donors to reduce the redox potential of groundwater. Yeast extract (YE) was added as a source of vitamins and minerals. Groundwater from MW-10S and MW-10D was pumped into four 55 gal barrels (approximately 200 L each) for preparing nutrient solution and anaerobic chase water. Injection of nutrient solution and chase water into the injection wells was carried out on Thursday, August 18, 2005 (considered as day 0). The injection process is explained in detail in Santharam (2008).

7. KB-1 injection

The KB-1 culture was purchased from SiREM, Ontario, Canada. After determining that the area around the injection wells had become reduced [based on the measured oxidation reduction potential (ORP) and dissolved oxygen (DO) values], and after migration of the tracer to down-gradient wells, a culture of KB-1 was injected through the injection wells, on October 13, 2005. The injection of KB-1 was preceded, as well as followed by, injection of low concentration of nutrient water. Each injection well first received 50 L of nutrient solution. The nutrient solution was prepared using groundwater from MW-9S and MW-9D that had been incubated, from October 10, 2005, with 1 L of SOME, 40 g of glucose, 0.5 L of lactate and 200 g of yeast extract in a 55 gal (approximately 200 L) barrel. Each injection well received 5 L of KB-1 culture; Flow of KB-1 was achieved by pressurizing the KB-1 vessel using a nitrogen cylinder. Injection of KB-1 was followed by injection of 50 L of the anaerobic chase water. The anaerobic chase water was prepared similar to the nutrient solution, described above, but without SOME and lactate.

8. Fall 2006

After demonstrating that lactic acid and SOME were successful in reducing PCE levels in samples collected from the pilot study area, we planned to use cheese whey as nutrient source in the field. Groundwater from MW-10 was used to dilute cheese whey for injection. Cheese whey inhibition at higher concentrations presents a problem in the field because higher concentrations are often introduced to account for dispersion that occurs within the aquifer. In the microcosm studies, the optimal concentration of cheese whey for PCE degradation (with and without KB-1) was 0.025%, with inhibition occurring at concentrations greater than 0.1%.

If we consider a 10-50 fold dilution, injection of about 0.5% cheese whey would disperse to the effective concentration range of 0.05% to 0.01%. In microcosms, 0.1% cheese whey resulted in a long lag time before reduction of PCE. While 0.05% whey supplies very little carbon, it is sufficient to fully reduce the levels of PCE typically observed in the field. Cheese whey contains about 50 g/L of sugars (mostly lactose). Dilution of cheese whey to 0.5% results in a concentration of about 250 mg/L or approximately 1.4 mM glucose equivalent. Depending on detailed reaction paths, this may be enough to reduce more than 1.4 mM of PCE because each glucose molecule provides a dozen active hydrogen molecules (H_2) as NADH, and each PCE needs four H_2. Theoretically, therefore, 0.05% cheese whey contains sufficient reducing power for 130 μM PCE.

On July 31, 2006, one day before the fourth nutrient injection, one liter of cheese whey, 40 g of glucose and 10 g of yeast extract were added to approximately 200 L of

groundwater pumped into a 55 gal barrel. The resulting concentration of cheese whey in the nutrient solution was 0.5%. The nutrient solution was prepared in four such barrels. On August 1, 2006 each injection well received 100 L of nutrient solution.

9. Analytical Methods

Gas chromatograph (Hewlett Packard 5890 Series II, Wilmington, DE) with FID detector and HP-1 column (Dimethyl Polysiloxane matrix, 30 m x 0.53 mm, Agilent Technologies, Wilmington, DE) was used to analyze chlorinated ethenes and methane. Hydrogen was used as the carrier gas. Injection temperature was 200 ºC and detector temperature was 300 ºC. Parameters were adjusted to obtain detectable peaks that could be distinguished from other compounds by elution time. Different isothermal temperatures were tested (80 ºC, 100 ºC, and 110 ºC). High column temperatures resulted in fast elutions but the peaks did not resolve very well from each other. Lower temperature allows good separation of the compounds, but took more time to finish the run. For example PCE elution time at 80 ºC was 4.1 min while at 110 ºC the PCE peak as detected after 2.2 min. At the end, a gas phase sample of 100 µL volume was taken with 100 µL Hamilton gas syringe, the column was set on an isothermal temperature of 100 ºC, and the run time was 5 min. The previous parameters were able to resolve chlorinated ethene peaks and methane. Gas flow rate was maintained at 1.5 mL/min. Detection limits were in the range of 1-10 µg/L for chlorinated ethenes; differences relate to the compounds and their Henry's constants. This analysis yields different headspace concentrations. Chlorinated ethene standards were prepared to determine elution times of different analytes of interest. A PCE standard was prepared once a month and run prior to each analysis to check the responses of the GC, and determine the relative elution times. The standard was prepared by injecting 10 µL of PCE liquid in a clean amber glass bottle of 4.2 L and allowing it to vaporize completely. The concentration of PCE in the standard bottle was 3.83 mg/L. At detection settings, elution times for chlorinated ethenes were as follow: PCE (2.7 min), TCE (1.6 min), DCE (1.1 min), VC (0.7 min) and Methane (0.6 min). Maintenance was done periodically to make sure that the gas chromatograph operation was uniform across the study. The injection septum (Thermogreen LB-2 / 11 mm diameter) was changed every 200 samples and inner glass column was cleaned every ~1000 samples. Methane and ethene were not resolved on this column at any temperature, and for that another GC was used. It was also difficult to create a calibration curve for vinyl chloride since the standard was prepared in methanol, and a large methanol peak masked the VC peak, even when water or sodium hydroxide was added to the standard.

10. Results and Discussion

Biostimulation Experiment

Water from MW-4D, MW-8S and MW-8D was used to study the extent of chlorinated ethene degradation upon stimulation of native microorganisms. In microcosms prepared with MW-4, methane was generated in the following treatments: SOME+YE, Glucose+ YE, Methanol, Methanol +YE, YE. About 50% of PCE decreased in SOME+YE treatment, and two thirds of PCE decreased in methanol and YE treatments. Trichloroethene (TCE) appeared after 6 weeks in SOME+YE, methanol+ YE and YE treatments. Unlike MW-4, addition of nutrients greatly enhanced reductive dechlorination of PCE in all vials except in SOME and methanol treatments. cis-Dichloroethene (c-DCE) was generated in the active microcosms in response to decrease of PCE concentrations during the second week of observation, but no further degradation of DCE was noted after 6 weeks. In general more frequent sampling events were needed to carefully monitor the variation of chlorinated ethene degradation. From this set of microcosms, wells had different responses to nutrient amendments. *Dehalococcoides* sp. that carries out complete degradation of PCE was either absent or not active under these conditions. Figure 3 shows microcosms results of MW-5 treated with nutrient solution with and without KB-1.

Cheese Whey

Cheese whey is a byproduct of the dairy industry and can be obtained inexpensively. Powdered whey is more costly, but easier to obtain, ship and store. First set of microcosms prepared with cheese whey was prepared to check if the lactate and vitamin B12 content in cheese whey was good for biostimulation and bioaugmentation studies. From here, several concentrations of cheese whey were tested (0.01%, 0.025%, 0.05%, 0.1% and0.25%) and compared to YE + SOME combinations used in previous studies. As expected, microcosms prepared without KB-1 bacteria were similar to control and PCE remained dominant in the system. On the other hand, PCE concentrations dropped almost 90% in 0.025% whey treatment and had a lag phase of 10 days, and were similar to YE+ SOME treatments. PCE concentrations also dropped in 0.05% and 0.01% whey treatments, but required a longer lag phase of 20 days (Figure 4). It was noticed that higher concentrations of cheese whey (above 0.05%) seemed to inhibit KB-1 bacterial culture and PCE remained through the study period. Meanwhile, 0.025% whey produced DCE when PCE concentrations dropped.

Groundwater Elevation

Precipitation affects the level of groundwater in the subsurface. Precipitation data was Variations in the data are due to rainfall events, but generally groundwater table in shallow zone was about 5 ft above that in the deep zone. In the pilot study area, the groundwater elevation is approximately 10 times higher in the shallow zones compared to deep zones as shown in Figure 3.60. The elevation grades between MW-8 and MW-12, and the general groundwater flow direction is to the east in both zones.

Chlorinated Ethenes in Pilot Study Area

Concentrations of PCE, TCE and DCE were plotted for three depths in deep and shallow wells. Deep well samples were collected at the following depths below top of casing: top (42 ft), mid (47 ft) and bottom (52 ft). Shallow wells sampled at the following depths: top (18 ft), mid (23 ft) and bottom (28 ft). Figures 5 to 7 represent chlorinated ethenes concentrations in deep zone of MW-8D, MW-9D and MW-10D respectively. In M-8D rapid decrease in PCE and increase in DCE concentrations were noticed

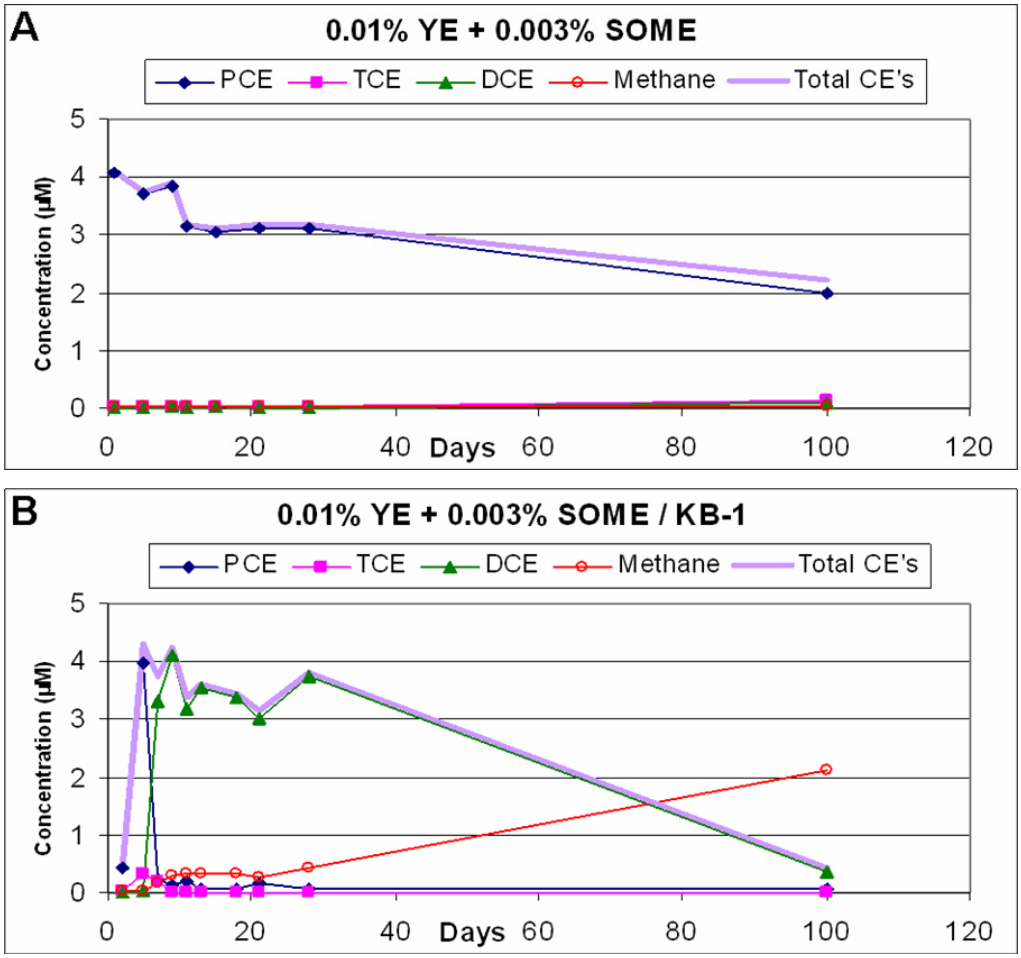

Figure 3. Microcosm data of MW-5D showing (A) biostimulation and (B) bioaugmentation with KB-1. Vials amended with 0.01% Yeast extract (YE)+ 0.003% Soy oil methyl ester (SOME).

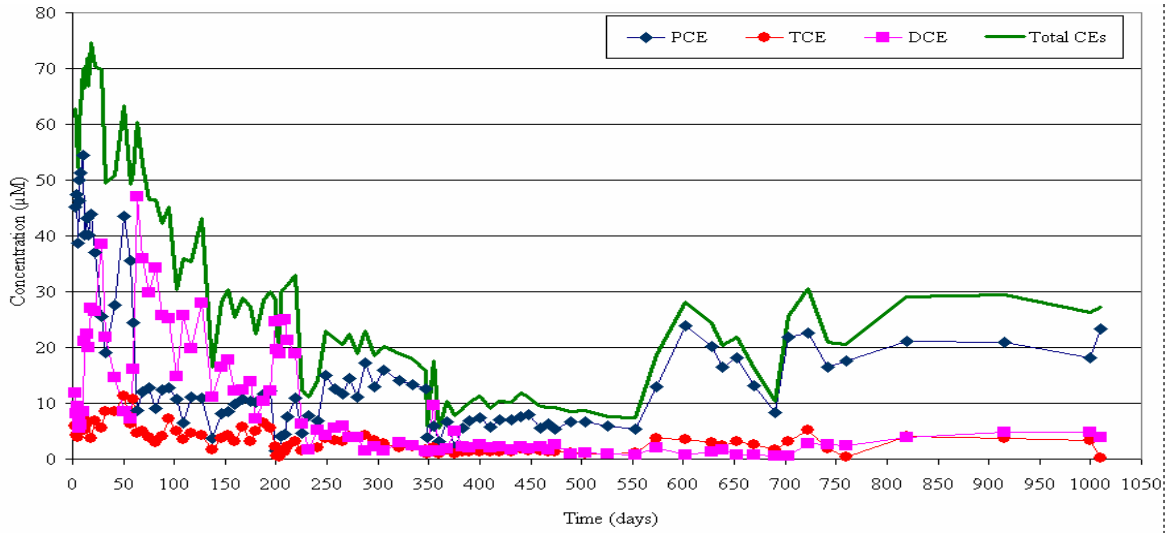

Figure 4. Cheese whey microcosms showing PCE degradation inhibition at concentrations greater than 0.05%.

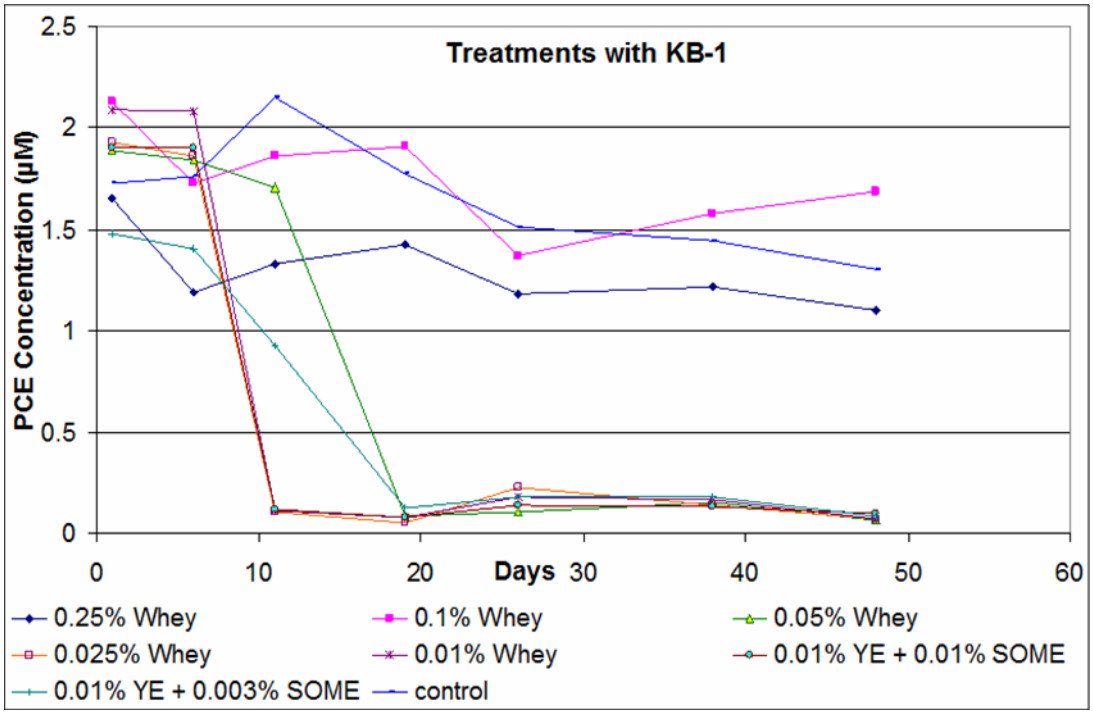

Figure 5. Mean concentration of chlorinated ethenes in MW-8D. Injection of nutrients and bromide between MW-8 and MW-9 on day 0 (August 18, 2005); nutrients and KB-1 on day 56 (October 13, 2005); nutrients and bromide on day 197 (March 3, 2006); nutrients on day 348 (August 1, 2006).

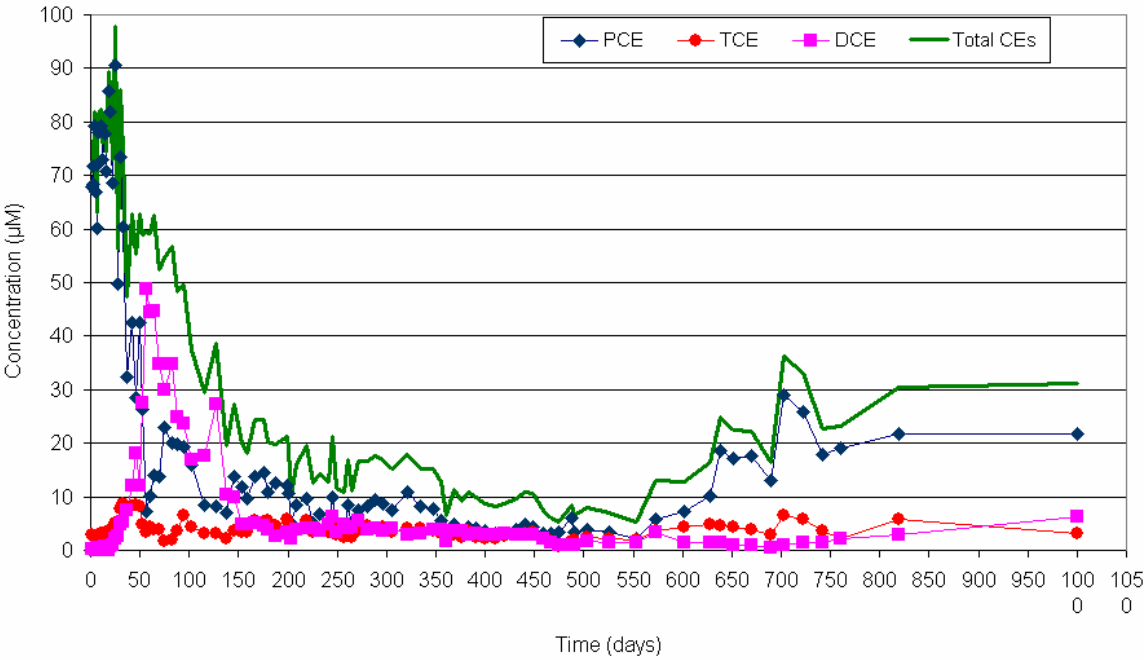

Figure 6. Mean concentration of chlorinated ethenes in MW-9D. Injection of nutrients and bromide between MW-8 and MW-9 on day 0 (August 18, 2005); nutrients and KB-1 on day 56 (October 13, 2005); nutrients and bromide on day 197 (March 3, 2006); nutrients on day 348 (August 1, 2006).

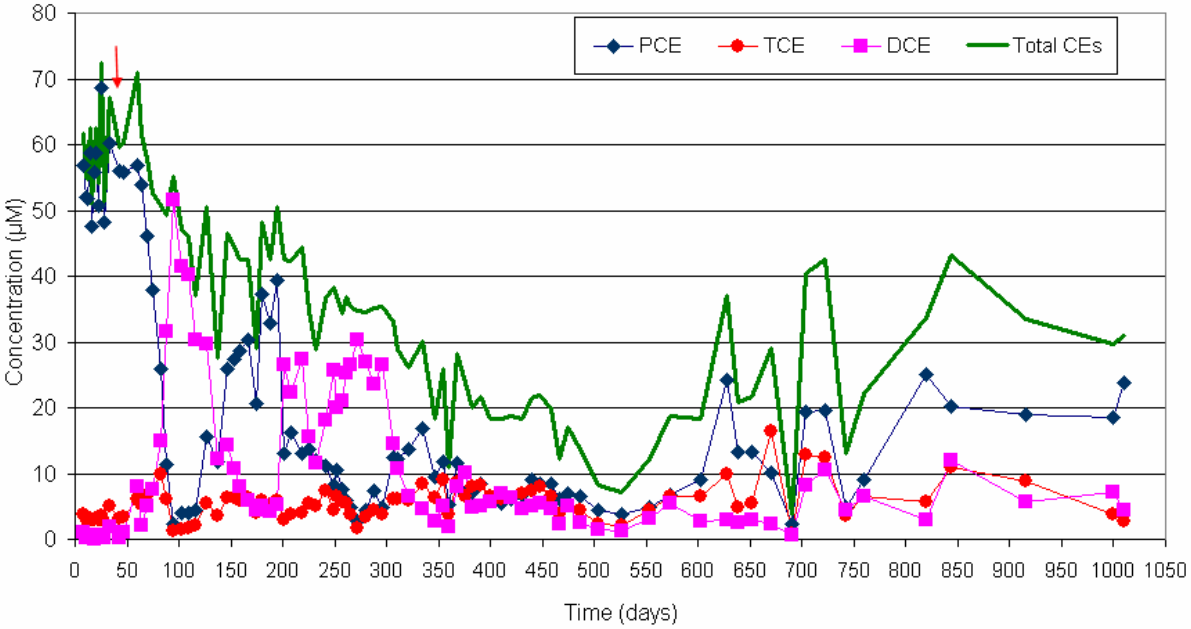

Figure 7. Mean concentration of chlorinated ethenes in MW-10D. Injection of nutrients and bromide between MW-8 and MW-9 on day 0 (August 18, 2005); nutrients and KB-1 on day 56 (October 13, 2005); nutrients and bromide on day 197 (March 3, 2006); nutrients on day 348 (August 1, 2006).

after first injection event in day 0. After second nutrient injection with KB-1 PCE remained low and DCE concentrations decreased. PCE concentrations then increased to about 10 µM before the third nutrient injection in day 197, and decreased rapidly after nutrient addition accompanied by DCE generation which soon decreased to lower levels and remain low for long time (750 days). Similar trend was also followed after last nutrient injection on day 348. Monitoring the well further we noticed that PCE concentrations are rebounding, but did not reach initial concentrations. This is perhaps due to decrease in microbial biomass and reducing conditions at the site.

MW-9D showed a dramatic response due to nutrient and KB-1 addition. PCE concentrations dropped from about 80 µM before KB-1 to about 10 µM after third nutrient feeding. DCE was generated after PCE decrease then decreased to low levels until about 750 days when concentrations start to rebound to about 7 µM for DCE after 1000 days and around 23 µM for PCE after the same time (Figure 3.78). In MW-10, PCE and DCE concentrations were fluctuating and not reflecting what is happening in MW-9D indicating that this well is receiving water from another path that can create that rebound of PCE concentration to about 40 µM before the nutrient injection in day 197. Total CEs concentrations decreased to 10 µM after 500 days and remained steady until they started to rise again.

Shallow wells in general had lower PCE concentrations than deep wells (< 10 µM) except for MW-10S that had a higher value of 17 µM. MW-8S was not affected much with nutrient addition and concentrations remain similar across the study. In MW-9S, PCE concentrations decreased following bacterial injection then rebounded. This was also the case when nutrients were added on day 348. After 1000 days PCE concentrations in this well were close to the starting point at around 6 µM. In MW-10S first response was detected after 230 days when PCE concentrations decreased and DCE increased. Now DCE has gone back to background values while PCE concentrations are reaching initial values.

11. Impact Downstream from the Point of Injection

The results that are presented for MW-9D, MW-10D, and MW-12D show that the nutrients and KB-1 move downstream with the water that is flowing to the east. For MW-10D, the concentrations of DCE, which are more than 20 µM between 200 and 300 days, are larger than those that are observed for MW-9D. Similarly, there are concentrations of DCE for MW-12D that exceed 30 µM between 350 and 450 days. This and other aspects of the data for MW-10D and MW-12D provide evidence that there is microbial action downstream of the injection point as one would expect. The observed times when the DCE concentration reaches 20 µM are about 20 days for MW-8D, 50 days for MW-9D, 80 days for MW-10D, and 300 days for MW-12D. The impact of KB-1 on the DCE concentration and CE concentration has a greater time lag; if we examine when the CE concentration is less than 30 µM, the values are about 130 days for MW-8D and MW-9D, 310 days for MW-10D, and 570 days for MW-12D. The KB-1 movement in the aquifer is slower than the nutrient movement, but there is evidence that both move downstream and have an impact downstream. The expectation is that the nutrients and the KB-1 are dispersed with time to locations that are north and south of MW-10D and MW-12D as well as at the well location.

12. Conclusions

Laboratory Studies

Microcosms experiments indicate that SOME, glucose, lactate, yeast extract, and cheese whey are good electron donors for chlorinated ethene biodegradation. Biostimulation of native microbes results in PCE conversion to DCE, while bioaugmentation with KB-1 bacterial culture was necessary to promote complete degradation of PCE to the end products methane and ethene. Cheese whey provided a good source of carbon and vitamins and can be used in biodegradation studies, though, inhibition of bacterial activity with high cheese whey concentrations was observed. This was due to acid formation and below optimal pH for growth. Therefore, use of cheese whey should be monitored in terms of concentration and perhaps frequency of addition. Adding small and frequent increments would work better than one bulk application that has a high chance of acidifying the aquifer. It seems that the complex nature of cheese whey would support microbial growth for a long time. It can be added monthly as recommended previously (Moretti, 2005 and AFCEE, 2004). Use of cheese whey will reduce cost of treatment, but this may not apply if pH control is needed. The soil has low buffering capacity at the pilot study area and therefore, careful optimal concentrations of cheese whey should be applied for remediation. Nutrients should be added to maintain KB-1 activity for long period; otherwise the microbial activity may be affected.

Field Studies

Soil tests at the pilot study area revealed that the subsurface is silty clay in the shallow zone grading to more silty sand soil in the deep zone. Tracer studies show that groundwater flow direction is toward the east in shallow and deep zones. Groundwater elevation is influenced by precipitation events. The hydraulic gradient is higher in the shallow zone than the deep zone and this may support the fact that ground water velocity is higher in the shallow zone than the deep zone. Two tracer studies, which were done during the bioremediation study, found that groundwater velocity decreased from 2004 to 2006 due to biomass growth near the injection sites. The results show that KB-1 was successfully established in this location as noted from the decrease in DCE and the total chlorinated ethenes concentrations. the rates of chlorinated ethene degradation in the field is slower than that of microcosms due to difference in temperature of groundwater of about 19 ºC and the incubation temperature of microcosms at 23 ºC that result in faster microbial growth and enhanced activity. When nutrient feeding was stopped CEs concentrations remained low for a long time after the last nutrient feeding, suggesting that substrates used may have provided a long term hydrogen source at the site. The biomass formed earlier would provide a source of organic substrates that can be used to sustain active dehalorespiring organisms and reduce biomass volume. This can also be noted when the final tracer study was conducted, which shows that ground water velocity is approaching the initial state.

13. Acknowledgments

We are grateful for financial support provided by the Kansas Department of Health and Environment and the Kansas Agricultural Experiment Station. We would like to extend our special thanks to Mr. Dan Nicoski (presently at USEPA, Region VII, Kansas City) and Bob Jurgens, Bureau of Environmental Remediation, KDHE, for their valuable inputs and assistance in this project. Thanks to Mr. Phil Dennis and Ms. Sandra Dworatzek at Geosyntec Consultants, for their valuable input during injection of KB-1. We would like to thank Dr. Stacy Hutchinson, Biological and Agricultural Engineering, Kansas State University for use of laboratory facilities for analyzing chlorinated ethenes and anions. And thanks to Dr. Fadi Aramouni for providing the cheese whey which was used in this work.

References

[1] AFCEE, 2004."Principles and practices of enhanced anaerobic bioremediation of chlorinated solvents." prepared for Air Force Center for Environmental Excellence, Brooks City-Base, Texas, September 2004.

[2] Bradley, P. M. and Chapelle, F. H. Methane as a product of chloroethenes biodegradation under methanogenic conditions. Environmental Science and Technology,Vol. 33, 1999, 653-656.

[3] Santharam, S. , Laboratory and field investigation of chlorinated solvents remediation in soil and groundwater. A Ph.D. Dissertation, Department of Chemical Engineering, Kansas State University, Manhattan, KS. http://hdl.handle.net/2097/910, 2008.

[4] SCRD. A chronology of historical developments in drycleaning. State Coalition for Remediation of Drycleaners. November 2007. http://www.drycleancoalition.org/download/drycleaning-historical_developments.pdf Accessed on 7/9/2008.

[5] Sutfin, J.A. , How methane injection attacks chlorinated solvents. International Ground Water Vol. 2, No. 4, 1996.

[6] Cupples, A.M., Spormann, A.M., & McCarty, P.L. Comparative evaluation of chloroethene, 2004.

[7] dechlorination to ethene by Dehalococcoides-like microorganisms. Environmental Science and Technology Vol. 38, 4768-4774.

[8] Lee, M.D., Quinton, G. E., Beeman, R. E., Biehle, A. A., & Liddle, R. L. Scale-up issues for in situ anaerobic tetrachloroethene bioremediation. Journal of Industrial Microbiology and Biotechnology Vol. 18 No. 2-3, 1997, 106–115.

[9] Major, D. W., McMaster, M. L., Cox, E. E., Edwards, E. A., Dworatzek, S. M., Hendrickson, E. R., Starr, M. G., Payne, J. A., & Buonamici, L.W. Field demonstration of successful bioaugmentation to achieve dechlorination of tetrachloroethene to ethene. Environmental Science and Technology Vol. 36, No. 23, 2002, 5106-5116.

[10] Maymó-Gatell, X., Chien, Y., Gossett, J. M., & Zinder, S. H. Isolation of a bacterium that reductively dechlorinates tetrachloroethene to ethene. Science Vol. 276, No. 5318, 1997, 1568-1571.

[11] Newell, C. J., Hass, P. E., Hughes, J. B., & Khan, T.. Results from two direct hydrogen delivery field tests for enhanced

dechlorination. Battelle Remediation of Chlorinated and Recalcitrant Compounds Conference, Monterey, CA, 2000.

[12] U.S. U.S. EPA. 1994. Chemical summary for perchloroethylene. US U.S. EPA, Office of Pollution Prevention and Toxics. Washington, DC. August, 1994. U.S. EPA 749-F-94-020a.

JJMIE

Volume 4, Number 1, Jan. 2010
ISSN 1995-6665
Pages 45 - 48

Jordan Journal of Mechanical and Industrial Engineering

Renewable Energy Potential and Characteristics in Jordan

M. Al zou'bi *

Hijjawi Faculty for Engineering Technology

Yarmouk University

Irbid-Jordan

Abstract

The current potential of various renewable energy resources in Jordan is discussed. New sites for wind energy exploitation are assessed and the pre-installation phase is started. On the other hand, it is shown that a large part of electrical load in Jordan is consumed during the daytime, when the solar power can be efficiently used. The pattern of wind energy variation is highly agreed with prevailing peak demands and corresponding peak hours. In this regard, the present paper investigates the degree of agreement between the load variation patterns and the power generated by the renewable energy sources. This includes the bulk power and the home scale consumption. Daily and seasonally load curves will be analyzed and correlated with solar and wind generated power curves. The data from existing wind farms will be used to enhance this study. Finally, the present paper highlights the necessity for reviewing and updating the energy strategies in Jordan

Introduction

Jordan is a key country in the Middle East region. Despite being adjacent to several oil-rich countries, Jordan struggles to secure its resources of energy especially when the prices of oil go up. A large portion of its budget is spent on importing oil from various countries. The problem is aggravated year after year due to the growth in population and increase in electricity demand. The industrial development requires more fuel consumption and continuous operation of power plants. Therefore, the search for alternative energy sources has become an imminent issue in Jordan.

Renewable energy sources are fundamentally different from fossil fuel or nuclear power plants because of their widespread occurrence and abundance. The primary advantage of many renewable energy sources are their lack of greenhouse gas and other emissions in comparison with fossil fuel combustion. Most of the renewable energy sources do not emit any additional carbon dioxide and do not introduce any risk such as nuclear waste.

Concerning the potential of renewable energy sources, they have the ability to supply several times the present world energy demand. They can enhance energy markets, secure long-term sustainable energy supplies, and reduce local and global atmospheric emissions. They can also provide commercially attractive options to meet specific needs for energy services (particularly in developing countries and rural areas), create new employment opportunities, and offer possibilities for local manufacturing of equipment [1].

Despite the significant progress achieved in renewable technologies, many fields are still at an early stage of development and not technically mature. If an effective research is applied in a modern way, renewable energy sources are considered highly responsive to overall energy policy guidelines and environmental, social, and economic goals [2]. One of the renewable energy critical issues is the degree of matching between renewable energy production and load patterns. Therefore, electrical grid storage was one of the most important storage methods advocated by the renewable energy community. With this method, it is possible to deeply exploit these resources in its 24-hour, 7-day cycle by using peak load equipment to meet the daily peaks.In the present work, a special emphasis is devoted to the assessment of renewable energy potential and the possibility of its deep exploitation in Jordan. This includes studying the potential of renewable energy, the variety of load patterns, their characteristics and matching schemes with renewable sources production. The daily and seasonally changes of renewable energy yield are compared with various loading curves for different sectors of consumers.

2.Renewable Energy Characteristics

Solar electric generation is a daylight process, whereas most homes have their peak energy requirements at night.

* Corresponding Auhtor: abder@yu.edu.jo

Domestic solar generation can thus feed electricity into the grid during grid peaking times during the day, and domestic systems can then draw power from the grid during the night when overall grid loads are down. This results in using the power grid as a domestic energy storage system, and relies on the 'net metering', where electrical companies can only charge customers for the amount of electricity used in the home that is in excess of the electricity and fed back into the grid.

Today's peak-load devices are used to provide infill capacity in a system relying heavily on renewables. The peak capacity would complement large-scale solar thermal and wind generation, providing power when they were unable to. Improved ability to predict the wind avaialability greatly enhances the utilization of this resource. Several countries have shown successful achievements in this field. In Germany, for instance, it is possible to predict wind generation output with 90% certainty 24 hours ahead. This means that it is possible to deploy other plants more effectively so that the economic value of wind contribution is increased.

3.Electrical Load Variation in Jordan

Electrical load forecasting is one of the major tasks, which continuously makes a challenge to the load management engineers in every electrical power system. There are several factors included in the load forecasting system which have demographic, political, climatic and economical attributes. The load curves are produced in daily, monthly and yearly forms. Figure 1 shows the daily load curves for typical working days in January, April, July and October months of the year 2005[3].

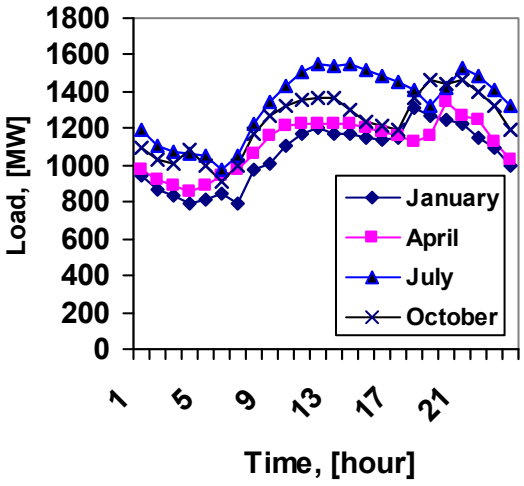

Figure1. Hourly variation of the Jordanian Electrical system load for typical days in different months.

Figure 2 illustrates the monthly variation of the Jordanian electrical load in year 2005, whereas Figure3 elucidates the distribution of this load in sector form. The daily and nightly patterns of load variation are closed to each other. A significant part of industrial, commercial and water pumping loads are mainly daily loads. Most of the organizations, official departments, educational and academic institutions consume their loads during the daytime. Figure 4 shows a sample of an hourly load variation in one of the faculties at Yarmouk University in Jordan [4].

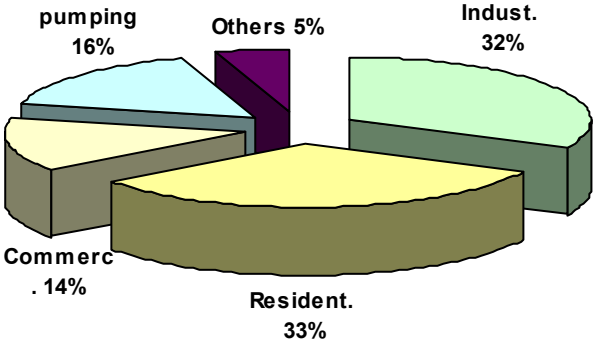

Figure 2. Monthly variation of the Jordanian Electrical system load for the year 2005.

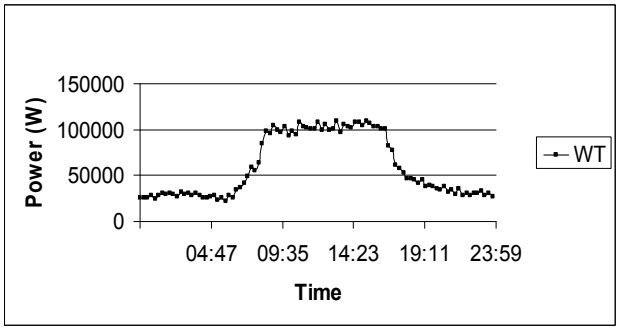

Figure3. The main sectors of the electrical load.

4.Power Supply using Renewables

The attempts to introduce a complete or partial replacement to the conventional sources of electrical energy did not stop since the 1950s. The intermittent nature of renewable energy was the main risk of these sources. However, several remarkable achievements have been done in the last two decades, which make the renewable energy one of the strong alternatives to the conventional sources.

The role of renewable energy in any country depends on the availability of the resources such as wind, solar radiation, geothermal and biomass. The assessment of load variation pattern is important to determine the best way of renewable energy exploitation. Therefore, it is important to find the degree of matching between the local loads and renewable energy generation schedule. In this context, it is known that the hot summer months in general, and July in particular, are associated with a high rate of electricity consumption in Jordan. With a mean temperature of more than 35^{o}C, most of the summer load consists of electric fans, water pumps and air conditioning [5, 6]. Luckily, the

best months for wind energy production in Jordan are the summer months as shown in Figure5. Therefore, the agreement between the wind energy production and the monthly load behaviour increases the importance of existing and planned wind farms. This is a good reason for promoting wind energy projects in Jordan.

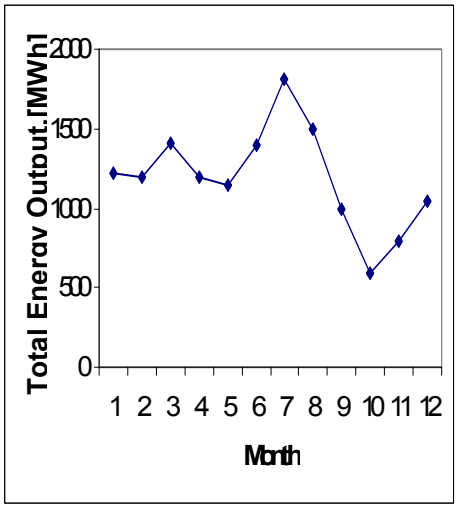

Figure 5. The monthly variation of wind energy production through the studied period

One of the most important factors to be considered in solar energy field is the sun shine period. Long hours of sun shine means more energy received from the sun. This factor is very important when comparing the long daytime in the summer with short days in winter. Table 1 shows Mean Daily Global Solar Energy Radiation KWh / m^2 as measured by the Jordanian Meteorological department stations.

Table 1. Mean Daily Global Solar Energy Radiation KWh / m^2, *JMD –Jordan, 2005*.

Station	J/F	M/A	M/J	J/A	S/O	N/D	Year
Dair ala	2.9/	4.9/	7.0/	7.3/	5.6/	3.1/	
	3.5	6.1	7.5	6.6	4.4	4.9	5.3
Ghor	3.0/	5.1/	7.0/	7.3/	5.7/	2.9/	
safi	3.7	6.2	7.5	6.7	4.4	2.3	5.1
Aqaba	3.5/	6.1/	7.4/	8.1/	6.6/	4.0/	
Airport	4.5	6.9	8.3	7.5	5.1	3.5	6.0
Irbid	3.1/	5.1/	6.9/	7.6/	6.0/	3.3/	
	3.7	6.4	7.7	7.5	4.6	2.9	5.4
Amman	3.2/	5.4/	7.1/	8.1/	6.0/	3.3/	
Airport	4.1	6.8	8.3	7.4	4.5	2.9	5.6
Wadi	3.2/	5.5/	7.5/	8.3/	6.5/	3.3/	
Dhulail	4.1	6.8	8.4	7.7	4.9	2.9	5.8
Rwished	3.3/	5.0/	6.3/	6.6/	5.5/	3.5/	
	3.9	5.9	6.8	6.3	4.4	2.9	5.0
Azraq	3.3/	5.7/	7.5/	8.1/	6.2/	3.7/	
	4.2	6.8	8.4	7.3	4.9	2.9	5.7

The following table shows the mean daily sun shine hours as measured by the Jordanian Meteorological department stations:

Station	J/F	M/A	M/J	J/A	S/O	N/D	Year
Dearalla	5.6/	7.7/	9.3/	12/	10/	6.5/	
	5.9	9.0	12	11.5	9.5	5.7	8.7
Ghorlsafi	5.2/	7.3/	9.7/	11.5/	9.5/	6.3/	
	5.4	8.9	11.7	10.7	8.7	5.1	8.4
Aqaba	6.8/	9/	9.6/	12/	11/	7.8/	
Airport	7.4	9.2	11.3	11.8	9.8	6.4	9.4
Irbid	5.5/	7.5/	9.6/	11.8/	10/	6.3/	
	5.2	9.0	11.3	12.2	8.5	4.2	8.4
Amman	5.1/	7.7/	9.8/	12/	10/	6.2/	
Airport	5.8	9.4	11.8	11.7	8.8	5	8.6
Wadidlail	5.5/	8.6/	9.9/	12/	11/	6.7/	
	6.5	9.7	11.7	11.6	9	5.7	9
Rwaishd	6.2/	7.6/	10/	12.4/	10.7	7.3/	
	6.9	8.5	12.2	11.8	/8.9	6	9.1
Azraq	6/	8.4/	9.6/	11.2/	9.7/	7/	
	6.6	9.3	11.1	11.1	8.7	5.5	8.7

5.Currentprojects in Renewable Energy

The distributed generation is a new trend in power systems, which is seriously looked to it as an alternative to conventional power generation. This concept is important to prevent blackouts, which can be avoided if an area did not depend only on one power plant. Renewable energy makes distributed systems more feasible because energy can be generated near the demand centers, reducing the need for long transmissions lines going through rural and urban landscapes, and by reducing the power loss across those lines. Moreover, the standard size for a new utility plant can be significantly reduced, and utilities are not eager to risk in such long-term investments.

Most renewable forms of energy, other than geothermal and tidal, are in fact stored solar energy. Renewable energy resources may be used directly as energy sources, or used to create other forms of energy. Examples of direct use are solar ovens, geothermal heat pumps and mechanical wind turbines. Examples of indirect use in creating other energy sources are electricity generation through wind turbines and photovoltaic cells.

6.Discussion

The continuous growth in electrical energy demand has put the decision makers in a critical situation. Therefore, the number of people who ask for exploitation new and renewable energy sources are in continuous increase day after day. With the presence of high potential sites, from the renewable energy point of view, there is no excuse for those who oppose this type of energy to wait more time.

The daily load variation has shown two peak-periods, one in the mid of the day and the other in the evening. The first peak period agrees well with the sunshine time in winter, whereas the two peak periods can lie in the long summer sunny hours. Jordan can be divided into five solar radiation regions. The first region is the southern region, which is located 29.0-30.5 N, 35.0-38 E. This region is represented by M'aan and Aqaba areas and has the highest solar

insolation in the country. In this regard, the annual daily average values of global irradiance are estimated between (6-7) KWh/m^2 and (1.2 – 1.35) KWh/m^2 for diffuse irradiance. The second region is the eastern region, which is located 30.5-32.5 N, 36.0-39 E. This region represents the semi desert and (Badia) remote areas in the country. Annual daily average values are about 5.5 and 1.5 KWh/m^2 for global and diffuse irradiance respectively. The annual daily average of sunny hours is about 9 hours. The third region is the middle region which is located at 30.5-32.0 N, 35.5-36.5 E. In comparison with other regions, this area has the highest annual average value of diffuse irradiance ranging between 1.6 and 1.9 KWh/m^2. The global irradiance is about 5.5 KWh/m^2 in this region. The fourth region is the northern region (32.0-33.0 N, 35.5-36.5 E). In this region the annual daily average values of global irradiance are about 5.0 KWh/m^2 and about 1.5 KWh/m^2 for diffuse solar irradiance. The last region is the western region (30.5-33.0 N, 35.0-35.5 E). This region represents the Jordan Rift Valley areas, where the elevation of areas is below the sea level (from –170m at Baqora to –250m at Ghor Safi). This region is very hot in summer and warm in winter.

The high values of solar energy radiation, shown in Table 1, illustrate that the solar energy exploitation in Jordan is possible and gives better results than that in other countries. Unfortunately, the projects in this field are still small and of experimental type rather than of commercial form. The long sunny days, shown in Table 2, add another incentive factor to employ this energy in large scale. It is worth mentioning here that, even the stand alone exploitation of solar energy is technically and commercially viable. The load pattern shown in Figure4 illustrates the possibility of employing solar energy for supplying large sector of loads with fixed pattern.

Concerning wind energy resources in Jordan, there are tens of places known by their high wind speed and long windy times. The existing wind farms in Hofa and Ibrahimia are good examples of wind energy projects. These farms are connected to the national grid and characterized by a high availability and excellent capacity factors. The agreement between the power output of these farms and the annual load curve shows that these farms can significantly participate in reducing the burden on the national grid in summer, when the load reaches its peak.

The preliminary research for new wind energy resources has revealed that tens of places have wind speed greater than 5m/s. Currently, there is a plan for three wind farms with Maximum capacity of 30MW each. These farms are distributed among three sites in the northern and southern regions of Jordan.

The exploitation of biomass and energy from waste was just started in Jordan. There are several projects in different places, mainly close to the big cities with heavy population.

7.Conclutions

The daily load curve of the Jordanian network has two peak periods, in midday and evening hours. Large sector of Jordanian electrical load can greatly benefited from the high irradiance and long sunny days whether these loads are connected to grid or stand alone. The existing and planned projects for small and large wind farms are important for establishing a good alternative for existing conventional sources of energy. The movement from small, pilot and experimental renewable energy projects is a must and inevitable.

References

[1] M. Barak and T. Swift-Hook, “Renewable energies: sources, conversion and application”, IEE Energy Series 2, 1986.

[2] G. Boyle, Renewable Energy: Power for a Sustainable Future. Open University, UK, 1996.

[3] Nepco Annual Report, 2005

[4] I. Abushmais, F. Kraidy and A. Abutaimeh, “Design a PV system to supply the Hijjawi Faculty with electrical energy” final year project, 2005.

[5]M.R.AL-Shakarchi, N.SH. ABU-Zeid, A Study of load management by direct control for Jordan's Electrical Network.Power System, Journal of Science & Technology, Vol. 7, No. 2, 2002, 25-30.

[6] M. Abderrazzaq, “Energy production assessment of small wind farms”, International Journal of Renewable Energy .Elsevier, Vol . 29, 2004., 2261-2272.

JJMIE

Volume 4, Number 1, Jan. 2010
ISSN 1995-6665
Pages 49 - 54

Jordan Journal of Mechanical and Industrial Engineering

Study and Control of a Power Electronic Cascade using Photovoltaic Cell-Multilevel Inverter

Dalila Beriber [a] Abdelaziz Talha [a] Farid Bouchafaa[a] Mohamed Seghir Boucherit[b]

[a] *Laboratoire d'Instrumentation, F.E.I, Université des Sciences et de la Technologie Houari Boumediene, Alger, ALGÉRIE*

[b] *Laboratoire de Commande des Processus, École Nationale Polyechnique, Alger, ALGÉRIE*

Abstract

In this paper, we study the performances of the cascade of the photovoltaic cell with the multilevel neutral point clamped (NPC) voltage source inverter (VSI).
In the first part, we remind the model of the double stator induction motors (DSIM). Then, we develop knowledge and control models of this inverter using the connection functions of the semi-conductors. After that, we propose a PWM strategy to control this converter. In this part, the inverter is fed by constant input DC voltages. In the last part, we study the performances of the constituted by two photovoltaic cells – two three-level NPC VSI - DSIM. The results obtained confirm the good performances of the proposed cascade.

Keywords: Multilevel inverter; Generator Cells; Photovoltaic; Control; DSIM.

1. Introduction

Nowadays, the main energy supplier of the worldwide economy is fossil fuel. This, however has led to many problems such as global warming and air pollution. Therefore, with regard to the worldwide trend of green energy, solar power technology has become one of the most promising energy resources. The number of PV installations has had an exponential growth [1]. One of the most important types of PV installation is the grid connected inverter configurations. These grid connected PV systems can be categorized from two viewpoints: PV cell and inverter configurations. The PV cell arrangements fall into four broad groups: centralized technology, string technology, multi-string technology and AC-module and AC-cell technologies [2].

All approaches have advantages and disadvantages [2], [3]; and will compromise various attributes such as harmonic generation, complexity, efficiency, flexibility, reliability, safety, modularity and cost. However, for residential PV installations, the most suitable configuration seems to be the string or multistring technologies where one or more strings of PV cells are connected to a single inverter. Using this type of configuration, there will be no losses associated with the string diodes compared to centralized technology. Moreover, independent Maximum Power Point Tracking (MPPT) is possible for all strings which might be installed in different sizes and orientations. This also increases the overall efficiency under special circumstances like partial shadowing.

There are different approaches to implement string and multi-string topologies. Usually, these modules consist of a solar array and a DC to DC converter controlled by a MPPT algorithm. Afterwards, the outputs of the DC/DC converters build up a DC voltage which is then converted to AC by means of an inverter [4]. The other possibility is to use multilevel. PV systems categorized by different PV cell configurations and inverter types topologies which are able to generate better output quality, while operating at lower switching frequency. This implies lower switching dissipation and higher efficiency. Moreover, this topology utilizes switches with lower breakdown voltage; therefore, it can be used in higher power applications at lower cost. It is worth mentioning that although the number of switches in this approach is higher than other two level topologies, for a sufficient high number of levels, the output filter can be avoided which means less weight, cost and space.

On the other hand, even with the same size of filter at the output, the switching frequency can be decreased which means higher efficiency. In general, a greater number of switches in multilevel converters can be justified since the semiconductor cost decreases at a much greater rate than the filter components cost. This project the total cost of multilevel converters to be comparable or even lower than that of two-level converters.

This paper presents the performances of the cascade of the photovoltaic cells with the multilevel NPC inverter.

Simulation results obtained confirm the good performance of the proposed cascade.

Corresponding Author. dberiber@yahoo.fr

2. Model of the DSIM

The model of the double stator induction machines (DSIM) is given in figure1 [5], [6].

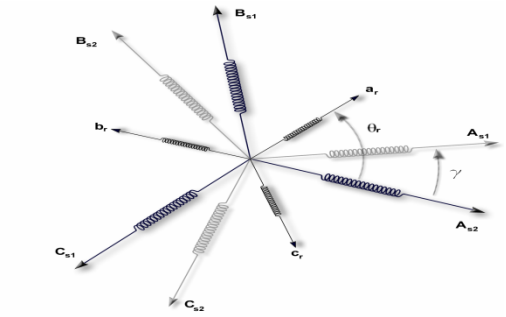

Figure 1. DSIM schema

Park model of the DSIM, with P pairs of poles, is defined by the following equations system [7], [8]:

$$\begin{cases} V_{sd1}=r_{s1}i_{sd1}+\dfrac{d\varphi_{sd1}}{dt}-\omega\varphi_{sq1} \\ V_{sq1}=r_{s1}i_{sq1}+\dfrac{d\varphi_{sq1}}{dt}+\omega\varphi_{sd1} \\ V_{sd2}=r_{s2}i_{sd2}+\dfrac{d\varphi_{sd2}}{dt}-\omega\varphi_{sq2} \\ V_{sq2}=r_{s2}i_{sq2}+\dfrac{d\varphi_{sq2}}{dt}+\omega\varphi_{sd2} \\ V_{rd}=r_{r}i_{rd}+\dfrac{d\varphi_{rd}}{dt}-\omega_{gl}\varphi_{rq} \\ V_{rq}=r_{r}i_{rq}+\dfrac{d\varphi_{rq}}{dt}+\omega_{gl}\varphi_{rd} \end{cases}$$

The electromagnetic torque is given by the following expression:

$$C_{em}=p\frac{L_m}{L_m+L_r}\left[\varphi_{rd}\left(i_{sq1}+i_{sq2}\right)-\varphi_{rq}\left(i_{sd1}+i_{sd2}\right)\right]$$

The model of the DSIM in the Park frame is given by figure2.

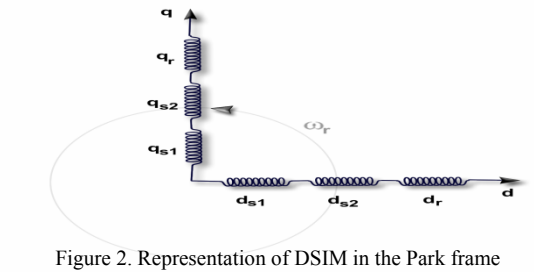

Figure 2. Representation of DSIM in the Park frame

3. Modelling of Three Level NPC VSI

3.1. The three-level NPC VSI structure

The three-level NPC VSI is constituted by three arms and two DC voltage sources [9], [10]. Every arm has four bi-directional switches in series and two diodes (Figure3) [7].

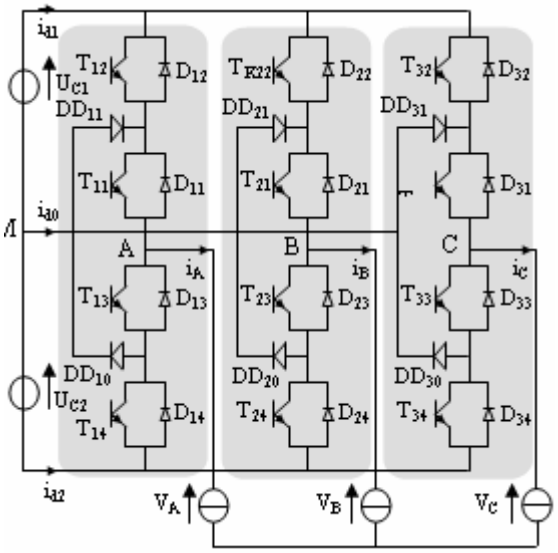

Figure 3. The three-level NPC inverter

3.2. Knowledge model

The switch connection function F_{ks} indicates the opened or closed state of the switch TD_{ks}.
We define two a half arm connection function F_{km}^{b} with: k : arm number

$$m = \begin{cases} 0 \text{ for the lower half arm} \\ 1 \text{ for the upper half arm} \end{cases}$$

For an arm k of the three-phase three-level NPC, several complementary laws controls are possible. The control law which lets an optimal control of this inverter is:

$$\begin{cases} B_{K4} = \overline{B}_{K1} \\ B_{K3} = \overline{B}_{K2} \end{cases}$$

Where B_{Ks} represents the gate control of the switch Tks.
We define the half arm connection function F_{i1}^{b} and F_{i0}^{b} associated respectively to the upper and lower half arms.
Where i is arm number (i=1, 2, 3).

$$\begin{cases} F_{11}^{b} = F_{11}F_{12} \\ F_{10}^{b} = F_{13}F_{14} \end{cases}, \quad \begin{cases} F_{21}^{b} = F_{21}F_{22} \\ F_{20}^{b} = F_{23}F_{24} \end{cases}, \quad \begin{cases} F_{31}^{b} = F_{31}F_{32} \\ F_{30}^{b} = F_{33}F_{34} \end{cases}$$

The output voltages of the inverter relatively to the middle point M are defined as follows:

$$\begin{bmatrix} V_{AM} \\ V_{BM} \\ V_{CM} \end{bmatrix} = \begin{bmatrix} F_{11}^{b} \\ F_{21}^{b} \\ F_{31}^{b} \end{bmatrix} U_{C1} - \begin{bmatrix} F_{10}^{b} \\ F_{20}^{b} \\ F_{30}^{b} \end{bmatrix} U_{C2}$$

This system shows that the three-level can be considered as two two-level voltage source inverters in series. This characteristic lets us to extrapolate the strategies used
The input currents of the inverter are given as follow

$$\begin{cases} i_{d1} = F_{11}^{b} i_1 + F_{21}^{b} i_2 + F_{31}^{b} i_3 \\ i_{d2} = F_{10}^{b} i_1 + F_{20}^{b} i_2 + F_{30}^{b} i_3 \end{cases}$$

The current i_{d0} is defined by the following relation:

$$i_{d0} = (i_1 + i_2 + i_3) - (i_{d1} + i_{d2}) \quad (1)$$

4. PWM Strategy of the Five Level NPC VSI

The inverter is controlled by the space vector modulation strategy which uses two bipolar carriers.

This strategy is characterized by two parameters [8], [11]:
- The modulation index m is defined as a ratio between the carrier frequency f_p and the reference voltage frequency f:

$$m = \frac{f_p}{f}$$

- The modulation rate r is the ratio between the magnitude V_m of the reference voltage and three times of the carrier's magnitude:

U_{pm}: $$r = \frac{V_m}{U_{pm}}$$

Figure4 shows the signals of this strategy.

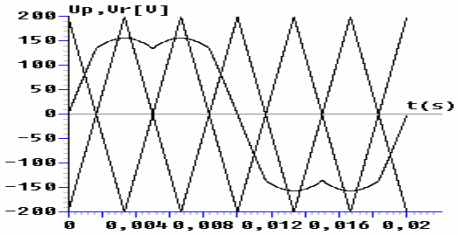

Figure 4. Space vector modulation strategy

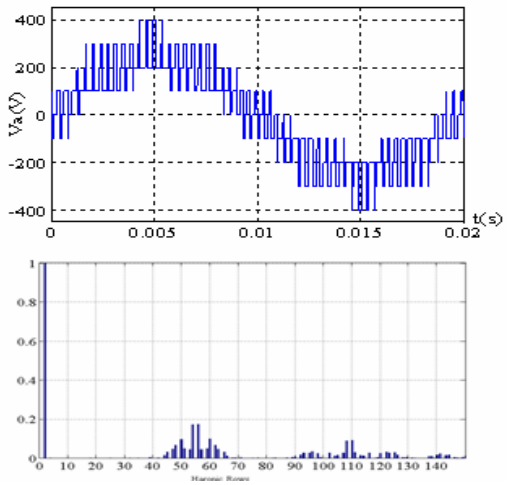

Figure 5. Simple voltage of the inverter and its spectrum

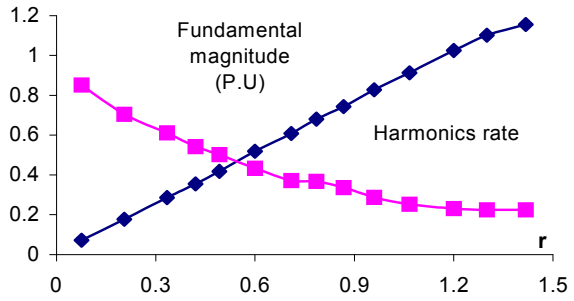

Figure 6 The adjusting characteristic of the output voltage of the inverter

For even values of m, the output voltages present symmetry relatively to the quarter of the period. Then, only odd harmonics exist. These harmonics gather by families centred around frequencies multiple of 4mf. The first family centred around frequency 2mf is the most important in view of its magnitude (Figure5).
The modulation rate r lets linear adjusting of fundamental magnitude from $r = 0$ to $r_{max} = 1{,}15$ (Figure6).
The harmonics rate decreases when r increases (Figure6).

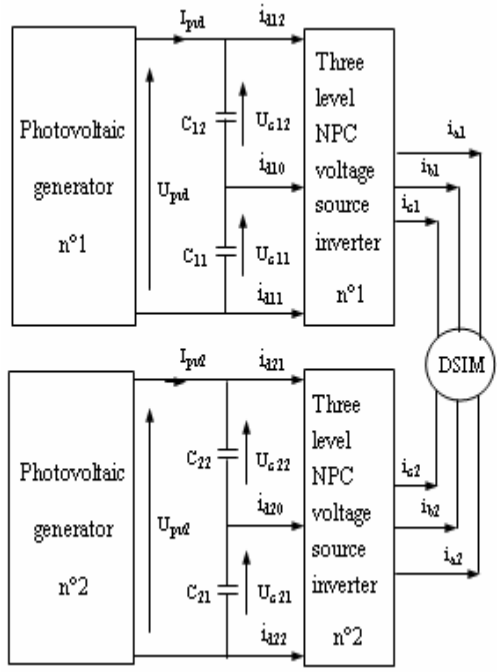

Figure 7. Two photovoltaic generator-filter-two three-level NPC VSI-DSIM cascade

5. Cascade of two Photovoltaic Generator – two Three-Level NPC VSI - DSIM

Until now, we have supposed the input DC voltages of the three-level NPC VSI constants. In this part, the authors study a generation input DC voltage technique. For this, we propose a cascade constituted by two photovoltaic generator-two three-level NPC VSI which feeds a DSIM (Figure7).

5.1. Modelling of Photovoltaic Generator

The building block of the PV array is the solar cell, which is basically a p–n semiconductor junction that directly converts light energy into electricity. Since the invention of solar cells, several models have been proposed to describe its function and behavior under different weather conditions (light and temperature) [12]. In this paper, we present the model with one exponential (diode) [13], [14]. The equivalent circuit is shown in figure8.

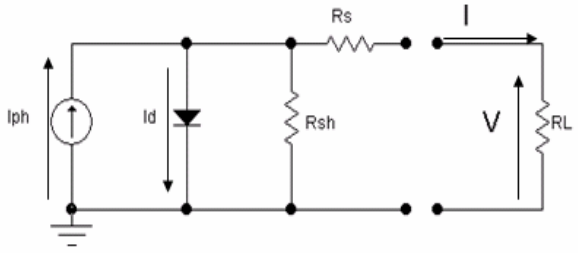

Figure 8. Electrical Scheme of a photovoltaic cell with one diode

To simulate a PV array, a PV simulation model which was obtained using Matlab/Simulink, was used based on the following equation:

$$I_g = I_{ph,g} - I_{s,g}\left[\exp\left(q\frac{V_g + R_{s,g}I_g}{AkN_{ms}T}\right) - 1\right] - \frac{V_g + R_{s,g}I_g}{R_{sh,g}}$$

where I is the PV array output current (A); V the PV array output voltage (V); Iph is the photocurrent depends on the solar radiation and the cell temperature; Is is the cell reverse saturation current varies with temperature; Rs is the series resistance; Rsh is the shunt resistance, q is the charge of electron = $1.602.10^{-19}$ C; K is the Boltzmanns constant $K=1.381.10^{-23}$ J/K; A is the pn junction ideality factor; T is the cell temperature (K) and g is the gap.

In our case, we have used photovoltaic generator MSX-83 composed by 36 cells in en series. The characteristics of a PV cell of changes in current and power based on the voltage of the PV cell is shown in figures 9 and 10(for a temperature T=25° and light E=1000W/m^2).

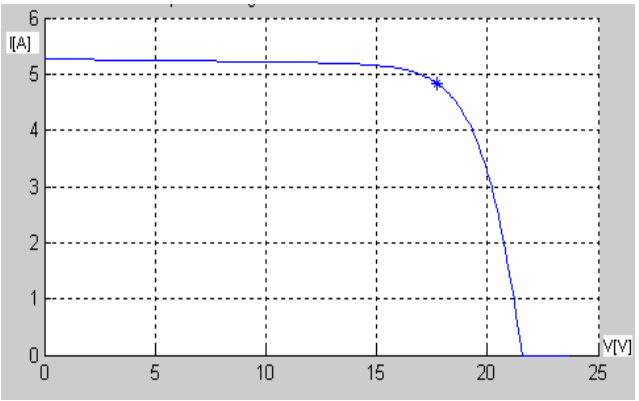

Figure 9. Current–voltage Characteristic PV

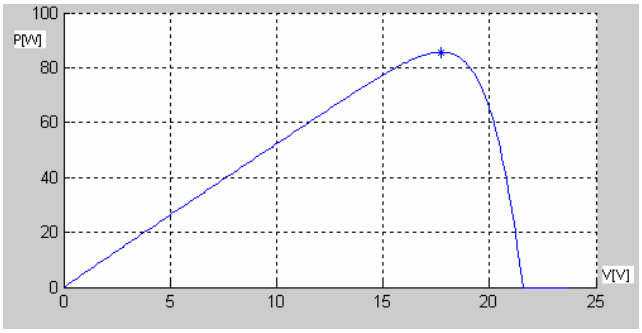

Figure 10. Power–voltage Characteristic PV

5.2. Modelling of Intermediates Filters

The model of these filters is defined by the following system:

$$\begin{cases} C_{K1}\dfrac{dU_{CK1}}{dt} = I_{pvK} - I_{dK1} \\ C_{K2}\dfrac{dU_{CK2}}{dt} = I_{pvK} - I_{dK2} \end{cases}$$

K: Number of the intermediate filters (K=1, 2).

5.3. Simulation Results

The parameters of the intermediate filter are: $C_{11}=C_{12}=C_{21}=C_{22}=10mf$.

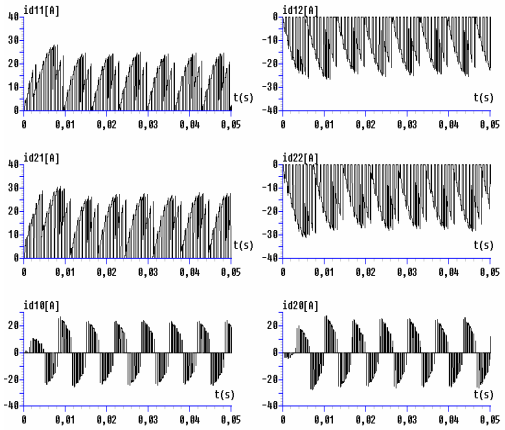

Figure11. Input currents of the two three-level inverter

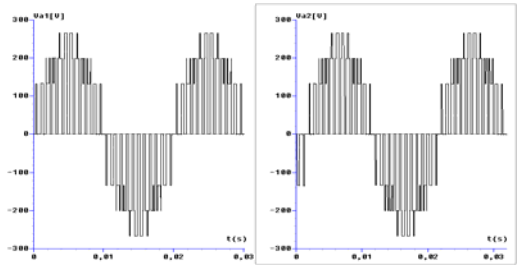

Figure 12. Output voltage of two three level inverter

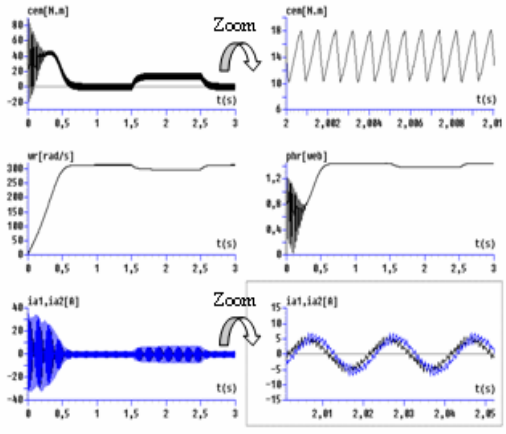

Figure 13. The DSIM performances

We note that the currents i_{d11} and i_{d21} are respectively the opposite of the currents i_{d12} and i_{d22}. The currents i_{d10} and i_{d20} have a mean value practically null (Figure11). The output voltages of inverter V_{a1} and V_{a2} are practically sinusoidal (Figure12). The performance of the speed control algorithm of the DSIM shows that the current of the machine nearly is sinusoidal; the speed follows quietly its reference. The speed and the torque effect for the charge variation between two instants t=1.5s and t=2.5s (Figure13).

6. Conclusions

After a brief introduction of different possible choices for inverters in Photovoltaic applications, it is shown that the Cascaded Multilevel Converter is a suitable choice for PV systems. The paper presents the performance of the cascade of the photovoltaic cell with the multilevel inverter.

The simulation results show that the performances obtained with this cascade are full of promise to be using this inverter in renewable energy.

References

[1] F. Blaabjerg, R. Teodorescu, M. Liserre, and A. V. Timbus, "Overview of control and grid synchronization for distributed power generation systems", IEEE Transactions on Industrial Electronics, vol. 53 No. 5, 2006, 1398–1409.

[2] S. B. Kjaer, J. K. Pedersen, and F. Blaabjerg, "A review of single-phase grid-connected inverters for photovoltaic modules", IEEE Transactions on Industry Applications, Vol. 41, No. 5, 2005, 1292–1306.

[3] Y. Xue, L. Chang, S. B. Kjaer, J. Bordonau, and T. Shimizu, "Topologies of single-phase inverters for small distributed power generators: an overview", IEEE Transactions on Power Electronics, Vol. 19 No. 5, 2004, 1305–1314.

[4] G. Walker and P. Sernia, "Cascaded DC/DC converter connection of photovoltaic modules", IEEE Transactions on Power Electronics, Vol. 19 No. 4, 2004, pp. 1130–1139.

[5] D. Hadiouche, H. Razik and A. Rezzoug, "Study and simulation of space vector PWM control of double-star induction motors", IEEE-CIEP'2000, Acapulco, Mexico, 2000, 42-47.

[6] A. Monti, A. P. Morando, L. Resta and M. Riva, "Comparing two level GTO-inverter feeding a double-stator asynchronous motor with a three level GTO-inverter feeding a single star asynchronous motor", EPE'1995, Sevilla, Spain, 1995, 2419-2425.

[7] D. Beriber, M. Berkouk, A. Talha and M. O. Mahmoudi, "Study and Control of Two Two - Level PWM Rectifiers – Clamping Bridge – Two Three Level NPC VSI Cascade. Application to Double Stator Induction Machine", IEEE 35th Power Electronics Specialists Conference, PESC'2004, Aachen, Germany, 2004, 3894-3899.

[8] A.Talha, D.Beriber and M.S.Boucherit, "Linear Feedback Control of Multi DC Bus Link Voltages of Multilevel NPC VSI Cascade", 14th IEEE International Conference on Electronics, Circuits and Systems ICECS'2007, Marrakech, Morocco, December 11 - 14, 2007, 355-358.

[9] J. Rodriguez, J. Lai, and F. Peng, "Multilevel inverters: A survey of topologies, controls, and applications", IEEE Transactions on Industrial Electronics, Vol. 49, No. 4, 2002, 724–738.

[10] S. Alepuz, S. Busquets-Monge, J. Bordonau, J. Gago, D. Gonzalez, and J. Balcells, "Interfacing renewable energy sources to the utility grid using a three-level inverter", IEEE Transactions on Industrial Electronics, Vol. 53, No. 5, 2006, 1504–1511.

[11] L.M. Tolbert, F.Z. Peng and T.G. Habelter, "Multilevel PWM methods at Low Modulation indices", in Proceedings of 1999 Applied Power Electronics Conference and exposition (APEC), 1999, 1032-1039.

[12] M. Bayegan, "Power electronic technologies for distributed Power", Keynote paper, 9th European conference on Power Electronics and Applications, EPE 01, 27th August 2001, Graz, Austria, 2001.

[13] B.Multon and al, "Analysis and Experimental Validation of Various Photovoltaic System Models", 7th International ELECTRIMACS'2002 Congress, Montréal, Canada, 2002, 1-6.

[14] E. Massada, "Power Converter for Renewable and Distributed Sources", 9th International Conference on Power Electronics and Motion Controls, EPE-PEMC'2000, Kosice, Slovak Republic, 2000.

JJMIE

Volume 4, Number 1, Jan. 2010
ISSN 1995-6665
Pages 55- 60

Jordan Journal of Mechanical and Industrial Engineering

The Measurement of Overall Elastic Stiffness and Bulk Modulus in Solar Photovoltaic Devices

Imad Alhayek [a], Mohamed S. Gaith [b,*]

[a] *Department of Mechanical Engineering, FET, Al-Balqaa Applied University, Amman, 11134 Jordan*

[b] *Department of Applied Sciences, FET, Al-Balqaa Applied University, Amman, 11134 Jordan*

Abstract

In this study, the correlation between macroscopic and microscopic properties of the II-IV semiconductor compounds ZnX (X=S, Se, Te) manufactured in photovoltaic window layers is investigated. Based on constructing orthonormal tensor basis elements using the form-invariant expressions, the elastic stiffness for cubic system materials is decomposed into two parts; isotropic (two terms) and anisotropic parts. A scale for measuring the overall elastic stiffness of these compounds is introduced and its correlation with the calculated bulk modulus and lattice constants is analyzed. The overall elastic stiffness is calculated and found to be directly proportional to bulk modulus and inversely proportional to lattice constants. A scale quantitative comparison of the contribution of the anisotropy to the elastic stiffness and to measure the degree of anisotropy in an anisotropic material is proposed using the Norm Ratio Criteria (NRC). It is found that ZnS is the nearest to isotropy (or least anisotropic) while ZnTe is the least isotropic (or nearest to anisotropic) among these compounds. The norm and norm ratios are found to be very useful for selecting suitable materials for electro-optic devices, transducers, modulators, acousto-optic devices.

Keywords: Overall Stiffness, Bulk Modulus, Anisotropic Materials, Window Layer Compounds.

1. Introduction

Nowadays, the necessity of alternative energy use is widely accepted. In solar energy technology, thin film solar technology based on the II-IV semiconductor compounds, is very promising due to lower production costs and shorter energy pay back times [1]. For these compounds, a successful interface between absorber and buffer layers with alternative and promising non-toxic materials requires compositional and electronic material characterization as a prerequisite for understanding and intentionally generating interfaces in photovoltaic devices [1]. On the other hand, stability of ZnTe/ZnS solar cells is of concern for their application in space, where the cells have to withstand high energy particles, mainly electrons and protons that can cause severe damage in solar cells up to a complete failure. Therefore, the radiation hardness and damage mechanism of the ZnTe solar cells is associated with the overall elastic stiffness and bulk modulus [3].

Most of the elastic materials in engineering applications are, with acceptable accuracy, considered as anisotropic materials such as metal crystals (due to the symmetries of the lattice), fiber-reinforced composites, polycrystalline textured materials, biological tissues, and photovoltaic materials. The wide-gap II-VI semiconductors, well known anisotropic materials used in high technology, have received much attention in the past decades since they have important applications in short-wavelength light-emitting diodes (LEDs), laser diodes and optical detectors [3]. Moreover, semiconductor materials constitute today basic components of emitters and receivers in cellular, satellite, solar cells, and photovoltaic systems. Their electronic and structural properties of such systems are subject of considerable interest in nanotechnology as well.

For the semiconductor compounds ZnS, ZnSe, and ZnTe, the zinc-blend structure (ZB) has the lowest minimum total energy. With respect to classical II- VI semiconductors, the ZnS, ZnSe, and ZnTe compounds have attracted much attention in recent years for their great potential in technological applications [3]. They have a high melting point, high thermal conductivity, and large bulk modulus. The hardness and large bulk modulus of these anisotropic materials make them ideal protective coating materials in photovoltaic applications [4]. These materials can, therefore, be used for optoelectric devices in which the availability of light sources in the mid-infrared spectral region is crucial for many applications, i. e., molecular spectroscopy and gas-sensor systems for environmental monitoring or medical diagnostics [5]. Being stable to high

* *Corresponding author. mgaith@coe.neu.edu*

.

temperatures and can be made of sufficiently insulating allows precise measurements of piezoelectric, elastic, and dielectric constants. For such data eventually a fully quantum-mechanical description is essential in order to serve to verify a quantative theory of piezoelectricity and elasticity in these structures.

These covalent materials have been extensively studied for their intrinsic structural, optical, and elastic properties such as energy gap, charge density, lattice constants and bulk modulus [1-36]. However, bulk modulus has been found to correlate well with strength and hardness in many materials and those with largest bulk moduli are usually expected to be the hardest materials [7]. Therefore, one of the important parameters that characterize the physical property of a material system is the material stiffness and its corresponding bulk modulus which measures the degree of stiffness or the energy required to produce a given volume deformation. The bulk modulus reflects important bonding characters in the material and, for many applications, is used as an indicator for material strength and hardness. Early experimental and theoretical investigations for bulk modulus were reported in [6,8]. Cohen [6] obtained an empirical expression for the bulk modulus based on the nearest-neighbor distance. His theoretical and experimental results were in agreement. Lam et al. [8] obtained an expression for bulk modulus using the total energy method with acceptable results. The bulk modulus for the semiconductor compounds was found to be inverse proportionally correlated to the lattice constants [8,17].

Historically, the study of anisotropic elastic materials has been synonymous with study of crystals. It is, therefore, natural to seek to characterize physical properties of crystal by constants (or invariants) whose values do not depend upon the choice of the coordinate system. Using several decomposition methods, these invariants were investigated such as photo elastic coefficients [37], piezoelectric coefficient [38] and elastic stiffness coefficients [39-42]. Physical properties are intrinsic characteristics of matter that are not affected by any change of the coordinate system. Therefore, tensors are necessary to define the intrinsic properties of the medium that relate an intensive quantity (i.e. an externally applied stimulus) to an extensive thermodynamically conjugated one (i.e. the response of the medium). Such intrinsic properties are the dielectric susceptibility, piezoelectric, and the elasticity tensors. Several studies were conducted to reveal the physical properties using decomposition methods for piezoelectric and elastic tensors [37-45]. An interesting feature of the decompositions is that it simply and fully takes into account the symmetry properties when relating macroscopic effects to microscopic phenomena. One can directly show the influence of the crystal structure on physical properties, for instance, when discussing macroscopic properties in terms of the sum of the contributions from microscopic building units (chemical bond, coordination polyhedron, etc). A significant advantage of such decompositions is to give a direct display of the bearings of the crystal structure on the physical property. For the stress and strain, for instance, the decomposition allows one to separate changes in volume from changes of shape in linear isotropic elasticity; the bulk modulus relates to the hydrostatic part of stress and strain while the shear modulus relates the deviatoric part [46].

It is often useful, especially when comparing different materials or systems having different geometrical symmetries, to characterize the magnitude of a physical property. One may also have to make, in a given material, a quantitative comparison of the contribution of the anisotropy to a physical property [42-44]. The comparison of the magnitudes of the decomposed parts can give, at certain conditions, valuable information about the origin of the physical property under examination [42,44]. These problems can be dealt with by defining the norm of a tensor. The norm is invariant and not affected by any change of the coordinate system. Invariance considerations are of primary importance when studying physical properties of matter, since these properties are intrinsic characteristics which are not affected by a change of the reference frame. Tu [42] and Jerphagnon et al. [43] proposed the norm criterion to quantify and then, quantitatively to compare the effect of piezoelectricity and elasticity using irreducible tensor theory. They compared the magnitude of piezoelectricity of two materials only of the same symmetry using Cartesian and spherical framework. However, their method seemed to be valid only for elastic tensor. Gaith et al. [44] developed a decomposition procedure based on constructing orthonormal tensor basis elements using the form-invariant expressions [37-41]. They introduced a method to measure the stiffness and piezoelectricity in fiber reinforced composite and piezoelectric materials, respectively, using the norm criterion on the crystal scale. In their method, norm ratios proposed to measure the degree of anisotropy in an anisotropic material, and compare it with other materials of different symmetries. They were able to segregate the anisotropic material property into two parts: isotropic and anisotropic parts. Of the new insights provided by invariance considerations, the most important is providing a complete comparison of the magnitude of a given property in different crystals. Such a comparison could be obvious for average refractive index, even birefringence, piezoelectricity, electro-optic effects, elasticity, etc. From a device point of view, the new insights facilitate the comparison of materials; one is interested in maximizing the figure of merit by choosing the optimum configuration (crystal cut, wave propagation direction and polarization, etc); and one wants to be able to state that a particular material is better than another for making a transducer or modulator [43]. It is most suitable for a complete quantitative comparison of the strength or the magnitude of any property in different materials belonging to the same crystal class, or different phases of the same material. The norm concept is very effective for selecting suitable materials for electro-optic devices, transducers, modulators, acousto-optic devices.

The goal of this study is to understand how qualitative ground state concepts, such as overall elastic stiffness, can be related to bulk modulus and lattice constants, An important observation for studying the respective semiconductors is the clear difference in the bulk modulus and lattice constants going from the group-IV to III-V and II-VI semiconductors. The relationship of the macroscopic characteristics of a covalent crystal (dielectric and elastic constants) and the microscopic ones (band gap, covalent,

atomic charge densities and lattice constants) is of interest. Therefore, using the elastic constant for anisotropic material, an elastic stiffness scale for such anisotropic material, and a scale to measure the isotropic elasticity within the material will be discussed. Besides, the microscopic origin of the overall elastic stiffness and bulk modulus calculation will be correlated with the structural properties parameter, i.e. lattice constant ***a***, which represents some fundamental length scale for the chemical bond of the unit cell.

2. Decomposition and Norm concept

The Orthonormal Decomposition Method (ODM) [44] is established through constructing an orthonormal tensor basis using the form-invariant expressions [37-39]. The basis is generated for the corresponding symmetry medium of the tensor, and the number of basis elements should be equal to the number of non-vanishing distinct stiffness coefficients that can completely describe the elastic stiffness in that medium. Accordingly, based on the Orthonormal Decomposition Method, the basis elements for isotropic material is obtained and consisted of two terms; shear and bulk moduli [44] and they are identical to those found in literature [46]. The elastic stiffness matrix representation for the isotropic system can be decomposed in a contracted form as:

$$C_{ij}=\begin{bmatrix} 2C_{44}+C_{12} & C_{12} & C_{12} & 0 & 0 & 0 \\ C_{12} & 2C_{44}+C_{12} & C_{12} & 0 & 0 & 0 \\ C_{12} & C_{12} & 2C_{44}+C_{12} & 0 & 0 & 0 \\ 0 & 0 & 0 & C_{44} & 0 & 0 \\ 0 & 0 & 0 & 0 & C_{44} & 0 \\ 0 & 0 & 0 & 0 & 0 & C_{44} \end{bmatrix} = A_1 \begin{bmatrix} 1&1&1&0&0&0 \\ 1&1&1&0&0&0 \\ 1&1&1&0&0&0 \\ 0&0&0&0&0&0 \\ 0&0&0&0&0&0 \\ 0&0&0&0&0&0 \end{bmatrix} + A_2 \begin{bmatrix} 4&-2&-2&0&0&0 \\ -2&4&-2&0&0&0 \\ -2&-2&4&0&0&0 \\ 0&0&0&3&0&0 \\ 0&0&0&0&3&0 \\ 0&0&0&0&0&3 \end{bmatrix} \quad (1)$$

where

$$A_1=\frac{1}{3}(C_{11}+2C_{12}),\ C_{11}\quad 2C_{44}\quad C_{12}\ =\qquad +$$
$$A_2=\frac{1}{15}(C_{11}-C_{12}\quad 3C_{44})\qquad +\qquad (2)$$

where A_1 and A_2 are the Voigt average polycrystalline bulk ***B*** and shear ***G*** modulus, respectively. The decomposed parts of Eq. (1) designated as bulk and shear modulus are identical to those found in literature [46-48].

For cubic crystals such as the II-VI semiconductor compounds, there are only three independent elastic stiffness coefficients C_{11}, C_{12} and C_{44} that can describe the mechanical elastic stiffness for these materials. The elastic coefficient C_{11} is the measure of resistance to deformation by a stress applied on the (100) plane, while C_{44} represents the measure of resistance to deformation with respect to a shearing stress applied across the (100) plane. These elastic coefficients are function of elastic material parameters, namely, Young's modulus, shear modulus, and Poisson's ratio. Thus, using the orthonormal decomposition procedure [44], the elastic stiffness matrix representation for cubic system can be decomposed in a contracted form as:

$$C_{ij}=\begin{bmatrix} C_{11} & C_{12} & C_{12} & 0 & 0 & 0 \\ C_{12} & C_{11} & C_{12} & 0 & 0 & 0 \\ C_{12} & C_{12} & C_{11} & 0 & 0 & 0 \\ 0 & 0 & 0 & C_{44} & 0 & 0 \\ 0 & 0 & 0 & 0 & C_{44} & 0 \\ 0 & 0 & 0 & 0 & 0 & C_{44} \end{bmatrix} = A_1 \begin{bmatrix} 1&1&1&0&0&0 \\ 1&1&1&0&0&0 \\ 1&1&1&0&0&0 \\ 0&0&0&0&0&0 \\ 0&0&0&0&0&0 \\ 0&0&0&0&0&0 \end{bmatrix} + A_2 \begin{bmatrix} 4&-2&-2&0&0&0 \\ -2&4&-2&0&0&0 \\ -2&-2&4&0&0&0 \\ 0&0&0&3&0&0 \\ 0&0&0&0&3&0 \\ 0&0&0&0&0&3 \end{bmatrix} + A_3 \begin{bmatrix} -4&2&2&0&0&0 \\ 2&4&-2&0&0&0 \\ 2&2&-4&0&0&0 \\ 0&0&0&2&0&0 \\ 0&0&0&0&2&0 \\ 0&0&0&0&0&2 \end{bmatrix} \quad (3)$$

where

$$A_1=\frac{1}{3}(C_{11}+2C_{12})$$
$$A_2=\frac{1}{15}(C_{11}-C_{12}\quad 3C_{44})\qquad +\qquad (4)$$
$$A_3=\frac{1}{10}(C_{12}-C_{11}\quad 2C_{44})\qquad +$$

It can be shown that the sum of the three orthonormal parts on the right hand side of Eq. (3) is apparently the main matrix of cubic system [47]. Also, the first two terms on the right hand side are identical to the corresponding two terms obtained in Eq. (1) for the isotropic system [47]. Hence, it can be stated that the cubic system is discriminated into the sum of two parts: isotropic part (first two terms), and anisotropic part (third term). The latter term resembles the contribution of the anisotropy on elastic stiffness in the cubic system. On the other hand, the first term on the right hand side of Eqs (1) and (3), designated as the bulk modulus, is identical to Voigt bulk modulus [47].

Since the norm is invariant for the material, it can be used for a Cartesian tensor as a parameter representing and comparing the overall stiffness of anisotropic materials of the same or different symmetry or the same material with different phases [42-44]. The larger the norm value is, the more the elastic stiffness of the material is. The concept of the modulus of a vector, norm of a Cartesian tensor is defined as [44]:

$$N=\|C\|=\ C_{ij}\square C_{ij}\ ^{1/2} \qquad (5)$$

3. Results and Discussion

Table 1 presents the materials elastic stiffness coefficients, calculated bulk B and overall elastic stiffness N moduli for the II-VI semiconductor ZnX (X=S, Se, and Te) compounds. Figure 1 shows clearly the correlation between overall elastic stiffness N and bulk modulus B. Quantitatively, the overall elastic stiffness increases as the calculated bulk modulus B increases. Besides, the calculated bulk moduli are identical to those found by theory of anisotropy [47], and are in agreement with experimental values [6] with maximum error of 8.5 % for ZnTe. The calculated bulk moduli obey the cubic stability

conditions, meaning that $C_{12} \le B \le C_{11}$. Figure 2 shows that the bulk modulus is inversely proportional to lattice constants a which was confirmed in several studies [8,14,17,21]. Consequently, from Figure 3 the overall elastic stiffness N is inversely proportional to lattice constants a, as well. Figures 1-3 indicate that among the three compounds under examination, ZnS has the largest elastic stiffness, largest bulk modulus (lowest compressibility), and lowest lattice constant, while ZnTe, in contrary, has the smallest elastic stiffness, smallest bulk modulus, and largest lattice constant. Therefore, the overall elastic stiffness and bulk modulus, the only elastic moduli possessed by all states of matter, reveal much about interatomic bonding strength. The bulk modulus also is the most often cited elastic constant to compare interatomic bonding strength among various materials [48], and thereafter the overall elastic stiffness can be cited as well.

For the isotropic symmetry material, the elastic stiffness tensor is decomposed into two parts as shown in Eq. (1), meanwhile, the decomposition of the cubic symmetry material, from Eq. (3), is consisted of the same two isotropic decomposed parts and a third part. It can be verified the validity of this trend for higher anisotropy, i.e., any anisotropic

Table 1 Elastic coefficients *(GPa)*[4], overall stiffness *N (GPa),* bulk modulus *B (GPa)*, and lattice constants *a* (*nm*).

	C_{11}	C_{12}	C_{44}	N	B	B_{exp}[6]	a[13]
ZnS	104	65	46.2	266.5	78	77	0.54
ZnSe	95.9	53.6	48.9	244.0	67.7	64.7	0.57
ZnTe	82	42	55	224.0	55.3	51	0.61

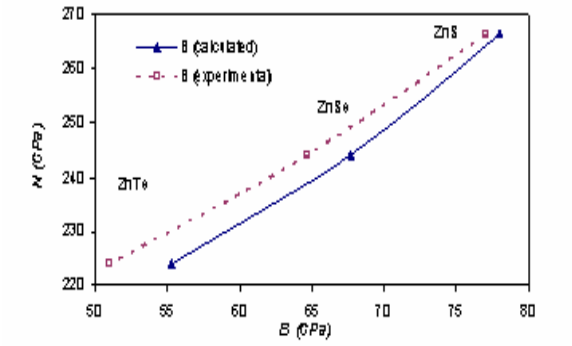

Figure 1 The overall elastic stiffness N versus bulk modulus B for ZnX (X=S, Se, Te).

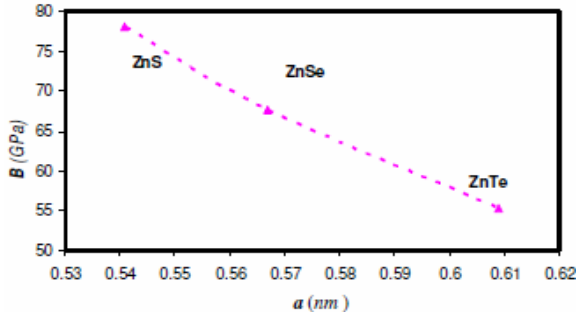

Figure 2 The bulk modulus B versus the lattice constants a for ZnX (X=S, Se, Te).

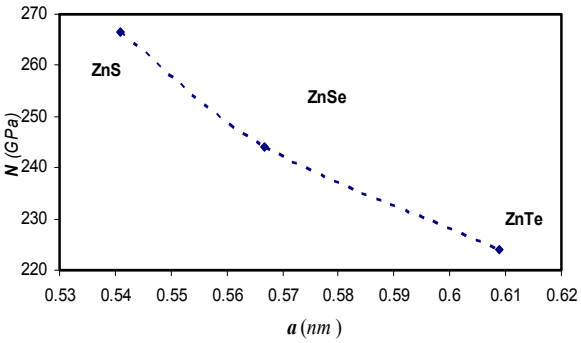

Figure 3 The overall stiffness N versus the lattice constants a for ZnX (X=S, Se, Te).

elastic stiffness will consist of the two isotropic parts and anisotropic parts. Their total parts number should be equal to the number of the non-vanishing distinct elastic coefficients for the corresponding anisotropic material. Anisotropic materials with orthotropic symmetry, for example, like fiber reinforced composites should have two isotropic parts and seven independent parts. Consequently, The Norm Ratio Criteria (NRC) used in this paper is similar to that proposed in [44]. For isotropic materials, the elastic stiffness tensor has two parts, Eq.(1), so the norm of the elastic stiffness tensor for isotropic materials is equal to the norm of these two parts, Eq.(5), i.e., $N = N_{iso}$. Hence, the ratio $\frac{N_{iso}}{N}$ is equal to one for isotropic materials. For cubic symmetry materials, the elastic stiffness tensor has the same two parts that consisting the isotropic symmetry materials and a third, will be designated as the other than isotropic or the anisotropic part. Hence, two ratios are defined as: $\frac{N_{iso}}{N}$ for the isotropic parts and $\frac{N_{aniso}}{N}$ for the anisotropic part(s). For more anisotropic materials (like orthotropic composites), the elastic stiffness tensor additionally contains more anisotropic parts, and then $\frac{N_{aniso}}{N}$ is defined for all the anisotropic parts. The norm ratios can also be used to assess the degree of anisotropy of a material property as a whole. In this paper the following criteria are proposed: when N_{iso} is dominating among norms of the decomposed parts, the closer the norm ratio $\frac{N_{iso}}{N}$ is to one, the more isotropic the material is. When N_{iso} is not dominating, norm ratio of the other parts, $\frac{N_{aniso}}{N}$, can be used as a criterion. But in this case the situation is reversed; the closer the norm ratio $\frac{N_{aniso}}{N}$ is to one, the more anisotropic the material is.

The norms and norm ratios for ZnS, ZnSe, and ZnTe are calculated and presented in Table 2. From the table, interesting phenomena are observed; as the isotropic ratio

$\frac{N_{iso}}{N}$ increases, the anisotropic ratio $\frac{N_{aniso}}{N}$ decreases, which confirms the definitions of these two ratios, and the bulk modulus increases at the same time. Therefore, the nearest material to isotropy (or least anisotropy) is ZnS, with $\frac{N_{iso}}{N}$ = 0.9830, in which corresponds to the largest bulk modulus B = 78 GPa. The least isotropic (or nearest to anisotropy) is ZnTe, with $\frac{N_{iso}}{N}$ = 0.9581, in which corresponds to the smallest bulk modulus B = 55.3 GPa. Since the cubic system is the nearest to isotropy among the anisotropic systems, the calculated values of isotropic norm ratio, $\frac{N_{iso}}{N}$, in Table 2 are very close to one (i.e., 0.9581 - 0.9830). Hence, it can be concluded that the closer the material is to isotropy, the larger the bulk modulus for the material is. A reverse trend correlating the norm ratios and lattice constants can be seen from the table; the closer the material is to isotropy, the smaller the lattice constant for the material is.

Table 2 The overall elastic stiffness *N* (*GPa*) and norm ratios for the II-IV semiconductor compounds ZnS, ZnSe, and ZnTe

	N_{iso}	N_{aniso}	N	$\frac{N_{iso}}{N}$	$\frac{N_{aniso}}{N}$	B	a
ZnS	262	49	266.5	0.9830	0.1836	78	0.54
ZnSe	238.7	50.9	244.0	0.9780	0.2084	67.7	0.57
ZnTe	214.6	64.2	224.0	0.9581	0.2865	55.3	0.61

4. Conclusions

An interesting feature of the decompositions is that it simply and fully takes into account the symmetry properties when relating macroscopic effects to microscopic phenomena. Therefore, the decomposition of elastic stiffness for cubic system materials into two parts; isotropic (two terms) and anisotropic parts is presented. A scale for measuring overall elastic stiffness is introduced and correlated with lattice constants and calculated bulk modulus. The overall elastic stiffness of II-IV semiconductor compounds ZnS, ZnSe, and ZnTe is calculated and found to be directly proportional to bulk modulus and inversely proportional to lattice constants. Among these compounds, ZnS has the largest overall elastic stiffness and bulk modulus and the smallest lattice constant. Meanwhile, ZnTe has the smallest overall elastic stiffness and bulk modulus and the largest lattice constant. The Norm Ratio Criteria (NRC) is introduced to scale and measure the isotropy in the cubic system material among the semiconductor compounds ZnS, ZnSe, and ZnTe. Hence, a scale quantitative comparison of the contribution of the anisotropy to the elastic stiffness and to measure the degree of anisotropy in an anisotropic material is proposed. ZnS is the nearest to isotropy (or least anisotropic) while ZnTe is the least isotropic (or nearest to anisotropic) among these compounds. These conclusions will be investigated on the II-IV semiconductor compounds CdX (X=S, Se, Te) in the next paper.

References

[1] C.H. Fischer, M. Batzer, T. Glatzel, I. Lauermann, M.C. Lux-Steiner, "Interface engineering in chalcopyrite thin film solar devices", Solar Energy Materials and Solar Cells Vol. 90, 2006, 1471-1585.

[2] D.L. Bätzner, A. Romeo, M. Terheggen, M. Döbeli, H. Zogg, A.N. Tiwari, "Stability aspects in CdTe/CdS solar cells", Thin Solid Films, Vol. 451, 2004, 536-543.

[3] H. Okuyama, T. Miyajima, Y. Moringa, F. Hiei, M. Ozawa, K. Akimot, "ZnSe/ZnMgSSe blue diode", Electronics Letters, Vol. 28, 1992, 1798-1799.

[4] S. Reich, A.C. Ferrari, R. Arenal, A. Loiseau, I. Bellom, J. Robertson, "Resonant raman scattering in cubic and hexagonal boron nitride", Physical Review B, Vol. 71, 2005, 205201-205212.

[5] R.L. Leitsmann, L.E. Ramos, F. Bechstedt, "Structural properties of PbTe/CdTe interfaces from first principles", Physical Review B, Vol. 74, 2006, 085309-085316.

[6] M.L. Cohen, "Calculation of bulk moduli of diamond and zinc-blende solids", Physical Review B, Vol. 32, 1985, 7988-7991.

[7] E. Kim, C. Chen, "Calculation of bulk modulus for highly anisotropic materials", Physics Letters A, Vol. 326, 2004, 442-448.

[8] P.K. Lam, M.L. Cohen, G. Martinez, "Analytic relation between bulk moduli" and lattice constants, Physical Review B, Vol. 35, 1987, 9190-9194.

[9] D. Berlincourt, H. Jaffe, L.R. Shiozawa, "Electroelastic properties of the sulfides, selenides, and tellurides of zinc and cadmium", Physical Review, Vol. 129, 1963, 1009-1017.

[10] Phillips, J.C. Bonds and bands in semiconductors. SD: Academic Press; 1973.

[11] P.K. Pandey, "Study of temperature dependence of interatomic separation and bulk modulus for ionic solids", Journal of Physics and Chemistry of Solids, Vol. 59, 1998, 1157-1160.

[12] S.B. Zhang, M.L. Cohen, "High-pressure phases of iii-v zinc-blende semiconductors", Physical Review B, Vol. 35, 1987, 7604-7610.

[13] J.R. Chelikowsky, "High-pressure phase transitions in diamond and zinc-blende semiconductors", Physical Review B, Vol. 35, 1987, 1174-1180.

[14] N.E. Christensen, O.B. Christensen, "Electronic structure of ZnTe and CdTe under pressure", Physical Review B, Vol. 33, 1986, 4739-4746.

[15] N.E. Zein, V.P. Antropov, "Self-consistent green function approach for calculation of electronic structure in transition metals", Physical Review Letters, Vol. 89, 2002, 126402-126405.

[16] S.R. Krishnakumar, R.N. Shanthi, D.D. Sarma, "Electronic structure of millerite Nis", Physical Review B, Vol. 66, 2002, 115105-11510.

[17] Y. Al-Douri, H. Abid, H. Aourag, " Empirical formula relating the bulk modulus to the lattice constant in tetrahedral semiconductors", Materials Chemistry and Physics, Vol. 87, 2004, 14-17.

[18] R. Dornhaus, G. Nimtz, W.Richter. Solid State Physics. Berlin: Springer; 1976.

[19] Harison, W.A. Electronic structure and the properties of solids. Toronto: General Publishing Company; 1989.

[20] T. Kobayasi, H. Nara. Bull. Coll. Sci., Tohuku University 2; 1993.

[21] H. Ledbetter, "Relationship between bulk-modulus temperature dependence and thermal expansivity", Physica Status Solidi B, Vol. 181, 1994, 81-85.

[22] Y. Al-Douri, H. Abid, H. Aourag, "Correlation between the bulk modulus and the charge density in semiconductors", Physica B, Vol. 305, 2001, 186-190.

[23] M. Ferhat, A. Zaoui, B. Khelifa, H. Aourag, "Band structure calculations of gexsi1−x", Solid State Communications, Vol. 91, 1994, 407-411.

[24] M. Kumar, "Temperature dependence of interatomic separation and bulk modulus for ionic solids", Physica B, Vol. 205, 1995, 175-179.

[25] A.M. Sherry, M. Kumar, "Analysis of thermal expansion for alkali halide crystals using the isobaric equation of state", Journal of Physics and Chemistry of Solids, Vol. 52, 1991, 1145-1148.

[26] J.L. Tallon, "The thermodynamics of elastic deformation—I: equation of state for solids", Journal of Physics and Chemistry of Solids, Vol. 41, 1980, 837-850.

[27] M. Kumar, S.P. Upadhyaya, "Analysis of the thermal expansion coefficient and its temperature dependence for alkali halides", Physica Status Solidi B, Vol. 181, 1994, 55-61.

[28] Q. He, Z. Yan, "Study of temperature dependence of bulk modulus and interatomic separation for ionic solids", Physica Status Solidi B, Vol. 223, 2001, 767-771.

[29] H. Ledbetter, "Sound velocities, elastic constants: temperature dependence", Materials Science and Engineering A, Vol. 442, 2006, 31-34.

[30] J.C. Collins, G.K. White, J.A. Birch, T.F. Smith, "Thermal expansion of ZnTe and HgTe and heat capacity of HgTe at low temperatures", Journal of Physics C, Vol. 13, 1980, 1649-1656.

[31] J.C. Jamieson, H.H. Demarest, "A note on the compression of cubic ZnS", Journal of Physics and Chemistry of Solids, Vol. 41, 1980, 963-964.

[32] S.H. Wei, A. Zunger, "Role of metal d states in II-VI semiconductors", Physical Review B, Vol. 37, 1980, 8958 - 8981.

[33] G.E. Engel, R.J. Needs, "Calculations of the structural properties of cubic zinc sulfide", Physical Review B, Vol. 41, 1990, 7876-7878.

[34] M.P. Tosi' Solid State Physics. Vol. 16, 1964, 1

[35] R. Khenata, A. Bouhemadou, M. Sahnoun, A. Reshak, H. Baltache, M. Rabah, "Elastic, electric and optical properties of ZnS, ZnSe, and ZnTe under pressure", Computational Materials Sciences, Vol. 38, 2006, 29-38.

[36] Landolt-Bornstein. Numerical data and functional relationships in science and technology—crystal and solid state physics. Vol. 22. Berlin: Springer-Verlag; 1987.

[37] T.P. Srinivasan, S.D. Nigam, "Invariant forms", J.ournal of Mathematical and Physical Sciences, Vol. 2, 1968, 311-320.

[38] T.P. Srinivasan, "Invariant piezoelectric coefficients for crystals", Physica Status Solidi B, Vol. 41, 1970, 615-620.

[39] T.P. Srinivasan, "Invariant elastic constants for crystals", Journal of Mathmatics and Mechanics, Vol. 19, 1969, 411-420.

[40] T.P. Srinivasan, "Invariant acoustic gyrotropic coefficients", Journal of Physics C, Vol. 18, 1985, 3263-3271.

[41] Spencer, A.T.M. Continuum mechanics. London: Longmans; 1983.

[42] Y.O. Tu, "The decomposition of anisotropic elastic tensor", Acta Crystallographica A, Vol. 24, 1968, 273-282.

[43] J. Jerphagnon, D.S. Chemla, R. Bonnevile, "The decomposition of condensed matter using irreducible tensors", Advances in Physics, Vol. 27, 1978, 609-650.

[44] M. Gaith,, C.Y. Akgoz, "A new representation for the properties of anisotropic elastic fiber reinforced composite materials", Review of Advance Material Sciences, Vol. 10, 2005, 138-142.

[45] S. Sutcliffe, "Spectral decomposition of the elasticity tensor", Journal of Applied Mechanics, ASME Vol. 59, 1992, 762-773.

[46] W. Voigt, "The relation between the two elastic moduli of isotropic materials", Annals of Physics, (Leipzig) Vol. 33, 1889, 573.

[47] Hearmon, R.F.S. An introduction to applied anisotropic elasticity. Oxford: University Press; 1961.

[48] C. Pantea, I. Mihut, H. Ledbetter, H.,J.B.Betts, Y.Zhao, L.L. Daemen, H. Cynn, A. Miglori, "Bulk modulus of osmium", Acta Materialia Vol. 57, 2009, 544-548.

JJMIE

Volume 4, Number 1, Jan. 2010
ISSN 1995-6665
Pages 61 - 68

Jordan Journal of Mechanical and Industrial Engineering

Thermodynamic Simulation Modelling of Low-Temperature Geothermal Source Located in Arid-Zone Area North Africa

S. Masheiti [a,*], B. Agnew [b]

[a] School of Mechanical and Systems Engineering, University of Newcastle upon Tyne,

Stephenson Building, Claremont Road, NE1 7RU, United Kingdom

[b] School of the Built Enviroment, Northumbria University, Ellison Building, Newcastle upon Tyne, NE1 8ST, United Kingdom

Abstract

This paper presents a thermodynamic modelling study of the utilization of an existing geothermal low-temperature heat source (114 kg/s and 73 °C) situated at Waddan city in Libya. Six models have been built and simulated using both IPSEpro refrigeration and power plant modelling libraries. All the models were validated in accordance to published literature and relevant fundamental thermodynamic tables and graphs. Results of five models have shown that the community in Waddan city could benefit from the geothermal source. For instance these models could provide 1284 ton of refrigeration at 5 °C, for air-conditioning use, or 835 ton of refrigeration at 0°C or 1324 kW of direct generated electricity. The sixth model has proved that this sustainable geothermal source could support a local electrical power station consisting of a natural gas fired turbine unit combined with an organic Rankin cycle. This station will provide Waddan city and surrounding villages with their demand of electrical and thermal energy of about 128MW (GT 85MW, ORC 18MW and District heating 25 MW at 75 °C).

Keywords: Arid-zone; low-temperature geothermal heat source; LiBr absorption chillers; air-conditioning; organic Rankin cycle; IPSEpro.

1. Introduction

In recent years, research has been devoted to improvement of absorption refrigeration systems. Mechanical vapour compression refrigerators require high grade energy for their operation. Apart from this, recent studies have shown that the conventional working fluids of vapour compression systems are causing ozone layer depletion and green house effect [1]. Absorption chillers powered by heat energy can be utilized. Since the temperature requirements for the cycle fell into the low to moderate temperature range, the water/air cooled lithium bromide water mixture single/half effect absorption chillers seem to be good prospect for geothermal application where heat inputs are at low temperatures. However most of these types of chillers, as mentioned by many researchers, were directly powered by low input mass flow rates of high or low temperature heat sources such as steam or hot water.

The most economical way to utilize geothermal source of energy is to use it as a powering source of single/half effect water/air cooled absorption chillers to produce air-conditioning, heating and hot water supply [2]. Many theoretical and experimental studies have been carried out on LiBr-H_2O absorption chillers powered by low heat sources. For instance, A.Kececiler et al. [3] performed experiments on LiBr-H_2O system in lab conditions used low temperature geothermal energy as a powering source. The obtained results showed that the maximum COP was gained when mass concentration of strong and weak solution in the generator and absorber were 0.44 and 0.48 respectively. They showed experimentally that the low-heat geothermal sources can not be used inefficiently in electricity generation, however could be used economically for refrigeration storing of fruits and vegetables at 4-10 °C as well as air conditioning. K. Sumathy et al. [4] developed prototype (cooling capacity = 100 kW) half effect LiBr-H_2O chiller powered by low temperature hot water source ranging from 60 to 75 °C. Test results indicated that the two-stage chiller could be powered by solar hot water system. Da-Wen Sun [5] simulated LiBr-H_2O absorption refrigeration systems. Detailed thermodynamic design data and optimum design maps were produced as a source of reference for developing new cycles and searching for new absorbent/refrigeration pairs. The derived tabulated thermodynamic design data showed that for low heat powering source at about 70 °C, the COP was 0.83 and the mass concentration of weak and strong solutions of LiBr were between 0.516 and 0.579 respectively when both condenser and absorber temperatures run at 30 °C. Figure 1 shows existing geothermal source at high potential and low-temperature heat situated at Waddan city 265 Km south of Libyan North coast.

* Corresponding Author. s.a.a.masheiti@ncl.ac.uk .

The well No. is T/2D/0013/0/88 at coordinates of X = 16 ° 09' 46'' ,Y = 29° 07' 06'' and at an elevation of 291 meters above sea level [6]. This existing sustainable freely available geothermal source was simulated using two IPSEpro power plant and refrigeration modelling libraries. Six schematic models, powered by this artesian hot water 12'' diameter well (1600 m deep) at constant flow rate of 114 kg/s and temperature of 73 °C, are presented in figures 5-10 respectively and they are namely as follows:

1- Water-cooled single effect LiBr-H_2O chiller.
2- Air-cooled single effect LiBr-H_2O chiller.
3- Water-cooled half effect LiBr-H_2O chiller.
4- Water-cooled half effect cascaded with CO_2 conventional compression cycle chiller.
5- Direct electrical generation organic Rankin cycle.
6- Water-cooled half effect cascaded with electrical generation gas turbine and R-245fa organic Rankin cycle.

Figures 2-4, show validation of simulated basic standalone models (single and half effect chillers), in accordance to the well known DÜhring temperature-pressure diagram [7]. The main state points of chillers cycle parameters were plotted at their state point locations on this diagram.

Figure 1. Well head of existing geothermal source

2. Modelling

The fundamental thermodynamic principles of mass and energy conservation were applied on all chiller cycle components. UA types of heat exchanger models were used for all of absorption chiller components except two components; the desorber unit which was modelled as an adiabatic flash drum for two-phase mixture where exiting streams are in equilibrium and exiting vapour is pure water, and in the absorber unit the restored poor solution takes up the occurring gaseous refrigerant mixture and leaves the absorber as a rich solution [8]. For heat exchangers, it is common to use UA formulation along with log-mean temperature difference (LMTD) as follows:

$$Q = UA\ \Delta T_{lm}$$

where Q : heat exchange capacity (w), U : overall heat transfer coefficient (w/m^2 k), A : heat transfer surface area (m^2), ΔTlm : logarithmic mean temperature difference (K)

$$\Delta T_{lm} = \frac{\left(T_{h,1} - T_{c,2}\right) - \left(T_{h,2} - T_{c,1}\right)}{\ln \dfrac{T_{h,1} - T_{c,2}}{T_{h,2} - T_{c,1}}}$$

where h: hot side, c : cold side, 1 & 2 : either end of heat exchanger.
The maximum possible heat transfer can be calculated from

$$Q_{\max} = \left(mc_p\right)_{\min} \Delta T_{inlet}$$

where m : mass flow rate (kg/s), c_p : specific heat at constant pressure (kJ/kg K), ΔT_{inlet} : inlet temperature difference (K).
The energy balance on each of heat exchangers is:

$$Q = \dot{m}\Delta h$$

where $\dot{m}$: mass flow rate (kg/s), Δh : the enthalpy difference between inlet and outlet of heat exchangers (kJ/kg).
The coefficient of performance of absorption chillers can be written as:

$$COP = \frac{Q_{evaporator}}{Q_{generator}}$$

The mass fraction of two-component (binary) mixture of LiBr/H_2O can be, in general, expressed as:

$$x = \frac{mass\ of\ one\ component\left(kg\right)}{Total\ mass\ of\ both\ components\left(kg\right)}$$

3. Simulated Models Results and Discussion

3.1 Water-cooled single effect

It can be seen from simulated results in figure 5, that the best obtained COP and refrigeration capacity, at outlet chilled water temperature of 5 °C, were 0.8245 and 563 ton respectively. In addition the useful rejected energy from the desorber was 15739 kW at outlet temperature of 68 °C. These output results achieved when the cycle operated between 0.51 and 0.55 of LiBr-H_2O solution mass fraction and between two low pressure levels of 0.04 and 0.007 bar. The cooling water supply, for removing excess heat from absorber and condenser, was in parallel connection to cycle components at an input mass flow rate of 258 kg/s and at 25 °C.

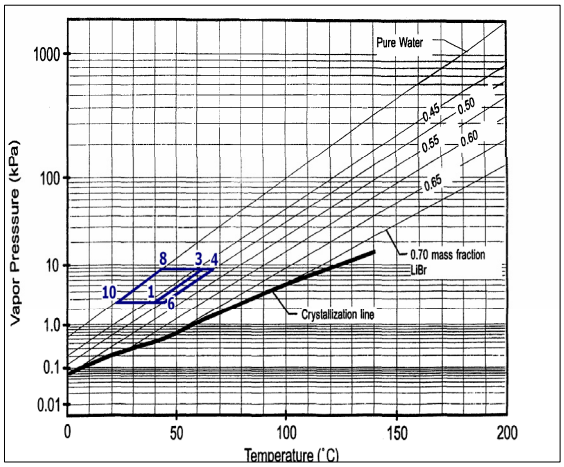

Figure 2. DÜhring plot for validation of Water-cooled single effect model

3.2 Air-cooled single effect

As shown in figure 6, the model was simulated at an outdoor average mean maximum dry bulb temperature of 40 ºC (design reference point according to ASHRAE). The range of LiBr-H2O solution mass fraction was between 0.47 and 0.5 which was less than that used in water-cooled single effect cycle due to higher weak solution outlet temperature of the absorber, hence higher heat transfer rate circulated in the cycle. The cycle was performed between two pressure levels 0.026 and 0.0865 bar. The achieved COP and refrigeration capacity were 0.845 and 628 ton respectively. The chilled water outlet temperature of the evaporator was noticeably high (22ºC) but still within the range of air-conditioning use in hot climate conditions such as Waddan city. The utilized output heating energy was roughly equals to that produced from water-cooled single effect chiller.

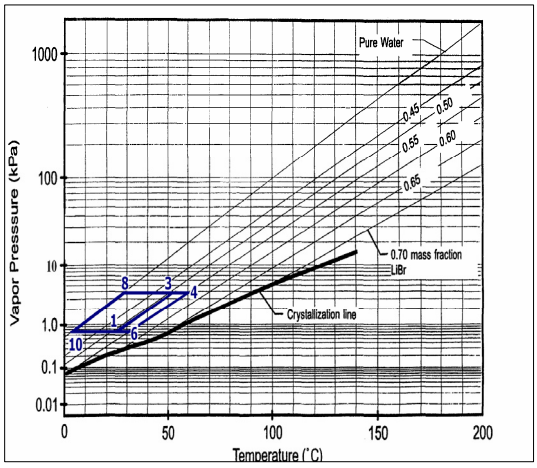

Figure 3. DÜhring plot for validation of Air-cooled single effect model

3.3 Water-cooled half effect

The schematic configuration of this model is shown in figure 7, the model is operated in three-pressure levels (0.07, 0.018 and 0.0071 bar). The high and low pressure levels function in the same way similar to the single effect one. The intermediate pressure level is the new feature of this cycle arrangement, and at this pressure level, the low desorber delivers refrigerant vapour to the high absorber. The obtained results have shown that a refrigeration capacity of 1284 ton was produced at outlet chilled water temperature of 5 ºC. This higher capacity was roughly double of water/air single effect chillers capacity. In this cycle more heat was extracted from the given powering source, hence no significant economical benefit of heat rejected from the desorber. A penalty must be paid when the cycle produced higher cooling capacity; the COP of the half effect is roughly half (0.424) of COP obtained from single effect chillers (0.8245-0.845). Both lower LiBr H2O mass fraction (0.41-0.44) in high pressure cycle and higher mass fraction (0.52-0.55) in low pressure cycle were circulated within modelled cycle.

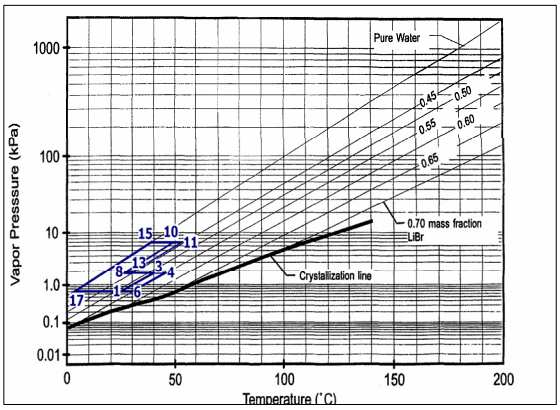

Figure 4. DÜhring plot for validation of Water-cooled half effect model

3.4 water-cooled half effect cascaded with conventional compression cycle CO2 chiller unit

To obtain further reduction of evaporator chilled water outlet temperature (≈ 0 ºC) in hot climate conditions, the half effect simulated absorption chiller model should be cascaded with carbon dioxide CO2 (R744) refrigeration compression cycle chiller model. The Selection of CO_2 as working refrigerant in the low temperature Rankin cycle, was based on the fact that this gas is natural, cheap, cause no damage to the environment, and is not hazardous. The complete schematic diagram for this combined cycle is shown in Figure 8. The results have shown that the refrigeration capacity was 835 ton at chilled temperature of roughly zero degrees centigrade.

3.5 Direct electrical generation organic Rankin cycle

The community in Waddan city could directly benefit from the existing geothermal source by simply installing an organic Rankin cycle (ORC) for direct electricity generation. R-245fa was found to be the most suitable working fluid among other related organic refrigerants, such as R134a. As shown in figure 9, the simulated results have indicted that a net electrical power of 1324 kW was produced at an ORC efficiency of 8.4 %.

3.6 Water-cooled half effect cascaded with gas turbine (GT) and R-245fa organic Rankin cycle (ORC)

Geothermal sources available in hot climate places and near natural gas fields could economically encourage local electrical investment companies to install combined cycle power plant (GT and ORC) to supply Waddan community

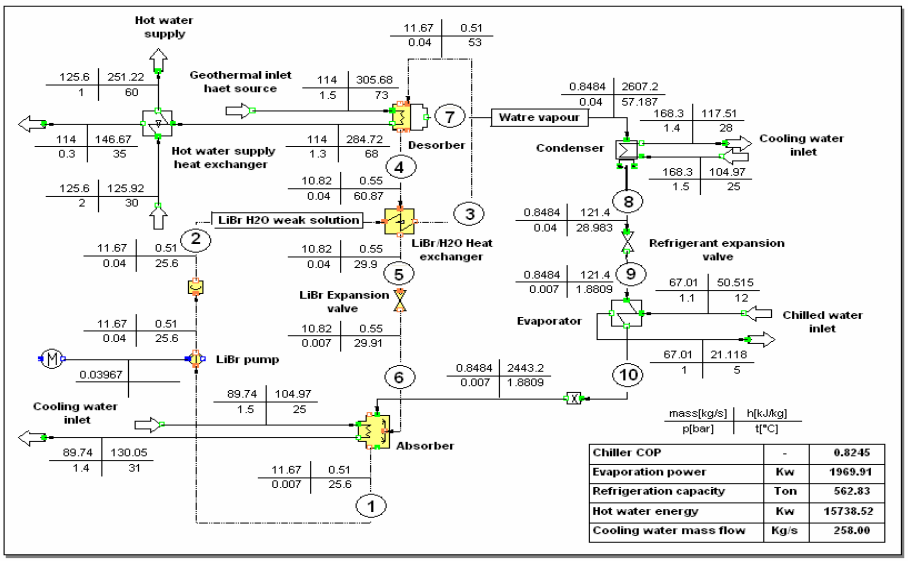

Figure 5. Water-cooled single effect LiBr-H2O absorption chiller

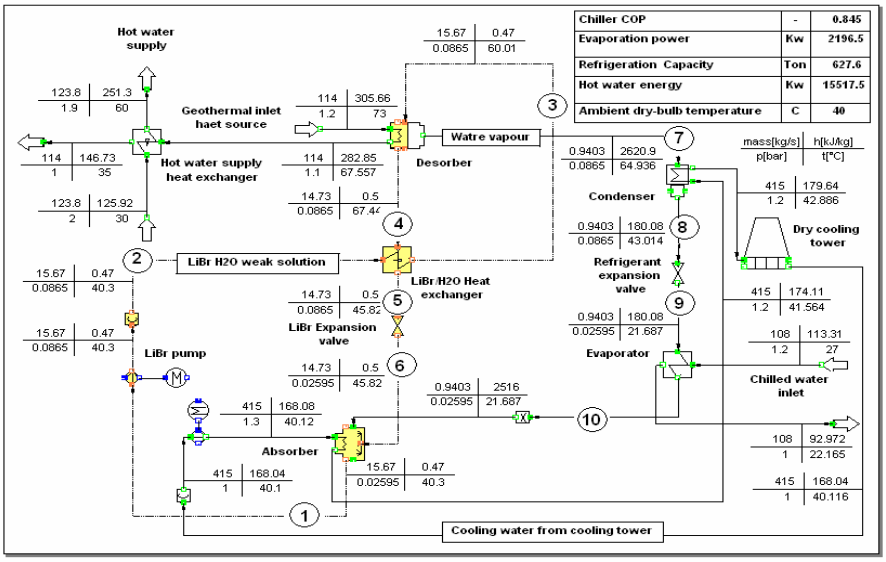

Figure 6. Air-cooled single effect LiBr-H2O absorption chiller

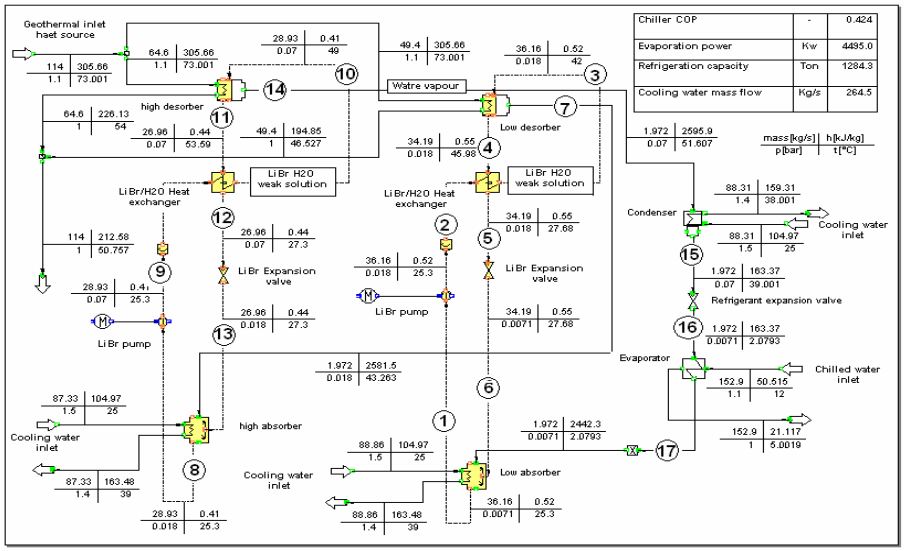

Figure 7. Water-cooled half effect LiBr-H2O absorption chiller.

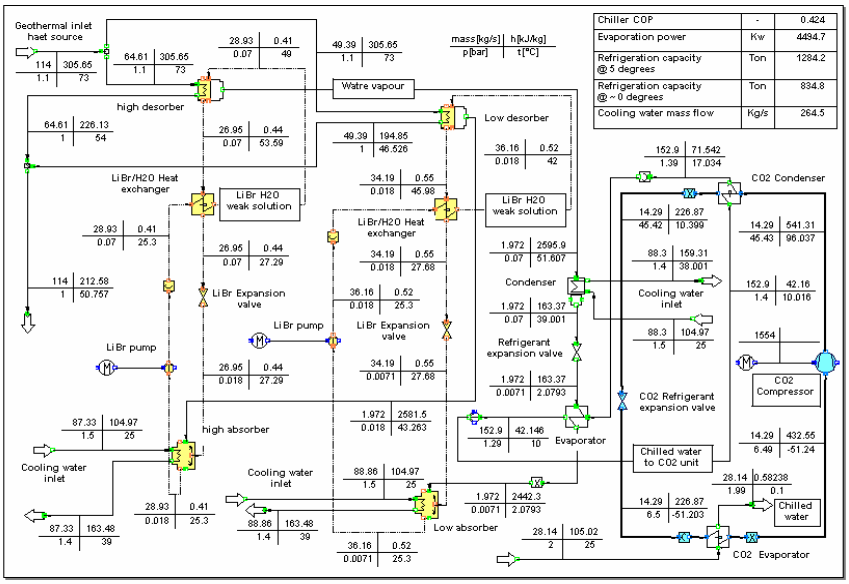

Figure 8. Water-cooled half effect cascaded with CO2 compression cycle chiller

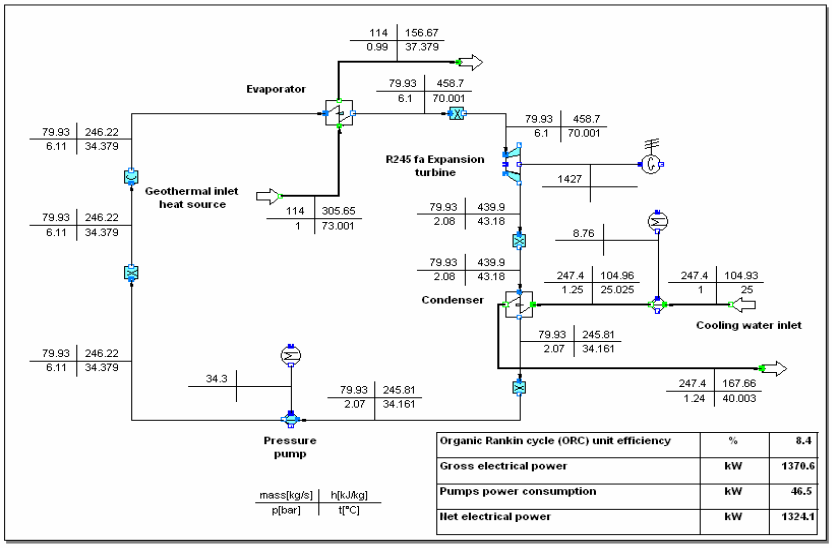

Figure 9. Direct electricity generation by R245fa organic Rankin cycle (ORC)

and surrounding villages with their demand of direct generated electricity and hot water supply. Results obtained in figure 10 have shown that the net output electrical energy and hot water energy were 103 MW and 25 MW respectively. Around 21% (18108 kW) of total produced electricity was from ORC unit. This can be considered as good achieved contribution in saving ozone layers from harmful LNG exhaust emissions.

4. Results summery

The obtained results of the proposed simulated models are displayed in figures 5-10 respectively and also summarized, for clarity, in two tables. Table 1 lists COP, chilled and hot water energies. Table 2 shows produced electrical energy. Graphical presentations for COP and refrigeration capacity are produced in figures 11 and 12 respectively.

5. Conclusion

A- For the stand alone absorption models (water and air cooled single and half effect chillers) the simulated results show, thermodynamically, that this low-temperature geothermal source can be used as heat source for both half and single effect Lithium bromide water mixture absorption chillers. The cooling capacities and coefficients of performance (COP) were found to be within acceptable published limits. The usable chilled water temperature difference a cross the evaporators, of water-cooled single/half effect chillers, was found within the range of air-conditioning use in hot climate conditions. The comparison between the three different models has indicated that the high cooling capacity was produced by water-cooled half effect chiller without any significant economical benefit of the heat rejected from the desorber.

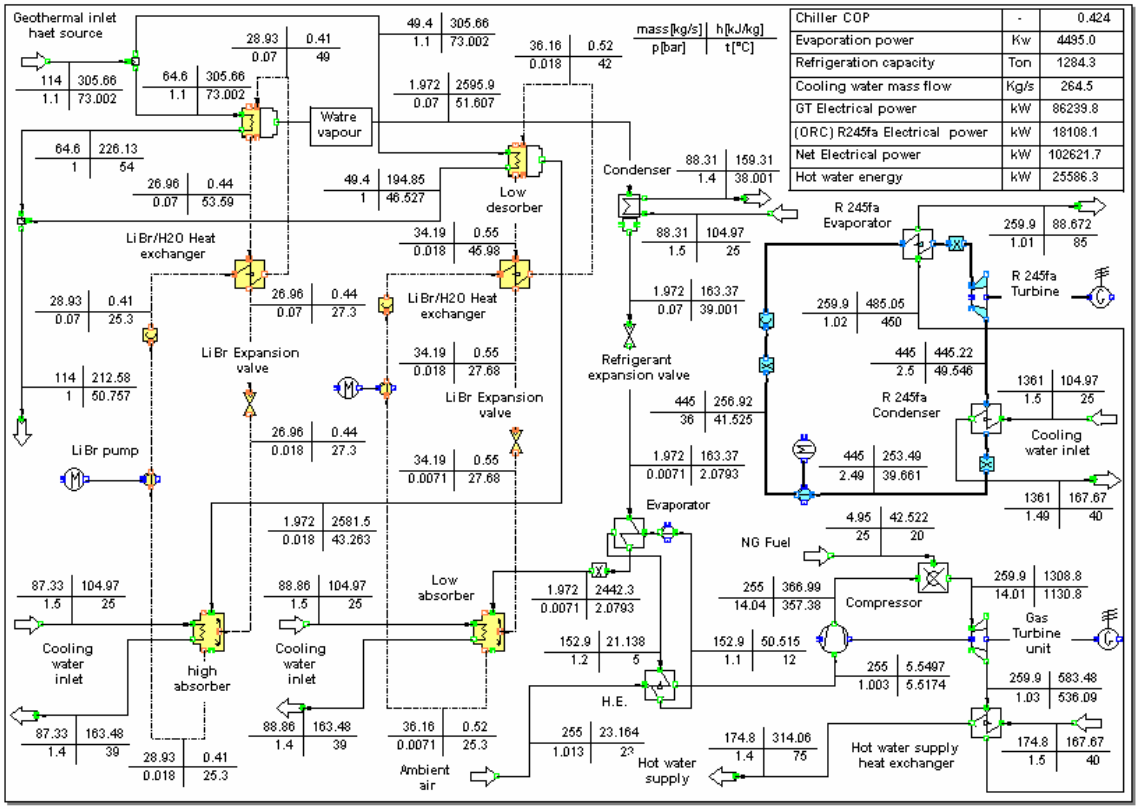

Figure 10. Water-cooled half effect cascaded with gas turbine (GT) and R-245fa organic Rankin cycle (ORC)

Table 1. Outlet results of thermal energy models

Output parameters	Absorption chiller model type			
	Water-cooled Single effect	Air-cooled Single effect	water-cooled Half effect	Water-cooled half effect cascaded with
COP	0.8245	0.845	0.424	0.424
Evaporation power (kW)	1970	2197	4495	4495
Refrigeration capacity (ton)	563	628	1284	835
Outlet chilled water temperature (ºC)	5	22	5	0
Hot water supply energy (kW)	15739	15518	-	-
Hot water supply Temperature (ºC)	68	67.5	-	-

Table 2. Outlet results of electricity generation models

Output parameters	Electrical power generation model type	
	R-245fa organic Rankin cycle (ORC) standalone	Water-cooled cascaded with gas turbine and R-245fa organic Rankin cycle (ORC)
ORC Efficiency (%)	8.4	16.74
ORC electrical power (kW)	1,324	18,000
Gas turbine electrical power (kW)	-	85,000
Total electrical power produced (kW)	1,324	103,000
Thermal hot water energy (kW)	-	25,000

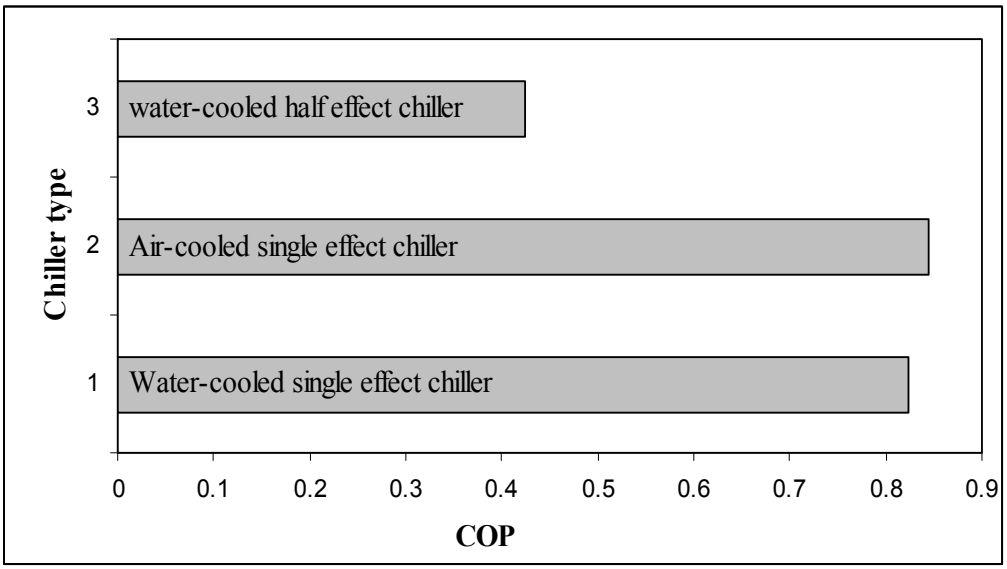

Figure 11. COP for different simulated chillers

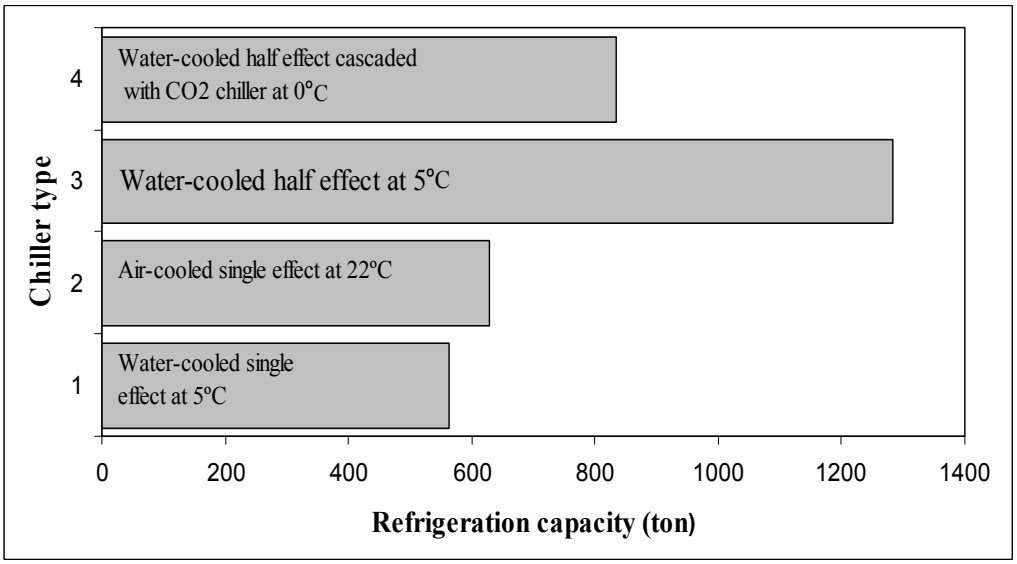

Fugure 12. Produced refrigeration capacity for different simulated chillers.

The low cooling capacity was obtained from both air and water-cooled single effect chillers with significant outlet temperatures (about 68 ºC) which can be furtherer used in central heating and domestic hot water supply. For further reduction in the value of evaporator outlet chilled water temperature (0° C or below) the absorption cycles need to be cascaded with conventional compression e.g. CO_2 cycle. If cooling air-conditioning system is decided to be the only suitable choice for Waddan communities, without utilizing hot water energy, then water-cooled half effect chiller is probably the best system to be installed. If air-conditioning and hot water supply systems are desired, in summer and winter seasons, then the water cooled single effect chiller has to be selected instead.

B- Low temperature artesian geothermal sources could be utilized to generate direct electricity using R-245fa organic Rankin cycle (ORC) without any further significant benefit of rejected heat from the evaporator using quite large evaporation surface area. This geothermal source, along with surrounding natural gas fields, seems technically, may be economically and environmentally very attractive to build clean combined power station (GT & ORC).

Acknowledgment

I would like to thank Eng. Abdul Salaam Alela from General water authority-Libya for his kind assistance

References

[1] Kaynakli, O. and M. Kilic, Theoretical study on the effect of operating conditions on performance of absorption refrigeration system. Energy Conversion and Management,. Vol. 48 No. 2, 2007, 599-607.

[2] Mary H. Dickson, M.F., Geothermal energy, ed. i. international institute for geothermal research pisa. 1996: John Wiley & sons.

[3] Kececiler, A., H.I. Acar, and A. Dogan, Thermodynamic analysis of the absorption refrigeration system with geothermal energy: an experimental study. Energy Conversion and Management,Vol. 41, No. 1, 2000, 37-48.

[4] Sumathy, K., Z.C. Huang, and Z.F. Li, Solar absorption cooling with low grade heat source -- a strategy of development in South China. Solar Energy, Vol. 72 No. 2, 2002, 155-165.

[5] Sun, D.-W., Thermodynamic design data and optimum design maps for absorption refrigeration systems. Applied Thermal Engineering, Vol. 17 No. 3, 1997, 211-221.

[6] GWA, Waddan geothermal artisian well techanical report, G.w. authority, Editor. 2007, Secretaries of Dams and Water resources. Libya.

[7] Keith E. Herold, R.R., Sanford A. Klein, Absorption Chillers and Heat Pumps. 1996, Florida: CRC Press Taylor & Francis Group. 283.

[8] SimTech, *IPSEpro Refrigeration Library manual*. 2003.

JJMIE

Volume 4, Number 1, Jan.2010
ISSN 1995-6665
Pages 69 - 74

Jordan Journal of Mechanical and Industrial Engineering

Solid Waste Landfills as a Source of Green Energy: Case Study of Al Akeeder Landfill

H. Abu Qdais *, F. Abdulla and L. Qrenawi

Civil Engineering Department, Jordan University of Science and Technology, P.O.Box 3030, Irbid 22110, Jordan

Abstract

The purpose of this paper is to estimate the amount of methane emitted from Al Akeeder landfill which is the second largest landfill in Jordan. To achieve that Gas-Sim model was used in predicting the amount of methane emissions. It was found that the methane emission will reach its peak value of 12 Million M^3/year by the year 2021, one year after the landfill closure. Furthermore, the power that can be obtained from the landfill in case ob methane recovery was estimated to be 5.6 MW in 2021. Utilizing the biogas will not only generate a green energy, but also will create a source of revenue through selling the CERs regulated by Clean Development Mechanism of Kyoto protocol.

Keywords: Landfills; AL Akeeder; Green Energy; Power; Greenhouse Gases.

1. Introduction

Landfills are remaining and will remain a common method for landfill disposal (Abu Qdais, 2007). Unless properly managed, landfills will pose serious environmental and health risks. Several gases are generated by decomposition process of organic materials in a solid waste landfill. The composition, quantity, and generation rates of the gases depend on several factors such as refuse quantity, density and composition, placement characteristics, landfill depth, refuse moisture content, temperature and amount of oxygen present (ASTDR, 2006) . Three processes form landfill gas, these are: bacterial decomposition, volatilization and chemical reactions. Table 1 outlines a typical landfill gas composition (El Fadel et al. 1997). It can be observed that methane forms the highest fraction of gases emitted from the landfill, followed by carbon dioxide.

Table 1. Typical Landfill Gas Composition (El Fadel, etal 1997)

Component	Concentration range (%)	
	Lower Limit	Upper Limit
Methane	40	70
Carbon dioxide	30	60
Carbon monoxide	0	3
Oxygen	0	5
Nitrogen	0	3
Hydrogen	0	5
Hydrogen sulfide	0	2
Trace compounds	0	1

* Corresponding author. hqdais@just.edu.jo

1.1. Health Impacts

Gases generated in landfills normally take the shortest or easiest route to the surface. Occasionally; the presence of fissures in or surrounding the filled land, possibly together with the presence of surface barrier will cause the evolved gases to travel large distances horizontally. In some cases, these gases found their way into basements of houses and buildings and deaths and injuries have resulted from asphyxiation, poisoning or from detonation of explosions of air methane mixtures. Numerous incidents of fires and explosions due to lateral gas migration away from landfills have been reported in the literature. (El – Fadel, 1997, Blumberga,2001)

Although landfill gas, rich in methane, provides an energy recovery opportunity, it has often been considered to be a liable because of its flammability and ability to form explosive mixtures with air in concentrations from 5 to 15 % by volume. Methane has the tendency to migrate away from the landfill boundaries by diffusion and advection. Diffusion and advection rates depend primarily on the physical properties and generation rates of the landfill gas, refuse permeability, internal landfill temperature, moisture content, surrounding soil formation and changes in barometric pressure.

1.2 Environmental Impacts

Emissions of methane and carbon dioxide from landfill surfaces contribute significantly to global warming or the greenhouse effect. Methane has received recent attention as a contributor to global warming because on a molecular basis, it has a relative effect 20 to 25 times greater than carbon dioxide, it is more effective at trapping infrared radiation and tends to persist longer in the atmosphere owing to other species (carbon monoxide) with a greater affinity for hydroxyl ions, the oxidizing agent for methane.

Recent increases of methane concentrations in the atmosphere have lead to extensive characterization studies of global methane sources and sinks. Atmospheric methane concentrations were reported to increase at an average rate of about 1 to 2% per year. It is estimated that methane contributes about 18% towards total global warming. This contribution represents 500 million tons per year approximately of which 40 to 75 million tons are attributed to emissions from landfills. Due to continuing trends in population increase and urbanization, solid waste landfills are becoming a significant contributor to atmospheric methane, unless recovery control systems are implemented (El Fadel Etal 1997).

Odors are mainly the result of the presence of small concentrations of odorous constituents (esters, hydrogen sulfide, organosulphurs, alkyl-benzenes, limonene and other hydrocarbons) in landfill gas emitted into the atmosphere. The odorous nature of landfill gas may vary widely from relatively sweet to bitter and acrid depending on the concentration of the odorous constituents within the gas.These concentrations will vary with waste composition and age, decomposition stage and the rate of gas generation and the nature of microbial populations within the waste. Although many odorous trace compounds may be toxic, they have historically been perceived more as an environmental nuisance than as a direct health hazard. The extent to which odors spread away from the landfill boundaries depends primarily on weather conditions; wind, temperature, pressure and humidity (Blumberga, 2001)

2. Al Akeeder Landfill

Al Akeeder landfill is located in the northern region of Jordan, near the main road to Mafraq Governorate. It is part of the Irbid and Mafraq Governorates; located in the boundaries of the Yarmouk Watershed with a Palestinian coordinates of $251^{\circ}\ 22'$ E and $216^{\circ}\ 33'$ N, Figure1. It is located at 27 km to the east of the city of Irbid, just at a distance of 1 km from the Syrian borders. It can be reached by a paved road about 7 km to the north of the Irbid-Mafraq highway. The nearest village is about 1.58 km to the south west called Al Akeeder village. This site was chosen because of low population density, low land cost and to minimize the leakage of contaminants into groundwater. Nowadays; the area near the landfill becomes populated and the impacts of the landfill on the public health and the surrounding environment should be investigated (METAP, 1998, Al Khaldi, 2001, Abu Rukha and Al Kofahi, 2001)

Al Akeeder landfill is the only official dump site for northern Jordan with an area of 806×10^3 m^2 used in almost equal proportions for disposal of industrial wastewater and municipal solid waste, see Figure 3.2. It serves the populations of Irbid city and another 62 villages and cities in Irbid, Mafraq, Jarash and Ajloun Governorates. Although by far the largest disposal site in the northern Jordan, Al-Akaider is not the only one. It is however believed to be the only site in the region which accepts liquid wastes. Municipal solid waste, small quantities of industrial waste and industrial wastewater are disposed of at the site. In the past; municipal wastewater was discharged with industrial wastewater, nowadays; municipal wastewater is discharged directly to a new treatment plant near the landfill [7, 39, 40, 41].

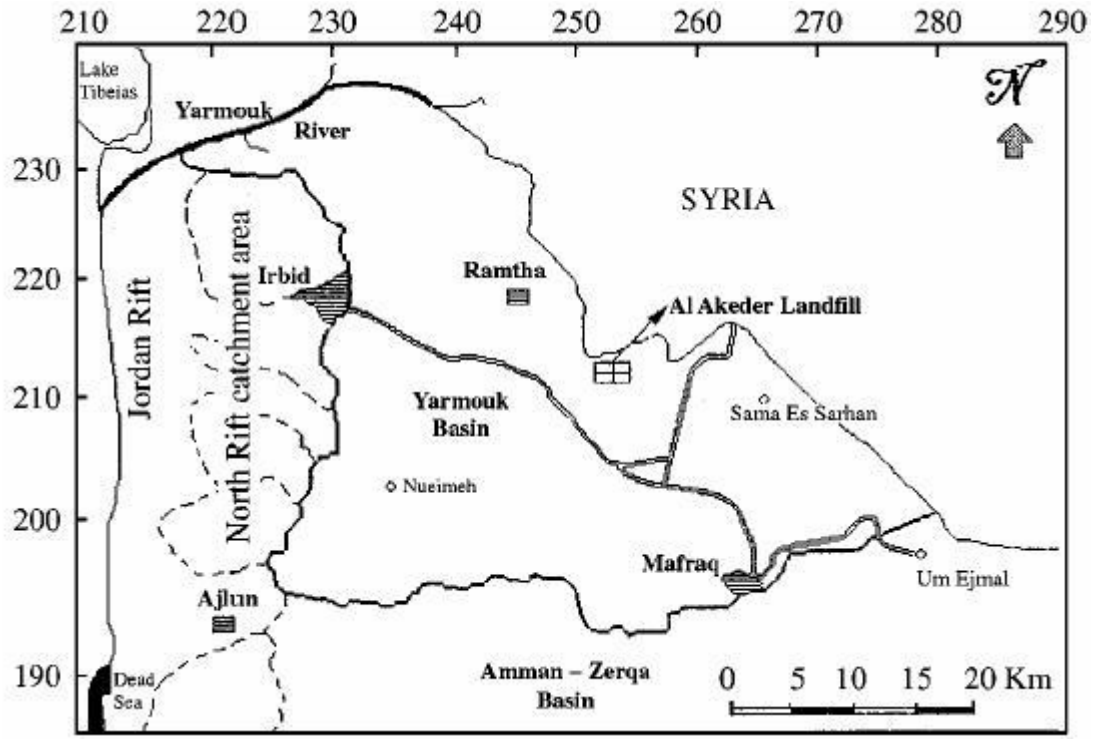

Figure 1. Location of AL Akeeder landfill site in Northern Jordan.

2.1. Solid Waste Composition and Quantities

Precise information on the waste composition disposed in the landfill is not available. Though, a study detained in 2001 shows that the landfilled waste is mostly organic. Figure 2 illustrates the composition and percentages of the solid waste (Chopra et al, 2001).

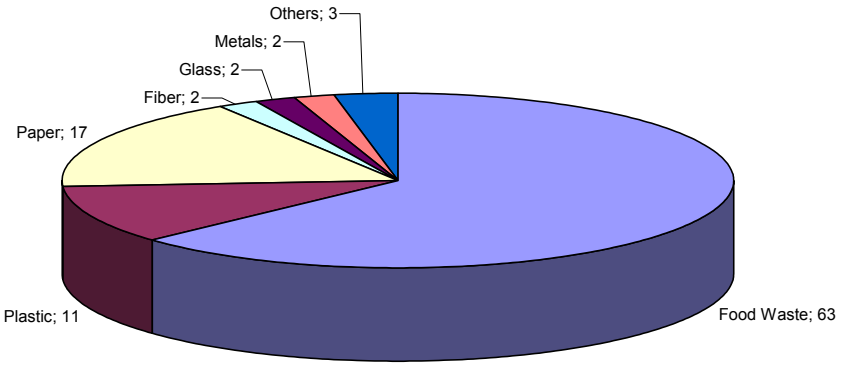

Figure 2. Composition of solid waste disposed at Al Akeeder landfill (Chopra et al, 2001)

Food waste has the highest percentage of total waste with percentage of 63 % while paper has the second highest percentage of 17 %. About 20 % of the waste is non-degradable materials. Industrial waste portion is about 10 % of the waste disposed at the landfill.

The per capita generation rate of municipal solid waste in Jordan ranges from 0.72 to 0.91 kg / capita / day. This range includes the increase of solid waste generation as a result of life changes., Abu Qdais (1987) estimated the daily per capita generation of municipal solid waste in Irbid; his estimates ranged from 0.78 to 0.92 kg/capita/day; which was reasonable and close to that found in literature.

3. Methane Gas Generation from Al Akeeder Landfill

To simulate the methane generation from the landfill, Gas-Sim model was used. Landfill gas generation was simulated from 1981 to 2055. The results of simulations presented in Figure 3

  - Volume 4, Number 1 (ISSN 1995-6665)

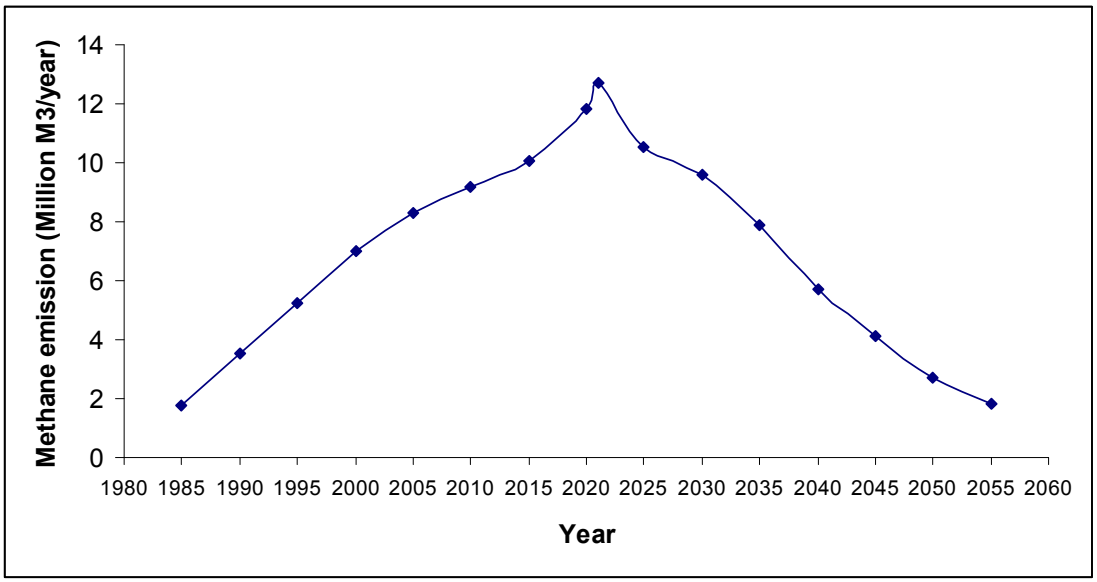

Figure 3. Simulated methane emission from the landfill using Gas-Sim Mode

It can be seen from Figure 3, that the trend of the simulation follows the triangular model theory. In the period from 1985 to 2021; the methane generation increases as well as the waste input quantities. At the beginning of simulation period (1985), the predicted amount of methane generation was found to be 1.75 million M^3/year. By the year 2020, it is assumed that the landfill will be reaching its full capacity and will be closed. Therefore, the peak methane generation will take place one year after the closure, namely the year 2021. The peak amount of methane was estimated to be 12 Million M^3/year. Then the methane production starts declining. This can be interpreted as the landfill enters a stage of stabilization, where methanogenic bacteria starts to produce less methane amounts due to low moisture content and low fresh biodegradable solid waste.

Gas-Sim model is capable of simulation the methane production for 100 years. However; methane generation has been estimated to a period of 35 years after the closure of the facility. The waste input quantity for the study period was entered to the model as a range to account for the uncertainty.

3.1 Power potential of the generated methane

Methane is a well known greenhouse gas. In addition it is a flammable gas with relatively high heat content. To minimize its adverse environmental impacts and make use of the energy recovery, it is assumed that a biogas plant will be constructed at Al Akeeder landfill and will start operation by the year 2015. Assuming the methane recovery of 40% from the emitted methane, the estimated amount of power that can be obtained from such a plant is illustrated in figure 4.

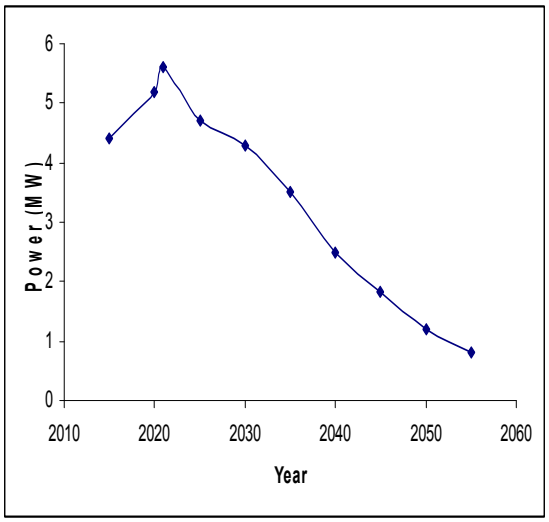

Figure 4. Estimated power that can be obtained from methane recovery at Al Akeeder Landfill.

It can be observed that about 4.3 MW of power can be obtained at the beginning of plant operation, while this value reaches 5.6 MW by the year 2021, directly after the landfill closure.

3.2 Global Warming Potential

Gas-Sim determines the effect of green house gases and compares the effect of each compound to carbon dioxide. For example; methane has 21 times the effect of carbon dioxide. Table 2 shows the species contributing to GWP and their CO_2 equivalence.

It is recognized that methane has the highest GWP (77.22 %) while carbon dioxide contributes to the total global warming potential by 12 %. It is recommended to best exploit the methane as a renewable source of energy and hence reducing the environmental problems resulting from its emission to the atmosphere.

Based on 40% methane recovery the amount of greenhouse gas emission reduction is illustrated in figure 5. It can be seen that by the beginning of the biogas plant operation (2015), the amount of emission reduction is about 62 thousand tons of CO_{2eq}, this amount will reach 80 thousand tons of CO_{2eq} by the year 2021. This suggest the possibility of making use from the Clean Development Mechanism of Kyoto Protocol, by selling the certified emission reduction. Assuming a cost of 12 US$ for each tone of CO_2 , the income from the carbon credit will be about 620,000 US$ in the year 2015 and will reach to about 800,000 by the year 2021

Table 2. GWP Species Emitted from Al-Akaider Landfill in 2006

Species	GWP (tones of CO_2)
Methane	150000
Carbon Dioxide	23300
1, 1, 1, 2 – Tetrafluorochloroethane	2.88
1, 1, 1 – Trichlorotrifluoroethane	54.3
1 – Chloro – 1, 1 – difluoroethane	155
Chlorodifluoromethane	4570
Chloroform	0.221
Chlorotrifluoromethane	1280
Dichlorodifluoromethane	13600
Dichloromethane	3.77
Trichlorofluromethane	956
Trichlorotrifluoroethane	325
Total	**194247**

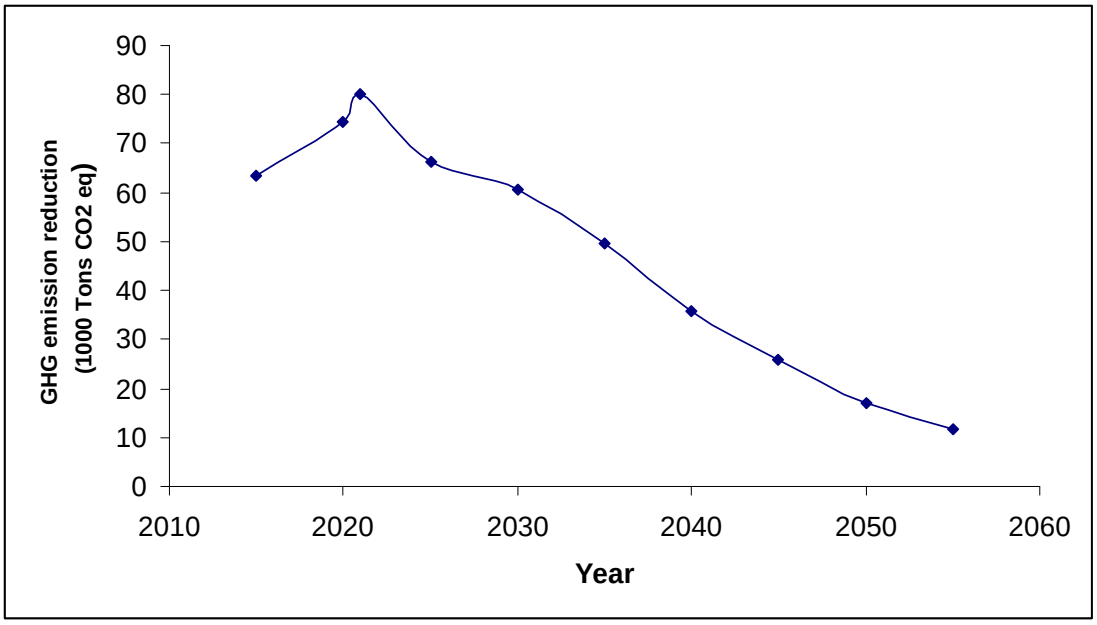

Figure 5. Greenhouse gas emission reduction based on 40% methane recovery

4.Conclusions and Recommendations

Landfills are source of greenhouse emissions. If biogas recovered from the landfill, adverse environmental impacts will be minimized. In addition, clean energy will be produced that will offset the polluting fossil fuel. In this study, methane emissions from AL Akeeder landfill were estimated using Gas-Sim model. It was estimated that the amount of methane that will be emitted by the year 2021 to be 12 Million M^3/year, while the power that can be obtained from the landfill in case of gas recovery will be 5.6 MW. In addition, the amount of greenhouse gas emission reduction will be about 80 thousand tones of CO_2 $_{eq}$ in the that year.

It is recommended to carry out a field study by conducting a pump test, so as to verify the results of methane modeling process.

References

[1] Abu Qdais H. A. Techno Economic Analysis of Municipal Solid Waste Management in Jordan, Waste Management, Vol. 27, 2007, 1666-1672

[2] ASTDR , (2006). Agency for Toxic Substances and Disease Registry (ASTDR). Landfill Gas Primer. An Overview for Environmental Health Professionals. [Online] [Accessed in June 2005]. Available from URL:http://www.atsdr.cdc.gov/HAC/landfill/html/ch2.html

[3] El-Fadel M., Findikakis A., Leckie J. Environmental Impacts of Solid Waste Landfilling. Environmental Management, Vol. 50, 1997, 1–25

[4] Blumberga, M. Risk Assessment of the Skede Landfill in Liepaja, Lativa MSc. Thesis, Stockholm: 2001

[5] Al khaldi L. Feasibility of Municipal Waste Recycling in Irbid City, MSc Thesis, Jordan, Jordan University of Science and Technology, November, 2001

[6] Abu Rukah Y., Al-Kofahi O. The assessment of the effect of landfill leachate on ground water quality. A case study. El-Akader landfill site – north Jordan. Arid Environments, Vol. 49, 2001, 615 – 630

[7] METAP, Mediterranean Environmental Technical Assistance Program (METAP). Northern Region Solid Waste Management Study. Supplementary Data Report, 1998.

[8] Chopra M., Reinhart D., El-Shaar W. US-Jordan Municipal Solid Waste Management Collaborative Research. The national Science Foundation (NSF), Final Report, 2001.

[9] Abu Qudais H. Solid Waste Management: An Evaluation and Possible Improvement for the City of Irbid, MSc thesis, Jordan University of Science and Technology, 1987.

JJMIE

Volume 4, Number 1, Jan. 2010
ISSN 1995-6665
Pages 75 - 78

Jordan Journal of Mechanical and Industrial Engineering

A Novel Dual Effect Soot Filtering System

Saud Aldajah*, Yousef Haik and Emad Elnajjar

Mechanical Engineering Department, United Arab Emirates University, Al-Ain, UAE

Abstract

A newly developed novel technique for filtering soot from an exhaust gas system is presented. The proposed filter surface is capable of synthesizing carbon nanotubes. Two filters were designed and tested; the first is made of carbon steel plate and the second was made of nanomagnetic particles mounted on a polymeric surface. The filters were placed along the pathway of an exhaust streamline with an inclination of 5o to ensure a laminar flow condition. The results showed that the proposed systems produced carbon nanotubes by converting the exhaust waste.

Keywords: Soot Filter; Carbon Nanotubes; Nanoparticles.

1. Introduction

The widespread use of compression-ignition-direct-injection (CIDI) diesel fueled engines in automotive and truck vehicles will have a major economic and environmental impact. Because of the higher efficiency of the CIDI engines, their use will result in significant reduction in both fuel consumption and consequently greenhouse gases emission. An estimate of as much as 30-35% reduction in greenhouse gases has been predicted as a result of this fuel consumption reduction from CIDI or diesel engines[1]. Lower fuel consumption will also translate to less dependence on imported oil, which has economic and security implications.

A major obstacle to the commercialization of diesel engines, especially for automotive applications, is their high level of nitrogen oxides (NOx) and particulate emissions, both of which have possible negative effects on health. Major efforts by governments and industry are thus currently being directed at development of technologies to reduce diesel engine emissions.

Among the newly developed technologies is the utilization of oxidation catalysts that convert hydrocarbon and carbon monoxide into carbon dioxide and water which are known in the literature. Ceramic filters that are known for their efficiency to remove 90% of the particulates require 500oC and oxygen rich exhaust condition. Another effective approach to reduce NOx emissions in both gasoline and diesel engines is exhaust gas recirculation (EGR). Oxides of nitrogen (NOx) are formed when the combustion chamber temperatures are too high. Any measure that reduces the combustion temperature will lead to reduction in NOx formation and emission. EGR involves recirculation of exhaust gas into the intake stream. The recirculated gas displaces some of the normal intake charge, which slows and cools the combustion process, thereby reducing NOx formation. However, recirculation of exhaust product back into the engine combustion chamber has detrimental effects. Engine durability is compromised by EGR due to oil contamination by engine exhaust products [4,5]. Additional technologies include Fuel switching which utilizes a lower fuel bound nitrogen, Combustion control techniques including low excess air firing, staged combustion, water/steam injection, Flue Gas Treatment methods including selective non-catalytic reduction and selective catalytic reduction (these are post combustion methods that reduce NOx emissions after formation), finally fuel reburning which involves injection of natural gas after primary fuel combustion. It is typically used on very large boilers firing residual oil or coal.

The proposed technology insinuates the utilization of a new effective filter which synthesizes the carbon nanotubes from the exhaust gas at low and moderate temperatures. During the past two centuries, carbon nanotubes have attracted the attention of many researchers because of their unique electrical and mechanical properties [6]. Traditionally, carbon nanotubes are synthesized via various techniques such as arc-discharge [7], laser ablation [8], plasma enhanced chemical vapor deposition (CVD) [9] and thermal CVD [10]. The proposed technique utilizes the use of nanomagnetic particles placed on a metallic plate as a catalyst in the exhaust system of an automotive engine. This filter will have a dual benefit of filtering the exhaust gas by reducing soot formation and the formation of carbon nanotubes.

* Corresponding author. s.aldajah@uaeu.ac.ae

2.Experimental Method

A simple single cylinder diesel engine is used to perform this experiment. The experimental setup is shown in figure 1. The specimen is carefully designed from a metallic plate with an adhesive to which Nanomagnetic particles were added. The specimen holder is designed as shown in figure 1, the holder services two purposes: it controls the position of the specimen (flat/ 5^{o} inclined with respect to the exhaust flow stream), also it is designed in such a way where it will eliminate any disturbance to the flow in order to ensure a laminar flow over the specimen. The holder is located close to the combustion chamber to ensure the highest possible temperature. All test samples are collected at similar engine operation conditions. The engine was running at 1100 rpm at an average load of 60N, the air temperature varied from 16^{o}C to 25^{o}C.

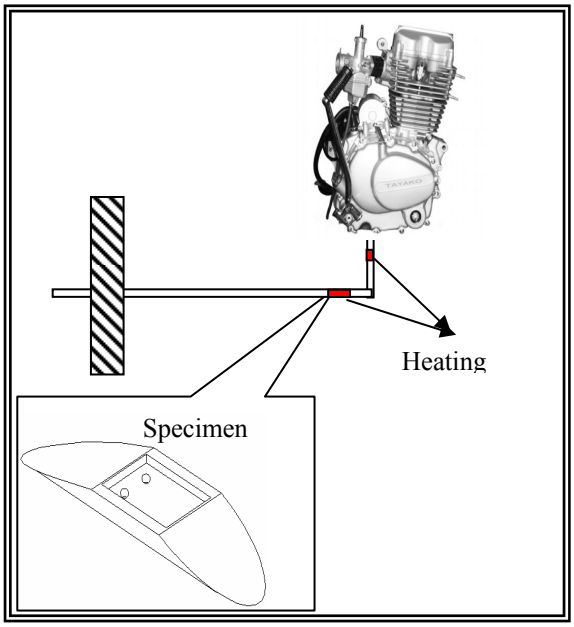

Figure 1.The experiment setup, with a zoomed view of the specimen holder.

2.1 Test Schedule

Two sets of samples were designed. The first samples were made of carbon steel which was highly polished and chemically itched in order to show the grains. The second set was made of samples were made out of iron oxide nanoparticles mounted on an adhesive on a plate. All samples were collected according to the conditions shown in table 1. The engine and flow parameters were the same for all tests (engine speed of 100 rpm, engine force of 60 N, air flow temperature of 37^{o}C and exhaust stream temperature of 96^{o}C).

3.Results and Discussion

The samples were characterized and analyzed using the scanning electronic microscope (SEM). SEM images of CNTs are shown in figure 2 (a), (b), (e) and (f), these images are shown an evidence of having CNT growing on the catalyst metal specimen. Images (c) and (d) are the base line where for these two samples the tests were reproduced under the same operation conditions without heating of the specimen. The two images are showing typical carbon particles without any trace of CNT. These two cases demonstrate the fact that having the metal catalysts specimen at the exhaust temperature (100oC) was not enough to produce CNT. Figure 3 shows the SEM images of sample 13 where it can be clearly seen that the CNTs had grown on the nanoparticles.

The right environment believed to enhance the growth of CNT using this technique can be summarized by the following: firstly, the precise design of the specimen and the holder to ensure quality laminar flow of the exhaust gas. Secondly, heating the sample to a temperature higher than 300oC and finally, the quality of the specimen surface which is polished to a very high levels of smoothness in the case of the metal plate.

4.Conclusions

This paper demonstrated an innovative, environmental friendly technique of producing carbon nanotubes from diesel engine exhaust stream flowing at a moderate temperature. The carbon nanotubes grew on a heated carbide metallic catalyst specimen and on a sample that contains nanoparticles positioned in the exhaust stream. The diesel exhaust stream temperature was kept at around 100^{o} C, whereas the specimens were heated to a moderate temperature of 250^{o} C (in the case where heating was applied to the sample). This filtering technique is a promising one; it can be used alone or in combination with other filters.

Table 1. The test samples conditions

Sample No.	Heating		Sample Position	Engine %Load	Comments
	Sample	Exhaust line			
1	Yes	No	Flat	75	
2	Yes	No	5º Inclination	75	
3	No	No	Flat	75	Base Line
4	Yes	Yes	Flat	75	
5	No	No	Flat	50	Base Line
6	No	No	Flat	100	Base Line
7	No	No	5º Inclination	50	Base Line
8	No	No	5º Inclination	100	Base Line
9	Yes	Yes	Flat	50	
10	Yes	Yes	Flat	100	
11	Yes	No	5º Inclination	50	
12	Yes	No	5º Inclination	100	
13	Yes	No	Flat	100	

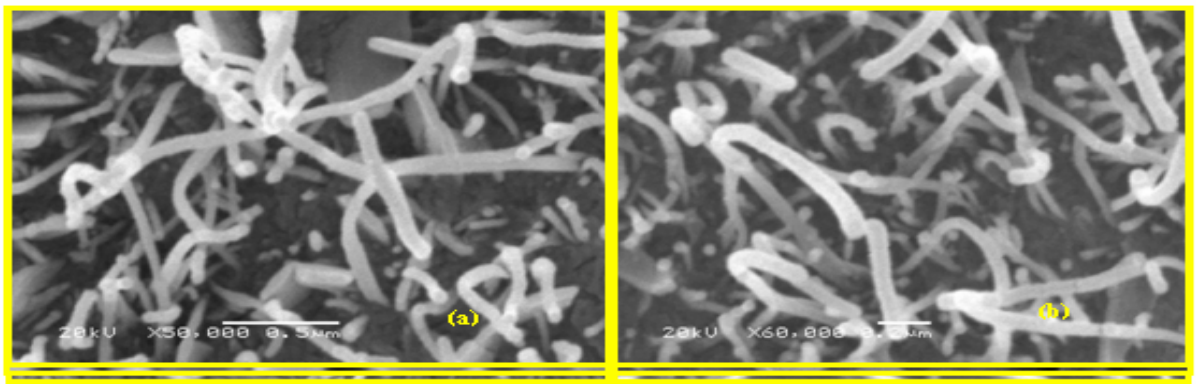

Figure 2. SEM images (a) sample 1 (Flat/ heated), (b) sample 2 (Inclined/ heated), (c) sample 4 (Flat/Non heated), (d) sample 6 (Inclined/Non heated), (e) sample 8 (Flat/ heated) and (f) sample 10 (Flat/ heated).

.

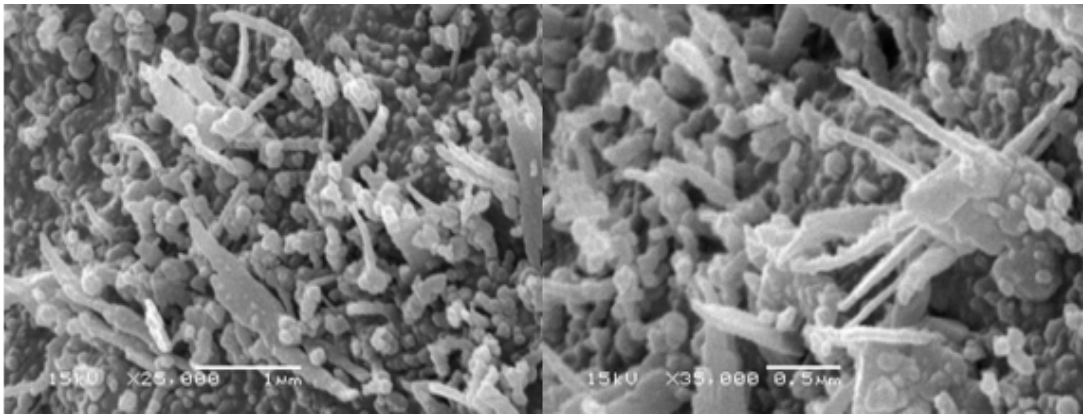

Figure 3. SEM images of sample 13

References

[1] C. J. Morey and J. Mark, "Diesel Passenger Vehicles – Can They Meet Air Quality Needs and Climate Change Goals," SAE Technical Paper # 2000-01-1599 2000.

[2] R. C. Yu and S. M. Shahed, "Effect of Injection Timing and Exhaust Gas Recirculation on Emissions from a D.I. Diesel Engine," SAE Technical Paper # 811234, 1981.

[3] S. Tullis and G. Greeves, "Improving NO_x Versus BSFC with EUI 200 Using EGR and Pilot Injection for Heavy-Duty Diesel Engines," SAE Technical Paper # 960843, 1996.

[4] A. J. Dennis, C. P. Garner, and D. H. Taylor, "The Effect of EGR on Diesel Engine Wear," SAE Technical Paper # 1999-01-0839, 1999.

[5] M. Gautam, K. Chitoor, M. Durbha, and J. C. Summers, "Effect of Diesel Soot Contaminated Oil on Engine Wear – Investigation of Novel Oil Formulations," Tribology International, Vol. 32, 1999, 687-699.

[6] R. Saito, G. Dresselhaus, Physical properties of carbon nanotubes, Imperial College Press, London, 1998.

[7] C. Journet,W.K. Maser, P. Bernier, A. Loiseau, M. Lamy de la chapelle, S. Lefrant, et al., Nature Vol. 388, 1997, 756.

[8] AThess, R. Lee, P. Nikolaev, H. Dai, P. Petit, J. Robert, et al., Science Vol. 273, 1996, 483.

[9] M. Meyyappan, L. Delzeit, A. Cassell, D. Hash, Plasma source Sci. Technol. ,Vol. 12, 2003, 205.

[10] E.F. Kukovitsky, S.G. L'vov, N.A. Sainov, V.A. Shustov, Appl. Surf. Vol. 215, 2003, 201.

JJMIE

Volume 4, Number 1, Jan. 2010
ISSN 1995-6665
Pages 79 - 90

Jordan Journal of Mechanical and Industrial Engineering

Characterization of Horizontally Grown Silicon Nanowires in Aluminum Thin Films

Khaleel N. Abushgair [a,*], Husam H. Abu-Safe [b], Hameed A. Naseem [b], Mahmoud A. EL-Sabagh [b], Brian L. Rowoen [b], Avnish K. Srivastava [c], Samir M. El-Ghazaly [b]

[a]*Department of Mechanical Engineering, Al-balqa Applied University, Amman, Jordan*

[b]*Department of Electrical Engineering, University of Arkansas, Fayetteville, AR, 72701, U.S.A*

[c]*National Physical Laboratory, New Delhi, India*

Abstract

Characterization of silicon nanowires grown horizontally through aluminum thin films was conducted. We show in our work that the fabrication process of these wires depends mainly on the thermally-activated silicon diffusion in-between the boundaries of aluminum grains. The diffusion of silicon through grain boundary is much lower than the grain bulk. Therefore, silicon starts to accumulate and form a wire shape structure along these grain boundaries. At 600□C, these accumulations form a continuous network of nanowires. The results are unique in the fact that these nanowires are pushed to grow horizontally instead of the more common vertical direction. The majority of obtained nanowires have a diameter of 75 nm and a length > 5 μm.

Keywords: Dead Sea; Water Volume and Surface Area Loss; SRTM-Based Model; Red-Dead Sea Channel; Renewable Energy and Sustainability.

1. Introduction

The continued scaling of silicon-based integrated circuit (IC) technology has produced need for a new generation of devices. Silicon nanowires (SiNWs) have proved to be valuable as research devices and as building blocks for nanotechnology [1]; this is proved by the recent progress of transistors and lasers built with nanowires [2]. However, fabrication of large amount of nanowires especially in an isolated form is still under research.

Self assembly of nanostructures provide a reasonably cost efficient and easy to implement way to fabricate nanoelectronic components [3, 4]. Many different attempts to fabricate silicon nanowires have been devised, including the vapor liquid solid method (VLS) [5] and the solid liquid solid method (SLS) [6] with metal catalysts, and laser ablation of powder silicon [7]. However, the fabricated nanowires using these methods are still in need to be incorporated into devices and to be tested as charge or signal carriers. There have been recent studies [8, 9] that report methods to fabricate aluminum-silicon nanowire networks. The method reported in reference 8 produced wires that can actually conduct currents. The web-like network was fabricated by de-alloying an aluminum-silicon thin film through selective chemical etching. The current that propagated through the network depends, in general, on the etch time of the alloyed film. However, lack of control over the design of this network, reduces its appropriateness when well designed architecture is required.

In this paper, we report a method similar to the one reported in reference 9 to grow horizontal network of silicon nanowires on silicon substrate. We also show that this method is similar to the SLS method but yet different in the temperature where this process takes place and also in using aluminum as a catalyst instead of gold or nickel commonly used in this process . Furthermore, we show that the use of aluminum as a catalyst results in a network of nanowires that grows in the horizontal direction rather than the vertical direction. Effect of the annealing temperature on the nanowire network is investigated and a possible growth mechanism is presented.

2. Experimental Parameters

In all our reported experiments, the used substrates were 5” silicon (100) wafers and 1”×1” Corning 7059 glass. Two sets of silicon samples were prepared. In the first set, the samples were cleaned with Acetone and the native oxide was removed by dipping the samples in a HF solution with 10% concentration for 2 minutes and then dried with filtered and compressed Nitrogen. In the second set a 300 nm of silicon oxide was thermally grown on the

* Corresponding authore-mail: khaleel45@yahoo.com.

silicon surface. In this oxidation process, the samples were placed inside a furnace with 3L/min oxygen flow at 950°C for 30 minutes. The oxide was patterned into various rectangular and circular shapes ranging in length from 12 μm to 200 μm. In one scheme the oxide was removed from the surface except those patterned regions (positive patterning). In the second scheme the oxide layer was removed only from the regions corresponding to those in the previous scheme (negative patterning). This was done using the negative mask of the one in the first scheme. The glass samples were cleaned with acetone and dried in a nitrogen flow. A thin layer of aluminum (40 nm) was thermally evaporated (using Edwards Auto 306 vacuum coater) on all silicon wafers and the glass samples. The prepared samples where then cut into 1 cm× 1 cm pieces using a diamond cutting saw. The samples were placed into a quartz tube for annealing. The temperature controller was able to maintain the sample temperature up to accuracy of ±0.1°C. To minimize the film oxidation, Argon was introduced in the annealing tube at a flow rate of 94 sccm and the pressure inside the tube was maintained at 200 Torr. Annealing time was fixed to 2 hours and the temperature range varied from 500°C to 600°C. To observe the morphology of the silicon surface, the samples were dipped for 2 minutes in an aluminum etchant solution (85% phosphoric acid, 5% nitric acid, 5% acetic acid, and 5% DI water at 40°C) and then dried in a nitrogen flow.

The features of the samples' surface morphology were examined using scanning electron microscopy (SEM) and atomic force microscopy (AFM). The compositional analysis was done using energy dispersive X-ray spectroscopy (EDX) and the crystalline structure of the samples was analyzed using cross sectional transmission electron microscopy (XTEM).

3. Results and Discussion

The overall results for the samples without the oxide layer are shown in SEM images of Figure 1. Figure 1a shows the calm and smooth texture of the film surface before annealing. After 2 hours of annealing at 600°C, dramatic changes in the surface morphology were observed. Figure1b shows the various confined structures on the silicon surface after this annealing. These structures can be divided into two main types with respect to their sizes. The smaller structures formed a web-like interconnected network that was observed all over the surface. Figure 2 shows 3D AFM image of these wires on the silicon surface. The wires making this network had an average diameter size of 75 nm. It is observed that these nanowires grow in a horizontal, rather than the more typical vertical direction. The individual nanowires seem to connect at various points to form this web. The lengths of these wires were comparable and reached few microns. The second type of structures is the larger island-like material clusters that also connect the individual wires and are part of the web structure. Figure1c shows the annealed samples after aluminum was removed. The nanowires web structure is still observed in these samples. However, the island structures seem to loss their cluster forms into a deformed crater shapes with hallow interior. When comparing these results to the ones obtained from the glass samples we found no structural formations created on the surface. Figure 3 shows the SEM image for the glass samples after annealing at 600°C for 2 hours. The major observation in these films was the cuts created in the film due to thermal coefficient mismatch between aluminum and glass ($\alpha_{aluminum}=23\times10^{-6}\ K^{-1}$, $\alpha_{glass}=0.46\times10^{-6}\ K^{-1}$).

To determine the elemental composition of the confined structures seen on the silicon samples before and after annealing, EDX spot measurements were taken at several locations on the surface of the various structures with an electron beam of 10 keV and spot size of 1.7 nm.

The EDX spectra of the samples before and after annealing are shown in Figure 4. Figure 4a shows the spectral pattern of the samples before annealing indicating the topical presence of the aluminum film on the sample. The oxygen peak in the pattern is due to the aluminum oxide on the film. Figure 4b is the pattern of a spot on the wire before aluminum is removed indicating the silicon composition of these wires. Nonetheless, this peak could come from the silicon wafer underneath the film as a result of film cracking. But no cracks were observed in the films even with very high magnification. The absence of the aluminum peak from this pattern suggests a unitary composition of these wire structures. The important concept from this is the idea that the silicon material can be confined to a nanosize diameter, micron-long, horizontal structures in the aluminum film. The confining locations had to be the grain boundaries of the metal film. The small oxygen peak in the pattern comes from the remaining aluminum oxide atop the wire. Figure 4c shows the elemental composites of the surface outside the wire and away from the island regions. These spot measurements were made before aluminum removal. The comparable aluminum and silicon peaks in this case indicate the thinning of the aluminum layer on these locations. This thinning behavior could come from the aluminum expansion, where stretching the film during annealing lead to the reduction of film thickness. However, this reduction is not sever and the surface is still going to be covered with an aluminum layer that shows a strong signal. Figure 4d is the EDX pattern coming from the islands on the surface; these formations are made mainly from aluminum as can be seen from the strong aluminum peak. However, the presence of the small silicon peak suggests a binary material composition existing as a result of silicon/aluminum alloying. Figure 4e is the EDX pattern coming from the annealed sample after aluminum was removed. This peak is representative of all confined structures indicating the dominant silicon composition in them.

Fabrication of SiNWs with catalysts has been described by other studies [10, 11]. In the VLS method the source for the vertically grown SiNWs is in the gas phase. In our samples, on the other hand, the source of silicon is the substrate itself, since there is no silicon in the ambient gas during annealing. While the SLS growth mechanism can be used as a possible explanation to describe the growth of these nanowires, the vast differences in the features of nanowires grown (vertical versus horizontal), annealing time, and process temperatures (typical SLS growth require temperatures on the order of 1000°C) would demand a different explanation of the growth mechanism.

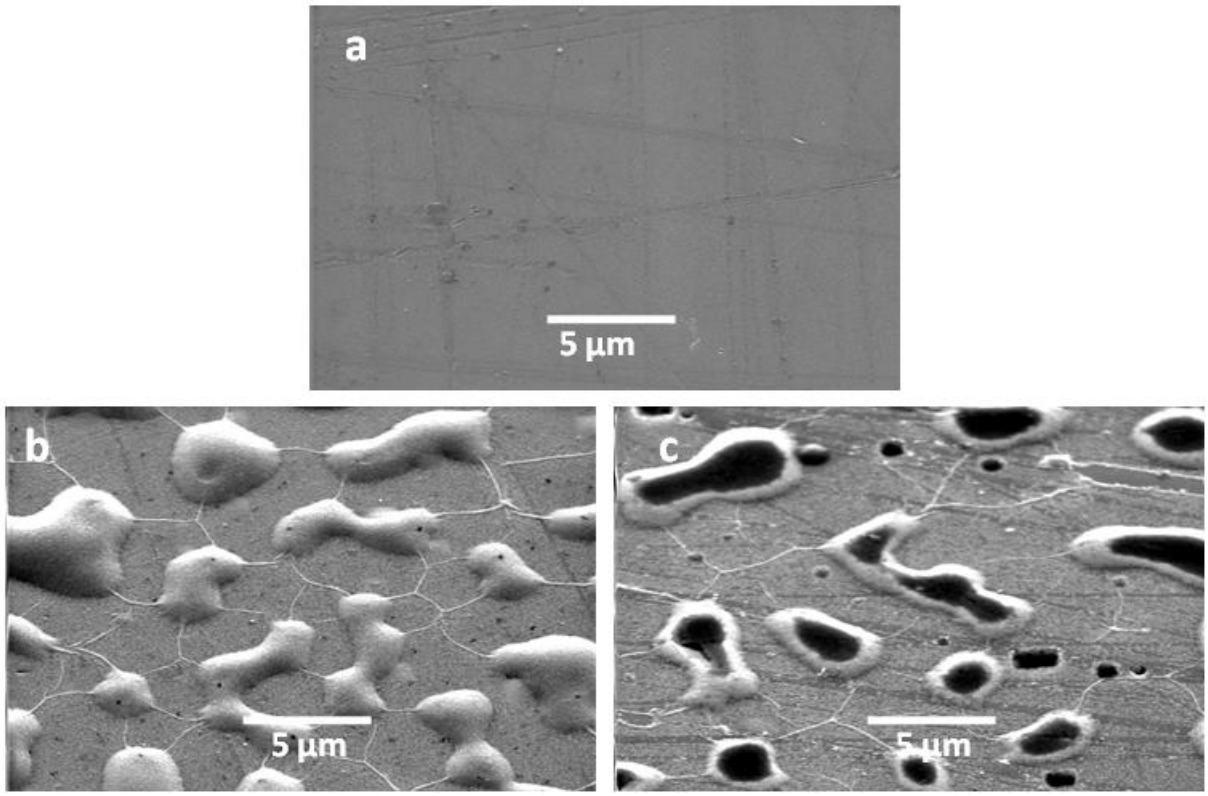

Figure 1. SEM image of the samples annealed at 600°C for 2 hours. The samples where tilted at 45° during imaging: a) SEM image of the sample before annealing, b) SEM image of the sample before aluminum was removed, c) SEM image of the sample after aluminum was removed. The black regions in c are where silicon had been etched at a faster rate.

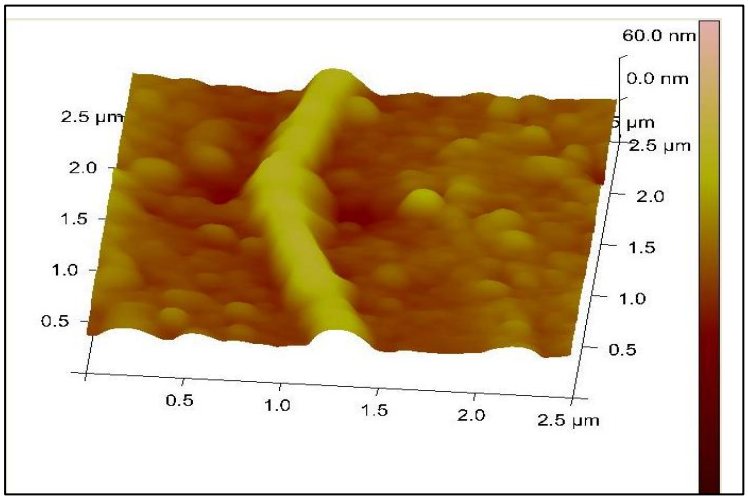

Figure 2. 3D AFM images of the samples annealed at 600°C for 2 hours after aluminum removal showing a wire formation created by the accumulations at the grain boundary.

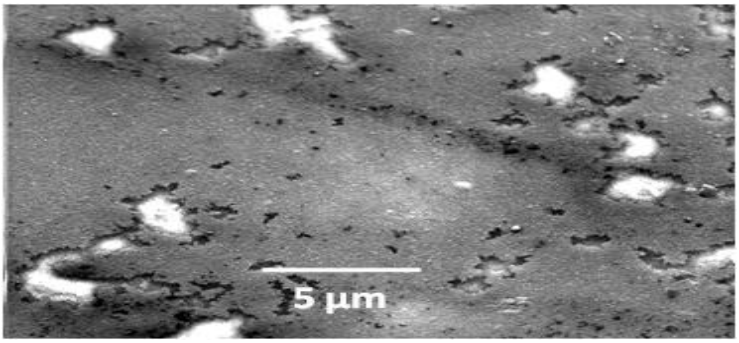

Figure 3. SEM of the glass sample after annealing at 600°C for 2 hours. The aluminum film did not show any confined structures on the film. The major observation is the cuts in the film due to thermal coefficient mismatch with the glass substrate.

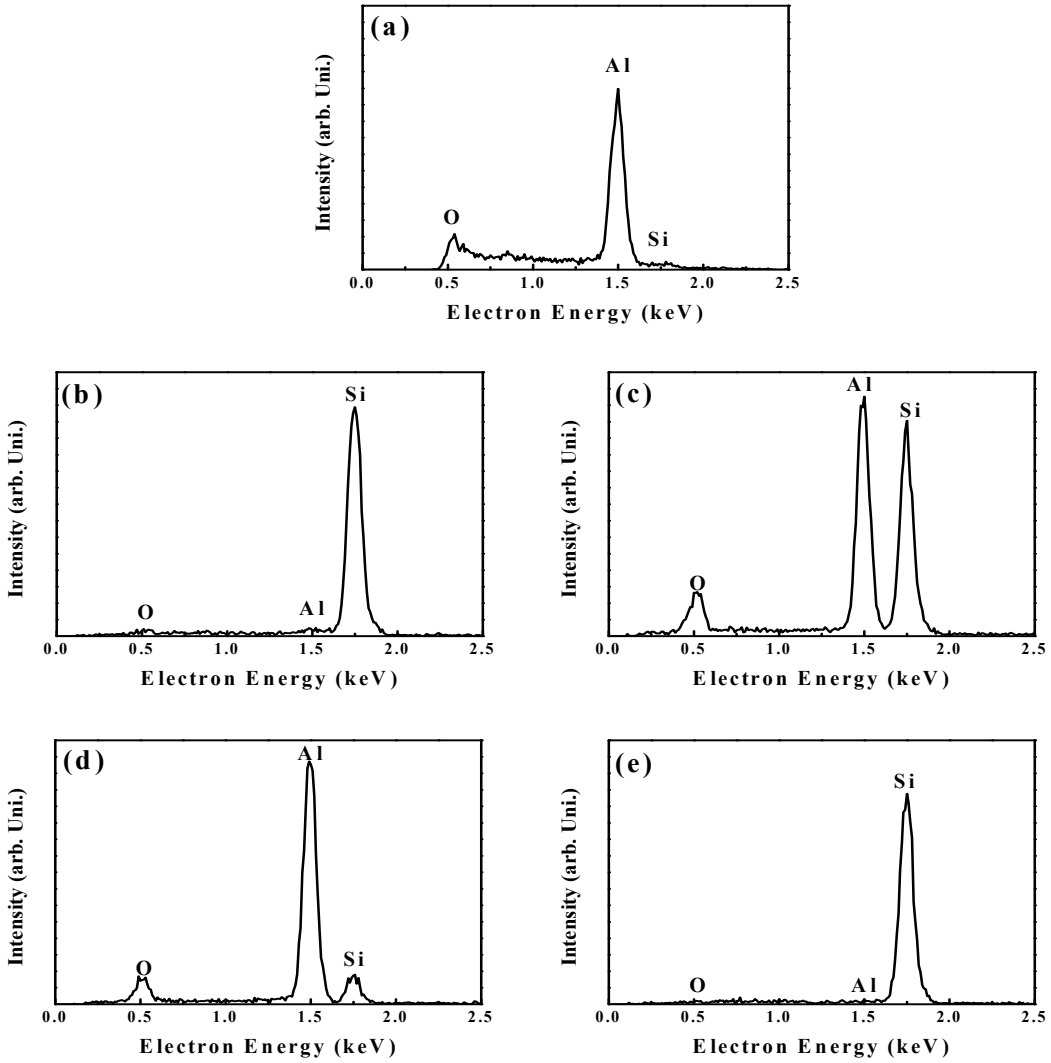

Figure 4. EDX spectrum pattern taken at a spot on the: a) aluminum surface before annealing, b) wire, c) off the wire, d) the island-like and d) surface after aluminum is removed.

To understand this mechanism, a temperature study of the silicon samples was conducted. Figure 5 shows the SEM images taken for the samples annealed at different temperatures for 2 hours. Starting with Figure 5a and the corresponding Figure 5a' which are the images of the silicon samples before and after removing the aluminum annealed at 500°C, respectively. In Figure 5a' (where aluminum is removed) the silicon surface appeared to have pitted regions indicating silicon etching during annealing. Also it is noted that the surface between the pitted regions is smooth which means that surface pitting occurred only at specific locations. These locations are where the silicon surface had defects that would increase the film internal stress locally. Mixing of silicon with aluminum on this location is provoked in this case. The etched silicon forms with the aluminum an alloy material where it fills the pitted region. From these alloy regions and as the silicon gradient concentration increases, silicon starts to diffuse through the aluminum film toward the grain boundaries in the film. However, the diffused amounts are not sufficient to reach the grain boundaries or even redeposit significantly on the silicon surface. Therefore, the etched silicon is washed off when aluminum removal process is performed. Figure 5b and the corresponding Figure 5b' are the SEM images at 550°C before and after aluminum removal, respectively. The islands in these samples (shown in Figure 5b) are larger but yet they are not well defined. The pitted regions in Figure 5b' are larger than the pitting in the previous sample indicating more etching at this temperature. Moreover, it is noted that a layer of silicon is deposited on the surface around the pitted regions. This second layer is not observed in the previous samples. However, the silicon surface between the pitted regions (partially shown in the image) is still smooth indicating the selective aluminum etching of the silicon surface.

Figure 5c and Figure 5c' shows the samples annealed at 580°C before and after aluminum is removed, respectively. On the sample with the aluminum film, a well-defined dark circular spots with a notch at its central region is shown. The diameter of these spots had an average of 3μm. When examined by EDX, these regions showed a dominant aluminum composition (see Figure 6a). The signal outside these circular spots (Figure 6b) showed only a strong silicon peak. As we have mentioned before, during high temperature annealing, the layer thickness reduces to the extent that aluminum signal becomes very weak. Most of the aluminum film cluster where silicon is being etched rapidly. This makes the aluminum film wear off in between regions. Therefore, these dark regions mark the locations where the large clusters will form.

As annealing temperature ramps up, silicon starts to erupt and diffuse from the aluminum clusters into the film. The size of these clusters increase and eventually forms an island-like structure. Figure 5d and Figure 5d' are the images of the sample annealed at 590°C before and after aluminum removal, respectively. The shapes of these islands are determined and defined by the grain boundaries of the aluminum film. On the other hand, as the silicon diffuses away from the highly concentrated regions and because diffusion is confined through aluminum film it forms a lib structure around the pitted regions as shown in Figure 5d'. Depending on the film thickness, the silicon will continue to diffuse until the film cannot hold any more silicon. Therefore, silicon deposition on the surface becomes imminent. A continuous second layer as the one seen in this figure will form. Figure 7 is schematic presentation of the formation mechanism of the clustered regions in the film. The erupted silicon etch from the walls of the crystalline silicon surface leaving behind inverted pyramids showing the (100) nature of the wafers.

The EDX patterns for the island formations are shown in Figure 8. The composites of the islands at the center and the edges are shown in Figure 8a and Figure 8b, respectively. The islands are mainly made of aluminum and silicon structure which could be in the form on an alloy. Since the solubility of silicon in aluminum is limited to 12.6 wt% [12] and due to the high silicon gradient concentration in these regions, silicon continues to diffuse through the aluminum layer until it redeposit on the surface or at the ground boundary forming the anticipated SiNWs. Pitted regions as well a second layer are observed everywhere on the surface but with different sizes. The smaller pitted regions are what make the surface between the larger regions look rough.

Figure 9a shows a XTEM image of the samples annealed at 600°C after aluminum was removed. The formation of a second silicon layer is clear in this image. Most of deposited silicon grows epitaxialy on the surface [13]. However, since the diffusion is random, the new layer will contain microcrystalline or even amorphous phases. The halos in the selected area diffraction (SAD) image shown in Figure 9b indicate the presence of these microcrystalline regions in the deposited layer.

Figure 10a and Figure 10b shows the SEM images of the positively patterned oxide (PPO) and negatively patterned oxide (NPO) of the silicon samples after aluminum was removed, respectively. During annealing, silicon and aluminum interacted only in the exposed regions where the oxide was absent. On the other hand, since silicon diffuses in aluminum films for long distances (typically 200 to 300 μm) [14], large accumulations of silicon were observed on top of the oxide layer. This can be seen in the NPO samples where most of the surface was covered with the oxide layer. The cuts in the oxide are the only openings from where silicon will diffuse. Therefore, the diffusion is faster and the silicon deposits further on top of the oxide. Moreover, since silicon diffusion through grain boundaries is much slower than the grain itself-due to grain boundary trapping-the main depositions near the openings is in the form of SiNWs. Figure 11a shows an SEM image of the NPO sample where 80μm×120μ rectangular cut was made in the oxide. Figure 11b is a higher magnification image of the dashed rectangular shown in Figure 11a. The SiNWs network is shown clearly without any island-like formations. The wire growth pattern in this case resembles the grain boundaries of the aluminum film. The only diffusion through these films is in the lateral direction therefore silicon diffuses from the openings through the film and deposits at the grain boundary. The silicon that accumulates in the grain boundaries starts to diffuse again further in the film leaving behind the accumulations in the grain boundary in the form of SiNWs. Nonetheless, far from these openings, the diffused silicon amounts become very small. Therefore, silicon tends to cluster forming silicon patches seen on top of the oxide away from the cut.

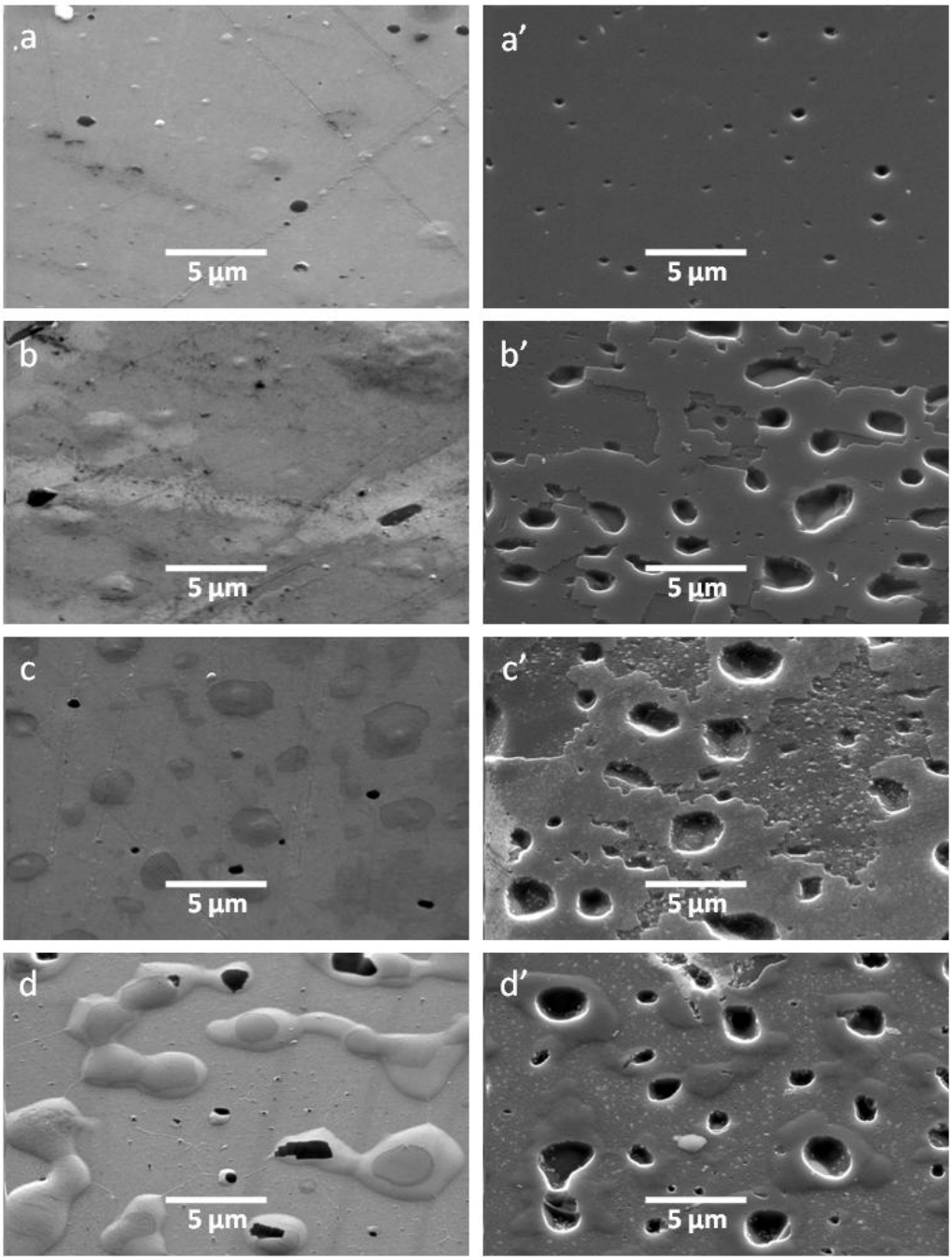

Figure 5. SEM images taken for the samples annealed for 2 hours at: a) 500°C, b) 550°C, c) 580°C, and d) 590°C. The primed letter indicate the image of the samples after aluminum was removed

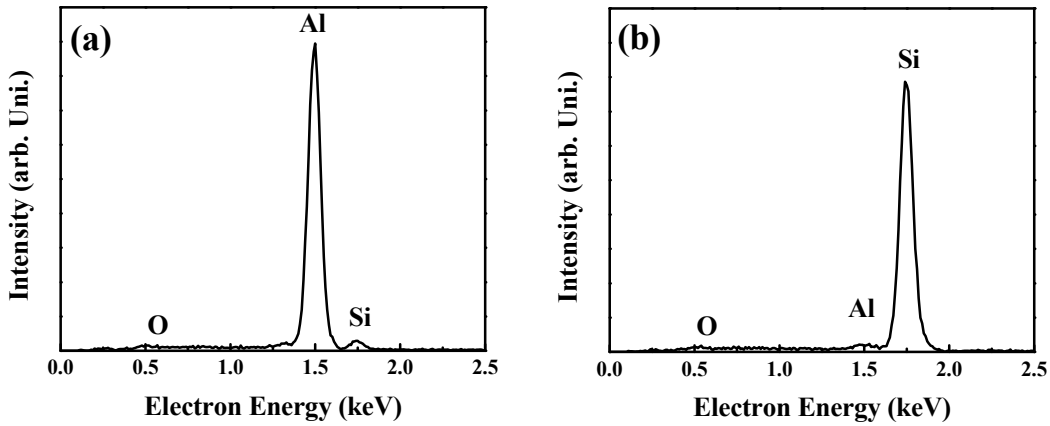

Figure 6. EDX pattern of the samples annealed a 580°C taken at: a) at the center of the dark circular region shown in Figure 5c and b) outside that circle.

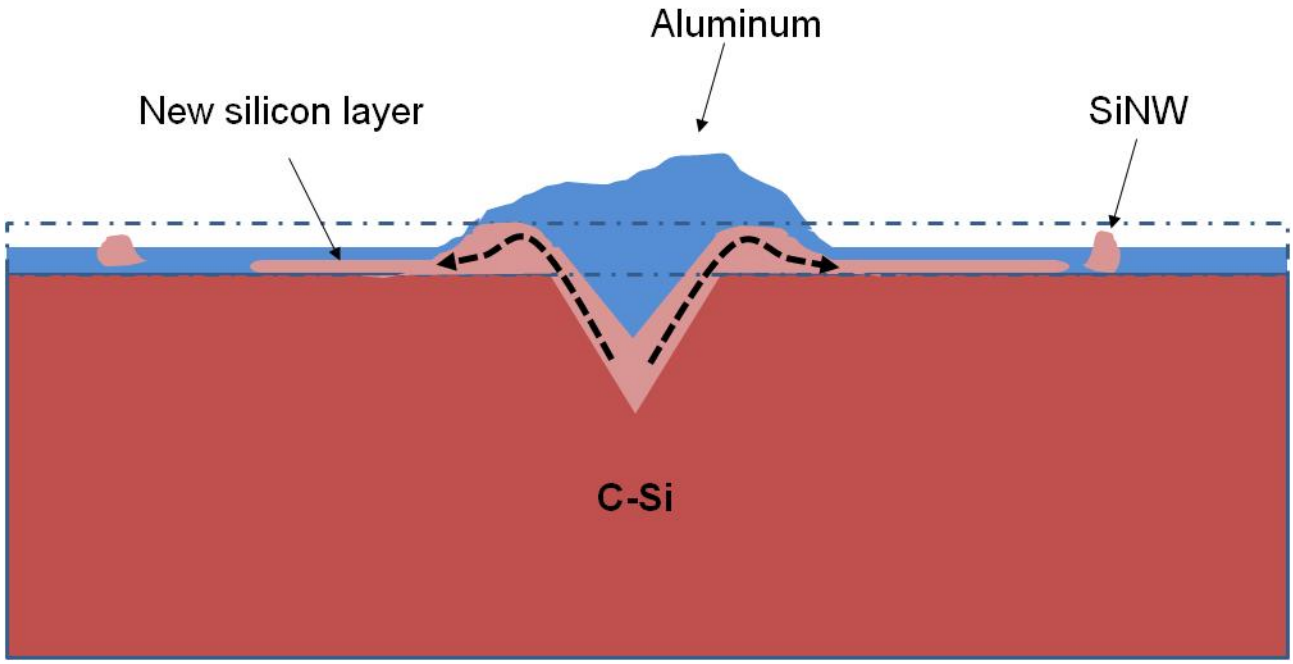

Figure 7. Schematic presentation of the material confined structures on the aluminum film. The dash dotted rectangle presents the thickness of the aluminum film before annealing.

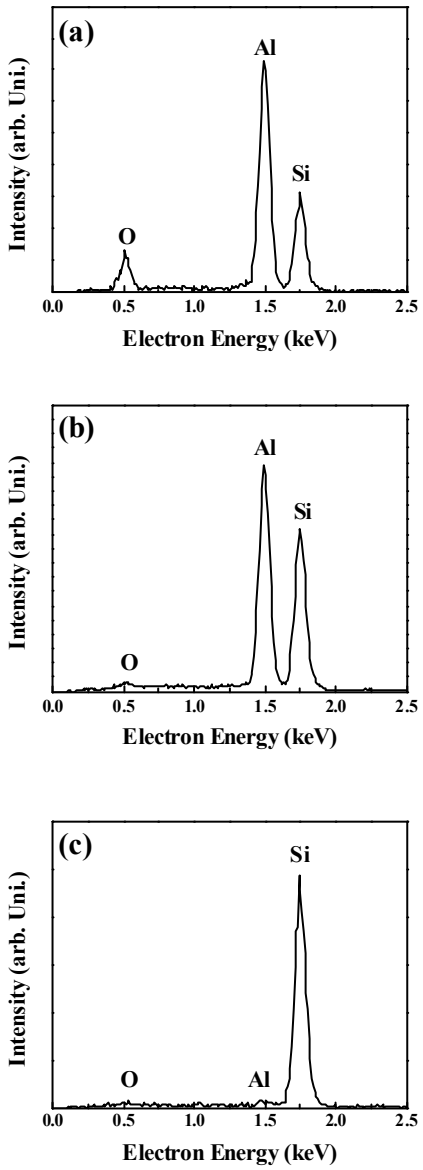

Figure 8. EDX pattern for the samples shown in Figure 5d. The spot measurements were taken at: a) the center of the circular spot, b) near the edge of the spot, c) on the silicon surface.

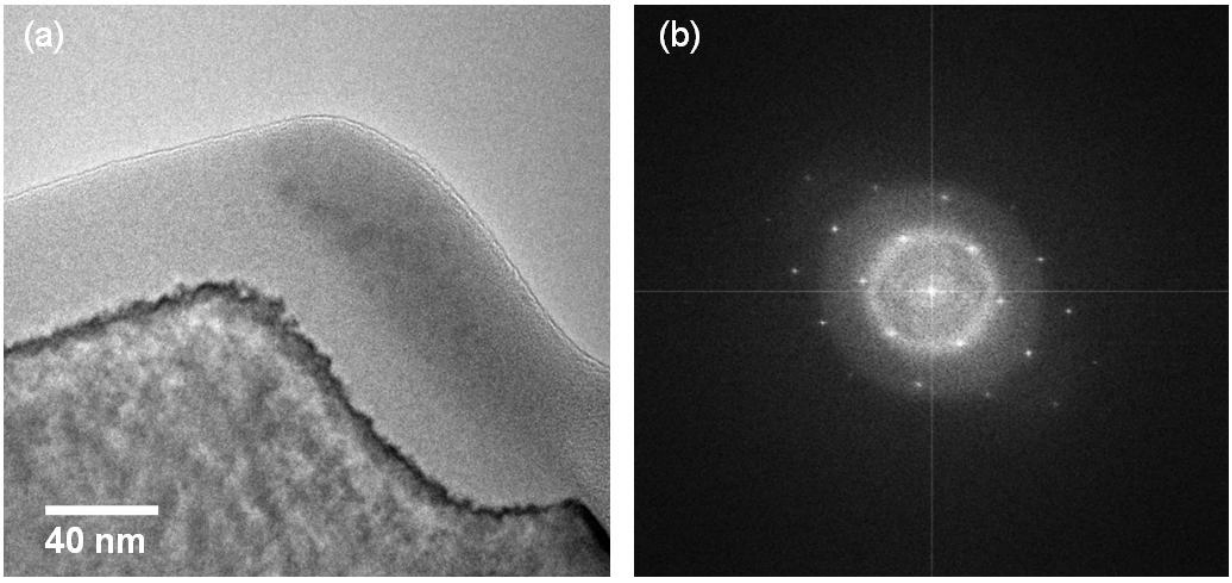

Figure 9. a) XTEM images of the samples annealed at 600°C for 2 hours after aluminum is removed. The image shows clearly the formation of a new layer on top of the silicon surface. b) SAD of the sample. The halos in the indicated a polycrystalline or even amorphous nature in this layer.

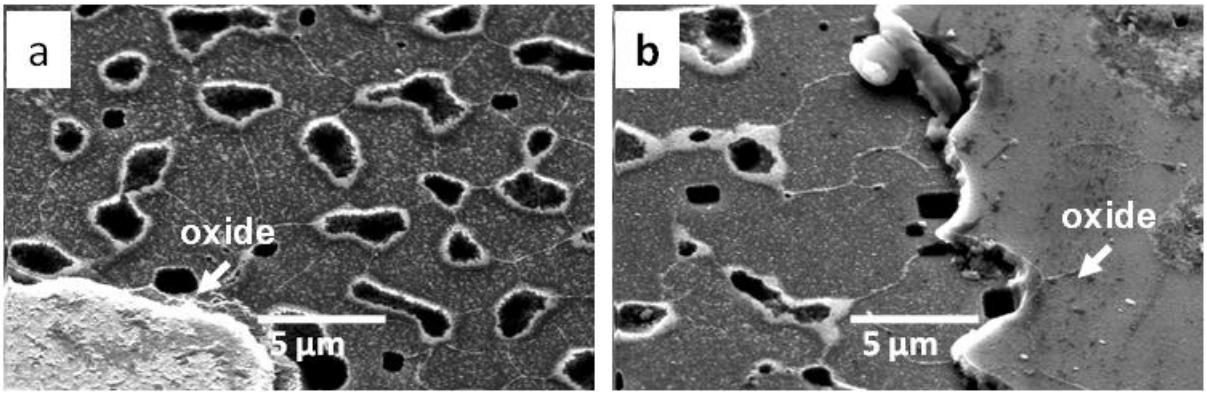

Figure 10. After aluminum removal, the silicon patches creating near the opening cuts in the oxide are removed also. The SEM images here are for a) PPO silicon samples and b) NPO silicon samples.

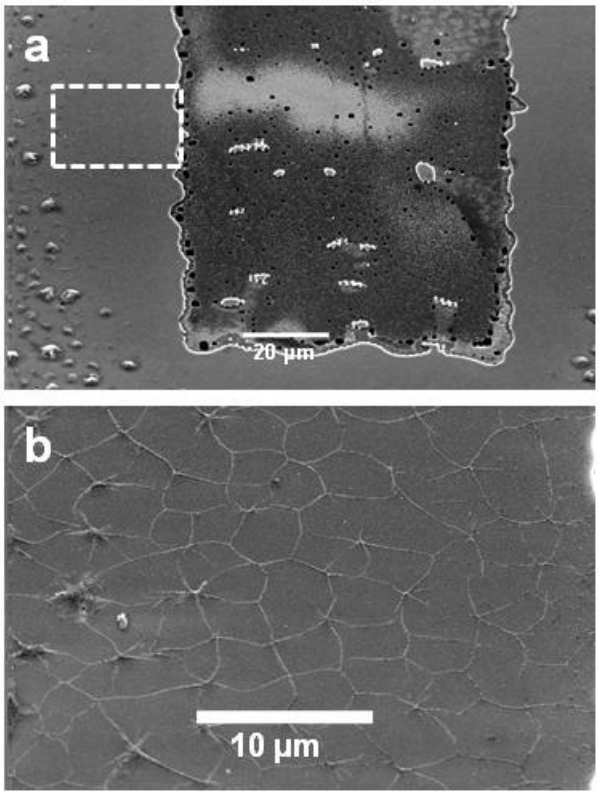

Figure 11. The opening cuts in the oxide acts as silicon source from where silicon will start to diffuser through the film. Near the cut most of the confined structures are in the form of SiNWs. The SEM images shown here for a) general overview and b) high magnification of the region indicated by the dashed rectangle shown in a.

The oxide covered surface is much less in the PPO samples. Therefore, the silicon does not have a preferred region to deposit. Silicon patch formation was observed near and away from the oxide edge. Small SiNWs were also observed on the oxide near the edge. Figure 12a and Figure 12b are the SEM images of the PPO before and after aluminum removal. The patches on the oxide seen near the cut before aluminum removal are the accumulated silicon and aluminum during annealing. When the aluminum was removed it took away the silicon parches leaving plane surface with no confined structures. The confided island-like and SiNWs are seen in the opened regions with no oxide where silicon and aluminum interacted in the same manner as the samples without the patterned oxide.

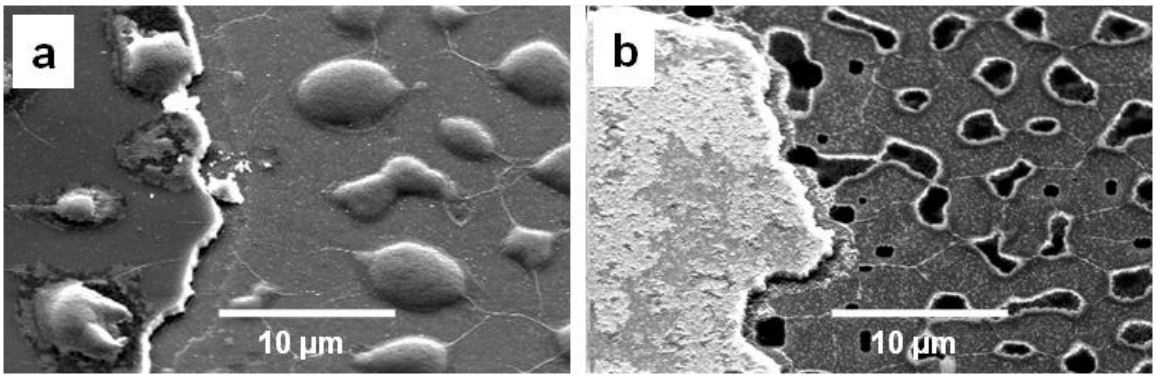

Figure 12. SEM images of the PPO silicon samples, a) before aluminum removal b) after aluminum removal. Small number of SiNWs were created near the edges of the oxide cuts since silicon had no preferred direction of diffusion.

4. Conclusion

In this experimental study, a horizontal network of SiNWs was grown on silicon substrate using aluminum as a platform for the growth process. The wires were grown at the grain boundaries of the aluminum film. The individual nanowires have lengths of few microns and a diameter of about 75 nm. As the silicon accumulates at these boundaries, it forms an interconnected web-like structure of SiNW. A comprehensive explanation of growth mechanism was presented in terms of silicon diffusion through aluminum and its subsequent deposition along the grain boundaries of the aluminum film.

Acknowledgements

The authors would like to thank Mourad Benamara for providing help in TEM sample preparation.

References

[1] G.Timp, Nanotechnology, (Springer, New York 1999)

[2] Y. Wu, Y. Cui, L. Huynh, C. J. Barrelet, D. C. Bell, C. M. Lieber," Controlled Growth and Structures of Molecular-Scale Silicon Nanowires", Nano Letters Vol. 4, 2004, 433436

[3] X. Duan, Y. Huang, Y. Cui, J. Wang, and C. M. Lieber, "Indium Phosphide Nanowires as Building Blocks for Nanoscale Electronic and Optoelectronic Devices", Nature, Vol. 409, 2001,66-73

[4] W. U. Huynh, J. J. Dittmer, A. P. Alivisatos," Hybrid Nanorod-Polymer Solar Cells" ,Science, Vol. 295, 2002 ,2425-2427

[5] K.K. Lew, C. Reuther, A.H. Carim, J.M. Redwing," Template-directed vapor-liquid-solid growth of silicon nanowires" J. vac. Sci. technology. B, Vol. 20, 2002, 389-342

[6] .J. Xing , D.P. Yu, Z.H. Xi, Z.Q. Xue," Controlled growth of nanowires using annealing and pulsed laser.". Appl. Phys. A, Vol. 76, 2003, 551-556

[7] X . Chen, Y. Xing, J. Xu, J.Xiang, D. Yu," Metal-Induced Nickel Silicide Nanowire Growth Mechanism**.**",Chem. Phys. Lett., Vol. 374, 2003 ,626-630

[8] K. Jang, S. Hwang, and Y. Joo," Effect of capping layer on hillock formation in thin Al films",Metals and Materials International, Vol. 14, 2008 ,147-151

[9] V. H. Liu, H. H. Abu-Safe, H. A. Naseem, and W. D. Brown," Fabrication of Silicon Nanowire Network in Aluminum Thin Films" Mat. Res. Soc. Proc., Vol. 862, 2005. 363-368

[10] M. Paulose, C. A. Grimes, O. K. Varghese and E. C. Dickey, "Self-assembled fabrication of aluminum–silicon nanowire networks", Appl. Phys. Lett., vol. 81, 2002 ,153-155

[11] N. Ozaki, Y. Ohno, and S. Takeda, " Silicon nanowhiskers grown on a hydrogen-terminated silicon {111} surface",Appl. Phys. Lett., Voll.. 72, 1998, 3700-3702

[12] T. B. Massalski Binary Alloy Phase Diagrams (Materials Park, OH: ASM International) 1990

[13] K. Sharif, H. H. Abu-Safe, H. A. Naseem, W. D. Brown, M. Al-Jassim, R. Kishore, " Epitaxial Silicon Thin Films by Low Temperature Aluminum Induced Crystallization of Amorphous Silicon",Mat. Res. Soc. Proc., Vol. 910, 2007, 517-521

[14] J. O. McCaldin and H. Sankur, Diffusivity and Solubility of Si in the Al Metallization of Integrated Circuits Appl. Phys. Lett. , Vol.19, 1971, 524-527

JJMIE

Volume 4, Number 1, Jan. 2010
ISSN 1995-6665
Pages 91 - 110

Jordan Journal of Mechanical and Industrial Engineering

Comparison of Biogas Supply Chains Using the Example of the Conditions of a Municipality

B. Noche * , A. Al Mansi, G. De La Torre

Universität Duisburg-Essen, IPE Transportsysteme und –logistik, Duisburg (Germany), Lotharstr. 1 – 21, 47057 Duisburg - Germany

1. Introduction

Due to scarcity of oil fields and the constant rise of energy needs of the industrialized countries, alternatives of power supply must be found. In addition, the rising energy demand provides a drastic increase of CO2 emissions, which among other reasons are also responsible for the climatic change. In the climatic protection package valid since 2008 a reduction of up to 40% in CO2 levels is aimed by the year 2020 [1]. In order to achieve this objetive, an increase of the portion of renewable energies is intended for the energy and heat supply. In the past five years the portion of renewable energies of the total energy consumption in Germany has doubled and is now 8,6 percent [2]. Waste management carries also a large portion of CO2 emissions in Germany besides industry. So called biogenous waste from nearly all areas such as households, industry and the waste water treatment indicate a great potential for energy supply and reduction of CO2 emissions [3] (See Figure1).

Biogenous waste in Germany (liquid manure, sewage sludge, forestal debris, industrial waste and old timber, straw, bio green waste, biogenous portion of the domestic house waste, leftovers from commercial sources among other materials) are estimated to represent 80 millions Mg (Megagram) of dry matter per year [4]. In the case of complete energetic utilization from this matter, an amount of 400 $TWh_{th/a}$ (Terawatt hour, thermic per Year) could be generated, constituting an approximate of 24% of the current consumption of the Federal Republic of Germany[5].

Due to the substitution of coal with biogenic waste, approximately 160 Million Mg CO_2 would be saved with an emission factor of 0,4 Mg CO_2 /Mwh_{th} (Megagram CO_2 per Megawatt hour, thermic) assumming for that, a closed CO_2-Cycle for the Bioenergy carriers and total utilization of biogenetic waste. With it the required emission reductions in both relevant sectors (Energy, and Waste management) will be by far surpassed[6]. With the prohibition of dumping of non pre-treated waste, which aim to strongly reduce a deposition of pre-treated biogenous waste and to prohibit the feeding of leftovers to animals in the entire European Union. New disposal ways for this waste fraction must be searched now.

The production of biogas in biological gas facilities or sewage purification plants represents a meaningful linkage between energy and waste management. The energetic use of biogenous waste opens possibilities of carrying out both the climatic protection and the power supply goals on a regenerative basis. Thus not only contribution is made to regenerative energy production, but also a new efficient utilization of biogenous waste is created. The climatic change and the discussion around the greenhouse effect moved the emission of CO_2 into the foreground. Transportation logistics importantly contributes to CO_2 emissions. In the past years optimization of transportation stood in focus for the minimization of costs. The mere adjustment of transport costs and posibilities without the consideration of the emission can no longer be justified. Route planning and transportation optimization are in the economy standard instruments for the improvement of logistics. In the area of the transportation of disposables, in particular during sewage sludge removal, this approach is rarely used. Large potentials for the disposal transportation due to successes in the past are therefore expected.

2. Objective

The efficient and ecological utilization of biogenous waste covers multiple logistic components such as points of collection, transportation, storage, drainage, hygienization, sterilization, cutting, and sorting, all of which are being part of the chain of valuable materials processing. The supply of the biogenous waste at the right time, with the correct quality and the proper place is associated with a large logistic effort because of cities with a high number of inhabitants where multiple sources of raw material are available. The costs, which are calculated for the supply of the biogenous waste, can be charged here against the yield from the production of biogas, so that profitability could be expected. Since there are multiple forms of biogenous waste, the collection of individual fractions is difficult to achieve efficiently. For example the waste fractions can belong to the food production, household, as well as that from hotel and restaurant industry combined. Therefore, it should be seeked for common disposal ways for the different waste fractions, in order to arrange more economical and more ecological forms of disposal and

Corresponding Author. bernd.noche@uni-due.de

  - Volume 4, Number 1 (ISSN 1995-6665)

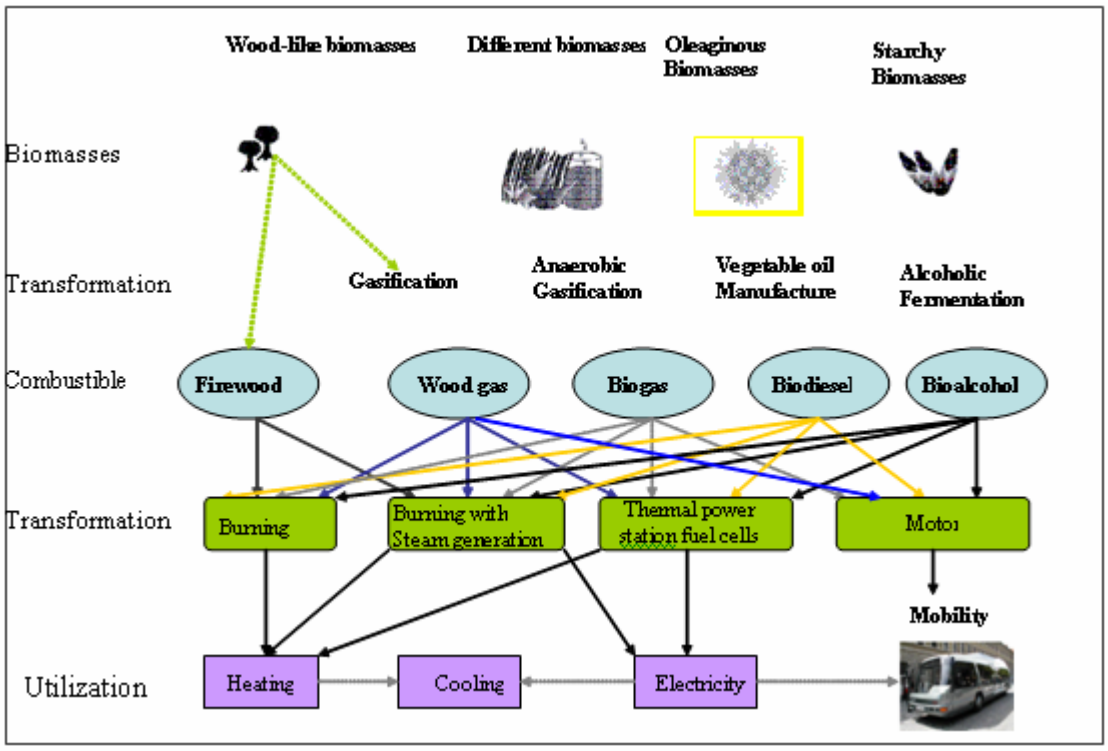

Figure 1.1 Energetic Utilization of Biomass.

utilization of organic resources. Consequently within the process chains in logistics, it is conceivable to collect the waste, mobilize it with large transportation units and bridging the spatial distance between waste deposits and reutilization points, according to the configuration of the technical components that aim to prepare the biogenous raw materials with the correct quality (pretreatment, e.g. to separate foreign matter, to adjust desired homogeneity). In this paper the biogenous waste fractions from "households", "gastronomy" and "sewage sludge from the waste water treatment" are limited to the area in Duisburg, according to the demand of logistic and plant-technical components which are going to be examined and their optimization potentials evaluated in the chain of processes to be analyzed. It will be shown how the different types of waste with collective reutilization steps could be supplied, where cost of plant-technical and/or logistic components are aimed to be reduced. In addition a mathematical model is suggested for the costs calculation, which are costs for the required logistic and the use of the technical components. For the maximization of the objective function (profit) it is also necessary to minimize the distances between accumulation and reutilization points, to be bridged. Considering the very high number of sources of raw material, heuristic procedures are usually applied. For the determination of the optimal collection and transportation routes a simulation tool is also suggested where all transportation and collecting procedures are ought to be adjusted. With this contribution a new concept for an economically and ecologically optimal supply of different biogenous waste for biogas production is presented, considering the logistic and configuration-technical components.

3. The Biogas Supply Chain

The biogas supply chain covers the integration of sources with reloading stations and destinations. The sources that are mentioned in this paper are, households, hotel and restaurant industries, including snack stands and pensions, the food industry, meat industry and slaughterhouses and the waste water treatment as well. From all these areas large quantities of biogenous raw materials result and this must be supplied to an optimal reutilization. Depending on the condition of the biomass and distance to production centers direct transportation or transportation through reloading stations have to be considered. In the reloading stations the individual raw materials from the different sources are conducted to larger transportation units to be mobilized to production stations (biogas facility). In addition, it is meaningful to submit the collected biogenous raw materials in the reloading stations for a short pretreatment. This short pretreatment could involve weight reduction and/or volume reduction, drainage of the damp biowaste, so the transport to the biogas facilities can be arranged more efficiently. The biogas is then used as fuel for gas engines or directly for the energy and heat production. The compost produced tfrom the process can further be used as fertilizer and used in agriculture. Figure 3.1 shows the biogas supply chain.

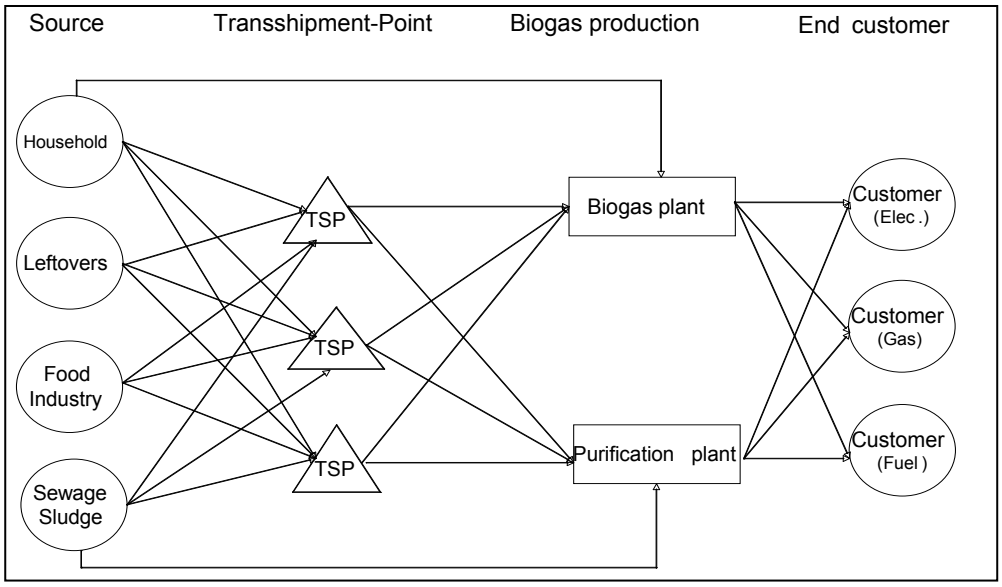

Figure 3.1. Biogas Supply Chain.

4. Area of Investigation

The area of investigation area is limited to the city of Duisburg. The city is divided into 48 urban districts, whereby identical postal zip codes are assigned to some districts. Therefore, only 25 different postal zip code areas with 492870 assigned inhabitants are considered [7]. Figure 4.1 shows the investigation area. Firstly, the waste fractions are separated, in order to differentiate their origins. Subsequently, the different sources of raw material and reutilization points in Duisburg are represented.

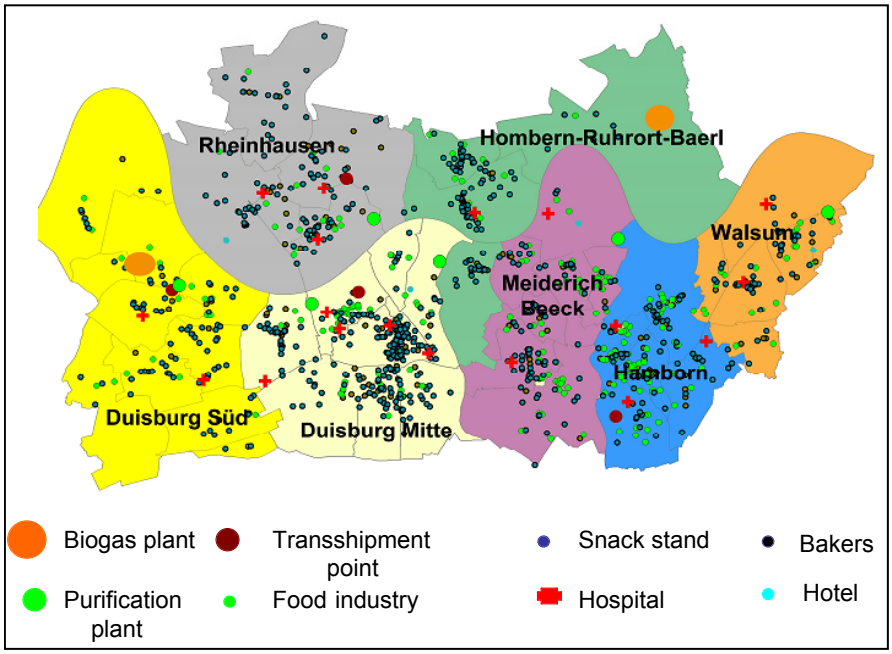

Figure 4.1 Map of the investigation area in Duisburg.

4.1. Database and Discussion

The relevance of the investigation is further increased in this paper on the basis of three selected districts with assistance of the GIS software (geographical information systems).

4.2. Waste from households

In 2006 36598.44 Mg (Megagram) of compostable waste was collected in Duisburg, where a third of the total was green waste that is accepted at the recycling points. This corresponds to about 11025 Mg of green waste in the year 2006. However this waste fraction is not considered in this paper. A small portion of 447.94 Mg was collected over the biowaste containers in the testing district. The rest of waste originates from two thirds of the total quantity from parks and cemetery maintenance as well as a small portion from Christmas tree collection. The collecting quantity from households is about 100 kg/inhabitant and year [8].

Waste from household in the three Districts

The number of inhabitants for each district and of the GIS derived number of houses is represented in figure 4.2.

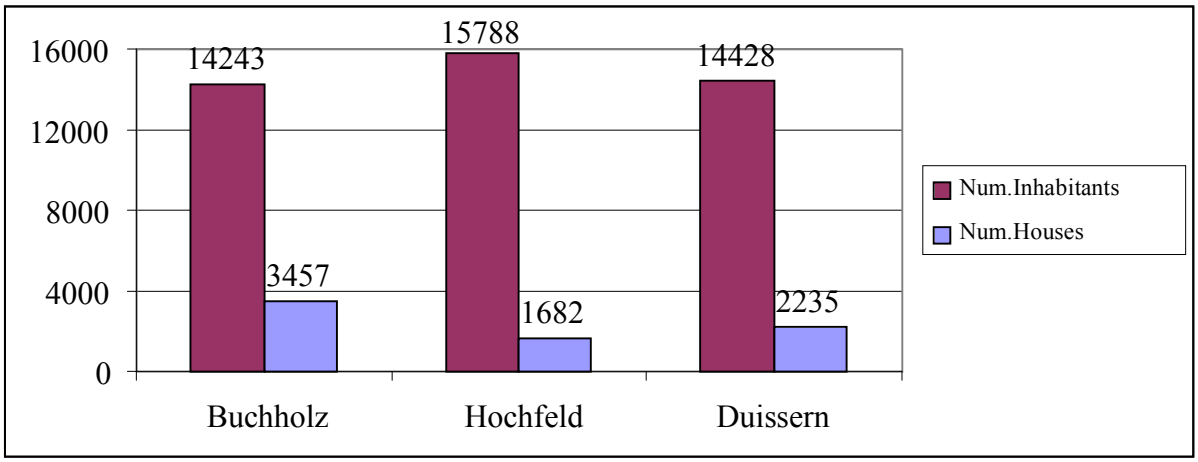

Figure 4.2. Number of inhabitants and houses in the districts of Duisburg.

The theoretical biowaste potential for the households from the three districts as provided by the Winzenhausen Institut is assumed to be 100 kg per inhabitant per year [8]. The quantity per house for a period of two weeks can be computed as following:

$$\text{Biowaste for each house in 14 days} = \frac{\text{Waste quantity per Inhabitant} \times \text{Number Inhabitants}}{\text{collect interval per year} \times \text{Number of Houses}}$$

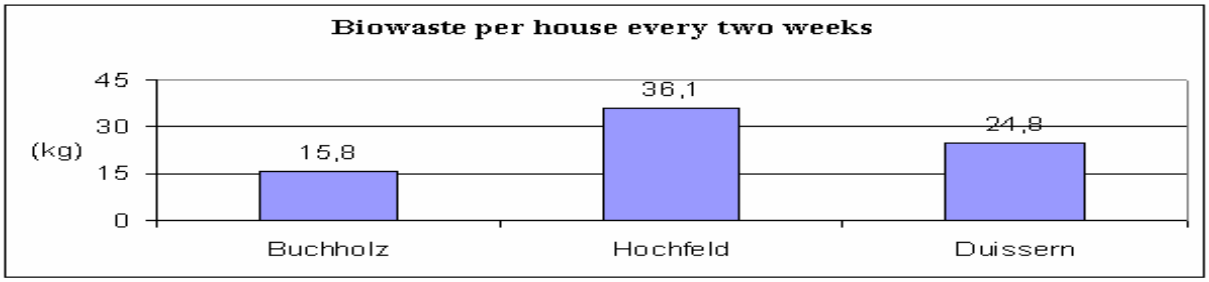

Figure 4.3. Biowaste of household per house every two weeks.

It is assumed that the biowaste of household is collected every two weeks. Thus it is represented with 26 collecting intervals per year and the biogenous quantities of waste for each house per district are represented in figure 4.3. After the computations it is to be determined that the quantity depends on each district. The reason for this is that there are more multi-family houses and buildings in Hochfeld. On the other hand although Buchholz holds more houses, fewer inhabitants per house are observed, thus this lowers the waste quantity per house. The entire quantity for the three districts is 170996 kg waste every two weeks.

4.1.2 Food Waste

The amount of hospitals, hotels, baking shops and snack stands are gathered within the range of the food wastes. The information from surveys on hospitals, hotels and snack stands are taken over. The average waste disposed per hospital was around 300 kg every two weeks that means 26 Periods in year. The 16 hospitals in Duisburg produce up to 124.8 Mg per year. Additionally there are 22 hotels that produce 114.4 Mg per year. That corresponds to 200 kg per hotel every two weeks. For each baking shop results a quantity of 80 kg every two weeks is expected. Thus 243 baking shops produce 505.4 Mg per year. For small snack stand a quantity of 160 kg results every two weeks. Resulting in 2121.6 Mg of waste per

year for 510 Snack stands. For Bars and Restaurants a quantity of 180 kg results every two weeks. So annually the waste production from 699 restaurants is 3271.3 Mg. Altogether the quantity of waste from the leftovers is approx. 6137,5 Mg/a.

Food waste in the three districts

The city of Duisburg has no information about the production of food waste, therefore the estimated value is derived from the number of gastronomic establishments. As an alternative to the estimated 25 kg/inhabitant·a [9], the production of waste can also be calculated from the number of inhabitants as follows:

$$\text{Waste per establishment} = \frac{\text{Waste quantity per Inhabitant} \times \text{Number Inhabitants}}{\text{collect interval per year} \times \text{Number of establishments}}$$

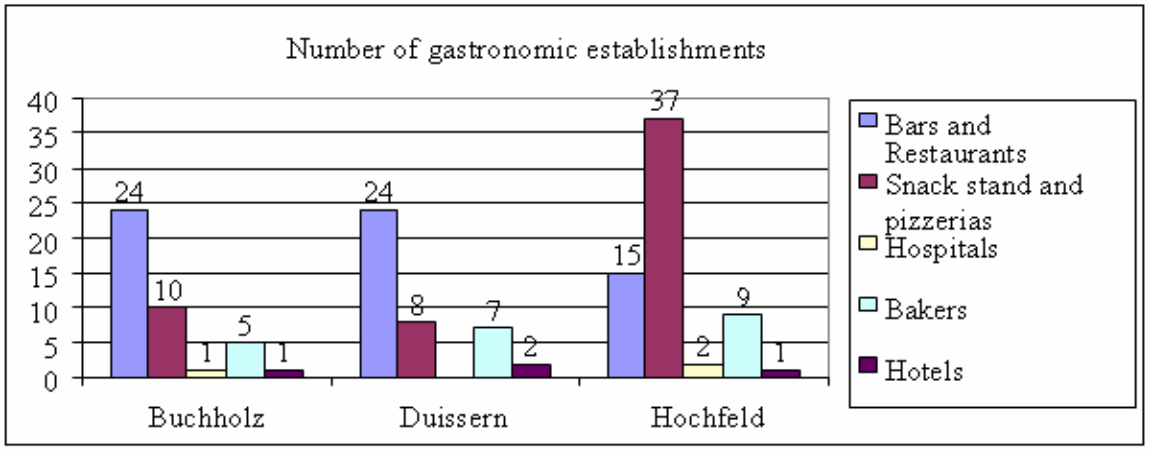

Figure 4.4 Number of gastronomic establishments in the three Districts.

The food waste is collected together with the household, therefore the geographic referencing uses only a node for each street section. Figure 4.8 shows the number of bars, restaurants, snack stands and pizzeria, hospitals, bakers shop and hotels. The entire collecting quantity every two weeks is 23520 kg.

4.1.3Waste from the food industry

From the biogenous waste from the food industry, (grocery stores and other food producers), all organic rests originate from sell and production of food. Among them also baking rests from the production of pasta and also beer's grains from the beer production are considered. Since no exact data for these quantities are available, the information from surveys on food industry is taken over. In relation to the individual food retailing a quantity of 80 kg every two weeks is estimated. The 912 food retailers produce annually approximately 1676.4 Mg. The grocery stores produce also a quantity of 80 kg every two weeks. The annually produced quantity of 261 stores is about 503.4 Mg. Thus the quantity of waste from the food industry is approx. 2179.8 Mg/a. The total quantity of produced waste from both fractions, food waste and waste from food industry, is then 8317.3 Mg/a. In the literature an amount of 20 kg per year per inhabitant is also considered and therefore the total quantity is about 9800 Mg/a [9]. This approximate value is determined by estimations, which is used as a comparative value in this paper.

Waste from the food industry in the three districts

The waste production is derived from the number of industries. As an alternative (20 kg/E·a) the waste production is calculated in relation to the quantity of inhabitants as follows:

$$\text{Waste per industry} = \frac{\text{Waste quantity per Inhabitant} \times \text{Number Inhabitants}}{\text{collect interval per year} \times \text{Number of industries}}$$

The waste of food industry like the leftovers is collected together with the waste of households. Figure 4.8 shows the number of food industries. The total collected quantity of 130 nodes every two weeks is about 10400 kg. A detailed representation of the quantity of the grocery stores is shown in figure 4.5.

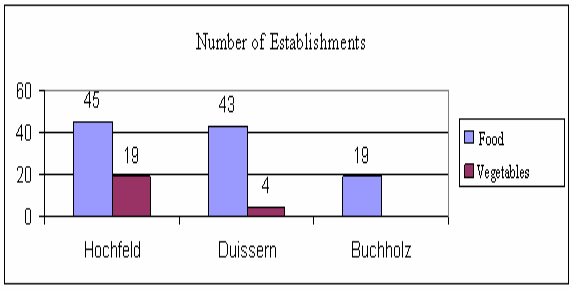

Figure 4.5. A detailed representation of the quantity of the grocery stores.

4.1.4Sewage sludge from waste water treatment

Sewage sludge is summarized under dredging from waste water treatment extracted in the Duisburger sewage purification plants. Six purification plants exist in Duisburg that are responsible for the waste water treatment of the city. The exact locations and produced quantities from these plants let themselve read off from the information platform in North-Rhine/Westphalia (AIDA) [10].

In this paper only the sewage sludge waste from waste water treatment plants is considered..

The well known Screenings and sand trap disposals were not included in the analysis. Sand trap disposals are washed in machines and used in the construction industry, for example in road construction. Screenings are washed likewise in machines and afterwards composted, deposited or incinerated [11]. For the total area in Duisburg an

amount of 16644.06 (Mg/a) results from the waste water treatment plants [10].

In order to examine more clearly and transparently the transportation, inventory and distribution costs, only three districts in Duisburg are examined (Duissern, Hochfeld and Buchholz). These three districts were afterwards processed with assistance of the GIS software

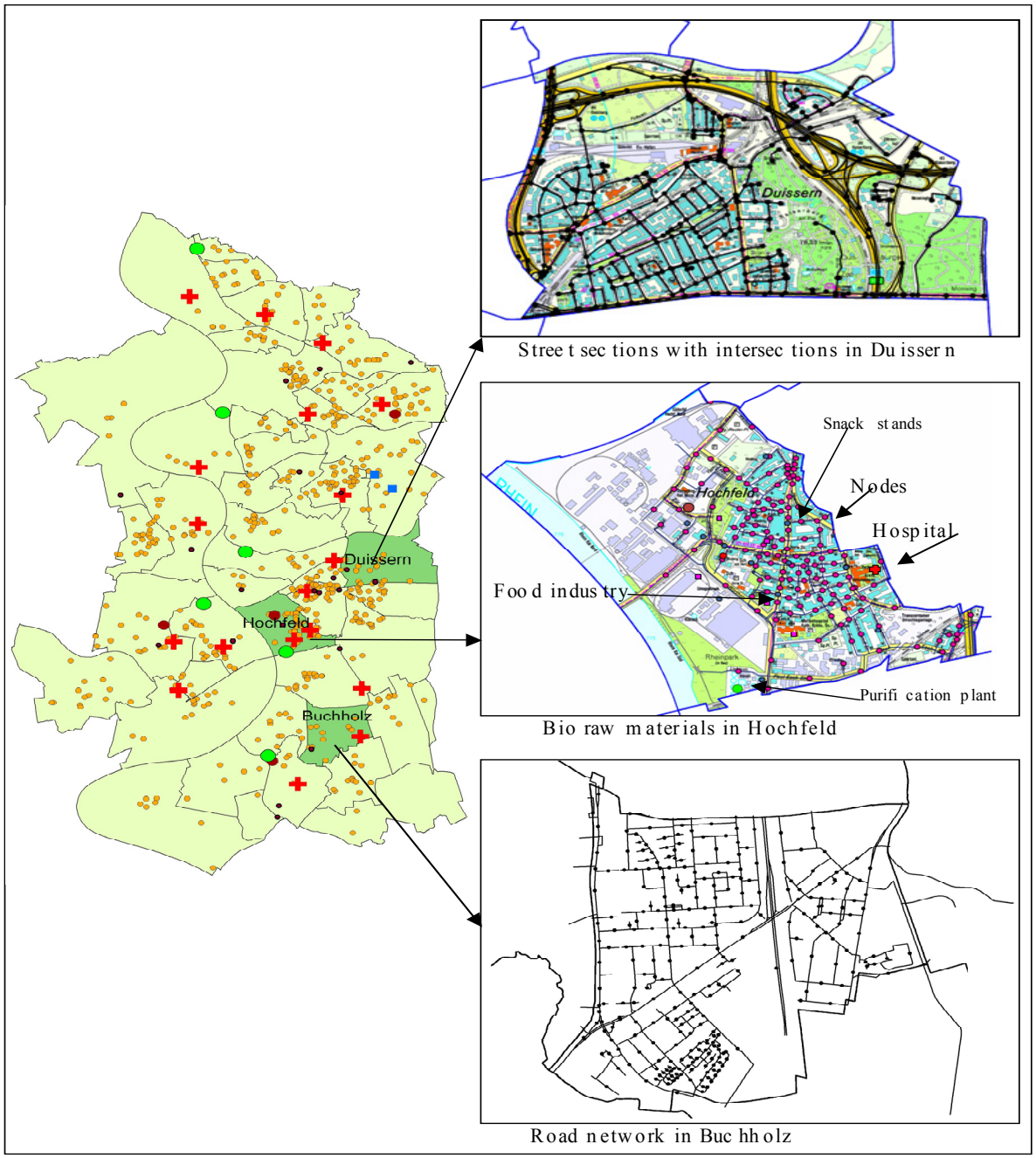

Figure 4.6 Investigation area.

4.2Data preparation with GIS Software

To increase the meaningfulness of the investigation, the model should have practical relevance where availability, actuality and accuracy of input data are required. The condition can be fulfilled and the production, administration and actualization of the data can be made possible by the application the digital information system. In order to calculate the biowaste quantity, two different methods are used in the literature, container-referred and inhabitant-referred calculations. Since the separate collection is accomplished only in four districts and no GIS data was made available, the investigation was accomplished regarding the number of inhabitants and surveys. To calculate the collecting costs and/or the covered driven distance, between two intersections (street section) they have to be represented as a node (in the middle of the road section) and the coordinates will be determined with assistance of the GIS software. Each house is assigned on a road section, which was labeled with a certain name. The data of the houses also contain the names of the road section, in order to avoid double allocation.

Duisburg has 6 purification plants and 4 recycling yards (transshipment stations). The investigation areas contain in total 666 nodes. The size of collecting surface is about 12.4 km² and has up to 44459 inhabitants [7].

4.3GIS-aided route planning

Three districts from Duisburg are selected for the investigation of the Biogas Supply chain (see Figure 4.14). Therefore 44459 inhabitants (9% of the total number of inhabitants of Duisburg), 12.4 km² surface (5% of entire surface), 7375 house, 63 bars and restaurants, 55 snack stands and pizzerias, 21 baker's shop, 4 hotels, 3 hospitals, and Grocery retailers are considered. The coordinates of nodes (in the middle of the road section) are determined with assistance of the GIS software and each house, hotel and hospitals were assigned to the nodes. A detailed representation of the Hochfeld district is shown in figure 4.6.

5. Analysis of The Process Chain

The 4 different process chains for biogenous wastes from the different areas are now considered.

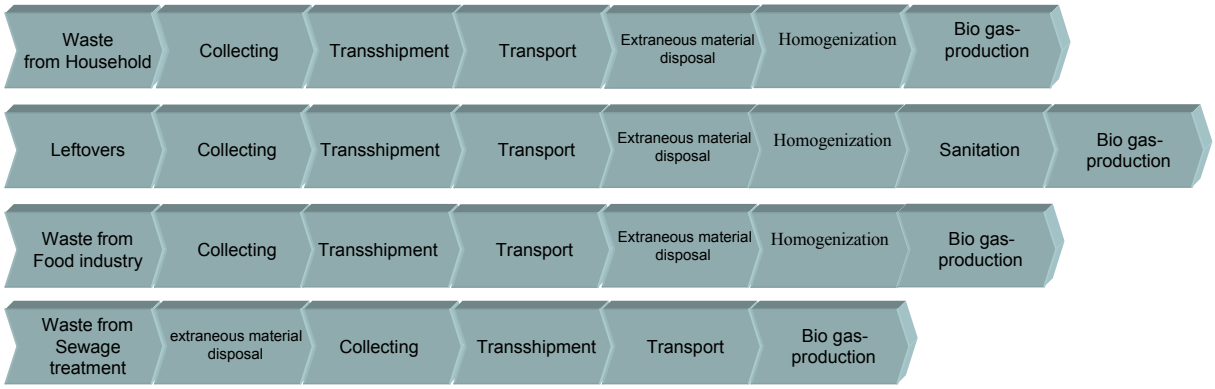

Figure 5.1 Biogas Process chain.

It should be seeked for optimization potentials for the collective utilization of waste. In addition different process chain scenarios are methodically run through to the end and in the observation of results regarding their cost-efficiency they will be compared one with another. If the four process chains are observed together, it is noticeable that those of the households, the hotel and restaurant industry and the meat industry are very similar. Only the pretreatment and processing of the biogenous waste materials from the hotel and restaurant industry and the meat industry are different due to legal regulations. There is no comparison between the pretreatment of sewage sludge from the waste water treatment with those of the other fractions and must always be observed therefore separately.

6. The mathematical model

For the computation of the entire process chains and the process chain scenarios a general mathematical model is suggested. This contains all collecting and transportation routes for transport over Transshipment stations (TSP) and direct transportation. The objective function is to maximize the net income from the disposal and utilization of waste. Some assumptions are done:

1. The Transshipment stations are temporarily limited. The material in the TSP stations should not be stored longer than two days, because if it is stored longer than two days, negative effects could occur. It could begin unpleasantly to smell for example.
2. The capacities of the TSP stations are equal in each point.
3. The production plant does not have a maximum capacity.
4. Each customer is served only by a vehicle.

The development of the mathematical model is based on an elaboration of Liu, Lin [12] and Liu, Lee [13], in which they solve a „Location Allocation problem“ (LAP) with consideration from inventory factors. Even if they pursue another objective in their article, then the approach appears also interesting for the solution of „Capacitive Multi-Depot Location Routing Problem“ (CMDLRP). Both articles were published in 2008 [14], [15].

Notations

M_s :Quantity of waste in the biological gas facility or purification plant s

M_q :Waste collecting quantity of customer q

E_{Biogas_s} :Fermentation gas yield per ton of biogas facility or purification plant s

$E_{Kompost_s}$:Compost yield per ton of the biogas or purification plant s

E_{Ent_q} : Income of the disposal fee of the customer q

U : Number of the transshipment station

Q : Number of customers

S :Number of the biogas or purification plants

R : Number of vehicles or route

D :Number of final customers

a : Vehicle capacity from source to the reloading station or biological gas facility

b :Vehicle capacity from transshipment station to the biological gas facility

$\max Serv$: Maximum service capacity of the vehicle

C_{fix_j} :Fixed costs of transshipment station j

c :Transport costs

cm : Travel cost per distance unit

C_{Lager} : Inventory carrying costs

$C_{\hom_j}$:Costs of the homogenization in the TSP station/biological gas facility

C_{hyg_j} :Costs ofthe hygienization in the TSP station/biological gas facility

C_{ster_j} :Costs of the sterilization in the TSP station/biological gas facility

C_{stgr_j} :Costs of the removal of extraneous materials in the transshipment station/biological gas facility

C_{entw_j} :Costs of the drainage in the transshipment station/biological gas facility

X_{ster_j} : 1, if the sterilization is needed, otherwise 0

X_{entw_j} :1, if drainage is needed, otherwise 0,

h :Index quantity of the TSP points or customers or biological gas facility

g :Index quantity of the TSP points or customers or biological gas facility

s :Index quantity of the biological gas facility

i :Index quantity of the customers

j : Index quantity of the transshipment points

k :Index quantity of the route

V_k :A row for route k with a transshipment point

Dis_{kgh} : Entire distance for route k

$V_{Kap_{gh}}$:Vehicle capacity

UL_{kgh} :Average demand for route k

D_{kgh} :Entire demand for route k

Y_{ij} :1, if customer j is assigned to depot i, otherwise 0

Z_j :1, if depot j is established, otherwise 0

X_{kgh} :1, if g is a direct successor of h on the route k, otherwise 0.

$$\max P = \overbrace{\sum_{s}^{S}\left(M_s \times E_{Biogas_s} + M_s \times E_{Kompost_s}\right)}^{\text{Biogas facilities revenue}} + \overbrace{\sum_{i}^{Q}\left(M_q \times E_{Ent_q}\right)}^{\text{Disposal fee}} - \overbrace{\sum_{j=Q+1}^{Q+U} C_{fix_j} x Z_j}^{\text{fixed costs}}$$

$$- \sum_{k=1}^{K}\sum_{g=1}^{Q+U+P}\sum_{h=1}^{Q+U+P}\left(\overbrace{\left(c + cm + Dis_{kgh}\right) \times \frac{D_{kgh}}{V_{Kap_{gh}}}}^{\text{Collecting costs}} + \overbrace{\left(\frac{V_{Kap_{gh}}}{2} + R_{kgh} - UL_{kgh}\right) \times C_{Lager}}^{\text{Inventory costs}}\right) \times X_{kgh}$$

$$- \overbrace{\sum_{j=Q+1}^{Q+U+P}\left(\left(C_{\hom_j} + C_{hyg_j} X_{hyg_j} + C_{ster_j} X_{ster_j} + C_{stgr_j} + C_{entw_j} X_{entw_j}\right)\left(\sum_{j=Q+1}^{Q+U+P} D_{gh} + \sum_{j=Q+1}^{Q+U+P} D_{gh}\right)\right)}^{\text{Pretreatment costs}}$$

$$+ \underbrace{\sum_{k=1}^{K}\sum_{(g=Q+U+P+1)}^{(Q+U+P+D)}\sum_{(h=Q+U+P+1)}^{(Q+U+P+D)}\left(\left(c + cm + Dis_{kgh}\right) \times \frac{D_{kgh}}{V_{Kap_{gh}}}\right)}_{\text{Distribution costs}}$$

$$V_{Kap_{gh}} \le a, \qquad g = 1,\ldots,Q, \;\; h = Q+U+1,\ldots,P \tag{1}$$

$$V_{Kap_{gh}} \le b, \qquad g = 1+Q,\ldots,U, \;\; h = Q+U+1,\ldots,P \tag{2}$$

$$D_{kgh} \le \max Serv \tag{3}$$

$$\sum_{k=1}^{K} \sum_{h=1}^{Q+U+P} X_{ikh} = 1, \qquad i = 1,\ldots,N \tag{4}$$

$$\sum_{g\,ev}^{K} \sum_{h\,ev}^{Q+U+P} \sum_{K=1}^{k} X_{ikh} \ge 1, \qquad \forall(v,\bar{v}) \tag{5}$$

$$\sum_{g=1}^{Q+U+P} X_{hgk} - \sum_{g=1}^{Q+U+P} X_{ghk} = 0 \qquad k = 1,\ldots,K, \;\; h = 1,\ldots,Q+U+P \tag{6}$$

$$\sum_{j=1+Q}^{Q+U} \sum_{i=1}^{K} X_{ijk} \le 1, \qquad k = 1,\ldots,k \tag{7}$$

$$\sum_{j=1+Q+U}^{Q+U+S} \sum_{i=1}^{K} X_{ijk} \le 1, \qquad k = 1,\ldots,k \tag{8}$$

$$\sum_{h=1}^{Q+U+P} X_{ihk} + \sum_{h=1}^{Q+U+P} X_{jhk} - Y_{ij} \le 1 \qquad \mathrm{i} = 1,\ldots,N, \;\; \mathrm{j} = N+1,\ldots,Q+U+P, \;\; k = 1,\ldots,K \tag{9}$$

$$X_{kgh} = \{0,1\}, \qquad g = 1,\ldots,Q+U+P, \;\; h = 1,\ldots,Q+U+P, \;\; k = 1,\ldots,K \tag{10}$$

$$Z_j = \{0,1\}, \qquad \mathrm{j} = Q+1,\ldots,Q+U+P \tag{11}$$

$$Y_{ij} = \{0,1\}, \qquad \mathrm{i} = 1,\ldots,Q, \;\; \mathrm{j} = Q+1,\ldots,Q+U+P \tag{12}$$

Constraints

The constraints (1) and (2) restrict the capacity of the vehicle. The constraint (3) ensures the fact that the capacity of the transshipment station is not exceeded. In order to fulfill the acceptance of the model, the constraint (4) guarantees that each customer is assigned only to one route. Then constraint (5) guarantees that each route with the same transshipment station and/or biological gas facility supplies. With the next constraint (6) it is assured that the point of arrival of the vehicle should be also the point of departure. The constraints (7) and (8) serve for the fact that a route serves no more than one transshipment station and/or biological gas facility. The constraint (9) is responsible for the fact that a customer is assigned only to one depot, if there is a route, which passes near this customer. Constraints (10), (11) and (12) secure that the decision variables take either the value 1 or 0.

7.Proposed Biogas Facilities in Duisburg

Two different biogas production scenarios are examined in this paper. In the first scenario, surrounding biogas plants are considered to be used as production locations. And in the second scenario, Duisburg's purification plants are used as production locations (see figure 7.1). The city of Duisburg had 492870 inhabitants in 2008. Since 1975 the number of inhabitant in the city has decreased by approximately 100000. The current inhabitant density is 2124 inhabitants/km². The total area is 232 km² and the agricultural area without grassland is about 21 km². In this area grain is cultivated predominantly [16]. Besides, in four districts inside the Duisburg-South region, biowaste is collected separately. And in 2006, the amount of collected biowaste was approximately 447.94 Mg. [17].

7.1 Possible plants

Agricultural biogas plant

The agricultural surfaces and raw materials are mostly located in the south region of Duisburg. Moreover, according to the area structure, it is possible that biowaste potential is higher, the biowaste containers have less extraneous materials and an agricultural biogas facility would be much more meaningful.

Since 1999, biowaste has been collected separately in four districts; Huckingen, Hüttenheim, Ungelsheim and Mündelheim. In these four districts, 22362 inhabitants are distributed to 10800 households. A possible plant is supposed to operate with not only renewable materials but also up to 49 % biowaste. Apart from the heat and electric

energy which are utilized from the biogas, this biogas may also be fed into the local gas network [10]

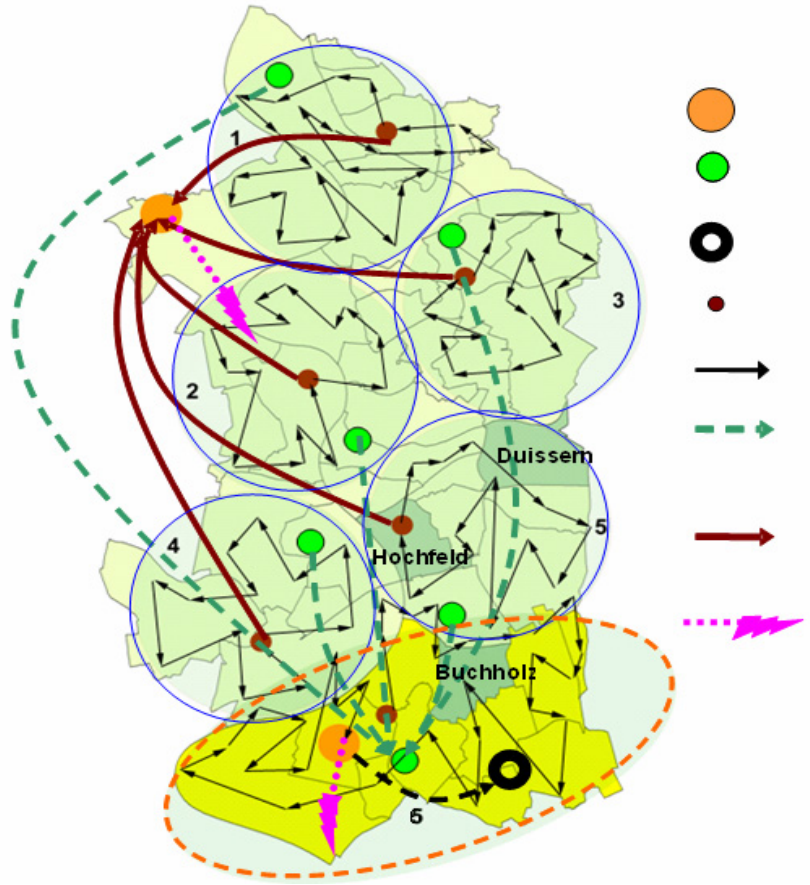

Figure 7.1 Proposal of biogas production models for Duisburg

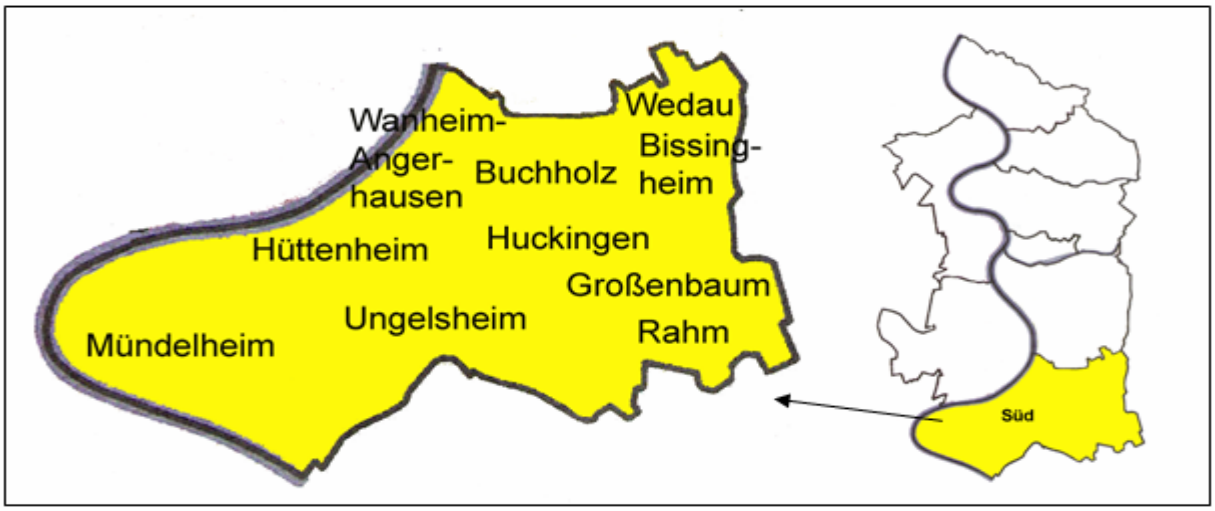

Figure 7.2 Overview of the district Duisburg south

Agricultural biogas facility has a cultivation area of approx. 801.5 hectares for the energy plants. These energy plants are corn, grass silage and rye. Besides, an annual harvest for these available plants is 22133 Mg/a. A substrate mixture, which is produced from these three plants, provides approximately 186 m³/Mg FM (fresh mass) of biogas. From this estimation, it is seen that a great amount of biogas production of 4116000 m³ can be achieved. The crop and its biogas yield are given in the table 7.1.

Table 7.1 overview of the crop and its biogas yield [16]

Possible supply from farmers		
Cultivation area	802	Ha
Average yield per hectare	28	t/ha
Usable potential	22133	t/a
Biogas facility		
Specific biogas yield for energy	186	m^3/t FM
Biogas yield for energy plants	4116000	m^3
Heat value	5.40	kWh/m^3
Energy yield	22229	MWh/a

Industrial biogas facility

The fermentation would be a possibility to use the bio waste which can be collected in Duisburg. The methane gas, which comes out during the fermentation, can be used for either heat or electric production. According to the other researches, the average amount of biogas can be 120 m³ /Mg [16]. A possible industrial biogas facility can be planned in Duisburg Baer, because the population density of Duisburg Bear is smaller than the other urban districts. Another reason is that it is very close to a natural gas net, so that the produced biogas can be fed into the natural gas network.

Purification plants

The purification plants can be used as an alternative for the biogas production. Although the production cost of purification plants are higher than those of biogas plants, there are savings possibilities with the transport costs.

7.2. Agricultural and industrial biogas plants model

In the first model, two biological gas plants for entire Duisburg are suggested. These plants are located in the south (agricultural) and in the northwest (industrial) area of Duisburg. In the agricultural biogas plant, renewable resources may be used with biowaste, which are collected in Duisburg south, in order to produce biogas. For the purpose of transport cost reduction, either the existing TSP stations can be used or after a cost analysis, any additional TSP stations may be built.

7.3 Biogas-purification plant model

As mentioned for the second alternative; Duisburg is divided into six areas, because six purification plants are available. Like in the first model, an agricultural biogas facility is placed in the south area and all biowaste is used in this plant. Subsequently, the biowaste in other districts are distributed to five different purification plants. For this purpose, the purification plants for biogas production (sewer gas production) are assumed to be suitable. In case of insufficient capacity, the 6th purification plant can be also used as a spare disposal option.

8. Development of a simulation tool

In the investigated areas, the biowaste is planned to be collected every 14 days. It means that the collecting vehicle visits at least once all nodes in every two weeks and afterwards it brings the collected raw materials to a TSP point or a purification plant. In order to determine a route, the following criteria could be considered:

- TSP point´s or purification plant´s capacity,
- Capacity of the collecting vehicle,
- Driver´s and collection personnel`s working hours,
- Unloading time per biowaste source (house, snack stand, etc.),
- Preparation time and driving time

The routes are planned with the developed software, which connects the customers, TSP points and biogas facilities. The operation sequence of the used algorithm is given in the Figure 8.1.

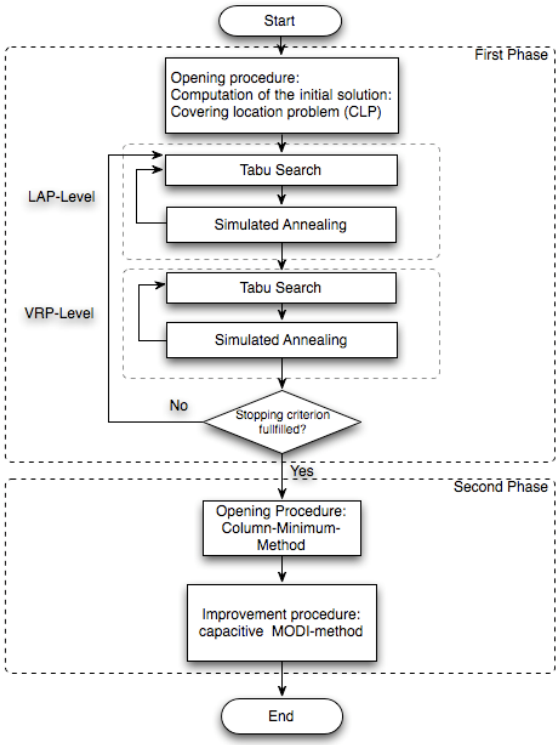

Figure 8.1 Process flowchart of the proposed heuristic approach

With the help of this process flowchart, the program can define the required TSP points (LAP) and compute the shortest route (VRP). In the second phase, the transport between transshipment points and biogas plants are handled. According to this phase some assumptions are done:

- All transshipment stations have the same capacity.
- All production plants have the same capacity.
- All collecting vehicles have the same capacity.
- All transport vehicles have the same capacity.
- All collecting vehicles have maximal three tours per day.
- The total capacity of the transshipment stations is equal to the whole capacity of all sources.
- The total capacity of the production plants is equal to the whole capacity of all sources.

8.1 First phase: Location and route planning

8.1.1 Constructive procedure:

„Covering location problem "The heuristic „Covering problem" possesses the following characteristics:

- Distances (and/or travel time) of nodes cannot exceed a fixed value.
- A minimum number of nodes and transshipment points must be specified, which ensure the service level.
- The distances between the biogenous raw materials sources and the TSP stations cannot be larger than 10 km (see Figure 8.2).

The distances between customers and transshipment points or biogas facilities will be first determined by using a shortest path method. Dijkstra's algorithm can be given as an example for this method. For each node, the reachability radius is given, it means that, there is a transshipment points set of U_i, which customer can reach.

$$U_i = \{j \in V : d(j,i) \leq S_i\}, i = 1,...,n$$

V is the set, which is the shortest path between i and j, can also be less or equal to the maximum distance S_i. It means that, the node is supplied by the transshipment point $j \in U_i$. The objetive function minimizes the total number of fixed nodes as transshipment points under the constraint that each Customers is served at least by a transshipment point.

8.1.2 Improvement procedure: Hybrid metaheuristic for the combined location and route planning

Step by step, it is tried to improve the initial solution from the constructive heuristics, with assistance of metaheuristics [18]. Hybrid metaheuristic consists of two subproblems; the location allocation problem (LAP) and vehicle routing problem (VRP). LAP problem is composed of location arrangement and customer assignment for the necessary location. Besides, VRP provides solution for customer-vehicle assignment and optimal sequence. The improvement method can be classified in two different procedures; special and general search methods. However, the special search methods are used for certain optimization problems. The general procedures, which are also called metaheuristics, are used for all problems [31]. In order to solve the NP-hard problems, numerous efficient procedures were developed; e.g. Simulated Annealing (which is based on a physical process in metallurgy) and Tabu Search (which was developed with assistance of artificial intelligence) [18]. In the Figure 8.3 it is shown, how the routes are generated by the simulation model for the three districts.

Possible transformation strategies are the following:

- Swapping: Two nodes are swapped between different routes.
- Insertion: A node is removed from one route and inserted into another.

In order to improve the solution of constructive heuristic, a hybrid heuristic, which consists of Tabu Search and Simulated Annealing, is used on both problem levels (LAP and VRP). With it both procedures share the same tabu list, whereby short cycles will be avoided and the search for better solutions can be arranged more effective.

8.2 Second phase: Transportation problem

The second phase of the model is a transportation problem which represents a single-step problem. The goal of the model is to keep the transport costs as low as possible. For this purpose, which TSP stations will satisfy which biogas or purification plants, should be determined by taking capacities into account.

8.2.1 Constructive Heuristics: Capacitated Column Minimum Method

In contrast to the simplest methods used to solve transport problems, the column minimum method considers not only the quantities but also the transport costs. The columns (transshipment stations) of the transport matrix are cyclically examined in the given order. If the biogas facility still exhibits demand, the most favorable feed connection from a still supplyable TSP station is arranged and the largest possible transportation quantity is planned.

8.2.2 Improvement procedures: capacitated MODI-method

The MODI method, also known as modifying distribution method, is a numeric procedure, which can solve a

standard transportation problem (with a given initial basic solution).

The MODI method reduces the total costs iteratively by exchange of one non-base variable with a base variable. If no more improvements can be achieved than an optimal solution was found..

8.3 Results of the simulation

With the aid of heuristic procedures, this simulation tool optimizes the entire route length so that the CO_2 emission will be reduced and the transport costs will be minimized

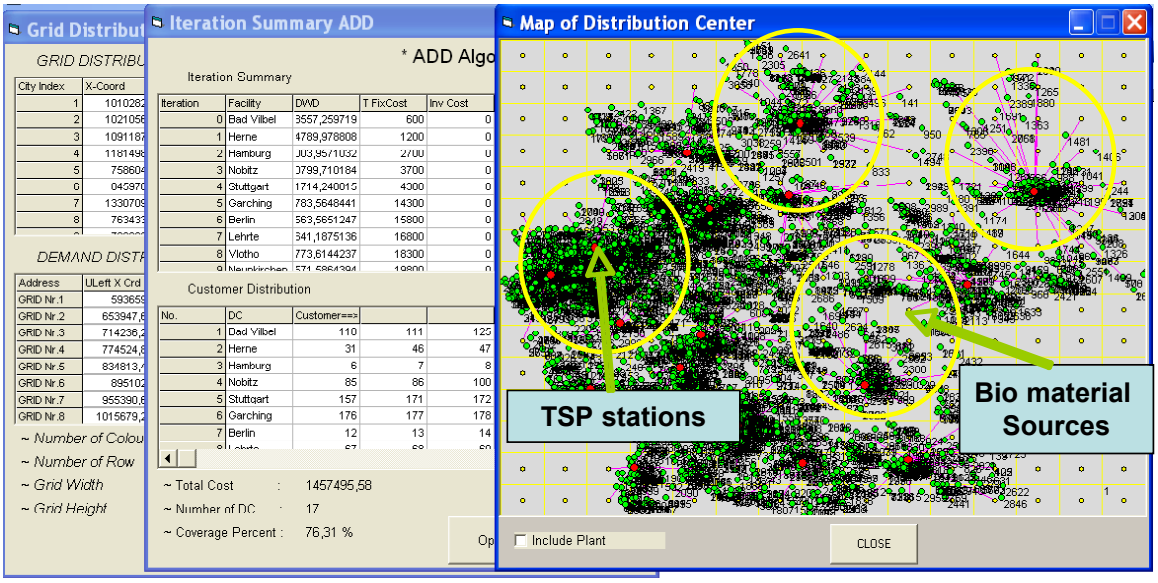

Figure 8.2 Distances between Sources and TSP stations.

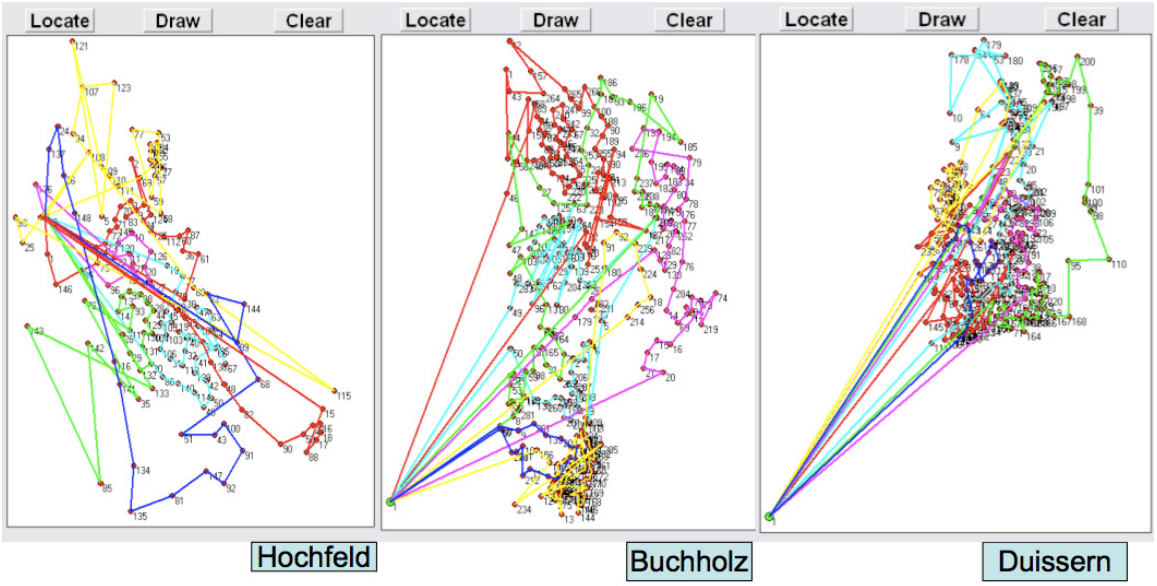

Figure 8.3 . Generated routes for the three districts.

In the simulation, three districts are considered. In these three districts, up to 206 Mg bio raw materials are collected every two weeks. Thus in these districts, up to 5376 Mg of bio raw materials can be collected annually (see figure 8.7). Maximum transportation distance of 114 km is calculated for a period of every two weeks. Due to the improvement procedures, the transportation distance is reduced to 103 km for a period (see fig 8.4). It is assumed that the bio waste is collected with a truck of 12 Mg collecting capacity.

In figure 8.5, Diesel consumption per 100 km is given for the whole year.

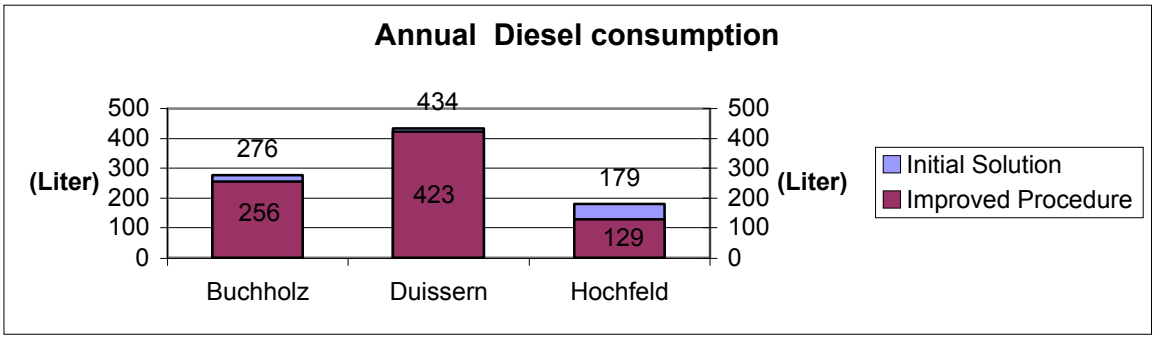

Figure 8.5 Annual consumption

Concerning the CO_2 emission, it is assumed that 1.138 kg CO_2 emission per kilometer is discharged in one year [19]. This results in total to 3365 kg of CO_2 emission per year. With the improvement procedures, the CO_2 emission is reduced to 307 kg (see figure 8.6).

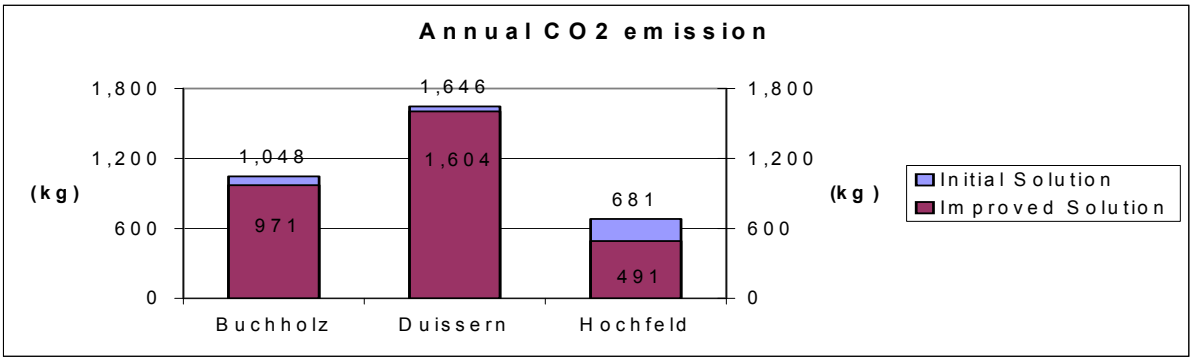

Figure 8.6. Discharge of CO_2 emissions

5376 Mg of bio waste collection results in a biogas potential of 537600 m^3. This quantity corresponds to 424704 kg (biogas). A truck with a capacity of 12 Mg, consumes 30 kg of biogas per 100 km. The total collecting distance, in the three districts per year, is about 2964 km. In order to cover the energy consumption of the truck, up to 889,2 kg of biogas will be needed.

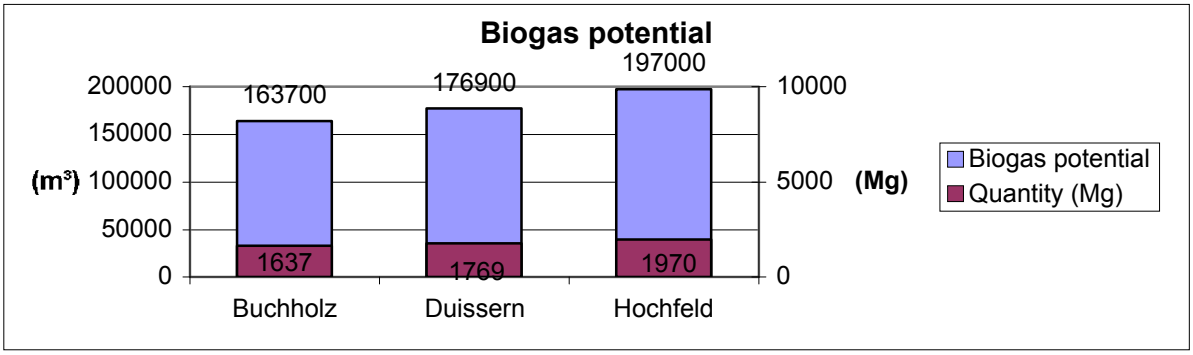

Figure 8.7 Biogas potential.

A gas-fueled waste collecting vehicle costs more than 15000 € to 30000 € in comparison with any vehicle with diesel engine. These price differences correspond from 4 to 9 % of the acquisition costs [20] [21]. However, the gas-fueled vehicles have fair fuel costs. If 20.25 € is saved for 100 km, it results a total saving of 5062.5 € per year for a covered distance of 25000 km. Therefore, the extra acquisition costs of 15000 € will be amortized after approximately 3 years. The average diesel price which is referred in this paper belongs to 2008. If a diesel price of 1.509 €/l is taken as a reference (this was the Diesel price before the economic crisis), 50.91 € per 100 km could be saved. In this case, the extra costs of 15000 € would have been already amortized after 1.2 years. So that 35.95 kg/100 km of CO_2-emission can be saved and the total saving results would become 135 Tons of CO_2 for a covered distance of 25000 km per year and a life span of 15 years.

9. Economical Efficiency

The collecting costs are derived from the waste quantity. In the literature, the collection costs are estimated to 77 € /Mg·km with an average population density [22]. The transport costs of 10 €/Mg·km are assumed in accordance to a declared information by a waste management service provider. The yield of fermenting residues from the purification plants is not considered. The tables 9.1, 9.2 and 9.3 show detailed balance information of biowaste.

Table 9.1 Balance for the biowaste household.

Balance for the biowaste from household			
	Agricultural Biogas facility	**Industrial biogas facility**	**Purification Plant**
Waste (Mg/a)	7.308	41.979	41.979
Sewage sludge (Mg/a)	-	-	16.644
Acquisition expense (€/a)	562.716	3.232.383	3.232.383
Acquisition fee (€/a)	1.249.668	7.178.409	7.178.409
Transport costs	-	419.790	-
Biogas potential (m^3)	876.960	5.037.480	5.753172
Elec. potential (kWh)	5.086.368	29.217.384	33.368.397
Production costs (€/a)	289.923	1.402.434	2.502.629
Biogas yield (€/a)	497.955	2.276.034	2.636.103
Fermenting residue (Mg/a)	2.192	12.593	-
Fermenting residue yield (€/a)	2.784	15.994	-
Profit	**897.769**	**4.415.829**	**4.079.500**

Production costs are 5.7 ct/kWh for the agricultural biogas facility, 4.8 ct/kWh for the industrial biogas facility and 7.5 ct/kWh for the purification plant [23]. From this information, the costs for an agricultural biogas facility are 1,72 million €, for an industrial biogas facility 1,88 million € and for the purification plant 3,25 million €.

Agricultural and industrial biogas facility model

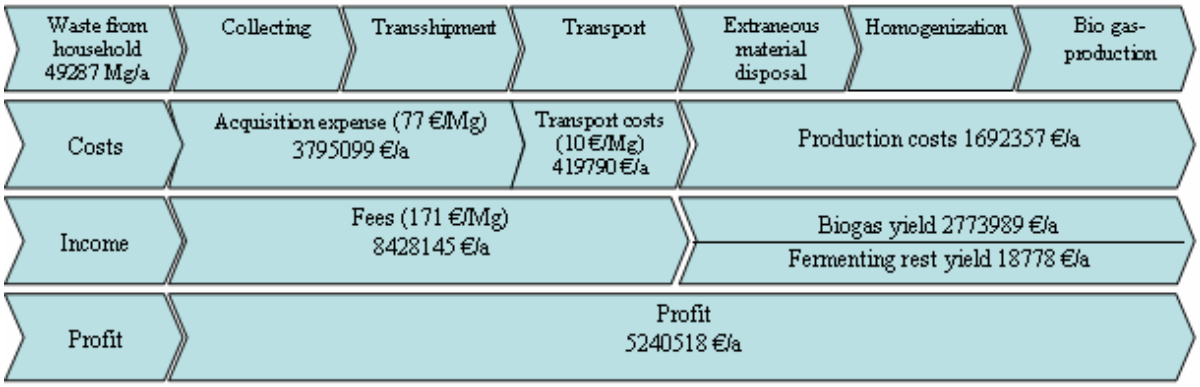

Biogas- and purification plant Model

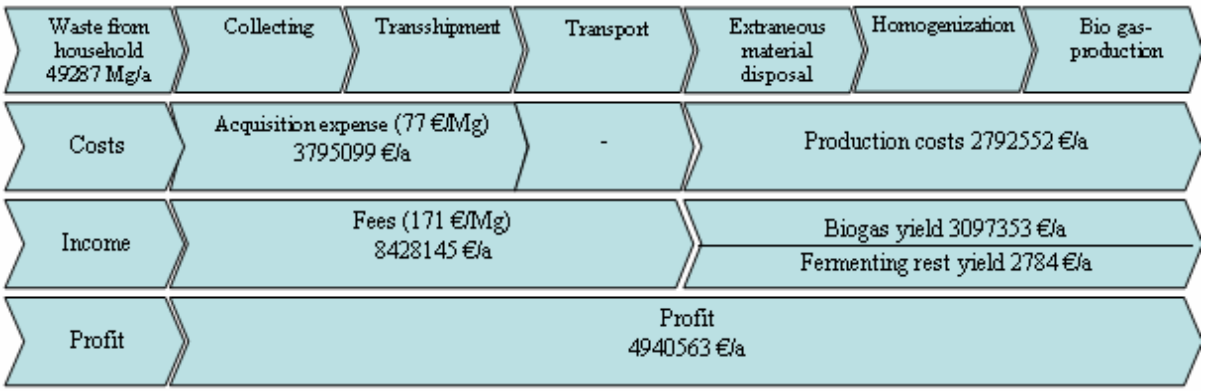

Table 9.2 Balance for Leftovers.

Balance for Leftovers			
	Agricultural Biogas facility	**Industrial biogas facility**	**Purification Plant**
Waste (Mg/a)	665	5472	5472
Sewage sludge (Mg/a)	-	-	16644
Acquisition expense (€/a)	51211	421381	421381
Acquisition fee (€/a)	113729	935794	935794
Transport costs	-	54725	-
Biogas potential (m^3)	176246	1450207	1450207
Elec. potential (kWh)	1022228	8411202	8411202
Production costs (€/a)	58267	403738	630840
Biogas yield (€/a)	100076	655233	655233
Fermenting residue (Mg/a)	200	1642	-
Fermenting residue yield (€/a)	253	2085	-
Profit	**104580**	**713268**	**550844**

Agricultural and industrial bio gas facility model

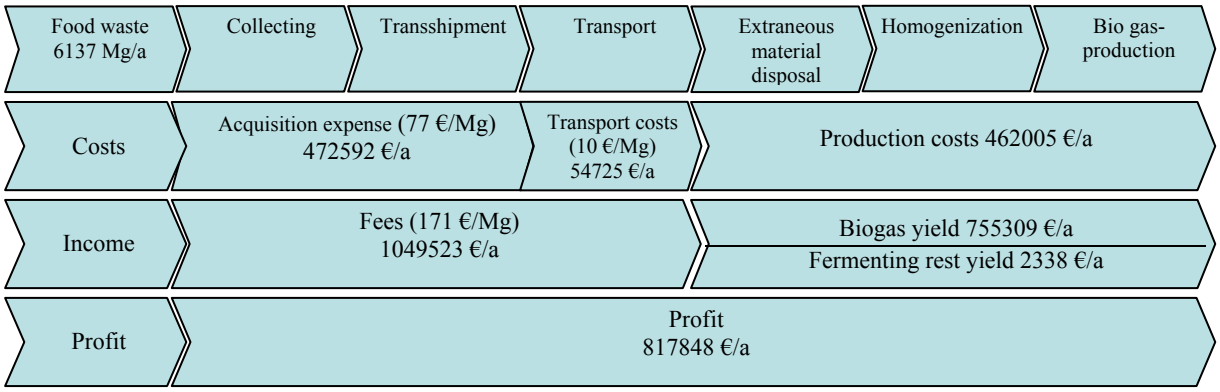

Bio gas- and purification plant Model

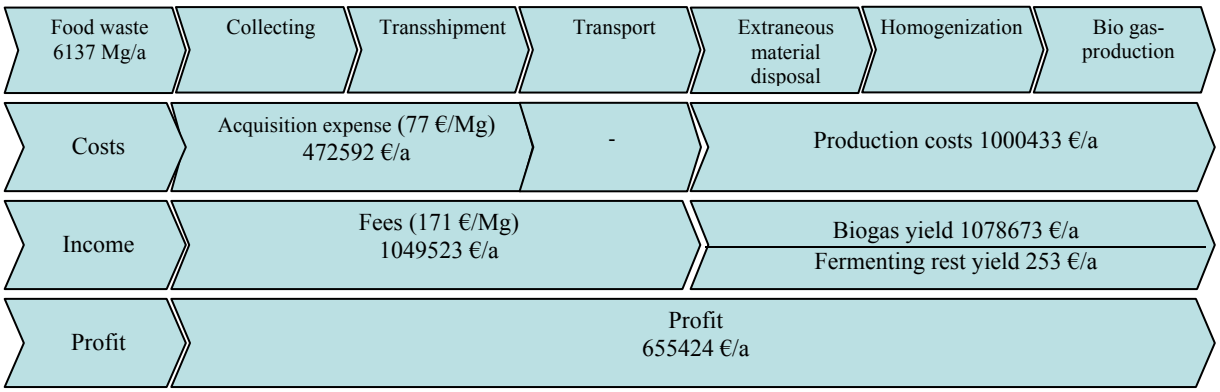

Table 9.3 Balance for waste from food industry

Balance for waste from food industry			
	Agricultural Biogas facility	Industrial biogas facility	Purification Plant
Waste (Mg/a)	260	1173	1173
Sewage sludge (Mg/a)	-	-	16644
Acquisition expense (€/a)	20020	90321	90321
Acquisition fee (€/a)	44460	200583	200583
Transport costs	-	11730	-
Biogas potential (m^3)	68900	310845	310845
Elec. potential (kWh)	399620	1802901	1802901
Production costs (€/a)	22778	86539	135218
Biogas yield (€/a)	39123	140446	140446
Fermenting residue (Mg/a)	78	352	352
Fermenting residue yield (€/a)	99	447	-
Profit	**40884**	**152886**	**127528**

Agricultural and industrial bio gas facility model

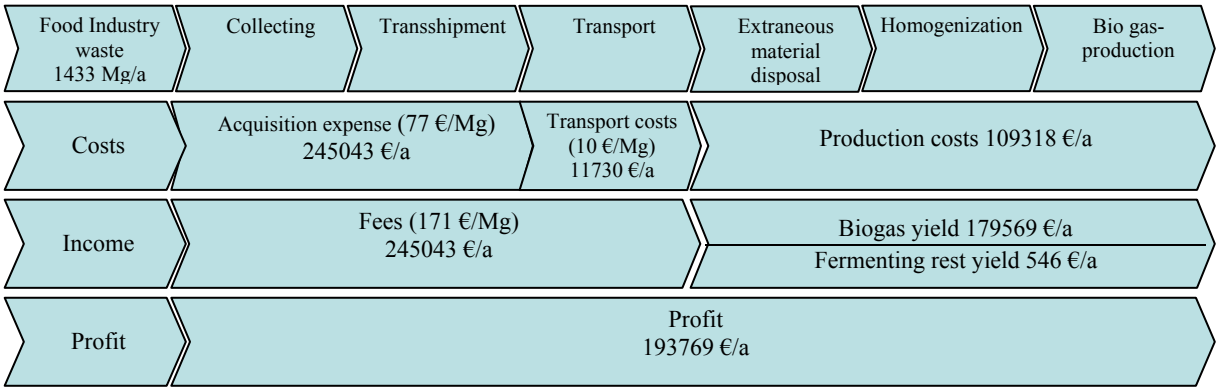

Biogas and purification plant Model

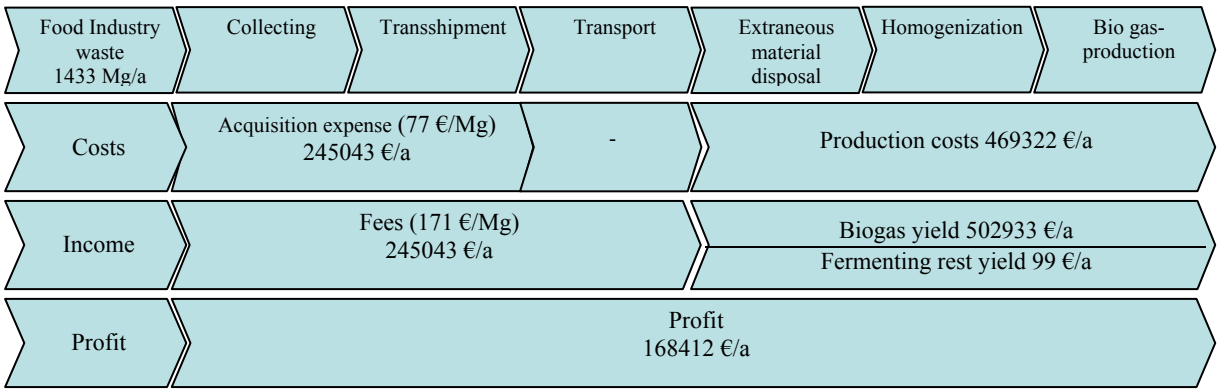

10. Summary and Outlook

The investigated waste quantity provides a theoretical biogas quantity of 863330 (m^3/a) for Duisburg. For the reality, it should be considered that raw material quantities can deviate clearly. The submitted paper suggests a total concept for the process chains simulation with logistic and plantspecific components for the biogenous waste materials supply. At the same time, the logistic components (collection, transport or storage) and the plantspecific components (drainage, cutting, sorting, hygienization and sterilization plants) are observed. It is possible to calculate the entire supply chain between the collecting points and the processing plants by using the extended mathematical model. The direct route between sources and processing plants are considered. The CO_2 emission which is caused by transport collecting process can be determined with the entire covered distance. The production of biogas in the water purification plants is extremely important, since the transportations of the sewage sludge would be omitted. With an appropriate pretreatment of the other three fractions in the transshipment stations, no new technical components in the sewage purification plants should be installed. Sludge from the waste water treatment is only suitable for one waste combination from the observed fraction. Thus, it can be seen that the preparation and pretreatment costs can deviate strongly from those of the other fractions. For this reason, it appears more economical, the biogenous wastes from the household, the leftovers and waste from the food industry, to transport collectively with the waste from the water treatment plant to the digestion towers of the sewage purification plants to produce biogas. The main idea is to observe the identification of the technical and logistic processes, which are necessary for the supply process. Meanwhile, the laws for treatment of biogenous waste materials are taken into account. However, the collective pretreatment of the different waste fractions comes along with some problems. So no hygenic conditions are needed to be fulfilled for the wastes from the household, while leftovers must be sanitized. In order to submit these, as a collective pretreatment, it must be ensured that the hygienc regulations are further observed.

This quantity of biogas is calculated with the assumption that 1 m³ biogas produces approximately 5.8 kWh electrical energy and supplies a theoretical electrical output of 50090716 kWh per one year production [24]. It is to be noted that, some part (20%) of the produced energy from the biogas is used for the pretreatment and preparation processes in the production plants. According to the North-Rhine Westphalia Energy Agency, the annual electric consumption per household per person is 2000 kWh without heat consumption [25]. With an electric potential of 40072573 kWh per year, up to 20000 inhabitants' electric consumption can be covered per year.

References

[1] Bundesministeriums für Umwelt, Naturschutz und Reaktorsicherheit (BMU), Wärme aus Erneuerbaren Energien, was bringt das neue Wärme Gesetz? Referat Öffentlichkeitsarbeit, Berlin , 2008.

[2] Bundesministeriums für Umwelt, Naturschutz und Reaktorsicherheit (BMU) ,Erneuerbare Energien kräftig im Aufwind: Anteil an der Stromversorgung bereits bei 14 Prozent, Berlin, 2008.

[3] Leible, L., A. Arlt, H. Seifert, S. Kälber, E. Nieke, D Wintzer und B. Fürniß, Stand und Perspektiven in Deutschland In: Deutsche Wissenschaftliche Gesellschaft für Erdöl, Erdgas und Kohle e.V. (Hrsg.): Tagungsbericht 2002-2.

[4] Leible, L.; Arlt, A., Fürniß, B.; Kälber, S.; Kappler, G.; Lange, S.; Nieke, E.; Rösch, C.; Winzer, D. Bereitstellung und energetische Nutzung organischer Rest- und Abfallstoffe sowie Nebenprodukte als Einkommensalternative für die Land- und Forstwirtschaft - Möglichkeiten, Chancen und Ziele, Kalsruhe: Forschungszentrum 2003 (Wissenschaftliche Berichte, FZKA 6882), 278 Seiten, 2003.

[5] Umweltbundesamt (UBA) : Umweltdaten Deutschland KOMAG Broschüre Berlin-Brandenburg, S. 57, 2002.

[6] Arlt, Andreas Systemanalytischer Vergleich zur Herstellung von Ersatzbrennstoffen aus biogenen Abfällen, am Beispiel von kommunalem Klärschlamm, Bioabfall und Grünabfall, Karlsruhe Forschungszentrum Karlsruhe 2003 (Wissenschaftliche Berichte, FZKA 6949), 2003.

[7] Stadt Duisburg (2008): Einwohnerstatistik, GFW Duisburg: Gesellschaft für Wirtschaftsförderung Duisburg mbh

[8] Kern, Michael Ausweitung der Bioabfallerfassung als Maßnahme zur Lösung von Kapazitätsengpässen bei der Restabfallbehandlung, Vortrag im Rahmen des "67. Informationsgespräch des Arbeitskreises für die Nutzbarmachung von Siedlungsabfällen (ANS) e.V. " Vol. 13 No. 15, 2006 in Weimar, 2006.

[9] Bidlingmaier, Werner : Manuskripte Biotechnologie in der Abfallwirtschaft, Weiterbildendes Studium Wasser und Umwelt, Bauhaus-Universität Weimar, 2008.

[10] AIDA - Informationsplattform Abfall in NRW, http://www.abfall-nrw.de/aida/

[11] Grundinformationen – Kläranlagen, http://members.aon.at/heideco/pics/grund info.pdf

[12] Liu, S.C.; Lin, C.C. : A heuristic method for the combined location routing and inventory problem, The International Journal of Advanced Manufacturing Technology, Vol. 26 No. 4, S. 372-381, 2005.

[13] Liu, S. C.; Lee, S. B. : A two-phase heuristic method for the multi-depot location routing problem taking inventory control decisions into consideration, The International Journal of Advanced Manufacturing Technology, Vol. 22 No.11-12, 2003, 941-950, 2003.

[14] Noche, B.; Al Mansi, A.; Rhoma, F. , Design of an Environmental Sypply Chain Network: A Biosolids Waste Case Study "Hamburg International Conference of Logistics" Hamburg/ Gemany, September 4-5, 2008.

[15] Noche, B.; Rhoma, F.; Al Mansi, A. , Biogas Logistics Supply Chain Network Design: A Framework Model, "Hamburg International Conference of Logistics" Hamburg/ Germany, September 4-5, 2008.

[16] GERTEC 2008, Potentialanalyse regenerative Energiequellen in Duisburg,

Endbericht, Essen

[17] Stadt Duisburg , Abfallwirtschaftskonzept der Stadt Duisburg, 2008.

[18] Aldarrat, H.; Goudz, A., Al Mansi, A..; Lorenz, M.; Noche, B. : Einsatz von metaheuristischen Lösungsverfahren bei der

simultanen Standort- und Routenplanung in: Trends und Strategien, S.80-85, 2008.

[19] Urban, A.I.; Halm, G.; Weber : Optimierung der Abfall-Logistik, Kassel University Press ,2005, 65 - 80

[20] Bundesverband Güterkraftverkehr Logistik und Entsorgung (BGL) e.V.Dieselpreis-Information:http://www.bgl-ev.de/images/downloads/initiativen/dieselpreisinformation.pdf?ms =206.

[21] http://www.wendland-elbetal.de/index.php?id=57,91,0,0,1,0

[22] Schimdt, Sonja : Ökobilanz Bioabfallentsorgung, Ibidem Verlag, 2006.

[23]http://www.hessen.de/irj/HMULV_Internet?cid=1dcbce373f6 d27e84653553a578 732c4

[24] http://www.voelklinger-vb.de/gav/biogasanlage/Haeufig_gestelle_Fragen/FAQs.h tml

[25] EAN : Kurzinfo 2007, Dortmunder Energie- und Wasserversorgung GmbH, 2007.

JJMIE

Volume 4, Number 1, Jan. 2010
ISSN 1995-6665
Pages 111 - 116

Jordan Journal of Mechanical and Industrial Engineering

A Comparison between the Electrical and Optical Properties of CdS: In Thin Films for Two Doping Ratios

Shadia J. Ikhmayies [a,*], Riyad N. Ahmad-Bitar [b]

[a] *Physics Department, Faculty of Basic Sciences, Applied Science Private University, Amman, Jordan.*

[b] *Physics Department, Faculty of Science, University of Jordan, Amman-Jordan.*

Abstract

Indium-doped cadmium sulphide CdS:In thin films were prepared by the spray pyrolysis (SP) technique on glass substrates at a substrate temperature T_s = 490˚C. A comparison between the electrical and optical properties of the films for two different doping ratios was made through measuring and analyzing the transmittance curves, photoluminescence spectra (PL) and I-V plots. It was found that the higher doping ratio results in a decrease in the transmittance and PL signal, and a slight increase in the optical bandgap energy. Also it results in a considerable reduction of the resistvity of the films. So choosing the proper doping ratio is important to produce high quality CdS:In thin films suitable for the use as windows in CdS/CdTe solar cells.

Keywords: Solar cells; cadmium sulphide; spray pyrolysis; II-IV compounds; doping

1. Introduction

Thin films of CdS have been extensively studied due to the variety of applications in optoelectronic devices. In particular heterojunction solar cells with a narrow bandgap base and a wide bandgap window such as CdS/CdTe and CdS/CuInSe solar cells [1].

There are several methods for depositing CdS thin films, such as; vacuum evaporation (VE) [2-4], chemical bath deposition (CBD) [1, 5, 6], spray pyrolysis (SP) [7-11], etc. However, the SP technique is a very low cost and simple technique that enables intentional doping and getting large area and uniform thin films [8].

In this work CdS:In thin films were produced by the SP technique, and a comparison between the effects of two different doping ratios on the electrical and optical properties of the films were investigated. The resistivity of the films was determined from the I-V plots which are linear. The optical bandgap energy was estimated from the transmittance curves and the PL spectra were recorded, deconvoluted and investigated.

2. Experimental Part

The precursor solution of CdS:In thin films was prepared by dissolving 2.06×10^{-2} moles of extra pure $CdCl_2.H_2O$ (MERCK Art. 2011) and 2.24×10^{-2} moles of thiourea $(NH_2)_2CS$ (>97% S) in 350 ml of distilled water. Indium chloride $InCl_3$ (MERCK Art.12471) was used as a doping compound. The ratio of the concentration of indium ions to that of cadmium ions in the solution which is not necessarily the same as their ratio in the films was considered as an estimation of the doping ratio. Two doping ratios were considered; 1.0×10^{-4} (light doping) and 1.5×10^{-2} (heavy doping). The solution was sprayed intermittently by using the spraying system described in [8] on glass substrates that were ultrasonically cleaned with methanol at a substrate temperature T_s= 490˚C.

The transmittance of the films was measured by using a double beam Shimadzu UV 1601 (PC) spectrophotometer with respect to a piece of glass of the same kind of the substrates in the wavelength range 400-1100 nm. The films' thickness was estimated by using Lambert law for absorption in a semiconductor. That is by making use of the relative transmittance through each film at a certain wavelength. The produced films have a thickness restricted in the range 0.2-1.0 μm.

The PL spectra were recorded at T= 23K by a system which consists of an Air Product He cryostat DISPLEX DE-202 capable of cooling down to 10 K, where the Ar ion laser of wavelength 488 nm was used as an excitation source. The laser power was 10 mW and the diameter of the laser beam on the sample was about 2 mm. The PL signal was collected by a multi-channel optical spectrometer (an Avantes Fiberoptic Spectrometer AVS-S2000) which hosts two gratings. The first grating has a range: 640 – 1280 nm and the second grating has a range: 190-860 nm. The spectrometer resolution (FWHM) ranges

Corresponding Author. shadia_ikhmayies@yahoo.com

from 0.3 - 10 nm depending on the recorded region and the grating.

Aluminum was chosen to make the contacts, where two strips were deposited on the surface of the film by vacuum evaporation. The contacts have a thickness of more than 0.4 μm, a length of 1 cm, a width of 1 mm, and a separation of 2-3 mm. The I-V measurements were taken by using a Keithley 2400 Source Meter, which was interfaced by an IBM personal computer and capable of measuring 10^{-11}A. The samples were placed in a brass cell that had a cover to enable measurements in the dark.

3. Results and Discussion

3.1. Electrical Properties

The I-V characteristics of indium-doped CdS:In thin films were taken in the dark at room temperature. The measurements were taken in the voltage range 0-10 V, and the curves are linear, which indicates the ohmic behavior of the contacts.

The I-V plots for two films with the doping ratios 10^{-4} and 1.5×10^{-2} were displayed in Figure 1. From the plot the resistivity was $\rho = 4.63\times10^{7}$ Ω.cm for the film of doping ratio 10^{-4} and $\rho = 900$ Ω.cm for the 1.5×10^{-2} doping ratio. So a huge decrease in the resistivity had occurred in the film of the higher doping ratio.

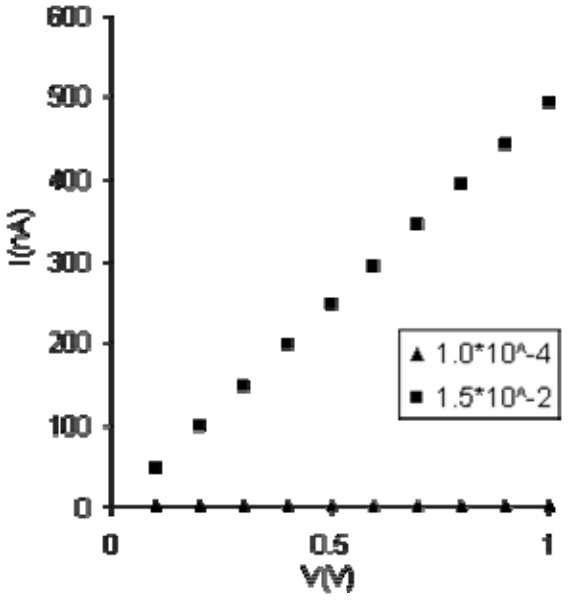

Figure 1. The I-V plots for CdS:In thin films of different doping ratios.

These results can be interpreted in terms of the decrease in the barrier height caused by doping. Josh et al [12] say that the decrease in the barrier height ϕ and hence the increase in the conductivity of the films can be explained on the bases of Waxman et al as,

$$\phi = kT\log(\frac{n1}{n2}) \quad \textbf{(1)}$$

where n_1 and n_2 are the numbers of carriers in the crystallite and in the grain boundary regions respectively. Indium will increase the number of charge carriers, because indium impurity atoms serve as strong donor impurities. If we assume the same extent of increase in the two regions (crystallite and grains), then ϕ will continue to decrease with increasing indium concentration.

The current will not continue increasing by increasing the concentration of indium atoms in the films, but beyond a certain limit the indium atoms will be incorporated in the crystal lattice as electrically inactive impurities (neutral impurity centers). The observations of Joshi et al [12] confirmed this thing. They observed that the Hall coefficient decreased with increasing indium content and finally saturates for large indium content.

3.2. 3.2 Optical Properties

3.2.1 Transmittance and Bandgap Energy

The transmittance of CdS:In thin films was measured at room temperature in the wavelength range 400-1100 nm and shown in Figure 2a for a film of thickness 0.5 μm. As we see there is a dependence of transmittance on the doping ratio; that is it reaches about 84% for the lower doping ratio, and about 72% for the higher doping ratio. The decrease in transmittance with doping is expected, because doping increases the number of charge carriers which increases the absorption in the films, and then decreases the transmission of light.

Figure 2b depicts the absorption coefficient of the two curves shown in Figure 2a. It is noticed that the absorption edge of the film of the higher doping ratio is red-shifted with respect to that of the film of the lower doping ratio. This is mainly due to the formation of band tails in doped semiconductors, which causes a strong modification of the joint density of states and, consequently the absorption spectrum [13].

The value of the optical energy bandgap was estimated from the plots of $\alpha h\nu$ versus $h\nu$ shown in Figure 3, where α is the absorption coefficient, h is Planck's constant and ν is the frequency of the radiation. Since the plots are linear, the direct nature of the optical transition is confirmed. The estimated values of the bandgap energy for films of different thickness are summarized in table 1. As we see in the table it is noticed that the bandgap energy was slightly larger for the higher doping ratio. The increase in E_g is due to the increase in the carrier concentration with doping, and can be attributed to the Moss-Burstein shift.

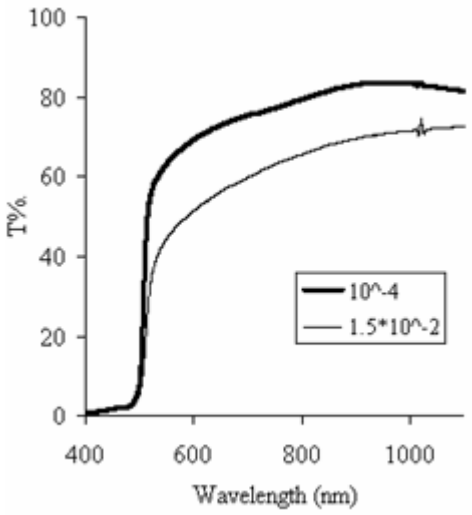

(a)

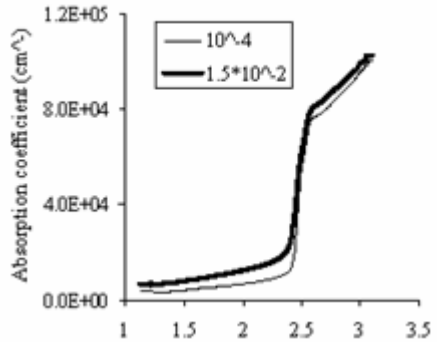

(b)

Figure2 a) The transmittance curves of CdS:In thin films of the two doping ratios. b) Absorption coefficient against energy for the transmittance curves in a.

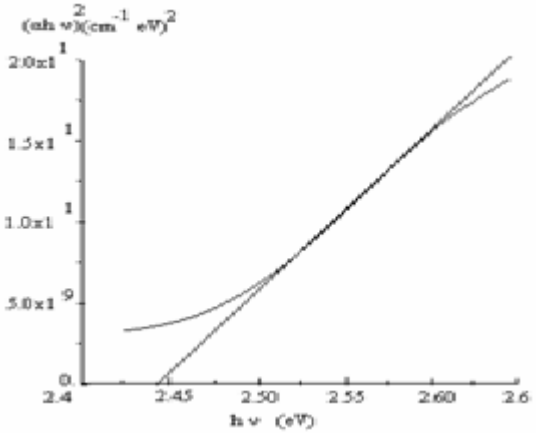

(a)

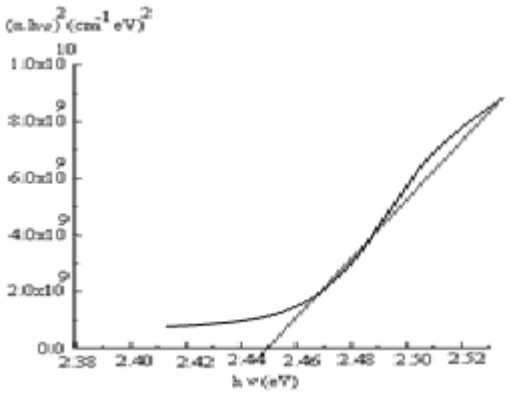

(b)

Figure 3 Plots of $(\alpha h\nu)^2$ versus hν for two films of thickness 0.50μm. (a) Doping ratio is 1.5×10^{-2}. (b) Doping ratio is 10^{-4}.

Table 1.The bandgap energy of CdS:In thin films of different thickness.

t(nm)	E_g(eV) for the 10^{-4} doping ratio	E_g(eV) for the 1.5×10^{-2} doping ratio
150	2.43	2.44
300	2.44	2.45
500	2.44	2.45

3.2.2 Photoluminescence

Figure 4 shows the PL spectra of two CdS:In thin films of different doping ratios. As the figure shows the PL signal had decreased with doping. A deconvolution peak fit was made (Figure5) to compare the effect of the two doping ratios on the PL spectra. The peak parameters obtained from the fit are inserted in table 2. At the higher doping ratio two peaks in the yellow region are attenuated and slightly red shifted, but the peak at 2.032 eV had slightly blue shifted and practically disappeared. The peak at 1.910 eV had completely disappeared and the peak at 1.961 eV had enhanced and blue-shifted. The peaks at 1.758 and 1.830 eV in the red region had completely disappeared, the peak at 1.712 eV had attenuated and two new peaks in the red region appeared which are 1.635 (but it is very weak) and 1.796 eV. The peak in the infrared region centered at 1.055 eV in Figure 4b was attenuated to more than half its original intensity.

Indium as other impurities (Fe and Zn) exhibits a quenching effect on the luminescence peak in mixed sulfide films were the In:Cd ratio is varying locally. This result was consistent with the results of Ahmed-Bitar [7] where he studied the PL with the doping ratio and he had a greatest signal for the undoped sample, and then the PL signal decreases with the doping ratio. He interpreted this result by saying that the doping level was found to produce structural changes which affect radiative transitions differently.

The disappearance of some peaks may mean that some defects had disappeared or reduced such as $I_{Cd}^{+}-V_{Cd}^{-}$ which is expected to be responsible about the orange emission and V_{Cd}^{2-} which is expected to be responsible about the infrared emissions. The new peaks and those that are enhanced are most probably associated to doping; that is new radiative transitions between doping levels and acceptor levels and/ or the valence band had

taken place. The red shift of some peaks is related to doping and it increases with doping [13].

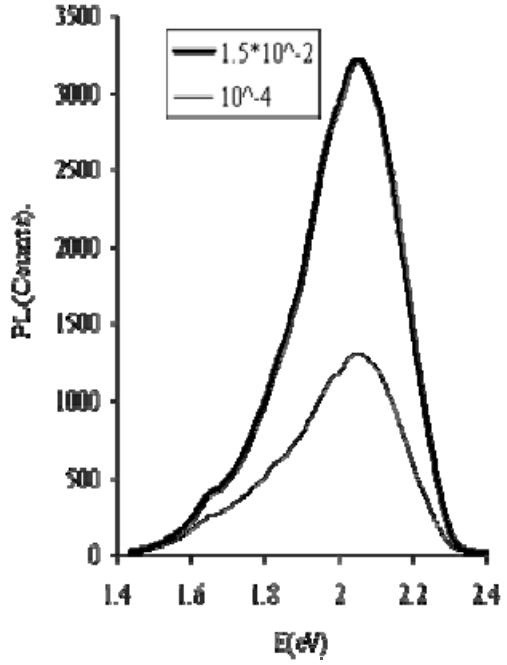

(a)

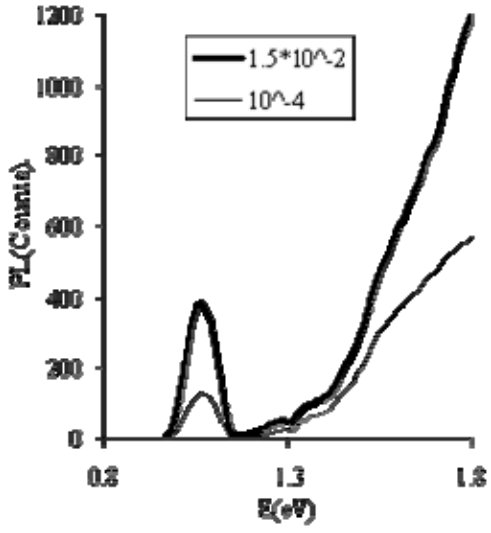

(b)

Figure 4 The PL spectra of CdS:In thin films of different doping ratio. a) Taken by the 2nd grating. b) Taken by the 1st grating.

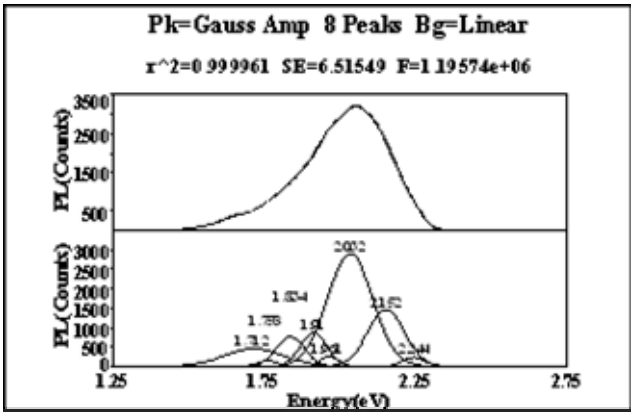

(a)

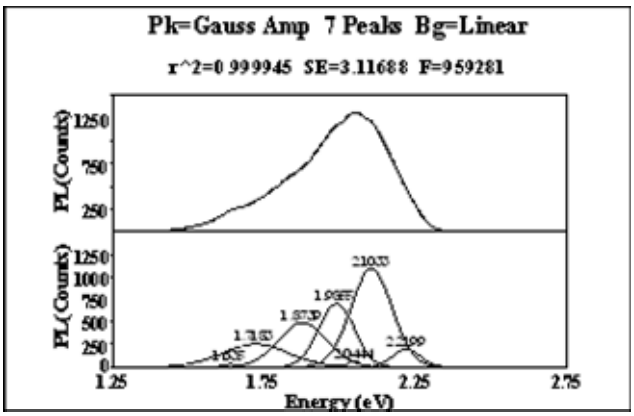

(b)

Figure 5 A deconvolution peak fit of the PL spectra in Figure 4a. a) Doping ratio is 10^{-4}. b) Doping ratio is 1.5×10^{-2}.

Table 2. Peak parameters obtained from the deconvolution peak fit in Figure5.

No	Position for the 10^{-4}	Amplitude	Position for the 1.5×10^{-2}	Amplitude
1			1.635	30
2	1.712	448	1.718	251
3	1.758	132		
4			1.796	181
5	1.834	757		
6			1.874	488
7	1.910	862		
8	1.961	267	1.986	702
9	2.032	2916	2.044	69
10	2.152	1458	2.103	1089
11	2.244	224	2.220	198

4. Conclusions

Indium-doped cadmium sulphide thin films were prepared by the spray pyrolysis technique with two different doping ratios on glass substrates at a substrate temperature T_s = 490˚C. A comparison between the effects of two different doping ratios on the electrical and optical properties of the films had been investigated. Higher doping had improved the electrical properties by

decreasing the resistivity of the films and slightly increased the bandgap energy. It attenuated the PL signal and caused the disappearance of some peaks and the appearance of new peaks, which means that doping levels had a significant role in the produced PL signal.

Acknowledgement

We want to thank Sameer Farrash in the University of Jordan for making the contacts by vacuum evaporation.

References

[1] H. Ariza-Calderon, R. Lozada- Morales, O. Zelaya-Angel, J. G Mendoza- Alvarez and L. Baños, "Photoluminescence measurements in the phase transition region for CdS thin films". J. Vac. Sci. Technol. A. Vol. 14, No.4, 1996, 2480-2482.

[2] M. Lepek, B. Dogil and R. Ciecholewski, "A Study of CdS thin film deposition". Thin Solid Films. Vol. 109, 1983, L103-L107.

[3] E. Bertran, J. L. Morenza, J. Esteve and J. M. Codina, " Electrical Properties of Polycrystalline Indium-Doped Cadmium Sulfide Thin Films". J. Physics. D. Vol. 17, No. 8, 1984, 1679-1685.

[4] D Patidar, R Sharma, N Jain, T P Sharma and N S Saxena, "Optical properties of thermally evaporated CdS thin films". Cryst. Res. Technol. Vol. 42, No. 3, 2007, 275–280.

[5] O. De. Melo, L. Hernández., O. Zelaya-Angel, R. Lozada-Morales, M. Becerril, and E. Vasco, "Low Resistivity Cubic Phase CdS Films by Chemical Bath Deposition Technique". Appl. Phys. Lett. Vol. 65, No. 10,1994, 1278-1280.

[6] O. Vigil, I. Riech, M. Garcia-Rocha, O. Zelaya-Angle, "Characterization of defect levels in chemically deposited CdS films in the cubic-to hexagonal phase transition". J. Vac. Sci, Technol. A. Vol. 15, 4, 1997, 2282-2286.

[7] Riyad. N. Ahmed-Bitar, "Effect of dopping and heat treatment on the photoluminescence of CdS films deposited by spray pyrolysis". Renewable Energy. Vol. 19, 2000, 579-586.

[8] Ikhmayies J. Shadia. Production and Characterization of CdS/CdTe Thin Film Photovoltaic Solar Cells of Potential Industrial Use. Ph.D Thesis, University of Jordan, Amman, Jordan, 2002.

[9] G. G. Slawh, W. Z. Manookian, and W. S. A. Abdul Ghafor, "Optical and Electrical Properties of CdS Thin Films Prepared by Spraying Pyrolysis Technique". Iraqi Soc. Of Phys. And Math., J. Math. Phys. Vol. 12, No.1,1991, 91-98.

[10] A. Ashour, "Physical Properties of Spray Pyrolysed CdS Thin Films". Turk J Phys. Vol. 27, 2003, 551-558.

[11] P Raji, C Sanjeeviraja and K Ramachandran, "Thermal and structural properties of spray pyrolysed CdS thin. Bull. Mater. Sci. Vol. 28, No. 3, 2005, 233–238.

[12] J. C. Joshi, , B. K. Sachar and Partap Kumar, "Electrical Transport Properties of Heavily Indium Doped Polycrystalline CdS Films". Thin Solid Films. Vol. 88, No. 3, 1982, 189-193.

[13] G.Perna, V.Capozzi, M.Ambrico, V.Augelli, T.Ligonzo, A.Minafra, L.Schiavulli and M.Pallara, "Structural and optical characterization of undoped and indium-doped CdS films grown by pulsed laser deposition". Thin Solid Films. Vol. 453-454, 2004, 187-194.

JJMIE

Volume 4, Number 1, Jan. 2010
ISSN 1995-6665
Pages 117 - 120

Jordan Journal of Mechanical and Industrial Engineering

Energy Management for Stand Alone PV System

Achour Mahrane *, Madjid Chikh, Ahmed Chikouche

UDES, Solar Equipment Development Unit,Route Nationale n°11, BP386, Bou Ismaïl, 42400, Tipaza, Algeria

Abstract

One of the crucial elements for mastering the performance of a Stand Alone PV System (SAPVS) is the control and management of the energy storage. We focus in this article on the energy control and management algorithm which is a part of a tool we have elaborated and which is devoted for simulation and performance evaluation of SAPVS.
For a given energy demand and power PV generator, the algorithm proceeds to several tests on parameters as SOC, I_{PV}, I_L in order to take the best decision for balancing the mismatch between the available energy produced by the source and the power required by the load. As example, the energetic behavior of a PV system applied in a local rural electrification is analyzed through the charge and discharge of the battery and the parameters SOC, I_{PV}, I_L, I_B for a typical day in winter and unfavorable day. We show that the elaborated algorithm allows us to avoid any shortage energy for the case treated.

Keywords: Stand Alone PV System, Energy Storage, Energy Management, System Performance.

Nomenclature

C	Battery capacity, AH
I_B	Charge and discharge current battery, A
I_L	Load current, A
I_{PV}	PV array current, A
P_{PV}	PV array power (W)
P_{NU}	PV array power non used (W)
R_I	Internal resistance of the battery, Ω
$S_{\min}$	Minimum value of the battery State of Charge
S_{Max}	Maximum value of the battery State of Charge
SOC	Battery State of Charge
SOC_0	Battery State of Charge at initial time
$SOC(n)$	Battery State of Charge at hour n
T_{amb}	Ambient temperature, °C
V_B	Battery voltage, V
V_R	Open circuit voltage, V

1. Introduction

Climate change and oil shortage have prompted the ever-growing awareness about the need to use non pollutant energy. This favorable economic background conducted to an impressive growth rates of the photovoltaic industry in the last decade and it is expected to continue in the upcoming years. In this context, the number of PV installations increases year after year but without noting a significant decrease in the PV system cost.
As the initial cost is high, the users need to be ensured that the PV system installed will be reliable and energetically efficient. To reach this goal, we have elaborated a helpful tool for the design and analysis, devoted as a first step, for SAPVS [1].
After having briefly described this tool, we will focus, in this article, on the energy storage and management of the PV system. We present an energy management strategy devoted for a Stand Alone PV systems based on a hierarchically structured control algorithm. The control strategy proposed to limit the charge/discharge batteries current is based on the test of the SOC, I_{PV}, I_L, I_d.
This algorithm has been designed with the aim of optimizing the energy efficiency and, at the same time, avoiding irregular working conditions that could reduce the life expectancy of the components.

2. Presentation of the SAPVS tool

The beginning of a system design is the preliminary studies where the needs and the requirements of the user are expressed. In the case of a SAPVS, we must know mainly the electrical power that the system must supply and its autonomy in case of lack of sunshine in other words the battery capacity. These data allow good sizing of the system in order to be efficient, reliable but without neglecting its cost.
After the sizing step, it will be useful, before the realization of the system, to proceed with the system simulation for the evaluation of its performances in order to bring any needed correction.

Corresponding Author. a_mahrane@yahoo.ca

We have elaborated this code to be used as a tool for the design of SAPVS and also for the follow up of the already installed systems.

2.1Architecture of the simulation program

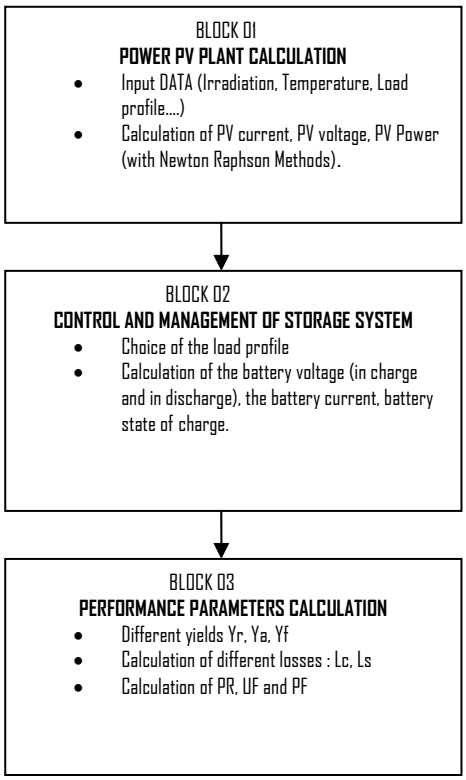

Figure 1. Synoptic of the SAPVS simulation program

The elaborated SAPVS simulation program is based on three main blocks (figure 1). The first block uses the Newton Raphson method to calculate the power PV field taking into account the global irradiation and the ambient temperature. The second block is devoted to the management and control of storage system based on an algorithm which will be presented in this article. The third block calculates the yields Y_A, Y_R, Y_F and the losses L_C and L_S for deducing the factors P_R, U_F and P_F used to evaluate the SAS performances. The results are presented as tables, graphs and histograms.

3. Control and Management strategy for the storage system

In SAPVS systems, a storage system is a solution for balancing the mismatch between the available energy by the source and the power required by the load. Both the power flows into and out of the storage device have to be designed accurately and controlled according to a global energy management strategy.

Control power flows can be easily obtained by interconnecting storage device (battery bank) and generation sources (PV plant) by means of algorithm which is implemented on a power converter. Control algorithm with a hierarchical structure has to adapt controlling actions in order to satisfy many constraints and critical conditions (low state of charge, over voltages, over currents...) with an assigned priority order[2].

3.1Storage system model

In most cases, the storage system is composed of several batteries. The common battery used is made of lead acid. Its charge is modelized by [3] - [5]:

$$V_B = V_R + \frac{I_B}{C}\left\{\frac{0.189}{1.142 - SOC} + R_I\right\} \quad (1)$$

Where

V_b: battery voltage, (V), I_B: current battery (A), C: battery capacity (A.H), V_R: open circuit voltage (V), SOC: State of Charge of the battery at given time. R_I: Battery internal resistance (Ω).

$$SOC = SOC_0 \pm \frac{I_B.\Delta t}{C_{nb}} \quad (2)$$

SOC_0: Battery State of Charge at initial time, Δt: time of charge or discharge (s).

When the voltage of each element is over 2.28V we add the following term:

$$(SOC - 0.9)\log\left\{\frac{300\ I_B}{C} + 1\right\} \quad (3)$$

Where,

$$V_R = 2.094\ \{1 - 0.001\ (T_{amb} - 25)\} \quad (4)$$

T_{amb} : Ambient temperature (°C)

$$R_I = 0.15\ \{1 - 0.02(T_{amb} - 25)\} \quad (5)$$

The battery discharge model is given by:

$$V_B = V_R - \frac{I_B}{C}\left\{\frac{0.189}{SOC} + R_I\right\} \quad (6)$$

3.2Control Strategy

to the load and the excess current will be used to charge the battery $(I_B = I_{PV} - I_L)$.

b- $SOC > S_{\min}$ and $I_{PV} < I_L$

As I_{PV} is lower than I_L, the PV array cannot feed the load so we disconnect the PV array from the load and the latter is supplied only by the battery (battery discharge).

Case 2: $SOC < S_{\min}$

In this case the battery is discharged and can't supply the load, so the load is disconnected and we proceed immediately to the recharge of the battery by the PV array.

4. Control and Management strategy applied to a practical Stand Alone PV system.

The example treated in this article concerns a small PV field devoted to rural electrification for a group of six houses, located at Tamanrasset (south of Algeria), whose daily energy needs is about 2 KWh (figure3). We present in the following the simulation results obtained with the control algorithm and we analyze by the means of the battery the energy behavior of this Stand Alone PV station.

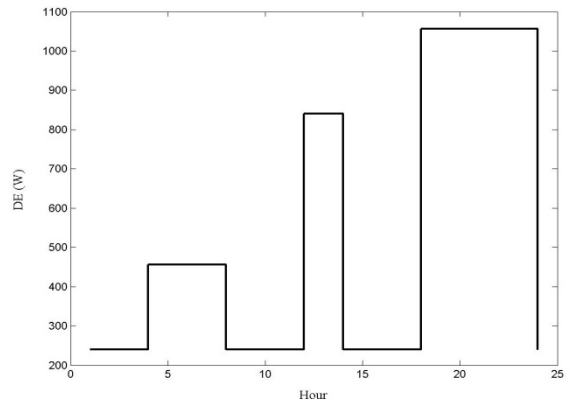

Figure 3. Daily village consumption.

4.1Description of the example treated

From the technical prescription manual and taking into account the meteorological data for the selected site and the autonomy requirements of the system (four days), we have sized the system by using PVSST 1.0 software developed by our team [6]. The results obtained conducted us to the following configuration:

- A PV field of 3.33KWp power installed must be composed by 24 branches in parallel. Each of them has 4 modules (36Wp) connected in series to have a voltage output of 48V.
- A set of 24 batteries elements of 2V connected in series having a nominal capacity of 1250Ah,

4.2Analysis of the energy management of the SAPVS studied by means of the battery behavior.

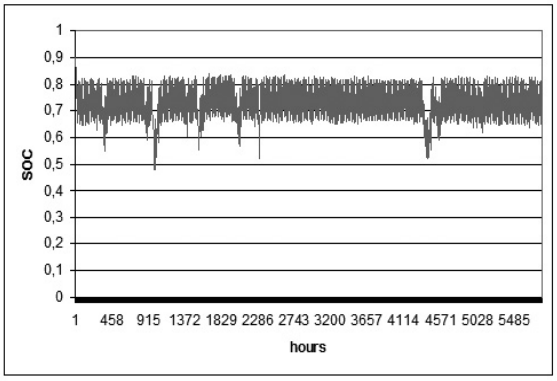

Figure 4. State of charge of a battery during a year

The battery is a key element in the SAPVS. It imposes the voltage for the whole system. The figure 4 represents the plot of the SOC of a battery on a period of one year for the energy needs profile given in figure 3. We notice that the SOC is comprised between 0.65 and 0.82. However, there are few days where the SOC is weak but it doesn't reach in any case the threshold value 0.2 of the battery. Its minimum value is of the order of 0.48. The low peaks of the SOC correspond to winter days where the irradiation is the lowest of the year. As shown on figure 5.

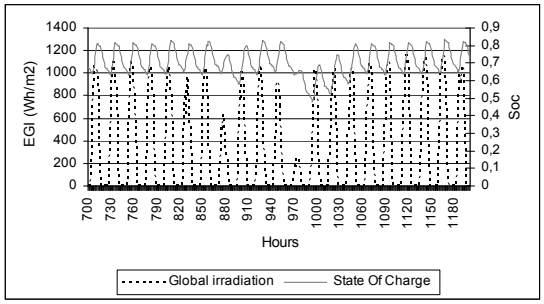

Figure 5. Variation of the battery SOC and the irradiation for the most unfavorable days of the year.

We can understand the energy management of the PV system by means of the battery charge and discharge for a given day. To show how our control algorithm is dealing with optimal manner, depending on the energy available, we analyse in the following the evolution of the system during the day successively for the case of '*a typical day*' and for the case of '*unfavourable*' day

4.2.1Case of typical day in winter

Figure 6 shows clearly that the PV system, while working, passes through several steps which depend on meteorological conditions, the currents I_{PV}, I_B, I_L and the SOC. That can be traduced by:

Region A: 0H – 7H

In this period of time there is an absence of irradiation that means $I_{PV} = 0$. The load is fed by the discharge of the battery which leads to the decrease of the SOC.

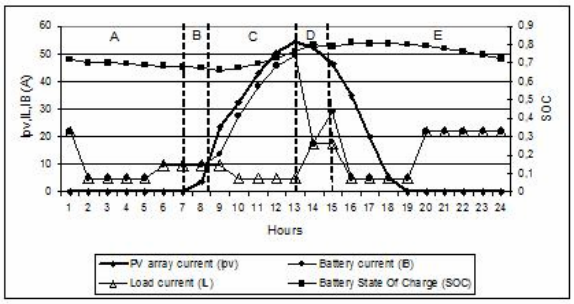

Figure 6. Variation of the battery SOC, I_{PV}, I_B and I_L for a typical day in winter.

Region B: 7H – 8H

In the beginning of the day, at the same time I_{PV} increases but I_{PV} is lower than I_L. The battery continues to discharge in the load $(I_B = I_L)$.

Zone C: 8H – 13H

In this zone $I_{PV} > I_L$. The load id fed by the PV current array I_{PV} while the battery is charging with a current $I_B = I_{PV} - I_L$.

Region D: 13H – 15H

As $I_{PV} > I_L$, while the $SOC < S_{Max}$ the battery continues to charge. When the $SOC > S_{Max}$, the PV array is disconnected from the battery and the battery begins to discharge in the load, $I_L = I_B$.

Region E: 15H – 21H

As soon as $SOC < S_{Max}$, the battery begins to charge again. We notice that the beginning of the region E matches with the day phase where the irradiation and consequently I_{PV} decreases. The battery is then discharging.

4.2.2 Case of the day whose SOC is the lowest of the year.

The figure 7 represents the evolution of the system in the case of the day where the SOC is the lowest of the year.

Region A: This zone concerns the day before and the beginning of the day on focus. We notice in this region that I_{PV} is very low, that means that the irradiation received by the PV array is absent or very low. In these conditions, as long as $(I_{PV} < I_L)$, The PV generator is disconnected from the load and the latter is supplied by the battery, whose discharge provoke the decrease of the SOC.

Region B:

This range time corresponds to the beginning of the day of interest. The irradiation begins to rise $(I_{PV} > 0)$ but is insufficient to feed the load $(I_{PV} < I_L)$, the PV array still being disconnected and the battery supplying the load with $(I_L = I_B)$. The battery continues to discharge and the SOC reaches its lowest value of the year (0.48).

Region C:

In this zone the irradiation has reached such a good level which allowed I_{PV} to increase and exceed I_L while the $SOC < S_{Max}$. In this case the PV array is able to supply the load and charge the battery with $(I_B = I_{PV} - I_L)$.

From the figure 6 and 7, we notice that the system doesn't show any situation of lack of energy, that means that the sizing of the PV system has been done correctly and the strategy adopted in the elaborated control and management algorithm seems to be efficient.

In order to characterize the operation of PV system, the Performance Ratio PR has been introduced. PR indicates how the energy produced by the PV system is used. The greater is PR the better the energy produced by the system is used. On the figure 8 we can see the ranges of the values taken by PR during one year for the SAPVS used for rural electrification. For the case treated, it appears clearly that for about 60% of the year PR is in the range (0.5-0.6) and that is in conformity with the figures recommended by the IEA for a SAPVS applied for rural electrification. A PR lower than 0.5 represents only 5% of all the cases.

5. Conclusion

An energy control and management algorithm devoted for Stand Alone PV System has been presented in this article. The algorithm is based on a strategy which deals with several parameters as the SOC, I_{PV}, I_L and I_B. We have shown, trough the presented example of rural electrification how the energy control and management algorithm deals with different situations for balancing the mismatch between the available energy produced by the source and the power required by the load requiring for certain cases the energy accumulated in the battery bank. This algorithm aims to optimize the use of the energy available from the PV generator and the battery while extending the lifetime of the latter and making the overall system more reliable and cost effective.

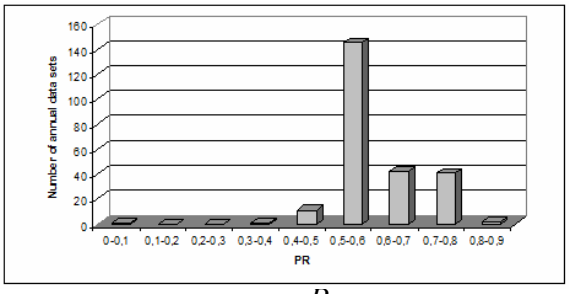

Figure 8. Range of values taken by P_R for one year in the case of SAPVS used in the example treated.

Acknowledgement

We would like to thank Mr. S. Elmetnani (UDES) for his valuable advices on the writings of this article.

References

[1] M. Chikh, A. Mahrane, A. Chikouche, A proposal for simulation and performance evaluation of stand alone PV systems. Proc. 23th EPVSEC, Valence, Spain, 2008,

[2] Energy management of stand-alone power systems with renewable energy sources. S. d'Arco, R. Rizzo, D. Coll-Mayor, P. Tricoli. Proc. ICREPQ, Mallorca, Spain, 2006.

[3] M. Chikh, Magister Thesis, CDER, 1994.

[4] M. A. Edigo, E. Lorenzo, Research Report, n°22/84, July 1986.

[5] J. P. Copetti, E. Lorenzo and F. Chenlo. Progress in Photovoltaics, Research and Applications, Vol 1, 1993, 283-292.

[6] M. Chikh, A. Mahrane, F. Z. Bouachri. Sizing tool for PV systems. Accepted for presentation in The ICRE 2010, April 5-8, 2010, Damascus, Syria.

JJMIE

Volume 4, Number 1, Jan. 2010
ISSN 1995-6665
Pages 121 - 128

Jordan Journal of Mechanical and Industrial Engineering

Evaluation of Solar Electric Power Technologies in Jordan

Omar Badran[a,*], Emad Abdulhadi[b], Rustum Mamlook[c]

[a] *Mechanical Engineering Department, Faculty of Engineering Technology, Al-Balqa Applied University P.O.Box 331006, Amman 11134 – Jordan*

[b] *Mechatronics Engineering Department, Faculty of Engineering Technology, Al-Balqa Applied University P.O.Box 331006, Amman 11134 - Jordan.*

[c] *Department of* ***Computer Engineering, College of computer Engineering and Sciences, Al-kharj University, Saudia Arabia***

Abstract

Jordan is considered one of the sun-belt countries, which possesses high solar radiation on its horizontal surface. The present study will be concerned on the uses of fuzzy sets methodology to perform evaluation between the most suitable solar technologies for power generation in Jordan, namely, solar ponds and photovoltaic (PV) technologies. The criterion of the evaluation were based on different parameters, i.e., power capacity, efficiency, availability, capacity factor, storage capability, cost, maturity, land usage and safety, they are planned as the technologies for the near foreseen term.
Based on benefit to cost ratios, the results showed that photovoltaic technology found to be the better choice in terms of generating electricity, research and development and more effective programs of support and installation.

Keywords: Fuzzy Sets Methodology; Solar Electric Power; Control Technology; Benefit to Cost Ratios; Power Plants; Renewable Energy.

1. Introduction

Jordan relies, almost completely, on imported oil from neighboring countries, which causes a financial burden on the national economy (Jaber et al, 2008). Domestic energy resources, including oil and gas, cover only 3–4% of the country's energy needs. Jordan spends more than 7.5% of its national income on the purchase of energy. The levels of energy and electricity consumption will probably double in 15 years, and it is probable that annual primary energy demand will reach $8x10^6$ ton of oil equivalent (toe) by 2010. Jordan accounts an average of $15.85x10^3$ ton of emissions, of which CO_2 constitutes around 97%; fossil-fuel combustion almost producing 85% by mass of the total GHG emissions (Jaber, 2002).

The solar energy flux reaching the Earth's surface represents a few thousand times the current use of primary energy by humans, earth receives 174 peta-Watt of incoming solar radiation at any given time, unfortunately, this huge amount of energy is not well utilized till now.

Electricity production using solar energy is one of the main research areas at present in the field of renewable energies, the significant price fluctuations are seen for the fossil fuel in one hand, and the trend toward privatization that dominates the power markets these days in the other hand, will drive the demand for solar technologies in the near term.

The great importance of electricity from solar technologies is due to the considerable associated benefits (Schott, 2006) (Haas, 2001) (NEPCO, 2006) (Badran, 2001) (Alrobaei, 2008), namely:

- Maximum power generation at peak load hours in hot climate countries like Jordan.
- The modular character of the solar field makes it possible to start at any power level.
- The off grid solar power production for remote locations maybe competitive to fossil fuel power due to the high cost of rural power since it requires to be distributed along far distance.
- Reduction of greenhouse gas emissions;
- Increases in local employment and income;
- enhanced local tax revenues;
- A more diversified resource base,
- Avoided risks of disruption in fossil fuel supply and association price instability
- Provision of infrastructure and economic flexibility by modular, dispersed and smaller scale technologies;
- The potential to greatly reduce, and perhaps eliminate, pollution associated with electricity services
- Contribution towards sustainability.
- Some solar technologies provides other benefits beside power generation i.e., fresh water.

Different types of solar power technologies need further improvements and cost reduction to be competitive with fossil fuel power plants in future power markets. The

* Corresponding author. badran@yahoo.com

National Renewable Energy Laboratory (NREL) evaluated the potential for the emerging photovoltaic (PV) technologies to meet the solar program's technical and economic targets; they discussed the current structure, capabilities, assumptions and made a linear programming model of capacity expansion plans (Braun and Skinner, 2007) (Blair et al, 2006).

Solar power has the advantage of electricity generation at peak load hours. Hot climate countries, like Jordan, have the highest electricity peak load consumption in demands during the hot summer days as shown in Figure1, (NEPCO, 2006).

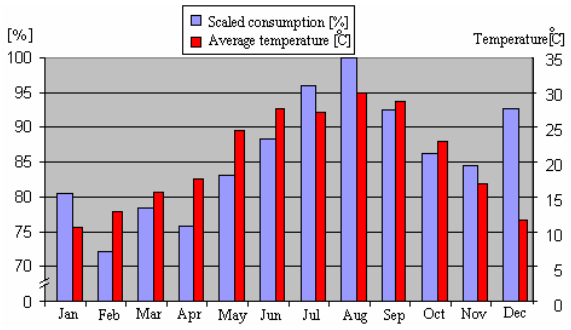

Figure 1. Monthly variations of electricity consumption in Jordan (NEPCO 2006**).**

Solar power plants play an important role in decreasing the environmental pollution; they contribute directly to the CO_2 reduction that caused by the conventional fossil fuel power plants. According to the Greenpeace study, the use of solar power plants can avoid 362 million tons of CO_2 emissions worldwide from 2002 to 2025. (Brakmann et al, 2005).

An evaluation study for different power production systems using fuzzy set methodology was prepared by Mamlook (2006). It shows that the solar power production is the best preferable option under the Jordanian climate in the basis of cost to benefit ratio. He also used the same mechanism under the same Jordanian climate for solar utilization applications; he showed that the solar power production is the second best choice that comes after the solar distillation (Mamlook et al, 2001).

Badran (2001) has studied different solar power technologies. He suggested that the Jordanian government needs to do more serious steps towards the utilization of industrial solar energy for power generation applications in arid regions.

Dead Sea is considered a perfect place for solar pond power plants due to its high salinity. The largest solar pond built so far is in Israel, and used to generate electricity, (Sukhatme, 1996). Other studies by (Khalil et al (1997) presented a theoretical study on the evaluation of electric solar pond power plant under Jordanian climate. Tahat et al (2000) built a mini solar pond in Jordan and studied its thermal performance to show its merits under Jordanian climate.

PV systems have wide range utilization in Jordan. They are used for water-pumping systems, powering radio–telephone stations, as well as supplying electricity to clinics and schools of very small communities in the remote regions (Hrayshat, 2007) (Jaber et al, 2004) (Badran 2001) (Abu-Khader et al, 2008). There are future plans consisting of installation of 1036 PV panels in remote villages (houses, schools, and other public buildings) each panel having an average generating capacity of 1050Wh/day (Hrayshat, 2007). Durisch et al (2007) performed calculations for five commercial PV modules for Al Qawairah site in Jordan and developed efficiency model for them.

In the present study, a fuzzy logic methodology is used to compare between photovoltaic (PV) and solar ponds in terms of their benefits (merits) and costs (barriers). The effect of different parameters on the power production of these technologies was taken from previous studies proposed for Jordanian climate, (Hrayshat, 2007) (Jaber et al, 2004) (Khalil et al, 1997) (Tahat et al, 2000) (Abu-Khader et al, 2008) (Badran 2001) (Durisch et al, 2007).

2. Solar Electric Power Technologies

Solar power technologies can be classified into direct (PV) and indirect electricity conversion, the indirect electricity conversion consists of concentrating and non-concentrating solar power systems (Quaschning, 2003).

2.1. Solar pond

A solar pond does not concentrate solar radiation, but collects solar energy in the pond's water by absorbing both the direct and diffuse components of sunlight; this is good for countries where the sky is frequently overcast. Solar ponds contain salt in high concentrations near the bottom, with decreasing concentrations closer to the surface (Figure 2).

This variation in concentration, known as a salt-density gradient, suppresses the natural tendency of hot water to rise, thus allowing the heated water to remain in the bottom layers of the pond while the surface layers stay relatively cool. Temperature differences between the bottom and top layers are sufficient to drive an organic Rankine-cycle engine that uses a volatile organic substance as the working fluid instead of steam. Temperatures of 90°C are routinely achieved in the pond bottom, and solar ponds are sufficiently large to provide some degree of energy storage. The potential of solar ponds to provide fresh water, heat and electricity, especially for island communities and coastal desert regions, appears promising, but has not been fully investigated (Zumerchik, 2001). Dead Sea is considered largest solar pond on earth, due to its high salinity. The largest solar pond built so far is the 250000 m^2 pond at Bet Ha Arava in Israel. The heat collected in this pond has been used to generate 5 MW of electrical power using an organic fluid Rankine cycle (Sukhatme, 1996). The principle of the collection and storage of solar energy in salt ponds where the salinity increases with depth is introduced, and the six polar ponds constructed by Israel since 1960 to test the theory of solar pond energy conversion are indicated. They examined the electric power, with attention given to the water layers, pumps, evaporator, organic vapor turbogenerator and condenser. The performance characteristics of solar pond power plants, which can be started up in a few minutes and deliver up to ten times or more of their rated output power, are pointed out as the basis for the suggestion that they can be used initially as peaking plants in the power grid. Respect to the Israeli plans, the accumulated generated

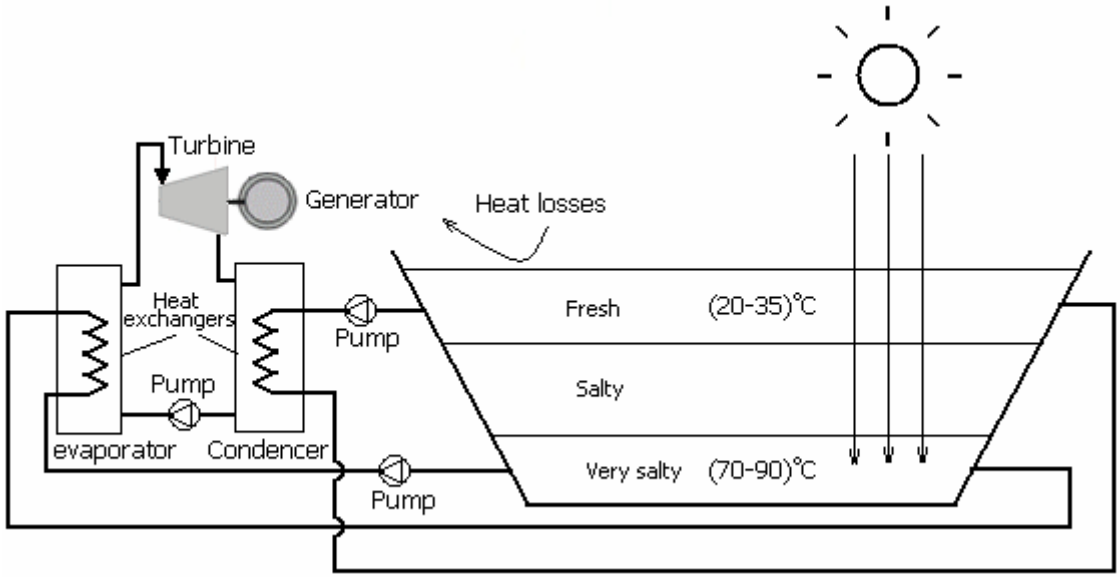

Figure 2. Solar pond power plant schematic for generating electricity

power by solar pond will be up to 2000 MW (Sukhatme, 1996) (Bronicki, 1981). Khalil et al (1997) presented 5 MWe electric solar pond power plant in the dead sea part of Jordan with surface area 1.5 km^2, they found that the solar pond could generate electricy with a levelized cost of 0.234JD/kWh under Jordanian climate.

In India, the first solar pond having an area of 1200 m^2 was built at the Central Salt and Marine Chemicals Research Institute in 1973. Experimental research ponds having areas of 100 and 240 m^2 respectively were operated for a few years at Pondicherry and at the Indian Institute of Science in Bangalore, while a 1600 m^2 solar pond was built in Bhavnagar again in the eighties. The largest pond built in India so far is located at Bhuj (Gujrat). The pond has an area of 6000 m^2. It has been operating since September 1993 and supplies the process heat need of a nearby dairy (Sukhatme, 1996).

2.2 Photovoltaic (PV)

Photovoltaic's (photo for light, voltaic for electricity) converts sunlight directly to electricity. Modules are mounted on a stationary array or on single- or dual-axis sun trackers (Abu-Khader et al 2008). Arrays can be ground-mounted on all types of buildings and structures. The DC output from PV can be conditioned into grid-quality AC electricity, or DC can be used to charge batteries or to split water to produce hydrogen (electrolysis of water) (Aabakken, 2006).

The photovoltaic (PV) market has grown extensively since 1992. R&D efforts, together with market deployment policies, have effectively produced impressive cost reductions: every doubling of the volume produced prompted a cost decrease of about 20%. But market deployment is concentrated: Japan, Germany and the United States account for over 85% of total installed capacity (Figure 3). PV still requires substantial R&D investments, as well as deployment supports, to gain market learning. In the near term, R&D efforts will focus on improving the balance-of-system components for both grid connected and stand-alone applications. Even with these supports, PV is not expected to be generally competitive until after 2025 – although it will continue to compete well in a growing range of market niches in which the cost of deployment supports is moderate (IEA, 2007) (Stierstorfer, 2006).

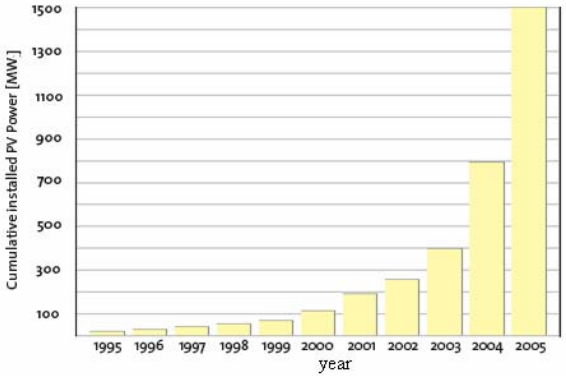

Figure 3. PV annual cumulative installation in Germany

Jordan utilizes PV cells for limited applications (water-pumping systems, powering radio–telephone stations, as well as supplying electrical energy for clinics, (Hrayshat, 2007) (Jaber et al, 2004). There are future plans consisting of installation of large number of PV for power generation connected to the grid line (Hrayshat, 2007), (Badran 2001). Durisch et al (2007) performed calculations for five commercial PV modules in Al Qawairah site in Jordan and developed efficiency model for them.

3. Fuzzy Methodology

After Zadeh's work on fuzzy sets (1965), many theories in fuzzy logic were developed in Japan, Europe, United States, and elsewhere. Since the 1970s Japanese researchers have been advancing the practical implementation of the fuzzy logic theory; they have been commercializing this technology and they have now over 2000 patents in the area from fuzzy air conditioner, fuzzy

washing machine, fuzzy toasters, fuzzy rice cookers, fuzzy vacuum cleaner, and many other industrial fuzzy control processes. They have a subway system that is totally controlled by fuzzy computer. It is smooth enough that riders do not need to hold straps, and the controller makes 70% fewer judgmental errors in acceleration and braking than human operators. The U.S. Space Administration has been involved in the use of fuzzy logic in space control decision making. Energy consumption could be analyzed using fuzzy sets (Oder et al, 1993). Also systems could be controlled using fuzzy (Mamlook et al, 1998).

3.1. Determining the linguistic variables and the fuzzy sets.

In order to decide between parameters which are fuzzy, vague, or ambiguous, MATLAB fuzzy toolbox was used to generate decision based on the benefit and the cost for each solar thermal power plant technology.

The fuzzy logic decision selection between PV systems and solar pond technology was applied according to benefits, namely, (B1= power plant capacity or size (MW), B2= Annual solar to electric efficiency, B3= Thermal efficiency, B4= Peak solar to electric efficiency, B5= Availability, B6= Annual capacity factor (CF), B7= storage hours, B8= maturity or popularity, B9= Temperature (T), B10= Safety, B11= Concentration ratio (CR)) to make a decision on the selection between the different solar technologies that cost less and have better benefits. Many factors affect the decision (costs) (Figure 4), i.e., (C1= Hardware cost, C2= Electricity cost, C3= Water usage, C4= Land usage, C5= Maintenance cost, and C6= environmental constrains).

The Fuzzy input/ output combination is shown in the Figure 4 as follows:

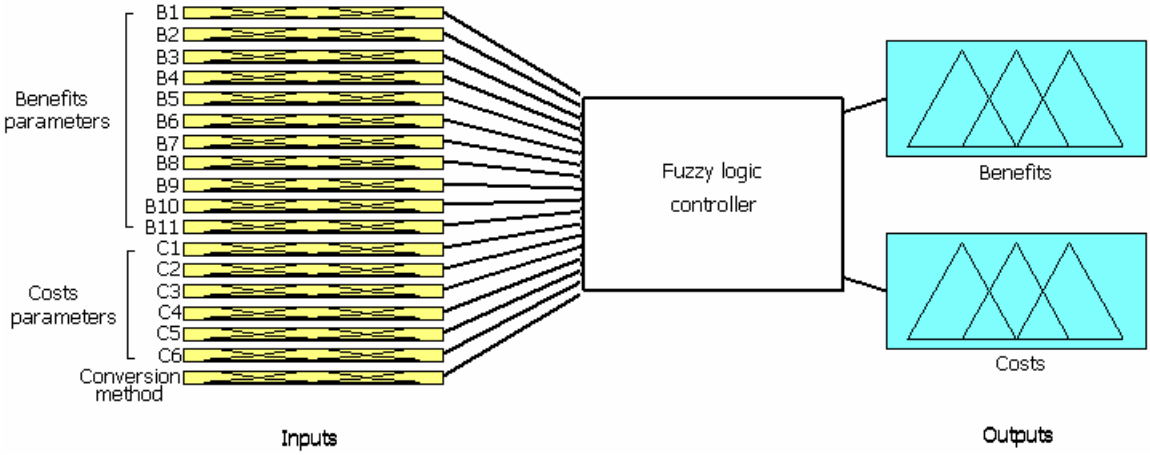

Figure 4. Fuzzy Inputs/Outputs Combination.

The fuzzy logic decision selection of the best solar technology options was applied according to their costs and benefits (Tables 1 and 2).

Table 1. Overall fuzzy weights of solar technologies for optimum benefits.

	Power	Annual efficiency	thermal efficiency	Peak efficiency	Availability	annual CF	storage h	Maturity	T	Safety	CR	Relative weight	Normalized relative weight*
Parameter importance	1.00	0.71	0.71	0.5	1.00	0.50	0.50	1.00	0.71	0.43	0.71	-	-
Pond	0.01	0.1	0.24	0.1	0.8	0.85	0.85	0.2	0.08	1	0.1	0.378	0.71
PV	0.05	0.7	-	0.97	1	0.19	0.42	0.65	-	0.35	-	0.532	1

* Normalized relative weight = relative weight/maximum relative weight

Table 2. Overall fuzzy weights of solar technologies for optimum costs

	Hardware Cost	Electricity Cost	Water Usage	Land Usage	Maintenance Cost	Environmental Constrains	Relative weight	Normalized relative weight*
Parameter importance	0.5	0.5	0.5	0.4	0.5	0.25	-	-
Pond	0.29	0.18	1	1	0.25	0	0.441	0.768
PV	0.84	1	0.05	0.36	1	0	0.574	1.000

* Normalized relative weight = relative weight/maximum relative weight

Data in Tables 1 and 2 are actual data obtained from different literature such as [(Braun and Skinner, 2007) (Schott, 2006), (Brakmann et al, 2005), (Dersch et al, 2004), (Mills, 2004),(Wibberley et al, 2006), (Mukund, 1999) (Porta, 2005), (Zumerchik, 2001), (Aabakken, 2006), (Groenendaal, 2002) (Sukhatme, 1996) (Badran 2001) (Hrayshat, 2007) (Jaber et al, 2004) (Khalil et al, 1997) (Tahat et al, 2000)

The inputs for fuzzy implementation in Table 1 and 2 are considered to be fuzzy variables, each of which can vary over a fixed weight (0-1), the inputs' and output's sets are shown in Figure 5.

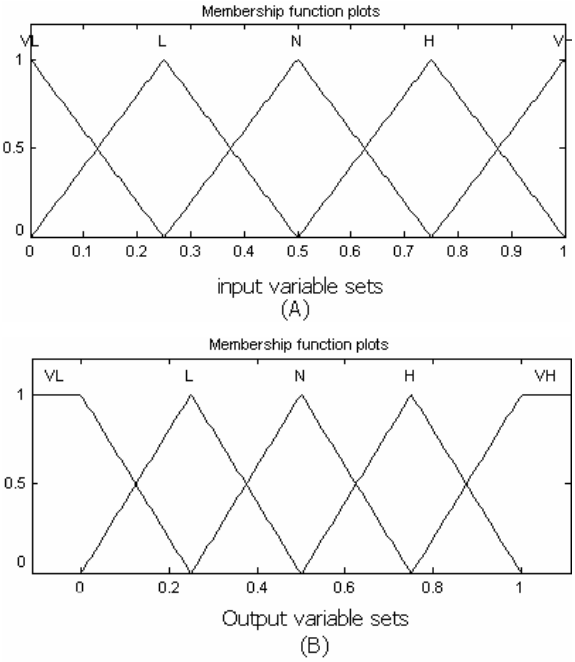

Figure 5. Fuzzy sets, (A) input sets (B) output sets.

The linguistic variables that were used to describe the fuzzy sets in Figure 5 are very low (VL), low (L), normal (N), high (H) and very high (VH).

The "conversion method" input shown in Figure 6 is responsible for determining the solar technology type; whether it is direct solar conversion (PV) or indirect (thermal conversion) excluding the "thermal efficiency", "temperature" and "concentration ratio" to have an accurate decision making as shown in Figure

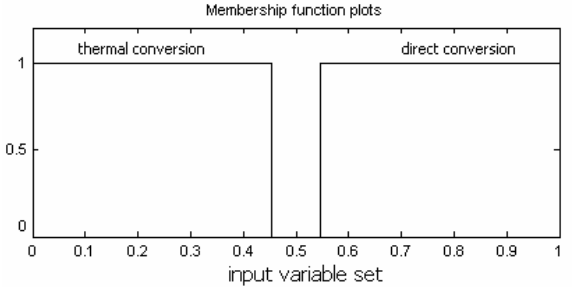

Figure 6. Binary fuzzy sets.

3.2. Constructing Fuzzy Rules

In the present section, 85 rules were used to predict the most preferable option(s) out of the two solar technologies, they are in a statements form as shown in the Figure 7.

```
1. If (B1 is VL) then (B is VL) (1)
2. If (B1 is L) then (B is L) (1)
3. If (B1 is N) then (B is N) (1)
4. If (B1 is H) then (B is H) (1)
5. If (B1 is VH) then (B is VH) (1)
:
55. If (C1 is VH) then (C is VH) (0.5)
56. If (C2 is VH) then (C is VH) (0.5)
57. If (C2 is H) then (C is H) (0.5)
58. If (C2 is N) then (C is N) (0.5)
59. If (C2 is L) then (C is L) (0.5)
60. If (C2 is VL) then (C is VL) (0.5)
:
80. If (C6 is VH) then (C is VH) (0.25)
81. If (B3 is VL) and (con is thermal_conv) then (B is VL) (0.71)
82. If (B3 is L) and (con is thermal_conv) then (B is L) (0.71)
83. If (B3 is N) and (con is thermal_conv) then (B is N) (0.71)
84. If (B3 is H) and (con is thermal_conv) then (B is H) (0.71)
85. If (B3 is VH) and (con is thermal_conv) then (B is VH) (0.71)
```

Figure 7. Fuzzy rules.

3.3. Performing Fuzzy Inference into The System

This procedure is used to compute the mapping from the input values to the output values, and it consists of three sub-processes, fuzzification, aggregation and defuzzification (Negnevitsky, 2005) as shown in the following figure.

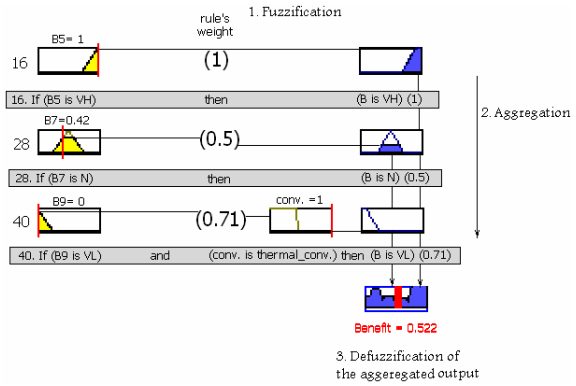

Figure 8. Fuzzy implementation sequence.

4. 4. Results and Discussion

The fuzzy sets enabled us to utilize large amount of collected data to compare between the two solar technologies systems, into a smaller set of variable rules (see Tables 1 and 2).

The benefit to cost ratio is shown in Table 3 as follows:

Table 3. Benefit to cost weight ratio.

Solar technology	Normalized benefits relative weight	Normalized costs relative weight	B/C
Pond	0.71	0.768	0.92
PV	1.000	1.000	1

The final results are shown in Figure 9 as follows:

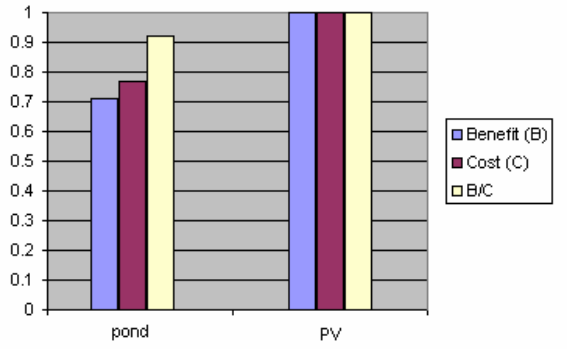

Figure 9. Comparison between benefits, costs and normalized benefit to cost ratios

As can be inferred from Table 3, Fig 9, and from the fuzzy sets analysis, photovoltaic technology (PV) has higher benefit to cost ratio than solar pond and it is considered to be better option for power generation. It has high growing rate in the world wide in spite of its high cost. Solar pond is considered to supply cheaper electricity that PV technology but in the other hand it has lower benefits (Figure 9). This is because the output power is lower in this technology and the maintenance cost is considered to be high, due to high salinity of water. So that the best option according to this study will be PV technology.

5.Conclusions

The foreseeable shortages due to the increased population and the industrial activities in the world, and today's already unreliable and distinctly expensive fossil resources are forcing a diversification of energy sources and driving the demand toward solar technologies in the near term.

Fuzzy logic methodology for evaluating the solar thermal power technology enabled us to condense huge amount of data into smaller sets, it has the ability to decide between different solar technologies in the bases of their benefits and cots. Based on fuzzy logic results, photovoltaic technology (PV) has the higher benefit to cost ratio than solar pond and it is considered to be better option for power generation. PV has high growing rate in the world wide in spite of its high cost. Solar pond is considered to supply cheaper electricity that PV technology but in the other hand it has lower benefits, due to its low solar energy.

References

[1] Aabakken J. Power Technologies Energy Data Book, report no. NREL/TP-620-39728. Colorado, CA: U.S. Department of Energy Office of Energy Efficiency and Renewable Energy by Midwest Research Institute ,2006.

[2] Abu-Khader M.M., Badran O.O. Abdallah S. Evaluating multi-axes sun-tracking system at different modes of operation in Jordan. Renewable and Sustainable Energy Reviews 2008; Vol. 12, No 3, 864-873.

[3] Alrobaei H. Novel integrated gas turbine solar cogeneration power plant. Desalination ; , Vol. 220, No. 1-3, 574-587, 2008.

[4] Braun G, Skinner D. Experience Scaling-Up Manufacturing of Emerging Photovoltaic Technologies, report no. NREL/SR-640-39165. Colorado, CA: U.S. Department of Energy Office of Energy Efficiency and Renewable Energy by Midwest Research Institute, 2007.

[5] Brakmann G, Aringhoff R, Tseke S. Concentrated Solar thermal power. Report no. 90-73361-82-6, Greanpeace. Netherlands, 2005.

[6] Badran O. Study in industrial applications of solar energy and the range of its utilization in Jordan. Renewable Energy Vol. 24, No. 3-4, 2001, 485-490.

[7] Bronicki Y. L., A solar-pond power plant IEEE Spectrum1981;18:56-59.

[8] Blair N, Mehos M, Short W, Heimiller D. Concentrating Solar Deployment System (CSDS) – A New Model for Estimating U.S. Concentrating Solar Power (CSP) Market Potential**.** Solar Conference, Cole Boulevard Golden, Colorado 80401-3393, National Renewable Energy Laboratory, NREL/CP-620-39682 2006.

[9] Dersch J, Geyer M, Herrmann U, Jones SA., Kelly B, Kistner R, Ortmanns W, Pitz-Paal R, Price H. Trough integration into power plants—a study on the performance and economy of integrated solar combined cycle systems. Energy 2004;29(5-6):947-959.

[10] Durisch W, Keller J, Bulgheroni W, Keller L, Fricker H. Solar irradiation measurements in Jordan and comparisons with Californian and Alpine data. Applied Energy, Vol. 52, No. 2-3, 1995, 111-124.

[11] Durisch W, Bitnar B, Mayor J, Kiess H, Lam K. Close J. Efficiency model for photovoltaic modules and demonstration of its application to energy yield estimation. Solar Energy Materials and Solar Cells, Vol. 91, No. 5, 2007, 79-84.

[12] Groenendaal B. Solar thermal power technologies, report no. ECN-C--02-062 Monograph in the framework of the VLEEM Project. Petten, the Netherlands, ECN Beleidsstudies, July. 39 p, 2002.

[13] Haas, R., T. Faber, J. Green, M. Gual, C. Huber, G. Resch, W. Ruijgrok, and J. Twidell , Promotion Strategies for Electricity from Renewable Energy Sources in EU Countries,. Institute of Energy Economics, Vienna University of Technology, 2001.

[14] Hrayshat E.S. Analysis of renewable energy situation in Jordan. Renew Sustain Energy Vol. 12, No. 1, 2007, 1873–1887.

[15] International Energy Agency (IEA) Fact Sheet. Renewables in Global Energy Supply. Report no. OECD-IEA, Paris, France.2007

[16] Jaber J.O., Jaber Q.M., Sawalha S.A., Mohsen M.S.. Evaluation of conventional and renewable energy sources for space heating in the household sector. Renewable and Sustainable Energy Reviews, Vol. 12, 2008, 278-289.

[17] Jaber J.O. Future energy consumption and greenhouse gas emissions in Jordanian industries. Applied Energy, Vol. 17, 2002, 15-30.

[18] Jaber J, Badran OO, Abu-Shikhah N. Sustainable energy and environmental impact: role of renewables as clean and secure source of energy for the 21st century in Jordan. Clean Techn Environ Policy Vol. 6, 2004, 174–86.

[19] Khalil R, Jubran B, Faqir N. Optimization of solar pond electrical power generation system. Energy Conversion and Management, Vol. 38, No. 8, 1997,787-798.

[20] Mills D, Morrison G, Lièvre P. Design of a 240 MW e Solar Thermal Power Plant Proc. Eurosun Conference, Freiburg, Germany, 2004.

[21] Mills D. Advances in solar thermal electricity technology. Solar Energy, Vol. 76, No. 1-3, 2004, 19-31.

[22] Mukund R. Wind and solar power systems. USA: CRC press, 1999.

[23] Mamlook R. Fuzzy Set Methodology For Evaluating Alternatives To Compare Between Different Power Production Systems. Journal of Applied Sciences 2006; Vol. 6, No. 9, 2006, 1686-1691.

[24] Mamlook R, Akash BA, Nijmeh S. Fuzzy Sets Programming to Perform Evaluation of Solar Systems in Jordan. International Journal of Energy Conversion and Management, Vol. 42, No. 14, 2001, 1717-1726.

[25] Mamlook R, Tao C, Thompson WE. An advanced fuzzy control1er. Int J Fuzzy Sets Systems, vol. 103, No. 3, 1998, 541-545.

[26] NEPCO. Annual report. Amman, Jordan; 2007.

[40] Negnevitsky M. Artificial Intelligence. England: Pearson Education, 2005.

[27] Oder C, Haasis HD, Renlz O. Analysis of the Lithuanian final energy consumption using fuzzy sets. Int J Energy Research, Vol. 17, 1993, 35-44.

[28] Porta F. Technical and economical analysis of future perspectives of solar thermal power plants. Master thesis,University of Stuttgart 2005 ,1-86.

[29] Photovoltaics Bulleti. Jordan's solar cogen 2002.

[30] Quaschning V. Technology Fundamentals - Solar Thermal Power Plants. Renewable Energy World Vol. 6, No. 1, 09-113, 2003.

[31] Schott A. Memorandum on Solar Thermal Power Plant Technology, report no. 0141 e 02053.0 ac/sk. Germany, 2006.

[32] Stierstorfer J. Solar generation: solar electricity for over one billion people and two million jobs by 2020, EPIA, Greenpeace, DLR, 2006

[33] Sukhatme S.P., Solar energy: principles of thermal collection and storage, McGraw-Hill, New Delhi , 1996.

[34] Tahat M.A., Kodah Z.H., Probert S.D., Al-Tahaineh H. Performance of a portable mini solar-pond. Applied Energy 2000; Vol. 66, No. 4, 299-310.

[35] Wibberley L, Cottrell A, Palfreyman D, Scaife P, Brown P. Techno-economic assessment of power generation options for Australia Technology Assessment Report 52: CRC for Coal in Sustainable Development, 2006.

[36] Zumerchik J. Macmillan encyclopedia of energy. USA: Macmillian Reference, 2001.

[37] Zadeh L. Fuzzy sets. Inf Control, Vol. 8, 1965, 338-853.

JJMIE

Volume 4, Number 1, Jan.2010
ISSN 1995-6665
Pages 129 - 134

Jordan Journal of Mechanical and Industrial Engineering

Interference Pigment Coated Solar Cells for Use in High Radiant Flux Environments

Faiz Rahman [a,*], Kamran Abid [a], Christoph Schmidt [b], Gerhard Pfaff [b], Friedrich Koenig [b]

[a] *Department of Electronics and Electrical Engineering, University of Glasgow, Oakfield Avenue, Rankine Building, Glasgow G12 8LT, United Kingdom*

[b] *Merck Research Laboratories, 64271 Dramstadt,Germany*

Abstract

We describe our development of heat-resistant solar cells made by depositing the interference filter pigment Solarflair on the surface of silicon and compound semiconductor solar cells. The coating is designed to reflect long wavelength components of solar radiation while admitting shorter wavelength visible and near-infrared components. This results in less heating of coated cells as compared to uncoated cells and consequently their maintaining high light-to-electricity conversion efficiency. Such coated cells have the potential to be usefully employed in concentrator type photovoltaic array systems. Details of the interference pigment used, coating techniques and results of measurements in simulated high heat load environments are described.

Keywords: Solar cells, Thermal Protection, Protective Films, Interference Pigments.

1. Introduction

With the proliferation of solar photovoltaic technology in recent years both the number and diversity of solar power installations has been increasingly rapidly. The emphasis on environmentally friendly i.e. green energy technologies has provided a big impetus to the development of semiconductor solar cell technology. A number of materials such as silicon, gallium arsenide and cadmium telluride have been used for the manufacture of solar photovoltaic cells[1]. Organic solar cells are also seeing a surge of interest even though their conversion efficiencies are significantly below that of inorganic cells. Silicon, however, remains the most popular material for solar cells and its prevalence in the industry will likely remain for at least several years to come. When used for solar photovoltaic applications distinction is usually made between monocrystalline, polycrystalline and amorphous silicon solar cells as these are very different from each other in terms of cost of production and power conversion efficiency. In general, compound semiconductor solar cells are more efficient than silicon solar cells in converting the energy in sunlight to electrical power. Again, monocrystalline silicon cells are more efficient that polycrystalline cells which are still more efficient than amorphous silicon cells. No matter which material technology is used for the construction of solar cells their efficient operation is dependent on their receiving an optimum amount and type of incident radiation. While large incident flux is usually desirable there is increasing realization that too high an intensity of solar radiation can lead to diminishing returns by heating up cells and thus causing loss of power conversion efficiency as well as a reduction in the cells useful lifetime. Selective spectral filtering of sunlight can go a long way towards addressing these issue and our work demonstrates that by forming appropriate filter coatings on the surface of solar cells it is indeed possible to make them more efficient under high input flux situations. This essentially implies an increase in cell operating efficiency and thereby a gain in overall electric power production. This issue will assume even more significance in the next few years when concentrator type solar cell installations become more widespread[2]. Concentrator solar cells have to endure much higher temperatures than cells simply exposed to the sun in large panels and their efficiency and lifetime can be greatly improved with this technology. We go on to describe the characteristics of our filter films and their effect on the operation of both GaAs and Si solar cells.

Corresponding author. f.rahman@elec.gla.ac.uk

2. Interference Pigments as Sunlight Filters

Incident light can be filtered in either intensity or wavelength by using either absorptive pigments or interference pigments. Transparent coatings containing ordinary colouring pigments have long been used for customising light for a variety of applications. Examples range from sun glasses to filters on infrared remote controls. In recent years, however, the idea of using interference pigments as light filters has gained much ground. These pigments are essentially small coated particles that act as multi-layer dielectric filters[3]. Instead of using the usual method of forming dielectric filters by depositing materials of appropriate refractive index on plane glass or other flat transparent substrate, interference filters are made by the chemical deposition of transparent oxides on particles of quartz or mica. By carefully sequencing and controlling reaction conditions it is possible to deposit a multi-layer stack of transparent oxide materials of precise thicknesses on transparent quartz or mica particles. The resulting material then exhibits thin film interference and displays selective transmission of light. The spectral response can be engineered by appropriate choice of coating oxides, their thicknesses and order of deposition. A variety of transmission and reflection profiles can be obtained when this kind of interference pigment is incorporated in transparent media such as glass, optically clear plastic or various synthetic lacquers. Several families of interference pigments for applications ranging from printing inks to car paints and decorative coatings are commercially available from various manufacturers. Merck produces perhaps the best known family of such pigments under its offering of special effect pigments. One of the sub-family called Solarflair has been specially developed for solar heat protection applications in high solar potential regions of earth. Translucent plastic sheets containing Solarflair, for instance, serve as effective material for the construction of green houses and sky lights in tropical and subtropical countries. These pigments have been designed such that their dispersions allow a large fraction of shorter wavelength visible radiation to pass through but longer wavelength heat-producing infrared radiation is very effectively attenuated through reflection. The result is cool green houses and other enclosed ambients. Our work has investigated the use of transparent filters containing Solarflair pigments for use in shielding solar cells from infrared radiation while letting most of the visible light through for photovoltaic generation to take place. Our experiments have involved work on preparing both plastic-based and glass-based filter films containing Solarflair that could be directly deposited on the top surface of solar cells.

3. Solarflair and Coatings Incorporating Solarflair

Solarflair, also known as Iriodin, is a multilayer synthetic pigment consisting of basal mica coated with silicon dioxide (SiO_2), titanium dioxide (TiO_2) and tin oxide (SnO_2) overlayers. Weather resistant grades are also available that contain an additional coating of zirconium dioxide (ZrO_2). This pigment is temperature stable up to 800 °C. The two main commercial offerings from Merck are called Solarflair 870 and Solarflair 875. These pigments have particle sizes in the range of 10-60 μm and 5-25 μm respectively. The former is suitable for general purpose infrared blocking applications while the later is tailored to have a transmission spectrum that matches photosynthesis requirements of vegetation quite closely. Figure 1 shows a plot of the transmission and reflection spectra of Solarflair x in the wavelength range from x nm to y nm.

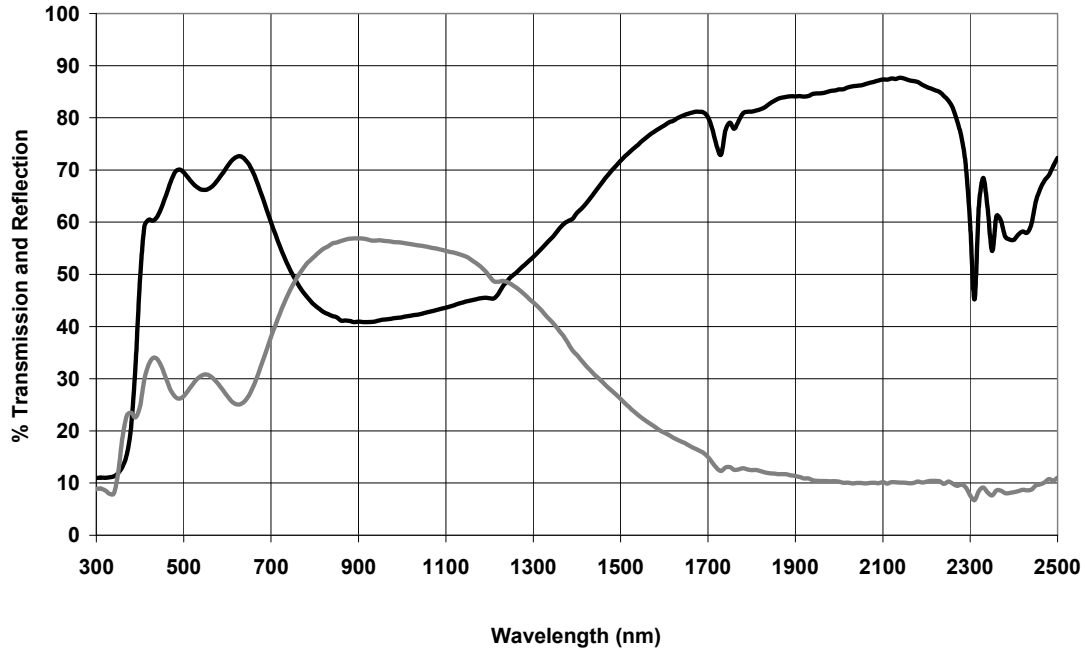

Figure 1. Spectral transmission and reflection of Solarflair 870 pigment particles

The actual pigments are inert, non-toxic, off-white powders that can be blended in plastics and glasses in various concentrations. It is possible to prepare a blend of Solarflair-containing acrylic plastic by mixing a desired amount of Solarflair in a solution of polymethyl methacrylate (PMMA) in a suitable solvent such as xylene or ethyl lactate. The loaded PMMA solution can then be coated on suitable substrates by any of a variety of coating techniques such as spray coating, roller coating or spin coating. With increasing Solarflair concentration the resulting films become less and less transmissive. An appropriate balance has to be struck with the Solarflair concentration such that as much infrared radiation as possible could be reflected away while attenuating as little as possible of visible light. With Solarflair itself is stable at temperatures in excess of 800 ºC, PMMA films containing Solarflair cannot withstand temperatures much above 100 ºC as the glass transition temperature of PMMA is only around 124 ºC. PMMA coatings also get scratched easily. Thus PMMA-based Solarflair coatings will clearly be unsuitable for use with solar cells exposed to aggressive outdoor environment. We, therefore, chose to work with silica-based coatings prepared from spin-on glass (SOG) precursors. Specifically, we used Intermediate Coating IC1-200 from Futurrex as the un-doped SOG. This is a polysiloxane-based polymer in n-butanol solvent. In usual application, it is spin coated at typically 4000 RPM on to cleaned substrates and then baked at 90 °C to remove any remaining solvent. A further anneal at 400 °C then converts it into silica. The resulting coating is tough and weather resistant. We investigated both PMMA and SOG coatings containing 10%, 15% and 20% by weight of Solarflair.

The transmission spectrum of each of these was measured and it was determined that SOG coatings containing 15% by weight of Solarflair, spun at 4000 RPM, were the most suitable for further experiments. However, it was also found that a 4-period stack of 5% Solarflair in SOG followed by un-doped SOG was even more suitable as it exhibited the largest contrast between the short wavelength pass-band and the long wavelength stop-band. A figure showing the transmission characteristics of these two types of films appears here as figure 2. Another feature that is seen here is the existence of a dip in transmission around 530 nm (green region) with single layer films. Such films have a distinct green hue in reflection. Multilayer films don't show such a dip and have a very flat pass-band.

  - Volume 4, Number 1 (ISSN 1995-6665)

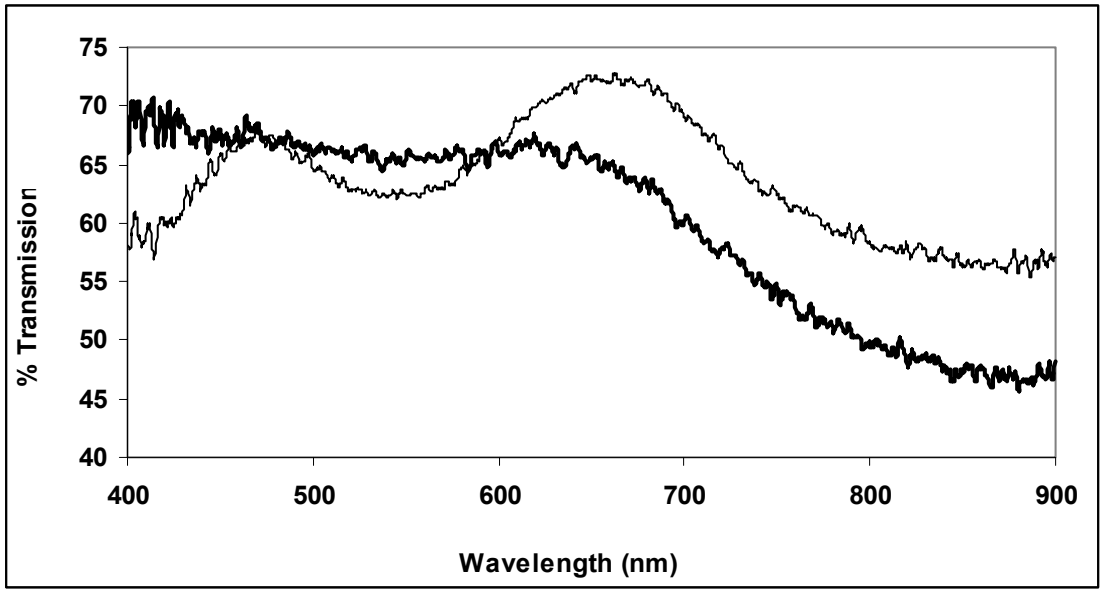

Figure 2. Spectral transmission of single layer (light curve) and 4-layer (bold curve) silica films containing 15% by weight of Solarflair

It is clearly seen from this figure that the multi-layer stack, though more laborious to deposit, was a better contender for infrared shielding applications. It features a relatively flat pass-band performance and a pronounced fall in transmission for longer wavelengths. However, the transition point – about 650 nm for the multi-layer coating – needs to move further towards the long wavelength side of the spectrum in order to better match with most inorganic solar cell materials. A shift of 100 nm would be very desirable.

4. Measurements on Solarflair-coated Solar Cells

We performed experiments on both GaAs and Si solar cells coated with Solarflair pigment embedded in SOG silica films. GaAs solar cells were fabricated from epitaxial structures grown at the University of Glasgow whereas amorphous silicon solar cells were purchased from Sanyo Corporation. The GaAs cells had a silicon nitride anti-reflection coating at the top whereas the Si cells were formed on 1 mm thick glass substrates. In both cases, Solarflair-containing SOG films were deposited and post-processed on solar cells through spinning from a butanol-based solution. A typical GaAs solar cell used in the experiments appears here in figure 3. The overlying Solarflair-containing silica films were only slightly translucent so they allowed a large amount of light to pass through to the cell.

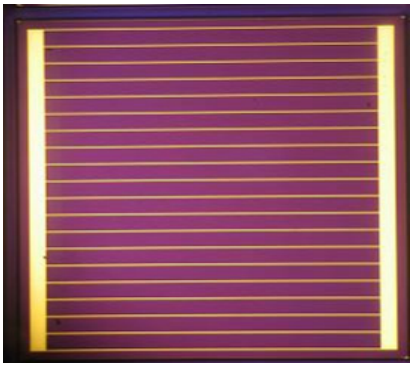

Figure 3. Epitaxial GaAs solar cell used in experiments

The optical responsivities of coated and uncoated cells were measured by illuminating them with a calibrated tungsten-halogen lamp as a light source[4]. The radiation contained both visible light and infrared radiation, as determined by a visible-infrared spectrometer. Open circuit terminal voltages (V_{OC}) were measured and plotted against incident optical power. Data was taken after the cells had stabilised in temperature. These results appear here in figure 4. The V_{OC} for coated cells was consistently measured to be about 0.5 volt higher than that for uncoated cells. This was also corroborated by the higher cell temperature measured for un-coated cells as compared to that for coated cells. Cells carrying a coating of Solarflair measured approximately 35 ºC lower in temperature than cells without the coating.

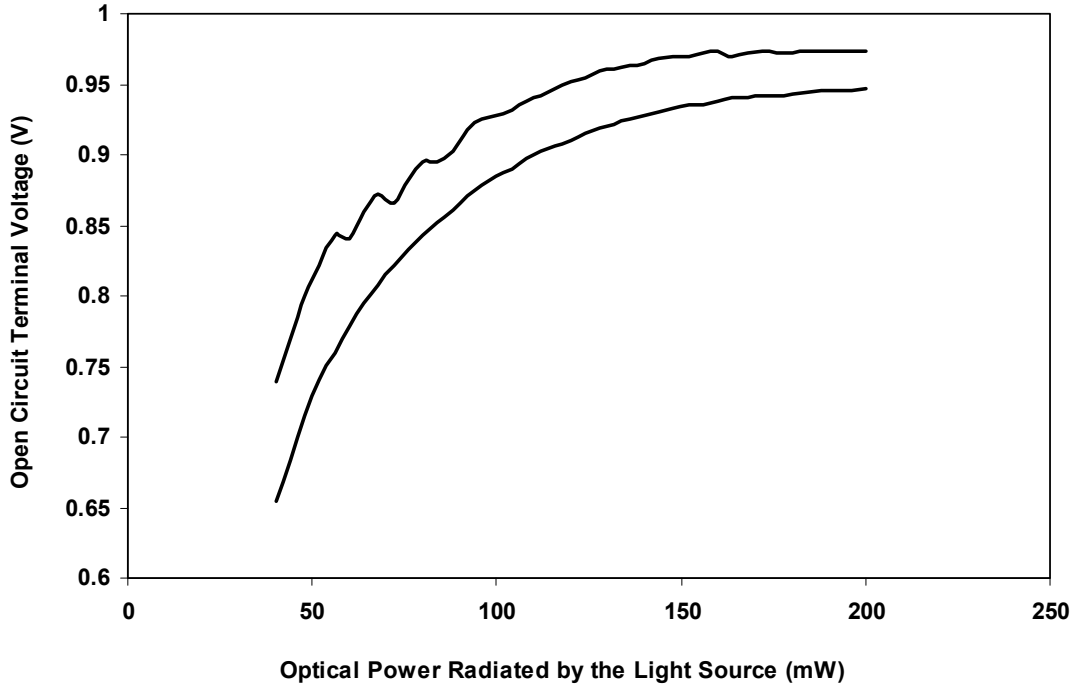

Figure 4. Responsivity curve showing open circuit terminal voltage as a function of illumination power for coated GaAs cells (top) and similar but uncoated cells (bottom)

This is clear evidence of the efficacy of Solarflair-based coatings in reducing photovoltaic cell temperature and raising their output voltage under radiant heating conditions.

The origin of the wavy structure in the optical responsivity of coated cells is not entirely clear but it is possibly due to interference effects in the Solarflair-loaded thin silica film. Silicon solar cells yielded similar results but showed even higher improvement in V_{OC}. Interestingly, the power output of silicon cells was seen to increase even under room light conditions once the cells were coated with Solarflair. It appears that the scattering of light by Solarflair particles enables better utilisation of light by these cells through a process of light trapping and results in the cells delivering higher electrical power output. This observation is very interesting because it suggests that by coating ordinary low performance solar cells intended for indoor applications in household gadgets it should be possible to obtain higher electrical power.

The effect of Solarflair films in shielding silicon photovoltaic cells from infrared radiation and thus maintaining them at lower temperatures compared to uncoated cells is seen in figure 5 where plats of temperatures reached by silicon cells under bright combined light-infrared radiation have been plotted as a function of time. The temperature of a reference uncoated cell is seen to climb to values at least 10 °C higher than that of coated cells. In high flux environments such as the interior of desert areas the ability of Solarflair coatings to keep photovoltaic cells cool and their efficiency high will evidently be of great value.

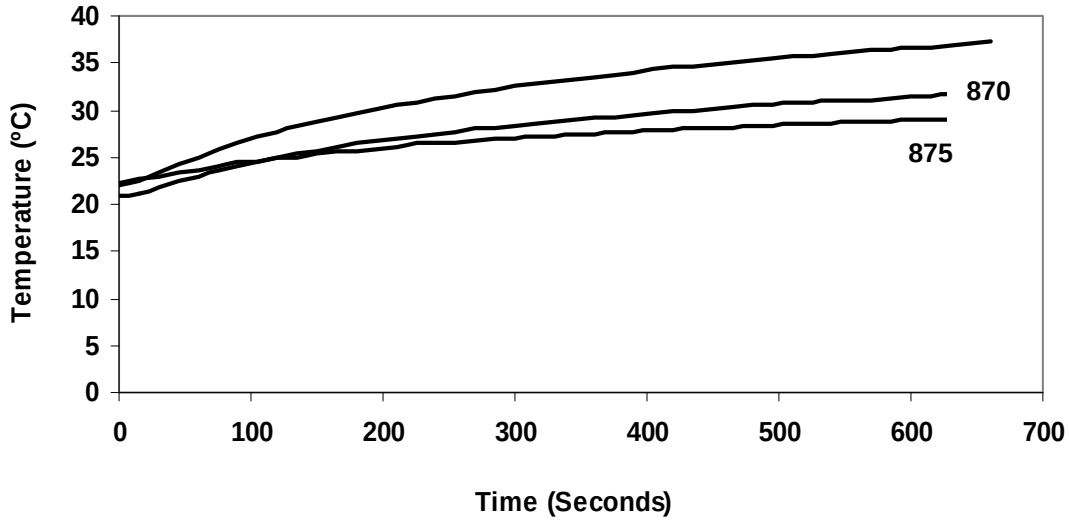

Figure 5. Plots showing temperatures reached by uncoated amorphous Si cell (top) and Solarflair-coated cells (bottom) as a function of elapsed time. 870 and 875 refer to two different versions of Solarflair.

5. Conclusions

Results of our experiments reported here show unambiguously that coating photovoltaic cells with silica films containing Solarflair pigments is very effective in keeping their temperatures down and thus enhancing their conversion efficiency in high flux environments. This results in higher open circuit terminal voltage and closed circuit cell current which lead to increased photovoltaic power output. Furthermore, the effect of light scattering and trapping leads to effective recycling of photons and that improves the functionality of even cells intended for room temperature operation.

References

[1] Hans Joachim Moller, Semiconductors for Solar Cells (Artech House, 1993), ISBN: 0890065748.

[2] R. Swanson, The promise of concentrators, Prog. Photovolt. Vol. 8, 93-111, 2000.

[3] Faiz Rahman, Nigel P. Johnson, The New Generation of Physical Effect Colorants, Optics and Photonics News, Vol. 19, 2008, 24.

[4] Faiz Rahman, Corrie Farmer, Nigel P. Johnson, Christoph Schmidt, Gerhard Pfaff and Colin R. Stanley, High Radiant Flux Photovoltaic Cells for Solar Proximity Missions, Semiconductor Science and Technology, Vol.22, 2007, 695.

JJMIE

Volume 4, Number 1, Jan. 2010
ISSN 1995-6665
Pages 135 - 142

Jordan Journal of Mechanical and Industrial Engineering

Development Chances of Distributed Energy Production on Small Scale

S. Alsaqoor [*,a], M. AlAjlouni [a], K. AlQdah [a], H. Kruczek [b], E. Pelińska-Olko [b]

[a] *Tafila Technical University, Jordan,* [b] *Wroclaw University of Technology, Poland*

Abstract

Distributed energy systems, nowadays, are very hot subject all over the world. They considered as a clean and sustainable energy. This kind of energy production will occur far from heat and power plants, in single houses or their small associations. This is not used, yet, in Jordan, put, regulations of power are under consideration and will hopefully appear very soon. A quick survey in the Jordanian markets and research bodies shows that the use of fuel cell compared with other distributed energy systems is very little. For this reason, the main part of this paper has been divorced to the discussion of the potentials of fuel cell systems in Jordan. The Poland experience in this subject has been studied in order to compare with the case of Jordan. The market and technical requirements for small-scale fuel cells in residential applications are investigated. In particular, the peculiar features of the Jordan situation are explored, with its specific energy resources and demands. The attributes and disadvantages are discussed, with a number of technology gaps being identified, and some solutions proposed. It is shown that various technologies could be applied. The obvious premium application of fuel cells in Jordan exists where grid connection is expensive. This study shows obviously many benefits can be gained if the distributed energy systems are applied to the Jordanian markets. These include, but not limited to, the improvements of the peak load, energy economy, and air pollutions. The study shows ,also, that Jordan can be gained a lot from using distributed energy systems.

Keywords: Emission Control; Carbon Dioxide; Fuel Cell Systems; Distributed Energy Production.

Nomenclature [*]

AFC	Alkaline Fuel Cell	n_{pi}	The amounts in kilo moles of products.
CH_4	Methane.	n_{si}	The amounts in kilo moles of substrates.
CO_2	Carbon Dioxide.	PAFC	Phosphoric Acid Fuel Cell.
DE	Distributed Energy	PEM	Proton Exchange Membrane
DMFC	Direct Methanol Fuel Cell	PV	Photovoltaic
EU	European Union.		
FC	Fuel Cell.	SOFC	Solid Oxide Fuel Cell.
GHG	Greenhouses Gases.		
GWP	Global Warming Potential.	ΔE	Energy Difference.
KOH	Potassium Hydroxide.	Ψ_{pi}	(divided by 100) times of staying in atmosphere of GHG, in products.
IC	Internal Combustion Engines	Ψ_{si}	(divided by 100) times of staying in atmosphere of GHG, in substrates.

[*] Corresponding author. kqdah@ttu.edu.jo

1. Introduction

Distributed energy systems (DE), nowadays, are very hot subject all over the world. They considered as a clean and sustainable energy. Distributed energy systems have already made a significant impact on the energy market and will certainly affect energy scenarios in the near future [1]. Pepermans et. al [2] extract an accurate definition for DE after a long survey. In their view, the best definition of distributed generation that generally applies seems to be 'an electric power generation source that is connected directly to the distribution network or on the customer side of the meter'. They also showed two major factors that contribute to the renewed interest in distributed generation i.e. electricity market liberalization and environmental concerns [2]. These DE systems include but are not limited to photovoltaic (PVS), wind, micro turbine, fuel cells (FC), and internal combustion (IC) engines. Although most of DE systems are not new in technological respect, they are receiving increased attention today because of their ability to provide combined heat and power, peak power, demand reduction, backup power, improved power quality, and ancillary services to the power grid. The visibility of renewable energy sources are increasing significantly due to common concerns about fossil fuel scarcity, increased pollution, weakened national security, and higher production of greenhouse gases related to the conventional power plants [1]. Even with all the benefits renewable energy has to offer, the decision on DE installations are still largely dependent on initial capital cost. Therefore the improvement of the DE economics strongly requires decreased costs for all of its components. Another important aspect to the life-cycle cost of the DE systems is reliability. Numerous researches all over the world deal with DE systems, components, improvement and applications. These works are not the scope of this paper but only few examples were presented in the references list(Italy [3], Poland [4], UK [5], Finland[6], Belgium [7], Spain[8 and 9] Greece[10] Iran[11] USA [1, 12, 13, 14, 15, and 16] China [17] France [18] Taiwan [19], Norway [20], Turkey [21], Algeria [22]. However, this paper is aimed to study the ability of use these ideas in Jordan. Concentration will be given for a comparison between Jordan and Poland [23-25]. Also discussed in this paper are the challenges that must first be overcome to reach the goal of good use of DE in Jordan in future. A quick survey in the Jordanian markets and research bodies shows that the use of FC compared with other DE systems is very little [26-35]. For this reason, the main part of this paper will be the discussion of the potentials of FC systems in Jordan. One must not forget that there are no DE in Jordan as the national electricity is isolated until now. The new law for power is under consideration and legal legislations will come to light very soon. The purpose of this paper is to provide a consolidated resource that describes the most common potentials in Jordan. The objective of this paper is looking for the above issues and study these challenges all around the world and special considerations will be given for Poland and Jordan as case studies. The paper layout will be as follows. The next section, after this introduction, will devoted for a theoretical background that contains ΔE_{GHG} , the chance for new technologies in a frame of distributed energy production and the properties of fuel cells. The next part will be about the properties of fuel cell on small scale. Finally, a summery and conclusions will be given.

2. Theoretical background

In this section, a theoretical background will be given. This will include , in addition to the literature review, the explanation of the main important concepts of the subject that will paved the way to this research.

2.1. *The Carbon dioxide(CO_2) concentration:*

In 2007 the announcement of the European Commission concerning the European strategy in frame of power industry was published. It contains the main priorities of energetic politics of EU even to 2050 [36]. That's the moment when the distributed energy production on small scale has a chance of development and serious treatment. This kind of energy production will occur far from heat and power plants, in single houses or their small associations. From the sixties of the last century an association of both systems (energetic and electric) in one entirety is possible.

The Carbon dioxide (CO_2) concentration in atmosphere changes every moment. It is influenced among other things by year's season, geographical position, the number of factories in a city and so on. The maximum of CO_2 concentration occurs in winter, in the states with a great number of conventional power plants. CO_2causes creating of "warm islands" because its specific gravity is bigger than specific gravity of mixture of oxygen with nitrogen (the air) and therefore CO_2 falls on the ground. So installations for measurement of the CO_2 concentration in atmosphere are installed on clean ecologically areas, a long distance from great cities, for example on the Antarctic. The air samples from ice of Antarctic and Greenland show that CO_2 concentration is twice bigger than in atmosphere from before 15 000 Years. Dakowski et. al [37] indicated that average time of CO_2 stay in atmosphere is 10 years, and main methods of its elimination belong to the group of biochemical methods. Perhaps the consequence of it is more violent growth of flora in the area with increased CO_2 concentration than in the other areas. The air samples of ice of Antarctic and Greenland show that CO_2 concentration is twice bigger than in atmosphere from before 15 000 Years. Counteraction of the climate warming according to means among other things emission decreasing of greenhouses gases (GHG). 80 % part of global emission GHG is according to CO_2 from power industry sector [36]. Therefore the EU ,as many other countries, proposes the using of ecological technology, which in consequence brings decreasing of GHG concentration in atmosphere. The EU project in this frame is ambitious. The EU wants in 2020 to achieve CO_2 emission decreasing in industrialized countries to the level of 30% in comparison with the level in 1990. These countries will have to decrease their own emission to 50% in 2050 in comparison with 1990. For Poland this level will be smaller but not smaller than 20 % to 2020 in comparison with 1990. For Jordan there are no formal statistics that indicate the actual figure but clear trend toward emission reduction can be seen.

2.2. *Challenges to be handled*

For both Poland and Jordan, there are a serious challenges and in all of the related sectors as follows.

Firstly, if the energetic sector is considered, these challenges means that it must propagation of new technologies of energy generation. These developments can be as follows:

- the extensive use of renewable sources,
- the use of biofuels,
- looking for a developed sources, that provide in combustion process with low GHG emission,
- improvement of hydrogen combustion and additionally the process should proceed with total steam condensation,
- the use of extensive power plants, that is conventional power plants storing 100% of CO_2 and H_2O from fuel combustion,
- looking for a safe fusion of light elements that so called thermonuclear power industry of the fourth generation.

Secondly, if the transport sector has been taken into considerations, these challenges means:

- propagation of using biofuels
- design and marketing of automotive vehicle with low petrol or gas consumption
- design of hybrid vehicle using conventional and renewable sources of energy.

Finally, if building industry sector is considered, this means:

- use of new building structures with better insulation properties
- improving insulation properties in existing buildings, houses
- application of energy saving technologies using the conventional and unconventional energy sources
- development of technology of warm accumulation.

In general for all of the above sectors, management of energy is crucial. This means working out and designing methods and management structures for observation activities in energetic sector in all around the world in order to introduction of corrections in Internal energetic strategy. The last point is very important. The World wants to stop the global climate warming by observing and eliminating reasons of GHG emissions. The main blame for disadvantageous climatic changes is ascribed to CO_2 and the globe will combat CO_2 sources with the help of all the available means. Meanwhile we know other, more harmful compounds, which are "treated" softer than CO_2. The world standpoint is not profitable for Poland taking into consideration the national energetic strategy because coal is still the main energetic fossil fuel, because the factor objectively assessing the technological process must be found.

2.3. The Greenhouse Gases energy difference (ΔE_{GHG})

The measure of warming up effect for chemical processes or advisable technologic process for example receiving large amount of warm could be a difference of the specific sums of the products consisting of the GHG amount multiplied by its characteristic features in burning products and substrates (ΔE_{GHG}). At ΔE_{GHG} construction we can use the gas factors GWP(G*lobal Warming Potential*) characterizing the ability of each of the gases to warm accumulation in the earth atmosphere in reference to CO_2 ability. The GWP value of any gas depends on the ability of stopping warm and its stay time in atmosphere. If at gas factor isn't given time that means the mentioned time is 100 years. For example $GWP_{100}(CO_2)$=1 means : the CO_2 influence on atmosphere is definite as 1 at its 100 year stay time in the atmosphere. For methane the analogical GWP value is 23. $GWP_{100}(CH_4)$=23. Therefore the influence of methane is 23 times bigger than for CO_2.

It should be emphasized that GWP_{100} (H_2O) is up to now undetermined. In the official announcements of the EU nothing or very little is said about water vapor in spite of the fact that H_2O is the main GHG and occurs in very large quantities in the earth atmosphere. Additionally it has perhaps a big GWP value. It is estimated that H_2O is responsible for from 36%– 60% to 96%-99% of the warming up effect. Scenarios of early phase of life on the earth assume evaporating of large quantities of water in consequence of sun radiation. It would be a cause of appearance of the earth atmosphere with specific composition and increasing of its temperature to the level which was suitable for life. One can propose to form the index informing about "goodness" of a process for the surrounding. The index could assess objectively a chemical or technological processes. For example as in formula (1) :

$$\Delta E_{GHG} = \left(n_{p1}\ GWP_{p1} + n_{p2}\ GWP_{p2} + \ldots\right) - \left(n_{s1}\ GWP_{s1} + n_{s2}\ GWP_{s2} + \ldots\right) \quad (1)$$

where:

n_{pi}, n_{si} are the amounts in kilo moles of products and substrates respectively.

GWP_{pi} GWP_{si} are Global Warming Potential of products and substrates respectively for 100 years stay of gases in the earth atmosphere.

The Formula(1) can be modified with the purpose of inputting the current data important for GHG effect. For example if we want to take into consideration the real stay time in atmosphere of the specific GHG we have to multiply each component by the true time of the gas staying in the atmosphere in years and divide it by 100:

$$\Delta E_{GHG} = \left(n_{p1}\ GWP_{p1}\ \psi_{p1} + n_{p2}\ GWP_{p2}\ \psi_{p2} + \ldots\right) + - \left(n_{s1}\ GWP_{s1}\ \psi_{s1} + n_{s2}\ GWP_{s2}\ \psi_{s2} + \ldots\right) \quad (2)$$

Where

ψ_{pi}, ψ_{si} are (divided by 100) times of staying in atmosphere of GHG, in products and substrates respectively. For the burning of the pure carbon it would be using data taken from reference [37] as:

$$\Delta E_{GHG} = n_{p1} * GWP_1 * \frac{7}{100} = 2 * \frac{7}{100} = \frac{14}{100}$$

The matter is very difficult in case of water vapor. For the uncomplicated chemical reaction :

$$CH_4 + 2O_2 \rightarrow CO_2 + 2H_2O$$

It is not easy to obtain the value ΔE_{GHG} . The cause is difficulties in determination of GWP value for water vapor and its real stay time in atmosphere. Up to now we don't have unequivocal opinion in the matter. We don't know how water vapor influences atmosphere of earth. Its

quantity changes in air seasonally. Excluding the stoichiometry cases we have problems with estimation whether the increase of the quantity of water vapor is in natural way or is it connected with the used technology. In which layers of atmosphere will it diffuse? Additionally we don't know "which " vapor have the greatest influence on the warming up, how much water vapor is in each atmosphere layer and how to count its summary GWP. In any case we know that water vapor quantity increases fast with temperature increasing. So its investigation from the point of view described above should be priority in short future. After them the classification the influence of the processes on surrounding will be easier.

The ΔE_{GHG} factor can have plus or minus value. The second means that the technological process is easy for the surrounding because it will run with elimination of warming climate effect.

2.4. The Properties of Fuel Cells

The following will be a description of few types of fuel cells that helps with a better understanding of this work [Details of fuel cells can be found in many references in the open literature and examples are given in reference [1,26-28, 38-63].

A fuel cell is an electro-chemical device that produces electricity without any intermediate power conversion stage. The most significant advantages of fuel cells are low emission of greenhouse gases and high power density. The energy density of a typical fuel cell is 200 Wh/l, which is nearly ten times of a battery. The efficiency of the fuel cell is also high in the range of 40–60%. If the waste heat generated by the fuel cell is used for cogeneration, the overall efficiency of such a system could be as high as 80% [1]. Fuel cells can be classified into five different categories based on the electrolyte chemistry, including proton exchange membrane fuel cell (PEMFC); solid oxide fuel cell; molten carbonate fuel cell; phosphoric acid fuel cell; and aqueous alkaline fuel cell.

The PEMFCs are rapidly becoming the primary power source in movable power supplies and distributed generation (DG), because of their high energy density, low working temperature, firm and simple structure [1].

One of these cells seems very special and has perhaps " the good future". This is Solid Oxide Fuel Cell (SOFC) with ceramic oxide electrolyte. SOFC have different shapes –flat, tubular [38-40], as shown in figure 1.They have advantages and drawbacks. However the solid electrolyte and work temperature lowering to $500\,^{0}C$ - $600\,^{0}C$ cause a rise of the prospective application range.

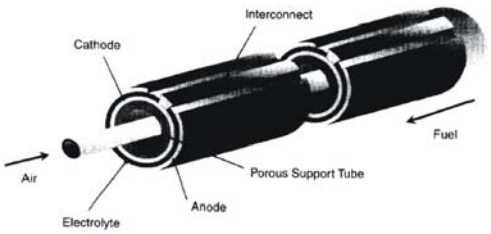

(a) Tubular

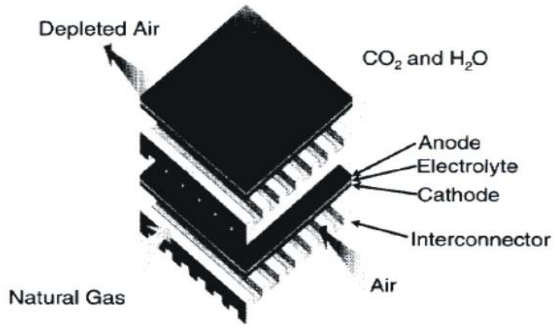

(b) Flat

Figure 1. The different shapes of solid oxide fuel cell (SOFC) [38]

In addition, CO_2 emission would have place only in a case of using fuel gases which contain methane. CO_2 is created as a by-product of oxidation and with water vapour is set off through a fuel canal. A cell tightness makes the CO_2 leading out easy. Presently, we don't know exactly how much CH_4 we need for installing 15-25kW electric power, which is indispensable for a middle class building. The research works connected with an efficiency increase and repeated usage of partly oxidized fuel gases are in progress. The SOFC construction for exploitation in single house and the possibility of a supply with different gases , among other biogas from sewage treatment plants of the houses are a additional trump, because biogases can include up to 60% methane. If CH_4 could be separated from the rest, one could use it theoretically in fuel cells, because SOFC now are very sensitive to sulfur compounds.

Alkaline Fuel Cell(AFC) is the oldest type of fuel cells. Its fast development has initiated from the Second World War. The cells are used for power supply on spaceships in 9 Moon missions (Apollo) and cars as shown in figure 2.

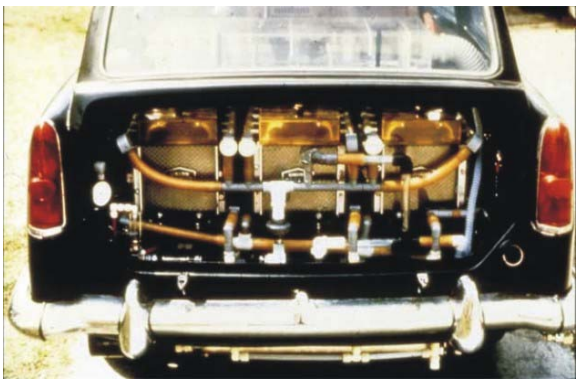

Figure 2. Karla Kordescha's car using fuel cell [41]

AFC electrolyte is KOH whose mass fraction determines the efficiency and work temperature in range $70\,^{0}C$ -$250\,^{0}C$ for power up to 12 kW. If work temperature of fuel cell is over $250\,^{0}C$ the mass fraction is about 85%.A susceptibility to CO_2 attack remains all the time, the technical problem to be resolved.CO_2 reacts with KOH and creates indissoluble salts as shown in equation(3).

$$2KOH + CO_2 \rightarrow K_2CO_3 + H_2O \quad (3)$$

The other problem is the displacement of water for the purpose of confinement of KOH concentration on specific level. The great advantage of AFC is relatively safe electrolyte and good tightness. It is connected with metallic construction which can be used for the sake of the low

work temperature. Reactions on electrode are described by equation (4,5 and 6).

$$A: 2H_2 + 4OH \rightarrow 4H_2O + 4\bar{e} \quad (4)$$

$$K: O_2 + 2H_2O + 4\bar{e} \rightarrow 4OH \quad (5)$$

$$Total: O_2 + 2H_2 \rightarrow 2H_2O \quad (6)$$

Figure3 shows the AFC system building .

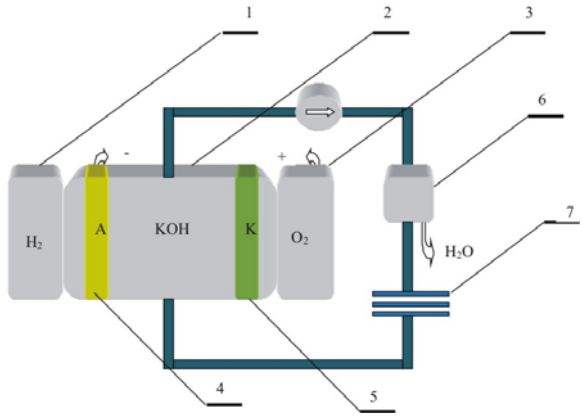

Figure 3. AFC system : 1- hydrogen tank, 2-electrolite, 3-oxygen tank , 4,5-electrode, 6 – water separator , 7- cooler.

Phosphoric Acid Fuel Cell(PAFC) achieves efficiency up to 40%, power up to 1 MW. A work temperature 130^0C - 220^0C. An electrolyte is concentrated H_3PO_4. It is in liquid state in porous silicon carbide. Electrodes are of graphite with platinum additives. Water vapour comes out directly to air and it doesn't thin a electrolyte which is relatively resistant to CO_2. The PAFC advantage is the chance to use hydrogen and natural gas as fuels.

Molten Carbonate Fuel Cell (MCFC) has electrodes from nickel and chromium. A electrolyte contains a molten carbonate of lithium and potassium. The cell is singular because addition of CO_2, for example in biogas, improves the work of cell. The carrying gas used in order to create the flow through the cell and to protect the specific level of CO_3 ions is CO_2. It gives chances to cooperation with conventional power plants on condition of complete separation, storage and dosage of CO_2. This fact is very important both for big power plants and for small systems in buildings. In the second case we can use biogas from biological treatment plant as fuel. A work temperature is high and averages 650^0C. The high temperature permits inner conversion of gases for hydrogen. A reforming of gases takes place in fuel cell directly. An outer installation of conversion like in PAFC isn't necessary. Additionally it excludes expensive catalysts from noble metals because the reaction is self-contained. Therefore costs of production decrease. It is very possible that they can decrease in short time up to 1000 -1500 US$/kW or below.

The membrane is the most important in Proton Exchange Membrane Fuel Cell (PEM, PEMFC). Membranes are chemically inert in both acid and basic environment. A work temperature is low and averages 70^0C -over 200 ^{0}C. Usually it is 120^0C -130^0C. This type of cells becomes resistant to CO. The other method causing increase of CO resistance is growth of work temperature. It influences a better protons ionic conductance without catalysts from platinum. Unfortunately the high temperature is harmful for membrane material. The temperature 200^0C is limiting and connected with thermal strength of membrane material. The development of this cell kind will connect with production of new electrode and catalysts materials , which permits the widening of work temperature range.

The construction of Direct Methanol Fuel Cell (DMFC) evolved from PEMFC .It is resistant to CO poisoning because CO doesn't occur in fuel – methanol. The fuel conversion to hydrogen doesn't occur too. The methanol as liquid is easier to store than gas - hydrogen. However DMFC has disadvantage. Methanol in air oxidizes to carboxylic acid and formaldehyde [42]. Both substances are toxic. They can cause blindness and even death. The big permeability through membrane material causes loss of energy, rated power decreases and its efficiency. The methanol diffusion produces products of methanol burning at both sides of membrane.

2.5. *Properties of fuel cell on small scale*

Technology requirements that must be fulfilled for fuel cell installations on small scale for the purpose of usage in building homes we can divide in some subgroups.

1. Operational safety, including non failure work of installation
2. Long time and low costs of exploitation
3. A possibility of creating hydrogen on place.

Hydrogen is a very lightweight and easy oxidable gas. The oxidation reaction is strongly exothermic. The bottom explosive limit average DGW [H_2]= 4% and the upper-GGW [H_2] =74%.

Some effluent and mixing with air is very dangerous. The small molar mass M H_2=2 kg/kmol causes a fast convection upwards. In rooms it cumulates under ceilings. Air grates should be under ceilings. In the best cases hydrogen tanks should stand in some distance from homes. A Leak proofness protection of a tank with the other fuel, methane is easier, because this gas is denser. The molar mass averages M CH_4=16kg/kmol and it is smaller than that of air. Air grates should be under ceilings too. The bottom explosive limit average DGW[CH_4]=5% and the upper - GGW[CH_4]= 15%. It is for the sake of explosion hazard safer than hydrogen. But after reforming CH_4 we get hydrogen. The place with hydrogen or methane tanks belongs to zone of potential explosion. Therefore non-failure work and specific safety devices are so important. This fact rises production costs.

Methanol as fuel demands a very good ventilation too. It oxidates to toxic compounds both in air and an organism. The leaky tank, cells or fuel pipes will cause health hazard for users of this type of cells.

The most convenient gas as fuel is methane because we know the technology of its storing in pressure vessels. Conversion to hydrogen can proceed in outer installations but it is the best if it will proceed in cells in which the conversion occurs inside, according to equation (7) and (8).

Fuel + water → hydrogen + carbon monoxide (7)

carbon monoxide + water → hydrogen + carbon dioxide(8)

The next method of hydrogen supply for homes is electrolysis of water proceeding in fuel cell in a process opposite to the process of energy production. One should take two possibilities into consideration. The first: on places in home there is one cell , which for some time works as electrolizer . It makes in this time some amount

of hydrogen . The gas is stored up in specific tank. During next portion of time the cell produces energy from hydrogen made earlier. We will need only one cell and installation for hydrogen accumulation. The next possibility is connected with two cells. The first works as electrolizer, the second creates energy. The cells must work synchronously and simultaneously. Hydrogen is created in suitable amount , which is safer . The disadvantage are a high costs of investment.

3. The Chance for New Technologies in A Frame of The Distributed Energy Production

The energetic crisis that people feel more painful from year to year is this moment when distributed energy production on small scale has a chance of development and serious treatment. This kind of power industry will occur far from heat and power plants, in single houses or their small associations. Costly power transmission lines will by needless, which is very positive for country economy. Additionally, the self-sufficient houses will lighten the heat and power plants, which from some time relatively frequently switch off the electric current. But for sector of the economy sector , that means:

1. "The equality of rights" for the conventional and the distributed energy production, which will jointly operate in a frame of the Common Market of Energy; that requires the specific legislative decision.
2. The system economic invitations for owners of houses (housing associations) – for example the expensive innovation should give back in real time (bank credits, taxes)
3. Information campaigns propagating new technologies in a frame of heat and power production.

The devices of the distributed energy production on small scale are these that can supply heat and power. The first ones are well-known and are constituents of hybrid heating systems. In our climatic zone those are heat pumps, fireplaces with water jacket or heat air divisions, pellet furnaces, solar collectors apart from the conventional furnaces using gas or coal .The electric power produce in this system will be more difficult but we can use solar cells for gate-ways or road lightings, small windmills to 3 kW. Usually both methods of energy supplying work in separate system. There are the heat and electric systems. From the sixties an association of both systems in one entirety is possible. This is enabled by fuel cells. The small sets can produce both electrical and heat energy in one place. Presently there are some cells constructions . They differ from each other with anode , cathode , electrolyte constructions, fuel gases and so on. Some cells have achieved market success and they can be used in building engineering in short time. The very important cells are hydrogen-oxygen cells, in which active substances are those two elements. The chemical reaction on the electrode is described with summary equation (9).

$$H_2 + 1/2O_2 \rightarrow H_2O \text{ + electric energy + heat (side-effect of electricity flow)} \quad (9)$$

In this case CO_2 don't occurs in exhaust gases completely but steam creates in big amount. In the moment we can not obtain ΔE_{GHG} of this process.

Power generated by the fuel cell is DC, hence similar to a PV system, the power conditioning systems, including inverters are required in order to supply normal customer load demand or send electricity into the grid. The simplest form of fuel system power electronics configuration, as shown in Fig. 4(a), consists of a fuel cell followed by the DC–AC converter [1]. A DC–DC converter is usually put between the fuel cell and the inverter, as shown in Fig. 4(b). The DC–DC converter performs two functions, one is the DC isolation for the inverter, and the second is to produce sufficient voltage for the inverter input, so that the required magnitude of the AC voltage can be produced. Power electronics costs { 18-40%, 20% for fuel cell} compared to total capital costs for DE system [1].

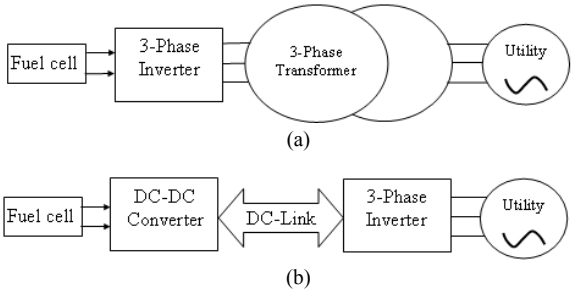

Figure (4) block diagrams of fuel cell systems (a) single inverter and (b) inverter and isolated DC-DC converter [1].

4. Summary and Conclusions

A dispersed energy production has its own group of followers. However bigger and bigger distance between homes and power plants causes the necessity of creation the new electro-energetic system on small scale, on scale of a single home. It is possible due to technical innovations in a frame of energy production , fuel cells among others.

In order to have a chance of adaptation in home's energetic systems fuel cells should be characterized by long-lasting, safe work, resistance to CO, CO_2 poisoning, resistance to other chemical compounds blocking ions flow through cells, safe fuel storage, inexpensive exploitation. The fuel cell having these specific features are DMFC and MCFC presently.

Very important for processes of energy production is obtaining of ΔE_{GHG} value at level near 0. In the main processes occurring in hydrogen-oxygen cells using hydrogen as fuel is created water vapor. In the heat recovery process we can condense H_2O and in the extreme case ΔE_{GHG} =0. In the cells working on methane, methanol can be create CO_2, CO, carboxylic acid and formaldehyde. That's why we have to develop ΔE_{GHG} more deeply. The precondition of the idea is the correct GWP estimation for each gases or chemical compounds and their time of stay in atmosphere. This is especially important in the case of water vapor.

References

[1] S. Chakraborty, B. Kramer, B. Kroposki, "A review of power electronics interfaces for distributed energy systems towards achieving low-cost modular design". Renewable and Sustainable Energy Reviews, Vol. 13, No. 9, 2009, 2323-2335.

[2] G. Pepermans, J. Driesen, D. Haeseldonckx, R. Belmans, W. D'haeseleer, "Distributed generation: definition, benefits and issues". Energy Policy, Vol. 33, No. 6, 2005, 787-798.

[3] C. Bossi, A. Del Corno, M. Scagliotti , C. Valli, "Characterisation of a 3kW PEFC power system coupled with a metal hydride H2 storage". Journal of Power Sources, Vol. 171, No. 1, 2007, 122-129.

[4] J. Paska, M. Sa"ek, T. Surma, "Current status and perspectives of renewable energy sources in Poland". Renewable and Sustainable Energy Reviews, Vol. 13, No. 1, 2009, 142-154.

[5] J. Godefroy, R. Boukhanouf, S. Riffat , "Design, testing and mathematical modelling of a small-scale CHP and cooling system (small CHP-ejector trigeneration)". Applied Thermal Engineering, Vol. 27, No. 1, 2007, 68-77.

[6] K. Alanne, A. Saari, "Distributed energy generation and sustainable development". Renewable and Sustainable Energy Reviews, Vol. 10, No.6, 2006, 539-558.

[7] T. Ackermann, G Andersson, L Söder, "Distributed generation : a definition". Electric Power Systems Research, Vol. 57, No. 3, 2001, 195- 204.

[8] D. Ramirez, L.F. Beites, F. Blazquez, J.C. Ballesteros, "Distributed generation system with PEM fuel cell for electrical power quality improvement". International Journal of Hydrogen Energy, Vol. 33, No. 16, 2008, 4433-4443.

[9]A. Angel, B. Jula "Future development of the electricity systems with distributed generation". Energy, Vol. 34, No. 9, 2009, 377-383.

[10] G.C. Bakos, "Distributed power generation: A case study of small scale PV power plant in Greece". Applied Energy, Vol. 86, No. 9, 2009, 1757-1766.

[11] S. Sanaye, M. R. Ardali, "Estimating the power and number of micro turbines in small-scale combined heat and power systems". Applied Energy, Vol. 86, No. 6, 2009, 895-903.

[12] R.J. Braun, S.A. Klein, D.T. Reindl, "Evaluation of system configurations for solid oxide fuel cell-based micro-combined heat and power generators in residential applications". Journal of Power Sources, Vol. 158, No. 2, 2006, 1290-1305.

[13] S. G. Chalk, F. James. Miller, "Key challenges and recent progress in batteries, fuel cells and hydrogen storage for clean energy systems". Journal of Power Sources, Vol. 159, No. 1, 2006, 73-80.

[14] P. Dondi, D. Bayoumi, Ch. Haederli, D. Julian, M. Suter, "Network integration of distributed power generation,". Journal of Power Sources, Vol. 106, No. 1-2, 2002, 1-9.

[15] D. Rankin, E. Martins, D. C. Walther, "Personal power systems". Progress in Energy and Combustion Science, Vol. 31, No. 5-6, 2005, 422-465.

[16] M.C. Williams, J.P. Strakey, S. Singhal, "U.S. distributed generation fuel cell program". Journal of Power Sources, Vol. 131, No. 1-2 , 2004, 79 - 85.

[17]Y. Ruan, Q. Liu, W. Zhou, R. Firestone, W. Gao, T. Watanabe, "Optimal option of distributed generation technologies for various commercial buildings". Applied Energy, Vol. 86, No. 9, 2009, 1641-1653.

[18] C.E. Hubert, P. Achard, R. Metkemeijer, "Study of a small heat and power PEM fuel cell system generator". Journal of Power Sources, Vol.156, No. 1, 2006, 64 -70.

[19] C. Laia, T. Lin, "Technical assessment of the use of a small-scale wind power system to meet the demand for electricity in a land aquafarm in Taiwan". Renewable Energy, Vol. 31, No. 6, 2006, 877-892.

[20] H. Miland, Øystein. Ulleberg, "Testing of a small-scale stand-alone power system based on solar energy and hydrogen". Solar Energy, Vol. 38, No. 9, 2008, 1815-1822.

[21] W. Lise, "Towards a higher share of distributed generation in Turkey". Energy Policy, Vol. 37, No. 11, 2009, 4320-4328.

[22] M. Mostefaoui, B. Belmadani, A. Babouri and A. Djerdir "Performance System Management: Fuel Cell / Photovoltaic". Global Conference of Renewable Energy and Energy Efficiency of Desert Regions, Amman, Jordan , 2009 .

[23] K. J. Chalvatzis, " Electricity generation development of Eastern Europe: A carbon technology management case study for Poland". Renewable and Sustainable Energy Reviews, Vol. 13, No.6-7, 2009, 1606–1612.

[24] K. Czaplicka, K., Krzysztof Stańczyk, K. Kapusta"Technology foresight for a vision of energy sector development in Poland till 2030. Delphi survey as an element of technology foresighting ". Technological Forecasting & Social Change, Vol. 76, No.3, 2009, 327–338.

[25] M. L. Murray, E. .Seymour, J. Rogut, S.W. Zechowska,"Stakeholder perceptions towards the transition to a hydrogen economy in Poland". International Journal of Hydrogen Energy, Vol. 33, No.1, 2008, 20 – 27.

[26] J. Al Asfar ,M. Hamdan, J. Yamin and Y. Abdullat. "Building and testing of a simple PEM Fuel Cell ". Global Conference of Renewable Energy and Energy Efficiency of Desert Regions, Amman, Jordan , 2009.

[27] J. Al Asfar J, M.Hamdan, and Y.Abdullat ". Theoretical Study of Hydrogen Flow in porous Media of Local Sweileh Sand". Global Conference of Renewable Energy and Energy Efficiency of Desert Regions, Amman, Jordan , 2009.

[28] Z. Abu-Hamatteh, M. Besieso , " Solar Hydrogen and Fuel Cells: A revolutionary and sustainable Source of Energy". Global Conference of Renewable Energy and Energy Efficiency of Desert Regions, Amman, Jordan , 2009 .

[29] E. S. Hrayshat, "Analysis of renewable energy situation in Jordan". Renewable and Sustainable Energy Reviews, Vol.11.No.8, 2007, 1873–1887.

[30] B. A. Akash, M. S. Mohsen, "Current situation of energy consumption in the Jordanian industry". Energy Conversion and Management, Vol. 44, No. 9, 2003, 1501–1510.

[31] J.O. Jaber, M.S. Mohsen, A. Al-Sarkhi, B.A. Akash, "Energy analysis of Jordan's commercial sector". Energy Policy, Vol. 31 No.9, 2003, 887–894.

[32] J.O. Jaber, S.D. Probert, "Purchased-energy consumptions in Jordan's commercial and public-service sector". Applied Energy, Vol. 71, No. 1, 2002, 31–43.

[33] A. Al-Ghandoor, J.O. Jaber, I. Al-Hinti, I.M. Mansour, "Residential past and future energy consumption: Potential savings and environmental impact". Renewable and Sustainable Energy Reviews, Vol. 13, No. 6-7, 2009, 1262–1274.

[34] E. S. Hrayshat, " Viability of solar photovoltaics as an electricity generation source for Jordan". Renewable Energy, Vol. 34, No. 10, 2009, 2133–2140.

[35] E. S. Hrayshat," Wind availability and its potentials for electricity generation in Tafila, Jordan". Renewable and Sustainable Energy Reviews, Vol. 9, No.1, 2005, 111–117.

[36] The announcement of the European Commission concerning the European strategy in frame of power industry. EUR 20245 EN, 2002.

[37] M. Dakowski, A. Wysokinski, " Climate change, greenhouse effect, whether human intervention". www.rurociagi.com.

[38]S. Badwal, K. Foger, K. " Solid Oxide Electrolyte Fuel Cell Review". , Ceramics International, Volume. 22, No. 3, 1996, 257-265.

[39] B.Frederic , Fuel cells , engines and hydrogen an energy approach. 3rd ed. John Wiley &Sons,LTD; 2006.

[40] Wojcik,W, "New directions manufacture and use of energy". Sustainable Systems Eenergy, Lublin Technical University, Technical Report, Poland, 2005.

[41] website , http://www.oeiizk.waw.pl.

[42] Sorsen , B., Hydrogen and Fuel Cells, Emerging technologies and applications,. "Sustainable World" series, Academic Press, 2005.

[43]W. J. Fergus, " Oxide anode materials for solid oxide fuel cells". Solid State Ionics, Vol. 177, No. 17-18, 2006, 1529–1541.

[44] N. Q. Minh, "Review: Solid oxide fuel cell technology—features and applications". Solid State Ionics, Vol. No.1-4, 174, 2004, 271–277

[45] A. Pramuanjaroenkij, S. Kakac, X.Yang. Zhou, "Mathematical analysis of planar solid oxide fuel cells". International Journal Of Hydrogen Energy, Vol. 33, No.10, 2008 , 2547 – 2565.

[46] B.D. Madsen, S. A. Barnett , "Effect of fuel composition on the performance of ceramic-based solid oxide fuel cell anodes". Solid State Ionics, Vol. 176, No. 36-36, 2005, 2545 – 2553.

[47] K. Eguchi, H. Kojo, T. Takeguchi, R. Kikuchi, K. Sasaki, "Fuel flexibility in power generation by solid oxide fuel cells". Solid State Ionics, Vol. 152–153, No.1- 4, 2002, 411 –416.

[48] Ch.Suna, U. Stimming , " Review: Recent anode advances in solid oxide fuel cells". Journal of Power Sources, Vol. 171, No. 2, 2007, 247–260.

[49] Q.Hu, Sh. Wang, T.L. Wen , " Analysis of processes in planar solid oxide fuel cells". Solid State Ionics,Vol. 179, No. 27-32, 2008, 1579–1587.

[50] F. Zink, Y.Lu, L. Schaefer , " A solid oxide fuel cell system for buildings". Energy Conversion and Management, Vol. 48, No. 3, 2007, 809–818.

[51] J. W. Fergus, " Electrolytes for solid oxide fuel cells". Journal of Power Sources, Vol. 162, No. 1, 2006, 30–40.

[52] A. B.Stambouli, E. Traversa, " Solid oxide fuel cells (SOFCs): a review of an environmentally clean and efficient source of energy". Renewable and Sustainable Energy Reviews, Vol. 6, No. 5, 2002, 433–455.

[53] P. Tomczyk , " MCFC versus other fuel cells—Characteristics, technologies and prospects". Journal of Power Sources, Vol.160, No. 2, 2006, 858–862.

[54] F. Bidault, D.J.L. Brett, P.H. Middleton, N. Abson, N.P. Brandon, " A new application for nickel foam in alkaline fuel cells ". International Journal of Hydrogen Eenergy, Vol. 34 , No. 16, 2009, 6799 – 6808.

[55] T. Burchardt, P. Goue´rec, E.Sanchez-Cortezon, Z. Karichev, J. H. Miners, " Alkaline fuel cells: contemporary advancement and limitations". Fuel, Vol. 81, No. 17, 2002, 2151–2155.

[56] B. Y.S. Lin, D. W. Kirk, S. J. Thorpe," Performance of alkaline fuel cells: A possible future energy system". Journal of Power Sources, Vol. 161, No.1, 2006, 474–483.

[57] C. Coutanceau, L. Demarconnay, C. Lamy, J.-M. L´eger, "Development of electrocatalysts for solid alkaline fuel cell (SAFC) ". Journal of Power Sources, Vol. 156, No. 1, 2006, 14–19.

[58] D. Mori, K. Hirose , " Recent challenges of hydrogen storage technologies for fuel cell vehicles". International Journal of Hydrogen Energy, Vol. 34, No. 10, 2009, 4569–4574.

[59] N. Rajalakshmi, S. Pandiyan, K.S. Dhathathreyan, "Design and development of modular fuel cell stacks for various applications". International Journal of Hydrogen Energy, Vol. 33, No. 1, 2008, 449 – 454.

[60] C.E. Hubert, P. Achard, R. Metkemeijer, " Study of a small heat and power PEM fuel cell system generator". Journal of Power Sources, Vol. 156, No.1 , 2006, 64–70.

[61] J.g.Wu, X. Z. Yuan, J. J. Martin, H.Wang, J. Zhang, J. Shen, Sh. hongWu,W.Merid, " A review of PEM fuel cell durability: degradation mechanisms and mitigation strategies". Journal of Power Sources, Vol. 184, No. 1, 2008, 104–119.

[62] Sh. Obara, I. Tanno, " Exergy analysis of a regional-distributed PEM fuel cell system". International Journal of Hydrogen Energy, Vol. 33, No. 9, 2008, 2300–2310.

[63] J. E. Brown, C. N. Hendry, P. Harborne, " An emerging market in fuel cells, Residential combined heat and power in four countries". Energy Policy, Vol. 35, No. 4, 2007, 2173–2186.

JJMIE

Volume 4, Number 1, Jan.. 2010
ISSN 1995-6665
Pages 143 - 150

Jordan Journal of Mechanical and Industrial Engineering

Modelling and Optimisation of Wind Energy Systems

A. Benatiallah, L.Kadi [a,*] , B. Dakyo [b]

[a] *Labo Energie et environnement et systeme d'information, Université d'Adrar, Algeria.*

[b] *labo énergie & environnement, université de Mostaganem, Algérie,* [b] *Labo GREAH, University of Havre, France*

Abstract

This paper presents the study of methodology for calculation the optimum size of a Wind system. A Long term data of wind speed for every hour of the day were used. These data were used to calculate the average power generated by a wind turbine for every hour of a typical day in a month. A load of a typical house in south of Algeria(desert area) was used as a load demand of the system. For a given load and a mixed multiple-criteria integer programming problem, the types and sizes of wind turbine generators (WTG) was calculated based on the minimum cost of system. In our research, we investigated the genetic algorithm (GA) for optimally sizing a wind power system.
We define that the objective function is the total cost, where the total cost is the sum of initial cost, an operation cost, and a maintenance cost. We determine an optimal configuration of wind generating systems, where total cost is more optimal using GA. A computer program has been developed to size system components in order to match the load of the site in the most cost. A cost of electricity, an overall system cost is also calculated for each configuration. The study was performed using a graphical user interface programmed in MATLAB

Keywords: Wind System; Optimal Configuration; Genetic Algorithm; Programming, Modelling,.

1. Introduction

The rapid depletion of fossil-fuel resources on a world has necessitated search for alternative energy sources. Wind energy has been considered as promising toward meeting the continually increasing demand for energy. The wind sources of energy are inexhaustible, the conversion processes are pollution-free, and their availability is free. For isolated systems such as rural electrification, the wind energy has been considered as attractive and preferred alternative sources.

Generally the main objectives of the optimization design are power reliability and cost.

In this paper an optimal sizing method using the genetic algorithm (GA) is proposed. The types and sizes of wind turbine generators, the highly of turbine can be optimized when sizing a standalone wind power system, which may be defined as a mixed multiple-criteria integer programming problem.

We propose the optimum configurations for wind generating systems in residences using hourly data over a year. We assume that a residence is one house consuming average electrical energy in south of Algeria (Sahara area). Genetic algorithm (GA) is used as an optimization method in this paper. The purpose of this study is to minimize the objective function of GA. The objective function is the total cost, which is the sum of initial cost, operation cost, and maintenance cost per year.

Minimizing the total cost, we can achieve an inexpensive and clean electric power system. In addition, the proposed method can adjust the variation in the data of load, location.

An alternative methodology for the optimal sizing of stand-alone Wind systems is proposed. The purpose of the proposed methodology is to suggest, among a list of commercially available system devices, the optimal number and type of units ensuring that the 20-year round total system cost is minimized subject to the constraint that the load energy requirements are completely covered. The 20- year round total system cost is equal to the sum of the respective components capital and maintenance costs. The decision variables included in the optimization process are the number and type of Wind turbine, the installation height of the WGs. The minimization of the cost (objective) function is implemented employing a genetic algorithms (GA) approach, which compared to conventional optimization methods, such as dynamic programming and gradient techniques, has the ability to attain the global optimum with relative computational simplicity.

* Corresponding Author. benatiallah@univadrar.org

The cost improvement of a wind system varies with the location and cost ratios of the wind power systems, and electrical machine. The present work provides the results of a study on the optimization of a wind system to meet a certain load distribution demand in the city of Bechar, Algeria. The method is applied to the satisfaction of a domestic load demand

2. System Configuration

The configuration of standalone wind power systems is shown in Figure 1. In this paper, we investigated the case that a system has permanent magnet synchronous generator (PMSG) directly coupled to the wind turbine shaft of the wind energy conversion chain.

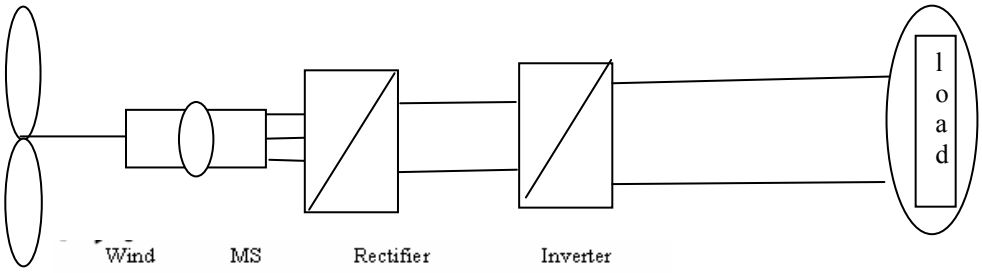

Fig 1. Wind power systems.

3. Modelling Of Wind Energy System Components

Various modelling techniques are developed by researchers to model components of Wind system. Performance of individual component is either modelled by deterministic or probabilistic approaches [1]. General methodology for modelling wind system components like wind turbine, machine generator, and inverter is described below:

3.1 MODELING OF THE WIND SPEED

The wind speed is one of the most important variables in the modeling of a wind energy conversion chain and is the main input variable in the chain synoptic diagram. Consequently, the simulation's accuracy depends on the representation of wind speed. Unfortunately, it has a random behavior inducing a fluctuating characteristic. So, in order to reproduce accurately the wind speed dynamic behavior, two approaches can help us. The first consists in considering measurements of long duration on an actual wind site and the second consists on representing the wind characteristic by an analytical model. The first solution is obviously more precise. Nevertheless, it does not easily permit to simulate various types of configurations of wind sites.

The speed of wind is a random process; therefore it should be described in terms of statistical methods.

The windspeed data were recorded near the ground surface. To upgrade wind speed data to a particular hub height, the following equation is commonly used:

$$v = v_i \cdot \left(\frac{h}{h_i} \right)^{\alpha}$$

Where:v: wind speed at projected height, $\boldsymbol{h}$
v_i: wind speed at reference height, $\boldsymbol{h_i}$
$\boldsymbol{\alpha}$: power-law exponent (- 1/7 for open land).
The wind speed distribution is assumed to be a Weibull distribution. Hence the probability density function is given by

$$f(v) = \frac{k}{c} \cdot \left(\frac{v}{c} \right)^{k-1} \cdot \exp\left[-\left(\frac{v}{c} \right)^{k} \right]$$

Where: c : scale factor, unit of speed
k : shape factor, dimensionless
v : wind speed.
The wind speed distribution functions were calculated for each hour of a typical day in every month

3.2 Modeling of the Wind Turbine

The mechanical quantities which will connect the wind turbine with the generator are the wind turbine torque and the rotational speed on the shaft. It should be noticed that the torque depends on the rotational speed. The wind turbine modeling consists on modeling the torque induced by the blades.
The available maximum wind power for a given wind speed is expressed by [1]:

$$S = \pi R^2$$

Where
ρ is the air density, R the blade radius and S the frontal area of the wind turbine.
This maximum power is defined by global aerodynamic coefficients. These two coefficients are bond by the following relation:

$$\lambda = \frac{R\Omega}{v}$$

Where
λ is the tip speed ratio, Ω the rotational speed of the shaft, C_p the power coefficient and C_Γ the torque coefficient.
The power and the wind turbine torque are then given by

$$P_t = P_w C_p = \tfrac{1}{2} \rho \pi R^2 v^3 C_p$$

$$\Gamma_t = \frac{P_t}{\Omega} = \tfrac{1}{2} \rho \pi R^3 v^2 C_\Gamma$$

If the power or torque coefficient is provided by the manufacturer, modeling can be made by a N order polynomial regression [1]:

$$C_\Gamma(\lambda) = a_0 + \sum_{i=1}^{N} a_i \lambda_i \quad (1)$$

The figure illustrates the wind speed torque obtained by modeling with 6 order polynomial regression. The inconvenient of this type of modeling resides on the fact that it does not make it possible to vary the blade pitch angle. The torque model obtained depends only on the wind speed and the shaft rotational speed

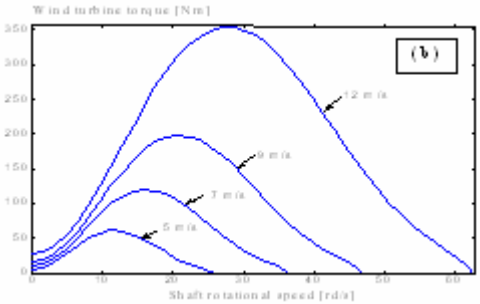

Figure 2 . wind turbine torque versus shaft speed rotational .

This type of modeling is computational time consuming. However, it allows parametric studies of the variation of the blade pitch angle of the turbine. In this case, the torque depends on three quantities: the wind speed, the rotational speed of the shaft and the blade pitch angleβ.

$$\text{where } [v_g] = \begin{bmatrix} v_a \\ v_b \\ v_c \end{bmatrix}; \ [i_g] = \begin{bmatrix} i_a \\ i_b \\ i_c \end{bmatrix};$$

$$[\Phi_A] = \Phi_M \begin{bmatrix} \sin(\theta) \\ \sin(\theta - 2\pi/3) \\ \sin(\theta + 2\pi/3) \end{bmatrix};$$

$$[r_g] = \begin{bmatrix} r_s & 0 & 0 \\ 0 & r_s & 0 \\ 0 & 0 & r_s \end{bmatrix}; \ [l_g] = \begin{bmatrix} l & m & m \\ m & l & m \\ m & m & l \end{bmatrix}$$

v_g is the stator voltages, i_g the stator currents, Φ_A the permanent magnet flux, θ the angular position, Φ_M the amplitude of the flux linkages established by a permanent magnet r_s the stator resistances, l the main stator phase inductance and m the stator mutual inductance between two stator phases.

To the previous equations, one must add the mechanical equation of the generator shaft

$$\frac{d\Omega}{dt} = \frac{p}{J}\left(\Gamma_t - \Gamma_{em} - f\,\Omega\right)$$

3.4 Modeling of the Static Converters

The static inverter used is a full wave three-phase voltage inverter (Figure) [ ]. Each switch is made up of IGBT in antiparallel with a free wheel diode. The switches are admitted as ideals, thus as in the case of the rectifier, their conduction correspond to a short circuit and their blocking corresponds in its turn to an open circuit. On the other hand, the overlapping is taken here into account. The following figure represents the inverter feeding a three-phase load which has Z_{ch} impedance.

At the output of the inverter, one obtains the three-phase and symmetrical voltage systems. The theory of the three-phase and symmetrical systems shows that the voltages and the currents of these systems have the

following properties:

$$\mathbf{i_{ach} + i_{bch} + i_{cch} = 0 \ ; \ u_{ab} + u_{bc} + u_{ca} = 0}$$

$$v_{cch} = \frac{u_{ca} - u_{bc}}{3} \qquad v_{bch} = \frac{u_{bc} - u_{ab}}{3} \qquad v_{ach} = \frac{u_{ab} - u_{ca}}{3}$$

i_{jch} and v_{jch} are respectively the load currents and load voltages where $j = a, b, c$.

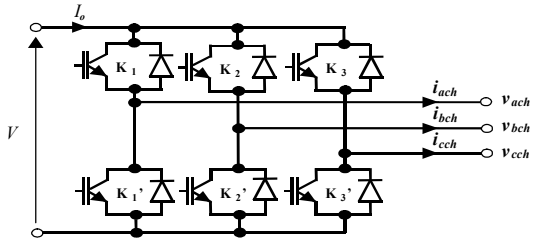

Figure 3. Electric scheme of the inverter.

$K_i = (T_i, D_i)$, $K_i' = (T_i', D_i')$, i = 1, 2, 3 and I_0 is the inverter input current Modeling of the wind energy converter

This part consists on implementing the wind energy converter (Figure1) by connecting the studied components. For that, the below equations are established in order to supplement the previous established equations.

The generator is connected with the rectifier by the following equation

$$\frac{dI}{dt} = \frac{1}{2(l-m)}\left(-\frac{d\Phi_{+A}}{dt} + \frac{d\Phi_{-A}}{dt} - 2rI - V\right)$$

Φ_{+A} and Φ_{-A} corresponds respectively to the PM flux passing by the stator phases which has the most positive potential and the most negative potential.

A filtering capacity is placed in the continues part, between the rectifier and the inverter. This is expressed as follows:

$$\frac{dV}{dt} = \frac{1}{C}\left(I - I_0\right)$$

The input inverter current is then obtained by this equation. For each case, this current is equal to the load current which corresponds to the load voltage which has the most positive potential (absolute value).

4. Optimal Sizing Using the Genetic Algorithm

4.1. Cost Analysis

A global cost model of a wind system has been derived from cost models of all the components for the wind

installation and of some other project costs. For most of the components the models are derived from electrical design laws and from the calibration of these models. For the generator and electrical equipment the price is derived from the value of the nominal power. The total wind system cost is the sum of all the costs, and a calibration factor F_{act} allows us to use real wind costs and take into account some unknown project parameters such as the manufacturer's margins [2]

$$C_{PV} = F_{act} \times \sum_{i} C_i$$

$$i : component$$

The evaluation of the total cost of a project must take into account some additional costs due to:

Land purchase and development of the site;
Transport of the wind generator;
Installation of the wind module;
Foundations building;
Financing and insurance;
Miscellaneous costs (engineering, unexpected costs, etc.).

The economic study should be made while attempting to optimize the size of integrated power generation systems favouring an affordable unit price of power produced. The economic analysis of the wind system has been made and the cost aspects have also been taken into account for optimization of the size of the systems.

The total cost of system takes into account the initial capital investment, the present value of operation and maintenance cost, the inverter replacement cost and the wind system replacement cost. The lifetime of the system is assumed to be 20 years.

The total system cost function is equal to the sum of the total capital, $C_c(x)$ (€), and maintenance cost, $C_m(x)$ (€), is given as follows [14]:

$$C_T = C_c + C_m + Co$$

Where Co *is* the total constant costs including the cost of power conditioning equipment, design and installation etc.

The initial capital investment for the integrated system, C_1 is given as

$$C_1 = N_w.C_w + N_w.h.C_h + C_{inv}\ (X_{inv}+1) + C_o$$

Where N_w : total number of WG

C_w : the capital costs (€) of one WG, h are the WG tower height limits (m)

C_h is the WG tower capital cost per meter (€/m) , C_o : other cost of installation.

The annual cost for all components that do not need certain items replaced is found by multiplying the total initial cost by the capital recovery factor (C_{RF}). The C_{RF} is defined as

$$C_{RF} = \frac{\left[i(1+i)^n\right]}{\left[(1+i)^n - 1\right]}$$

Where i is the annual interest rate (5% in this study) , n is the lifetime of the component.

The operation and maintenance cost is calculated as follows[3]:

$$C_2 = \frac{\beta(P_m)}{8766}.t + \sum_{0}^{t} \gamma(x(\tau)).\nabla\tau$$

Where β , γ maintenance and operation coefficients, for 20-year system lifetime

$C_2 = 20.C_{mw} + 20.h.C_{hm}) + C_{m\_inv}(20\text{-}X_{inv}\text{-}1)$.

Where C_{mW} are the maintenance costs per year (€/year) of one WG

C_{hm} is the WG tower maintenance cost per meter and year (€/m/year), X_{INV} are the expected numbers of DC/AC inverter replacements during the 20-year system lifetime, CINV is the capital cost of the DC/AC inverter, (€),

C_{m_INV} maintenance costs per year (€/year) of one DC/AC inverter

The optimization procedure is to determine the sizes of wind system, then to use the GA to compute the type and sizes of Wind Turbine and higher, and then to recalculate the optimal fixed system configuration

4.2. The Genetic Algorithm

The GA is a stochastic global search method that mimics the metaphor of natural biological evolution and does not require derivative information or other auxiliary knowledge [4].

Genetic algorithms are very different from traditional search and optimization methods used in engineering design problems. Fundamental ideas of genetics in biology are borrowed and used artificially to construct search algorithms that are robust and require minimal problem information. A typical constrained, single variable optimization problem can be outlined as follows:

Maximise $_x$ or Minimise $_x$ f(x)

Subject to the constraint: $x_{\min} \le x \le x_{\max}$

For the solution of such a problem with GAs the variable x is typically coded in some string structures. Binary-coded or floating point strings can also be used, while the length of the string is usually determined according to the accuracy of the solution desired. The GA, as any evolution procedure for a particular problem, must have the following components (Michalewicz, 1994)[5]:

• A generic representation for potential solutions to the problem, similar to the system modelling presented in the previous section.

• Genetic operators (such as crossover and mutation) that alter the composition of children. In the proposed method, the GA optimal sizing methodology outputs the optimum number of WGs, WGs installation height and comprising the set of decision variables, such that the 20-year round total system cost itial population of potential solutions.

• An evaluation function that plays the role of the environment, rating solutions in terms of their ''fitness '' and function.

Multi-objective optimization is achieved by minimizing the total cost function consisting of the sum of the individual system devices capital and 20-year round maintenance cost:

$C_T = N_w.C_w + N_w.h.C_h + C_{inv}\ (X_{inv}+1) + 20.C_{mw} + 20.h.C_{hm}) + C_{m\_inv}(20\text{-}X_{inv}\text{-}1) + C_o$

$$F(N_w, h) = \min\{C_T(N_w, h)\}$$

Subject to the constraints

$$N_w \geq 0$$

$$h_{max} \leq h \leq h_{min} \qquad \forall t \in [0, t]$$

$$P_{cons} = \eta[P_w].P_w \quad [\quad]$$

And $$|P_{cons}| \leq P_w$$

Where h_{max}, h_{min} are the WG tower upper and lower height limits (m), respectively, specified by the WG manufacturer, P_{cons} the load consumption , P_w the wind power production[6]

The flowchart of the GA optimization process is depicted in Figure4. An initial population of 50 chromosomes, comprising the 1st generation, is generated randomly and the constraints described by inequalities ( ) are evaluated for each chromosome. If any of the initial population chromosomes violates the problem constraints then it is replaced by a new chromosome, which is generated randomly and fulfils these constraints. The first step of the algorithm iteration is the fitness function evaluation for each chromosome of the corresponding population. If any of the resulting

fitness function values is lower than the lowest value obtained at the previous iterations then this value is considered to be the optimal solution of the minimization problem and the corresponding chromosome consists of the hybrid system optimal operational parameter values. This optimal solution is replaced by better solutions, if any, produced in subsequent GA generations during the program evolution. In order to select the chromosomes, which will be subject to the crossover and mutation operations in order to produce the next generation population, a selection operation is applied based on the roulette wheel method (Michalewicz, 1994). The crossover mechanism uses the Simple Arithmetical Crossover with initial probability psac = 85%.[7],[8]

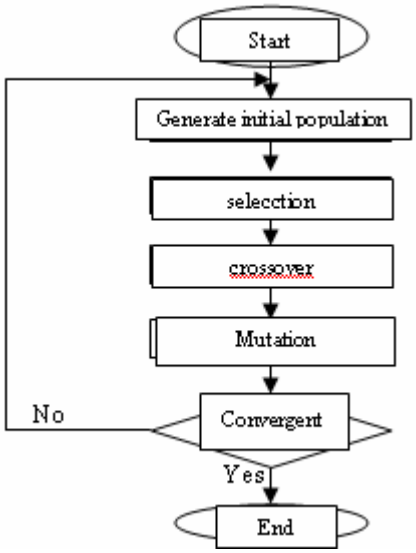

Figure 4 Flowchart of GA.

Next, the selected chromosomes are subject to the mutation mechanism: Uniform Mutation, a gene is randomly selected and it is assigned a new value, randomly selected from the corresponding range of values which fulfil the optimization problem constraints. This range of values is calculated for the selected gene, considering the values of the other genes within the chromosome constant. The mutation probability, P_m is 5.[9]

In case that the application of the crossover or mutation operators, results in a chromosome which does not satisfy the optimization problem constraints, then a ‘‘repair’’ procedure is performed and that chromosome is replaced by the corresponding parent. In case of SC operation, where each new chromosome is generated by two parents, then the chromosome is replaced by the parent with the best fitness function value. The GA optimization process described above is repeated until a predefined number of population generations have been evaluated

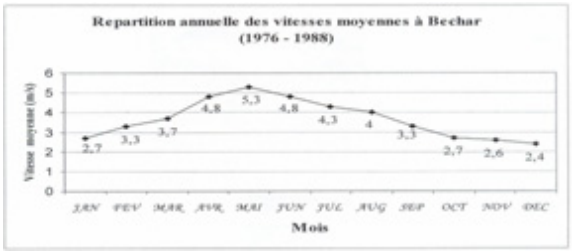

Fig .5: Wind speed in Bechar area.

5. Simulation Results

The proposed method has been applied to the design of a stand alone wind system in order to supply a house located in the south of Algeria (Bechar, Sahara area).

The crossover rate is 0.85. The mutation rate is 0.05. Number of possible different wind types is 3, number of inverter types is 2. The wind turbine lifetime is 15 years. The inverter lifetime is 6 year. The effective interest rate considered is 3%. The wind price (< $5kw_c$) is 10 Euro/w_c. The O&M cost of wind is 1 c€/Wc/year. The cost of the invertors is given related to power [10],[11],[12]

The developed method was used to calculate the optimum number of wind turbine and titles for a stand-alone wind system of the Bechar cite, Algeria. Wind speed data for Bechar obtained from the National Meteo ONM were utilized. The Simulation was specified at the value of 1 year. The load of typical house in Bechar cite, profile plot is shown in Figure6.[13]

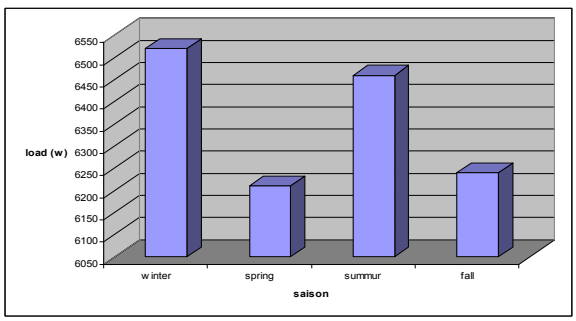

Figure 6 Load profile for all seasons.

highest load demand values occur in winter. Therefore, the higher of the wind generator was optimising for winter

for the considered site. With the use of the program described in the former section, we calculated a series of possible combinations of the number of wind, higher and inverter. For a given unit price of turbine and machine, an optimum solution that minimizes the cost of the system was found. The optimum numbers of wind and higher as indicated in Figure7.

The numbers of wind turbine and higher are determined previously. The GA's results are [1.3, 11] with the total capital cost of wind system as 4715 Euro. The type wind turbine yields the lowest cost for the system.

The optimal configuration is [2, 11]. The cost of Power Supply in the simulation is shown in Figure7, and this is in accordance with the situation that both the solar energy and wind energy are abundant in summer at this location.

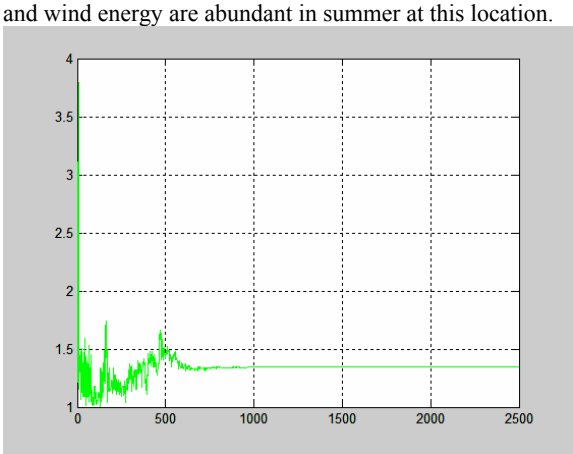

(a)

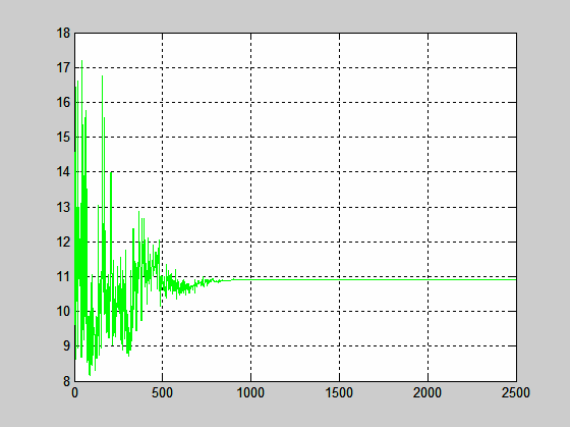

(b)

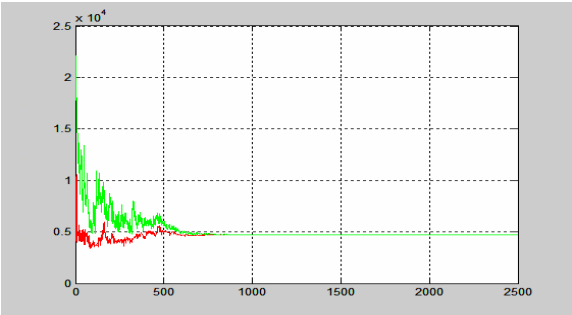

(c)

Figure7 a.optimal number of wind, b. higher of turbine, c. Total cost.

6. Conclusions

A methodology of sizing standalone wind power systems using the genetic algorithm is proposed in this paper. Studies have proved that the genetic algorithm converges very well and the methodology proposed is feasible for sizing standalone wind power systems.

A procedure for optimizing the size of a wind-energy system was presented. The procedure was applied for the sizing of wind system that is considered to produce a power to domestic load in the Bechar area, Algeria. The analysis indicates that a wind system power output can be optimized to suit specific applications with variable or constant power loads. For the specific system considered in this study, the results indicate that the optimal wind system that resulted in the minimum capital cost is (2, 11).

References

[1] J.K. Kaldellis, G.Th. Vlachos, "Optimum sizing of an autonomous wind–diesel hybrid system for various representative wind-potential cases", Applied Energy 83 ,2006, 113–132.

[2] S.R. Vosen, J.O. Keller, "Hybrid Energy Storage Systems for Stand-Alone Electric Power Systems: Optimization of System Performance and Costs Through control Strategies," *International Journal of Hydrogen Energy*, Vol 24, No. 12, 1999, 102-106.

[3] Th.F. El-Shatter, M.N. Eskandar, M.T. El-Hagry, "Hybrid PV/Fuel Cell System Design and Simulation," *Renewable Energy*, 2002, Vol. 27, No. 3.

[4] M. Wang, M. H. Nehrir, D. B. Nelson, "A Simulink-Based Model for a Stand-Alone Wind-Photovoltaic/Fuel Cell Generating System", *Proceedings*, NAPS 2001, Texas A&M University, College Station, October 15-16.

[5] F. Giraud, Z.M. Salameh, "Steady-State Performance of a Grid-Connected Rooftop Hybrid Wind-Photovoltaic Power System with Battery Storage," *IEEE Transactions on Energy Conversion,* Vol. 16, No. 1, 2001.

[6] W.D. Kellogg, M.H. Nehrir, G. Venkataramanan, V. Gerez, "Generation Unit sizing and Cost Analysis for Stand-Alone Wind, Photovoltaic, and Hybrid Wind/PV Systems," *IEEE Transactions on Energy Conversion*, Vol. 13, No. 1, 1998.

[7] R. Chedid, H. Akiki, S. Rahman, "A Decision Support Technique for the Design of Hybrid Solar-Wind Power Systems", *IEEE Transactions on Energy Conversion,* Vol. 13, No. 1, 1998.

[8] M.T. Iqbal, "Simulation of a Small Wind Fuel Cell Hybrid Energy System," *Renewable Energy*, Vol. 28, No. 4, 2003.

[9] A N Celik, Optimization and Tecno-Economic Analysis of Autonomous Photovoltaic Wind Hybrid Energy Systems in Camparison to Single Photovoltaic and Wind Systems, Energy Convers Manage , Vol. 43, No. 18, 2002, 2453-2468.

[10] A.N. Celik, Techno-economic Analysis Of Autonomous PV-Wind Hybrid Energy Systems Using Different Sizing Methods, Energy Conversion and Manage, Vol.44, 2003, 1951-1968.

[11] M.K. Deshmukh, S.S. Deshmukh «Modeling of hybrid renewable energy systems», Renewable and Sustainble Energy Reviews, Vol. 12, No. 1, 235-249**,** 2008.

[12] K.Eftichios and all, Methodology For Optimal Sizing Of Stand- Alone Photovoltaic/Wind-Generator Systems Using Genetic Algorithms » Solar Energy, Vol. 8, 2006, 1072-1088,.

[13] Y. Himri, A .Boudghene Stambouli, B .Draoui, S .Himri. « Techno-Economical Study Of Hybrid Power System For A Remote Village In Algeria », Energy.Vol. 33, 2008, 1128–1136,

[14] F .Youcef Ettoumi and all, Comparative Simulation Of Wind Park Design And Setting In Algeria, Renewable Energy, Vol. 33, 2008, 2333–2338.

[15] Tsung-Ying Lee, Short term hydroelectric power system scheduling with wind turbine generators using the multi-pass iteration particle swarm optimization approachEnergy Conversion and Management, Vol. 49,No. 4, 2008, 751-760.

[16] Hongxing Yang, Lin Lu, Wei Zhou, A novel optimization sizing model for hybrid solar-wind power generation system Solar Energy, Vol. 81, No.1, 2007, 76-84.

JJMIE

Volume 4, Number 1, Jan. 2010
ISSN 1995-6665
Pages 151 - 154

Jordan Journal of Mechanical and Industrial Engineering

New Method for Quality Evaluation of Mc-Si Wafers Implied in the Fabrication of Photovoltaic Cells

Mohamed FATHI *, Ahmed CHIKOUCHE

UDES, Solar Equipments Development Unit

Route National N11, Bouismaïl, BP 386, 42415 Tipaza, ALGERIA

Abstract

We have developed a new method for quality evaluation of mc-Si wafers implied in the fabrication of photovoltaic cells. This method is based on the exploitation of the variation of the sheet resistance ($\Delta R\square$) of chemically etched wafers. We have presented specific classification connecting directly $\Delta R\square$ bands to the crystalline defect types and densities. These results are in good accordance to physically observed defect density and grain boundaries repartition. Previously, with special process experimentation, we have shown that the best sensitivity to crystalline extended defects in mc-Si material is supported by the "Secco Etch" chemical solution. This chemical is very sensitive to crystalline defects and was applied to the development of our new characterization method of mc-Si wafers.

Keywords: Multicrystalline Silicon Wafers; Crystalline Defect Density; Four Probes Technique; Chemical Delineation; Photovoltaic.

1. Introduction

Crystalline extended defects of a mc-Si wafer can affect various aspects of photovoltaic cells manufacturing, from device performance to production yield [1]. Indeed, the presence of crystalline defects and impurities leads to losses of energetic efficiency in the photovoltaic cells [2]. Many investigations have shown that the final electrical properties of these devices are directly correlated with the crystalline defect density in the bulk material [3, 4]. This study has two main objectives. The first one was the selection of a more sensitive chemical agent in order to localize, identify and calculate the crystalline defect density. The second one was the implementation of a new technique for the identification and mapping of crystalline defect density on the whole mc-Si wafer area, all in one step. The mc-Si ingots analyzed here have been produced in our laboratory by the Heat Exchanger Method (HEM) [5].The Observation with an optical or a scanning electron microscope (SEM) of the crystalline extended defects (dislocations, stacking faults, twins, precipitates, etc...), requires a chemical etch called delineation step [6]. Several chemical solutions such as, Dash, Sirtl, Secco, Yang, Wright etc.., are commonly used for silicon defect delineation. However, the defect delineation process depends on silicon surface crystallographic orientation and topography [7]. The first used etch was Dash Etch which reveals dislocations in all crystallographic orientations but necessitates very long etching times [8]. Sirtl reveals dislocations only on (111) surfaces [9]. Secco etches defects in all orientations and gives circular defect pits [10]. Yang solution gives good defect delineation in all orientations and its etch pit shapes (triangular, quadratic, etc...) are function of surface orientation [11, 12]. Wright etch [13] is widely used in the semiconductor failure analysis field and especially for high temperature induced defect analysis; it is effective in all orientations but its composition is more complex than Secco and Yang. Furthermore, Wright etch is less sensitive to dislocations generated during crystal growth than Secco and Yang solutions [12, 13].

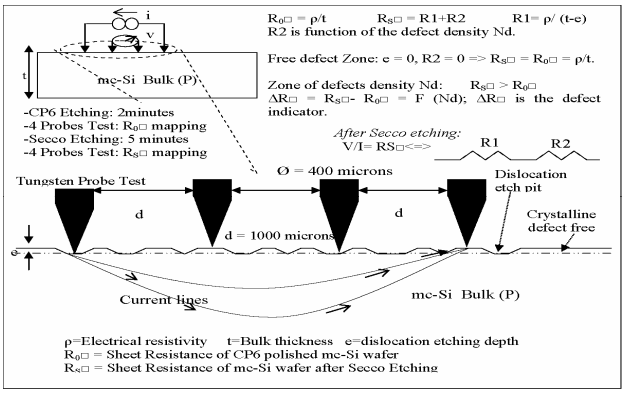

Figure 1. Principle of crystalline defects detection by sheet resistance variation.

We have chosen to develop our defect analysis process with the Secco and Yang etches, because our first interest was studying dislocations induced by HEM mc-Si growth, and also variable grain crystallographic orientations on

Corresponding author. Email: dr_fathimohamed@yahoo.fr

mc-Si material. Both etching solutions are sensitive to all kind of crystalline defects and also to all crystallographic orientations. The specificity of mc-Si HEM material has necessitated a special adjustment of Yang and Secco etching process parameters (time, agitation, temperature, etc…).

The principle of the developed technique for the mapping of crystalline defects is based on the exploitation of the sheet resistance variation in the delineated zones of crystalline defects. The delineation process consists of the action of a selective etching agent which will attack more quickly the crystalline defected zones than the other zones. This is due to the fact that in defected regions, the disturbance of the crystal lattice causes weak atomic bonds. The decoration of defect will take place only on the crystal grains levels; the zones of grain boundaries will be uniformly and more quickly etched than the grain surface because the atomics bonds are too weak there. Thus, the measurement of sheet resistance on the etched area should indicate a variation compared to the initial value obtained before application of the delineation solution on the wafer. A more defected area should lead to a higher increase in sheet resistance. In order to obtain a significant increase of sheet resistance, it is important to cause major perforations at the defect sites. Therefore, longer etching times than used for SEM defect inspection are necessary.

This new concept for crystalline defect mapping would provide time reduction and easy automation for defects analysis. It would be applied for the study of the defect density variation with the wafer position along the ingot. It would also be useful for the control of defects induced by each processing step during photovoltaic device manufacturing.

The sheet resistance measurement technique and crystalline defects delineation are both well established techniques in semiconductor characterization field. However, the combination of these two techniques for mapping crystalline defects is a new and useful approach. Indeed, in comparison to other techniques such as automated light scattering [14] or Sopori scanning machine [15], our technique is more economic in terms of time and cost. It is also more adapted for a first diagnostic to make a qualitative and fast study of the defect

2. Experimental

We have used P-type Boron doped mc-Si wafers of 10 x 10 cm2 in dimension and of about 1 Ω.cm in electrical resistivity. They were sawed from ingots grown by the Heat Exchanger Method (HEM). In order to remove the sawing process damage, we have begun by thinning and polishing these wafers. During this step, we have used an acidic polishing solution (known as "CP4 Etch") made by mixing nitric acid (HNO3), acetic acid (CH3COOH) and hydrofluoric acid (HF) with respectively 50%, 30% and 20% concentrations. After 6 min of etching, we rinsed thoroughly the mc-Si wafers with deionized water and dried them under a nitrogen gun. In order to test the Secco and Yang solutions, samples were cut from a polished mc-Si wafer. Mainly, the etching time and the agitation mode were varied. Before each delineation trial, the samples were immersed in diluted HF (10%) solution for 30 seconds in order to remove the native silicon dioxide (SiO2) and then rinsed in deionized water. The Secco [10] formulation is HF/potassium bichromate (K2Cr2O7)/H2O, obtained by mixing 2 parts of HF with 1 part of K2Cr2O7/H2O at (0.15Moles) or (44grams of K2Cr2O7 in 1litre of H2O). The Yang [11] formulation is HF/chromic acid (CrO3)/H2O, obtained by mixing 1 part of HF with 1 part of CrO3/H2O at (1.5Moles) or (150grams of CrO3 in 1litre of H2O). After the Secco or Yang etching process the samples were immediately rinsed in deionized water and nitrogen dried. Subsequently, SEM observation and other analysis have been performed.

For the development and study of defect density mapping technique, we have used a mc-Si wafer previously polished by "CP4 Etch", with a final thickness of about 325µm (±5µm). By using an automated four probes tester, we have measured the sheet resistance at 25 different positions which were well defined and regularly distributed across the wafer surface. Stamp marks were applied on the probe tester carrier as a reference to allow positioning of the wafer exactly at the same place during the next measurement step (following the crystalline defects etching). Once the sheet resistance mapping of the polished mc-Si wafer was over, we carried out a desoxidation of the wafer with HF (10%) during 30 seconds followed by water rinsing. Then, we proceeded to the delineation of the crystalline defects. For this step, we have chosen to apply "Secco Etch" during 5 minutes. The etched mc-Si wafer by Secco solution was then precisely positioned under the 4 probe tester, and the sheet resistance was measured again at the same 25 initially selected positions. Thereafter, we calculate and plot the sheet resistance variation (ΔR□) mapping. This result and its correlation is presented and discussed below. Figure 1 is a typical representation of this developed technique.

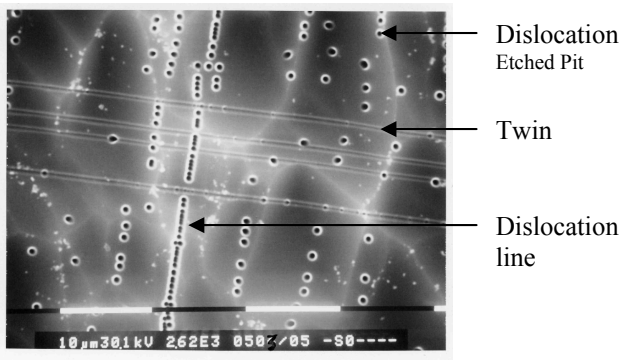

Figure 2. Secco defects delineation on mc-Si

3. Results and Discussion

The results of Yang and Secco delineation studies confirm the revelation of crystalline defects for an immersion time from 1 to 2 minutes, by clearly delineating dislocations, twins, grain boundaries and dislocation lines. We observed that dislocation pits etched with the Yang solution have mainly triangular or quadratic forms, whereas the dislocation pits are circular when using the Secco solution. Figure 2 is an illustration of Secco defect delineation process under the optimized conditions.

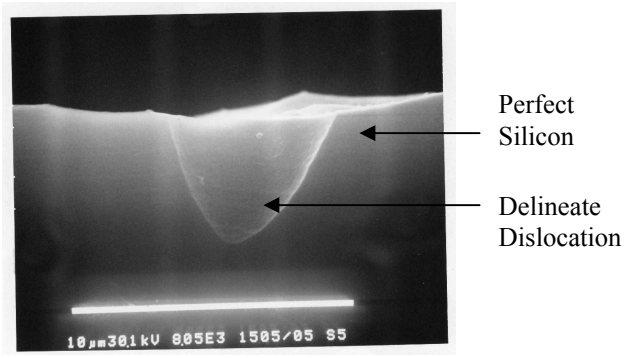

Figure 3. Cross section of dislocation delineated by Secco Etch for 5 minutes

In order to compare the action of dislocation localization between Secco and Yang solutions, we carried out a Secco revelation on a sample previously revealed with Yang Etch and vice-versa. The aim was to enable us to make a choice between Secco and Yang Etches for the calculation of the maximum density of defects. These tests showed that the action of Secco is higher than Yang's and lead us to choose Secco for the calculation and mapping of dislocation density. The profile of etched dislocation pits revealed by this solution is shown on Figure 3. The dipping time of the Secco delineation process was fixed at 5 minutes for the following defect mapping study. Such dipping time removes 5 µm of the dislocation zone as shown by the SEM micrograph of Figure 3. This fine knowledge and control of crystalline defect decoration by "Secco Etch" on mc-Si wafers were directly applied to the development of defect detection by the sheet resistance variation technique.

Once the sheet resistance mapping of a polished mc-Si wafer (10x10 cm2) was completed, we submitted the wafer to a Secco etch during 5 minutes. We chose this revelation time in order to strongly mark the defected zones and thus obtain an appreciable variation of sheet resistance. The mc-Si wafer revealed in this way was then precisely placed under the 4 probes tester, and measurement of the sheet resistance was carried out at the initially selected positions. We plotted the mapping of sheet resistance variation (ΔR□) on the 25 selected points of the mc-Si wafer. The Figure 4 shows the layout obtained for ΔR□. The next step was the superposition of the physical image of decorated mc-Si wafer with that of the ΔR□ mapping. In order to accomplish this, we have taken a digitalized photo of the whole Secco etched wafer surface, scaled it, and finally successfully superposed it to ΔR□ mapping. The Figure 4 illustrates this original result. The SEM analysis of these results allowed us to make the first classification for ΔR□ bands according to the revealed crystalline defect type and average dislocation density. This classification is summarized on Table 1.

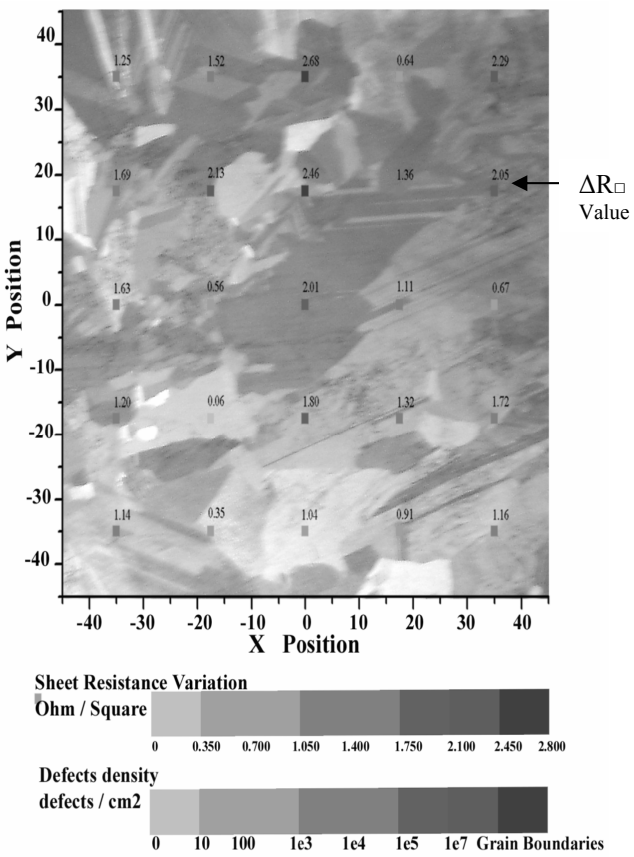

Figure 4. Superposition of the physical image of the defects area with ΔR□ mapping

Finally, by using this interesting correlation between sheet resistance variation (ΔR□) and defect density, we have plotted the mapping of the average defects density mapping on a whole mc-Si wafer (see Figure 5). These mapped values are in good agreements with those obtained from SEM analysis by counting etch pits. Sheet resistance mapping with the four probe technique has less resolution (it is about 3 mm) than the automated optical microscopy mapping technique. However, it gives sufficient information about defect distribution for photovoltaic device manufacturing. We can say that our developed technique is a good tool for making a quick diagnostic of the average dislocation density repartition in the mc-Si wafer and grown ingots.

Table 1. Classification of defects types according to sheet resistance variation bands

ΔR□ BANDS[Ω/□]	IDENTIFICATION AND DENSITY OF DEFECTS (Nd).
ΔR□ ≤ 0.35	Clean area without any defects
0.35≤ ΔR□ ≤ 0,7	Area with very low dislocations density $10cm^{-2} < Nd < 100cm^{-2}$
0.7≤ ΔR□ ≤ 1,050	Area of low dislocations density $100cm^{-2} < Nd < 10^3cm^{-2}$
1,050 ≤ΔR□ ≤ 1.400	Area of medium dislocations density $10^3cm^{-2} < Nd < 10^4cm^{-2}$
1.400 ≤ΔR□ ≤ 1,750	Area of high dislocations density $10^4cm^{-2} < Nd < 10^5cm^{-2}$
1.750 ≤ΔR□ ≤ 2.100	Area of very high dislocations density. $10^5cm^{-2} < Nd < 10^7cm^{-2}$
2.100 ≤ΔR□ ≤ 2.450	Twins area and / or grain boundaries
2.450 ≤ΔR□ ≤ 2.800	Area of grain Boundaries

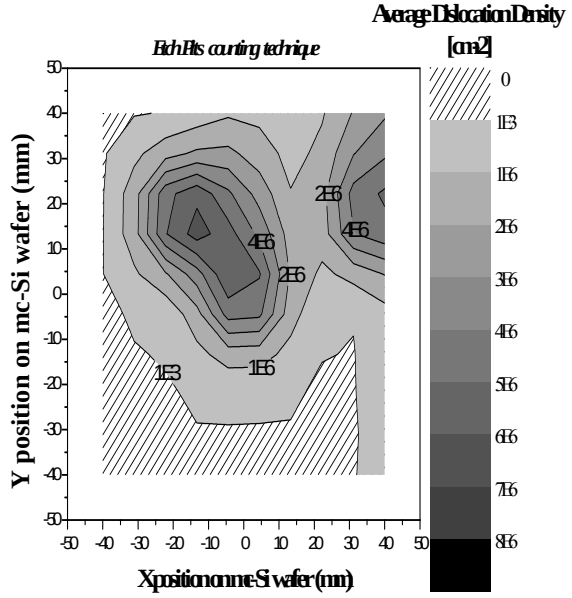

Figure 5. Plotting of the average defects density mapping by using sheet resistance technique.

Conclusion

By specific experimentations on mc-Si wafers, we have optimized chemical delineation process of crystalline extended defects. It appeared that Secco Etch is the more sensitive solution to crystalline defects. Therefore, it was applied for calculation and mapping of dislocation density. We have demonstrated the feasibility of a new technique for detection and mapping of the crystalline defects on a whole mc-Si wafer area. This method is based on the exploitation of the variation of the sheet resistance (ΔR□) of Secco delineated defective zones. We have presented the first classification connecting directly ΔR□ bands to crystalline defect types and densities. These results are in good accordance to physically observed defects density and grain boundaries repartition.

References

[1] M. Karilahti, PhD Thesis, Helsinki University of Technology, February 2003

[2] D.H. Macdonald, PhD Thesis, the Australian National University, May 2001

[3] M. Spiegel, PhD Thesis, Konstanz University of Physics, October 1998

[4] E.B. Yakimov, J. Phys. III France, December 1997, 2293-2307

[5] V.G. Popov, Quantum Electronics & Optoelectronics, Semiconductor Physics, Vol.3 , No. 4, 2000, 479-488

[6] M.S. Klukarni, J. Libbert, S. Keltner, J.Electrochem. Vol. 149 No.2, G153-G165 , 2002.

[7] Semiconductor Materials and Process Technology Handbook, Edited by Gary E., McGuire, 1988

[8] W.C. Dash, J. Appl.Phys. 27, 1956, 1193

[9] E. Sirtl, A.Z. Adler, Metallkd. 52 , 1961, 529

[10] [F.Secco d'Aragona, J. Electrochem. Vol. 119, 1972, 948.

[11] K.H. Yang, J. Electrochem. Vol. 131, 1984, 1140

[12] K.H. Yang, Semiconductor Processing, ASTM STP 850, Dinesh C. Gupta, Ed., American Society for Testing and Materials, 1984

[13] W.M. Jenkins, J. Electrochem. Vol. 124, 1979, 479

[14] B.L Sopori, J .Electrochem. Vol. 135 , 1988, 2601-2607

[15] B.L. Sopori, R. Murphy, C. Marshall, 23rd IEEE Photovoltaic Specialists Conference, 1993, 190

JJMIE

Volume 4, Number 1, Jan. 2010
ISSN 1995-6665
Pages 155- 162

Jordan Journal of Mechanical and Industrial Engineering

Numerical Modeling of Coal Tire-Shred Co-Gasification

Ilham Talab, Zaki Al-Nahari, Rana Qudaih, Isam Janajreh *

Mechanical Engineering Program, Masdar Institute of Science & Technology (MIST), Sas Al Nakhl Area

Abu Dhabi, Abu Dhabi, P.O.Box 54224,United Arab Emirates

Abstract

Tires, plastics, cellulosic materials, i.e., papers and cardboards are rich in hydrocarbon yet land filling of the waste of these materials is still practiced causing potential risk to our ecosystem through gas emissions (essentially CH_4) and ground water leaching. Co-Gasification within the existing infrastructure of pulverized coal utility gasifiers is considered a practical near-term solution for these rich hydrocarbon waste materials while minimizing capital requirements and maintaining the high efficiency of pulverized coal reactors. Systematic and numerical modeling of coal/tire shred fuel blend gasification is presented in this study. Co-combustion and gasification of tire shred and coal is a complex problem that involves gas and particle phases, along with the effect of turbulence on the chemical reactions. Coal/tire shred gasification modeling involves the prediction of volatile evolution and char burnout from the co-pulverized coal/biomass particles along with simulation of the gasification chemistry occurring in the gas phase. The mathematical models used for co-pulverized coal/tire shred particle gasification consist of models for turbulent flow (RNG k-ε model); gas phase gasification (Species Transport model); particles dispersion by turbulent flow (Cloud Tracking model); coal/biomass particles devolatilization (Constant Rate model); heterogeneous char reaction (Multiple surface reactions model); and radiation (Discrete Ordinates model). The coal was blended with 5, 10, and 20% tire shred (mass basis) for co-gasification. The effect of the percentage of tire shred blended with coal on the temperature distribution, products distribution, particle burnout rate, and pollutant emissions at the exit of the furnace will be presented.

Keywords: Cogasification, numerical modeling, systematic modeling, char-burnout.

1. Introduction

A relatively new technology for electricity production that is gaining prominence in the world is that of gasification. Waste tires and coal co-gasification within the existing infrastructure of pulverized coal utility boilers or gasifiers is viewed as a practical near-term means of encouraging renewable energy while minimizing capital requirements and maintaining the high efficiency of pulverized coal boilers/gasifiers [1-3]. The wide availability of pulverized coal boilers (in number and capacity) translates into significant opportunities for waste tire utilization even at levels of only 5 to 20% of thermal input. Coal/tire co-gasification has several benefits: it is the fastest way to increase the use of the humongous quantities of tire disposed every year for electric power generation; it saves capital cost by utilizing existing plant infrastructure; and it offers environmental advantages, such as reducing No_x emissions [4]. Co-pulverized coal and tire particles gasification modeling is a complex problem that involves gas and particle phases along with the effect of turbulence on the chemical reactions. In addition to solving the transport equations for the continuous phase (gas), the discrete second phase (spherical solid particles) in the Lagrangian frame of reference is also predicted. Discrete phase modeling is used for the prediction of particle trajectories and the individual conservation equations for the chemical species are solved utilizing the species convection-diffusion equation.

Corresponding Authors. ijanajreh@masdar.ac.ae.

  - Volume 4, Number 1 (ISSN 1995-6665)

2. Governing Equations and Solution Procedures

Modeling of gasification involves the application of conservation laws, and accounting for volatile evolution, char particles burnout, and coupling the homogeneous chemistry occurring in the gas phase as well as the heterogeneous in the solid phase.

Systematic Analysis Equations:
Systematic analysis or zero-dimension-modeling is an equilibrium analysis which quantitatively estimates the associated oxidizer and moderator feedstreams and syngas yields in the case of gasification. It predicts species and determines the needed oxygen and moderator (CO_2 or H_2O) per mole of feedstock at the operating temperature and pressure of a given gaisifier. There are several gasification technologies that classified according to their operating temperature as low, intermediate, and high temperature such as fixed bed (moving bed) gasifier, fluidized bed gasifier and entrained flow gasifier, respectively. The high operating temperature (~1250-1600°C) of the entrained flow gasifier reduces the residence time that make them popular for high throughput application. Entrain gasifiers are amenable for equilibrium due to the fast chemical reactions and the calculations of syngas composition are reasonably accurate [5]. Whether accommodating pulverized solid hydrocarbon or in slurry and with the addition of oxidizer, the goal of systematic analysis is to determine the equilibrium species concentrations as well as the temperature and pressure of the products. While the reactions consist of several hundreds of steps and hundreds of species and radicals, the following general three step reactions represent the predominant reaction pathway.

$$\text{water gas reaction } C_{(solid)} + H_2O \underset{k_{b,r}}{\overset{k_{f,r}}{\Leftrightarrow}} CO + H_2 \quad +131 MJ/Kmole \quad (1a)$$

$$\text{Boudouard reaction } C_{(solid)} + CO_2 \underset{k_{b,r}}{\overset{k_{f,r}}{\Leftrightarrow}} 2CO \quad +173 MJ/Kmole \quad (1b)$$

$$\text{Methanation reaction } C_{(solid)} + 2H_2 \underset{k_{b,r}}{\overset{k_{f,r}}{\Leftrightarrow}} CH_4 \quad -75 MJ/Kmole \quad (1c)$$

(1)

The feedstock (whether is mixed or homogenous) consumes all the available oxygen in a series of three heterogeneous reactions. In the above reactions the feedstock is represented by a solid carbon and the products are limited to six species (unconverted solid $C_{(solid)}$, CO,CO_2, CH_4, H_2, and H_2O). The Methanation reaction is several orders of magnitude slower than the Boudouard and Water gas reactions (Smooth and Smith 1985). Each of these reaction equations is independent, and has an associated equilibrium equation in terms of either their molar concentration or partial pressure as follow:

$$K_c(T) = \frac{[C]^c[D]^d}{[A]^a[B]^b} \quad or \; K_p(T) = \frac{p_C^c . p_D^d}{p_A^a . p_B^b} \qquad (2)$$

$$and K_c(T) = K_p(T).(RT)^{c+d-a-b}$$

Where [X] indicates the molar concentration of species X, lower case c, d, a , and b are the stoichiometric coefficients, and K_c is generally expressed in Arrhenius rate as:

$$k_c(T) = A_r T^{\beta_r} e^{-\frac{E_r}{RT}} \qquad (3)$$

where A_r is the pre-exponent constant, β is temperature exponent constant, E_r is the activation energy, R is the universal gas constant (R = 8.313kJ/kmol. K), T is the absolute temperature. At equilibrium K_c is expressed in terms of Gibbs free energy ($\Delta g^o = \Delta h^o - T\Delta s^o$) that ties 1st and 2nd thermodynamic quantities to indicate reaction spontaneousity as:

$$k_c(T) = e^{-\frac{\Delta g^o}{RT}} \qquad (4)$$

Where Δh_o and Δs_o are the standard enthalpy and entropy change of reactions. The three elemental mass conservation equations for C, H and O add another three equations to the three reactions equilibrium equations. The total molar fractions and energy equation warrant the solution of the system (6 species and any two variables of four: Temperature, pressure, and moderator oxidizer molar concentration per mole of feedstock). The steady form of the energy equation is written as:

$$\sum_{i=1}^{n\ product} \dot{n}_i h_i = \sum_{i=1}^{n\ reactant} \dot{n}_i h_i + \dot{Q} \qquad (5)$$

Where the enthalpy terms, h, include enthalpies of formation and sensible enthalpies.

Continuous Phase and CFD Equations:
The continuous phase is governed by Navier-Stoke equation that associated with source term:

$$\frac{\partial}{\partial t}(\phi) + \frac{\partial}{\partial x_i}(u_i \phi) = -\frac{\partial}{\partial x_i}\left(\Gamma_\phi \frac{\partial \phi}{\partial x_i}\right) + S_\phi \qquad (6)$$

Time rate advective diffusion source

where ρ is the density and upper case S_φ is the source terms due to the dispersed/discrete phase interaction. Φ is the dependent variable corresponding to density (ρ), the density velocity multiple (ρ,*ui*), and the temperature (T), representing the conservation of mass, momentum, and energy respectively. Φ can also represent turbulent scalars, i.e. turbulent kinetic energy (k) and turbulent dissipation rate (ε). These two equations in steady state flow regime are written as:

$$\rho u_i \frac{\partial k}{\partial x_i} = \mu_t \left(\frac{\partial u_j}{\partial x_i} + \frac{\partial u_i}{\partial x_j}\right)\frac{\partial u_j}{\partial x_i} + \frac{\partial}{\partial x_i}\left(\frac{\mu_t}{\sigma_k}\frac{\partial k}{\partial x_i}\right) - \rho\varepsilon$$

$$\rho u_i \frac{\partial \varepsilon}{\partial x_i} = C_{1z}\frac{\mu_t \varepsilon}{k}\left(\frac{\partial u_j}{\partial x_i} + \frac{\partial u_i}{\partial x_j}\right)\frac{\partial u_j}{\partial x_i} + \qquad (7)$$

$$\frac{\partial}{\partial x_i}\left(\frac{\mu_t}{\sigma_z}\frac{\partial \varepsilon}{\partial x_i}\right) - C_{2z}\frac{\rho \varepsilon^2}{k}$$

The right hand terms represent the generation, the diffusion, and destruction respectively. In these equations, μ_t is the turbulent or eddy viscosity $\mu_t = f_\mu C_\mu \rho k^2 / \varepsilon$. Where f and C are constants and C_{1z}, C_{2z}, σ_κ, and σ_z, are empirical constants. The transportation of species m_i is written as:

$$\frac{\partial}{\partial t}(\rho m_i) + \frac{\partial}{\partial x_i}(\rho u_i m_i) = \frac{\partial}{\partial x_i}\left(\rho D_{i,m} + \mu_t / Sc_t\right)\frac{\partial m_i}{\partial x_i} + \qquad (8)$$

$$R_i + S_i$$

Where $D_{i,m}$ is the diffusion coefficient. Sc_t is the turbulent Schmidt number which is a ratio of the eddy viscosity μ_t to the eddy diffusivity $D_{ti,m}$. These transport equations

incorporate a reaction source term R_i in addition to the S_i which accounts for discrete phase interaction. The R_i term is governed by the stoichiometric reaction below:

$$\sum_{i=1}^{N} v'_{i,r} S_i \underset{k_{b,r}}{\overset{k_{f,r}}{\Leftrightarrow}} \sum_{i=1}^{N} v''_{i,r} S_i \quad (9)$$

The i^{th} species production/destruction due to the reaction r is written as:

$$R_{i,r} = M_{i,r}(v''_{i,r} - v'_{i,r})\left(k_f \prod_{j=1}^{N} [C]_{j,r}^{\eta^*_{rj}} - k_b \prod_{j=1}^{N} [C]_{j,r}^{v''_{j,r}}\right) \quad (10)$$

where k is the reaction constant described in equation 3, and $[C]_j$ is the molar concentration of j_{th} specie raised to stoichiometric coefficients ν and reaction order η, and M_i is the molecular weight of species i.

Discrete Modeling Justification:

Gasification processes are typically turbulent and hence require modeling avoiding the exhaustive and numerical intensive direct numerical simulation (DNS). For example the length scale, velocity and Reynolds number of gas turbine combustor, after burner, and utility furnace are (0.1m, 50m/s, 250,000), (0.5m, 100m/s, 2,500,000), and (10m, 10m/s, 5,000,000) respectively. The smallest turbulent scale, known as Kolmogorov scale, denoted with η is expressed as:

$$\eta = L \,.\, \mathrm{Re}^{-\frac{3}{4}} \quad (11)$$

where L is the characteristic length scale. Solving the flow field down to η scale requires $\mathrm{Re}^{9/4}$ computational node for each dimension, $\mathrm{Re}^{9/4}$ nodes for three dimensional, and it is impractical at Re=10,000 (10^9 nodes). The discrete Lagrangian method is used for the solid phase. At low volume fraction (α) the average particle distance is greater than twice its diameter, therefore, particle-particle interaction can be neglected. Small particulate loading $(\alpha_d \rho_d / \alpha_c \rho_c << 1)$ implies a reasonable one-way coupling. Small value of the Stokes number (Ratio of the dispersed phase relaxation time $\tau_d = \alpha_d d_d^2 / 18\mu_c$ to that of the flow time $(\tau_c = U/D)$ indicates particles will closely follow the fluid, otherwise particles will move independently of the flow field.

Discrete/Particulate Phase Equations:

The discrete phase is solved in a Lagrangian frame of reference. This phase consists of spherical particles of 10μm to 100μm in diameter dispersed in the continuous phase. Their trajectory is predicted by integrating the force balance on the particle. This force balance equates the particle inertia with the forces acting on the particle and can be described as:

$$\frac{d\vec{u}_P}{dt} = F_D(\vec{u} - \vec{u}_P) + \vec{g}(\rho_P - \rho)/\rho_P + \vec{F} \quad (12)$$

Where F_D $(u - u_p)$ is the drag force per unit particle mass; u is the fluid phase velocity; u_p is the particle velocity; ρ is the fluid density, and ρ_p is the density of the particle. Equation (12) incorporates additional forces (F) in the particle force balance that can be important (thermophoretic and Brownian forces). The trajectory equations are solved by stepwise integration over discrete time steps. Integration of Eq. (12) yields the velocity of the particle at each point along the trajectory, with the trajectory itself predicted by

$$\frac{dx}{dt} = u_P \quad (13)$$

Equations similar to (12) and (13) are solved for each coordinate direction to predict the trajectories of the discrete phase. The trajectories of the discrete phase particles are computed as well as the heat and mass transfer to and from them. Inert heating law is applied while the particle temperature is less than the vaporization temperature. Devolatilization law is applied to the combusting particle mass (m_p) when the temperature of the particle reaches the vaporization temperature, T_{vap} . It is written as:

$$-\frac{dm_p}{dt} = Ae^{-(E/RT)}[m_p - (1 - f_v^0)m_p^0] \quad (14)$$

Where $f_{v,}$ and $m_p{}^o$ are the volatile fraction and initial mass, respectively. It remains in effect while the mass of the particle, m_p, exceeds the mass of the non-volatiles in the particle.

The heat transfer to the particle during devolatilization process governs the contributions from convection, radiation, and the heat consumed during devolatilization. It is written as:

$$m_p c_p \frac{dT_p}{dt} = hA_p(T_\infty - T_p) + \frac{dm_p}{dt} h_{fg} + \varepsilon_p A_p \sigma(T_R^4 - T_p^4) \quad (15)$$

Where c_p, $h_{fg,}$ ε, A, and σ are after the volatile component of the particle is completely evolved, a surface reaction begins, which consumes the combustible fraction of the particle until the combustible fraction is consumed. Heat, momentum, and mass transfer between the solid fuel particles and the gas will be included by alternately computing the discrete phase trajectories and the continuous phase equations.

The reactive two phase flow modeling is achieved within the framework of Fluent code [13].

3. Results and Discussion

Systematic analyses results:

Table 1 shows the proximate and ultimate analysis of the fuels used in this study. The lower heating values for the 0%, 5%, 10% and 20% coal and tire fuel blends are 31.91, 32.03, 32.15, and 32.38 MJ/kg respectively. It is noted in the proximate analysis that the amount of volatile matter and the ash content increase while fixed carbon and moisture content decrease when the amount of tire fuel blended with coal increases. As for the ultimate analysis, the percentage by weight of carbon, oxygen, and nitrogen decrease and the percentage of hydrogen and sulfur to a lesser extend increase when the amount of tire fuel blended with coal increases.

  - Volume 4, Number 1 (ISSN 1995-6665)

Table 1 – proximate and ultimate analysis of the fuel.

	Coal	Tire	Coal + 5%Tire	Coal + 10% Tire	Coal + 20% Tire
Proximate Analysis					
Fixed Carbone	0.5292	0.2293	0.5142	0.4992	0.4692
Volatile	0.3666	0.6731	0.3819	0.3973	0.4279
Moisture	0.0200	0.0102	0.0195	0.0190	0.0180
Ash	0.0842	0.0874	0.0844	0.0845	0.0848
Total	1.0000	1.0000	1.0000	1.0000	1.0000
Ultimate Elemental Analysis					
Carbon	0.7315	0.7299	0.7314	0.7313	0.7312
Oxygen	0.1058	0.0977	0.1054	0.1050	0.1042
Hydrogen	0.0531	0.0690	0.0539	0.0547	0.0563
Nitrogen	0.0153	0.0026	0.0147	0.0140	0.0128
Sulfur	0.0101	0.0124	0.0102	0.0103	0.0106
Ash	0.0842	0.0883	0.0844	0.0846	0.0850
Total	1.0000	1.0000	1.0000	1.0000	1.0000

The three coal/tire blends are modeled at a baseline temperature and pressure of 1,250C^{o} and 30bars, respectively. Four co-firing conditions (0, 5%, 10%, and 20% tire/coal) sweeping three operating temperatures (1,250 $\pm$ 250C^{o}) were carried out. The results suggest that there is negligible or no effect of adding tire on the production of CO. Figure 1(a) for example shows similar trends for the three coal/tire fuel blends for CO production at various temperatures. However, as the tire percent blended with coal increases, more H_2 is produced as shown in figure 1(b) mainly due to the increase in hydrogen as tire content increase. On the other hand, systematic analysis results demonstrate trends in NH_3, and H_2S produced from each fuel blend as depicted in figure 2 (a & b).

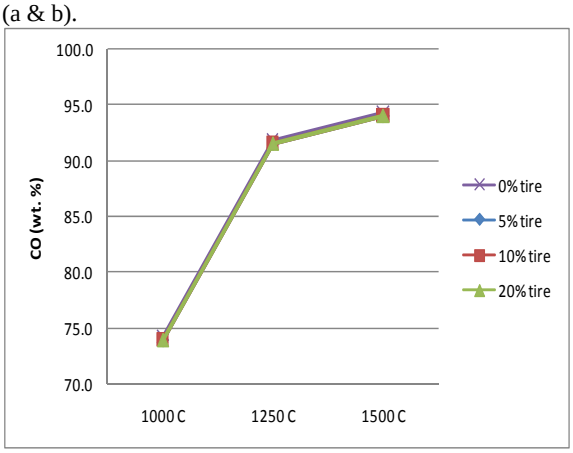

Fig. 1 (a). CO mass fraction.

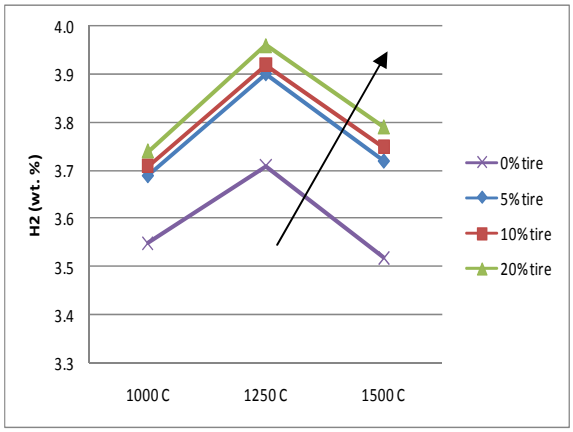

Fig. 1 (b). H_2 mass fraction.

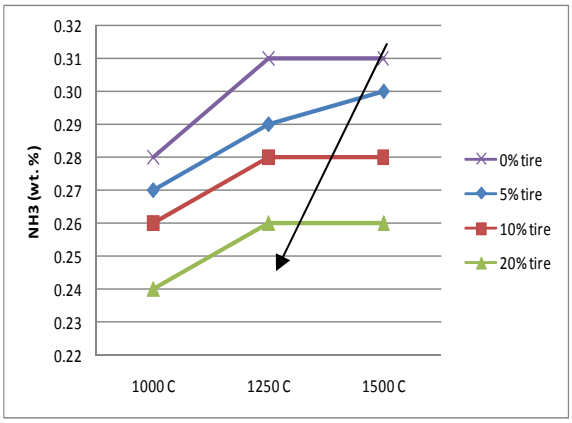

Fig. 2 (a). NH_3 mass fraction.

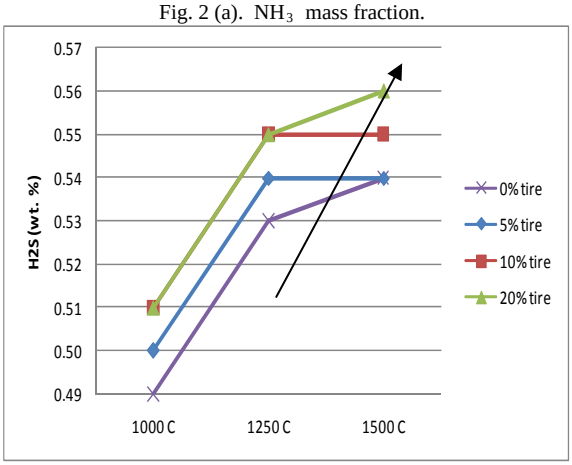

Fig. 2 (b). H_2S mass fraction.

Since the nitrogen content decreases as tire content increases in the fuel blend, it is anticipated that the formation of NH_3 will decrease as amount of tire blended with coal increases which is depicted in figure 2(a). Unlike nitrogen, sulfur content increases slightly as tire content increases and hence more H_2S is produced as percent of tire blended increases as shown in figure 2(b).

Reactive flow simulation results:

The geometry of the gasifier is depicted in figure 3. It was selected from the work of Chen et al. and Bockelie et al. [6,7,8,9]. The topology of the selected gasifier geometry is fitted with a multi-blocking mesh methodology. Multi-blocking provides a better grid resolution/clustering control, improves mesh structuring, and eases the use of the hexagonal mesh type for better inter cell communications and accuracy. The axisymmetrical meshing posses no complexity in construction, the 3-dimensional mesh, however, is more complex and must follow a general method that permits parametric studies without the need for reconstruction [10]. Flexibility in number of inlet ports, their radial distributions, and axial positioning are amongst the parameters that the 3 dimensional mesh is designed to offer.

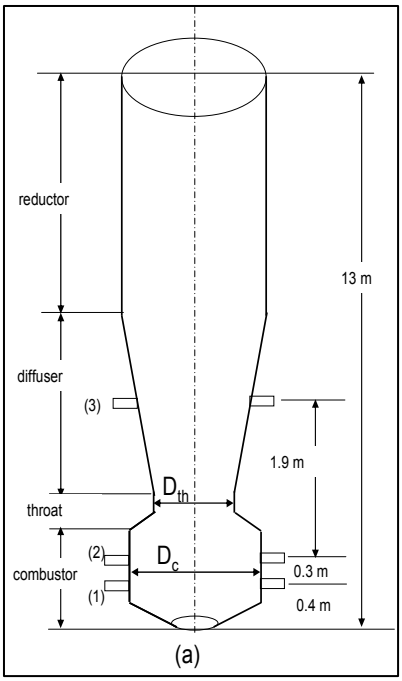

Fig. 3. Two-stage air blown gasifier and nozzle geometry.

The same fuel blends of coal with 5%, 10%, and 20% (mass basis) tire chips were studied assuming uniform particle diameter of 10 µm. For each case, the initial and boundary conditions were kept constant, and only the fuel composition had been changed. Table summarizes the boundary and operating conditions.

Table 2 – boundary and operating conditions.

Coal Feed	
Fuel flow rate (kg/s)	4
Fuel inlet temperature (K)	300
Oxidant & moderator: 23wt% O_2, 77wt% H_2O	
Flow rate at inlet 1 (m/s)	6
Flow rate at inlet 2 (m/s)	6
Flow rate at inlet 3 (m/s)	4
Turbulent intensity (%)	10
Flow inlet temperature (K)	1000
Gasifier pressure (bar)	30
Gasifier Wall temperature (K)	1600
Radiation model	Discrete Ordinates

The general conversion pathways of gasification can be summarized into the general global gas phase and solid phase reactions listed below [11, 12]:

$$Fuel \rightarrow CH_xO_yN_z + C_{(s)}Ash \quad (16)$$

For oxygen-rich conditions, combustion occurs:

$$CH_xO_yN_z + wO_2 \rightarrow CO_2 + \frac{x}{2}H_2O + zNO_2 \quad (17)$$

Where *w* can be readily calculated following simple elemental mass balance.

Heterogeneous reactions are:

$$C_{(s)}Ash + CO_2 \rightarrow 2CO + Ash \quad (18)$$

$$C_{(s)}Ash + H_2O \rightarrow CO + H_2 + Ash \quad (19)$$

$$C_{(s)}Ash + 2H_2 \rightarrow CH_4 + Ash \quad (20)$$

The volatiles react immediately to form CO_2 and H_2O in O_2 rich conditions at the bottom of the gasifier. The simulations revealed 100% conversion of both volatiles and char reactions. The effects of tire blended with coal on gas temperature; CO, NO emissions; and particle burnout rate, are discussed next.

The results show a higher gas temperature for lower tire content fuel mainly due to the increase in char content as percentage of tire decreases as tabulated in Table 1. The peak centerline gas temperature is 664K, 620K, 617K, and 611K for 0% tire, 5% tire, 10% tire and 20% tire coal blends respectively as shown in figure 4. The peak centerline gas temperature for the coal gasification decreases by 6.6% when 5% of tire is blended with coal. On the other hand, the effect of tire addition on the amount of CO produced was not found to follow a simple pattern. As depicted in figure 5, it is evident that more CO is produced right next to the inlets (0-3 m axial distance), however, as the reactions progress along the gasifier, different trends are noticed. One reason can be the close ratio of volatiles/char for tires used in this study and the simulation of more than one reaction which makes the prediction of CO produced a function of more than one variable.

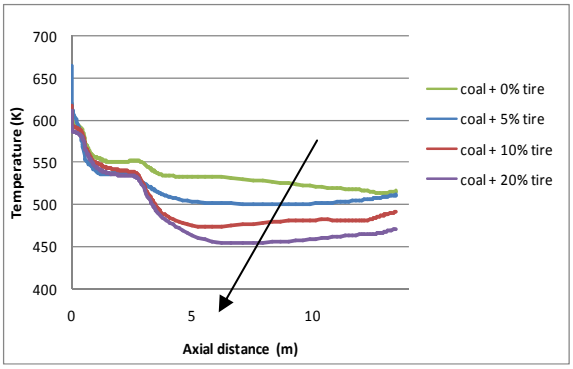

Fig. 4. Centerline gas temperature.

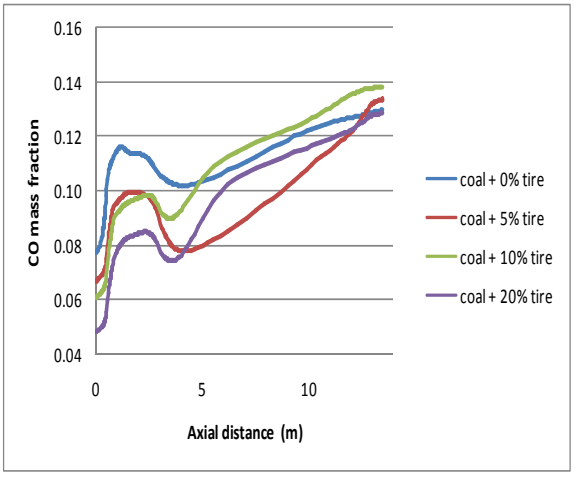

Fig. 5. Centerline CO mass fraction.

Better burnout rates are obtained as shown in figure 6 when tire chips are blended with coal. Compared with the baseline case of 0% tire, tire-coal blends show more homogeneous burnout along the gasifier centerline. Practically, char particles resulting from the devolatilization of tire are more porous than those resulting from coal and hence more reactive.

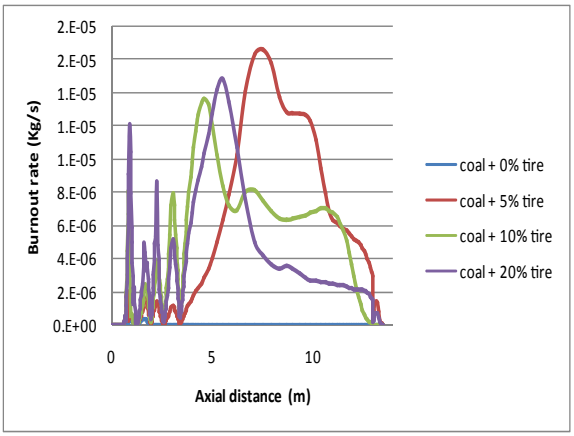

Fig. 6 . Centerline particle burnout rates.

Finally, the effect of adding tire to coal gasification on the pollutant NO production was investigated. Figure 7 shows NO mass fraction for each of the four cases along the gasifier centerline. In this study, it was noted that the NOx emissions consist mostly of NO. In general, the formation of thermal NOx is determined by a set of highly-temperature dependant chemical reactions known as the extended Zeldovich mechanism. For the fuel NOx, the nitrogen containing organic compounds present in the solid fossil fuel can contribute to the total NOx formed during the gasification process. This fuel nitrogen is particularly an important source of nitrogen oxide emissions for coal used in this study, which contains 1.53% nitrogen by weight.

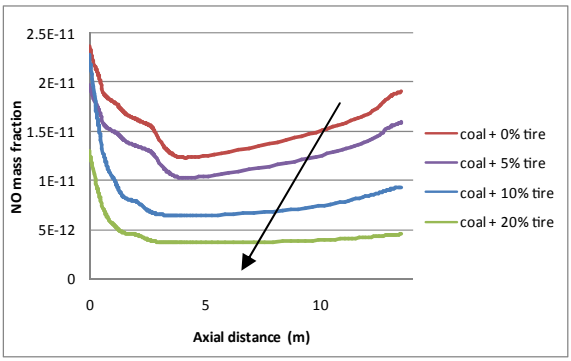

Fig. 7. Mass fraction contours of NO for 0%, 5%, 10% and 20% tire-coal blends.

Similar to the gas temperature, the mass fraction of the NO decreases with the increase in the fraction of tire fuel blended with coal. The NO mass fraction at the gasifier outlet is 1.93×10^{-11}, 1.61×10^{-11}, 9.32×10^{-12}, and 4.53×10^{-12} for 0%, 5%, 10%, and 20% tire-coal fuel blends respectively. NO mass fraction at the outlet decreases by 17% when 5% of tire is blended with coal and by 52% for 10% tire-coal blend. The reduction of NO mass fraction for coal/biomass co-gasification is due to the reduction of both thermal and fuel NOx. In fact the gas temperature decreased by 6.6% for the coal +5% tire compared to coal gasification without tire as depicted previously in figure 4. Consequently, the thermal NOx will also be reduced because it is highly temperature dependent. In addition to that there is also a reduction of fuel NOx for the coal-tire blends because of the net decrease of the amount of nitrogen as summarized in Table 1. The results obtained in this study show clearly the benefits of co-gasification on the reduction of traditional pollutant (NOx).

4. Conclusion

A numerical investigation of co-gasification of coal with 5, 10, and 20% (mass basis) tire is presented in this study. Systematic analysis in addition to CFD using Species Transport model along with discrete phase modeling are used for the investigation of this complex problem that involves gas and particle phases along with the effect of the turbulence on the chemical reactions. Systematic results show negligible effect of blending tire with coal on the production of CO, whereas H_2 and H_2S production increased with higher content of tire. On the other hand, less NH_3 is produced as tire content increases. These results follow the variation of ultimate composition of the fuel as the tire content increases, i.e., as the sulfur content increases with higher percentage of tire, H_2S produced increase. On the other hand, the CFD results were in general agreement with systematic analysis except that they represent a more realistic model which causes some differences compared to the ideal systematic approach. The results show a reduction of gas temperature and the pollutant NO mass fraction as more tire is blended with coal. The producer gas temperature decreased by 6.6% when 5% tire was blended with coal and by 52% when 10% tire was blended. Whereas the effect of blending tire with coal on CO production didn't result in a specific trend, the model showed a general increase in the rate of particle burnout as more homogeneous and stable burnout was noticed for high tire content fuels mainly due to the higher porosity and thus reactivity of char produced from tire than that produced from coal.

References

[1]Boylan, D., Bush, V., and Bransby, D. I., Biomass and Bioenergy, 19 (2000), pp. 411-417.

[2] Freeman, MC., Chister, D.C., James, R.A., Ekmann, J.M., and Walbert, G. F., "Results of pilot-scale Biomass Co-Firing for P.C. Combustors," DOE/FETC, Advanced Coal Base Power & Environmental Systems Conference, 1997, Pittsburgh, Pennsylvania.

[3] Sami, M., Annamalai, K., and Wooldridge, M., Progress in Energy and Combustion Science, 27 (2001), pp. 171-214.

[4] Hein, K.R.G., Bentgen, J.M., "EU clean coal technology, combustion of coal and biomass," Fuel Process Technology, 54 (1998), pp. 159

[5] M. J. Bockelie, M. K. Denison, Z. Chen, T. Linjewile, C. L. Sensior, A. F. Sarofim, "CFD Modeling of Entrained Flow Gasifiers in Version 21 Systems", Report reaction Engineering International, 77 West 200 south, suite 210, Salt Lake City, UT 84101

[6] C. Chen, M. Horio, T. Kojima, Chem. Eng. Science Vol. 55 No. 18, 2000, 3875-3883

[7] C. Chen, M. Horio, T. Kojima, Fuel Vol. 80 , no. 10 , 2001, 1513-1523

[8] M. J. Bockelie, M. K. Denison, Z. Chen, T. Linjewile, C. L. Sensior, A. F. Sarofim, "CFD Modeling of Entrained Flow Gasifiers in Version 21 Systems", Report reaction Engineering

International, 77 West 200 south, suite 210, Salt Lake City, UT 84101

[9] H. Watanabe, M. Otaka, Fuel 85 , 2006), pp. 1935-1943

[10] I. Janajreh, I. Talab, R. Qudaih, "Waste Representation and Numerical Simulation of Entrained Flow Gasifier", Proceedings of the Inaugural US-EU-China Thermophysics Conference, ASME May 28th-30th , Beijing , ChinaUECTC-RE '09.

[11] C. Ghenai, I. Janajreh, "CFD Analysis of the Effects of Co-firing Biomass with Coal", Golabal Conference on Renewable Energy Approaches for Desert Regions March 31st –April 2nd, 2009 Amman Jordan.

[12] C. Ghenai, and I. Janajreh, "Numerical Modeling of Coal/Biomass Co-Firing", FEDSM2008-55204, Symposium on Transport Phenomena in Energy Conversion From Clean and Sustainable Resources Jacksonville, Florida, August 10-14, 2008.

[13] Fluent 6.3.26, Fluent Inc. 2007.

JJMIE

Volume 4, Number 1, Jan. 2010
ISSN 1995-6665
Pages 163 - 168

Jordan Journal of Mechanical and Industrial Engineering

Performances of Photovoltaic Generator Multi-Level Cascade

Abdelaziz Talha[a,*] , Dalila Beriber[b], Mohamed Seghir Boucherit[b]

[a]*Laboratoire d'Instrumentation, Faculté d'Electronique et d'Informatique, Université des Sciences et de la Technologie Houari Boumediene, B.P.32, El-Alia, 16111 Bab-Ezzouar, Alger, Algérie*

[b]*Laboratoire de Commande des Processus, École Nationale Polyechnique, Alger, Algérie*

Abstract

In this paper, we study the performances of the cascade of the solar cell panels with the multilevel inverter. In the first part, we develop a knowledge model of the inverter by using connection functions of this converter. A PWM strategy which uses four bipolar carriers is developed to control this converter. In this part, the inverter is fed by constant input DC voltages. The performance of the algorithm is studied on the base of the harmonic rate. Then, we present the solar cell model. In the last part, we study the stability problem of the input DC voltages of the inverter. Thus, we study a cascade constituted by two photovoltaic cell panels – five-level NPC VSI - permanent magnet synchronous machine (PMSM). This studied lets to find a solution to solve this problem. The performances obtained with this cascade are full of promise to be using this inverter in renewable energy

Keywords: Multilevel inverter; Generator Cells; Renewable; PMSM.

Nomenclature

I : Current delivered by photovoltaic cell,
V : Voltage delivered by photovoltaic cell,
I_{ph} : Photo-current,
I_s : Saturation current of diode dependants of temperature,
R_s : Series resistance,
R_{sh} : Shunt resistance,
q : Charge of electron = $1.602.10^{-19}$C,
K : Boltzmann Constant = $1.381.10^{-23}$J/K,
A : Quality factor of diode,
T : Cell Temperature in °K.
g : gap.

1.Introduction

During last century, the consumption of electrical energy has greatly increased because the industry growth. The energy demand predictions for next years confirm the growth of the energy consumption. Consequently, the traditional energy sources (fossil) will last few more decades. And this will produce an outage of the energy in the word. On the other hand the consumption of the traditional sources contributes greatly to the greenhouse effect, for this reason, it is necessary to use the renewable energy sources no polluting such as solar cell. The industrial consumers need to be fed by sinusoidal voltage generators. In the last decade the power electronic technology has made a very important advance their development. On the one hand, the power switches used in the structures of converters are able to switch more quickly, On the other hand, new structures have emerged converters. Some of them promote high switching frequencies. And instead to transfer significant levels of power (multi-level structures,…).

In this paper, we are interested to study the cascade of a multilevel inverter and solar cell generator.

The performances obtained with this cascade are full of promise to be used in renewable energy production systems.

2.Modelling of Five Level NPC Voltage Source Inverter

The three-phase five-level NPC VSI is a new conversion structure used to feed, with variable frequency and voltage, power alternating current machines. Several structures are possible for five-level inverters [1]. In this paper, we study the Neutral Point Clamping (NPC) structure (Figure1). This converter is constituted by three arms and four DC voltages sources. Every arm has eight bi-directional switches, six in series and two in parallel, and two diodes DD_{k0} and DD_{k1} which let to have zero voltage for V_{kM}. Every switch is composed by a transistor and a diode in anti-parallel. For an arm k of the three-phase five-level NPC VSI, several complementary laws controls are possible. The control law which lets an optimal working of this inverter is [1]:

$$\begin{cases} B_{K4} = \overline{B}_{K2} \\ B_{K5} = \overline{B}_{K1} \\ B_{K6} = \overline{B}_{K3} \end{cases}$$

Where B_{ks} represents the gate control of the switch T_{ks}

* Corresponding Author. abtalha@hotmail.com

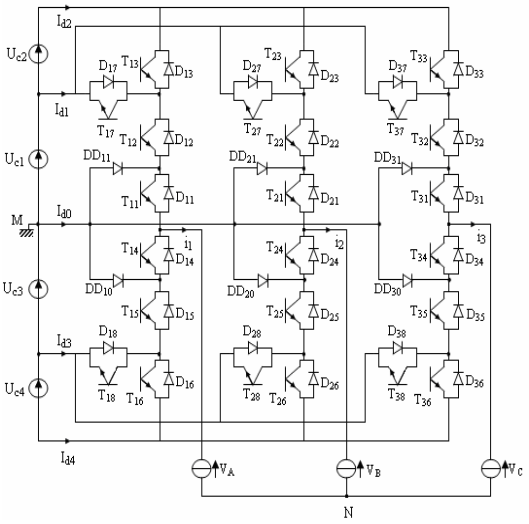

Figure 1. A Five-level NPC voltage source inverter

The switch connection function F_{ks} indicates the opened or closed state of the switch TD_{ks}. We define two a half arm connection function F^b_{km} with:
k : arm number

$$m = \begin{cases} 0 \text{ for the lower half arm} \\ 1 \text{ for the upper half arm} \end{cases}$$

and:

$$\begin{cases} F^b_{K1} = F_{K1}F_{K2}F_{K3} \\ F^b_{K0} = F_{K4}F_{K5}F_{K6} \end{cases}$$

The output voltages of the inverter relatively to the middle point M are defined as follows:

$$\begin{bmatrix} V_{AM} \\ V_{BM} \\ V_{CM} \end{bmatrix} = \begin{bmatrix} F_{17}+F^b_{11} \\ F_{27}+F^b_{21} \\ F_{37}+F^b_{31} \end{bmatrix} U_{c1} + \begin{bmatrix} F^b_{11} \\ F^b_{21} \\ F^b_{31} \end{bmatrix} U_{c2} - \begin{bmatrix} F_{18}+F^b_{10} \\ F_{28}+F^b_{20} \\ F_{38}+F^b_{30} \end{bmatrix} U_{c3} - \begin{bmatrix} F^b_{10} \\ F^b_{20} \\ F^b_{30} \end{bmatrix} U_{c4}$$

The system (3) shows that a five-level NPC VSI can be considered as four two-level voltage source inverters in series. This characteristic lets us to extrapolate the strategies used for the two-level inverter to the five-level NPC inverter.
The input currents of the inverter are given as follows:

$$\begin{cases} i_{d1} = F_{17}i_1 + F_{27}i_2 + F_{37}i_3 \\ i_{d2} = F^b_{11}i_1 + F^b_{21}i_2 + F^b_{31}i_3 \\ i_{d3} = F_{18}i_1 + F_{28}i_2 + F_{38}i_3 \\ i_{d4} = F^b_{10}i_1 + F^b_{20}i_2 + F^b_{30}i_3 \end{cases}$$

The current i_{d0} is given as follows:

$$i_{d0} = (i_1 + i_2 + i_3 + i_4) - (i_{d1} + i_{d2} + i_3)$$

3. PWM Strategy of the Five Level NPC VSI

In this part, we present a PWM algorithm of the five-level NPC VSI: the space vector modulation strategy with four bipolar carriers. This strategy is characterized by two parameters [1], [2]:
- The modulation index m is defined as a ratio between the carrier frequency f_p and the reference voltage frequency f:

$$m = \frac{f_p}{f}$$

The modulation rate r is the ratio between the magnitude V_m of the reference voltage and three times of the carrier's magnitude U_{pm}: .

$$r = \frac{V_m}{U_{pm}}$$

Figure2 shows the signals of this strategy

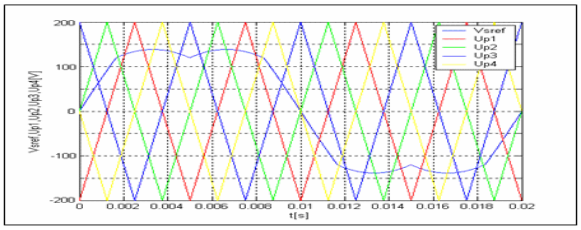

Figure 2. Space vector modulation strategy associated to four bipolar carriers

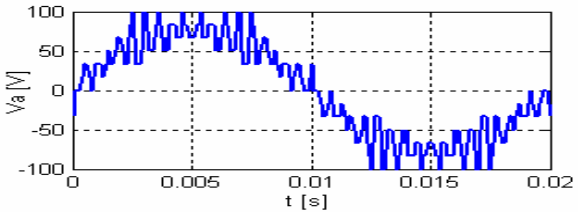

(a)

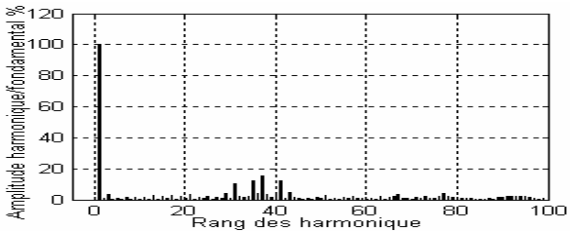

(b)

Figure 3.(a,b) The simple voltage of the inverter and its spectrum (m=10)

For even values of m, the output voltages present symmetry relatively to the quarter of the period. Then, only odd harmonics exist. These harmonics gather by families centred around frequencies multiple of 4mf. The first family centred around frequency 4mf is the most important in view of its magnitude.

4. Modelling of Photovoltaic Generator

Since the invention of solar cells in en 1954, several models have been proposed to describe its function and behavior under different weather conditions (light and temperature) [3]. In this paper, we present the model with one exponential (diode) [4], [5]. The electrical scheme is given in figure 4.

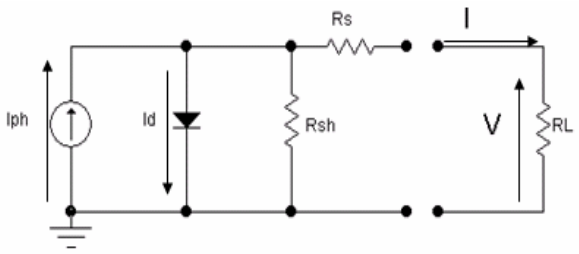

Figure 4. Electrical Scheme of a photovoltaic cell with one diode

The expression of the current-voltage characteristic is given as follows:

$$I = I_{ph} - I_S \times [\exp(\frac{q \times (V + R_s \times I)}{A \times k \times T}) - 1] - \frac{V + R_s \times I}{R_{sh}}$$

Thus, the equivalent scheme of a photovoltaic generator (PG) is given in figure5.

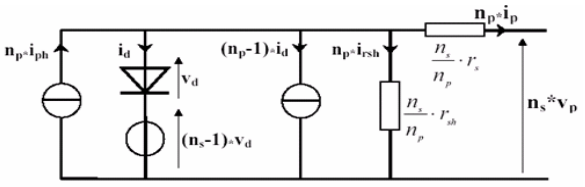

Figure 5. Equivalent scheme of photovoltaic generator

The expression of the current-voltage characteristic of photovoltaic generator is given as follows:

$$I_g = I_{ph,g} - I_{s,g}[\exp\left(q\frac{V_g + R_{s,g}I_g}{AkN_{ms}T}\right) - 1] - \frac{V_g + R_{s,g}I_g}{R_{sh,g}}$$

The functional scheme of photovoltaic generator uses Matlab/Simulink is given in figure6.
In this paper, we have used photovoltaic generator MSX-83 composed by 36 cells in en series

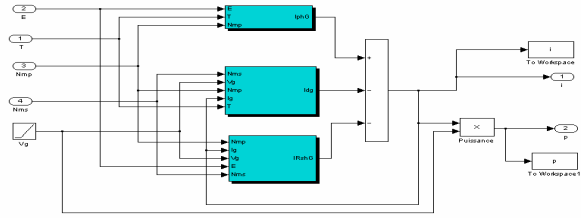

Figure 6. Functional Scheme of photovoltaic generator

The figures 6, 7 and 8 represents respectively current–voltage characteristics, power–voltage and current–voltage (reel case) of panel MSX-83, for a temperature T=25° and light E=1000W/m^2.

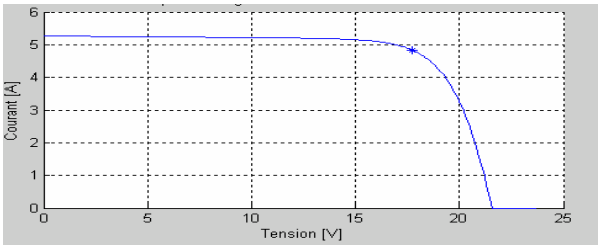

Figure 7. Current–voltage Characteristic PG

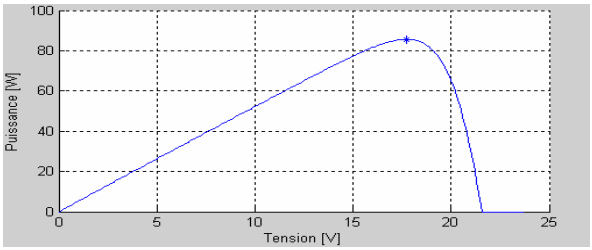

Figure 8. Power–voltage Characteristic PG

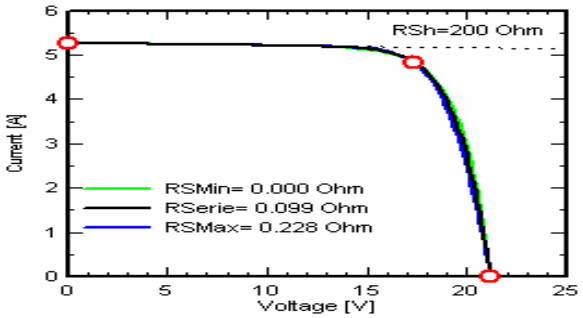

Figure 9. Real Characteristic current–voltage of PG

We can note that the simulation results used the proposed model are nearly of the real case and then we can validate our model.

5. Cascade of Two Photovoltaic Generator – Five-Level NPC VSI - PMSM

Until now, we have supposed the input DC voltages of the five-level NPC VSI constants. In this part, the authors study a generation input DC voltage technique. For this, we propose a cascade constituted by two photovoltaic generator-five-level NPC VSI which feeds a PMSM (Figure10).

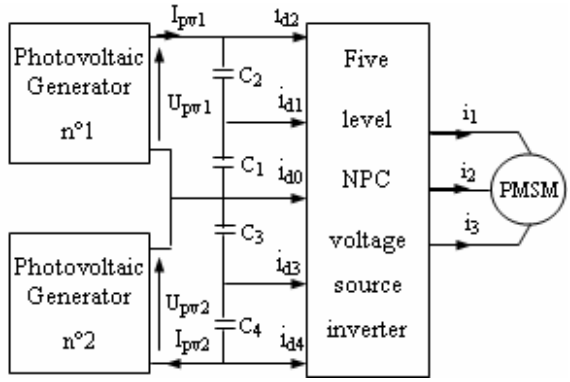

Figure 10. Two photovoltaic generator-filter-five-level NPC VSI-PMSM cascade

5.1. Modelling of Intermediate Filter

Figure11 shows the structure of the intermediate filter of the studied cascade.

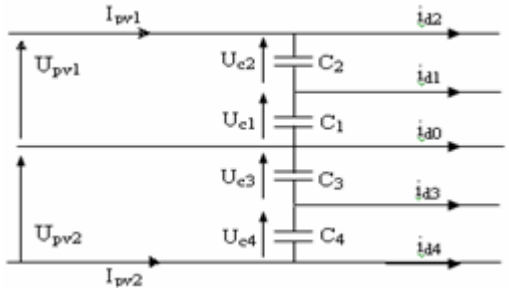

Figure 11. Structure of the intermediate filter

The model of this filter is defined by the following system:

$$\begin{cases} C_1 \dfrac{dU_{c1}}{dt} = I_{pv1} - i_{d2} - i_{d1} \\ C_2 \dfrac{dU_{c2}}{dt} = I_{pv1} - i_{d2} \\ C_3 \dfrac{dU_{c3}}{dt} = I_{pv2} - i_{d2} - i_{d1} - i_{d0} \\ C_4 \dfrac{dU_{c4}}{dt} = I_{pv2} - i_{d2} - i_{d1} - i_{d3} - i_{d0} \end{cases}$$

5.2. Simulation results

The five-level NPC inverter is controlled by the space vector modulation strategy with four bipolar carriers, any photovoltaic generator delivered a voltage V_{pvi}=140V.

We note : $U_{c13}=U_{c1}-U_{c3}$, $U_{c24}=U_{c2}-U_{c4}$ et $U= U_{PV1}+U_{PV2}$.

The parameters of the intermediate capacitors filter are: $C_1=C_2=C_3=C_4$=20mF.

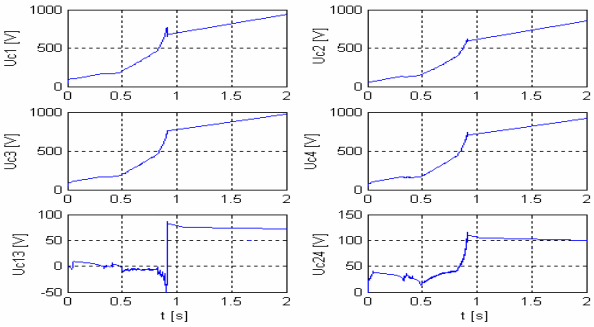

Figure 12. Input voltages of the inverter and their differences

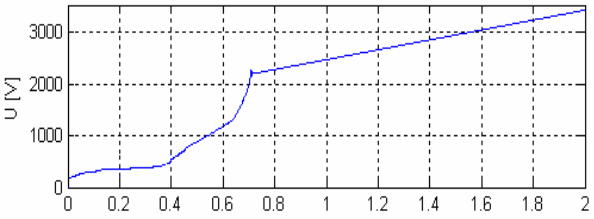

Figure 13. Output voltage of photovoltaic generator

The different input voltages of the VSI are not stables and their differences are not null (Figure12). The output voltages of the photovoltaic generator decrease continually (Figure13).

6. Stabilisation of Input Voltage of Five Level NPC VSI

To improve the input voltages of the five-level NPC inverter, we propose to use a clamping bridge, constituted by a transistor and a resistor [1]. The transistors are controlled to maintain equal the different input DC voltages of the inverter (Figure14).

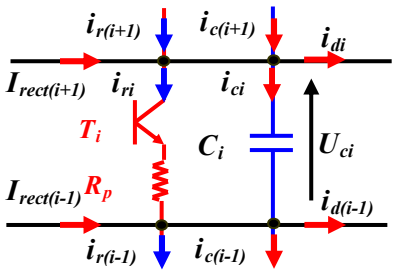

Fig. 14. Clamping bridge cell

The model of the clamping bridge-filter set is defined by the following equation:

$$\begin{cases} C_1 \dfrac{dU_{c1}}{dt} = I_{PV1} - i_{d2} - i_{d1} - i_{r1} \\ C_2 \dfrac{dU_{c2}}{dt} = I_{PV1} - i_{d2} - i_{r2} \\ C_3 \dfrac{dU_{c3}}{dt} = I_{PV2} - i_{d2} - i_{d1} - i_{d0} - i_{r3} \\ C_4 \dfrac{dU_{c4}}{dt} = I_{PV2} - i_{d3} - i_{d2} - i_{d1} - i_{d0} - i_{r4} \end{cases}$$

Where $i_{r1} = \dfrac{U_{ci}}{Rp}$

The control algorithm of the resistive clamping circuits can be summarized as follows:

if $U_{c1} > \dfrac{U_{PV1}}{2} \Rightarrow$ (T1=1) & (T2=0)

if $U_{c2} > \dfrac{U_{PV1}}{2} \Rightarrow$ (T2=1) & (T1=0)

if $U_{c3} > \dfrac{U_{PV2}}{2} \Rightarrow$ (T3=1) & (T4=0)

if $U_{c4} > \dfrac{U_{PV4}}{2} \Rightarrow$ (T4=1) & (T3=0)

The parameters of the intermediate capacitors filter are: $C_1=C_2=C_3=C_4=20$mF and $R_p=25\Omega$. The figures 15 and 16 show the simulation results when using the clamping bridge

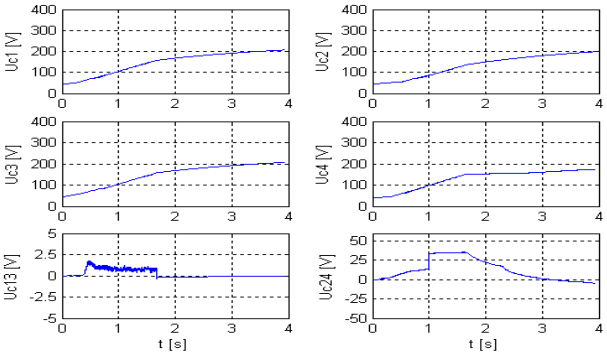

Figure 15. Tensions du pont de clamping et leurs différences

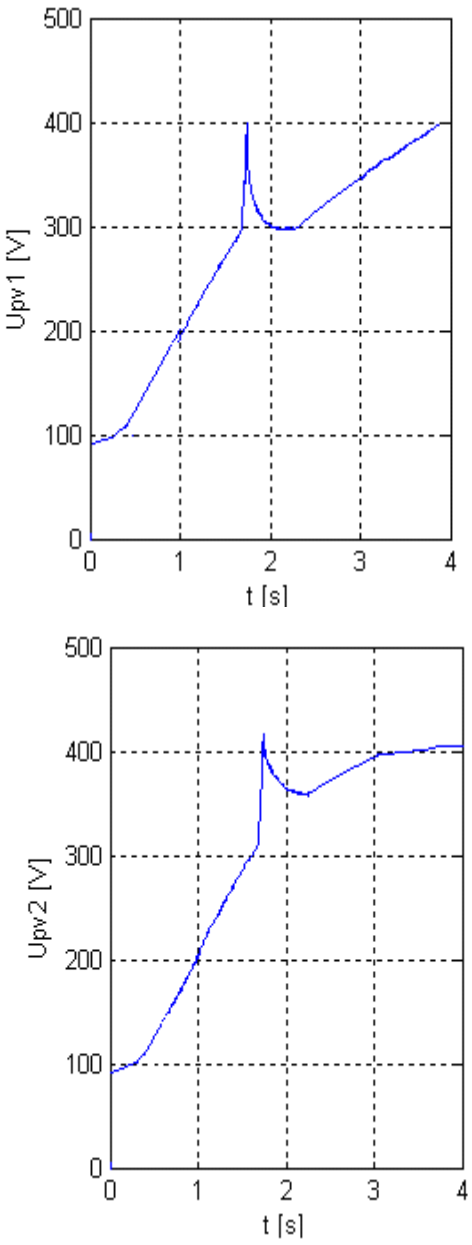

Figure 16. Output voltage of two Photovoltaic generator

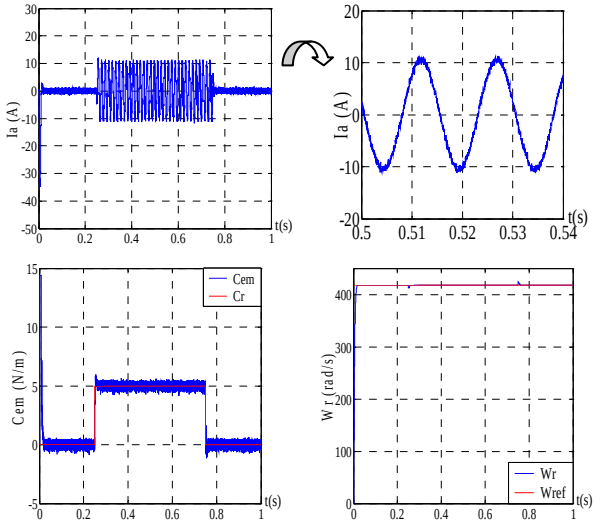

Figure18. Performances of PMSM

We observe that the differences between the input voltages of the five-level NPC inverter are decreased to have a value practically null in steady state (Figure15). The output voltage of the three two-level rectifiers is lightly increased (Figure16). The current i_{d0} has a mean value practically null (Figure17). The performance of the speed control algorithm of the PMSM shows that the current of the machine nearly is sinusoidal. The speed and the torque effect for the charge variation between two instants t=1.5s and t=2.5s (Figure18).

7. Conclusions

In this paper, we have studied the performances of the cascade of the photovoltaic cell panels with the multilevel inverter. The modelling of the five-level NPC inverter shows that it is equivalent to four two-level inverters in series. This characteristic lets us to extrapolate the strategies used for the two-level inverter to the five-level NPC inverter. Also, we have presented a space vector modulation strategy with four bipolar carriers.

The study of the stability problem of the input DC voltages of five-level NPC inverter using a cascade constituted by two photovoltaic generator-five-level NPC VSI shows that the different input voltages of this VSI are not stables and their differences are not zero. To solve this problem, we propose to use clamping bridge, because this bridge allows improve the input voltage of five-level inverter.

The performances obtained with this cascade are full of promise to be using this inverter in renewable energy

References

[1] A. Talha, E.M. Berkouk, M.S. Boucherit and G. Manesse, “Study and control of two two-level PWM rectifier – clamping bridge - seven-level NPC VSI cascade. Application to PMSM speed control", European Transactions on Electrical Power Journal (ETEP) by John Wiley & Sons, Ltd, vol.16, No.1, 2006, 93-107.

[2] L.M. Tolbert, F.Z. Peng and T.G. Habelter, "Multilevel PWM methods at Low Modulation indices", in Proceedings of 1999 Applied Power Electronics Conference and exposition (APEC),Dallas, Texas, March 14-18, 1999, 1032-1039.

[3] M. Bayegan, "Power electronic technologies for distributed Power", 9th European conference on Power Electronics and Applications, EPE 01, 27th August 2001, Graz, Austria 2001.

[4] B.Multon and al, "Analysis and Experimental Validation of Various Photovoltaic System Models", 7th International ELECTRIMACS’2002 Congress, Montréal, Canada, 2002, 1-6.

[5] E. Massada, "Power Converter for Renewable and Distributed Sources", 9th International Conference on Power Electronics and Motion Controls, EPE-PEMC’2000, Kosice, Slovak Republic 2000.

JJMIE

Volume 4, Number 1, Jan. 2010
ISSN 1995-6665
Pages 169 - 176

Jordan Journal of Mechanical and Industrial Engineering

Power Quality and Stability Improvement in Wind Park System Using STATCOM

V.Suresh Kumar [a,*], Ahmed F.Zobaa [b], R.Dinesh Kannan [a], and K.Kalaiselvi [c]

[a]Thiagarajar College of Engineering, India , [b]University of Exeter, UK , [c]Sethu Institute of Technology, India

Abstract

Operation of wind turbines has an impact on the power quality and reliability at the connected electric network. Power quality problems such as voltage flicker and harmonic distortion along with reliability issues are some major concern and in this work the flicker & harmonics issues are considered. Wind turbine connected to an induction generator and synchronous generator is modeled using PSCAD to analyze power quality and reliability problems. STATCOM unit is developed to inject reactive power to mitigate power quality problems and to get stable grid operation. Due to continuously varying wind speed components, the active and reactive power along with terminal voltage fluctuates continuously. By connecting STATCOM into the grid, the active power, reactive power and terminal voltage is maintained constant. The wind electric generators have power electronic converters which are used to sweep maximum power at the available speed and for efficient control introduce harmonics. The STATCOM modified as shunt active filter which is used for mitigating harmonics provides good results

Keywords: Wind Energy; Simulation; Modelling; Power Quality; STATCOM

1. Introduction

In recent years wind power generation has experienced a very fast development in the whole world. As the wind power penetration into the grid **is** increasing quickly, the influence of wind turbines on the power quality is becoming an important issue. One of the important power quality aspects is flicker [1-2]. Flicker is induced by voltage fluctuations, which are caused by load flow changes in the grid. Grid connected wind turbines may have considerable fluctuations in output power, which depend on the wind power generation technology applied [3-4].

The flicker emission produced by grid connected wind turbines during continuous operation is mainly caused by fluctuations in the output power due to wind speed variations, the wind gradient and the tower shadow effect [5]. Regarding to variable speed wind turbines, which have the ability to reduce power fluctuations, flicker emission is quite different from that generated by fixed speed wind turbines. Variable speed operation of the rotor has the advantage that the faster power variations are not transmitted to the grid but are smoothed by the flywheel action of the rotor. Variable speed wind turbines fed induction generators and synchronous generators, the most popular installed variable speed wind turbines worldwide, are the main research interest here [6]. Even' though variable speed wind turbines have good performance with respect to flicker emission, flicker mitigation becomes necessary as the wind power penetration level increases. Flicker mitigation can be realized by appropriate reactive shunt compensation [7].

The most commonly used device for flicker mitigation is the Static Var Compensator (SVC). However, the STATCOM has received much more attention recently. Compared with the SVC, the STATCOM has many advantages, such as overall superior functional characteristics, better performance, faster response, smaller size, cost reduction, and capable of providing both active and reactive power [8-10]. The STATCOM, consisting of a voltage source converter, uses advanced power switches to provide fast response and flexible voltage control for power quality improvement, which is suitable to application with rapidly fluctuating loads. Using high frequency PWM, the converter will create smooth current with low harmonic content.

In this paper, a wind turbine fed induction generator and synchronous generator is modeled using PSCAD and flicker emission of grid connected wind turbines fed induction generators is investigated during continuous operation. The factors that affect flicker emission of wind turbines, such as wind speed, turbulence intensity, short circuit capacity and grid impedance angle, are analyzed [11]. Simulation results prove that STATCOM is an effective means to mitigate the flicker level during continuous operation of grid connected wind turbines. Also the converters, which are used to extract maximum power at the available speed, are connected between the induction generator and grid. Harmonics due to the non-linear load (converters) are compensated by designing STATCOM as a shunt active filter [12]

* Corresponding author. *vskeee@tce.edu*

2. Power Quality Issues

When a non-linear load or distorting load is connected to the power system fundamental sinusoidal waveform of current flowing through system will change. This will rise non-sinusoidal voltage drop across various network element connected to the system resulting in distorted waveform propagation through out the system to buses remote from the original source. Although the main issues of power quality are common to distribution networks, whether active or passive the addition of wind generation can have a significant impact on power quality. For wind turbine fed induction generator designs, which use power electronics converters, the issues of harmonic distortion of the network voltage must be carefully considered while the connection of fixed-speed turbines to the network needs to be managed carefully if excessive transients are to be avoided.

During normal operation wind turbines produce a continuously variable output power. The power variations are mainly caused by the effects of turbulence in the wind and tower shadow. These effects lead to periodic power pulsations at the frequency at which the blades pass the tower ,which are superimposed on the slower variations caused by meteorological changes in wind speed. There may also be higher frequency power variations (at a few Hz) caused by the dynamics of the turbine. Variable-speed operation of the rotor has the advantage that many of the faster power variations are not transmitted to the network but are smoothed by the flywheel action of the rotor. However, fixed speed operation using a low-slip induction generator, will lead to cyclic variations in output power and hence network voltage. A voltage dip is a sudden reduction in the network voltage to a value between 100 per cent and 0 per cent followed by a voltage recovery after a short period of time, conventionally 1ms to 1 min. Dips between 10 per cent and 15 per cent of the terminal voltage are commonly due to switching of loads, whereas larger dips may be caused by faults.

2.1 Voltage flicker

Voltage flicker describes dynamic variations in the network voltage. Traditionally it was of concern when the connection of large fluctuating loads (e.g. arc furnaces, rock crushing machinery sawmills, etc.) was under consideration. However, it is of considerable significance for wind farms, which: (i) often use relatively large individual items of plant compared to load equipment; (ii) may start and stop frequently; (iii) may be subject to continuous variations in input power. Flicker produced during continuous operation is caused by power fluctuations, which mainly emanate from variations in the wind speed, the tower shadow effect and mechanical properties of the wind turbine. Flicker due to switching operations arises from the start and shut down of the wind turbines.

2.2 Harmonics

A wind turbine with an induction generator directly connected to the grid without an intervening power electronic converter is not expected to distort the voltage waveform. Power electronics applied for soft start may generate short-duration high-order current harmonics but their duration and magnitude are usually small. Hence for a system with fixed-speed wind turbines emission limits for harmonics are not a constraint. However, variable-speed wind turbines using power electronic converters should be assessed against given or calculated limits for harmonics. New wind turbine designs use transistor-based converters, which are operated at switching frequencies above 3 kHz and their impact on the voltage waveform is usually negligible. However, connection of electric equipment does in general change the harmonic impedance of the network. For example, capacitor banks employed in fixed-speed wind turbines may shift the resonant frequency of the harmonic impedance. Therefore, possible harmonic sources already present in the network may cause unacceptable harmonic voltages. Consequently, for networks with significant harmonic sources, connection of wind turbines with suitable filter should be carefully designed to avoid an ill-conditioned modification of the harmonic impedance..

3. Power Quality Improvement

The FACTS device are based on power electronic controllers that enhances the capacity of the transmission line .These controllers are fast and increases the stability operating limits of the transmission systems when their controllers are properly tuned. FACTS devices are mostly used to regulate voltage and schedule power flow through some lines. FACTS device has the potential to operate the more flexible and economic way.

STATCOM is a voltage source inverter which means a DC capacitor voltage source regularly switched by gate turn off thyristor to generate alternating voltage and by surrounding the capacitor with four GTOs, each with a reverse diode, its voltage can be switched in the positive or negative direction. By connecting six or seven of these in series and switching them at different times with in each 50 Hz cycle an accurate sine wave is developed. If the developed voltage is higher than system voltage the STATCOM will supply reactive power like a rotating synchronous compensator and improve the voltage and conversely if lower it will remove reactive power. STATCOM has potential to maintain its reactive current at low voltage since it has an essentially constant current characteristics while a thyristor SVC is constant impedance.

Reduced land use to about 40% of a thyristor SVC requirement gives the potential for limited storage, if batteries replace capacitor

Be applied as an active filter because each step can be switched in response to a harmonics

A STATCOM can provide fast capacitive and inductive compensation and is able to control its output current independently of the AC system voltage.

There are mainly two approaches to mitigate power quality problems. The first approach is load conditioning, which ensures that equipment is made less sensitive to power disturbances, allowing the operation even under significant voltage distortion. The other solution is to

install line conditioning system that suppresses the power disturbances.

3.1 Mitigation of Flicker

The most basic configuration of the STATCOM consists of a two-level VSC with a DC energy storage device; a coupling transformer connected in shunt with the AC system, and associated control circuits. It is possible to change the reactive power flow on the connection line by using reactive shunt compensators, such as STATCOM, to mitigate the flicker level during continuous operation of grid connected wind turbines. Figure. 1 shows the block diagram of STATCOM based wind generator.

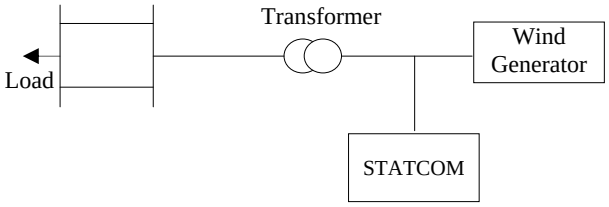

Figure. 1 Voltage Fluctuation Mitigation with STATCOM

The STATCOM consists of a controllable PWM voltage source converter. The voltage source converter is preferred to the current source converter because the devices are clamped against over-voltages by the voltage across the DC-link capacitor bank. The losses are lower and the devices do not have to able to withstand a large reverse voltage.

3.2 Harmonics mitigation

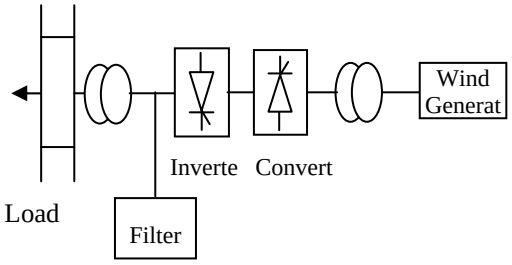

Figure. 2 Harmonics mitigation with shunt active filter

Among the different technology available active filters prove to be flexible to compensate current harmonic components compared to passive filters whose performance is limited to few harmonics and they can also introduce resonance in power system. Figure. 2 shows the active shunt filter system which is used to mitigate harmonics. Harmonics, one of the most important power quality problems results from the basic operating principle of converters in the wind energy generator-grid can be reduced by appropriately designing a shunt active filter. The shunt active filter has topology similar to that of STATCOM. Shunt active filter compensates current harmonics by injecting equal and opposite harmonic current acting as current source injecting harmonic current by the load but phase shifted by 180^0

4.Modeling and Simulation of Wind Power System

4.1 Induction generator

In this study, wind induction generator is modeled using PSCAD as shown in Figure. 3 and case studies are carried out in regarding to power quality and stability using STATCOM

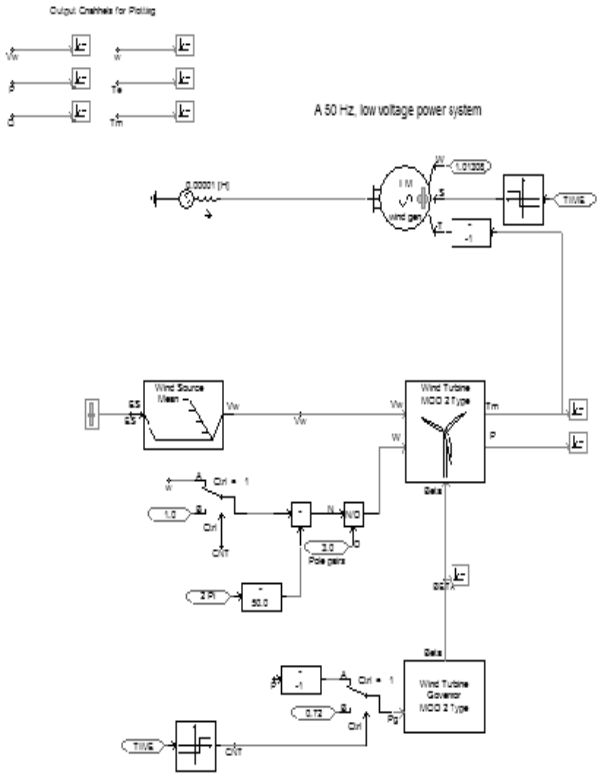

Figure. 3 modeling of wind induction generator

Case A: In this case wind induction generator connected to a grid is modeled. The results indicates the active power, reactive power and the terminal voltage varies continuously due to varying wind speed and the synchronization problem associated with wind generator connected to a grid.

Case B: In this case, wind induction generator connected to a grid with STATCOM is modeled. The results indicates the active power, reactive power and the terminal voltage variations are regulated by means of STATCOM which injects reactive power to regulate the system under study as shown in Figure. 5

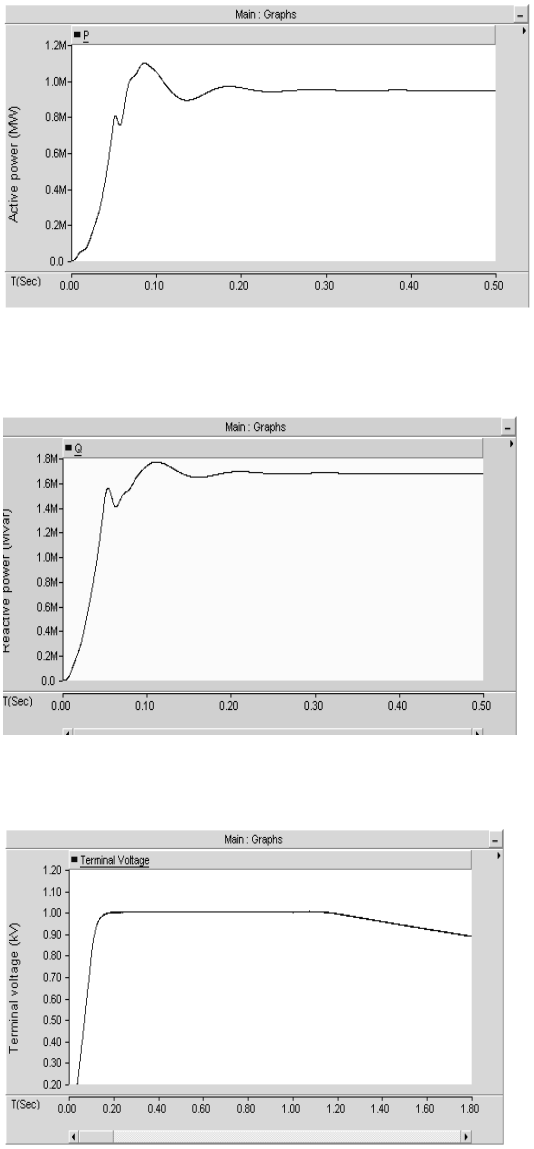

Figure. 4 Variation of Active power, Reactive power and terminal voltage of a induction generator connected to a grid

Figure 5 Variation of active & reactive power and terminal voltage of an induction generator connected to a grid with STATCOM.

Case C: In this case the induction generator driven by a wind turbine connected to a grid with converters is modeled. The main use of converters is to sweep maximum power at the available speed but such converters acting as a non-linear load will result in harmonics. The effect of harmonics is studied with and without active filter which is shown in Figure. 6. The current harmonics spectrum analyzed on both source side and load side due to the non-liner converters without filter is given in Figure. 7.

Case D: In this case, the induction generator driven by a wind turbine connected to a grid with converters and filters is modeled. The filter connected to the grid side will reduce the harmonics as shown in Figure. 8. shows the active shunt filter modeled using PSCAD and current harmonics spectrum with filter is shown in Figure. 8.

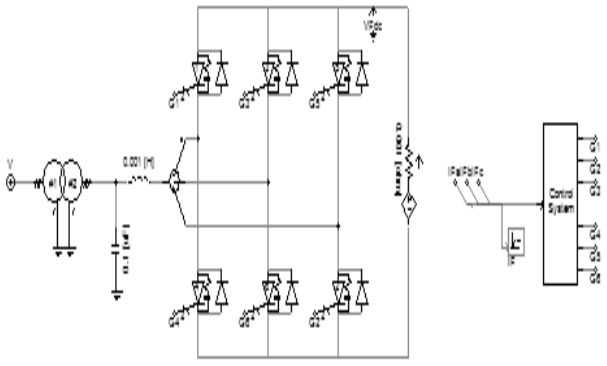

Figure. 6 STATCOM as a shunt active filter

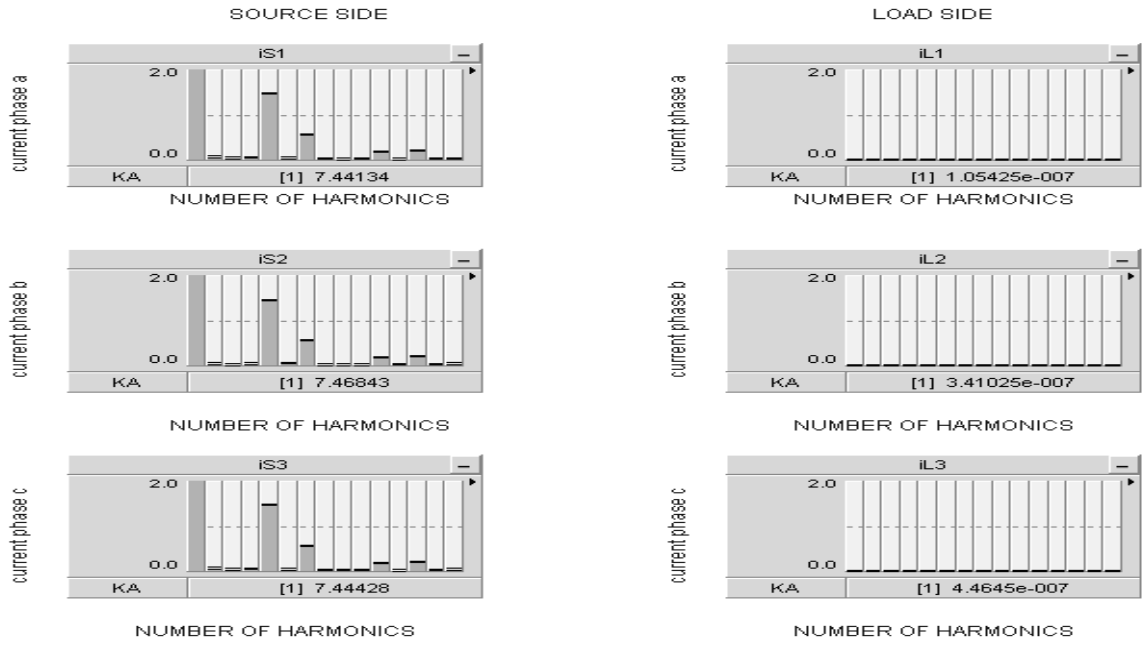

Figure. 7 Current harmonics spectrum without filter

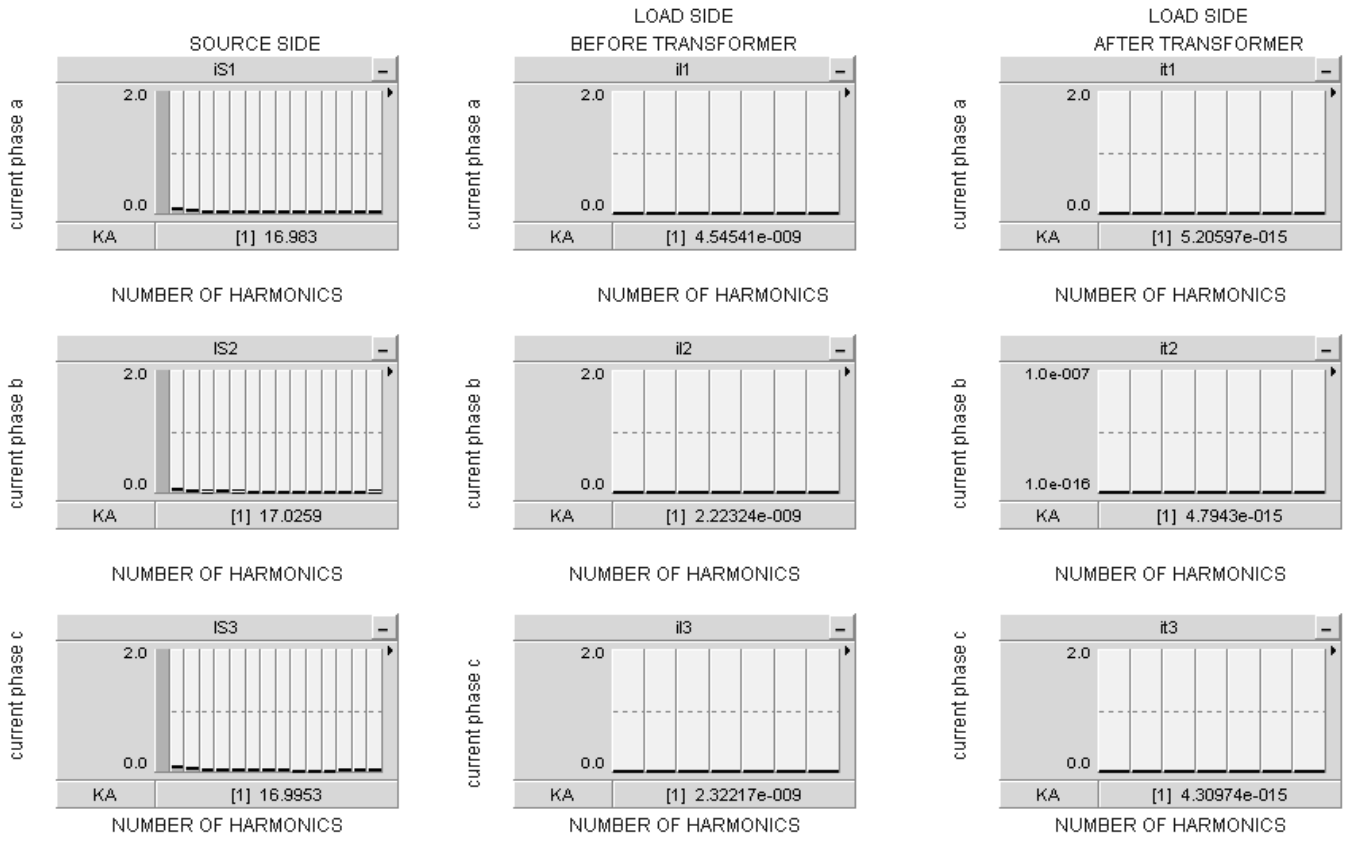

Figure. 8 Current harmonic spectrum with filter

  - Volume 4, Number 1 (ISSN 1995-6665)

5.2 Synchronous generator

Synchronous generator based wind turbine which is more advantageous than induction generator, supplies reactive power and the maintenance is high. In this study wind synchronous generator is modeled using PSCAD and case studies have been carried out in regard to power quality and stability

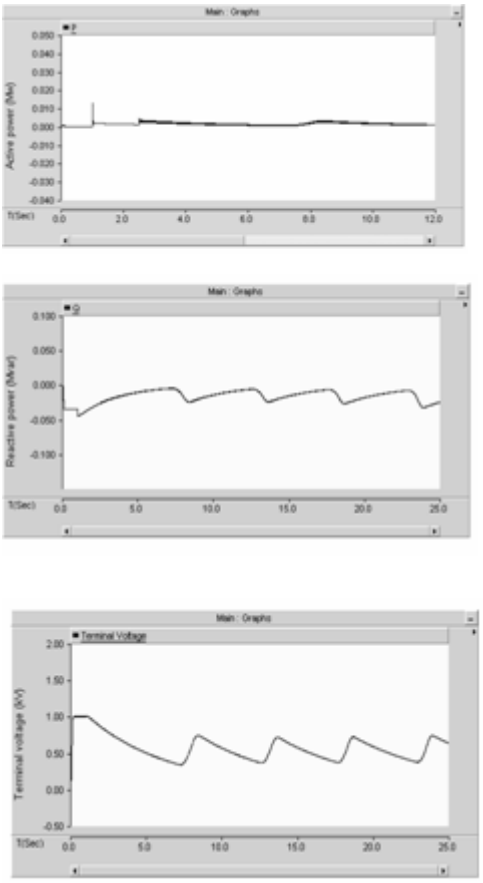

Figure. 9 Variation of active power, reactive power and terminal voltage of a wind synchronous generator connected to a grid

Case A: In this case wind synchronous generator connected to a grid without STATCOM is modeled. Results indicates the active power, reactive power and the terminal voltage varies continuously due to varying wind speed and the synchronization problem associated with wind generator connected to a grid as shown in Figure. 9.

Case B: In this case wind synchronous generator Connected to a grid with STATCOM is modeled. Here the STATCOM is connected to compensate the voltage fluctuation and maintain the voltage with in limits. The results indicates the active power, reactive power and the terminal voltage variations are regulated by means of STATCOM which injects reactive power to regulate the system under study as shown in Figure. 10

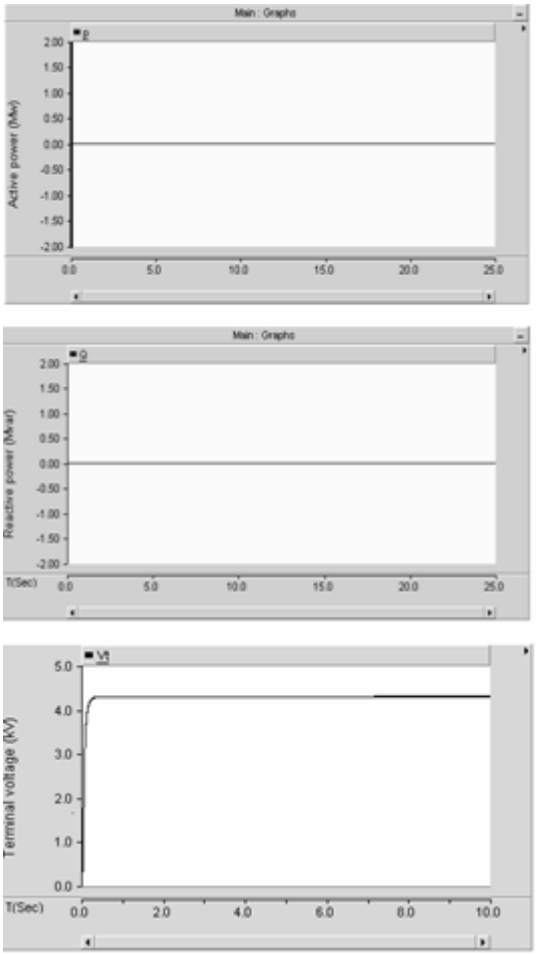

Figure. 10 Variation of active power, reactive power and terminal voltage of a wind synchronous generator connected to a grid with STATCOM

Case C: In this case the synchronous generator driven by a wind turbine connected to a grid with converters is modeled. The converters used to seep maximum power act as non-linear load. Figure. 11 shows the current harmonics spectrum on both source side and load side due to the non-liner converters. High amount of harmonics are measured due to power electronic converters

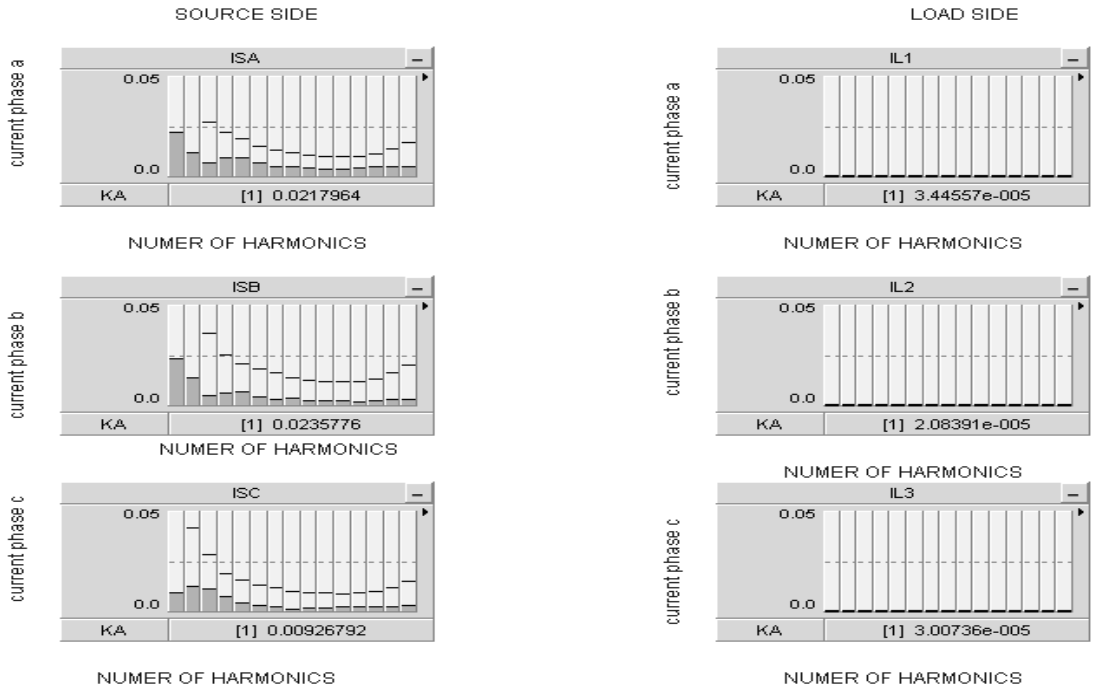

Figure. 11 Current harmonics spectrum without filter

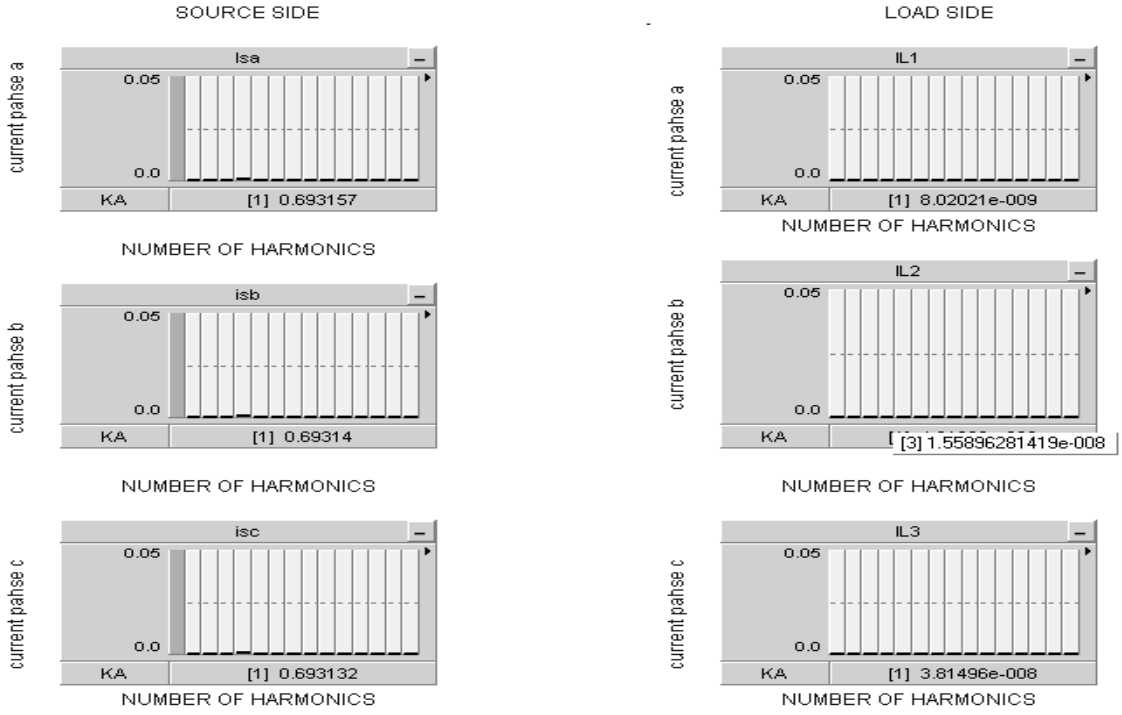

Figure. 12 Current harmonic spectrum with filter

Case D: In this case, the synchronous generator driven by a wind turbine connected to a grid with converters and shunt active filter are modeled. The filter connected to the grid side is reducing the harmonics. It is clearly reflected in the current harmonics spectrum shown in Figure. 12

5. Conclusions

In this work, power quality issues such as voltage fluctuation, harmonics are analyzed with respect to wind generator connected to a grid. The modeling and simulation techniques of a wind power converter and connected power system had been analyzed using PSCAD.

From this analysis, it was found that voltage fluctuation occurs frequently due to synchronization problem associated with connection of wind generator to grid. Hence STATCOM was used to inject reactive power to maintain voltage level with in limits and also eliminates power fluctuations and this confirms the excellent performance of the proposed system for power quality improvement. It was proved that the STATCOM modified as a shunt active filter can be used to eliminate the harmonics generated by the power converters.

Acknowledgement

Authors are thankful to All India Council for Technical Education, India for their financial support (project grant: 1-51/FD/CA/(13)/2006-07) to carry out this work

References

[1] C.Carrillo, A.E.Feijoo & J.Cidras, Power fluctuations in an isolated wind plant, IEEE Trans. on Energy Conversions, Vol. 19, No. 1, 2004, 217-221.

[2] Z. Chen & E. Spooner, Grid interface for renewable energy sources, Proc. 2nd International conf. on Power Electronics and Motion Control Conference(IPEMC'97), Hangzhou, China, 1997, 256–261.

[3] M. P. Papadopoulos, Investigation of the flicker emission by grid connected wind turbines, Proc. 8th International conf. on Harmonics & Quality Power, Athens, Greece, 1998, 14–16.

[4] Neris, N. Vovos, & G. Giannakopaulos, A variable speed wind energy conversion scheme for connection to weak ac systems, IEEE Trans. Energy Conversions, Vol. 14, No. 1, 1999, 122–127.

[5] Z. Chen & E Spooner, Grid power quality with variable speed wind turbines, IEEE Trans. Energy Conversions, Vol. 16, No. 2, 2001, 148–153.

[6] M.Davidson, Interaction of a wind farm with the distribution network and its effect on voltage quality, Proc. IEE Colloquium on the impact of Embedded Generation on Distribution Networks (Digest 1996/194), 1996, 9/1–9/5.

[7] S.K.Salman, & A.L.J.Teo, Windmill modelling consideration and factors influencing the stability of a grid-connected wind power based embedded generator, IEEE Trans. Power Systems, Vol. 18, No. 2, 2003, 793–802.

[8] A.Arulampalam, M.Barnes & N.Jenkins, Power quality and stability improvement of a wind farm using STATCOM, Proc. IEE Generation, Transmission & Distribution, Vol. 153, No.6, 2006, 701-710.

[9] Z.Saad-Saoud, M.L.Lisboa, J.B.Ekanayake, N. Jenkins & G.Strbac, Application of STATCOMs to wind farms, Proc. IEE Generation, Transmission & Distribution, Vol.145, No. 5, 1998, 511–516.

[10] A.Arulampalam, J.B.Ekanayake & N.Jenkins, Application study of a STATCOM with energy storage, Proc. IEE Generation, Transmission & Distribution, Vol. 150, No. 3, 2003, 373–384.

[11] Z. Chen & S.B. Tennakoon, Harmonic filter considerations for voltage source inverter based advanced static Var compensator, Proc. International Universities Power Engineering Conference (UPEC'92), Bath, UK, 1992, 640–643.

[12] Z. Chen & E. Spooner, Wind turbine power converters: comparative study, Proc. IEE Conf. on Power Electronics and Variable Speed Drives (PEVD'98), London, UK, 1998, 471–476.

JJMIE

Volume 4, Number 1, Jan. 2010
ISSN 1995-6665
Pages 177- 192

Jordan Journal of Mechanical and Industrial Engineering

Solar Net Collective Flux and Conversion Efficiency of the Nickel-Pigmented Aluminium Oxide Selective Absorber Prepared by Alternate and Reverse Periodic Technique in Different Prototype Volumes

A. Wazwaz [a, *], J. Salmi [b], R. Bes [c]

[a] *Department of Chemical Engineering, College of Engineering, Dhofar University, P.O.Box 2509, Postal Code 211, Salalah, Sultanate of Oman.*

[b] *Marion Technologies Nanomaterials, Nanostructured Materials & Ceramic Powders, Cap Delta - Parc Technologique Delta Sud, F-09340, Verniolle, France*

[c] *CIRIMAT/LCMIE, Université Paul Sabatier, 31062 Toulouse Cedex 4, France*

Abstract

Different constructed prototypes of different volumes were used to test different nickel- pigmented aluminium oxide selective absorber samples for photo thermal conversion. Different types of solar net collective flux (average, accumulative, maximum, minimum) were calculated. We found that there is a good linear mathematical relationship between the solar net collective fluxes with the prototype volume in the range 500 – 8000 ± 1 cm^3. Comparison between aluminium alloy, copper sheet, and the nickel-pigmented aluminium oxide selective absorber for net collective flux with nickel content and prototype volume were done. The highest net collective flux is for the sample of nickel content 60μg/cm^2 where: during a day, the accumulative net collective flux is 5586±1 W/m^2; while the average net collective flux is 372.4±0.1 W/m^2 in prototype of volume 500±1 cm^3. The lowest net collective flux is for the sample of nickel content 92μg/cm^2, where: during a day, the accumulative net collective flux is 4393±1 W/m^2; the average net collective flux is 292.9±0.1 W/m^2 in prototype of volume 8000±1 cm^3 .The percent conversion efficiency and absorption of merit are constants for all samples in all prototypes. The maximum average percent conversion efficiency is for sample of nickel content 60μg/cm^2 which lies in the range (72.0-74.0±0.1) %. However the least average percent conversion efficiency is for the sample of nickel content 92μg/cm^2 which lies in the range of (61.0-69.0±0.1) %. The best mathematical relations between the net collective flux and prototype volume were calculated. The correlation coefficients squared for all calculations are 0.91 on average.

Keywords: Selective Absorber; Nickel-Pigmented Aluminium Oxide, Prototype, Net Collective Flux, Conversion Efficiency, Absorption of Merit.

1. Introduction

Solar energy is an important, cheapest, and safe source of renewable energy. Therefore, it plays an important role in many different branches of our life. Solar energy materials are used commercially for photothermal, photoelectric energy production and for achieving energy efficiency in buildings. Developments in architecture with buildings are achieved using electrochromic and thermotropic windows. In agriculture, growths of plants are affected by being tuned to the spectral sensitivity for photosynthesis. The solar energy source is electromagnetic radiations that interact with matter.

We can utilize the solar energy by means of collectors. These collectors may be flat [12] or concentrating.

There are four basic types of concentrating collectors:

1. Parabolic trough [15].
2. Parabolic dish.
3. Power tower.
4. Stationary concentrating collectors.

The main part of the collector is the absorber. The absorber can be selective [1, 2] or non-selective, black or colored [3].

Selective surfaces/films/coatings form the basis of a wide range of very useful optical coatings and interference filters. Many fields such as chemistry, physics, and

* Corresponding author. arefwazwaz@hotmail.com.

technology are used to develop the optical coatings scientifically and industrially.

The selective coating may be ideal or non-ideal. The selectivity depends on the application we interested in [4, 11, 14].

The collector can be glazed, unglazed, or insulated. The glazed, insulated collector with absorber, which is selective, gives the best solar thermal performance. In our study the selective absorber is the nickel-pigmented aluminium oxide selective absorber.

We studied the optical properties (Absorptance, Reflectance, and Transmittance) of nine samples of nickel-pigmented aluminium oxide selective absorber, environmental conditions, and the configuration of our system (prototype) on the heating power and the conversion efficiency [5] of the selective absorber.

The cover used is a commercial polyethylene, because it reduces the convective loss, of low cost, flexible and can protect the selective absorber from degradation caused by exposing the absorber directly to the environment.

The performance of the flat-plate collector with an absorber for photothermal conversion can be described by the conversion efficiency (η) [13]. The conversion efficiency depends on the collective flux which in turn depends on the radiation flux and the heat loss. The radiation losses can be calculated using the Stefan-Boltzmann law and the other losses can be easily calculated, because they are dependent on the configuration and environment of the system. These losses are also linearly proportional to the temperature.

The effective role of the selective absorbers in photothermal conversion can be described by two cases. Both of them are concerned with the calculation of the collector efficiency. One is where the conduction and convection losses are assumed to be negligible compared to the radiation losses. This is also valid if the collector is operating at a high temperature. To maximize the conversion efficiency for both flat-plate and concentrating collectors, the loss of heat must be reduced while the absorptance-transmittance product must be increased to be close to unity. The performance of photothermal converters is also dependent on absorptivity (α) and emissivity (ε) separately.

The second case is where the conduction and convection losses are not neglected. These losses are strongly dependent on the environment (wind velocity, humidity, ambient temperature) and on the configuration of the systems [6].

Many scientists have discussed the thermodynamic equations governing the efficiency of solar collectors. Advances and development in fundamental physics and chemistry can lead to new and more efficient solar energy materials that have very widespread applications [6-8].

In this paper we study the relationship between the net collective fluxes (average, accumulative, and maximum), percent conversion efficiency, and absorption of merit with nickel content and the prototype volume.

2. Experimental

The constructed models were tested outdoors during daylight under clear sky at Bethlehem University from June to October. All measurements are done at steady state conditions. The selective absorbers were put on a horizontal plane. The experimental model for the flat-plate collector (prototype) is consisting of the selective absorber, the insulated box, the transparent cover, and the data logger.

2.1. Selective Absorber

Nickel-pigmented alumina was prepared on aluminium alloy substrate. Samples of different optical properties were used. These samples were prepared using an electrochemical process. Anodic aluminium (alumina) was first formed followed by pigmentation of alumina by nickel using alternate or reverse periodic current.

Scanning electron microscopy was used to determine the structure of the selective absorber surface and the thickness of the coatings. The thickness measured was found to be in the range from 0.350 to 0.400 μm.

The optical properties (hemispherical absorptivity α and hemispherical emissivity ε) were measured using an absorptiometer (EL 510 Elan Informatique) and an emissiometer (EL 520 Elan Informatique) at 70^{o}C, respectively. X-ray diffraction was used to test the presence of impurity phases [5].

The following block diagram illustrates preparation of aluminium alloy surface.

Figure 1. The electrochemical cell for the anodization of aluminium alloy.

The pigmentation of alumina with nickel was done using alternate and reverse periodic currents [5].
The schematic of the resulted layers from anodization and pigmentation is shown in Figure 2.

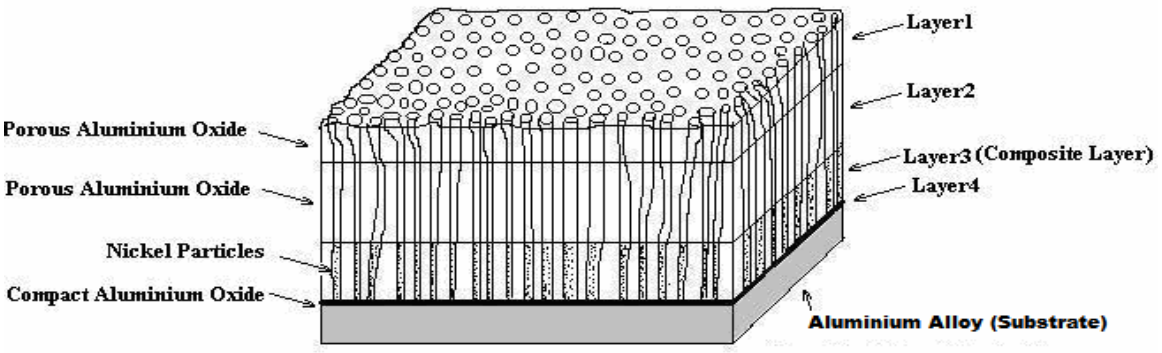

Figure 2. Schematic of the cross-section of the prepared selective absorber.

2.2. Insulated Box (Prototype).

Four different types (by volume) of prototypes were used. Figure 3 illustrates schematically the structure of the prototype. Table1 gives the dimensions for each prototype.

Table1. Dimensions of the prototypes used in the solar thermal performance.

Box type	Length(cm)xWidth(cm)x Height(cm)	Volume ($\pm$1cm^3)	Shield Area ($\pm$1cm^2)
A	10x10x5	500	100
B	15x15x5	1125	225
C	20x20x5	2000	400
D	40x40x5	8000	1600

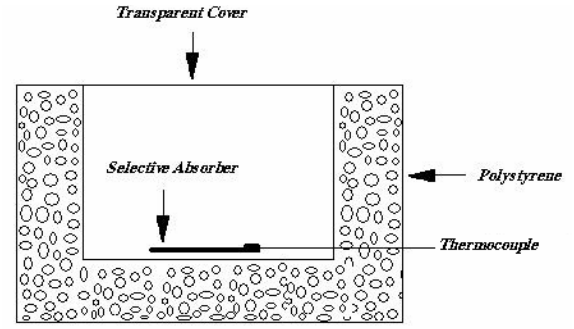

Figure 3. Schematic drawing of the prototype.

2.3. The Transparent Cover

A commercial polyethylene shield of thickness 50 µm and average transparency of 0.80 (in the solar range) was used. It is usually used to reduce the heat loss and to protect the absorber from degradation caused by exposing the absorber directly to the environment.

2.4. The data logger

The data logger used was HANDY-LOG DB-525 version 4 with DB-Lab WINDOWS^{TM} software. This data logger is coupled with temperature sensors DT013 of temperature range -25^{o}C to 125^{o}C ($\pm$0.01^{o}C). In addition to, it is equipped with a relative humidity sensor (DT 041). The temperature of the selective absorber, the temperature Inside and outside the box, and the relative humidity were measured at the same time.

All the set-up components for the solar net collective flux (net heating power) measurements are shown in Figure 4.

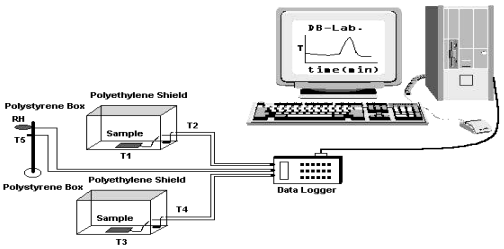

Figure 4. Schematic of all set-up components for the solar net collective flux measurements.

3. Method of Calculations

The performance of the selective absorber for photo-thermal conversion can be described by the conversion efficiency (η) which is defined as [6]:

$$\eta = \frac{\text{Energy extracted from the system}}{\text{Energy input}} = \frac{Ee}{A\,Is} \qquad (1)$$

Where
A is the area of the absorber exposed to the flux.
I_s is the incident flux. E_e is the extracted energy from the system (also, called net collective flux or net heating power).

E_e = (Energy absorbed) - (Energy lost)

$$E_e = (t\alpha)\,A\,I_s - U_L \qquad (2)$$

Where $t\alpha$ is the effective transmittance-absorptance coefficient product for a single covered collector.
t is the transmittance of the cover. U_L is the overall loss of energy from the absorber. U_L is the sum of three parameters that involved in the heating process, namely, radiation, conduction, and convection losses.

The radiation losses can be calculated using Stephan-Boltzmann law and the other losses are dependent on the configuration and environment of the system. Moreover, these losses are linearly proportional to the temperature.

The effective role of the selective absorbers in photo-thermal conversion can be described by two cases. Both of them are concern with the calculation of the collector efficiency.

The first case is where the conduction and convection losses are assumed to be negligible compared to the radiation losses. It is also valid if the collector is operating at high temperatures. In this case the extracted energy (heating flux, E_e) can be calculated as in the following relation:

$$E_e = (t\alpha)\, A\, I_s - \sigma A \epsilon\, (T_s^4 - T_a^4) \qquad (3)$$

Where
A is the area of the absorber.
σ is Stephan-Boltzmann constant ($5.678\ 10^{-8}$ W.m^{-2} K^{-4}).
Є is the thermal emittance at temperature Ts of the absorber.
T_a is the temperature of the ambient.
T_s is the temperature of the selective absorber.
The conversion efficiency (η) becomes:

$$\eta = t\alpha - \frac{\sigma\varepsilon(Ts^4 - T^4 a)}{Is} \qquad (4)$$

If the absorber is illuminated with a concentrated solar flux of concentration ratio X, then relation 4 becomes:

$$\eta = t\alpha - \frac{\sigma\varepsilon\,(Ts^4 - T^4 a)}{XIs} \qquad (5)$$

To maximize η for both flat plate and concentrating collectors, U_L must be reduced while the absorptance-transmittance product must be increased to be close to unity.
The performance of photo-thermal converters is also depending on absorptivity (α) and emissivity (Є) separately. Therefore, the term absorptance of merit (α_m) [6] was used to indicate the conversion efficiency (η) when there is no cover (t=1). It gives the upper limit for the conversion efficiency of a solar converter.

The output heat can be measured in terms of the mechanical work by using the Carnot efficiency which can be calculated for a particular reversible thermodynamic cycle as:

Where
W is the output work. Q_s is the heat of the selective absorber.

$$\eta(\text{Carnot}) = \frac{W}{Qs} = \frac{Qs-Qa}{Qs} = \frac{Ts-Ta}{Ts} \qquad (6)$$

T_s, T_a are the temperatures of the selective absorber and ambient; respectively.
The second case is where the conduction and convection losses are not neglected. In this case the extracted heating energy (Ee) (net collective flux or net heating power) can be calculated as

$$E_e = (t\alpha)I_s - B(T_s - T_a) - \sigma\epsilon_{eff}\,(T_s^4 - T_a^4) \qquad (7)$$

Where

B is the conduction-convection loss coefficient.

ϵ_{eff} is the effective emittance of the absorber and the atmosphere [9] which is given by:

$$\in_{eff} = \left[\frac{1}{\in_s} + \frac{1}{\in_a} - 1\right]^{-1} \qquad (8)$$

Where
$Є_s$ is the average emissivity of the selective absorber and
$Є_a$ is the average atmospheric emissivity.
The experimental model for testing the selective absorber consisting of: the insulated box, the transparent cover and the data logger are discussed in the previous section.
In addition to, the heat capacity of the system and the conduction-convection coefficient (B), for each prototype, were determined and used from previous study [5]. We wrote computer software to do all the calculations [5]

4. Results and Discussion

The relation between the accumulative and average net heating power (net collective flux) with prototype volume for aluminium alloy is shown in figure 5.
Linear regression for the accumulative and average net heating power for aluminium alloy gives the following relations:
Pac = -0.0291 V + 874.8 with $R^2 = 0.97$
Pav = -0.0019 V + 58.4 with $R^2 = 0.97$
Where
$\mathbf{P_{ac}}$ is the accumulative net heating power per square meter of aluminium alloy during a day.
$\mathbf{P_{av}}$ is the average net heating power per square meter of aluminium alloy per hour during a day.
V is the volume of the prototype in cubic centimeter. $\mathbf{R^2}$ is the correlation coefficient square.
These relations represent the accumulative and average net heating power for aluminium alloy; respectively.
The accumulative net collective flux is 874.8 W/m^2 and the average net collective is 58.4 W/m^2 when heat loss is neglected (V = 0.0 cm^3).
In addition to, we can do the same calculations for copper sheet. The comparison between aluminium alloy and copper sheet substrates is shown in figure 6.
As we see from figure 6, copper sheet has higher net collective flux (net heating power) by approximately one and half more than that of aluminium alloy. Therefore, copper sheet is a better substrate; this because copper has greater thermal conductance than aluminium alloy.
The effect of prototype volume on using nickel pigmented anodized aluminium selective absorber instead of aluminium alloy substrate is shown in the following tables and figures.
The variation of **Ts, Ta, ΔT, P, η** and $\boldsymbol{\alpha_m}$ with day time for nickel pigmented anodized aluminium selective absorber sample of nickel content 82 μg/cm^2 ,inside prototype A, is shown in table 2.

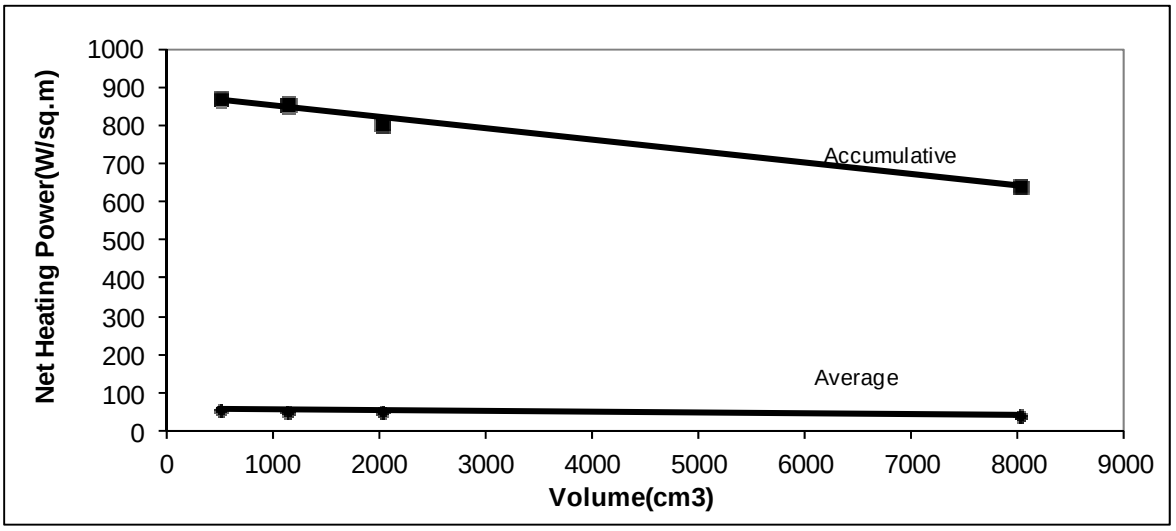

Figure 5. Variation of accumulative and average net heating power for aluminium alloy with prototype volume.

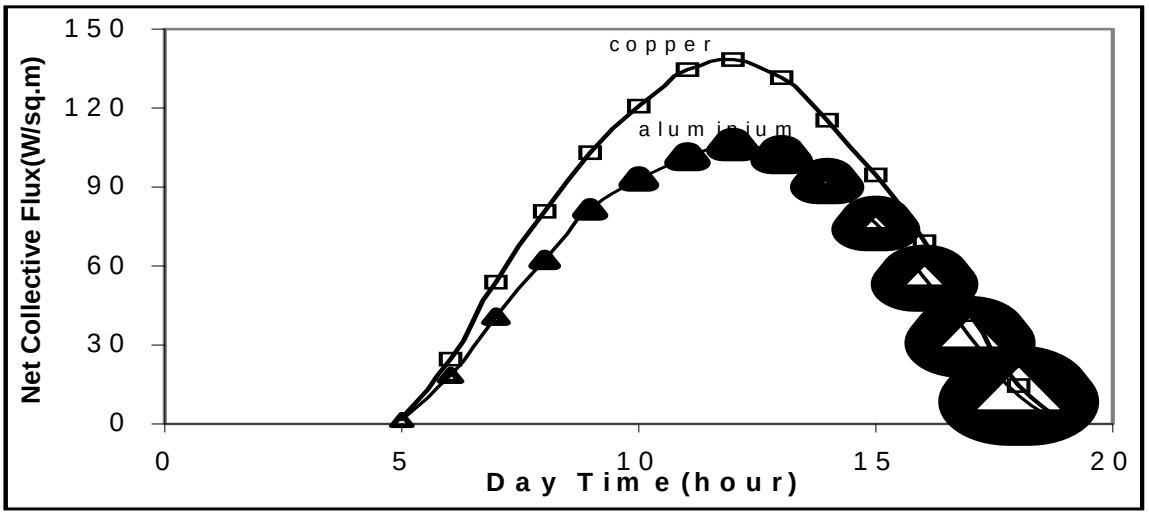

Figure 6. Variation of the net collective flux with the day time for aluminium alloy and copper sheet.

Table 2.Variation of Ts, Ta, ΔT, P, η and α_m with day time for selective absorber sample of nickel content 82 μg/cm^2 using prototype A.

Time(h)	Ts(^{o}C) (±0.01)	Ta(^{o}C) (±0.01)	ΔT(^{o}C) (±0.01)	P(W/m^2) (±0.01)	η (±0.01)	α_m (±0.01)	RH (%) (±0.01)
5.00	24.82	23.54	1.28	16.02	0.76	0.96	33.47
6.00	24.66	23.06	1.60	119.68	0.77	0.96	37.25
7.00	29.79	27.55	2.24	264.01	0.77	0.96	34.73
8.00	37.00	30.31	6.69	399.58	0.77	0.96	24.20
9.00	46.00	32.51	13.49	506.54	0.77	0.96	24.04
10.00	64.86	31.87	32.99	600.94	0.76	0.96	33.32
11.00	68.07	29.79	38.28	656.57	0.76	0.96	39.76
12.00	35.72	29.31	6.41	667.63	0.77	0.96	41.17
13.00	32.83	28.83	4.00	639.42	0.77	0.96	44.48
14.00	30.75	28.03	2.72	571.94	0.77	0.96	46.68
15.00	30.11	27.55	2.56	459.82	0.77	0.96	46.68
16.00	29.31	26.91	2.40	340.03	0.77	0.96	47.46
17.00	28.19	26.11	2.08	204.12	0.77	0.96	47.46
18.00	27.07	24.82	2.25	68.17	0.77	0.96	50.60
19.00	25.79	23.70	2.09	0.00	0.00	0.79	54.85

From table 2:

Accumulative net collective flux (accumulative net heating power) is 5403±1 W/m^2.

Average net collective flux (average net heating power) is 360.2±0.1 W/m^2.

Average conversion efficiency is 69.0±0.1 %. Average absorption of merit is 95.0±0.1 %.

Average relative humidity is 40.4±0.1%.

The effect of adding the selective coating (nickel pigmented alumina), in comparison with aluminium alloy substrate, on the net collective flux (using prototype A) is shown in figure 7.

As we see from figure 7, adding the nickel pigmented anodized aluminium layer over the substrate will increase the net collective flux approximately eight times greater than that of using aluminium alloy alone.

In all measurements, we found that the maximum net collective flux obtained during a day is in the time interval 11:00AM to 13:00PM.

The behavior of sample of nickel content 82 μg/cm^2 compared with aluminium alloy substrate using prototype B is shown in figure 8.

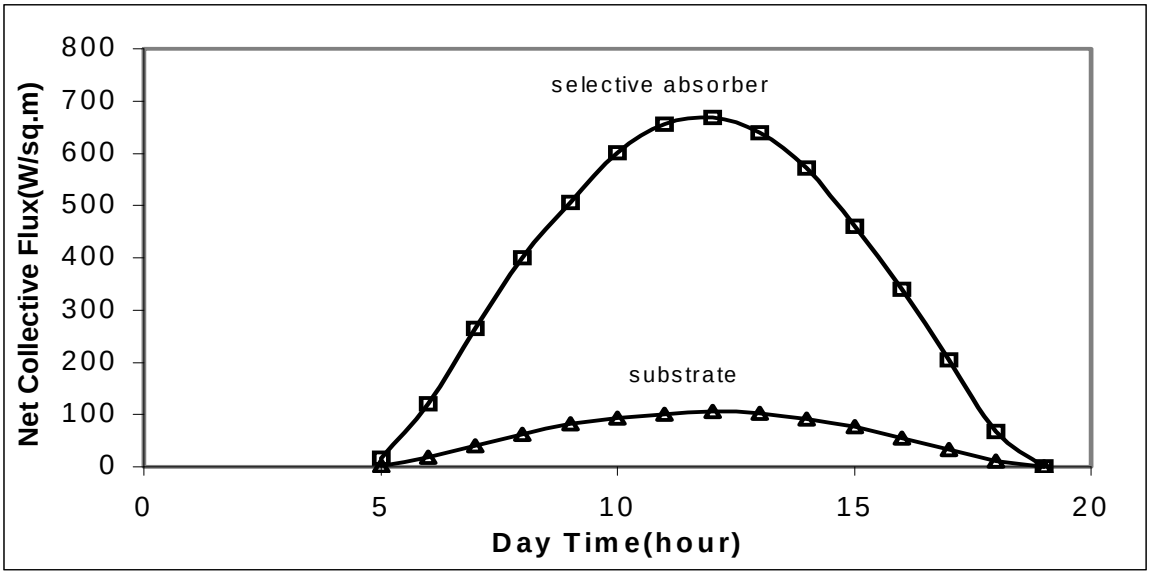

Figure 7. Effect of adding nickel pigmented anodized aluminium layer over aluminium alloy substrate on the net collective flux using prototype A.

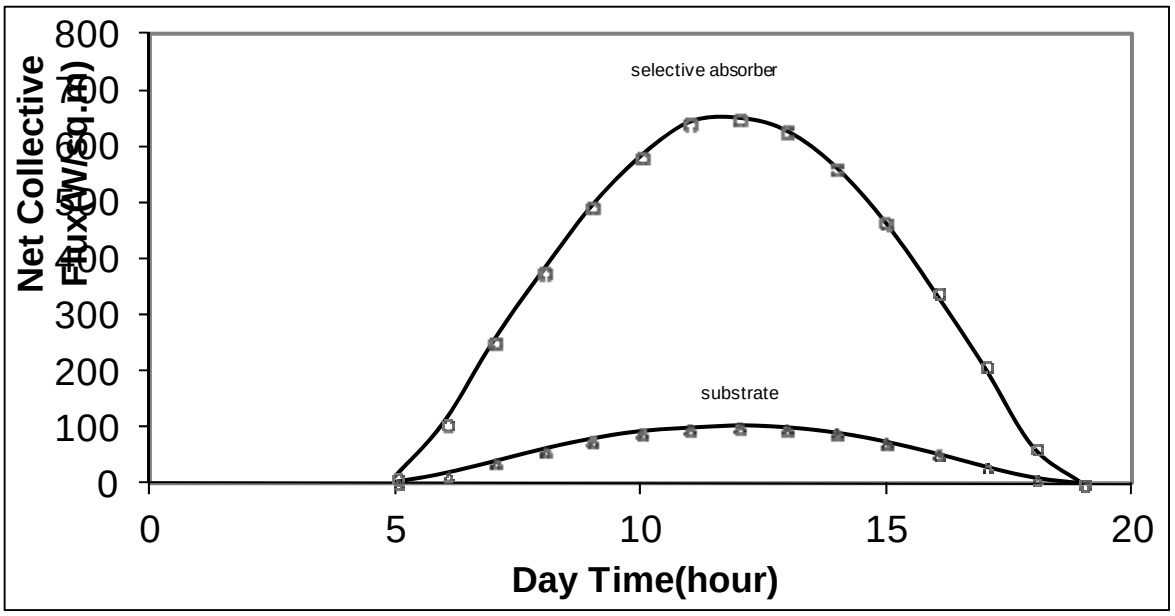

Figure 8. Variation of net collective flux with day time for selective absorber sample of nickel content 82 μg/cm^2 and aluminium alloy substrate using prototype B.

Comparing figure 8 with figure 7, prototype B gives less net collective flux than prototype A. This is because the conduction-convection and radiation losses are increased by increasing the prototype volume.

The same behavior will be obtained if we use prototypes C and D , but with less net collective flux during the day. The behavior of sample of nickel content 82 μg/cm^2 compared with the aluminium alloy during a day light inside prototype C is shown in figure 9.

Less net collective flux is obtained for both samples of nickel content 82 μg/cm^2 and the aluminium alloy substrate using prototype C.

However, using prototype D gives the same behavior but with less net heating power during a day because of the increase in the conduction-convection and radiation losses as we will see in table 3. Average relative humidity is 37.9±0.1%.

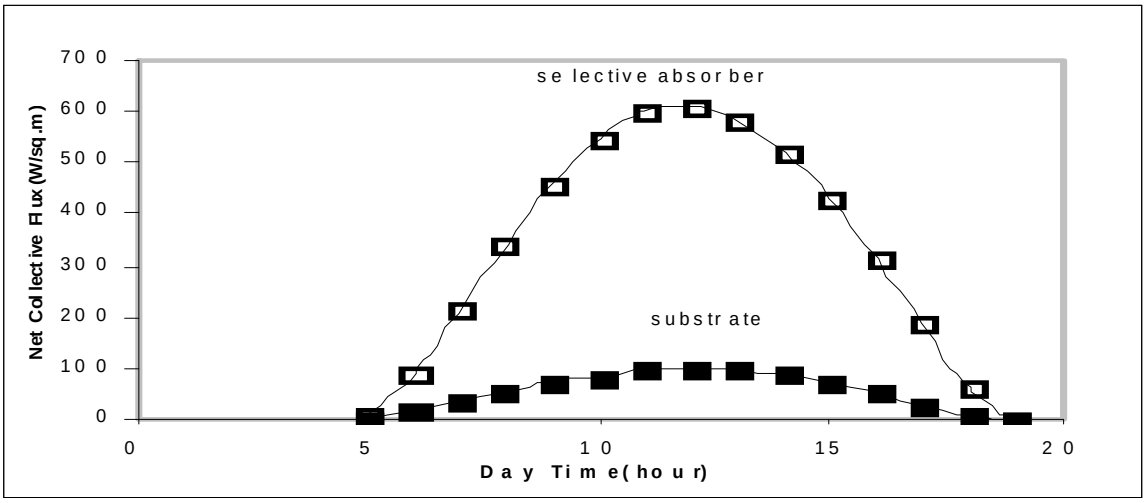

Figure 9. Variation of net collective flux with day time for selective absorber sample of nickel content 82 μg/cm^2 and aluminium alloy substrate using prototype C.

Table 3. Variation of Ts, Ta, ΔT, P, η and α_m with day time for selective absorber sample of nickel content 82 μg/cm^2 using prototype D.

Time(h)	Ts(^{o}C) (±0.01)	Ta(^{o}C) (±0.01)	ΔT(^{o}C) (±0.01)	P(W/m^2) (±0.01)	η (±0.01)	α_m (±0.01)	RH (%) (±0.01)
5.00	27.07	27.07	0.00	0.00	0.00	0.96	38.50
6.00	27.23	27.23	0.00	60.67	0.77	0.96	38.82
7.00	28.35	27.55	0.80	184.91	0.76	0.96	37.72
8.00	35.23	35.07	0.16	331.59	0.77	0.96	30.33
9.00	56.62	42.12	14.50	436.01	0.74	0.93	24.83
10.00	73.99	38.44	35.55	504.87	0.71	0.90	26.25
11.00	69.51	37.64	31.87	561.43	0.72	0.91	28.76
12.00	41.64	34.43	7.21	606.66	0.76	0.95	34.73
13.00	39.08	33.95	5.13	580.70	0.76	0.95	35.36
14.00	37.48	33.79	3.69	505.60	0.76	0.95	35.99
15.00	36.04	33.63	2.41	394.21	0.76	0.95	37.56
16.00	35.07	32.51	2.56	271.92	0.76	0.95	46.99
17.00	33.15	31.39	1.76	135.40	0.76	0.95	50.45
18.00	31.71	30.43	1.28	23.07	0.72	0.91	50.60
19.00	30.27	29.47	0.80	0.00	0.94	0.02	52.02

Figures 8, 9 and 10 show that as the prototype volume increased (from A to D), the net collective flux is decreased during the day since the conduction-convection (B) and the radiation losses are increased. However, the nickel pigmented layer on aluminium alloy increases the net collective flux by approximately eight times in comparison with the aluminium alloy alone.

The behavior is the same in figures 8 to 10 for all nickel pigmented anodized aluminium selective absorber samples, but with different numerical results.

The variation of percent conversion efficiency with day time for sample of nickel content 82 μg/cm^2, using prototype A, is shown in figure 11.

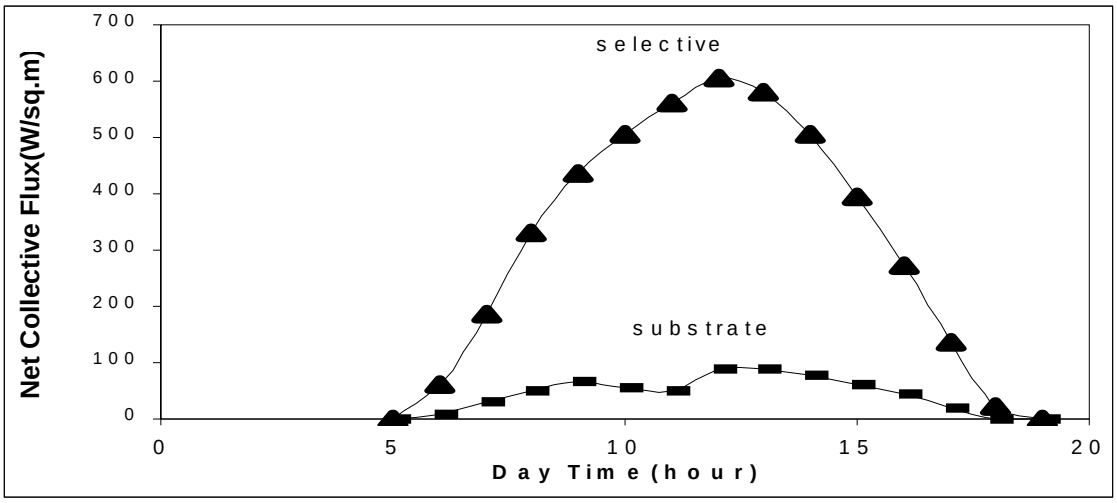

Figure 10. Variation of net collective flux with day time for sample of nickel content 82 μg/cm^2 and aluminium alloy substrate using prototype D.

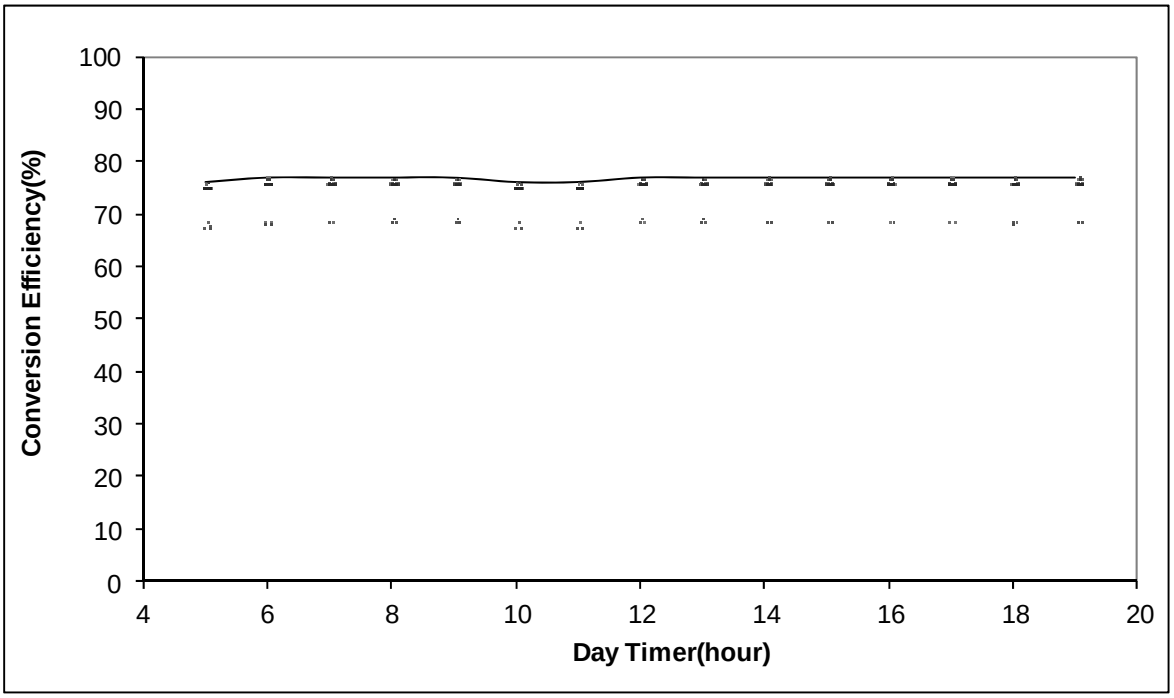

Figure 11. Variation of percent conversion efficiency as a function of day time for selective absorber sample of nickel content 82 μg/cm^2 using prototype A.

From figure 11, the percent conversion efficiency is constant during the day and this behavior is the same for all selective absorber samples using all prototypes, because the conversion efficiency depends, mainly, on the optical property of the sample.

The behavior of the percent absorption of merit during a day light for selective absorber sample of nickel content 82 μg/cm^2 using prototype A is shown figure 12.

As we see from figure 12, the percent absorption of merit is constant during a day and this is the same behavior for all other samples in all different prototypes, but with different numerical results. Absorption of merit depends, mainly, on the optical properties of the selective absorber sample and does not on the shield. It represents the maximum conversion efficiency that can be obtained if there is no shield on the prototype.

The accumulative net collective flux results for selective absorbers including copper sheet and aluminium alloy substrates are summarizes in table 4. These results represent all types of prototypes used.

Table 4 shows that the highest accumulative net collective flux (per day) is obtained using the selective absorber sample of nickel content 60μg/cm^2 which gives 5586±1W/m^2 in prototype A ; while the lowest value obtained with the selective absorber sample of nickel content 92μg/cm^2 which gives 4393±1W/m^2 in prototype D.

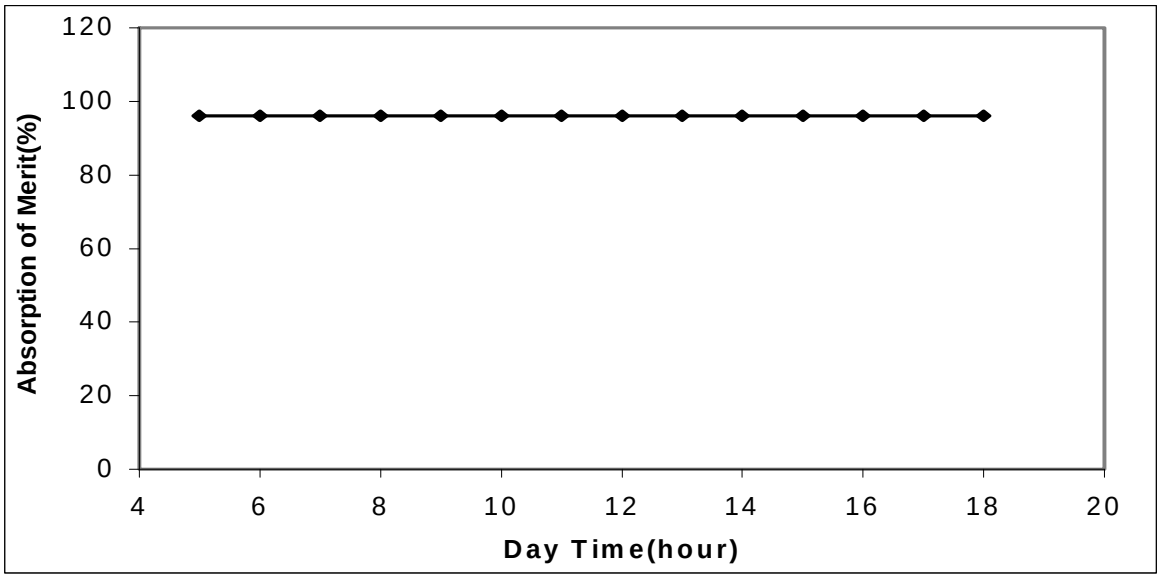

Figure 12. Variation of percent absorption of merit as a function of day time for selective absorber sample of nickel content 82 μg/cm^2 sample using prototype A.

Table 4: Accumulative net collective flux (per day) for all samples in different prototypes (A, B, C and D).

Sample of Nickel Content(±1μg/cm^2)	$P_{ac}(A)^1$±1	$P_{ac}(B)^1$±1	$P_{ac}(C)^1$±1	$P_{ac}(D)^1$±1
0 (Al alloy)	875	851	788	647
0 (Cu sheet)	1125	1109	1038	824
55	5568	5566	5511	4976
60	5586	5574	5528	5017
70	5535	5518	5469	4880
73	5531	5455	5336	4841
76	5516	5451	5041	4631
80	5515	5395	4953	4597
82	5403	5395	4826	4561
86	5300	5343	4762	4402
92	5292	5037	4713	4393

[1]Represent the accumulative net collective flux (accumulative net heating power) in different prototypes (A, B, C and D).

For the substrates, the highest value is obtained with copper sheet which gives 1125±1W/m^2 in prototype A; while the lowest value is obtained with aluminium alloy which gives 647±1W/m^2 in prototype D.

Since each selective absorber sample has a certain nickel content, we will see in the following figures the effect of nickel content on the accumulative collective flux, conversion efficiency and the absorption of merit.

The net collective flux (per day) as a function of the nickel content is shown in figure 13. As the nickel content increased, the accumulative net collective flux is increased to certain nickel content then it decreased after this limit. In other words, there is an optimum value of nickel content that gives the highest accumulative net collective flux.

As we see from figure 13, the nickel content limit is 60μg/cm^2. This value is in accordance with the previous study [10].

The average net collective flux (during a day and per hour) for all samples in different prototypes is shown in table 5.

Table 5 is with accordance with table 4 where the highest average net collective flux (during a day and per hour) is obtained for the selective absorber sample of nickel content 60 μg/cm^2 which gives 372.4±0.1W/m^2 in prototype A; while the lowest value is obtained for the selective absorber of nickel content 92 μg/cm^2 which gives 292.9±0.1W/m^2 in prototype D.

For the substrates, the highest value is obtained for Cu sample which gives 75.0±0.1 W/m^2; while the lowest

value is obtained for aluminium sample which gives 43.1±0.1 W/m^2 in prototype D.

The variation of the average net collective flux (during a day and per hour) with the nickel content is shown in figure 14.

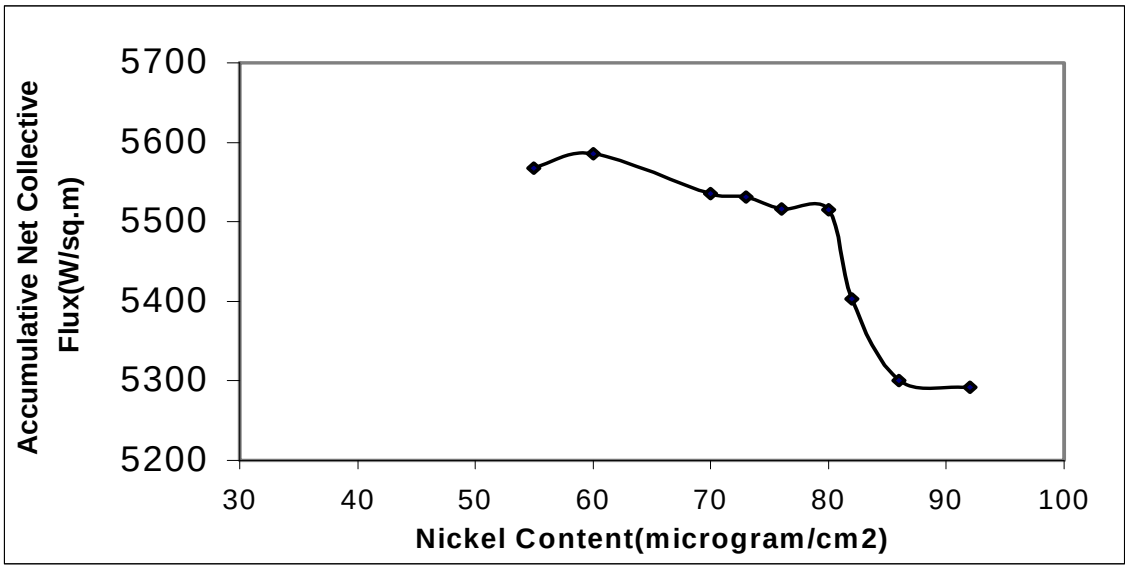

Figure 13. Variation of accumulative net collective flux with the nickel content using prototype A.

Table 5. The average net collective flux (during a day and per hour) for the substrates and the selective absorber samples in different prototypes (A, B, C and D).

Sample of Nickel Content(±1μg/cm^2)	$P_{av}(A)^1$±0.1	$P_{av}(B)^1$±0.1	$P_{av}(C)^1$±0.1	$P_{av}(D)^1$±0.1
0 (Al alloy)	58.3	56.8	52.6	43.1
0 (Cu sheet)	75.0	74.0	69.2	54.9
55	371.2	371.1	367.4	331.7
60	372.4	371.6	368.6	334.5
70	369.0	367.9	364.6	325.3
73	368.7	363.6	355.8	322.7
76	367.8	363.4	336.0	308.7
80	367.6	359.7	330.2	306.5
82	360.2	356.2	321.7	304.1
86	353.3	341.1	317.5	293.5
92	352.8	335.8	314.2	292.9

[1]Represent the accumulative net collective flux (accumulative net heating power) using different prototypes (A, B, C and D).

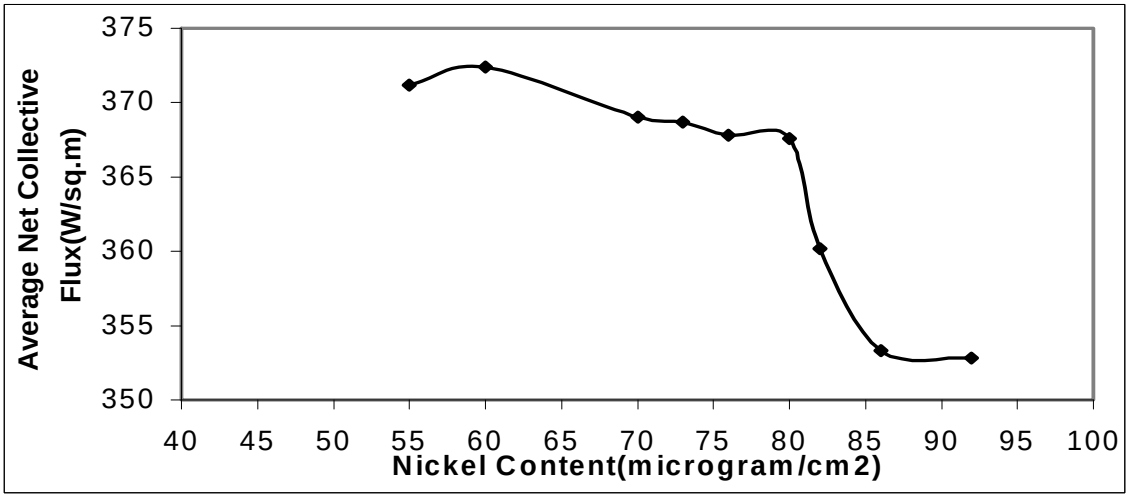

Figure 14: Variation of average net collective flux with the nickel content using prototype A.

Figure 14 is in accordance with figure 13.

The variation of the accumulative net heating power and the average net heating power (for the sample of nickel content 73 μg/cm^2 with prototype volume) is shown in figure 15. Linear regression for the accumulative and average net heating power for the sample of nickel content 73 μg/cm^2 leads to the following relations:

$\mathbf{P_{ac} = -0.0896\ V + 5551.2}$ with $\mathbf{R^2 = 0.99}$

$\mathbf{P_{av} = -0.0060\ V + 370.1}$ with $\mathbf{R^2 = 0.99}$

Where

P_{ac} is the accumulative net heating power per square meter of the selective absorber during a day.
P_{av} is the average net heating power per square meter of the selective absorber and per hour during a day.
V is the volume of the prototype in cubic centimeter. R^2 is the correlation coefficient square.
The above relations represent the accumulative and average net heating power for one sample of nickel content 73 μg/cm^2. The accumulative net collective flux is 5551.2 W/m^2 and the average net collective flux is 370.1 W/m^2, when heat loss is neglected (V = 0.0 cm^3).
The extracted relations of the accumulative and average net heating power for nickel pigmented anodized aluminium selective absorber samples are illustrated in table 6 and 7, respectively.

Where

P_{ac} is the net accumulative heating power per square meter of the selective absorber during a day.
V is the volume of the prototype in cubic centimeter.
R^2 is the square of the correlation coefficient.

From table 6, the sample of nickel content 60 μg/cm^2 is of the highest value. It gives 5656.0 W /m^2 , when there is no heat loss (V = 0.0 cm^3). However, the lowest value is for sample of nickel content 92 μg/cm^2. This sample gives 5151.6 W/m^2, when there is no heat loss (V = 0.0 cm^3). This value of the nickel content inside the alumina pores is sufficient to grade the refractive index of the layers from the base on aluminium alloy to the top porous alumina layer. Therefore, it gives the optimum selectivity and in turns the maximum solar net collective flux.

The relations can be best described by a linear relationship, because the correlation coefficient square is very close to 0.91 on average.

The relations for all selective absorber samples and substrates are illustrated in table7. Table 7 is in accordance with table 6.
The correlation coefficient squared in the above two tables' shows that the relation between the net heating power and the prototype volume is linear since it is very close to one.
The average percent conversion efficiency is calculated (during a day and per hour) for the substrates and the selective absorber samples as shown in table 8.

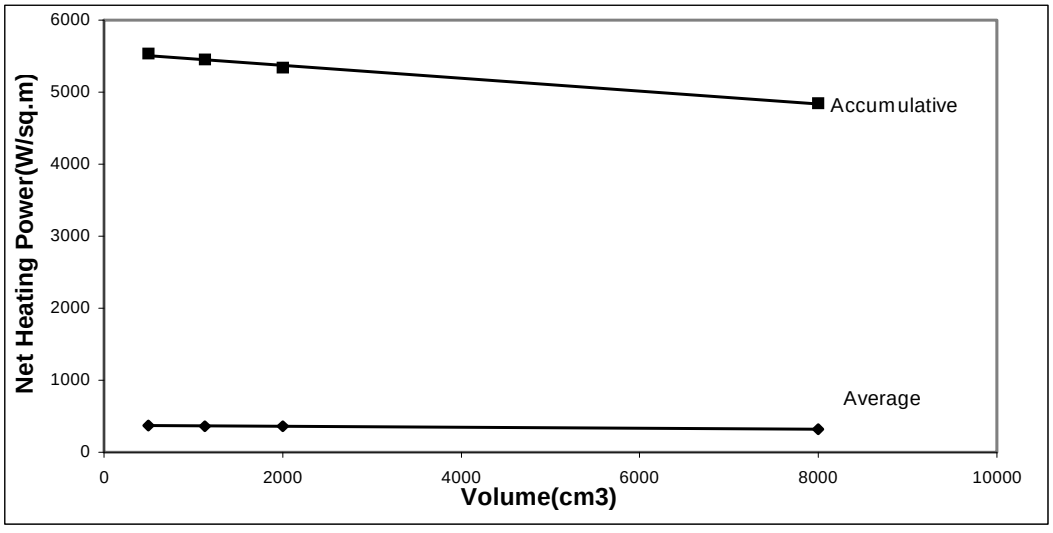

Figure 15. Variation of accumulative and average net heating power for the sample of nickel content 73 μg/cm^2 with prototype volume.

Table 6. Extracted relations of the accumulative net heating power for substrates and selective absorber samples during a day.

Sample of Nickel Content(±1μg/cm^2)	Extracted Relation	R^2
0 (Al alloy)	P_{ac} = -0.0291 V + 874.8	0.97
0 (Cu sheet)	P_{ac} = -0.0399 V + 1140.0	0.99
55	P_{ac} = -0.0829 V + 5646.0	0.99
60	P_{ac} = -0.0790 V + 5656.0	0.99
70	P_{ac} = -0.0909 V + 5614.5	0.99
73	P_{ac} = -0.0896 V + 5551.2	0.99
76	P_{ac} = -0.1109 V + 5482.0	0.87
80	P_{ac} = -0.1106 V + 5436.5	0.82
82	P_{ac} = -0.1050 V + 5351.4	0.75
86	P_{ac} = -0.1173 V + 5292.6	0.80
92	P_{ac} = -0.1008 V + 5151.6	0.80

Table 7. Extracted relations of the average net heating power for substrates and selective absorber samples during a day and per hour.

Sample of Nickel Content(±1μg/cm^2)	Extracted Relation	R^2
0 (Al alloy)	P_{av} = -0.0019 V + 58.4	0.97
0 (Cu sheet)	P_{av} = -0.0027 V + 76.0	0.99
55	P_{av} = -0.0055 V + 376.4	0.99
60	P_{av} = -0.0053 V + 377.1	0.99
70	P_{av} = -0.0061 V + 374.3	0.99
73	P_{av} = -0.0060 V + 370.1	0.99
76	P_{av} = -0.0074 V + 365.5	0.87
80	P_{av} = -0.0074 V + 362.4	0.82
82	P_{av} = -0.0068 V + 355.4	0.76
86	P_{av} = -0.0070 V + 346.7	0.84
92	P_{av} = -0.0067 V + 343.4	0.80

Table 8. Average percent conversion efficiency (during a day and per hour) for substrates and selective absorber samples in different prototypes (A, B, C and D).

Sample of Nickel Content(±1μg/cm^2)	$\%\eta_{av}$(A) ± 0.1[1]	$\%\eta_{av}$ (B) ± 0.1[2]	$\%\eta_{av}$ (C) ± 0.1[3]	$\%\eta_{av}$ (D) ± 0.1[4]
0 (Al alloy)	12.5	11.0	13.0	12.0
0 (Cu sheet)	15.0	15.5	17.0	12.8
55	72.0	74.0	72.0	65.0
60	72.0	74.0	73.0	73.2
70	72.0	73.0	72.0	64.0
73	72.0	73.0	72.0	64.0
76	71.0	72.0	72.0	61.0
80	71.0	71.0	72.0	61.0
82	69.0	68.0	71.0	61.0
86	69.0	68.0	71.0	61.0
92	69.0	68.0	68.0	61.0

Where : [1]Average percent conversion efficiency using prototype A. [2]Average percent conversion efficiency using prototype B. [3]Average percent conversion efficiency using prototype C. [4]Average percent conversion efficiency using prototype D.

Table 8 shows that the highest average percent conversion efficiency (during a day and per hour) obtained is (74.0±0.1)%, and the lowest value is (61.0±0.1)% for different selective absorber samples in different prototypes.

For the substrates, the highest value is obtained with Copper substrate which is (17.0±0.1)%, while the lowest value is obtained with Aluminium alloy substrate which is (11.0±0.1)%.

From table 8, the maximum net collective flux obtained is (699.2±0.1)W.m2 for sample of nickel content 60 μg/cm2 using prototype A; while the lowest value is (590.3±0.1)W.m2 for sample of nickel content 92 μg/cm^2 using prototype D.

Concerning substrates, the maximum value obtained is (138.4±0.1) W.m^2 for Cu sheet using prototype A; while the lowest value obtained is (89.4±0.1) W.m^2 for Al alloy in prototype D.

The relation between the maximum net collective fluxes (during a day) with prototype volume (for one sample of nickel content 73 μg/cm^2) is shown in figure 16.

The relation between the maximum net collective fluxes with prototype volume is given by:

$P_{max} = -0.0072\ V + 676.0$ with $R^2 = 0.99$

The relations for all selective absorber samples are illustrated in table 9.

These relations are fall in the interval time 11:00 to 13:00 during a day.

The effect of the nickel content on the maximum net collective flux obtained during a day is shown in figure 18.

The variation of the maximum net collective flux with nickel content in figure 15 has the same behavior as in previous figures.

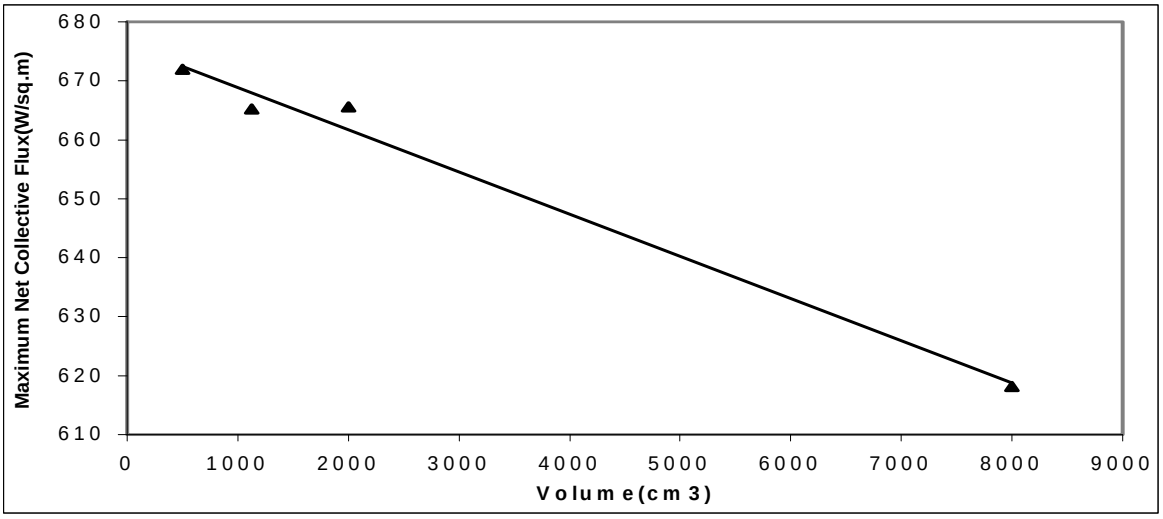

Figure 16. Variation of the maximum net collective flux with prototype volume for sample of nickel content 73 μg/cm^2.

Table 9. Extracted relations of the maximum net heating power for the selective absorber samples during a day.

Sample of Nickel Content(±1μg/cm^2)	Extracted Relation	R^2
55	$P_{max} = -0.0064\ V + 683.2$	1.00
60	$P_{max} = -0.0071\ V + 694.6$	0.93
70	$P_{max} = -0.0063\ V + 679.2$	0.97
73	$P_{max} = -0.0072\ V + 676.0$	0.99
76	$P_{max} = -0.0074\ V + 669.6$	0.96
80	$P_{max} = -0.0073\ V + 662.4$	0.83
82	$P_{max} = -0.0069\ V + 657.5$	0.75
86	$P_{max} = -0.0060\ V + 638.4$	0.91
92	$P_{max} = -0.0055\ V + 632.1$	0.81

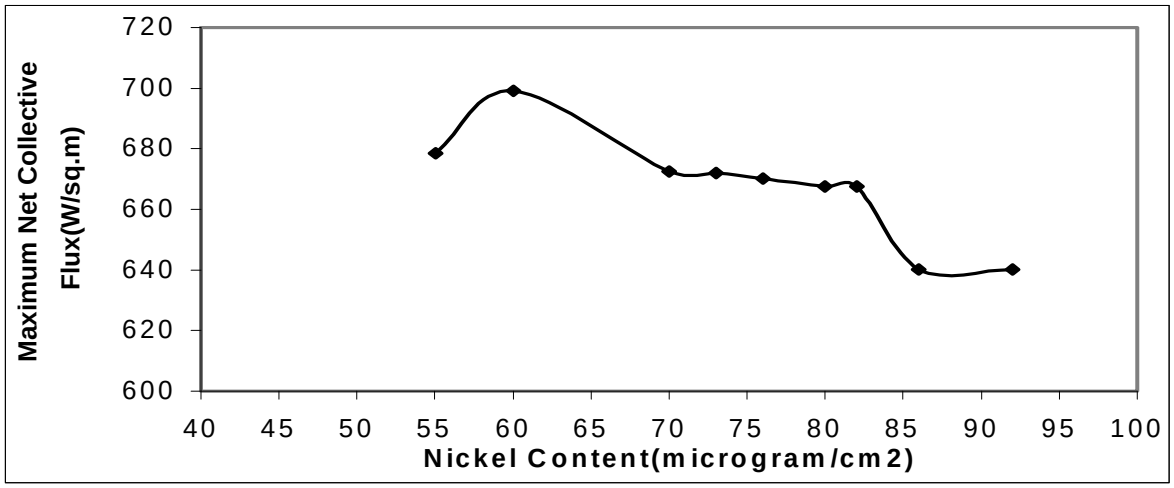

Figure 17.Variation of maximum net collective flux obtained during a day with the nickel content using prototype A.

5. Conclusions

Nickel pigmented anodized aluminium alloy selective absorbers prepared by dc anodization (using dilute phosphoric acid) followed by electrolysis in nickel sulphate solution (coloration) using ac and prc currents were used.

The substrates and the selective absorber samples are tested at Bethlehem University at a horizontal level where certain experimental set-up is used. The substrates selective absorber samples were tested inside prototypes of volume in the range of 500–8000±1cm^3.

The net heating power (net collective flux) (average, accumulative and maximum), conversion efficiency (average and maximum) and absorption of merit (average and maximum) were studied.

Comparing aluminium alloy with copper sheet shows that copper sheet gives higher net collective flux, conversion efficiency and absorption of merit than aluminium alloy.

Prototype of volume 500±1 cm^3 is of the most suitable prototype because it has the least conduction-convection losses. The highest conversion of the solar flux is found for the selective absorber of nickel content 60 μg/cm^2. However, the lowest conversion of the solar energy into thermal energy is found for sample of nickel content 92μg/cm^2 due to its high emissivity.

The effects of nickel content, in the alumina pores, on the converted solar flux is that as the nickel content increased the absorptivity is increased. However, there is a nickel content limit that gives the optimum net collective flux and selectivity. This limit is 60μg/cm^2.This limit of nickel content is sufficient to decrease the refractive index gradually from the barrier alumina (at the bottom) to the upper porous alumina. Therefore the solar radiation can be trapped inside the alumina pores that have certain nickel content (nickel particles). This trapping gives good opportunity for the radiation to be absorbed by multi reflection of the radiation inside the pores and by the resonant scattering of radiation among nickel particles embedded in the alumina pores (figure2).There is a linear relationship between the net heating power (collective flux) (average, accumulative and maximum) and average absorption of merit with prototype volume.

The commercial polyethylene is used because it is a good shield for glazed insulated prototype reduces the connective loss and protects the selective absorber against degradation.

References

[1] C.M. Lampert, Solar Energy Materials Vol. 1, 1979, 319.

[2] Sten Löfving, Solar Energy Materials Vol. 5, 1981, 103.

[3] C.M. Lampert, Solar Energy Materials Vol.2, 1979, 1.

[4] C.G. Granqvist, Physica Scripta. , Vol. 32, 1985, 401.

[5] A. Wazwaz, PhD Thesis, Paul Sabatier, Toulouse, France, 2001.

[6] M.S. Sodha, S.S. Mathur and M.A.S. Malik, "Reviews of Renewable Energy Resources", John Wiley and Sons, Vol. 2, 1983, 237- 239 and 297-319.

[7] A.S. Elasfouri and M. M. Hawas, Energy Convers. Mgmt Vol. 27, No. 1, 1987, 1.

[8] H.C. Hottel and A. Whillier, "Evaluation of flat-plate solar collector performance", Trans. Of Conference on the Use of Solar Energy, University of Arizona 2, 1958, 74.

[9] P.K. Gogna, S. C. Mullick and K.L. Chopra , Int. J. Energy Research, Vol. 4, 1980, 317.

[10] J .Salmi, "Elaboration Et Caracterisation De Couches Absorbante Selectives Solaires Sur L'Alliage D'Aluminium 1050", Thesis, Paul Sabatier University, Toulouse, France 1999.

[11] A. Abene, V. Dobois, M. Le Ray and A. Ouagued, Journal of Food Engineering, Vol. 1, No. 65, 2004, 15.

[12] K. Srithar, A. Mani, Journal of Zhejiang University Science A, Vol. 11, No. 7, 2006, 1870.

[13] Sia, Toh Ching, Velautham, Sanjayan, Darus, and Amer Nordin, International Energy Journal, Vol. 8, No. 2, 2007, 125.

[14] S.A. Kalogirou, S. Lalot, G. Florides, and B. Desmet, Solar Energy, Vol. 2, No. 82, 2008, 164.

[15] D. Kruger, Y. Pandian, K. Hennecke, and M. Schmitz, Desalination, 1-3(220), 612(20.

JJMIE

Volume 4, Number 1, Jan.2010
ISSN 1995-6665
Pages 193 - 204

Jordan Journal of Mechanical and Industrial Engineering

Transient Analysis and Output Characteristics of DC Motors Fed by Photovoltaic Systems

Mohammad S. Widyan [a,*], Anas I. Al Tarabsheh [a], Issa Y. Etier [a], Rolf E. Hanitsch [b]

[a] *Electrical Engineering Department , The Hashemite University, 13115 Zarqa, Jordan*

[b] *Institute of Energy and Automation Technology , Berlin University of Technology,Einsteinufer 11, D-10587 Berlin , Germany*

.

Abstract

This paper presents the dynamical analysis of DC shunt, series and permanent-magnet PM motors fed by photovoltaic PV energy systems at different illuminations. At the full solar intensity, the maximum power point of current/voltage I/V characteristic of the PV modules is designed to be at the rated conditions of the machines. The nonlinear behavior of I/V characteristics of the PV modules and that of the magnetization curve of the ferromagnetic materials of the machines are approximated by polynomial curve fitting. The dynamical analysis of the machines fed by fixed terminal voltage has also been carried out and a comparison between the cases of supplying the motors by fully illuminated solar cells, partially illuminated solar cells and fixed terminal voltage is addressed. The steady-state output characteristics, the torque-speed characteristics, of the three DC motors with the two inputs are presented and compared.

Keywords: Dynamical Analysis of DC machines; Photovoltaic Cells; Steady-State Output Characteristics.

1. Introduction

DC motors are electrical machines that consume DC electrical power and produce mechanical torque. Historically, DC machines are classified according to the connection of the field circuit with respect to the armature circuit. In shunt machines, the field circuit is connected in parallel with the armature circuit while DC series machines have the field circuit in series with the armature where both field and armature currents are identical. Permanent-magnet machines, on the other hand, have only one circuit (armature winding) and the flux generated by the magnets is constant. Compared with conventional electrical machines, permanent-magnet machines exhibit higher efficiency, higher power to weight ratio and simpler construction.

The use of PV systems as a power source for electrical machines is considered a promising area in photovoltaic applications due to the ongoing growth of PV-market [1]. The dynamical and steady-state characteristics of PV-powered DC motors at different solar intensities, different loading conditions and different system controllers & configurations have been proposed [2]-[8]. Similar studies for permanent-magnet and AC machines are presented [9]-[13]. PV arrays comprise several parallel/series connected solar cells to provide sufficiently high output power for operating common loads and devices [14]. In this paper, the main contributions are the dynamical analysis and the steady-state output characteristics of DC shunt, series and permanent-magnet motors fed by photovoltaic cells at different solar intensities as compared with the case of supplying the motors by fixed terminal voltage. Additionally, the maximum power point of the photovoltaic cells is designed to be at the rated conditions of the machines when the PV array is fully illuminated. The nonlinearity of the magnetization curve of the ferromagnetic materials of the machines in case of shunt and series motors and that of the *I/V* characteristics of the photovoltaic cells have been included by polynomial curve fitting. The steady-state output characteristics when the motors are fed by solar cells at different illuminations and fixed terminal voltage have been depicted and compared for the three motors. The paper is structured as follows: The nonlinear dynamical model of the DC shunt, series and permanent-magnet motors are presented in Section II. Section III outlines the design and main characteristics of the photovoltaic cells. The numerical simulation results are addressed in Section IV. Section V depicts the steady-state output characteristics of the three machines fed by fixed voltage and by photovoltaic cells at two solar intensities. Finally, conclusions are drawn in Section VI.

Corresponding Author. mohammadwidyan@yahoo.com

2. Dynamical Model of DC Shunt, Series and Permanent-Magnet Motors

This section presents the dynamical model of the DC shunt, series and permanent-magnet motors including the nonlinearity of the magnetization curve of the ferromagnetic materials.

a) DC Shunt Motor

In shunt machine, the field circuit is connected in parallel with the armature circuit. It has the following equivalent circuit:

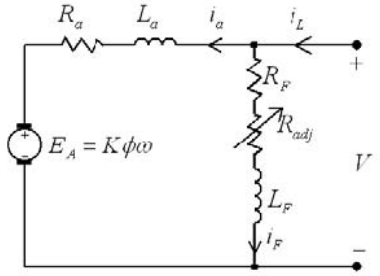

Figure 1. Equivalent Circuit of DC Shunt Motor

The equation of the field circuit is:

$$L_F \frac{di_F}{dt} = V - (R_F + R_{adj})i_F \quad (1)$$

where L_F: field winding inductance, i_F: field current, V: terminal voltage and $R_F + R_{adj}$: field winding resistance. The equation of the armature circuit is:

$$L_a \frac{di_a}{dt} = V - R_a i_a - K\phi\omega \quad (2)$$

where L_a: armature winding inductance, i_a: armature current, R_a: armature resistance, K: constant related to the design of the machine, ϕ: flux per pole and ω: rotational speed of the rotor. The motion equation of the motor is:

$$J \frac{d\omega}{dt} = K\phi i_a - T_L \quad (3)$$

where J: rotor and load moment of inertia and T_L: load torque.

The magnetization curve is the relation between the flux ϕ and the field current i_F. However, it is usually obtained experimentally in terms of the induced voltage $E_A = K\phi\omega$ as function of i_F at a certain rotational speed ω at no load. In this paper, $K\phi$ is expressed as function of the field current i_F based on the data given in [15] after dividing the induced voltage $E_A = K\phi\omega$ by the given rotational speed. $K\phi$ as function of i_F has then been polynomially fitted using MATLAB. It is found that the following second order polynomial is accurate enough to represent them as:

$$K\phi = \alpha_1 i_F^2 + \alpha_2 i_F + \alpha_3 \quad (4)$$

where $\alpha_1 = -0.3084$, $\alpha_2 = 1.0272$ and $\alpha_3 = 0.0049$.

Substituting for $K\phi$ in Eq. (2) yields:

$$L_a \frac{di_a}{dt} = V - R_a i_a - (\alpha_1 i_F^2 + \alpha_2 i_F + \alpha_3)\omega \quad (5)$$

and for $K\phi$ in Eq. (3) gives:

$$J \frac{d\omega}{dt} = (\alpha_1 i_F^2 + \alpha_2 i_F + \alpha_3) i_a - T_L \quad (6)$$

Eqs. (1), (5) and (6) represent the nonlinear dynamical behavior of a DC shunt motor including the nonlinearity of the magnetization curve of the ferromagnetic material of the machine.

b) DC Series Motor

DC series motor, with its own characteristics of high starting torque which makes it suitable for high inertia as well as traction systems, has a nonlinear dynamical model. As its name indicates, the field circuit is connected in series with the armature and therefore the armature and field currents are the same. The equivalent circuit of a DC series motor is:

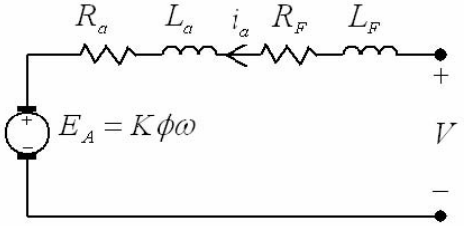

Figure 2. Equivalent Circuit of DC Series Motor

The equation of the armature:

$$(L_F + L_a)\frac{di_a}{dt} = V - (R_a + R_F)i_a - K\phi\omega \quad (7)$$

where L_F: field winding inductance, L_a: armature winding inductance, i_a: armature current, V: applied terminal voltage, R_a: armature winding resistance, R_F: field winding resistance, K: constant depends of the design of the machine, ϕ: flux per pole and ω: rotational speed of the rotor. The motion equation is:

$$J \frac{d\omega}{dt} = K\phi i_a - T_L \quad (8)$$

where J: rotor and load moment of inertia and T_L: load torque.

Based on the data presented in [15] and using MATLAB, it is found that $K\phi$ can be expressed as function of i_a as:

$$K\phi = \beta_1 i_a^2 + \beta_2 i_a + \beta_3 \quad (9)$$

where $\beta_1 = -0.0017$, $\beta_2 = 0.0938$ and $\beta_3 = 0.0062$.

Substituting for $K\phi$ in Eq. (7) yields:

$$(L_F+L_a)\frac{di_a}{dt}=V-(R_a+R_F)i_a-(\beta_1 i_a^2+\beta_2 i_a+\beta_3)\omega \quad (10)$$

and for $K\phi$ in Eq. (8) yields:

$$J\frac{d\omega}{dt}=(\beta_1 i_a^2+\beta_2 i_a+\beta_3)i_a-T_L \quad (11)$$

Eqs. (10) and (11) represent the nonlinear dynamical behavior of a DC series motor including the nonlinearity of the ferromagnetic material of the machine.

c) Permanent-Magnet DC Motor

Due to absence of the field current and field winding, permanent magnet machines exhibit high efficiency in operation, simple and robust structure in construction and high power to weight ratio. The attractiveness of the permanent-magnet machines is further enhanced by the availability of high-energy rare-earth permanent-magnet materials like SmCo and NdFeB [16]. However, the speed control of permanent-magnet DC motor via changing the field current is not possible. The equivalent circuit of the permanent-magnet DC motor is:

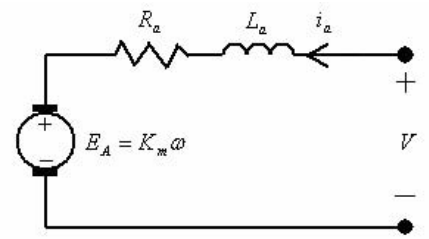

Figure 3. Equivalent Circuit of Permanent-Magnet DC Motor

Applying KVL provides the armature equation as:

$$L_a\frac{di_a}{dt}=V-R_a i_a-K_m\omega \quad (12)$$

where L_a: armature winding inductance, i_a: armature current, V: terminal voltage, R_a: armature resistance, K_m: constant related to the design of the machine and ω: rotational speed. The motion equation is:

$$J\frac{d\omega}{dt}=K_m i_a-T_L \quad (13)$$

where J: rotor and load moment of inertia and T_L: load torque. Eqs. (12) and (13) represent the dynamical model of permanent-magnet DC motor.

The complete numerical parameters of the DC shunt, series and permanent-magnet motors are given in appendix A.

3. Photovoltaic Cells Design and Main Characteristics

Figure 4, (a) shows an example of a commercial amorphous silicon (a-Si:H) PV module where twelve single p-i-n cells are incorporated. Figure 4,(b) presents the equivalent circuit generally applied for photovoltaic modules; it consists of 12 current sources in parallel to 12 diodes. Including the resistive elements and in the circuit of Figure 4, (b) represents very well the behavior of real solar cells [17] and [18]. As a simplification, the PV module is represented as a symbol shown in Figure 4, (c). The specifications of this module are listed in Table I. To increase the voltage and current capabilities of the PV cells, modules are connected in parallel and series as shown in Figure 5.

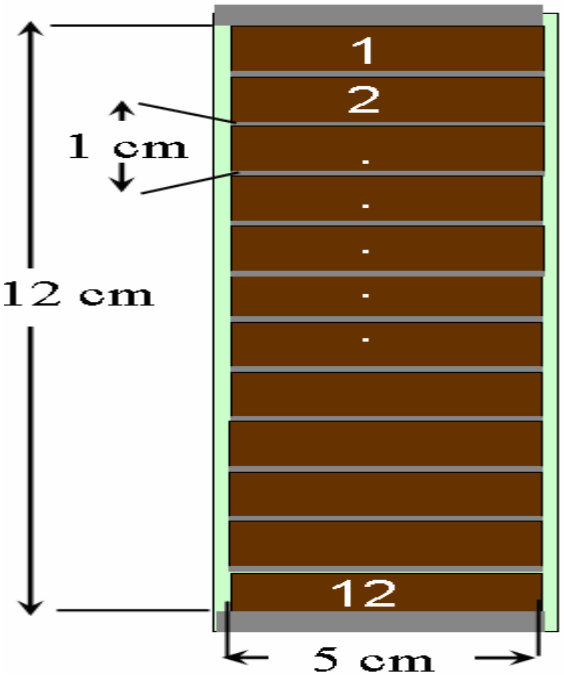

(a)

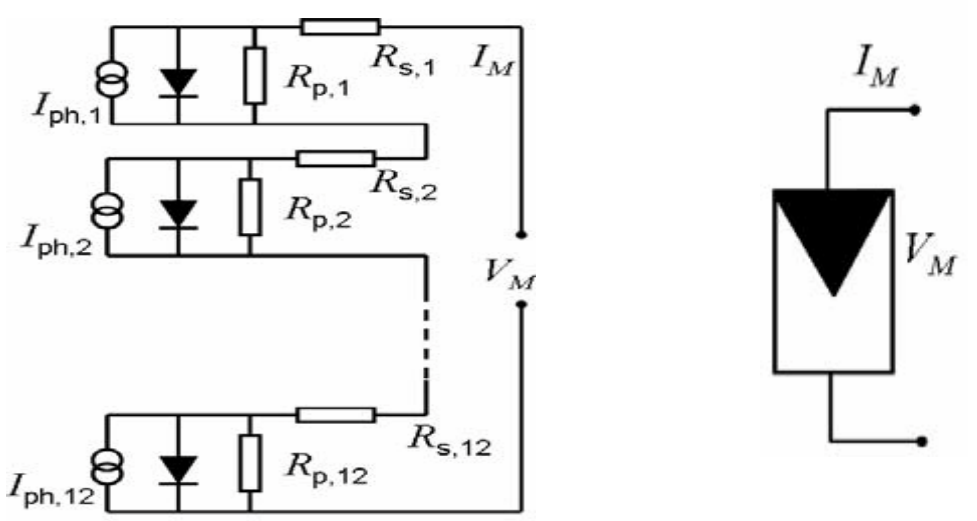

(b) (c)

Figure 4. (a) Thin film amorphous silicon a-Si:H PV module consisting of 12 series-connected solar cells (b) its equivalent circuit and (c) its symbol. The effective area of the module is $60cm^2$ where the area of each cell is $5cm^2$.

Table I. Specifications of the PV module shown in Figure 4

Nominal power (mW)	Voltage at max. power (V)	Current at max. power (mA)	Short circuit current (mA)	Open circuit voltage (V)	Dimensions (cm^2)
431	6.78	63.55	74.2	9.15	5×12

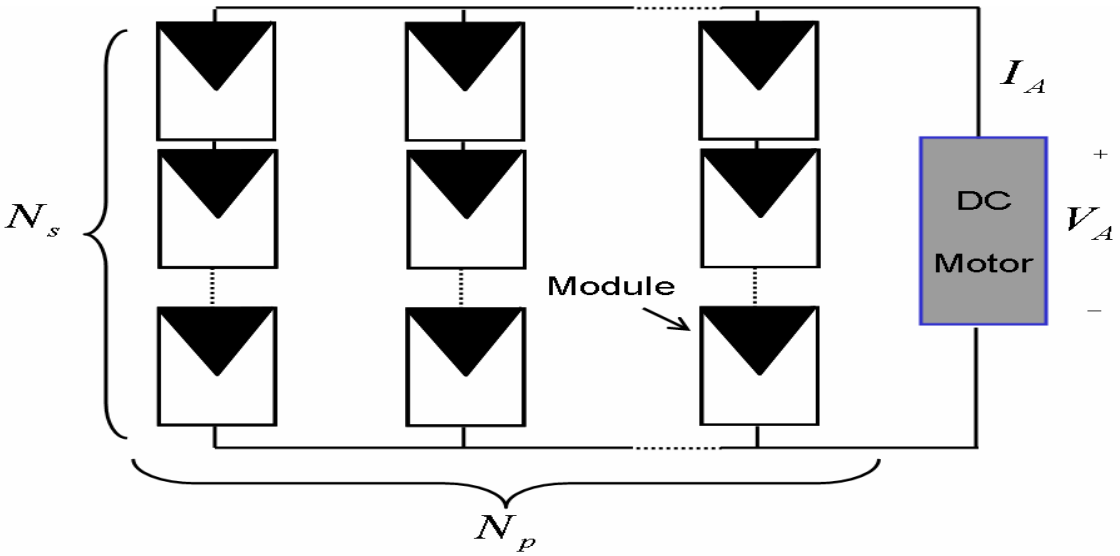

Figure 5. A PV array consisting of series- and parallel-connected modules loaded by dc motor

The I/V characteristics of the PV module are expressed as:

$$I_M = I_0 \exp\left\{\frac{V_M - I_M R_s}{n_M V_t} - 1\right\} + \frac{V_M - I_M R_s}{R_p} - I_{phM} \quad (14)$$

where I_M is the output current of the module, I_0 is the reverse-saturation current, V_M is the output voltage of the module, R_s is the series resistance per module, n is the ideality factor per module, V_t is the thermal voltage equals 25.9 mV at T=300K, R_p is the parallel resistance per module and I_{phM} is the generated current per module. Therefore, the relationship between the current and the voltage of a PV array is written as:

$$I = N_p \left(I_0 \exp\left\{ \frac{\frac{V}{N_s} - \frac{I}{N_p} R_s}{n_A V_t} - 1 \right\} + \frac{\frac{V}{N_s} - \frac{I}{N_p} R_s}{R_p} - I_{phM} \right) \quad (15)$$

In this paper, the rated conditions of the load are 130V and 16A. To generate this rated values and are selected as shown in Table II.

Table II. Parameters of the designed PV array

Design voltage (V)	Design current (A)	N_s	N_p	Area of PV array (m^2)
130	**16**	**19**	**252**	**5.8**

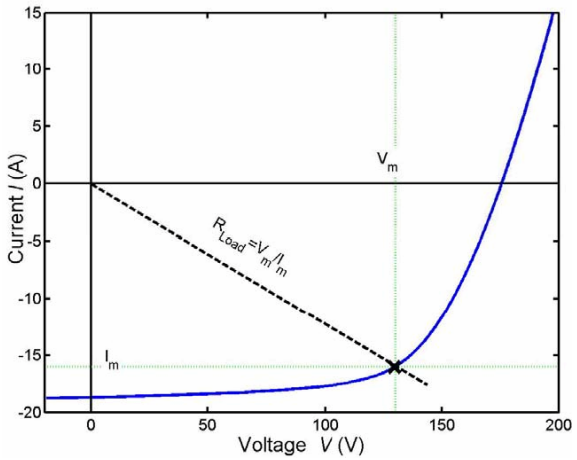

Figure 6. Current/voltage characteristics of the designed PV array consisting of 19 series- and parallel-connected modules

Apparently, the output characteristic of the photovoltaic cells is highly nonlinear. Using the MATLAB instruction 'polyfit' it is found that a polynomial of the 9^{th} order is accurate enough to represent the output voltage as function of the current at full illumination as:

$$V = \gamma_1 I^9 + \gamma_2 I^8 + \gamma_3 I^7 + \gamma_4 I^6 + \gamma_5 I^5 + \gamma_6 I^4 + \gamma_7 I^3 + \gamma_8 I^2 + \gamma_9 I + \gamma_{10} \quad (16)$$

where V is the terminal voltage of the photovoltaic cells, I is the output current, $\gamma_1 = -1.352 \times 10^{-6}$, $\gamma_2 = 1.0779 \times 10^{-4}$, $\gamma_3 = -3.5926 \times 10^{-3}$, $\gamma_4 = 6.4851 \times 10^{-2}$, $\gamma_5 = -0.6865$, $\gamma_6 = 4.3097$, $\gamma_7 = -15.4538$, $\gamma_8 = 28.6745$, $\gamma_9 = -24.1155$ and $\gamma_{10} = 179.9758$.

Fig. 7 shows the polynomially fitted V/I characteristics of the designed cells at different illuminations. The terminal voltage V of Eqs. (1), (5), (10) and (12) is replaced by the expression of Eq. (16) when the motors are fed by photovoltaic cells. In shunt motor, I represents $i_F + i_a$ and in series & permanent-magnet motors I represents i_a.

IV. Numerical Simulations

The numerical simulation results of the DC shunt, series and permanent-magnet motors are presented in this section.

a) DC Shunt Motor

Figure 8, (a) shows the field current of the DC shunt motor after a step change in the load torque from 5Nm to the rated torque of 10.4Nm subjected at $t = 5s$ for the two cases of fixed terminal voltage and a terminal voltage supplied by the photovoltaic cells at full solar illumination and 0.75 of the full illumination with a field resistance of $100\,\Omega$. As the load increases, the current withdrawn by the motor increases. The terminal voltage of the photovoltaic cells decreases as a result. At light loads, the terminal voltage of the photovoltaic cells is higher than the nominal voltage of the machine. This justifies the higher field current at the light load of 5Nm in case of photovoltaic cells. The armature current is shown in Figure 8, (b) and the corresponding rotational speed is shown in Figure 8, (c). In all responses, the steady-state values at the rated load torque are in good agreement at full illumination as the photovoltaic cells are designed to provide the rated voltage at the rated current of the motor at the full solar illumination. At 0.75 of the full illumination the response is lower than that when the motor is fed by fixed terminal voltage and so is the rotational speed as shown in Figure 9, (b).

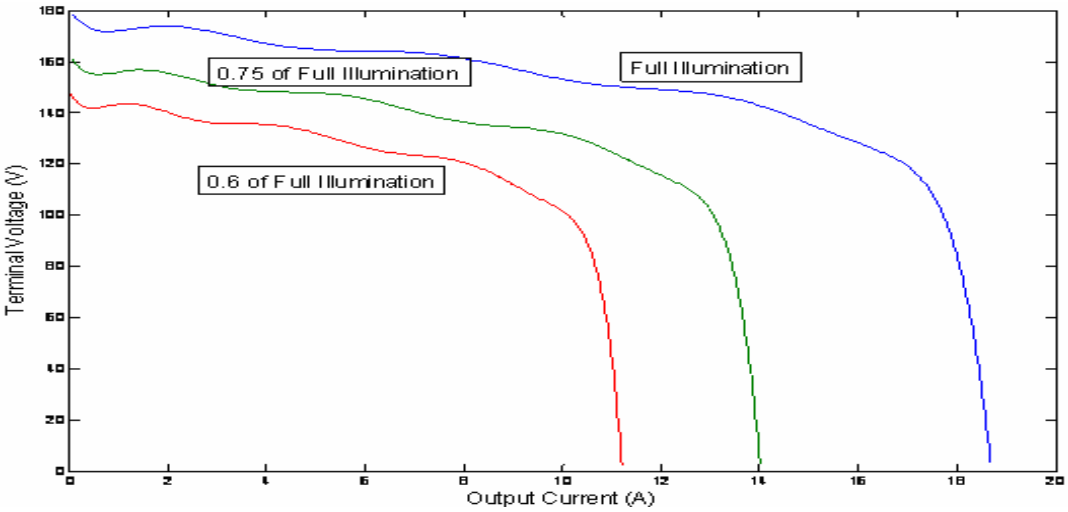

Fig 7: Polynomially fitted I/V characteristics of the designed photovoltaic array at different illuminations

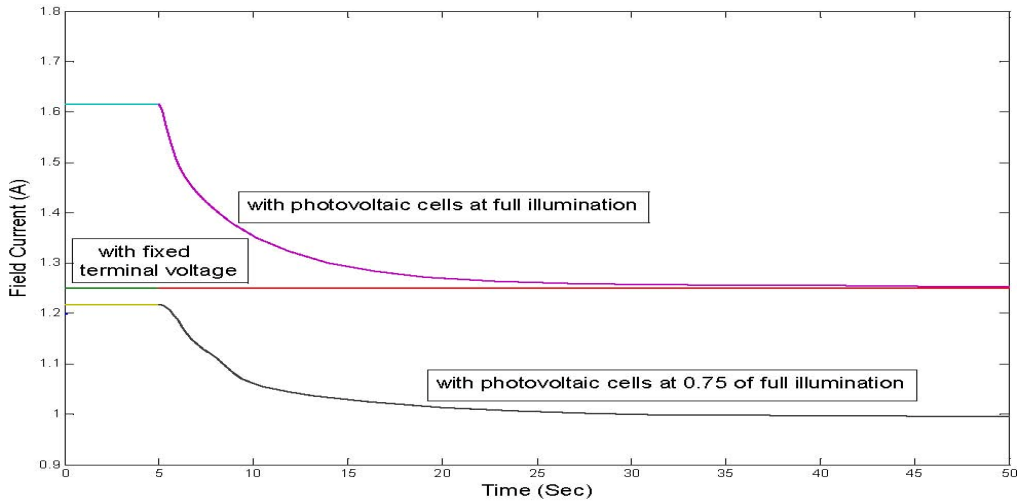

(a)

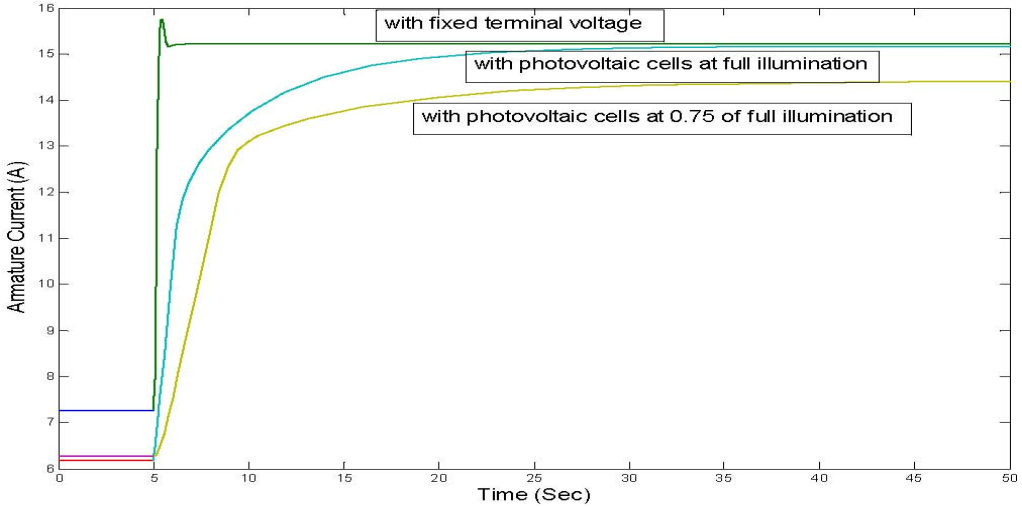

(b)

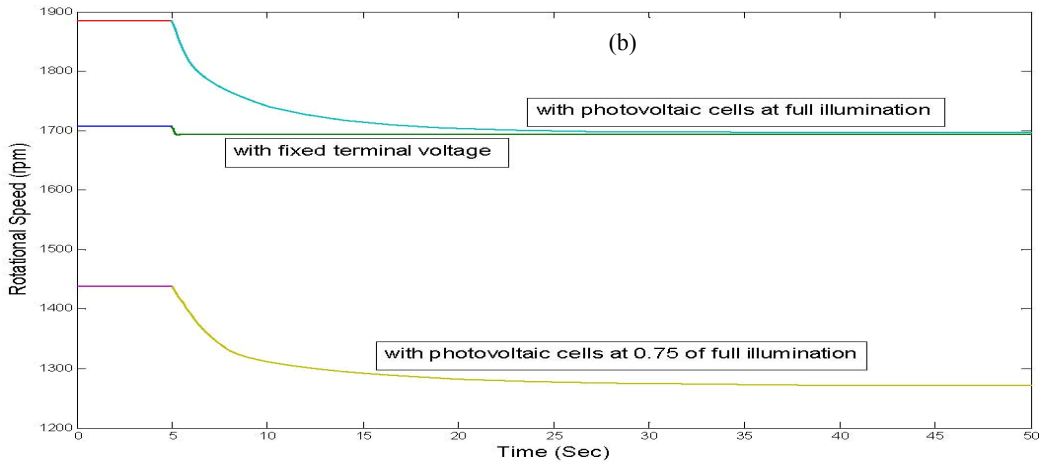

(c)

Figure 8. (a) Field current, (b) armature current and (c) rotational speed of DC shunt motor after a step change on the load torque from 5Nm to 10.4Nm with a total field resistance of 100 Ω

b) DC Series Motor

The simulations executed on the DC shunt motor are repeated for the series motor. Figure 9, (a) shows the armature current of the series motor after a step increase in the load torque from 5Nm to 17Nm for the cases of fixed terminal voltage and a terminal voltage supplied by photovoltaic cells at full solar illumination and 0.75 of the full illumination. The steady-state armature current in case of photovoltaic cells and full illumination is slightly higher These small deviations are justified by the small difference in the voltage supplied by the photovoltaic cells compared with the fixed rated voltage of 125V as shown in Figure 9, (c). This difference comes as result of the fact that the output voltage of the photovoltaic cells is function of the output current. At 0.75 of the full illumination the response is lower.

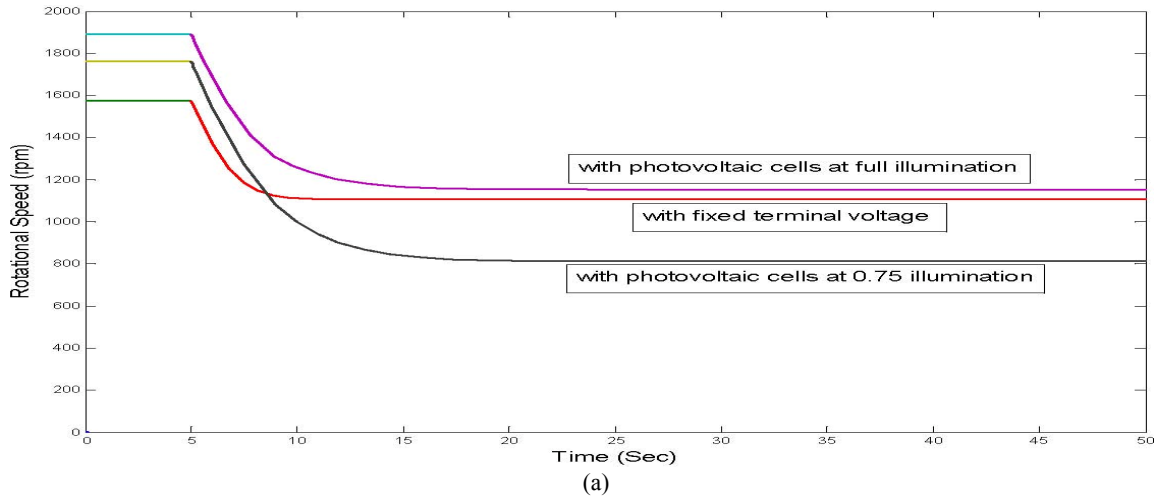

(a)

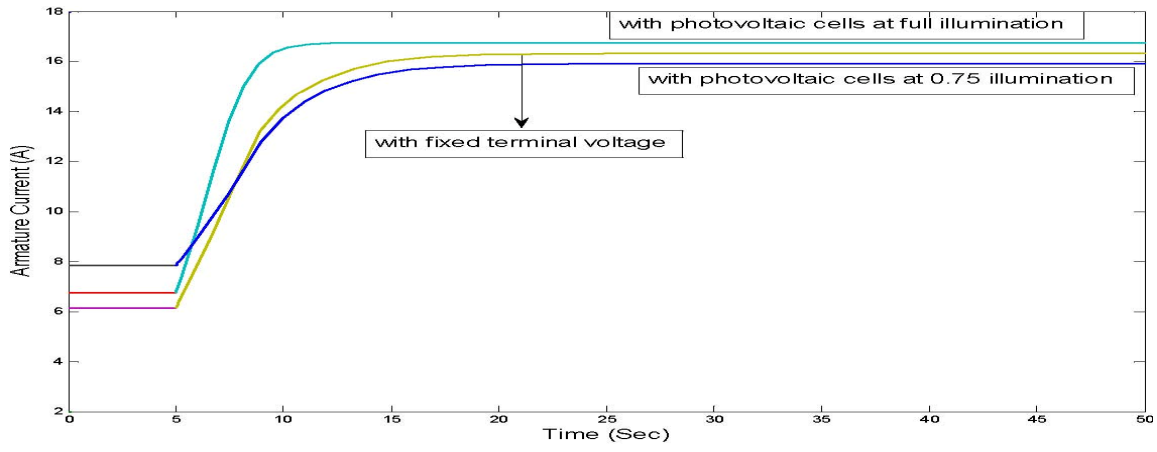

(b)

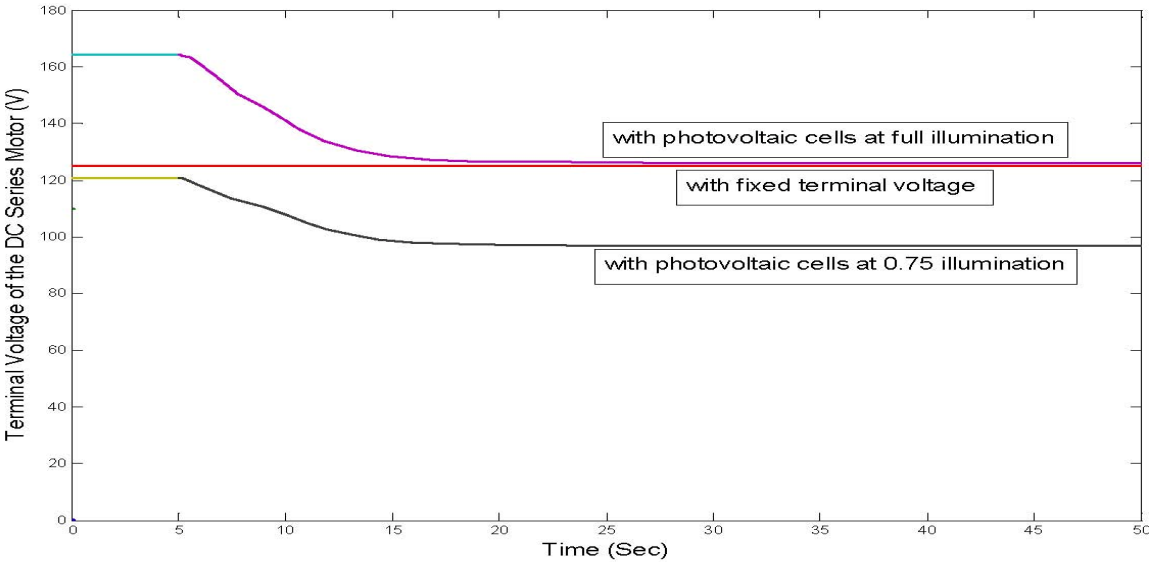

(c)

Figure 9: (a) Armature current, (b) rotational speed and (c) terminal voltage (photovoltaic cells voltage) of the DC series motor after a step increase in the load torque from 5Nm to 17Nm

c) Permanent-Magnet DC Motor

Figure 10, (a) shows the armature current of the permanent-magnet DC motor after a step increase in the load torque from 5Nm to 11.9Nm for the cases of fixed terminal voltage and a terminal voltage supplied by photovoltaic cells at full solar illumination and 0.75 of the full illumination. The steady-state armature current in case of photovoltaic cells and fixed terminal voltage is identical because it is independent of the input voltage as can be concluded from Eq. (13). The deviation in the rotational speed shown in Figure 10, (b) comes as a result of the difference in the applied voltage.

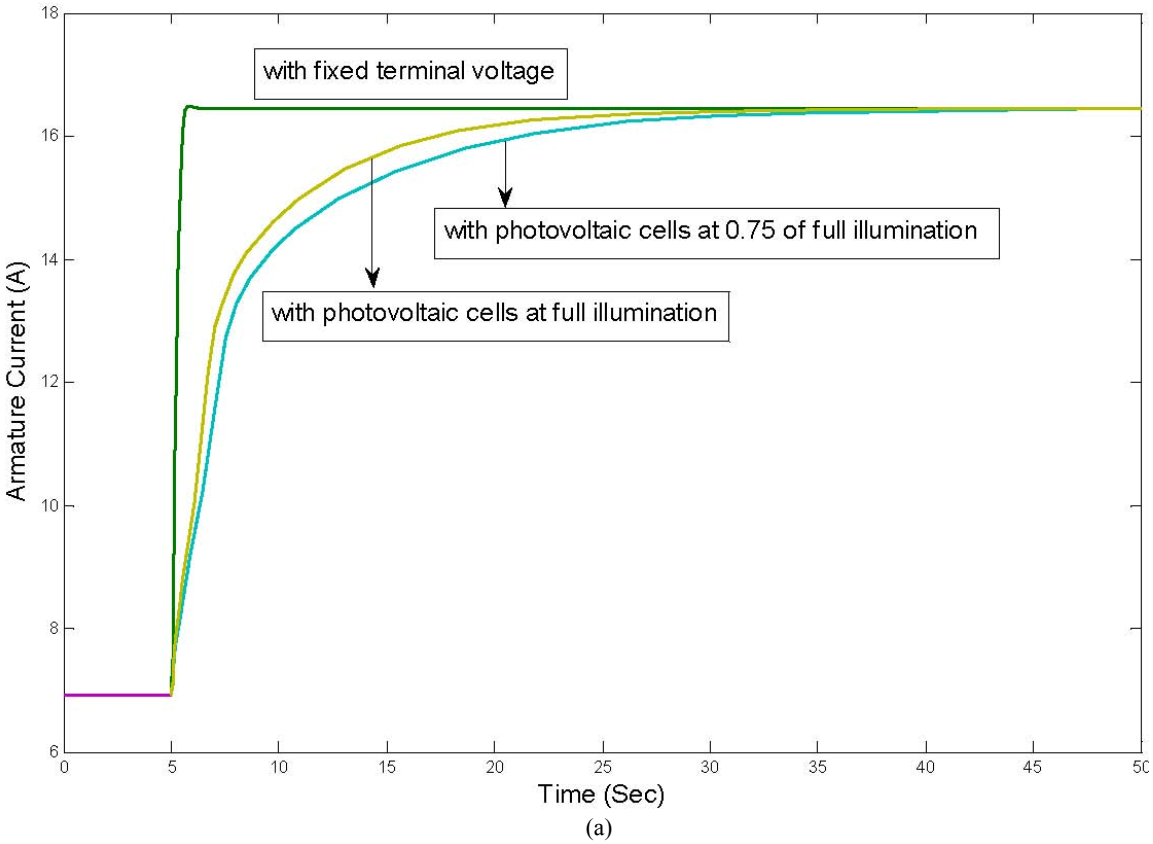

(a)

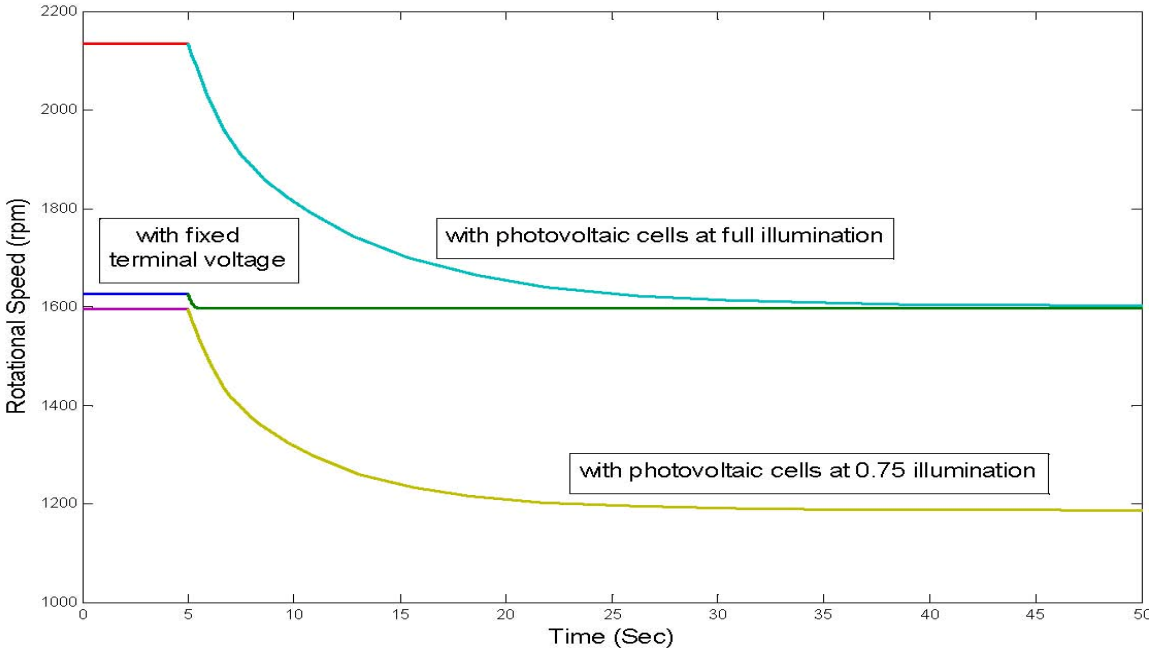

(b)

Figure 10: (a) Armature current and (b) rotational speed of the permanent-magnet DC motor after a step increase in the load torque from 5Nm to 11.9Nm.

4. Steady-State Output Characteristics

The steady-state output characteristics (torque-speed characteristics) of the three motors when fed by fixed terminal voltage and photovoltaic cells at different illuminations are studied. The operating points of the systems are obtained by dropping out all the time derivative terms of the dynamical differential equations and solving the resulting nonlinear algebraic equations. This has been carried out using the MATLAB Symbolic Math Toolbox instruction 'solve'. Figure 11 shows the torque-speed characteristics of the DC shunt motor and, Figure 12 shows that of the DC series motor and Figure 13 shows that of the permanent-magnet DC motor. Clearly, at the rated load torque the rotational speed of the motors in both cases are in good agreement as the terminal voltage of the photovoltaic cells at full illumination is very close to the rated voltage supplied in case of fixed terminal voltage. At lighter loads, the speed in case of photovoltaic cells is higher for the motors at full illumination. This takes place because the terminal voltage of the photovoltaic cells is higher at light loads as the current withdrawn from the cells is lower. In all cases, the characteristics in case of 0.75 of the full illumination is lower as the voltage supplied by PV cells is smaller.

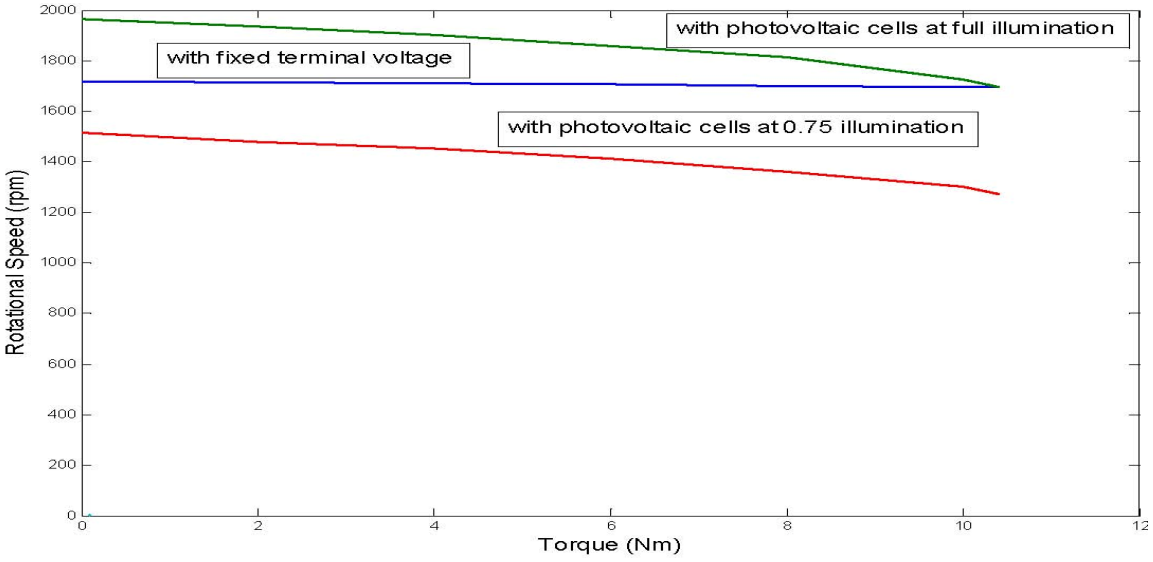

Figure 11. Torque-speed characteristics of DC shunt motor with photovoltaic cells at different illuminations and fixed terminal voltage

Figure 11. Torque-speed characteristics of DC shunt motor with photovoltaic cells at different illuminations and fixed terminal voltage

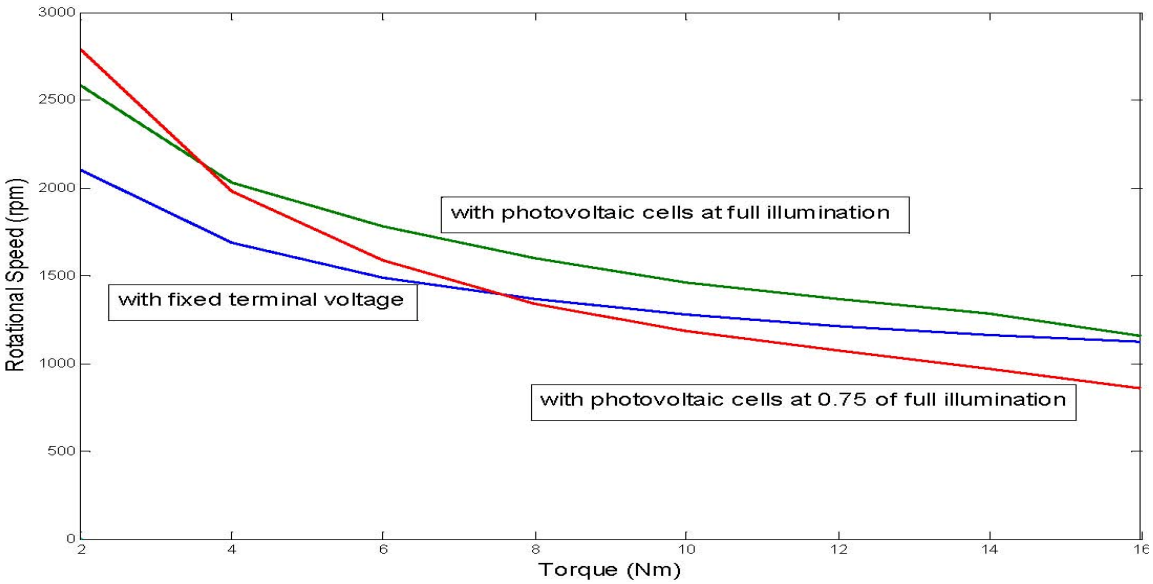

Figure 12. Torque-speed characteristics of DC series motor with photovoltaic cells at different illuminations and fixed terminal voltage

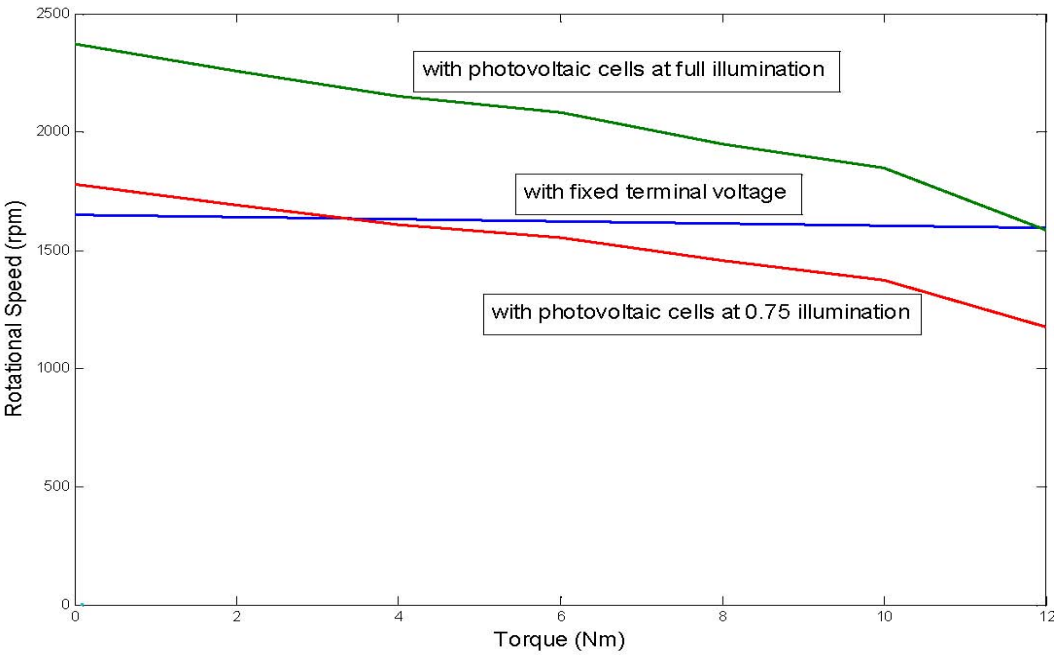

Figure 13.Torque-speed characteristics of permanent-magnet DC motor with photovoltaic cells at different illuminations and fixed terminal voltage .

5. Conclusions

The dynamical analysis of PV-powered DC shunt, series and permanent-magnet motors are studied. At the full solar intensity, the photovoltaic cells are designed to provide their maximum power at the rated conditions of the machine. The simulation results at two solar intensities are compared with the case of supplying the motors by fixed terminal voltage. The nonlinearity of the output characteristics of the photovoltaic cells and that of the magnetization curve of the DC machines are included in all simulations by polynomial curve fitting. The results show that when the machine is run at the rated conditions, the steady-state values are in good agreement in both cases of fully illuminated photovoltaic cells and fixed terminal voltage. At light loads with photovoltaic cells and full illumination, the responses of the machines are higher as the voltage supplied is higher. The output steady-state characteristics, torque-speed characteristics, of the three motors are outlined and compared in the cases of feeding them by fully illuminated solar cells, partially illuminated solar cells and fixed terminal voltage. All simulations are carried out using MATLAB.

References

[1] A. Al Tarabsheh, "Amorphous Silicon Based Solar Cells", Doctoral Diss., Institute of Physical Electronics, University of Stuttgart, Stuttgart, Germany, 2007.

[2] M. Bello and I. Davidson, "Dynamics of Solar-Powered Fractional Horse Power Motor", Int. Conf. on Electrical and Electronics Engineering, 7-9 , 2005, 273-277.

[3] M. Akbaba and M. C. Akbaba, "Dynamic Performance of a Photovoltaic-Boost Converter Powered DC Motor-Pump System", IEEE Int. Conf. Electrical Machines and Drives, 2001, 356-361.

[4] V. Badescu, "Dynamic Model of a Complex System Including PV cells, Electric Battery, Electrical Motor and Water Pump", Solar Energy, Vol. 28, 2003, 1165-1181.

[5] W. Anis and H. M. B. Metwally, "Dynamic Performance of a Directly Coupled PV Pumping System", Solar Energy, Vol. 53, No. 3, 1994.

[6] H. M. Metwally and W. R. Anis, "Dynamic Performance of Directly Coupled Photovoltaic Water Pumping System Using D.C. Shunt Motor", Energy Convers. Mgm. Vol. 37, No. 9, 1996, 1407-1416,.

[7] H. Hilmer, A. Ratka, K. Vajen, H. Ackermann, W. Fuhs and O. Melsheirner, "Investigation of Diretly Coupled Photovoltaic Pumping System Connected to a Large Absorber Filed", Solar Energy, Vol. 61, 1997, 65-76.

[8] M. Akbaba, I. Qamber and A. Kamal, "Matching of Separately Excited DC Motor to Photovoltaic Generators for Maximum Power Output", Solar Energy, Vol. 63, 1998, 375-385.

[9] M. Akbaba, "Matching Induction Motors to PVG for Maximum Power Transfer", The 9th Arab Int. Conf. Solar Energy , Vol. 209, 2007, 31-38.

[10] A. Betka and A. Moussi, "Performance Optimization of a Photovoltaic Induction Motor Pumping System" Renewable Energy, Vol. 29, 2004, 2167-2181.

[11] C. Hua, J. Lin and C. Shen, "Implementation of a DSP Controlled Photovoltaic System with Peak Power Tracking", IEEE Trans. Ind. Electronics, Vol. 45, No. 1, 1998, 99-107.

[12] E. Muljadi, "PV Water Pumping with a Peak Power Tracker Using a Simple Six Step Square-Wave Inverter", IEEE Trans. Industrial Applications, Vol. 33, No. 3, 1997, 714-721.

[13] C.L.P. Swamy, B. Singh and B.P. Singh, "Dynamic Performance of a Permanent Magnet Brushless DC Motor Powered by a PV Array for Water Pumping", Solar Energy Mater, Solar Cells, Vol. 36, 1995, 187-200.

[14] L. D. Partain, Solar cells and their applications, John Wiley & Sons, Inc., 1995.

[15] Chee-Mun Ong, Dynamic Simulation of Electric Machinery, Prentice Hall PTR, Upper Saddle River, New Jersy 07458, 1998.

[16] M. S. Widyan, "Design, Optimization, Construction and Test of Rare-Earth Permanent-Magnet Electrical Machines with New Topology for Wind Energy Applications", Doctoral Diss., Institute of Energy and Automation Technology, Berlin University of Technology, Germany, 2006.

[17] J. Merten, M. Asensi, C. Voz, A. V. Shah, R. Platz, and J. Andreu, "Equivalent Circuit and Analytical Analysis of Amorphous Silicon Solar Cells and Modules", IEEE Transactions on Electron Devices Vol. 45, 1998, 423.

[18] R. M. Swanson, Handbook of Photovoltaic Science and Engineering, edited by A. Luque and S. Hegedus, Wiley, West Sussex, England, 2003.

Appendix A

1) The numerical parameters of the DC shunt motor are:

$L_F = 10H$, $R_F + R_{adj} = 80 \to 120\Omega$, $V = 125V$, $L_a = 18mH$, $R_a = 0.24\Omega$, $J = 0.5kgm^2$.

2) The numerical parameters of the DC series motor are:

$L_F = 44mH$, $R_F = 0.2\Omega$, $V = 125V$, $L_a = 18mH$, $R_a = 0.24\Omega$, $J = 0.5kgm^2$.

3) The numerical parameters of the permanent-magnet DC motor are:

$L_a = 18mH$, $R_a = 0.24\Omega$, $K_m = 0.7237$ Vs, $V = 125V$, $J = 0.5kgm^2$.

JJMIE

Volume 4, Number 1, Jan. 2010
ISSN 1995-6665
Pages 205 - 209

Jordan Journal of Mechanical and Industrial Engineering

Wind-Solar Hybrid Electrical Power Generation in Jordan

Ghassan Halasa *

Electrical Engineering Department, University of Jordan, Amman, Jordan

Abstract

The paper presents the electrical power generation using solar- and wind-energy for the country of Jordan. Presently with the oil prices are on the rise, the cost of electrical power production is very high. The opportunity of a large wind and solar hybrid power production is being explored. Sights are chosen to produce electricity using, the wind in the Mountains in Northern Jordan and the sun in the Eastern Desert. It is found that the cost of windmill farm to produce 100-150 MW costs $290 million, while the solar power station to produce 100MW costs $560. The electrical power production costs per kWh are 2 cents for the wind and 7.7 cents for the solar. The feasibility for using wind energy is now, solar energy when price of oil reaches $100 per barrel. The paper also discusses different control methods to link with the national grid.

Keywords: Hybrid power production system; wind energy, solar energy; power production cost; Jordan.

1. Introduction

The concept of solar and wind energies dates back to nearly 7,000 years ago [1]. However, in the late 1800s the Danes developed the first wind turbines to produce commercial electricity [1] – [4]. In the early 1900s small-scale wind turbines became more widely used around Europe especially in the rural areas for producing electricity using old car generators and carved rotors. The wind power brought electricity to the rural areas and the electrical power was used to charge batteries to run radios and to draw water from deep wells [2]. Except in Denmark where wind power production and research continued, wind power did not play any major role in the generation of electricity until the late 1900s.

The rapid growth of solar and wind powers is due in part to favorable global political climate towards these energies, efforts to reduce carbon dioxide (CO_2) and greenhouse gases (GHG) and other power plant pollutants, global awareness of climate changes, and the urgency to develop renewable energy sources. Other factors such as lucrative tax incentives and legislation mandating national renewable energy standards have accelerated the march towards solar and wind energies. For example in the US, some states have enacted "renewable portfolio standard (RPS)" law that requires utilities to sell a certain percentage of the energy from sustainable energy sources within reasonable stipulated times. Even though Europe and North America have the largest installed capacity of wind turbine capacity, China, India, and developing world have the biggest potential for wind power [5].

This paper examines the capacity and potential for electricity-generating solar- and wind-turbines installed In the Eastern and Northern part of the country. Wind Solar alternatives are essential for growth, finance, and the political environment. The cost of wind power has reduced from the cost of power production from 9.5 cents per kilowatt-hour to 2 cents for wind energy production and to 7.7 cents for solar power production. This is very significant because developing countries, which depend on external sources to finance major energy projects, may be able to finance small scale solar and wind energies projects from their own resources and faster. In this paper the electrical and power calculations for solar and wind utilization to support the national grid in Jordan will be analyzed. This paper also looks at some of the modern power electronics converters and electrical machines which have improved significantly solar and wind energy technologies to make them acceptable and embraced as cost effective and renewable energy.

2. The Existing Jordan' National Grid

Jordan is interconnected in one national grid. The grid covers most of the populated areas of the country from Aqaba, on the far south to Irbid in the far north. Overhead transmission line link Syria in the north, Palestine in the west, while undersea cable links Egypt in the south. Future countries to be connected to Jordan national grid include Lebanon, Iraq and Turkey.

The major generation centers are the Aqaba Thermal Power Station in the far south, Al-Hussein Thermal Power Station in Zarka near Amman, and Al-Risha near the Iraqi border. The Aqaba Power Station uses gas supplied through pipelines from Egypt. The pipeline extends to Amman. Future expansion of this gas line is expected to go to Syria, and eventually Turkey. Al-Hussein power station uses fuel oil imported from Iraq. Al-Risha power station uses locally produced gas. There are several small

* Corresponding Authors. halasa@ju.edu.jo.

units scattered in different districts belonging to older utilities. These units are used during peak demands.
The oldest and the highest power production plant in Jordan is the Al-Hussein Thermal Power Station. It is the most expensive because it uses imported oil and also uses air-cooling systems, that consume quite amount of energy, to cool the turbines. A small pilot plant uses biogas produced by sewerage treatment plant. Another pilot plant uses wind energy near the sight proposed in North Jordan.

3. Conventional Electrical Production Cost

The Kingdom of Jordan is considered an emerging country in the Middle East; it has almost no natural resources. The country imports most of its oil needs from neighboring countries at market prices. Oil and gas imports are huge burden on the country's national economy. Electricity is generated by burning imported gas and oil, limited generation from hydro, wind mills, and biogas. When oil prices rose to extremely high levels last summer, Jordanians experienced continuous increases in electricity prices. It is now urgent and essential to deploy other alternatives for electrical generation, which is the use of solar and wind energy for electrical generation.
As shown in Table 1 Jordan in 2007 produced a total of 13,001 GWh of electrical energy and consumed 10,553 GWh. The average per capita electricity consumption in Jordan in 2007 was 2277 kWh as compared to 2075 KWh in 2006[18], resulting in annual growth rate of 9.7%. Table 1 shows generating capacity and electrical energy production by type of generation for 2007.

Table 1 .Energy Production In 2007 By Generation Type [18]

Fuel Type	Generating Plants Capacity (MW)	Electrical Production (GWh)
Steam Units	1013	6,904
Gas Turbines/Diesel	193	45
Gas Turbines/Natural Gas	310	916
Diesel Engines	43	1
Hydro Units	12	61
Windmills	1.4	3
Biogas	4	10
Combined Cycle	600	5,061
Total Generation	2176.4	13,001

Almost all electricity production in Jordan currently is carried out by the state-owned utility National Electric Power Company (NEPCO). Al-Hussein Power Plant (with capacity of 400 MW) and the Aqaba Power Plant (with capacity of 650 MW) are the country's two main power generation facilities. Jordan has modest reserves of natural gas, of 230 billion cubic feet, and has developed one gas field at Al-Risha in the eastern desert near the Iraqi border. The current output of this field is around 30 million cubic feet per day. Al-Risha field is used to fuel one nearby power plant, which generates about 10% of Jordan's electricity. For several years, Jordan has been exploring the option of importing natural gas from Egypt. In 1999, a decision was made to delay imports until a more thorough evaluation of reserves at Al-Risha field was completed. When this review showed that quantities available were not sufficient to meet the country's needs, Jordan decided to reopen talks on imports from Egypt. A pipeline was constructed and completed in 2006. Aqaba thermal power station, a major generating center, currently uses Egyptian gas. Jordan imports about 150,000 barrels of oil per day mostly from Iraq and Saudi Arabia. The Zarka refinery near Amman, the only refinery in the country, refines the imported oil. Table 2 shows electrical generation fuel consumption in 2007. Gas and oil imports pose a huge burden on the national economy.

TABLE 2 FUEL CONSUMPTION IN 2007 FOR ELECTRICAL GENERATION [18]

Fuel Type	Consumption in Thousands Tons Oil Equivalent
Heavy Fuel	621
Natural Gas	2,396
Diesel	9
Total	3,026

According to 2007 data supplied by NEPCO[18], electrical production cost is USr$0.073 per KWh; out of which fuel cost is US$0.0386 per KWh. This figure is considered expensive as compared to production cost in other countries. As the oil prices surged to more than double in the summer of 2008, accordingly the production cost increased to US$ 0.11 per KWh. If it is assumed that the true value of oil price is $100 per barrel, the production cost would be about US$0.095 per KWh. This figure will be used in cost comparison.

4. Assesment Of Wind And Solar Energies

In Jordan electricity demand grew around 9.7% in 2007. The Jordanian government has been seeking ways to attract foreign capital to fund additional capacity. Wind and solar energies as main source of electricity generation are currently set as government priorities. The government implemented the following actions [19]:

- Developing new wind and solar maps for Jordan.
- Developing a legal framework for renewable energy.
- Developing incentives for renewable energy projects.
- Securing an appropriate fund to implement the 1st commercial wind energy project in Jordan.
- Secure an appropriate fund to implement the feasibility
- Study of the hybrid solar power plant.

Because of the government enthusiasm to promote renewable energy, a thorough investigation has been conducted to study the possibility for a hybrid system of windmills and solar arrays for electricity generation. Data collected over many years by the Jordan Meteorological Department [20] has helped in locating the sights for both windmills and solar arrays.

The wind farm location was set in the area of Ras-Munif where the annual wind speed average is 10.6 knots which is equivalent to 5.5 meters/second according to data collected by the Meteorological Department in Jordan. With the exception of the months of September and October, where the wind speed is low, the other 10 months the speed is 6-6.5 m/s. Remembering that this speed represents the village ground level speed. If the windmills are sighted at higher elevation and in the valley curvature between mountains running west to east where wind tunnel effect exists, the average wind speed might rise to comfortable levels where windmills run near full capacity. The windmill tower height of 100 meters also increases wind speed to levels close to the 7-9 m/s [22] which might bring the wind turbine power output to 1 Mw or more for ten months of the year. Experience indicates that wind speed tend to be higher during the night time. Therefore, during the day time the deficiency in windmills' power output can be augmented by solar cells electrical production.

5. The Wind-Solar Hybrid System

A. Proposed Windmill-Solar Hybrid

The proposed non-conventional electrical generation will supply 100-150 Mw. As it was pointed out earlier, the sight is chosen in a high valley curvature in the mountainous range where wind tunnel effect exists where continuous high speed wind prevails all year round. An array of 100 windmills was chosen for this work. Each unit has a capacity 1.5 Mw. Several windmill suppliers were investigated and the choice was set on SAIP Electric Group [21]. Figure 1 shows the windmill chosen for this project. Since the average annual wind speed characteristics at location is 6 m/sec and might average about 7-9 m/sec as was pointed out in section 4 above. The cut in wind speed for the units is 3 m/sec, which is way above the annual average wind speed at the chosen sight guaranteeing continuous power output. The cutout speed is 25 m/sec where this average is over 10 minutes span average. In that location wind never reach that high. Consequently the chosen units are suited for the proposed sight. Figure 2 indicates that with the wind speed average at sight, the windmill average power output would be about 1 Mw for year round. This power may increase up to 1.5 Mw, which is the maximum power output of the generator. Therefore the proposed windmills farm may produce a continuous power output between 100-150 Mw. The blade length is 37.5 m, making the windmill side clearance 75 m, and at a height of 100 m. Leaving additional side clearance of 100 m so that windmills do not form wind obstacles between each other. Therefore the wind farm array should be about 2 Km long. Land appropriation for this sight would be about 200,000 m2. This is easily accommodated in the proposed sight.

Figure 1. The 1.5 MW Windmill.

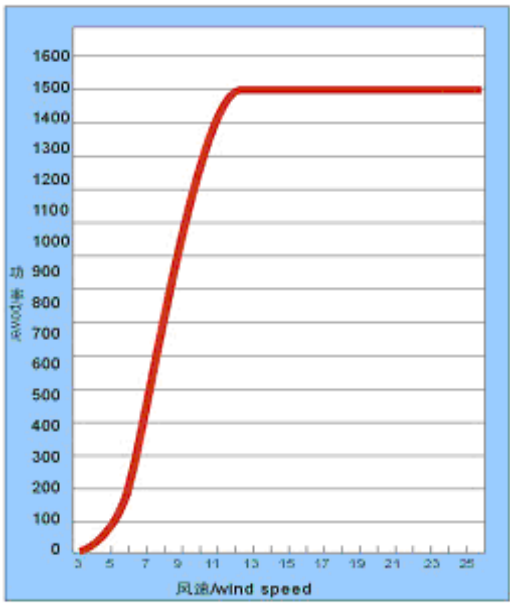

Figure 2 The Power-Wind Speed Characteristics

In case the windmills' output is reduced a solar cells array may be an alternative for additional support and reliability. Experience had told us that whenever the wind speed drops means a fair weather where sun shine is a maximum. For a reliable renewable energy power supply, the windmills farm is supported by solar cells array. Table 3 shows the solar array type specifications to be used. The decision was to install solar array to produce 100Mw to support the windmill farm. A total of 500,000 arrays are needed to supply this required power.

Since Ras Munif, the location of the windmills is mountainous area, is unsuitable location for the solar arrays, because they are used for agricultural plantations. A better location is in the Easter Jordanian Desert. In desert land is readily available and the yearly average daily sunshine is 9.3 hours[20]. By installing east-west sun tracing system, a full 8 hours daily average maximum power output can be obtained. Accounting for the modules

Table *3*. Solar Module Speifications.

Maximum power (Wp)	200W
Maximum power voltage (V)	42
Maximum power current (A)	5.24
Open circuit voltage (V)	50
Short circuit current (A)	5.7
Number of cells (Pcs)	91(7x13)
Size of module (mm)	1702x945x45
Weight per piece (kg)	19

surface area and spaces between modules, the solar installation requires land appropriation of 1 km2.

Location of the solar power station is chosen to be near Al-Risha Power Station currently in operation in the Eastern Jordanian Desert. This sight is chosen for easier link to the national grid. Al-Risha is located on 32˚ latitude. This requires the modules to be installed inclined toward the South at 32˚ with the horizontal, facing southward. Modules inclination adjustments of ±15˚ are needed to track the sun's seasonal variations. East-West tracking motors may be used to increase full capacity power production to 8 hours per day.

The proposed hybrid wind-solar installation is needed to supply Jordan with low cost renewable electric power. The two installations are capable to supply 10% of the country's electricity peak demand needs for the year 2009.

B. Cost Estimation

The cost of one windmill is US$ 1.85[21]; additional 20% of the price may cover shipping and installation. In addition and US$200,000.00 per unit for controllers and other supporting equipment needed for grid link. Result is a total cost per unit ready to supply the grid may be set around US$2.4 million. Another 10% for maintenance, 6% for capital investment, and another 5% Administration may be added to the 2.4 million; the result is a net cost of US$2.9 million per unit. A total of US$290 million are needed for the wind farm installation to produce 100 – 150MW of electrical power. The average life-time of the windmill is 20 years. Simple calculations, after the assumption that the full wind power out is for 20 hours per day, result in electrical production cost US$0.02/kWh. This figure is much lower less than the current conventional electrical production cost of US$0.095/kWh.

As for the solar power station, the cost of 500,000 modules needed to produce 100 MW is US$370 million. This cost includes the controllers for grid link. In addition to the 370 million solar modules cost, 20% for installation, 10% for the sun tracking system, 10% maintenance, 6% capital investment and 5% administration may bring the total cost of the solar power station to $560 million. The high percentage for installation is to cover the cost of frames upon which the modules will be installed. Remembering that the power production is for 8 hours per day and the life time of the solar cells is 25 years; then the production cost will be US$0.077/kWh. This production cost is almost the same as the present conventional production cost., but lower than the projected production cost of US cents 9.5, for when the price of oil reaches $100 per barrel.

Comparing the wind and solar power production costs, it seems that wind power production cost is much lower than the solar power production. Therefore wind energy production is feasible now even with the oil prices at $40 per barrel. In the future when oil prices rise, even with the high cost of solar energy, solar power is important for power flow reliability.

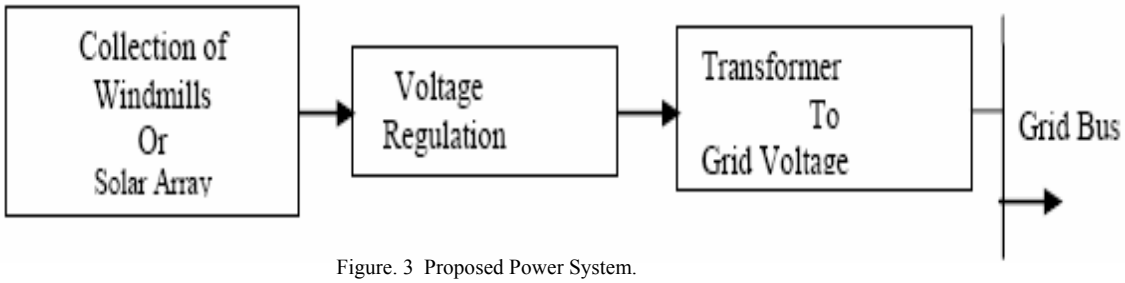

Figure. 3 Proposed Power System.

6. Conclusion

Jordan have high electric production cost that is directly linked with the oil prices. An alternative is renewable wind and solar electric power production. The possibility was thoroughly investigated. The result is to install windmill farm in the mountainous area in the north, where wind speed proved to be viable, while the eastern desert is suitable to install solar power station. The cost for the windmill farm to produce 100-150MW for 20 hours per day is US$290 million. The cost of the solar power station to produce 100MW for 8 hours per day is US$560 million. The production cost per kWh (in US cents) is 2 cents for the windmill and 7.7 cents for the solar. The conventional production cost 9.5 cents projected when the price of oil is $100 per barrel. For reliable energy system, hybrid power production is essential.

Aknowledgment

This work was partially supported by University of Jordan through sabbatical leaf offered to Dr. Ghassan Halasa spent on the campus of Western Michigan University for the academic year 2008/2009

References

[1] N. Kodama, T. Matzuzaka, and N. Inomita, “Power Variation Control of a Wind Turbine Using Probabilistic Optimal Control, Including Feed-forward Control for Wind Speed,” Wind Eng., Vol. 24, No. 1, 13 – 23, Jan 2000.

[2] L. L. Freris, Wind Energy Conversion Systems, Englewood Cliffs, NJ: Prentice-Hall, 182 – 184, 1990.

[3] E. Koutroulis and K. Klaitzakis, “ Design of a Maximum Power Tracking System for Wind-Energy-Conversion Applications,” IEEE Trans. on Indust. Elect., Vol. 53, No. 2, 2006, 486 – 494, April.

[4] E. Muljadi and C. P. Butterfield, “Pitch-controlled Variable-speed Wind Turbine Generation,” IEEE Trans. Ind. Appl., Vol. 37, No. 1, 2001, 240 – 246.

[5] W. Lin, H. Matsuo, and Y. Ishizuka, “Performance Characteristics of Buck-Boost Type Two-input DC-DC Converter With an Active Voltage Clamp,” IEICE Tech. Rep., Vol. 102, No. 567, 2003, 7 – 13.

[6] J. A. Baroudi, V. D. Dinavahi, and A. M. Knight, “A review of Power Converter Topologies for Wind Generators,” Renewable Energy 32, Science Direct, January, 2007, 229 – 2385.

[7] Z. Chen and E. Spooner, “Current Source Thyristor Inverter and its Active Compensation System,” Proceedings of IEE Generation, Transmission, and Distribution, Vol. 150 , 2003, 447 – 454.

[8] K. Tan and S. Islam, “Optimum Control Strategies in Energy Conversion of PSMG Wind Turbine System Without Mechanical Sensors,” IEEE Trans Energy Convers, Vol. 10, 2004, 392 – 399.

[9] Z. Chen and E. Spooner, “Grid Power Quality with Variable Speed Wind Turbines,” IEEE Trans Energy Convers, Vol. 16, 2001, 148 – 154.

[10] Z. Chen and E. Spooner, “Wind Turbine Power Converters: A comparative Study,” Proceedings of IEE Seventh International Conference on Power Electronics and Variable Speed Drives, 1998, 471 – 476.

[11] S. H. Song, S. Kang, and N. Hahm, “Implementation and Control of Grid Connected AC-DC-AC Power Converter for Variable Speed Wind Energy Conversion System,” Proceedings of IEEE AIPEC’03, Vol. 1, 2003, 154 – 158.

[12] Y. Higuchi, N. Yamamura, M. Ishida, and T. Hori, “An Improvement of Performance of Small-scaled Wind Power Generating With Permanent Magnetic Type Synchronous Generator,” Proceedings of IEEE IECON’00, Vol. 2, 2000, 1037 – 1043.

[13] G. L. Johnson, Wind Energy Systems, Englewood Cliffs, NJ, Prentice-Hall Inc., 1985

[14] N. Mutoh, T. Matsuo, K. Okada, and M. Sakai, “Prediction-data-based Maximum-Power-Point-Tracking Method for Photovoltaic Power Generation Systems,” Proc. 33rd IEEE PESC2002, Vol. 3, 1489 – 1494.

[15] K. Kobayashi, H. Matsuo, and Y. Skine, “An Excellent Operating Point Tracker of Solar-Cell Power Supply System,” IEEE Trans. on Indust. Elect., Vol. 53, No. 2, 2006, 495 – 499.

[16] G. R. Walker and P. C. Sernia, “Cascaded DC-DC Converter Connection of Photovoltaic Modules,” Proc. 33rd IEEE PESC2002, Vol. 3, 24 - 29.

[17] A. Hirofumi, etc., Instantaneous Power Theory and Applications to Power Conditioning, 2007 Edition.

[18]http://www.nepco.com.jo/showImageTC.aspx?imageURL=Statistics_files/Englishalbums/2/, Retrieved on 2/3/2009.

[19] http://www.ren21.net/iap/commitment2.asp?id=93, Retrieved 3/3/2009

[20] The Hashimite Kingdom of Jordan, Meteorological Department, Climate Division, Jordan Climatic Data , 2007.

[21] SAIP Electric Group Limited, Huifeng Road, Luishi Industrial Zone, Wenzhou, Zhejiang, 325604, China.

[22] Peterson, E.W. and J.P. Hennessey, Jr., , On the use of power laws for estimates of wind power potential, J. Appl. Meteorology, Vol. 17, 1978.

JJMIE

Volume 4, Number 1, Jan. 2010
ISSN 1995-6665
Pages 211- 216

Jordan Journal of Mechanical and Industrial Engineering

Rapidly Shrinking Dead Sea Urgently Needs Infusion of 0.9 km^3/a from Planned Red-Sea Channel: Implication for Renewable Energy and Sustainable Development[1]

Shahrazad Abu Ghazleh[a,*], Stephan Kempe[a], Jens Hartmann[b], Nils Jansen[b]

[a]Institute for Applied Geosciences, FB 11 Materials and Geosciences, Darmstadt University of Technology, Schnittspahnstr. 9, 64287 Darmstadt, Germany
[b] Institute for Biogeochemistry and Marine Chemistry, Hamburg University, Bundesstr. 55, 20146 Hamburg, Germany

Abstract

The Dead Sea has been experiencing a severe drop in level since 1978 with an average of 0.7 m/a due to the accelerating water consumption in its catchment and stood in 2008 at -420 m. In this study, a terrain model of the surface area and water volume of the Dead Sea was developed from the SRTM data using ArcGIS. The model shows that the lake shrinks on average by 4 km^2/a in area and by 0.47 km^3/a in volume, amounting to a cumulative loss of 14 km^3 in the last 30 years. The receding level leaves almost annually shoreline terraces recorded here for the first time by DGPS field surveys. The terrace altitudes were correlated among the different profiles and dated to specific years of the lake level regression, illustrating the tight correlation between the morphology of the terrace sequence and the receding lake level. Our volume-level model and previous work on groundwater inflow suggest that the projected Dead Sea–Red Sea channel must have a carrying capacity of >0.9 km^3/a in order to slowly re-fill the lake to its former level. The channel will also exploit the net altitude of 400 m to produce hydro-energy and create a sustainable system of electricity generation and freshwater production by desalinization. Moreover, such a channel will maintain tourism and potash industry of the Dead Sea and reduce the natural hazard caused by the lake recession.

KEYWORDS: Dead Sea; Water Volume And Surface Area Loss; SRTM-Based Model; Red-Dead Sea Channel; Renewable Energy And Sustainability.

1. Introduction

The Dead Sea surface is the lowest terrestrial point on Earth at 420.86 m below sea level as of 20 January 2008 (Arab Potash Company records) and it is shrinking rapidly. It is well-known for its unique geographical, ecological and historical characteristics. The Dead Sea occupies the central part of the Jordan Rift Valley and serves as a terminal lake for a catchment area of 40,650 km², with the Jordan River as the main tributary (Figure. 1a). It used to deliver 1.21 km³/a (Salameh and El-Naser 1999) [1] to the Dead Sea, to which water of several wadis draining to the lake from the western and eastern peripheral mountains is added (Figure. 1a). The salt concentration of 34% is 10 times as salty as the ocean. Despite the lack of life in the Dead Sea, it is rich in a wide variety of minerals, making it an important source for salt industries and an attraction point for visitors wishing to benefit from the therapeutic qualities of its minerals. The distinctive cultural and historical heritage of the Dead Sea basin make it very important place not only for the riparian countries but also for the entire world. Many historical sites are located in the lake area such as Jesus's baptism site, Mount Nebo and Lot village. The excessive consumption of the water in the Dead Sea basin caused a rapid drop of the Dead Sea with severe environmental consequences. Therefore, an international effort should be done to save this unique eco-system and reserve its historical and natural treasures. This study aims at : (a) developing a terrain model of the Dead Sea water volume and surface area in order to determine the water input requirements of the shrinking Dead Sea and consequently the projected Red-Dead Sea Channel; (b)

[1] Reprinted with permission Springer Science + Business Media from Naturwissenschaften 96: 637-643

investigating the most recent changes in the Dead Sea level and the shore morphology by surveying the modern shoreline terraces and dating them according to the Dead Sea hydrograph; and (c) Evaluating the environmental impacts of the Dead Sea lowering and those of the projected channel as well as implication of the channel with respect to renewable energy and sustainable development.

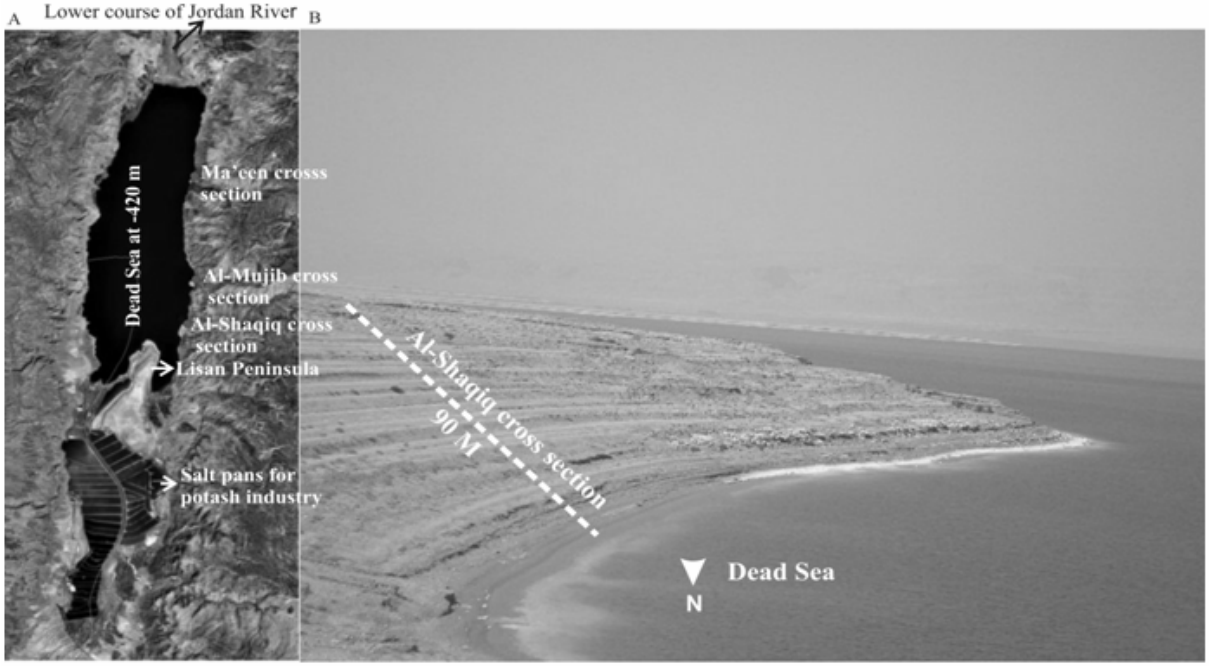

Figure 1 a. Location of the Dead Sea and the measured terrace profiles. The image was taken from w.NASA World Wind. b. Recent Dead Sea terraces north of Wadi Al-Shaqiq fan delta.

2. Material and Methods

To calculate the volume and area loss functions of the Dead Sea, a model of the rift valley volume and surface area in meter intervals was developed from SRTM data (3 arc second; CIAT 2004)[2]. ArcGIS (3D)-Analyst-"Surface Volume" tool-functionality was used to calculate the surface area and water volume of the Dead Sea below a certain altitude. The tool was applied for each meter change of the level from −389 to −415 m. Since the bathymetric contours of the Dead Sea below −415 m are not available in the SRTM data, the water volume of the current Dead Sea below −415 m (Dead Sea Data Summary. International Lake Environment Committee Foundation)[3] was added to our calculated volume in order to determine the total volume of the Dead Sea. The calculated water volume and surface area were plotted against the altitude. A polynomial function was derived that best fits the calculated graph using a least-square method.

Three profiles of the Dead Sea terraces were surveyed with the DGPS rover (Leica SR-20) at (1) Wadi Al-Shaqiq fan delta, (2) Wadi Al-Mujib fan delta, and (3) Wadi Ma'een fan delta (Figures. 1a & 3). The terrace altitudes were correlated among the different profiles and dated to specific years of the lake level regression according to the Dead Sea hydrograph as made available by the Hydrological Survey of Israel (personal communication, Eliyahu Wakshal) and previous publications.

3. Results and Discussion

3.1. Surface Area and Water Volume of The Dead Sea

The level of closed lakes—such as the Dead Sea—is a result of the hydrological balance between runoff into the lake plus direct precipitation on the lake surface minus evaporation; therefore, it serves as an indicator of climatic conditions. However, the recent Dead Sea level change (and its associated changes in surface area and volume) is mainly due to (a) transferring 500 Mio m³/a of water from the upper Jordan River by the Israel National Water Carrier project to the Mediterranean coastal plain; (b) diverting an additional water amount of 75 Mio m³/a from the Yarmouk River to the same carrier; (c) diverting 110 Mio m³/a of the Yarmouk River water to the King Abdullah Channel in Jordan and an additional 135 Mio m³/a from the same resource by Syria; (d) consuming (cumulative from 1976 to 1997) 2.4 km³ of the surface and ground water inflow to the Dead Sea from the eastern coast and Wadi Araba by Jordan and 3.3 km³ from the same resource in the western side by Israel; and (e) abstracting 5 km³ from the Dead Sea water for the potash industry by both Israel and Jordan [4]. The level change is therefore mainly due to human water consumption and not a result of climate change. The terrain model shows that water volume and surface area correlate highly with the lake level (volume R^2=0.9993, area R^2=0.9899; Figures. 2a, b) reflecting the bathymetry of the flanks of the former Dead Sea and the morphology of the rift valley, according to Eqs. 1 and 2 developed based on our model.

$$WV = 0.0077x^2 + 6.8905x + 1,688.8 \quad (1)$$

$$SA = -0.0008x^5 - 1.6141x^4 - 1,301.9x^3 - 524,930x^2 - 1*10^8x - 9*10^9 \quad (2)$$

where WV: water volume, SA: surface area
x: Dead Sea level.

According to our GIS data analysis, the Dead Sea has lost 9.7 km³ (0.2 km³/a) from its volume and 365 km² (7.9 km²/a) from its area during the period between 1932 and 1978. Since 1978, the volume decreased dramatically from ~157.7 to ~147 km³ with an average of 0.47 km³/a (Figures. 2a, b). Meanwhile, the surface area shrank from 729.4 to 636.7 km² with 4 km²/a on average. The recession of the lake level caused additional groundwater inflows of about 0.5 km³/a (Salameh and El-Naser 2000)[5]. This, plus our calculated volume loss, suggests that surface water inflow has to increase by more than 150% or by ~0.9 km³/a, in order to stop the continuous drop of the Dead Sea. However, this is unlikely to happen due to the current intensive consumption of water resources in the Dead Sea basin that is still increasing, e.g., by population growth and recent migrations to Jordan from Iraq and Lebanon.

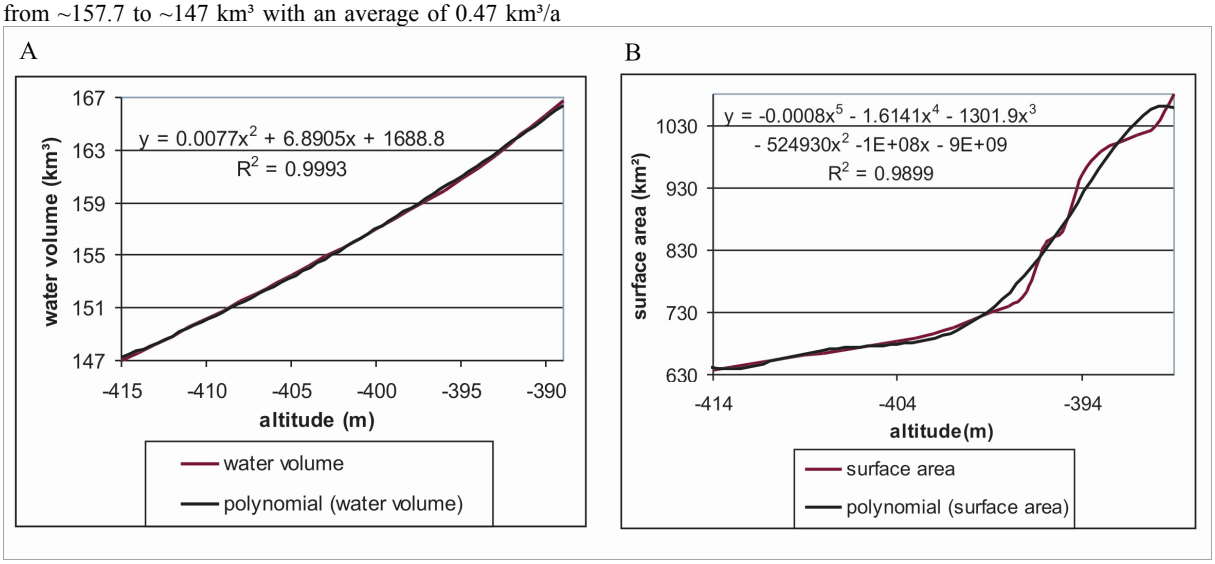

Figure 2 a. Volume–altitude model of the Dead Sea. b. Surface area–altitude model of the Dead Sea

3.2. Shoreline Terraces And Level Changes

The wadis draining to the Dead Sea experienced rapid erosion due to the lowering of the base level during the Holocene. Consequently, Gilbert-type fan deltas were formed in front of the mouths of the main wadis such as Al-Mujib, Al-Shaqiq, and Ma'een (Figure. 3a). Along some shore sections of these deltas with easily erodable lacustrine and alluvial deposits, a unique set of shore-line terraces formed that can serve as a tool to investigate this level change in details (Figures. 1b, 3a). These terraces were formed during the last 77 years as a result of a lake level drop of 30 m with an average of 0.4 m/a. Recorded levels [6] and [7] Hydrological Survey of Israel) suggest that the highest terrace at −389 m formed in 1932 (and previous years). The recorded level curve allows correlating most of the terraces to specific years (Figure. 3b). The lowest here documented terrace at −419 m formed in winter 2006–2007. Some years show a more pronounced recession than others but many of the terraces represent one winter season only. The average of lake level recession increased in rate throughout time: From 1932 to 1977, the Dead Sea level dropped relatively slowly from −389 to −399 m with an average of 0.2 m/a. In this relatively long period, only seven larger terraces can be recognized in the different profiles. This could be due to the prolonged times of stable water level that allowed the waves to abrade wide terraces.

The intensive water consumption in the Dead Sea basin in the last 30 years caused an accelerated drop from −399 m in 1978 to −419 m in 2007 with an average of 0.7 m/a. In this short period, 25 terraces formed, but with smaller dimensions. This is interpreted as a result of the fast recession and of the short period of constant water level that has not allowed the waves to form wide terraces.

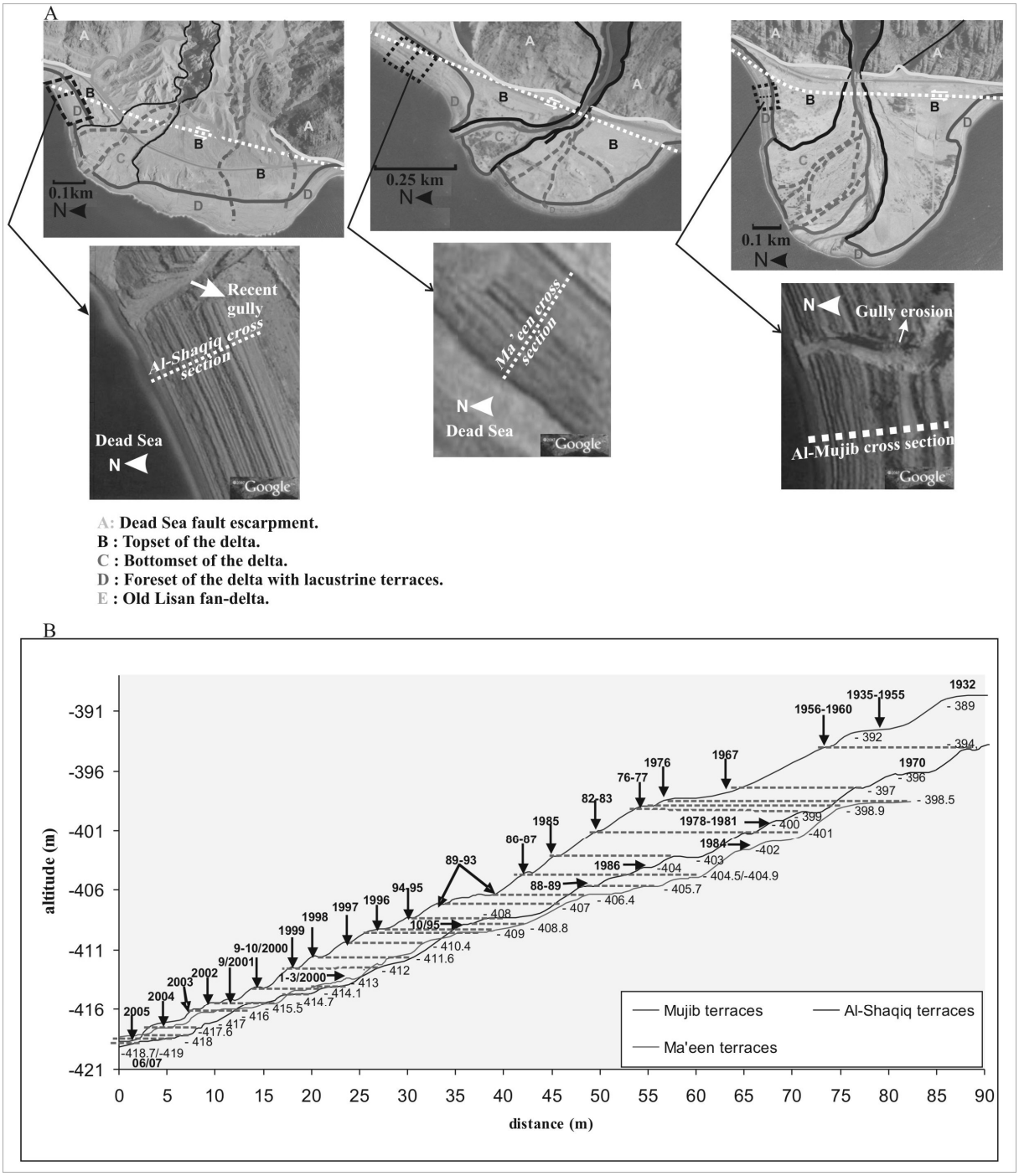

Figure 3 a. Gilbert fan deltas and sequences of lacustrine terraces north of Wadi Al-Shaqiq (upper left), north of Wadi Ma'een (upper middle), and north of Wadi Al-Mujib (upper right). Note roads crossing the deltas on the landward sections at positions near to the presumed trace of the Dead Sea eastern boundary transform fault. The lower images in this figure were taken from Google Earth. The date of these photos is 16 January 2007 http://earth.google.com. b. Three profiles of Dead Sea terraces surveyed by DGPS, correlated among each other and dated according to the recorded Dead Sea levels.

3.3. The Effects of The Dead Sea Lowering and The Implications of The Projected Channel

The rapid lowering of the Dead Sea level in the last 30 years has caused and will continue to cause severe detrimental effects both to its function as a resource and to the natural state of its shores. These effects include:

- Higher pumping costs for the factories using the former southern sections of the Dead Sea to extract potash, salt, and magnesium.
- The declining water level causes an accelerated outflow of fresh water from surrounding aquifers, thus causing a loss of this important resource.
- The receding shoreline makes it difficult (and in some places even dangerous) for tourists and hotel guests to access the water of the Dead Sea for medical bathes.
- The freshwater outflow has enhanced the dissolution of buried salt deposits creating a treacherous landscape of sinkholes and mud along the entire shore of the Dead Sea (Closson et al. 2005;[8] Yechieli et al. 2004)[9] that caused severe damage to roads, salt pans, and other civil engineering structures.

- The rapid emergence of delta bodies and the thereby caused decrease in buoyancy could cause sudden (or earthquake-triggered) slips (mass waste movement and landslides, such as what happened in the north of the Dead Sea in 2000) of sections of the deltas with the prospect to trigger small tsunamis within the lake.
- The rapid down-cutting of the west-draining wadis due to the lake level lowering threatens the bases of the bridges built at the mouths of these wadis.
- The lake could soon become halite-saturated, causing incrustation along its entire perimeter (today only spray water forms intermittent salt deposits).

Given the mounting stress on the water resources in the Dead Sea basin and the environmental hazard caused by its lowering, two projects were suggested to maintain the Dead Sea and stop its lowering: the Red Sea–Dead Sea Channel (RSDSC) and the Mediterranean–Dead Sea Channel (MDSC). Two alignments were suggested for the MDSC: in the north from the Mediterranean coast through Bet She'an to the Jordan River and in the south from the Gaza strip to Masada at the Dead Sea [10]. Although the northern route of the MDSC is the shortest and the cheapest one, the RSDSC would be under the control of all riparian countries, and its benefits could therefore be distributed fairly. Such projects cannot only stop the level decrease, but can also utilize the altitude difference of 400 m to produce renewable hydro-static energy and hence freshwater by desalinization. It also introduces new salt to the lake, ensuring the long-term sustainability of the salt extraction and tourism industry in both sides of the lake. Furthermore, it reduces the severe environmental hazards caused by the lake level lowering. Based on the water volume loss calculated by our model and the ground water inflow to the Dead Sea, we suggest that the RSDSC should have a capacity of more than 0.9 km^3/a in order to slowly fill the lake back to levels as of 30 years ago and to ensure its long-term sustainability.

However, the building of this channel raises a number of questions with respect to the negative impacts on the lake itself and on the lake basin:

- One of the long-term negative impacts of the channel might be the continuous infiltration of seawater into underground aquifers. Since this would diminish energy output, the channel should be planned with an impermeable bed to begin with.
- Possible ruptures of the RSDSC bed during earthquakes along the Dead Sea Fault would not be such a risk since the channel would be segmented by pumping and turbine stations, thus sections of it could temporarily be emptied and repaired.
- The possibility of lake water stratification for a long period is not expected. This depends on the rate at which the lake level will be raised. A slow and gradual pumping rate reduces the possibility of surface water dilution. Once the target level is attained, the volume of inflowing seawater will be adjusted to maintain a constant level. Incoming seawater will evaporate and the seawater-derived salts will accumulate in the upper water column. Thus the salinity and density of the surface water will continuously increase and reach that of the lower one. Consequently, the mixing of the water layers will occur [11].
- The mixing of sulphate-rich seawater with calcium-rich Dead Sea water could lead to gypsum precipitation. Halite precipitation may also take place during the steady state period, once the salinity of the upper water has increased enough to attain saturation with respect to this mineral. However, overturn of the water column will decrease the precipitation of both minerals due to the effect of mixing of seawater with the entire water body of the Dead Sea [11].
- Blooming of algae and bacteria could occur, causing a high turbidity, and therefore a higher rate of evaporation [11]. Since the possible dilution of the Dead Sea will be limited to the filling period, the blooming is expected to be a minor problem.

4. Conclusion

The hydrological balance of the Dead Sea significantly changed since the beginning of the twentieth century mainly due to intensive consumption of water resources in the lake basin mainly by Israel and secondarily by Jordan and Syria. During the last 30 years, water consumption caused an accelerated decrease in the water level, volume, and surface area amounting to 0.7 m, 0.47 km^3, and 4 km^2 per year, respectively. Our model function can also be used to predict near-future volume and area losses. Thus, in 2020, the lake will have dropped presumably to −427.8 m and will have lost 5.6 km^3 and 48 km^2 of its current volume and area, successively. Based on the water volume loss calculated by our model and the ground water inflow to the Dead Sea, we suggest that the RSDSC should have a capacity of more than 0.9 km^3/a in order to slowly fill the lake back to levels as of 30 years ago and ensure its long-term sustainability. The channel can also benefit from the net altitude difference of 400 m to generate renewable hydro-static energy and hence freshwater by desalinization. If the diversion of Jordan water to the Mediterranean coast would be stopped (replacing the water need by desalinization of seawater), then the recession of the Dead-Sea could be considerably slowed, buying time to consider the long-term alternatives.

Acknowledgments

The field work for this research was made possible by grants from the (DAAD) and (DFG), Germany. We thank Prof. E. Wagshal, Jerusalem, for providing the Dead Sea hydrograph; Prof. I. Sass, Darmstadt, for the DGPS equipment; Prof. A. Al-Malabeh, the Hashemite University/Al-Zerqa', and Dr. M. Nawasrah, (NRA) Amman, for fieldwork support; and Dr. M. Abo Kazleh for assistance in the field work and GPS post-processing. We also thank the Natural Resource Authority, Amman, for allowing us to use their GPS base station and field house at Ghour Al-Hadithah. This article was originally published as: "Abu Ghazleh S., Hartmann J., Jansen N., and Kempe S. (2009) Water input requirements of the rapidly shrinking Dead Sea. *Naturwissenschaften* 96: 637-643". Reprint with kind permission of Springer Science + Business Media.

References

[1] E. Salameh, H. El-Naser, "Does the actual drop in Dead Sea level reflect the development of water sources within its drainage basin?" Acta Hydrochim Hydrobio., Vol. 27, 1999, 5–11.

[2] International Centre for Tropical Agriculture (CIAT), "Voidfilled seamless SRTM data V1". Available from the CGIAR-CSI, 2004.

[3] Dead Sea Data Summary. International Lake Environment Committee Foundation: http://www.ilec.or.jp/eg/index.html, Accessed 1 Jun 2008.

[4] R. A. Al-Weshah, "The water balance of the Dead Sea: an integrated approach". Hydrol Process., Vol. 14, 2000, 145–154.

[5] E. Salameh, H. El-Naser, "Changes in the Dead Sea level and their impacts on the surrounding groundwater bodies". Acta Hydrochim Hydrobiol., Vol. 28, 2000, 24–33.

[6] C. Klein, "Fluctuations of the level of the Dead Sea and climatic fluctuations during historical times". Ph.D. Dissertation, Hebrew University, Jerusalem, 1986, (in Hebrew, English abstract).

[7] M. Hassan, M. Klein, "Fluvial adjustment of the lower Jordan River to a drop in the Dead Sea level". Geomorphology, Vol. 45, 2002, 21–33.

[8] D. Closson, N. Ab0ou Karaki, Y. Klinger, M. J. Hussein, "Subsidence and sinkhole hazard assessment in the southern Dead Sea area, Jordan". Pure Appl Geophys., Vol. 162, 2005, 221–248.

[9] Y. Yechieli, M. Abelson, A. Bein, V. Shtivelman, O. Crouvi, D. Wachs, G. Baer, R. Calvo, V. Lyakhovsky, Formation of sinkholes along the shore of the Dead Sea. Geological Survey of Israel, Vol. 21, 2004, 34 pp.

[10] The Harza JRV Group, "Red Sea-Dead Sea Canal Project, Draft Prefeasibility Report". Main Report. Jordan Rift Valley Steering Committee of the Trilateral Economic Committee, 1996.

[11] Gavrieli, A. Bein, A. Oren, "The expected Impact of the Peace Conduct Project (The Red Sea- Dead Sea pipeline) on the Dead Sea. Mitigaton and Adaption Strategies for Global Change". Vol. 10, 2005, 3-22.

JJMIE

Volume 4, Number 1, Jan.2010
ISSN 1995-6665
Pages 217 - 224

Jordan Journal of Mechanical and Industrial Engineering

Seawater Desalination System Integrated to Single Effect and Double Effect Absorption Heat Transformers

Rabah GOMRI *

School of Electrical and Electronic Engineering,Engineering Campus, Universiti Sains Malaysia,14300 Nibong Tebal, Seberang Perai Selatan, Pulau Pinang, Malaysia

Abstract

In this paper the performance and thermodynamic analysis of seawater desalination system combined to single effect and double effect absorption heat transformers are investigated. Energy and exergy analysis of the two systems were performed. Simulation results were used to study and to compare the influence of the absorber temperature and the intermediate heat source temperature (evaporator and generator temperature) on the energy efficiency, exergy efficiency, and fresh water production of the two systems

Keywords: Desalination; Energy; Exergy; Single Effect Heat Transformer; Double Effect Heat Transformer, Absorption; Simulations.

Nomenclature

Cp	Specific heat, Kj/Kg.K
ex	Specific exergy, Kj/Kg
Ex	Exergy, Kw
DAHT	Double absorption heat transformer
h	Specific enthalpy, Kj/Kg
HEX	Heat exchanger
m	Mass flow rate, Kg/s
N	Number
P	Pressure, Pa
Q	Heat load, Kw
SAHT	Single absorption heat transformer
T	Temperature, °C
T_{abm}	Absorber mean temperature, K
T_{evm}	Evaporator mean temperature, K
T_{gm}	Generator mean temperature, K
T_{hsm}	Heat source mean temperature, K
T_{hs}	Temperature of the intermediate heat source, °C
W	Mechanical work, Kw
X	mass fraction, % LiBr
ε	Effectiveness
η	Efficiency
ρ	Mass density, kg/m^3

Subscripts

0	Reference conditions
ab	Absorber
AHT	Absorption heat transformer
auxcd	Auxiliary condenser
cd	Condenser
ex	Exergetic
d	Destructed
ev	Evaporator
g	Generator
i	i^{th} Spice
j	j^{th} heat source
LiBr	Lithium Bromide
pump	Pump
wp	Water production

* Corresponding author. wael_sal@eng.usm.my.

1. Introduction

Water and energy are two inseparable items that govern our lives and promote civilisation.
Desalination of sea or brackish water is the method used currently to produce potable water [1].
The most developed and widely used technique for seawater desalination is the distillation process. The distillation of sea or brackish water can be achieved by utilising a thermal energy source [2].
Among the numerous options to improve the energy efficiency of desalination plants stands out the absorption heat transformer. A heat transformer is a device, which can deliver heat at a higher temperature than the temperature of the fluid by which it is fed. Absorption heat transformer systems are attractive for using waste heat from industrial processes and renewable energy such as solar energy and geothermal energy.
Bourouis et al. [4] studied by numerical simulation the purification of seawater using AHT working with the solution Water-(LiBr+LiI+$LiNO_3$+LiCl) and low temperature heat sources. This study is limited to evaluate the variation of the coefficient of performance (COP) of the AHT. Romero et al. [5] and Siquerios et al. [6] investigated the increase of the COP of the AHT in water purification systems, with and without increasing the low heat source temperature.
In this paper a comparative study between single effect and double effect absorption Heat Transformer Systems used for Seawater Desalination is carried out. Mathematical models of single absorption heat transformer (SAHT) and double absorption heat transformer (DAHT) operating with the Water/Lithium bromide solution and the overall desalination system (WP) were developed to simulate the performance of these combination systems. For the two systems identical heat source temperature was used to simulate the heat input to an absorption heat transformer. Energy and exergy analysis of the two systems were performed. Simulation results were used to study and to compare the influence of the various operating parameters on the energy efficiency, exergy efficiency, exergy losses of the two systems components and fresh water production of the two systems

2. System description

Figure 1. shows schematic diagram of seawater desalination system integrated to a single effect absorption heat transformer. The system consists of two parts. The first part is the absorption heat transformer and the second part is water desalination (Water Production).

As shown in Figure 1. the main components of a single effect absorption heat transformer system are the generator (G), absorber (Ab), condenser (Cd), evaporator (Ev), two pumps (pump1 and pump2), an expansion valve (V) and a solution heat exchanger (HEX-II).

The AHT operates at two pressure and three temperature levels when the heat is supplied to the generator and evaporator at the same temperature. The generator and the evaporator are supplied with heat (Q_g and Q_{ev} respectively) at the same temperature and the upgraded heat is delivered from the absorber (Q_{ab}), with part of the heat flowing into the process removed at ambient temperature from the condenser (Q_{cd}).

The desalination system consists of an auxiliary condenser, a separation vessel, a heat exchanger (HEX-I) and the absorber of AHT. In the absorber Q_{ab} is used to heat the seawater until it reaches its boiling point and partly evaporates. The two phases (liquid water and steam) leave the absorber and are separated through a vessel separator.

Figure 2. shows schematic diagram of seawater desalination system integrated to a double effect absorption heat transformer. The system consists of two parts. The first is the absorption heat transformer and the second part is water desalination (Water Production).

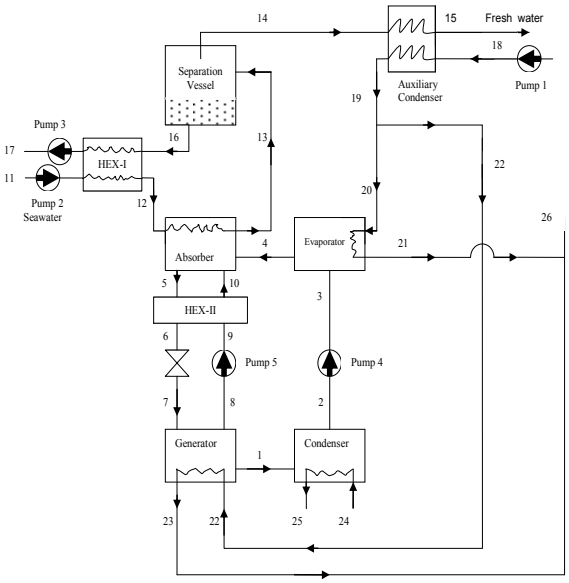

Figure 1. Schematic diagram of water purification integrated to a single effect absorption heat transformer.

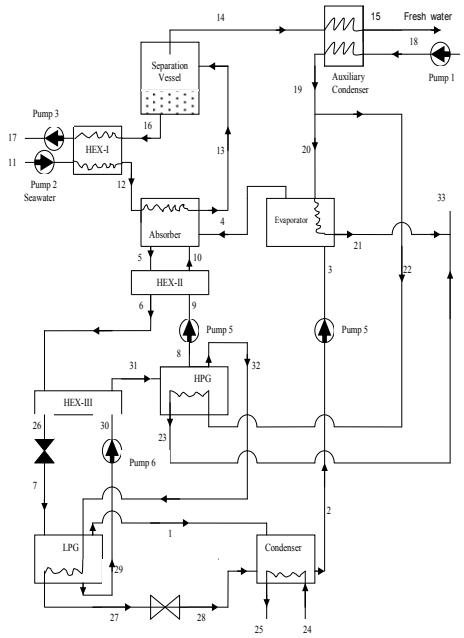

Figure 2. Schematic diagram of water purification integrated to a double effect absorption heat transformer

Corresponding Author. wael_sal@eng.usm.my.

As shown in Figure 2. the main components of a double effect absorption heat transformer system are the High pressure generator (HPG), the low pressure generator (LPG), absorber (Ab), condenser (Cd), evaporator (Ev), three pumps (pump1 pump2 and pump3), an expansion valve (V) and two solution heat exchangers (HEX-II and HEX-III). The AHT operates at three pressure and four temperature levels when the heat is supplied to the high pressure generator and evaporator at the same temperature. The HPG and the evaporator are supplied with heat (Q_g and Q_{ev} respectively) at the same temperature and the upgraded heat is delivered from the absorber (Q_{ab}), with part of the heat flowing into the process removed at ambient temperature from the condenser (Q_{cd}).

The desalination system consists of an auxiliary condenser, a separation vessel, a heat exchanger (HEX-I) and the absorber of AHT. In the absorber Q_{ab} is used to heat the seawater until it reaches its boiling point and partly evaporates. The two phases (liquid water and steam) leave the absorber and are separated through a vessel separator.

3. Mathematical model

The process mathematical model consists of two parts. The first part is the absorption heat transformer and the second part is water desalination

3.1. Mathematical model for the absorption heat transformer

The system is simulated assuming the following conditions:

The analysis is made under steady conditions.

The refrigerant (water) at the outlet of the condenser is saturated liquid.

The refrigerant (water) at the outlet of the evaporator is saturated vapour.

The Lithium bromide solution at the absorber outlet is a strong solution and it is at the absorber temperature

The outlet temperatures from the absorber, from the HPG and from the LPG correspond to equilibrium conditions of the mixing and separation respectively.

Pressure losses in the pipelines and all heat exchangers are negligible.

Heat exchange between the system and surroundings, other than in that prescribed by heat transfer at the generator, evaporator, condenser and absorber, does not occur.

The reference environmental state for the system is water at an environment temperature T_0 of 23°C (seawater temperature) and 1 atmosphere pressure (P_0)

Fixed data used in the analysis are summarised in Table 1

Table 1. Fixed data used in the analysis

	Evaporator heat load	Q_{ev}	500	Kw
	Seawater temperature	T_{11}	23	°C
	Seawater mass flow rate	m_{11}	0.03	Kg/s
	Condensation temperature	T_{cd}	29	°C
Condenser	Inlet temperature of cooling water	T_{24}	23	°C
	Outlet temperature of cooling water	T_{25}	26	°C
	Evaporation temperature	T_{ev}	$T_4=T_{21}-3$	°C
Evaporator	Inlet temperature of hot water	T_{20}	$T_{20}=T_{19}$	°C
	Outlet temperature of hot water	T_{21}	$T_{21}= T_{20}-5$	°C
	Generator temperature (HPG)	T_g	$T_8=T_{23}-3$	°C
Generator (HPG)	Inlet temperature of hot Water	T_{22}	$T_{22}=T_{19}$	°C
	Outlet temperature of hot Water	T_{23}	$T_{23}= T_{22}-5$	°C
HEX-I	Heat exchanger effectiveness	ε_I	80	%
HEX-II	Heat exchanger effectiveness	ε_{II}	80	%
HEX-III	Heat exchanger effectiveness	ε_{III}	80	%
Separation Vessel	Liquid water and steam	T_{13}	100	°C
	Liquid phase	T_{16}	100	°C
	Vapour phase	T_{14}	100	°C

Verify the energy balance for LPG

$$Q_{gl} = m_7.h_7 + m_{13}.h_{13} - m_1.h_1 - m_{27}.h_{27} - m_{29}.h_{29} = 0 \quad (1)$$

In this analysis, the equations for the thermal-physical properties of lithium bromide/water solution and liquid water developed by Patek and Klomfar [14] are used in this work. The equations for the thermal properties of steam are obtained from correlation provided by Irvine and Liley [15].

The first law of thermodynamics yields the energy balance of each component of the AHT system as follows

$$\left(\sum m_i.h_i - \sum m_0.h_0\right) + \left(\sum Q_i - \sum Q_0\right) + W = 0$$

The thermal efficiency of the absorption heat transformer is obtained by

$$\eta_{th-AHT} = COP_{AHT} = \frac{Q_{ab}}{\left(Q_g + Q_{ev} + W_{pump_s}\right)}$$

Where:

For Single effect absorption heat transformer

$$W_{pumps} = W_{pump1} + W_{pump2}$$

For double effect absorption heat transformer

$$W_{pumps} = W_{pump1} + W_{pump2} + W_{pump6}$$

3.2. Mathematical model for the global system (seawater desalination)

For this part, the mathematical model is based on the following assumptions:

The distillate product is salt free.

Absorber heat (Q_{ab}) is transferred always to seawater as latent and sensible heat (Q_{abL} and Q_{abS} respectively).

The distillate vapour always condenses completely.

The system operates at atmospheric pressure.

Heat transferred as steam condenses (Q_{abL}) in auxiliary condenser is transferred to the outgoing flow from solar flat plate collectors

The vessel separator is well insulated.

The mass and energy balance for the desalination system (see Figure 1.) is expressed as follows:

Absorber sensible heat (Q_{abS}):

$$Q_{absS} = m_{11}.C_p.\left(T_{12} - T_4\right)$$

m_{11} : mass flow rate of seawater feed (see Table 1)

Absorber latent heat (Q_{abL}):

Distilled water m_{15}

$$m_{15} = \frac{Q_{abL}}{L_v}$$

$$Q_{abL} = Q_{ab} - Q_{absS}$$

Auxiliary condenser:

$$Q_{auxcd} = Q_{abL} = m_{15}.L_v$$

L_v is the latent heat of vaporisation of sea water. An average value of L_v equal to 2414.4 KK/Kg was used for the calculations [16].

The first law efficiency of the desalination plant can be formulated as:

$$\eta_{th-WP} = \frac{Q_{ab}}{\left(Q_{WP} + W_{pumps}\right)}$$

Q_{WP}: heat consumed by the water production system.

$$Q_{WP} = m_{18}.\left(h_{18} - h_{32}\right)$$

Where:

For Single effect absorption heat transformer

$$W_{pumps} = W_{pump1} + W_{pump2} + W_{pump3} + W_{pump4} + W_{pump5}$$

For double effect absorption heat transformer

$$W_{pumps} = W_{pump1} + W_{pump2} + W_{pump3} + W_{pump4} + W_{pump5} + W_{pump6}$$

4. Exergetic analysis

The exergetic analysis reveals important information about the plant total irreversibility distribution among the components, determine which component weights on the overall plant inefficiency. According to Bejan et al. [19] the exergetic balance applied to a fixed control volume is given by the following equation:

$$ExD = \sum_j \left(1 - \frac{T_0}{T_j}\right).Q_j + \left(\sum_i m_i.ex_i\right)_{in} - \left(\sum_i m_i.ex_i\right)_{out} - W$$

Where the first term is the exergy of heat. The second and the third terms are the sum of exergy input and output rates of the flow, respectively. W is the mechanical work transfer to or from the system and ExD is exergy destroyed due to the internal irreversibility.

For each individual component of the global system (seawater desalination system) the exergy loss is calculated using equation 14. The total exergy loss of the global system is the sum of the exergy loss in each component. The exergy efficiency of the global system is defined as follows:

$$\eta_{ex-pw} = \frac{Ex_{desired,outpout}}{Ex_{used}} = 1 - \frac{ExD}{Ex_{used}}$$

Where:

$Ex_{desired,output}$ is the desired exergetic effect

Ex_{used} is the exergy used to drive de process

For Single effect absorption heat transformer:

$$W_{pumps} = W_{pump1} + W_{pump2} + W_{pump3} + W_{pump4} + W_{pump5}$$

For double effect absorption heat transformer

5. Results and discussion

Mass, energy and exergy balance equations and the various complementary relations constitute the simulation models of single effect and double effect absorption heat transformer systems used for seawater desalination. To solve the large set of equations simultaneously a computer program, which is written in FORTRAN was developed. Computer simulation was carried out in order to determine the various stream properties and the amount of heat and work exchanged by all equipments of the the tow systems. The results obtained from the present study may be presented as follows.

Figure 3 shows the effect of absorber temperature (T_{ab}) and generator and evaporator temperatures (intermediate heat source temperature) on energy efficiency (η_{WP}) of water production system integrated to single effect heat transformer (SAHT-WP) and water production system integrated to double effect absorption heat transformer (DAHT-WP). It can be seen that the η_{WP} of the DAHT-WP system is higher then that SAHT-WP system. For a given intermediate heat source temperature the operating absorber temperature interval of SAHT-WP is larger than that for DAHT-WP. In this study and when the intermediate heat source temperature is varied from 74°C to 96°C the maximum η_{WP} values of the SAHT-WP system are in the range of 0.799-0.833 and for DAHT-WP system are in the range of 1.276-1.308.

Figure 4 shows the effect of absorber temperature (T_{ab}) and generator and evaporator temperatures (intermediate heat source temperature) on exergy efficiency ($\eta_{ex\text{-}WP}$) of water production system integrated to single effect heat transformer (SAHT-WP) and water production system integrated to double effect absorption heat transformer (DAHT-WP). It can be seen that the $\eta_{ex\text{-}WP}$ of the DAHT-WP system is higher then that SAHT-WP system. For a given high generation temperature (HPG temperature), the operating interval of SAHT-WP is large than that for DAHT-WP. The water production system is more

efficient for high generator and evaporator temperature. In this study and when the intermediate heat source temperature is varied from 74°C to 96°C the maximum $\eta_{ex\text{-}WP}$ values of the SAHT-WP system are in the range of 54.1%-46.9% and for DAHT-WP system are in the range of 60.8%-58.5%

Figure 5 shows the water production of the two systems versus absorber temperature (T_{ab}). At the reverse of the energy efficiency and exergy efficiency the production of water for single effect absorption heat transformer integrated to desalination system (SAHT-WP) is more important than that for double effect absorption heat

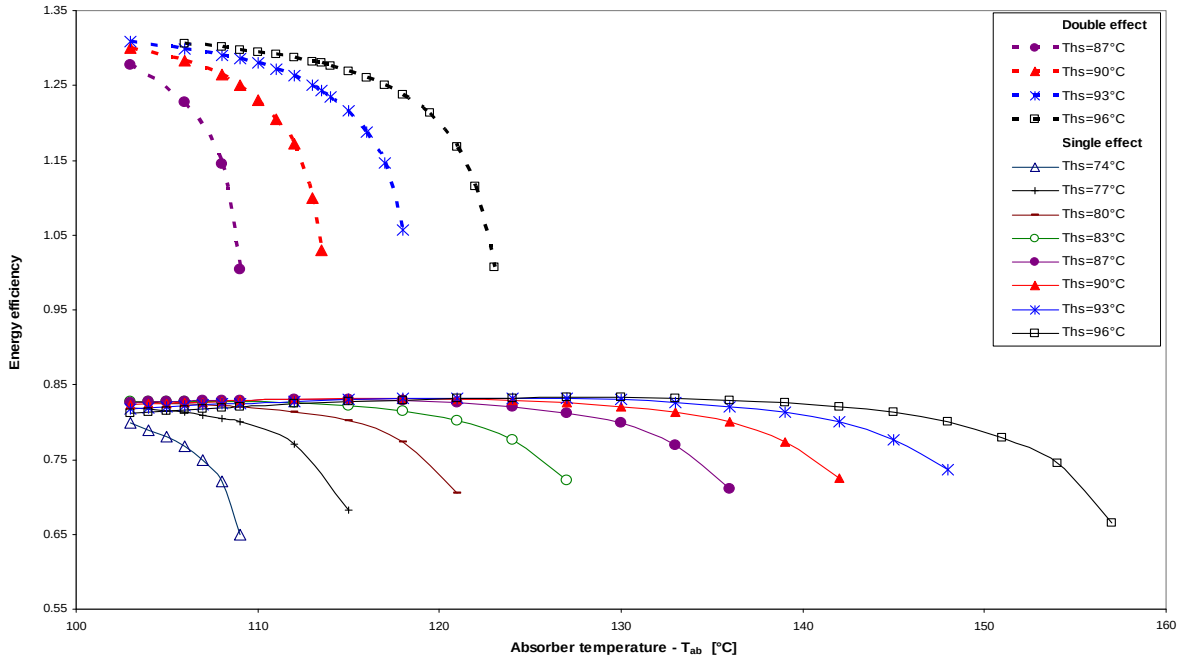

Fig 3. Effect of Tab on the water production system integrated to a single effect and double effect absorption heat transformers

transformer integrated to desalination system (DAHT WP). For SAHT-WP the production of water is almost constant for a wide range of temperature but for the second system (DAHT-WP) the water production decreases quickly when the absorber temperature increases. In this study and when the intermediate heat source temperature is varied from 74°C to 96°C the maximum fresh water production values of the SAHT-WP system are in the range of 0.168Kg/s-0.179Kg/s and for DAHT-WP system are in the range of 0.164Kg/s-0.167Kg/s

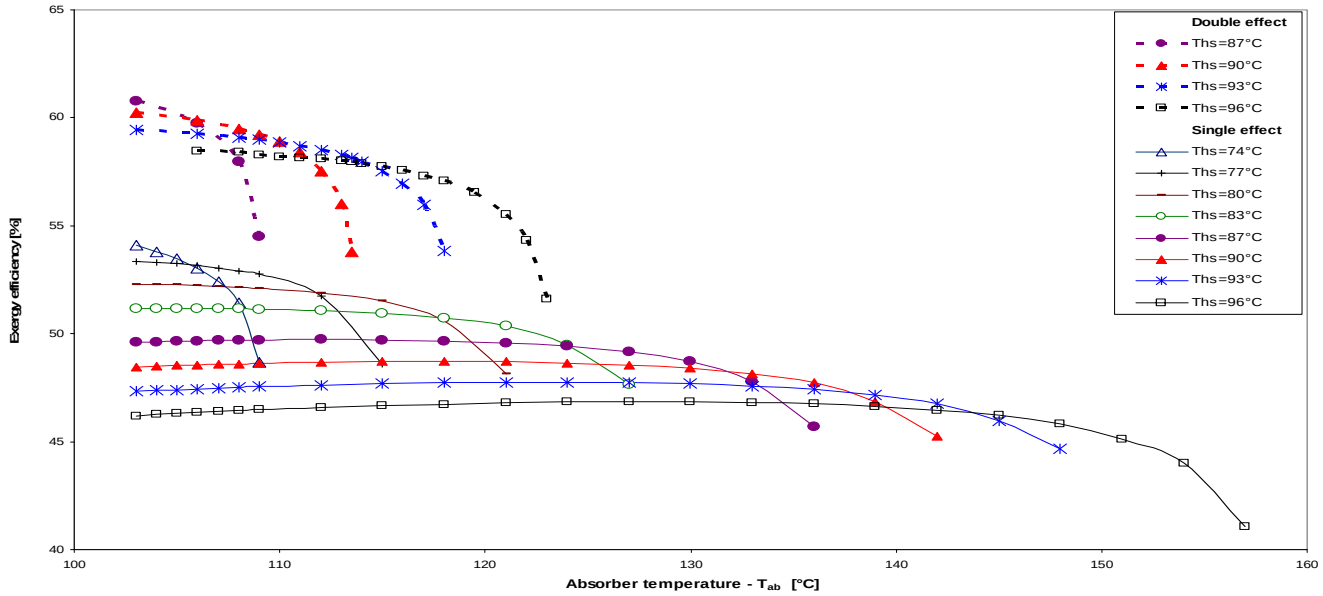

Figure 4. Effect of Tab on exergy efficiency of the water production system integrated to a single effect and double effect absorption heat transformer

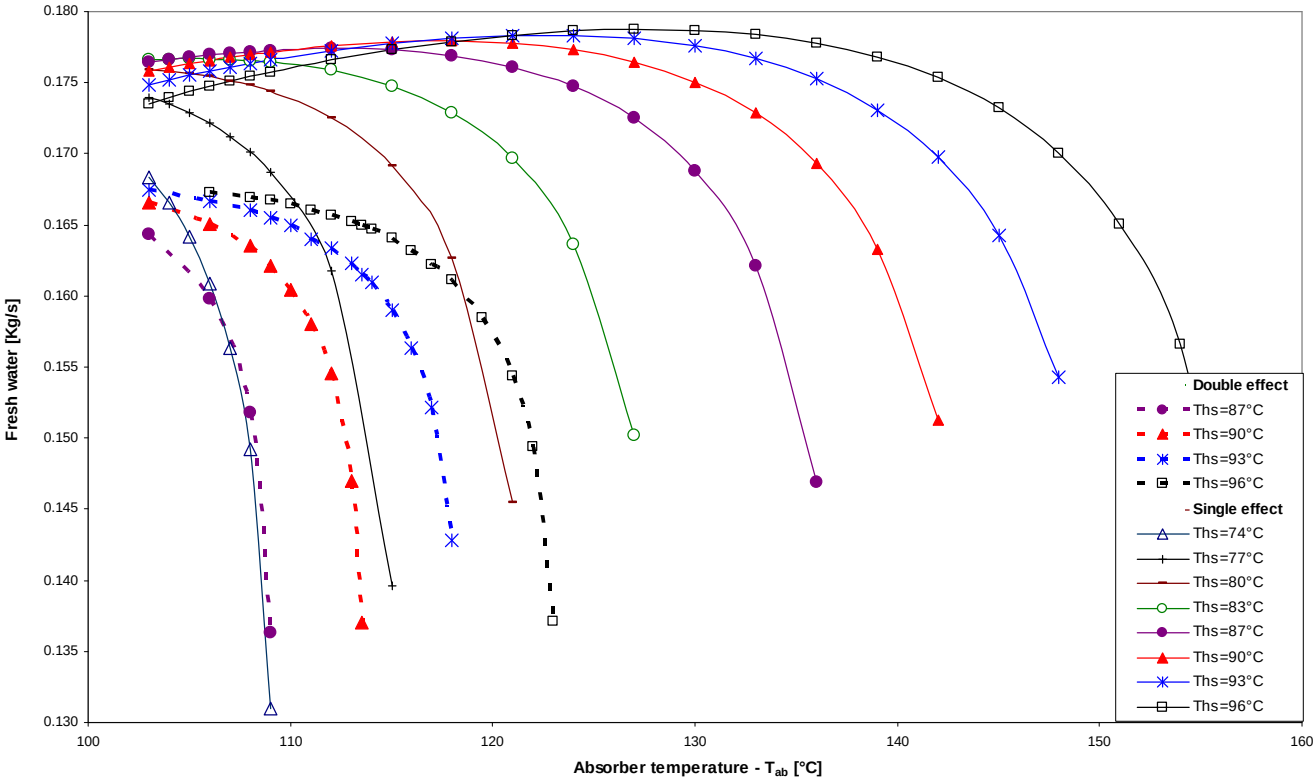

Figure 5. Effect of Tab on the quantity of fresh water produced

6. Conclusions

In this paper comparative study between single effect and double effect absorption Heat Transformer Systems used for Seawater Desalination is carried out

The energy efficiency and the exergy efficiency of the double effect absorption heat transformer (DAHT) are higher then that for single effect absorption heat transformer (SAHT). For a given high generation temperature (HPG temperature), the operating interval (absorber temperature) of SAHT is large than that for DAHT.

At the reverse of the energy efficiency and exergy efficiency the production of water for single effect absorption heat transformer integrated to desalination system (SAHT-WP) is slightly higher than that for double effect absorption heat transformer integrated to desalination system (DAHT-WP). For SAHT-WP the production of water is almost constant for a wide range of temperature but for the second system (DAHT-WP) the water production decreases quickly when the absorber temperature increases

References

[1] Khalil EE. Potable water technology development in Egypt. Desalination , Vol. 136, 2001, 57-62.

[2] Garcia-Rodriguez L, Gomez-Camacho C. Preliminary design and cost analysis of a solar distillation system. Desalination Vol. 126, 1996, 109-114.

[3] Nafey AS, Mohamad MA, El-Helaby SO, Sharaf MA. Theoretical and experimental study of a small unit for solar desalination using flashing process. Energy Conversion and Management Vol. 48, 2007, 528-538.

[4] Bourouis M, Coronas A, Romero RJ, Siqueiros J. Purification of seawater using absorption heat transformers with water-(LiBr+LiI+$LiNO_3$+LiC1) and low temperature heat sources. Desalination 166, 2004, 209-214.

[5] Romero RJ, Siqueiros J, Huicochea A. Increase of COP for heat transformer in water purification systems. Part II – without Increasing heat source temperature. Applied Thermal Engineering Vol. 27, 2007, 1054-1061.

[6] Siqueiros J, Romero RJ. Increase of COP for heat transformer in water purification systems. Part I – Increasing heat source temperature. Applied Thermal Engineering, Vol. 27 , 2007, 1043-1053.

[7] Frederick FS. Flat plate solar collector performance evaluation with a solar simulator as a basis for collector selection and performance prediction. Solar Energy, vol. 18, 1976, 451-466.

[8] Kalogirou SA. Solar thermal collectors and applications. Progress in energy and combustion science; Vol. 30, 2007, 231-295.

[9] Uca A., Inalli M. Thermo-economical optimization of a domestic solar heating plant with seasonal storage. Applied Thermal Engineering; Vol. 27, 2007, 450-456.

[10] Karatasou S, Santamouris M, Geros V. On the calculation of solar utilizability for south oriented flat plate collectors tilted to an angle equal to the local latitude. Solar energy 2006; 80:1600-1610.

[11] Akhtar N, Mullick SC. Computation of glass-cover temperatures and top heat loss coefficient of flat-plate solar collectors with double glazing. Energy , Vol. 32, No. 7, 2006, 1067-1074.

[12] Sartori E. Convection coefficient equations for forced air flow over flat surfaces. Solar Energy Vol. 80, 2006,1063-1071.

[13] Bernard J. Energie Solaire – Calculs et Optimisation, France, Ellipse, 2004.

[14] Patek J, and Klomfar J. Computationally effective formulation of the thermodynamic properties of LiBr-H2O solution from 273 to 500K over full composition range. Int. J. of Refrigeration; Vol. 29, 2006, 566-578.

[15] Irvine TF, Liley PE. Steam and gas tables with computer equations. USA, Academic Press, 1984.

[16] Orfi J, Galanis N, Laplante M. Air humidification dehumidification for water desalination system using solar energy. Desalination, Vol. 203, 2007, 471-481.

[17] Kotas JT. The exergy method of thermal plant Analysis, Paris, Lavoisier, 1987.

[18] Bejan A, Tsatsaronis G, Moran, M. Thermal design and optimization, New York, Wiley, (1996).

[19] Vidal A, Best R, Rivero R, Cervantes J. Analysis of a combined power and refrigeration cycle by the exergy method. Energy, Vol. 31, 2006, 3401-3414.

JJMIE

Volume 4, Number 1, Jan. 2010
ISSN 1995-6665
Pages 225 - 229

Jordan Journal of Mechanical and Industrial Engineering

A Study of Fuel Cell Hybrid Auto Rickshaws Using Realistic Urban Drive Cycles

Mohammed Abu Mallouh [a,*], Bradley Denman [b], Brian Surgenor[b], Brant Peppley[b]

[a] *Department of Mechatronics Engineering , Hashemite University , Zarqa, Jordan*

[b] *Department of Mechanical and Materials Engineering , Queen's University, Kingston, Ontario, Canada*

Abstract

The popular three-wheeled vehicles known as auto rickshaws are common in Asian cities where due to their older two-stroke engines they have been significant contributors to the current air quality issues that plague the urban areas. Recent changes to four-stroke engines as well as those powered by diesel, compressed natural gas (CNG) or liquefied petroleum gas (LPG) reduce the pollution and greenhouse gas emissions. However, because of the large number of vehicles emission of such vehicles is still an important issue.

Some studies about converting an internal combustion engine (ICE) rickshaw to an electrical or fuel cell rickshaw have been done recently. Most of the rickshaw conversion studies used one of the standard urban drive cycles. Such drive cycles do not accurately portray the demands on a rickshaw. Thus, results with unrealistic drive cycles may be misleading.

In this study a comparison between ICE and hybrid fuel cell rickshaw configuration was done using a realistic drive cycle. An ICE and two candidate fuel cell rickshaw models were created and assessed using the Powertrain System Analysis Toolkit (PSAT) software. Two drive cycles that would closely emulate the true demands on a rickshaw operated in an urban environment were developed in order to more accurately simulate the performance of conventional and fuel cell hybrid rickshaws as a means of determining the current feasibility of fuel cells for use in rickshaws.

Keywords: Rickshaw; Fuel Cell, PSAT; Hybrid Vehicle; Drive Cycle.

Nomenclature

CNG	compressed natural gas
LPG	liquefied petroleum gas
ICE	internal combustion engine
Ni-MH	nickel metal hydride
Li-ion	lithium-ion
FC	fuel cell
PEM	proton exchange membrane
SOC	state of charge

1. Introduction

Alternative energy solutions received a great deal of attention in the last decade due to the need of sustainable and environmental friendly energy sources. The main pollutant source in urban areas is the emission of vehicles with ICE 0. Increased concerns over global and local pollution, depletion of fossil fuels, and higher gas prices have motivated ambitious plans for new vehicle types with alternative energy sources. Hybrid electrical vehicles that combine the advantages of two power sources, ICE and electrical motors, have been the focus of attention recently. Nowadays, such vehicles are available in the auto market and are becoming more popular due to high fuel prices and the increasing concerns about he environment. Fuel cell and electric hybrid driven vehicles is another promising alternative technology. These vehicles have been proposed as the next generation of vehicles since they promise clean performance and show higher energy efficiency than conventional vehicles 0[2].

Auto rickshaws are one of the most popular vehicles in developing Asian countries where they are used as taxis and to transport goods. In India alone there are about 2.5 millions rickshaws currently on the road and 250,000 new vehicles are sold each year 0[3]. Figure 1 shows a typical three-wheel auto rickshaw. Due to their small size and maneuverability they are popular method of transportation in large urban centers.

A two or four stroke gasoline engine usually powers these vehicles. Thus, rickshaws are typically highly polluting. In recent years, alternatives such as CNG and LPG models have been introduced to deal with the pollution problem. While these vehicles reduce the amount of particulate matter and other harmful pollutants they do not eliminate them and cities where rickshaws are numerous will continue to have poor air quality. The capital city of New Delhi is one of the most polluted cities in the world although the majority of the public transport is currently

*Corresponding Author. mmallouh@hu.edu.jo

based on the CNG technology [4]. Some studies about converting an ICE rickshaw to an electrical or fuel cell vehicle have been done recently. In [5] a photovoltaic battery powered rickshaw was investigated. Results showed the proposed hybrid battery/photovoltaic configuration was more efficient and resulted in fewer emissions than the ICE rickshaw.

A hybrid fuel cell/battery rickshaw was studied in [4]. Using the Highway Fuel Economy Test as the drive cycle the results showed promise in creating a hydrogen fuel cell vehicle, with respect to both the environment and cost. It is known that the high costs and fuel storage requirements for the fuel cell vehicle have hindered their use in four-

Figure 1: Standard three-wheel auto rickshaw

wheel light duty vehicles. However, these drawbacks are partially mitigated in a rickshaw since the lower power demand results in a reduced cost for the fuel cell compared to a four-wheel vehicle. Daily rickshaw ranges are between 70 and 150 km with a maximum speed of 60km/hr at most which does not necessitate as much hydrogen to be stored on board for a full run 0[1].

Most of the rickshaw conversion studies used one of the standard urban drive cycles. Such drive cycles do not accurately portray the demands on a rickshaw since they are primarily located in urban centers where they are subjected to mostly stop-and-go traffic and a large amount of braking and acceleration. In 0[6] a driving cycle that represents the driving pattern of the auto rickshaw in India was proposed and compared to the India urban drive cycle that is commonly used for rickshaws analysis.

In this study a comparison between ICE and hybrid fuel cell rickshaw configurations was done based on running cost using a realistic drive cycle. Two drive cycles based on 0[6] were developed in order to more accurately simulate the performance of conventional and fuel cell hybrid rickshaws as a means of determining the current feasibility of fuel cells for use in rickshaws.

2.System Main Components

2.1 Fuel Cell

Fuel cells (FC) are electrochemical devices that convert chemical energy of a reaction directly into electrical energy. Among the various types of fuel cells, Proton Exchange Membrane (PEM) fuel cell has drawn the most attention due to its simplicity, viability, quick start up, higher power density and lower temperature operation 0[2]. Inputs to a PEM fuel cell are oxygen and hydrogen while the outputs are electricity and water. A PEM fuel cell is capable of using both oxygen directly from air, or purified oxygen. At the anode, hydrogen is electrochemically oxidized to form protons and electrons. At the cathode, oxygen is electrochemically reduced and combined with the protons transported through the membrane and the electrons that pass through an external circuit. The overall reaction in the cell is the electrochemical oxidation of hydrogen to form water. The electrons flowing through the external circuit are capable of performing useful work due to the energy released by reaction 0[4].

A standalone FC system may not be sufficient to satisfy the load demands, especially during start-up and transient events. Moreover, the FC system would have to supply all of the power demand thus increasing the size and cost of the FC system. As a result, downsizing the FC system and hybridizing it with an energy storage system decreases system cost and improves performance.

2.2 Battery

The two primary battery competitors for use in both electric vehicles and hybrid-electrics are nickel metal hydride (Ni-MH) and lithium-ion (Li-ion). While Ni-MH currently has an edge over Li-ion in terms of production readiness, Li-ion has twice the energy density of Ni-MH 0[7]. One great advantage of Li-ion batteries is their low self-discharge rate of only approximately 5% per month approx compared to over 30% per month and 20% per month in nickel metal hydride batteries and nickel cadmium batteries respectively 0[7].

3.Auto Rickshaw Configuration Models

Conventional ICE Rickshaw

A Mahindra Alfa is a three-wheel rickshaw that is powered by a diesel engine. Figure 2 shows the PSAT generated configuration of the conventional vehicle and its components.

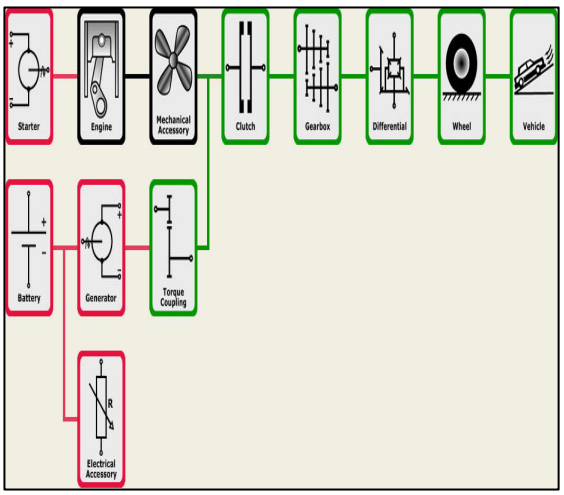

Figure 2: PSAT component configuration for conventional rickshaw

Table 1 provides the primary auto rickshaw specifications used in the vehicle model from manufacturer specifications and experimental results.

Table 1: Auto rickshaw parameters used in the model as taken from 0[6] and (www.mahindrasmallcv.com).

Engine Type	4-stroke, Single Cylinder, diesel
Max. Power (kW)	5.51 KW±5% @ 3600 rpm
Max. Torque (Nm)	16.7 Nm±5% @ 2200-2800 rpm
Transmission	Constant Mesh, 4 Forward
Tire Size	4.50" x 10", 8PR
Maximum Speed	53 km/h
Battery	12 V, 50 Ah
Headlights	2 x 35 W
Fuel Capacity	10.5 L
Max GVW	800 kg
Curb Weight	480 kg
Frontal Area	2.09 m^2
Coefficient of Drag	0.5
Max Acceleration	2.1 m/s^2
Average Payload	100 kg

3.2 Fuel Cell Hybrid Rickshaw

A hybrid configuration was selected in order to utilize a lower power PEM FC. The FC provides power to the vehicle's motor and battery. PSAT can only create a series fuel cell hybrid vehicle configuration therefore no parallel configurations have been tested. Figure 3 shows the configuration for the fuel cell hybrid rickshaw.

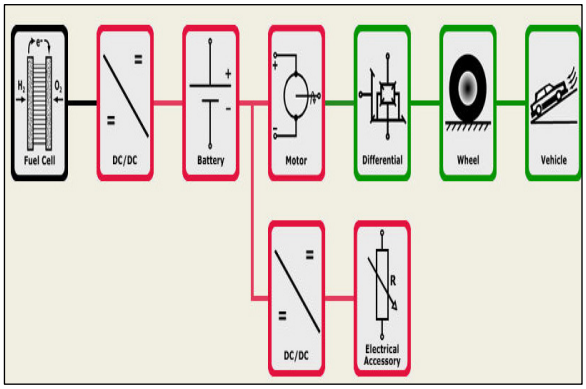

Figure 3: PSAT component configuration for series fuel cell hybrid rickshaw

It is expected that the fuel cell will be the most critical component in the hybrid configuration. In order to match the performance of the conventional diesel rickshaw the power supply of the hybrid must be appropriate. The effect of the FC power was investigated by considering two sizes of the PEM FC. An 8.8 kW high power rickshaw configuration where the bulk of the vehicle power is provided by the FC and a 4.4 kW FC low power version that would only be able to provide part of the power when the maximum is demanded. FCs with both specifications are commercially available.

Onboard hydrogen fuel is in the form of pressurized gas with a mass of 1.79 kg in a 38 kg cylinder. Li-ion batteries were integrated into the models with a capacity of approximately 8.4 kWh. With the batteries there is a concern when it comes to deep discharging and its effect on capacity over time. Therefore a maximum discharge has been considered to be a drop in the state of charge (SOC) by 40% in order to maintain their lifespan.

An AC electric induction motor with an 8 kW maximum power output was selected based upon the specifications of the conventional rickshaw. Additionally the DC/DC converters operate at an efficiency of 95%. A single final drive differential was selected as opposed to a full transmission, which reduces the overall weight of the vehicle. The rickshaw, however, was not entirely changed from the specifications of the conventional model. Passenger and driver masses were also kept the same to maintain a direct comparison between the conventional and FC hybrid models.

4.Drive Cycles

A drive cycle is the series of conditions a vehicle will experience in a set amount of time that can be used a reflection of the conditions over a longer period of time. The drive cycle defines when the vehicle is at rest, accelerating, decelerating or at a constant speed. Most existing drive cycles were designed for four-wheel light duty vehicles. The maximum acceleration, deceleration and top speed in such drive cycles are above the capabilities of rickshaws. Thus such drive cycles do not accurately portray the demands on a rickshaw. In 0 new drive cycles for rickshaws in India were designed. The new drive cycles were developed using GPS data that was collected from rickshaws in operation. The study looked at rickshaws driving in New Delhi at different times and developed daytime and evening drive cycles.

In this study two drive cycles were designed based upon the results presented in 0. The daytime drive cycle was based upon the periods of peak traffic when speeds were limited. By comparison the evening cycle allows for higher speeds when there is less traffic on the roads and shorter stop durations. The statistics of both drive cycles and the India urban drive cycle that is usually used in rickshaw analysis are shown in Table 2.

Table 2: Drive cycles statistics

Parameter	India Urban cycle	Day cycle	Evening cycle
Time (s)	2689	5650	4849
Distance (km)	17.4	8.7	17.40
Maximum Speed (km/h)	62.2	44.0	49.96
Average Speed (km/h)	23.3	5.5	12.92
Maximum Acceleration (m/s^2)	1.7	7.0	7.0
Maximum Deceleration (m/s^2)	-2.1	-7.0	-7.0
Average Acceleration (m/s^2)	0.3	0.8	1.02
Average Deceleration (m/s^2)	-0.4	-0.9	-1.0449
Idle Time (s)	267	405	222
Number of Stops	52	31	31

5.Simulation Results

The ICE conventional rickshaw model was designed to replicate the baseline for comparison to all the alternative powered vehicles. The main results for comparison based upon the rickshaw drive cycles are displayed in Table 3. The "LP FC" and "HP FC" columns represent the low and high power FC hybrid configurations. "Conv" represents the conventional model.

5.1 Comparison of Drive Cycles

The three drive cycles described in Section 4 were simulated using the conventional vehicle model. Results are shown in Table 3. There was a distinctive difference between the two developed realistic drive cycles and the mainstream cycle. The fuel economy for the India Urban cycle was significantly less than that of the two other cycles. Based upon a typical rickshaw routine the conventional rickshaw needs additional fuel every day. This conflicts with the India Urban cycle results thatindicate that a rickshaw could travel for almost three days without refueling. It is unrealistic to expect that in heavy traffic with a great deal of acceleration and braking that a conventional rickshaw would achieve a remarkable 2.43 L/100 km diesel fuel economy when loaded with passengers. The intensity of the two developed cycles is made clear from the high demands for fuel and significant amounts of exhaust shown in the simulation results. Based upon the results from the developed cycles the need for refueling is greater, which more accurately portrays the usage of auto rickshaws in urban Indian streets. The intensive drive cycle shows a marked increase in rate of carbon dioxide released which are higher than that reported in [8], which indicated that a typical four-stroke gasoline auto rickshaw would release 78.5 g/km.

5.2 LP FC versus HP FC

As shown in Table 3 the LP FC configuration has better fuel economy, cost/km, and range than the HP FC configuration for both daytime and evening drive cycles. While both configurations utilized the braking energy almost at equal percentage, the electrical consumption in the case of the HP FC configuration was negative. This negative value indicates that the HP FC configuration inevitably wastes fuel by charging the battery when it is already sufficiently charged. On the other hand while the LP FC configuration provided just enough power to keep the SOC constant it was still greater than was required. The first 80 seconds of the daytime drive cycle is plotted in Figure 4, in it the speeds and accelerations are relatively low and the intensity of the drive cycle is at a minimum.

Figures 5 and 6 show the plot of the power outputs with respect to the same eighty seconds of the daytime drive cycle. The fuel cell output approaches its peak power and is used in greater proportion than the batteries are despite the low power requirements. The emphasis on the fuel cell in both the LP and HP FC models results in greater fuel consumption than may have been required if the control strategy were optimized for greater hybridization. The LP FC configuration was found to be better than the HP FC configuration in almost every aspect, thus it will be used for comparison with the conventional configuration.

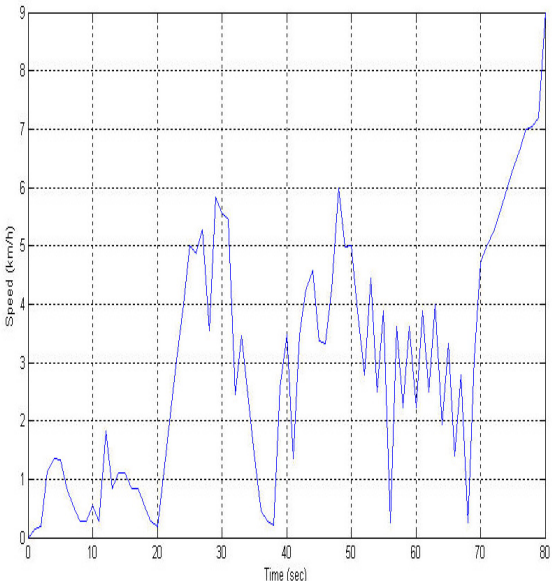

Figure 4: Speed versus Time for the Daytime Drive Cycle Simulation

Table 3: Summary of Simulation Results

Result	Conventional			LP FC		HP FC	
	India Urban Cycle	Day Cycle	Evening Cycle	Day Cycle	Evening Cycle	Day Cycle	Evening Cycle
Fuel Economy (L/100km)	2.4	6.2	4.3	44.9	36.2	50.7	42.1
Fuel Economy Gasoline Equivalent (L/100km)	2.7	6.9	4.8	3.0	2.5	3.4	2.9
Range based on fuel capacity (km)	432.1	170.2	244.8	268.6	332.5	237.7	286.5
CO_2 Emissions (g/km)	64.8	164.7	114.5	0	0	0	0
Final SOC (%)	NA	NA	NA	69.18	68.99	70.07	71.69
Distance Traveled (km)	16.1	7.6	15.0	8.1	16.1	8.1	16.1
Percentage of Braking Energy Recovered at Battery (%)	0	0	0	4.9	11.3	5.6	11.5
Fuel Mass Consumed (kg)	0.3281	0.3894	0.5384	0.0655	0.1050	0.0739	0.1218
Electrical Consumption (Wh/km)	NA	NA	NA	8.4	4.8	-1.4	-9.9

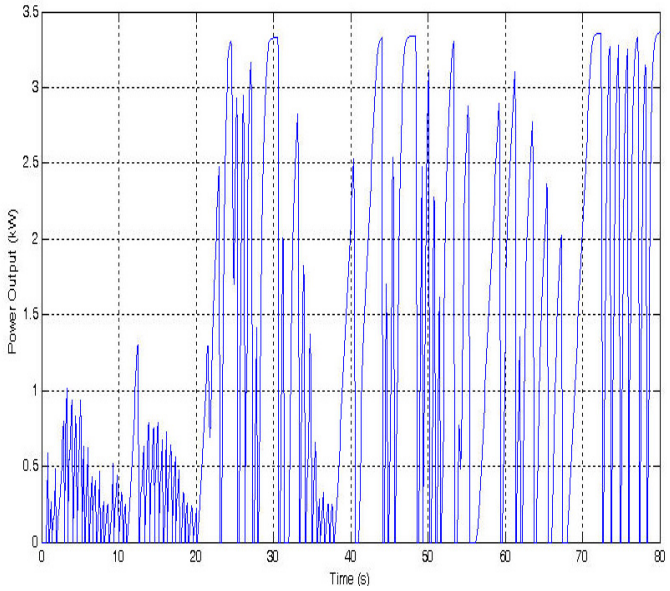

Figure 5: FC output versus time for LP FC model on daytime drive cycle

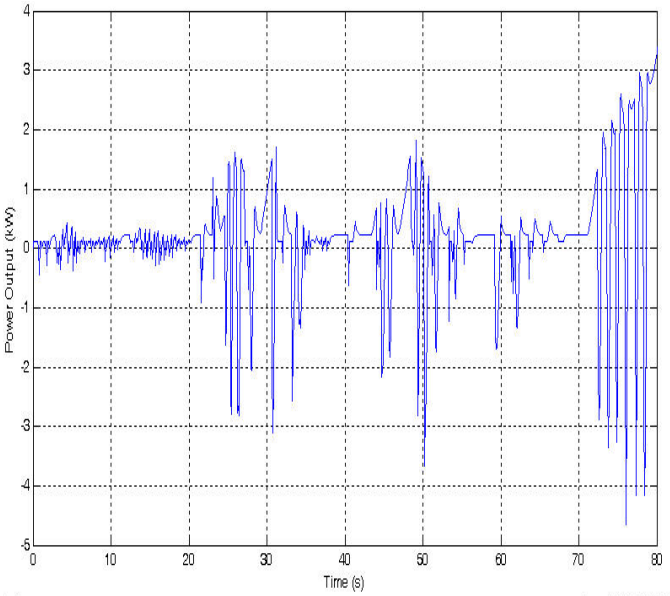

Figure 6: Battery output versus time for LP FC model on daytime drive cycle

5.3 Fuel Cell versus Conventional Models

During the daytime drive cycle, as shown in Table 3, the gasoline equivalent fuel economy and range for the LP FC was better than the conventional model by 57% and 58%, respectively. For the evening drive cycle it was 48% and 36% better. The conventional configuration releases 164.65 and 114.47 g/km of carbon dioxide for the daytime and evening drive cycles respectively while there are no vehicular emissions of carbon dioxide for either FC configuration. Thus the LP FC configuration is better than the conventional configuration when considering both the performance efficiency and the environment.

The running cost per km was calculated based upon standard rates. The cost per liter of diesel fuel is 32.86 Rs/L 0[9], electricity is sold at an average rate of 4.8 Rs/kWh [10] and the cost of hydrogen when converted into Rupees is 240 Rs/kg of hydrogen using an exchange rate of 48 Rs to 1 USD [11]. It was estimated that the charging process would be approximately 90% efficient therefore there is a loss factor equal to 1.1. The respective costs per kilometer of travel for the two drive cycles are listed in Table 4. The values were calculated based upon the equation of Cost/km = (Fuel Consumed x Fuel Price + Electricity Consumption x Loss Factor x Cost of Electricity) / Distance Traveled.

Table 4: Cost/km for each rickshaw model

Vehicle Model	Cost (Rs/km)	
	Daytime cycle	Evening cycle
Conventional Rickshaw	1.98	1.38
Low power Li-ion Rickshaw	1.98	1.59
High power Li-ion Rickshaw	2.19	1.91

The running cost of the LP FC configuration is seen to be equal to that of the Conv. configuration for the daytime cycle (both at 1.98 Rs/km). However, for the evening cycle, LP FC is 15% more expensive than Conv. (1.59 compared to 1.38 Rs/km)". This is mainly due to the higher cost of hydrogen compared to diesel fuel in India. In order to decrease the cost/km the use of the hydrogen has to be reduced. It is expected that utilizing the batteries more than the fuel cell will reduce the hydrogen consumption and in turn the cost per kilometer. Altering the control strategy to activate the fuel cell only after the batteries have been drained to a sufficient point after which all the power will be supplied by the fuel cell and the battery will recharge can do this. Less reliance on the hydrogen and more on the electricity is a critical parameter to any control scheme modifications. The fuel cell must be used only when recharging is required and emphasize it as a range extender as opposed to the primary source of power. While these modifications will improve the fuel cell model's economic feasibility the price of diesel must also increase to make the fuel cell alternative more viable based upon the costs.

6.Conclusions

A study of auto rickshaw conversion using a realistic drive cycle was conducted. The intensity of rickshaw driving is captured more accurately by the two developed drive cycles as opposed to a standard urban drive cycle.

It was found that the LP FC configuration is better than the HP FC model in both performance and cost. The significant advantage of both FC models compared to ICE rickshaws is their lack of carbon dioxide emissions.

However, the operating cost of FC hybrid rickshaws is significantly higher than the conventional one. Since most rickshaws are privately owned and do not generate significant income the higher initial investment and operating costs currently make it an unrealistic option. The combination of a reduction in hydrogen consumption and increase in diesel and fossil fuel prices is needed to make the current technology more viable in the application. These changes together with decreasing costs in fuel cell technology will result in more favorable economics that will generate more consumer interest.

References

[1]Y. Wu, B. Chen and K. D. Huang, "The effect of control strategy and driving pattern on the fuel economy and exhaust emission of a hybrid electrical bus", SAE World Congress: Advanced Hybrid Vehicle Powertrains, Detroit, Michigan, 2008.

[2]M. C. Kisacikoglu, M. Uzunoglu and M. S. Alam, "Fuzzy logic control of a fuel cell/battery/ultra-capacitor hybrid vehicular power system", Proc. IEEE Vehicle Power and Propulsion Conference, Arlington, Texas, 2007.

[3]P. Mulhall, M. Naviwala, S. M. Lukic, J. Braband and A. Emadi, "Entrepreneurial projects program at Illinois Institute of Technology: solar/battery hybrid three-wheel auto rickshaw for India", Proc. IEEE Vehicle Power and Propulsion Conference, Arlington, Texas, 2007.

[4]M. S. Alam, T. Moeller and A. Maly, "Conversion of an Indian three wheeler scooter into hybrid fuel cell Ni-MH battery vehicle and validation of the Vehicle model for the Baja three wheeler scooter", Proc. IEEE Conference on Electric and Hybrid Vehicles, Pune, India, 2006.

[5]Y. Gurkayank, O. Onar and A. Khaligh, "A photovoltaic-battery powered all-electric rickshaw for Indian market", SAE World Congress: Advanced Hybrid Vehicle Powertrains , Detroit, Michigan, 2009.

[6]S. Lukic, P. Mulhall, G. Choi, M. Naviwala, S. Nimmagadda, and A. Emadi "Usage pattern development for three-wheel auto rickshaw taxis in India", Proc. IEEE Vehicle Power and Propulsion Conference, Arlington, Texas, 2007.

[7]M. Alam , T. Taher, M. Khader, A. Lateef, R. Kizilel, "Analysis and hardware development of a novel prototype hybrid PEM fuel cell Li-Ion battery scooter", Proc. IEEE Conference on Electric and Hybrid Vehicles, Pune, India, 2006.

[8]T.V. Ramachandra and Shwetmala, "Emissions from India's transport sector: Statewise synthesis", Atmospheric Environment, Vol. 43, No. 34, 2009, 5510-5517.

[9]Weeks Update India, "New petrol/diesel price India New Delhi, Mumbai, Bangalore, Chennai, Kolkata", 2009.

[10]Corporate Catalyst India, "Cost of doing business in India", http://www.cci.in/pdf/cost-of-doing-business-india.pdf, 2007.

[11]M. Qadrdan and J. Shayegan "Economic assessment of hydrogen fueling station, a case study for Iran" Renewable Energy, Vol. 33, No. 12, 2008, 2525-2531.

المملكة الأردنية الهاشمية

الجامعة الهاشمية

المجلة الأردنية
للهندسة الميكانيكية والصناعية

JJMIE

مجلة علمية عالمية محكمة

http://jjmie.hu.edu.jo/

ISSN 1995-6665

المجلة الأردنية للهندسة الميكانيكية والصناعية
مجلة علمية عالمية محكمة

المجلة الأردنية للهندسة الميكانيكية والصناعية: مجلة علمية عالمية محكمة أسستها اللجنة العليا للبحث العلمي في وزارة التعليم العالي والبحث العلمي،الأردن، وتصدر عن عمادة البحث العلمي والدراسات العليا، الجامعة الهاشمية، الزرقاء، الأردن.

ترسل البحوث إلى العنوان التالي :

رئيس تحرير المجلة الأردنية للهندسة الميكانيكية والصناعية
عمادة البحث العلمي والدراسات العليا
الجامعة الهاشمية
الزرقاء - الأردن
هاتف : 3903333 5 00962 فرعي 4147
Email: jjmie@hu.edu.jo
Website: www.jjmie.hu.edu.jo